

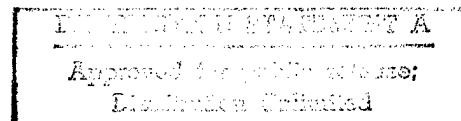
**MODELING TEMPERATURE AND STRAIN RATE HISTORY EFFECTS IN
OFHC CU**

A THESIS

Presented to the Academic Faculty

By

Albert Buck Tanner



19980608 086

In Partial Fulfillment
of the Requirements for the Degree
Doctor of Philosophy in Mechanical Engineering

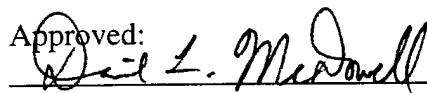
DTIC QUALITY INSPECTED 3

Georgia Institute of Technology
June 1998

REPORT DOCUMENTATION PAGE			Form Approved OMB No. 0704-0188	
<small>1. The reporting burden for this collection of information is estimated to average 1 hour per response, including the time for reviewing instructions, searching existing data sources, gathering and maintaining the data needed, and completing and reviewing the collection of information. Send comments regarding this burden estimate or any other aspect of this collection of information, including suggestions for reducing this burden, to Washington Headquarters Services, Directorate for Information Operations and Reports, 1215 Jefferson Davis Highway, Suite 1204, Arlington, VA 22202-4302, and to the Office of Management and Budget, Paperwork Reduction Project (0704-0188), Washington, DC 20503.</small>				
1. AGENCY USE ONLY (Leave blank)		2. REPORT DATE 28 May 1998		3. REPORT TYPE AND DATES COVERED Final Report
4. TITLE AND SUBTITLE Modeling Temperature and Strain Rate History Effects in OFHC Cu			5. FUNDING NUMBERS	
6. AUTHOR(S) Albert Buck Tanner LTC				
7. PERFORMING ORGANIZATION NAME(S) AND ADDRESS(ES) Georgia Institute of Technology Atlanta, GA			8. PERFORMING ORGANIZATION REPORT NUMBER	
9. SPONSORING/MONITORING AGENCY NAME(S) AND ADDRESS(ES) US Army Military Personnel Center Alexandria, VA			10. SPONSORING/MONITORING AGENCY REPORT NUMBER	
11. SUPPLEMENTARY NOTES Ph.D. Thesis				
12a. DISTRIBUTION/AVAILABILITY STATEMENT Distribution Unlimited Approved for Public Release			12b. DISTRIBUTION CODE	
13. ABSTRACT (Maximum 200 words) Linking macro-scale material behavior with the evolution of microstructure has proven effective in obtaining an appropriate mathematical structure for constitutive relationships. Incorporation of strain rate, temperature, and deformation path history effects are especially critical to accurately predict material responses for arbitrary nonisothermal, variable strain rate conditions. Material constitutive equations contain numerous parameters which must be determined experimentally, and often are not fully optimized. The goal of this research was to develop more physically descriptive kinematics and kinetics models for large strain deformation based on internal state variable (ISV) evolution laws which include strain rate and temperature <i>history</i> dependence. A unique and comprehensive set of experiments involving sequences of different strain rates, temperatures, and deformation paths, as well as, constant strain rate, isothermal and experiments characterizing restoration processes, were conducted on OFHC Cu.				
14. SUBJECT TERMS Temperature History Effects, Strain Rate History Effects, OFHC Cu, Internal Variable Models, Optimization, Parameter Determination			15. NUMBER OF PAGES State 426	
			16. PRICE CODE	
17. SECURITY CLASSIFICATION OF REPORT UNCLASS		18. SECURITY CLASSIFICATION OF THIS PAGE UNCLASS		19. SECURITY CLASSIFICATION OF ABSTRACT UNCLASS
20. LIMITATION OF ABSTRACT				

**MODELING
TEMPERATURE AND STRAIN RATE HISTORY EFFECTS
IN OFHC CU**

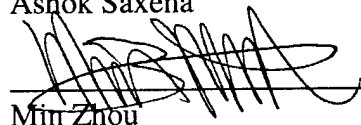
Approved:



David L. McDowell, Chairman



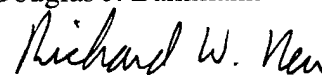
Ashok Saxena



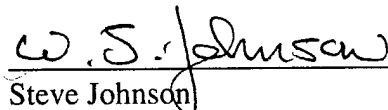
Min Zhou



Douglas J. Bammann



Richard W. Neu



Steve Johnson

Date Approved 28 MAY 98

DEDICATION

This thesis would not have been possible without the loving support and constant understanding, guidance, and love from my wonderful wife, Lisa. Throughout the years, I could always depend on Lisa for her encouragement, compassion, and selfless sacrifices for the family. Not only has she been devoted to me and my work, but also to our five great children: Maria, Melissa, Melinda, Buck, and Margaret. She has been the model mother and wife, and a wonderful example for us all. Yet, even while balancing a home, children, and a Ph.D. candidate, Lisa was able to earn her Masters degree from Kennesaw State University.

ACKNOWLEDGMENTS

I would like to thank my advisor and friend David L. McDowell, for his encouragement, instruction, and understanding. His broad level of knowledge, expertise, and interests are unmatched. I look forward to a continued relationship. I also thank the members of my reading committee; Dr. Douglas J. Bammann, Dr. Steve Johnson, Dr. Ashok Saxena, Dr. Richard W. Neu, and Dr. Min Zhou. I appreciate the United States Army for a fulfilling career and for providing this educational opportunity, as well as, the Army Research Office and the program monitor, Dr. Kailasam Iyer, for sponsoring this research.

I am grateful to Dr. Daniel A. Mosher for his sound instruction on experimental techniques and to Dr. Wendell Kawahara for the use and support of the Sandia National Laboratory material test facility. I also thank George Butler and Laurent Cretegny for the micrograph instruction and Rick Brown for his support in conducting experiments here at Georgia Institute of Technology.

My parents provided the love of education and appreciation for hard work, both of which were essential. My daughters Maria and Melissa were invaluable for their help and long hours preparing this thesis.

I am especially thankful for my wife and family. They are most important to me and make everyday a wonderful experience.

CONTENTS

DEDICATION.....	iii
ACKNOWLEDGMENTS.....	iv
TABLES.....	x
FIGURES.....	xiii
NOMENCLATURE.....	xxxviii
SUMMARY.....	xliv
CHAPTER I INTRODUCTION.....	1
CHAPTER II INELASTIC DEFORMATION PROCESSES.....	6
II.1 Introduction.....	6
II.2 Dislocation Substructures.....	10
II.2.1 Dislocation Obstacles.....	11
II.2.2 Stacking Faults.....	15
II.3 Strain Hardening Processes.....	16
II.4 Restoration Processes.....	17
II.4.1 Dynamic Restoration.....	18
II.4.2 Static Restoration.....	22
II.5 Thermal Activation.....	26
CHAPTER III OFHC COPPER EXPERIMENTS.....	29
III.1 Introduction.....	29
III.2 Experimental Procedures.....	32
III.2.1 Material.....	33
III.2.2 Test Matrices.....	36
III.2.2.1 Constant True Strain Rate and Isothermal Experiments..	38
III.2.2.2 Restoration Experiments.....	40

	III.2.2.3 Sequence Experiments.....	42
	III.2.3 Experimental Procedures.....	44
	III.2.3.1 Compression Experiments.....	45
	III.2.3.1.1 Quasi-static (Low) Strain Rate.....	45
	III.2.3.1.1.1 Quasi-static (Low) Strain Rate Apparatuses.....	45
	III.2.3.1.1.2 Quasi-static (Low) Strain Rate Specimens.....	52
	III.2.3.1.1.3 Homogeneous Compression.....	55
	III.2.3.1.2 High Strain Rate.....	57
	III.2.3.2 Quasi-static Torsion Experiments.....	61
	III.2.3.3 Specimen Temperature Histories.....	65
	III.2.3.4 Sequence Experiments.....	69
	III.2.3.5 Experiment Consistency.....	81
III.3	Experimental Results.....	85
	III.3.1 Restoration Experimental Results.....	85
	III.3.1.1 Static Restoration Experimental Results.....	85
	III.3.1.2 Dynamic Restoration Experimental Results.....	90
	III.3.2 Constant True Strain Rate, Isothermal Experimental Results.....	107
	III.3.2.1 Compression.....	107
	III.3.2.2 Torsion Experiments.....	112
	III.3.3 Results of Sequence Experiments.....	114
	III.3.3.1 Strain Rate Sequence Results.....	114
	III.3.3.2 Temperature Sequence Results.....	120
	III.3.3.3 Deformation Path Sequence Results.....	125
	III.3.3.3.1 Compression/Torsion Deformation Path Sequence.....	125
	III.3.3.3.2 Reverse Compression/Tension Deformation Path Sequence Results.....	132
	III.3.3.3.3 Reverse Torsion Deformation Path Sequence Results.....	140
	III.3.3.4 Combined Strain Rate, Temperature and/or Deformation Path Sequence Results.....	142
III.4	Data Analysis.....	147
III.5	Comparison With Other Experimental Data.....	157
III.6	Very High Strain Rate Data.....	164
III.7	Discussion.....	156
III.8	Experimental Results Summary.....	170

CHAPTER IV	MICROSTRUCTURAL ANALYSIS.....	171
IV.1	Specimen Preparation.....	171
IV.2	Results.....	175
IV.3	Discussion.....	186
 CHAPTER V	 CONSTITUTIVE MODELS.....	 188
V.1	Introduction	188
V.2	Parameter Determination.....	190
V.3	Constitutive Models	200
V.3.1	Johnson and Cook Model.....	203
V.3.2	Zerilli-Armstrong Model.....	204
V.3.3	Mechanical Threshold Stress Model.....	206
V.3.4	Bammann, Cheisa, and Johnson Model.....	213
V.3.5	McDowell Model.....	215
V.4	Correlation to Constant Strain Rate, Isothermal Data and Parameter Sensitivity.....	222
V.4.1	Johnson and Cook Model.....	223
V.4.1.1	Johnson/Cook Model Correlation to Experimental Data.....	223
V.4.1.2	Johnson/Cook Model Predictions.....	225
V.4.1.3	Johnson/Cook Model Parameter Sensitivity.....	229
V.4.2	Zerilli-Armstrong Model.....	231
V.4.2.1	Zerilli-Armstrong Model Correlation to Experimental Data.....	231
V.4.2.2	Zerilli-Armstrong Model Sequence Predictions.....	232
V.4.2.3	Zerilli-Armstrong Model Correlation to High Strain Rate Data.....	236
V.4.2.4	Zerilli-Armstrong Model Sequence Predictions (using parameters fit with very high strain rate data).....	237
V.4.2.5	Zerilli-Armstrong Model Parameter Sensitivity.....	241
V.4.3	Mechanical Threshold Stress Model.....	243
V.4.3.1	MTS Model Correlation to Experimental Data.....	243
V.4.3.2	MTS Model Sequence Predictions.....	246
V.4.3.3	MTS Model Parameter Sensitivity.....	250
V.4.4	Bammann, Cheisa, and Johnson Model.....	251
V.4.4.1	BCJ-SNL Model Correlation to Experimental Data.....	251
V.4.4.2	BCJ-SNL Model Sequence Predictions.....	255
V.4.4.3	BCJ-SNL Model Parameter Sensitivity.....	259

	V.4.5	McDowell Model.....	261
		V.4.5.1 McDowell Model Correlation to Experimental Data.....	261
		V.4.5.2 McDowell Model Sequence Predictions.....	264
		V.4.5.3 McDowell Model Parameter Sensitivity.....	268
		V.4.5.4 McDowell Model Sequence Predictions (modified data set).....	270
		V.4.5.5 McDowell Model Sequence Predictions (high strain rate).....	274
V.5		Discussion.....	277
CHAPTER VI		CONSTITUTIVE MODEL IMPROVEMENTS.....	281
	VI.1	Modeling Approaches.....	281
	VI.2	Design of Experiments.....	285
		VI.2.1 DOE Analysis Factors.....	287
		VI.2.1.1 Temperature Dependence.....	287
		VI.2.1.2 Isotropic Variable Saturation.....	289
		VI.2.1.3 Kinematic Variable.....	290
		VI.2.1.4 Isotropic Variable Evolution Rate.....	290
		VI.2.1.5 Isotropic Variable Activation Energy.....	291
		VI.2.1.6 Kinematic Variable Activation Energy.....	291
		VI.2.1.7 Variation in Isotropic Variable Activation Energy.....	291
		VI.2.2 Macroscopic Responses.....	292
	VI.3	Artificial Neural Networks.....	299
	VI.4	Modeling Improvements.....	302
		VI.4.1 BCJ-SNL Modeling Improvements (split parameters).....	302
		VI.4.2 Recrystallization ISV Modeling.....	308
		VI.4.2.1 BCJ-SNL Model with Recrystallization Parameter.....	318
		VI.4.2.2 McDowell Model with Recrystallization Parameter McDowell Model.....	322
		VI.4.2.2.1 McDowell Model with Recrystallization Parameter Correlation and Sequence Predictions (limited data set).....	325
		VI.4.2.2.2 McDowell Model with Recrystallization Parameter Correlation and Sequence Predictions.....	330
		VI.4.3 Very High strain Rate Regime.....	335
	VI.5	Data Set Requirements for Predicting History Effects.....	339
		VI.5.1 DOE Analysis Factors.....	339

	VI.5.1.1 Quantity of Experimental Data Points.....	339
	VI.5.1.2 Objective Function Form.....	340
	VI.5.1.3 Experimental Deformation Conditions used for Optimization: Isothermal, Constant True Strain Rate (25°C; 6000 s ⁻¹ and 0.0004 s ⁻¹ and 269°C; 0.0004 s ⁻¹ less than 0.5 strain, 0.1 s ⁻¹ and 5200 s ⁻¹).....	340
	VI.5.1.4 Experimental Deformation Conditions used for Optimization: Strain Rate Sequence (269°C; 0.0004 s ⁻¹ to 0.5 strain then 269°C; 0.1 s ⁻¹).....	340
	VI.5.1.5 Experimental Deformation Conditions used for Optimization: Temperature Sequence (269°C; 0.0004 s ⁻¹ to 0.5 strain then 25°C; 0.0004 s ⁻¹).....	341
	VI.5.1.6 Experimental Deformation Conditions used for Optimization: Isothermal, Constant True Strain Rate (269°C; 0.0004 s ⁻¹ 0.5 to 1.0 strain).....	341
	VI.5.1.7 Experimental Deformation Conditions used for Optimization: Temperature Sequence (25°C; 0.0004 s ⁻¹ to 0.5 strain then 269°C; 0.0004 s ⁻¹ with hold times of 1.5 and 20 minutes).....	341
	VI.5.2 Macroscopic Responses.....	342
VI.6	Summary.....	347
CHAPTER VII	SUMMARY AND CONCLUSIONS.....	350
VII.1	Overview of Experimental Results.....	350
VII.2	Summary of Constitutive Modeling.....	352
VII.3	Recommendations.....	354
	REFERENCES.....	356
	VITA.....	380

LIST OF TABLES

<u>Table</u>	<u>Page</u>
III.1: SPECIMEN CONFIGURATION	36
III.2: COMPRESSION: STRAIN, STRAIN RATE AND TEMPERATURE EFFECTS	38
III.3: TORSION EXPERIMENTS: STRAIN AND TEMPERATURE EFFECTS (von Mises equivalent true strain rate and true strain are shown)	39
III.4: STATIC RESTORATION: LOAD, UNLOAD, HOLD, RELOAD EXPERIMENTS (Conducted in compression at 0.0004 s^{-1}. Hold time after pre-strain)	40
III.5: DYNAMIC RESTORATION: LOAD, HOLD, AND RELOAD EXPERIMENTS (Conducted in compression at 0.0004 s^{-1})	41
III.6: QUASI-STATIC (0.0004 s^{-1}) TWO STEP TEMPERATURE SEQUENCE (von Mises equivalent true strain rate and true strain are shown)	42
III.7: HIGH RATE (1000 s^{-1}), FOLLOWED BY QUASI-STATIC (0.0004 s^{-1}) TWO STEP STRAIN RATE SEQUENCE (von Mises equivalent true strain rate and true strain are shown)	42
III.8: STRAIN RATE CHANGE SEQUENCE (Compression at 269°C)	43
III.9: REVERSE PATH EXPERIMENTS (von Mises equivalent true strain rate and true strain are shown. All strain rates were 0.0004 s^{-1}.)	43
III.10: CONTINUOUSLY VARYING TEMPERATURE AND/OR STRAIN RATE (All experiments were conducted in compression to a true strain of 1.0)	44
III.11: COMPRESSION SPECIMEN LUBRICANT	53

IV.1: GRINDING AND POLISHING PROCEDURES.....	173
IV.2: ETCHING PROCEDURES.....	173
IV.3: SPECIMEN GRAIN SIZES.....	174
V.1: ELASTIC SHEAR MODULUS	203
V.2: JOHNSON/COOK MODEL PARAMETER COMPARISON FOR OFHC Cu.....	225
V.3: ZERILLI-ARMSTRONG MODEL PARAMETER COMPARISON FOR OFHC Cu.....	232
V.4: MTS MODEL PARAMETER COMPARISON FOR OFHC Cu.....	245
V.5: BCJ-SNL OPTIMIZED MODEL PARAMETERS FOR OFHC Cu FOR STRAIN RATES 4×10^{-4} TO $6 \times 10^3 \text{ s}^{-1}$ AND TEMPERATURES 25°C TO 269°C	254
V.6: MCDOWELL MODEL PARAMETER COMPARISON FOR OFHC Cu.....	263
V.7: COMPARISON MODEL PARAMETER COMPARISON OF ERROR NORM (NORMALIZED TO SMALLEST VALUE).....	280
VI.1: ORTHOGONAL ARRAY.....	286
VI.2: PARAMETER MATRIX.....	296
VI.3: RESPONSE MATRIX.....	296
VI.4: CORRELATION OF FACTOR AND PARAMETER.....	299
VI.5: CRITICAL STRAIN PARAMETERS FOR RECRYSTALLIZATION INITIATION.....	313
VI.6: NORMALIZED OBJECTIVE FUNCTION VALUES FOR BCJ-SNL.....	319
VI.7: MCDOWELL MODEL HIGH STRAIN RATE TERM PARAMETERS.....	337
VI.8: MCDOWELL MODEL HIGH STRAIN RATE TERM PARAMETERS WITH ADIABATIC HEATING.....	338

VI.9: PARAMETER MATRIX.....	342
VI.10: RESPONSE MATRIX.....	343
VI.11: CORRELATION OF FACTOR AND PARAMETER.....	346

LIST OF FIGURES

<u>Figure</u>	<u>Page</u>
I.1: Strain rate and temperature history effects of f.c.c. metals (Klepaczko, 1975 and Duffy, 1979).....	2
II.1: Influence of thermal assistance on dislocation motion past obstacles.....	9
II.2: Diagram of microstructure. Grain subdivision into geometrically necessary boundaries including dense dislocation walls (DDW's) and microbands (MB's) which delineate cell blocks (CB's) containing incidental dislocation boundaries in the form of cell walls (Bay <i>et al.</i> , 1992).....	14
II.3(A - D): Microstructure changes during deformation. (A) During deformation, a cellular substructure develops as the strain increases, (B and C) the cells become smaller and the walls more dense, achieving a limit in cell size (D) (McQueen and Jonas, 1975). At increasing strain, some dense dislocation walls develop into microbands (Bay <i>et al.</i> , 1992).....	20
II.4 (A - D): Recovery process. Recovery begins with the annihilation of dislocation in the cell walls which become subboundaries (A - B). As recovery continues, the subgrains grow in diameter and the overall dislocation density decreases (C - D) (McQueen and Jonas, 1975).....	21
II.5(A - D): Recrystallization. In metals of low SFE, straining creates localized high densities of dislocations. The high misorientation of the cell walls become capable of migrating. The driving force for the migration is provided by the difference in dislocation density between the interior of the new grain and the surrounding worked area (McQueen and Jonas, 1975).....	24
II.6: Categories of static restoration. The proportions of each softening mechanism are shown. On initial straining (A - B), static recovery can occur. At strains above B, which reflects the critical strain for recrystallization, both recovery and recrystallization occurs. C is the strain associated with the peak stress. Between C and D, both meta-dynamic and static recrystallization along with recovery occurs.....	25

III.1: Annealing schedule for OFHC copper.....	34
III.2a,b: Micrographs of the initial grain structure of annealed OFHC Cu material (50 and 100 magnification).....	35
III.3: Initial texture of annealed OFHC Cu material. Pole figure for (111) orientation.....	35
III.4: MTS servo-hydraulic test machine and controller at SNL.....	47
III.5: MTS extensometer modified for use within a three zone furnace.....	47
III.6: MTS 810 Test machine at SNL used for continuously varying temperature and strain rate experiments and load, hold, and reload experiments. Three-zone furnace used for elevated temperature experiments is shown mounted.....	50
III.7: True strain rate for strain rate variation sequences in compression (vs strain).....	51
III.8: True strain rate for strain rate variation sequences in compression (vs time).....	51
III.9: Compression specimen detail.....	54
III.10: Compression specimen end grooving details.....	54
III.11: Typical compression specimens at 0, 0.5, and 1.0 true strain.....	55
III.12: Examples of non-uniform deformation: Barreling (left) and hour-glassing (right).....	56
III.13: Effect of barreling on flow stress of copper. The % barreling and barreling rate are given in the legend.....	57
III.14: Configuration of the Hopkinson Bar.....	59
III.15: Hopkinson bar experiment setup at SNL. Induction heater coil and water cooling system are shown.....	59
III.16: Configuration of the modified split Hopkinson pressure bar apparatus at SNL.....	60

III.17: Sample Hopkinson bar experimental results showing the strain gage measurements from the incident and transmitted bars.....	61
III.18: Drawing of a 50.8 mm diameter Lindholm specimen. All dimensions are in mm.....	64
III.19: 50.8 mm diameter Lindholm specimen before deformation.....	64
III.20: Specimen temperature response after insertion into three-zone furnace at 269°C and after removal from three-zone furnace at 269°C.....	67
III.21: MTS Servo-Hydraulic test machine with 2.5kW induction heater at MPRL.....	68
III.22: 50.8 mm Lindholm copper specimen with induction heater coil and steel susceptor.....	68
III.23: Diagram of the second phase sequence specimens (quasi-static following high strain rate).....	70
III.24: Picture of three pre-strained Hopkinson bar specimens (left) which are then made into the quasi-static compression specimen (right - shown after compression).....	70
III.25: Specimen design for path sequence; compression/tension and tension/compression (all dimensions are in mm).....	72
III.26: Top: large compression specimen (type 4) before deformation. Bottom: picture of reverse path (compression/tension) specimens, (left) machined from virgin material then annealed, (right) machined from pre-strained compression specimen.....	73
III.27: 10M pound MTS test frame at SNL. Used for compression of large (type 4) specimens.....	74
III.28: MTS 880 Test machine at SNL used for reverse path compression/tension experiments.....	75
III.29: Diagram and picture of preparation of the second sequence specimens from pre-strained material.....	77
III.30: Double shear specimen design for path and strain rate sequence experiments.....	79

III.31: Double shear specimen for path and strain rate sequence experiments, shown after deformation, and bracket used to maintain alignment.....	79
III.32: Diagram showing the removal of a Lindholm specimen from a pre-strained compression specimen.....	80
III.33: Picture of one inch diameter Lindholm specimen removed from a 30.48 mm (1.2 inch) diameter compression specimen (shown before deformation).....	80
III.34: Repeatability of compression tests. Five experimental results are shown.....	81
III.35: Load, unload and remachine, and reload at same temperature and strain rate conditions. Both 25°C at 0.0004 s ⁻¹ and 269°C at 0.0004 s ⁻¹ are shown.....	82
III.36: Effect of unload and remachining on material response. Experimental data for compression at 25°C and 0.0004 s ⁻¹ strain; unload and remachine into specimen type 6; then reload in compression at 25°C and 0.0004 s ⁻¹	84
III.37: Static restoration results at 269°C, 0.0004 s ⁻¹ and different hold times at 0.3 strain.....	87
III.38: Static restoration results for OFHC Copper at 0.0004 s ⁻¹ , 269°C, 541°C and 676°C for different hold times at 0.5 strain.....	88
III.39: Static restoration results for OFHC Copper at 541°C, 0.0004 s ⁻¹ , and different hold times at 0.5 strain.....	88
III.40: Static restoration results for OFHC Copper at 676°C, 0.0004 s ⁻¹ , and different hold times at 0.3 strain.....	89
III.41: Experimental results for OFHC Cu in compression at 0.0004 s ⁻¹ , 25°C, and hold under load control for 20 minutes at 1.0 strain compared to hold under stroke control.....	92
III.42: Experimental results for OFHC Cu in compression at 0.0004 s ⁻¹ , 25°C, and hold under load control for 20 minutes at 0.5 strain compared to 1.0 strain.....	92
III.43: Experimental results for OFHC Cu in compression at 0.0004 s ⁻¹ , 25°C, and hold under load control for 20 minutes at 1.0 strain compared to hold under stroke control.....	93

III.44: Experimental results for OFHC Cu in compression at 0.0004 s^{-1} , 25°C , and hold under load control for 20 minutes at 1.0 strain compared to hold under stroke control.....	93
III.45: Experimental results for OFHC Cu in compression at 0.0004 s^{-1} , 25°C , load and hold sequences to 0.3, 0.5, 0.7, and 1.0 strain, and hold for 10 minutes under load control compared to hold under stroke control.....	95
III.46: Experimental results for OFHC Cu in compression at 0.0004 s^{-1} , 25°C , load and hold sequences to 0.3, 0.5, 0.7, and 1.0 strain, and hold for 10 minutes under load control compared to hold under stroke control.....	95
III.47: Experimental results for OFHC Cu in compression at 0.0004 s^{-1} , 269°C , and hold under load control for 20 minutes at 1.0 strain compared to a no hold experiment, shown in solid symbols.....	96
III.48: Experimental results for OFHC Cu in compression at 0.0004 s^{-1} , 269°C , and hold under load control for 20 minutes at 1.0 strain compared to a no hold experiment, shown in solid symbols.....	96
III.49: Experimental results for OFHC Cu in compression at 0.0004 s^{-1} , 269°C , load and hold sequences to 0.5 and 1.0 strain, with hold for 60 minutes under stroke control compared to a no hold experiment, which is shown in solid symbols.....	98
III.50: Experimental results for OFHC Cu in compression at 0.0004 s^{-1} , 269°C , load and hold sequences to 0.5 and 1.0 strain, with hold for 60 minutes under stroke control compared to a no hold experiment, which is shown in solid symbols.....	98
III.51: Experimental results for OFHC Cu in compression at 0.0004 s^{-1} , 269°C , load and hold sequences to 0.5 and 1.0 strain, and hold for 60 minutes under load control compared to a no hold experiment. Reload curves are compared with annealed material shown shifted to the reload strain with open symbols.....	99
III.52: Experimental results for OFHC Cu in compression at 0.0004 s^{-1} , 269°C , load and hold sequences to 0.5 and 1.0 strain, and hold for 60 minutes under load control compared to a no hold experiment. Reload curves are compared with annealed material, shown shifted to the reload strain (open symbols).....	99

III.53: Experimental results for OFHC Cu in compression at 0.0004 s^{-1} , 269°C , load and hold sequences to 0.5 and 1.0 strain, and hold for 60 minutes under load control compared to a no hold experiment. to 1.0 and hold. Hold under load control for 60 minutes. Strain rate is 0.0004 s^{-1} and temperature is 269°C	100
III.54: Experimental results for OFHC Cu in compression at 0.0004 s^{-1} , 269°C , load and hold sequences to 0.5 and 1.0 strain, and hold for 60 minutes under stroke control compared to a no hold experiment and to the response to hold under load control.....	100
III.55: Experimental results for OFHC Cu in compression at 0.0004 s^{-1} , 269°C , load and hold sequences to 0.5 and 1.0 strain, and hold for 60 minutes under stroke control compared to a no hold experiment and to the response to hold under load control.....	101
III.56: Experimental results for OFHC Cu in compression at 0.0004 s^{-1} , 269°C , load and hold sequences to 0.3, 0.5, 0.7, and 1.0 strain, and hold for 10 minutes under stroke control compared to a no hold experiment.....	101
III.57: Experimental results for OFHC Cu in compression at 0.0004 s^{-1} , 269°C , load and hold sequences to 0.3, 0.5, 0.7, and 1.0 strain, and hold for 10 minutes under stroke control compared to a no hold experiment, shown with solid symbols.....	102
III.58: Experimental results for OFHC Cu in compression at 0.0004 s^{-1} and 405°C . Four experiments are shown.....	103
III.59: Experimental results for OFHC Cu in compression at 0.0004 s^{-1} , 405°C , load and hold sequences to 0.1, 0.2, and 0.3 strain, and hold for 50 minutes under stroke control compared to a no hold experiment, shown with solid symbols.....	103
III.60: Experimental results for OFHC Cu in compression at 0.0004 s^{-1} , 405°C , load and hold sequences to 0.1, 0.2, and 0.3 strain, and hold for 50 minutes under stroke control.....	104
III.61: Experimental results for OFHC Cu in compression at 0.0004 s^{-1} , 405°C , load and hold sequences to 0.1, 0.2, and 0.3 strain, and hold for 50 minutes under stroke control compared to a no hold experiment. Reload curves are compared with annealed material, shown shifted to the reload strain, shown with open symbols.....	104

III.62: Experimental results for OFHC Cu in compression at 0.0004 s^{-1} , 405°C , load and hold sequences to 0.3 strain and hold for 15 minutes under stroke control and 0.5 strain and hold for 15 minutes under load control compared to a no hold experiment, shown with solid symbols.....	105
III.63: Experimental results for OFHC Cu in compression at 0.0004 s^{-1} , 405°C , load and hold sequences to 0.3 strain and hold for 15 minutes under stroke control and 0.5 strain and hold for 15 minutes under load control.....	105
III.64: Experimental results for OFHC Cu in compression at 0.0004 s^{-1} , 405°C , load and hold sequences to 0.3, 0.5, 0.7, and 1.0 strain, and hold for 1000 seconds under stroke control compared to a no hold experiment, shown with solid symbols.....	106
III.65: Experimental results for OFHC Cu in compression at 0.0004 s^{-1} , 405°C , load and hold sequences to 0.3, 0.5, 0.7, and 1.0 strain, and hold for 1000 seconds under stroke control.....	106
III.66: Strain rate dependence of OFHC Cu in compression at 25°C	108
III.67: Strain rate dependence of OFHC Cu in compression at 269°C	108
III.68: Strain rate dependence of OFHC Cu in compression at 541°C	109
III.69: Temperature dependence of OFHC Cu in compression at $\dot{\epsilon} = 0.0004 \text{ s}^{-1}$	109
III.70: Temperature dependence at $\dot{\epsilon} = 0.01 \text{ s}^{-1}$	110
III.71: Temperature dependence at 0.1 s^{-1}	110
III.72: Temperature dependence at 1.0 s^{-1}	111
III.73: Temperature dependence at 1000 s^{-1}	111
III.74: Torsion experimental data at elevated temperatures and a von Mises equivalent strain rate of 0.0004 s^{-1}	113
III.75: Comparison of compression and torsion experiment data for OFHC Cu at elevated temperatures. Von Mises equivalent strain rate was 0.0004 s^{-1}	113

III.76: Compression strain rate history effects at 25°C from high strain rate (6000 s ⁻¹) to quasi-static (0.0004 s ⁻¹).....	116
III.77: Compression strain rate history effects at 25°C from high strain rate (6000 s ⁻¹) to quasi-static (0.0004 s ⁻¹).....	116
III.78: Experimental results for OFHC Cu compressed at 25°C while strain rate continuously varied from 0.0004 s ⁻¹ to 0.1 s ⁻¹	117
III.79: Experimental results for OFHC Cu compressed at 25°C while strain rate continuously varied from 0.1 s ⁻¹ to 0.0004 s ⁻¹	117
III.80: Experimental results for OFHC Cu compressed at 25°C while strain rate continuously increased from (0.0004 s ⁻¹ to 0.1 s ⁻¹) are compared to results while the strain rate continuously decreased from (0.1 s ⁻¹ to 0.0004 s ⁻¹).....	118
III.81: Experimental results for OFHC Cu compressed at 405°C while strain rate continuously varied from 0.0004 s ⁻¹ to 0.1 s ⁻¹	118
III.82: Experimental results for OFHC Cu compressed at 405°C while strain rate was continuously decreased from 0.1 s ⁻¹ to 0.0004 s ⁻¹	119
III.83: Experimental results for OFHC Cu compressed at 405°C while strain rate continuously increased from (0.0004 s ⁻¹ to 0.1 s ⁻¹) are compared to results while the strain rate continuously decreased from (0.1 s ⁻¹ to 0.0004 s ⁻¹).....	119
III.84: Temperature history effects of OFHC Cu in compression at 269°C and 0.0004 s ⁻¹ pre-strained to 0.5 and then in compression at 25°C and 0.0004 s ⁻¹	121
III.85: Temperature history effects of OFHC Cu in compression (25°C, 0.0004 s ⁻¹ then 269°C, 0.0004 s ⁻¹).....	122
III.86: Temperature history effects of OFHC Cu in compression at 25°C and 0.0004 s ⁻¹ pre-strained to 0.5 and then in compression at 269°C and 0.0004 s ⁻¹ after 20 minutes in furnace (axis transformed to zero strain) compared to initial response of annealed material.....	122
III.87: Experimental results for OFHC Cu compressed at 0.0004 s ⁻¹ while temperature was continuously reduced from 405°C.....	123

III.88: Experimental results for OFHC Cu compressed at 0.0004 s^{-1} while temperature was continuously increased from 25°C	123
III.89: Temperature sequence effects. Experiment results for OFHC compressed at 0.0004 s^{-1} while temperature was continuously increased from 25°C	124
III.90: Deformation path sequence experiments on OFHC Cu conducted in high rate compression followed by quasi-static shear (von Mises equivalent responses are shown).....	127
III.91: Deformation path sequence experiments on OFHC Cu conducted in quasi-static compression and 25°C to 0.3 and 0.5 strain followed by quasi-static shear to 1.0 strain (von Mises equivalent responses are shown). The von Mises equivalent strain rate was 0.0004 s^{-1}	128
III.92: Deformation path sequence experiments on OFHC Cu conducted in quasi-static compression to 0.5 strain followed by quasi-static shear to 1.0+ strain are compared for various temperatures (von Mises equivalent responses are shown). The von Mises equivalent strain rate was 0.0004 s^{-1}	129
III.93: Deformation path sequence experiments on OFHC Cu conducted in quasi-static compression to 0.5 strain followed by quasi-static shear to 1.5 strain are compared to the shear response of initially annealed material (von Mises equivalent responses are shown). The von Mises equivalent strain rate was 0.0004 s^{-1}	130
III.94: Deformation path sequence experiments on OFHC Cu conducted in quasi-static compression and 269°C to 0.5 strain followed by quasi-static shear to 1.0 strain (von Mises equivalent responses are shown). The von Mises equivalent strain rate was 0.0004 s^{-1}	131
III.95: Deformation path sequence experiments on OFHC Cu conducted in quasi-static tension and 25°C followed by quasi-static compression. The specimen remained in the test machine during the deformation path sequences.....	134
III.96: Deformation path sequence experiments on annealed OFHC Cu conducted in quasi-static tension and 25°C followed by quasi-static compression are compared to material after a compressive, quasi-static pre-strain of 0.5.....	135

III.97: Deformation path sequence experiments on OFHC Cu conducted in quasi-static compression and 25°C followed by tension. The specimen remained in the test machine during the deformation path sequences.....	136
III.98: Deformation path sequence experiments on OFHC Cu conducted in quasi-static compression at 25°C to 0.5 strain followed by compression at 25°C then tension.....	136
III.99: Deformation path sequence experiments on OFHC Cu conducted in quasi-static compression and 25°C followed by tension are compared to the response after a compression pre-strain at 25°C to 0.5 strain.....	137
III.100: Deformation path sequence experiments on OFHC Cu conducted in compression, 25°C, and 0.0004 s ⁻¹ to 0.5 strain followed by tension until necking initiated.....	137
III.101: Cyclic deformation path sequence experiments on annealed OFHC Cu conducted in compression, 25°C, and 0.0004 s ⁻¹ followed by tension under stroke control.....	138
III.102: Cyclic deformation path sequence experiments on pre-strained (0.5 compression at 25°C and 0.0004 s ⁻¹) OFHC Cu conducted in compression, 25°C, and 0.0004 s ⁻¹ followed by tension under stroke control. Twenty complete cycles are shown.....	138
III.103: Cyclic deformation path sequence experiments on pre-strained (0.5 compression at 25°C and 0.0004 s ⁻¹) OFHC Cu conducted in compression, 25°C, and 0.0004 s ⁻¹ followed by tension under stroke control. Twenty complete cycles are shown relative to the initial compressive pre-strain.....	139
III.104: Cyclic deformation path sequence experiments on pre-strained (0.5 compression at 25°C and 0.0004 s ⁻¹) OFHC Cu conducted in compression, 25°C, and 0.0004 s ⁻¹ followed by tension under stroke control are compared to annealed material under the same deformation conditions.....	139
III.105: Reverse deformation path sequence experiments on annealed OFHC Cu conducted in torsion at various temperatures. The von Mises equivalent strain rate was 0.0004 s ⁻¹	141

III.106: Reverse deformation path sequence experiments on annealed OFHC Cu conducted in torsion at 25°C are compared for two strain levels, 0.5 and 1.0. The von Mises equivalent strain rate was 0.0004 s ⁻¹	141
III.107: Strain rate and temperature history effects for OFHC Cu in compression from 25°C and 6000 s ⁻¹ followed by 269°C and 0.0004 s ⁻¹	143
III.108: Strain rate and temperature history effects for OFHC Cu in compression from 269°C and 5200 s ⁻¹ followed by 25°C and 0.0004 s ⁻¹	144
III.109: Strain rate and temperature history effects for OFHC Cu in compression. The deformation conditions continuously changed from 405°C and 0.1 s ⁻¹ to 350°C and 0.0004 s ⁻¹	144
III.110: Strain rate and temperature history effects for OFHC Cu in compression. The deformation conditions continuously changed from 405°C and 0.0004 s ⁻¹ to 250°C and 0.1 s ⁻¹	145
III.111: Strain rate and temperature history effects for OFHC Cu in compression. The deformation conditions continuously changed from 70°C and 0.0004 s ⁻¹ to 305°C and 0.1 s ⁻¹	146
III.112: Strain rate sensitivity for OFHC Cu deformed in compression at 25°C. The stress was measured at the indicated (in boxes) strain levels, ranging from 0.05 to 1.0.....	148
III.113: Strain rate sensitivity for copper deformed in compression at 25°C to a strain of 0.15. Data from Follansbee and Kocks, 1988, shown in close symbols, are compared to the current experimental data, open symbols.....	150
III.114: Strain rate sensitivity for OFHC Cu deformed in compression at 269°C. The stress was measured at the indicated (in boxes) strain levels, ranging from 0.05 to 1.0.....	151
III.115: Strain rate sensitivity for OFHC Cu deformed in compression at 541°C. The stress was measured at the indicated (in boxes) strain levels, ranging from 0.05 to 1.0.....	151
III.116: Strain hardening for OFHC Cu in compression at 25°C and 0.0004 s ⁻¹	152
III.117: Strain hardening for OFHC Cu in compression at 269°C and 0.0004 s ⁻¹	153

III.118: Strain hardening for OFHC Cu in compression at 25°C and various strain rates (0.0004, 0.01, 0.1 and 1.0) s ⁻¹	154
III.119: Strain hardening for OFHC Cu in compression at 269°C and various strain rates (0.0004, 0.01, 0.1 and 1.0) s ⁻¹	154
III.120: Strain hardening for OFHC Cu in compression at 541°C and 0.0004 s ⁻¹	155
III.121: Strain hardening for OFHC Cu in compression at 541°C and various strain rates (0.0004, 0.01, 0.1 and 1.0) s ⁻¹	155
III.122: Strain hardening for OFHC Cu in compression at 0.0004 s ⁻¹ and various temperatures (25°C - 541°C)	156
III.123: Strain hardening for OFHC Cu in torsion at 0.0004 s ⁻¹ and various temperatures (25°C - 405°C). (The von Mises equivalent strain levels are shown)	156
III.124: Oxygen-free-electronic (OFE) copper (0.9999 Cu) with an initial average grain size of 30 - 50 µm deformed in compression at room temperature, 25°C (Follansbee, 1985)	159
III.125: Compression data from Follansbee, 1985, are shown with lines, and the current experimental data are shown with open symbols	159
III.126: OFHC Cu (0.9995) with an initial average grain size of 20 µm deformed in tension at room temperature, 25°C (Christodoulou, <i>et al.</i> , 1982)	160
III.127: Compression data from Christodoulou, <i>et al.</i> , 1982, are shown with lines, and the current experimental data are shown with open symbols	160
III.128: OFE Cu (0.9999) with an initial average grain size of 40 µm deformed in compression at room temperature, 25°C (Follansbee and Kocks, 1988)	161
III.129: Compression data from Follansbee and Kocks, 1988, are shown with lines, and the current experimental data are shown with open symbols	161
III.130: OFHC Cu (0.9999) with varying initial average grain sizes deformed in shear at room temperature, 25°C, and 3000 s ⁻¹ (Meyers, <i>et al.</i> , 1995). The von Mises equivalent stress and strain are shown	162

III.131: Compression data from Meyers, <i>et al.</i> , 1995, are shown with lines, and the current experimental data at 6000 s^{-1} , are shown with open symbols. The von Mises equivalent stress and strain are shown.....	162
III.132: OFHC Cu (0.9999) with varying initial average grain sizes deformed in shear at room temperature, 25°C , and 0.001 s^{-1} (Meyers, <i>et al.</i> , 1995). The von Mises equivalent stress and strain are shown.....	163
III.133 Comparison of compression data from Meyers, <i>et al.</i> , 1995, are shown with lines, and the current experimental data, 0.01 s^{-1} , are shown with open symbols. The von Mises equivalent stress and strain are shown.....	163
III.134: Pressure-shear OFHC Cu data (Frutschy and Clifton, 1998).....	165
III.135: Pressure-shear OFHC Cu data (Frutschy and Clifton, 1998).....	165
III.136: Comparison of OFHC Cu data near 269°C (Frutschy and Clifton, 1998). The von Mises equivalent stress and strain are shown.....	166
III.137: Comparison of OFHC Cu data $495 - 541^{\circ}\text{C}$ (Frutschy and Clifton, 1998). The von Mises equivalent stress and strain are shown.....	166
IV.1: Average grain sizes for OFHC Cu from compression at constant strain rate, 0.0004 s^{-1} , isothermal experiments. The sizes (μm) are shown at the corresponding strain and temperature at completion of strain. Two values are shown at 0.5 strain, 25°C and 269°C , which were determined from separate experiments. The standard deviation on the measurements was $4\text{ }(\mu\text{m})$	176
IV.2: Micrograph of OFHC Cu annealed at 600°C for four hours. The micron bar corresponds to $20\text{ }\mu\text{m}$ and a magnification of $100\times$	177
IV.3: Figure IV.3: Micrograph of OFHC Cu annealed at 600°C for four hours. The micron bar corresponds to $20\text{ }\mu\text{m}$ and a magnification of $100\times$	177
IV.4: Micrograph of OFHC Cu compressed at 25°C and 0.0004 s^{-1} to a strain of 0.5. The micron bar corresponds to $50\text{ }\mu\text{m}$ and a magnification of $50\times$	178
IV.5: Micrograph of OFHC Cu compressed at 236°C and 0.0004 s^{-1} to a strain of 1.0. The micron bar corresponds to $50\text{ }\mu\text{m}$ and a magnification of $50\times$	178

IV.6: Micrograph of OFHC Cu compressed at 286°C and 0.0004 s ⁻¹ to a strain of 1.0. The micron bar corresponds to 100 µm and a magnification of 20 x.....	179
IV.7: Micrograph of OFHC Cu compressed at 25°C and 0.0004 s ⁻¹ to a strain of 0.5. The micron bar corresponds to 50 µm and a magnification of 50 x.....	179
IV.8: Micrograph of OFHC Cu compressed at 405°C and 0.0004 s ⁻¹ to a strain of 1.0. The micron bar corresponds to 50 µm and a magnification of 50 x.....	180
IV.9: Micrograph of OFHC Cu compressed at 676°C and 0.0004 s ⁻¹ to a strain of 1.0. The micron bar corresponds to 50 µm and a magnification of 50 x.....	180
IV.10: Average grain sizes for OFHC Cu from compression at 269°C and various constant strain rates, 0.0004 s ⁻¹ experiments. The sizes (µm) are shown at the corresponding strain and temperature at completion of strain. The value shown at 0.5 strain was determined from a separate experiment. The standard deviation on the measurements was 4 (µm).....	181
IV.11: Average grain sizes for OFHC Cu from compression at constant strain rate, 0.0004 s ⁻¹ , isothermal experiments at 269°C with various hold times after unloading at 0.3 strain before reloading to a final strain level of 0.7 or 1.0.. The sizes (µm) are shown at the corresponding strain and temperature at completion of strain. The value shown at 0.5 strain was determined from a separate experiment. The standard deviation on the measurements was 4 (µm).....	182
IV.12: Average grain sizes for OFHC Cu from compression at constant strain rate, 0.0004 s ⁻¹ and 269°C isothermal experiments. The specimens were compressed to 1.0 strain and then held for 20 minutes while maintained under a constant load. The sizes (µm) are shown at the corresponding strain and temperature at completion of strain.	183
IV.13: Average grain sizes for OFHC Cu from compression at constant strain rate, 0.0004 s ⁻¹ and 269°C isothermal experiments. The specimens were compressed to 0.5 strain and then held under constant temperature under either load or stroke control for 60 minutes and then reloaded for an additional 0.5 strain and held for another 60 minutes. The sizes (µm) are shown at the corresponding strain and temperature at completion of strain. The standard deviation on the measurements was 4 (µm).....	184

IV.14: Average grain sizes for OFHC Cu from compression at constant strain rate, 0.0004 s^{-1} and sequences of temperature experiments. The specimens were first pre-strained at 25°C to 0.5 strain. The specimens were unloaded and subsequently reloaded at 269°C after the indicated periods at 269°C before deformation. The sizes (μm) are shown at the corresponding strain and temperature at completion of strain. Two values are shown at 0.5 strain, 25°C and 269°C , which were determined from separate tests. The standard deviation on the measurements was 4 (μm). Indicated sizes for the reloaded specimens correspond to the average grain size (μm) at 1.0 true strain.....	186
IV.15: Relationship between softening and fractional amount of recrystallized grains in Cu (Kwon and DeArdo, 1990). Numbers in boxes represent the volume percentage of recrystallization.....	187
V.1: Optimization schemes: Gradient and Downhill Simplex.....	193
V.2: Two dimension parameter sensitivity example. The global minima, $\text{OBJ}_{\text{global}}$, is the objective function value resulting from the optimization of the parameters. A consistent offset, $\text{OBJ}_{\text{offset}}$, is calculated using parameters adjusted ± 0.01 from the optimized parameter values. This offset objective function value is greater than $\text{OBJ}_{\text{global}}$. Another optimization is calculated using the offset parameters as the initial values and with certain parameters held fixed. The resulting objective function, OBJ_s , is a measure of the sensitivity of the objective function to that parameter set.....	199
V.3: Typical minimization of the objective function (shown normalized to the minimum value) using the Pointer Optimization software.....	200
V.4: Effect of temperature and variations in p and q on activation energy for the MTS model.....	210
V.5: Variation in diffusivity parameter with temperature and activation energy variations.....	218
V.6: Correlation to OFHC Cu data using Johnson/Cook model. The model correlation are shown using solid lines, while the experimental data are shown with open symbols.....	224
V.7: Strain rate sequence prediction for OFHC Cu using the Johnson/Cook model. Solid lines represent the model prediction, while symbols represent data.....	226

V.8: Strain rate sequence prediction for OFHC Cu using the Johnson/Cook model. Solid lines represent the model prediction, while symbols represent data.....	226
V.9: Temperature sequence prediction for OFHC Cu using the Johnson/Cook model. Solid lines represent the model prediction, while symbols represent data.....	227
V.10: Temperature sequence prediction for OFHC Cu using the Johnson/Cook model. Solid lines represent the model prediction, while symbols represent data.....	227
V.11: Strain rate and temperature sequence prediction for OFHC Cu using the Johnson/Cook model. Solid lines represent the model prediction, while symbols represent data.....	228
V.12: Strain rate and temperature sequence prediction for OFHC Cu using the Johnson/Cook model. Solid lines represent the model prediction, while symbols represent data.....	228
V.13: Parameter sensitivity for OFHC Cu using the Johnson/Cook model. Light and dark bars reflect a $\pm 10\%$ offset from the optimized parameter values corresponding to a minimum of the objective function. First two bars show ability of indicated parameter, alone, to achieve the global minimum while the second two bars show ability of the remaining parameters, with the indicated parameter held constant, to reach the minimum.....	230
V.14: Correlation to OFHC Cu data using the Zerilli-Armstrong model. The model correlations are shown using solid lines, while the experimental data are shown with open symbols.....	231
V.15: Strain rate sequence prediction for OFHC Cu using the Zerilli-Armstrong model. Solid lines represent the model prediction, while symbols represent experimental data.....	233
V.16: Strain rate sequence prediction for OFHC Cu using the Zerilli-Armstrong model. Solid lines represent the model prediction, while symbols represent experimental data.....	233
V.17: Temperature sequence prediction for OFHC Cu using the Zerilli-Armstrong model. Solid lines represent the model prediction, while symbols represent experimental data.....	234

V.18: Temperature sequence prediction for OFHC Cu using the Zerilli-Armstrong model. Solid lines represent the model prediction, while symbols represent experimental data.....	234
V.19: Strain rate and temperature sequence prediction for OFHC Cu using the Zerilli-Armstrong model. Solid lines represent the model prediction, while symbols represent experimental data.....	235
V.20: Strain rate and temperature sequence prediction for OFHC Cu using the Zerilli-Armstrong model. Solid lines represent the model prediction, while symbols represent experimental data.....	235
V.21: Correlation to OFHC Cu data using Zerilli-Armstrong model. The model correlations are shown using solid lines, while the experimental data are shown with open symbols.....	236
V.22: Strain rate sequence prediction for OFHC Cu using the Zerilli-Armstrong model correlated with the additional high strain rate data. Solid lines represent the model prediction, while symbols represent experimental data.....	238
V.23: Strain rate sequence prediction for OFHC Cu using the Zerilli-Armstrong model correlated with the additional high strain rate data. Solid lines represent the model prediction, while symbols represent experimental data.....	238
V.24: Temperature sequence prediction for OFHC Cu using the Zerilli-Armstrong model correlated with the additional high strain rate data. Solid lines represent the model prediction, while symbols represent experimental data.....	239
V.25: Temperature sequence prediction for OFHC Cu using the Zerilli-Armstrong model correlated with the additional high strain rate data. Solid lines represent the model prediction, while symbols represent experimental data.....	239
V.26: Strain rate and temperature sequence prediction for OFHC Cu using the Zerilli-Armstrong model correlated with the additional high strain rate data. Solid lines represent the model prediction, while symbols represent experimental data.....	240

V.27: Strain rate and temperature sequence prediction for OFHC Cu using the Zerilli-Armstrong model correlated with the additional high strain rate data. Solid lines represent the model prediction, while symbols represent experimental data.....	240
V.28: Parameter sensitivity for OFHC Cu using the Zerilli-Armstrong model. Light and dark bars reflect a $\pm 10\%$ offset from the optimized parameter values corresponding to a minimum of the objective function. First two bars show ability of indicated parameter, alone, to achieve the global minimum while the second two bars show ability of the remaining parameters, with the indicated parameter held constant, to reach the minimum.....	242
V.29: Correlation to OFHC Cu compression data using the MTS model. The model correlations are shown using solid lines, while the experimental data are shown with open symbols.....	244
V.30: Strain rate sequence prediction for OFHC Cu using the MTS model. Solid lines represent the model prediction, while symbols represent experimental data.....	247
V.31: Strain rate sequence prediction for OFHC Cu using the MTS model. Solid lines represent the model prediction, while symbols represent experimental data.....	247
V.32: Temperature sequence prediction for OFHC Cu using the MTS model. Solid lines represent the model prediction, while symbols represent experimental data.....	248
V.33: Temperature sequence prediction for OFHC Cu using the MTS model. Solid lines represent the model prediction, while symbols represent experimental data.....	248
V.34: Strain rate and temperature sequence prediction for OFHC Cu using the MTS model. Solid lines represent the model prediction, while symbols represent experimental data.....	249
V.35: Strain rate and temperature sequence prediction for OFHC Cu using the MTS model. Solid lines represent the model prediction, while symbols represent experimental data.....	249

V.36: Parameter sensitivity for OFHC Cu using the MTS model. Light and dark bars reflect a $\pm 10\%$ offset from the optimized parameter values corresponding to a minimum of the objective function. First two bars show ability of indicated parameter, alone, to achieve the global minimum while the second two bars show ability of the remaining parameters, with the indicated parameter held constant, to reach the minimum.....	251
V.37: Correlation to OFHC Cu compression data using the BCJ-SNL model. The model correlations are shown using solid lines, while the experimental data are shown with open symbols. The ratio α/κ is displayed using short dashed lines.....	251
V.38: Strain rate sequence prediction for OFHC Cu using the BCJ-SNL model. Solid lines represent the model prediction, while symbols represent experimental data.....	256
V.39: Strain rate sequence prediction for OFHC Cu using the BCJ-SNL model. Solid lines represent the model prediction, while symbols represent experimental data.....	256
V.40: Temperature sequence prediction for OFHC Cu using the BCJ-SNL model. Solid lines represent the model prediction, while symbols represent experimental data.....	257
V.41: Temperature sequence prediction for OFHC Cu using the BCJ-SNL model. Solid lines represent the model prediction, while symbols represent experimental data.....	257
V.42: Strain rate and temperature sequence prediction for OFHC Cu using the BCJ-SNL model. Solid lines represent the model prediction, while symbols represent experimental data.....	258
V.43: Strain rate and temperature sequence prediction for OFHC Cu using the BCJ-SNL model. Solid lines represent the model prediction, while symbols represent experimental data.....	258

V.44: Parameter sensitivity for OFHC Cu using the BCJ-SNL model. Light and dark bars reflect a $\pm 10\%$ offset from the optimized parameter values corresponding to a minimum of the objective function. First two bars show ability of indicated parameter, alone, to achieve the global minimum while the second two bars show ability of the remaining parameters, with the indicated parameter held constant, to reach the minimum.....	260
V.45: Correlation to OFHC Cu compression data using the McDowell model. The model correlations are shown using solid lines, while the experimental data are shown with open symbols. The softening data, beginning at 269°C above 0.5 strain, was included in the calculation of the objective function during the optimization.....	262
V.46: Strain rate sequence prediction for OFHC Cu using the McDowell model. Model correlations are given by solid lines while symbols represent experimental data.....	265
V.47: Strain rate sequence prediction for OFHC Cu using the McDowell model. Model correlations are given by solid lines while symbols represent experimental data.....	265
V.48: Temperature sequence prediction for OFHC Cu using the McDowell model. Model correlations are given by solid lines while symbols represent experimental data.....	266
V.49: Temperature sequence prediction for OFHC Cu using the McDowell model. Model correlations are given by solid lines while symbols represent experimental data.....	266
V.50: Strain rate and temperature sequence prediction for OFHC Cu using the McDowell model. Model correlations are given by solid lines while symbols represent experimental data.....	267
V.51: Strain rate and temperature sequence prediction for OFHC Cu using the McDowell model. Model correlations are given by solid lines while symbols represent experimental data.....	267

V.52: Parameter sensitivity for OFHC Cu using the McDowell model. Light and dark bars reflect $\pm 10\%$ offset from optimized values corresponding to a minimum of the objective function. First two bars show ability of indicated parameter, alone, to achieve the global minimum while the second two bars show ability of the remaining parameters, with the indicated parameter held constant, to reach the minimum.....	269
V.53: Correlation to OFHC Cu compression data using the McDowell model. The model correlations are shown using solid lines, while the experimental data are shown with open symbols. The softening data, beginning at 269°C above 0.5 strain, was eliminated from the calculation of the objective function during the optimization.....	270
V.54: Strain rate sequence predictions for OFHC Cu using the McDowell model. Solid lines represent the model predictions, while symbols represent experimental data.....	271
V.55: Strain rate sequence predictions for OFHC Cu using the McDowell model. Solid lines represent the model predictions, while symbols represent experimental data.....	271
V.56: Temperature sequence predictions for OFHC Cu using the McDowell model. Solid lines represent the model predictions, while symbols represent experimental data.....	272
V.57: Temperature sequence predictions for OFHC Cu using the McDowell model. Solid lines represent the model predictions, while symbols represent experimental data.....	272
V.58: Strain rate and temperature sequence predictions for OFHC Cu using the McDowell model. Solid lines represent the model predictions, while symbols represent experimental data.....	273
V.59: Strain rate and temperature sequence predictions for OFHC Cu using the McDowell model. Solid lines represent the model predictions, while symbols represent experimental data.....	273

V.60: Correlation to OFHC Cu compression data including the very high strain rate data 692820 s^{-1} at 298°C and 461°C (Frutschy and Clifton, 1988). The model correlation are shown using solid lines, while the experimental data are shown with open symbols. The optimization was conducted only using the data to a strain of 0.5.....	275
V.61: Correlation to OFHC Cu compression data including the very high strain rate data 692820 s^{-1} at 298°C and 461°C (Frutschy and Clifton, 1988). The model correlation are shown using solid lines, while the experimental data are shown with open symbols. The optimization was conducted only using the data to a strain of 0.5.	276
VI.1: Flow chart for constitutive model development using advanced algorithms.....	285
VI.2: Temperature factor variance with temperature. Solid symbols reflect the dependence for χ_2 and the open symbols for χ_1	290
VI.3: DOE results showing the relative importance that each factor has on the minimization of the objective function. The correlation of factor numbers to parameters are given in Table VI.4.....	297
VI.4: DOE results showing the relative importance each factor has on the objective function. The correlation of factor numbers to parameters are given in Table VI.4.....	298
VI.5: Correlation to OFHC Cu compression data using the BCJ-SNL model. The model correlations are shown using solid lines, while the experimental data are shown with open symbols. The ratio α/κ is displayed using short dashed lines.....	304
VI.6: Strain rate sequence prediction for OFHC Cu using the BCJ-SNL model. Solid lines represent the model prediction, while symbols represent experimental data.....	305
VI.7: Strain rate sequence prediction for OFHC Cu using the BCJ-SNL model. Solid lines represent the model prediction, while symbols represent experimental data.....	305
VI.8: Temperature sequence prediction for OFHC Cu using the BCJ-SNL model. Solid lines represent the model prediction, while symbols represent experimental data.....	306

VI.9: Temperature sequence prediction for OFHC Cu using the BCJ-SNL model. Solid lines represent the model prediction, while symbols represent experimental data.....	306
VI.10: Strain rate and temperature sequence prediction for OFHC Cu using the BCJ-SNL model. Solid lines represent the model prediction, while symbols represent experimental data.....	307
VI.11: Strain rate and temperature sequence prediction for OFHC Cu using the BCJ-SNL model. Solid lines represent the model prediction, while symbols represent experimental data.....	307
VI.12: Prediction of critical strain for the initiation of recrystallization using OFHC Cu data at strain rates from 0.0004 s^{-1} to 1.0 s^{-1} and temperatures from 134°C to 541°C . Actual peak strain values are shown in closed symbols and those which were estimated from strain data limited to 1.0 are shown with open symbols.....	312
VI.13: Microstructural deformation mechanism map for establishing the character of recrystallization (Jonas and Sakai, 1984).....	316
VI.14: Correlation to OFHC Cu using the BCJ-SNL model. Solid lines are model predictions which shows the optimized fit to experimental data without the recrystallization softening variable.....	320
VI.15: Correlation to OFHC Cu compression data using the McDowell model. The model correlations are shown using solid lines, while the experimental data are shown with open symbols.....	321
VI.16: Correlation to OFHC Cu compression data using the McDowell model with recrystallization parameter. The model correlations are shown using solid lines, while the experimental data are shown with open symbols. Data was correlated to the five isothermal, constant true strain rate experimental data.....	321
VI.17: Correlation to OFHC Cu using the McDowell model, without the recrystallization softening variable. The predictions are shown using solid lines, while the experimental data are shown using open symbols.....	323
VI.18: Correlation to OFHC Cu using the McDowell model, without the recrystallization softening variable. The predictions are shown using solid lines, while the experimental data are shown using open symbols.....	324

VI.19: Correlation to OFHC Cu compression data using the McDowell model. The model correlations are shown using solid lines, while the experimental data are shown with open symbols.	326
VI.20: Correlation to OFHC Cu compression data using the McDowell model. The model correlations are shown using solid lines, while the experimental data are shown with open symbols.	326
VI.21: Strain rate sequence prediction for OFHC Cu using the McDowell model with recrystallization parameter. Solid lines represent the model prediction, while symbols represent experimental data.....	327
VI.22: Strain rate sequence prediction for OFHC Cu using the McDowell model with recrystallization parameter. Solid lines represent the model prediction, while symbols represent experimental data.....	327
VI.23: Temperature sequence prediction for OFHC Cu using the McDowell model with recrystallization parameter. Solid lines represent the model prediction, while symbols represent experimental data.....	328
VI.24: Temperature sequence prediction for OFHC Cu using the McDowell model with recrystallization parameter. Solid lines represent the model prediction, while symbols represent experimental data.....	328
VI.25: Strain rate and temperature sequence prediction for OFHC Cu using the McDowell model with recrystallization parameter. Solid lines represent the model prediction, while symbols represent experimental data.....	329
VI.26: Strain rate and temperature sequence prediction for OFHC Cu using the McDowell model with recrystallization parameter. Solid lines represent the model prediction, while symbols represent experimental data.....	329
VI.27: Correlation to OFHC Cu compression data using the McDowell model. The model correlations are shown using solid lines, while the experimental data are shown with open symbols.	331
VI.28: Strain rate sequence prediction for OFHC Cu using the McDowell model with recrystallization parameter. Solid lines represent the model prediction, while symbols represent experimental data.....	332

VI.29: Strain rate sequence prediction for OFHC Cu using the McDowell model with recrystallization parameter. Solid lines represent the model prediction, while symbols represent experimental data.....	332
VI.30: Temperature sequence prediction for OFHC Cu using the McDowell model with recrystallization parameter. Solid lines represent the model prediction, while symbols represent experimental data.....	333
VI.31: Temperature sequence prediction for OFHC Cu using the McDowell model with recrystallization parameter. Solid lines represent the model prediction, while symbols represent experimental data.....	333
VI.32: Strain rate and temperature sequence prediction for OFHC Cu using the McDowell model with recrystallization parameter. Solid lines represent the model prediction, while symbols represent experimental data.....	334
VI.33: Strain rate and temperature sequence prediction for OFHC Cu using the McDowell model with recrystallization parameter. Solid lines represent the model prediction, while symbols represent experimental data.....	334
VI.34: Correlation to OFHC Cu compression data using the McDowell model with the high strain rate term incorporated. The model correlations are shown using solid lines, while the experimental data are shown with open symbols.....	337
VI.35: Correlation to OFHC Cu compression data using the McDowell model with the high strain rate term incorporated. A temperature increase of approximately 200°C due to adiabatic heating was included. The model correlations are shown using solid lines, while the experimental data are shown with open symbols.....	338
VI.36: DOE results showing the relative importance that each factor has on the minimization of the objective function. The correlation of factor numbers to parameters are given in Table VI.11.....	344
VI.37: DOE results showing the relative importance each factor has on the objective function. The correlation of factor numbers to parameters are given in Table VI.11.....	345

NOMENCLATURE

Abbreviations

ANN	Artificial neural networks
b.c.c.	Body centered cubic
BCJ-SNL	Bammann, Chiesa, Johnson - Sandia National Laboratory
CB	Cell block
Comp	Compression
DDW	Dense dislocation wall
EDM	Electro discharge machining
f.c.c.	Face centered cubic
HRS	Hot rolled steel
ISV	Internal state variable
J/C	Johnson and Cook
MB	Microband
MPRL	Mechanical Properties Research Laboratory
MTS	Mechanical threshold stress
OFE	Oxygen-free-electronic
OFHC	Oxygen-free high conductivity
Rev C/T	Reverse compression/tension

RVDT	Rotary variable differential transformer
SFE	Stacking fault energy
SNL	Sandia National Laboratory
Z-A	Zerilli and Armstrong

Symbols

α	Back stress, kinematic hardening
A	MTS model parameter
A_1	McDowell model parameter
A_2	McDowell model parameter
A_3	McDowell model parameter
A_4	McDowell model parameter
b	Burger's vector
B	J/C model parameter
B_0	McDowell model parameter
B_1	McDowell model parameter
B_2	McDowell model parameter
B_3	McDowell model parameter
B_4	McDowell model parameter

C	J/C model parameter; McDowell model parameter
C_0	Z-A model parameter
C_1	MTS model parameter
C_2	Z-A model parameter; MTS model parameter
C_3	Z-A model parameter; MTS model parameter
C_4	Z-A model parameter
D	McDowell model parameter
D_1	McDowell model parameter
D_2	McDowell model parameter
γ	Engineering shear strain
d	Average grain diameter/size; diameter of specimen
$\dot{\epsilon}$	Strain rate
$\dot{\epsilon}_i$	Initial strain rate
$\dot{\epsilon}_0$	Reference strain rate, constant
$\dot{\epsilon}_f$	Final strain rate
$\dot{\epsilon}_{s0}$	MTS model constant
ϵ	Strain
ϵ_a	Axial engineering strain
ϵ^P	Plastic strain
ϵ^N	Inelastic strain
ϵ_t	True strain

f	BCJ-SNL model parameter
g_0	Normalized activation energy; Initial gage length of the specimen
η	Parameter sensitivity; viscosity partitioning factor
h	BCJ-SNL model parameter
H	BCJ-SNL model parameter
Θ	Diffusivity coefficient; strain hardening rate
Θ_0	Initial strain hardening rate
θ	Rotation angle
θ_g	Rotation angle of gage section
κ	Isotropic hardening variable
k	Boltzmann's constant; Hall-Petch strengthening parameter
L	Specimen length
$L\alpha$	McDowell model parameter
$L\chi$	McDowell model parameter
$\bar{\lambda}$	Mean grain intercept
m	J/C model parameter
ξ	Internal state variable
μ	Elastic shear modulus; McDowell model parameter
μ_0	Reference shear modulus
μ_{293}	Elastic shear modulus at 293°C
n	J/C model parameter; Z-A model parameter

n_1	McDowell model parameter
n_2	McDowell model parameter
ν	Poisson ratio; McDowell model parameter
$OBJ_{constrained}$	Objective function when certain parameters are fixed
$OBJ_{minimized}$	Global minimum
OBJ_{offset}	Objective function value for specified parameter set
P_L	Number of grain intercepts per unit length
p	MTS parameter, defines obstacle profile
Q	Activation energy
Q_0	Total energy barrier; activation energy
ΔQ_α	Activation energy for McDowell model parameter
ΔQ_χ	Activation energy for McDowell model parameter
q	MTS parameter, defines obstacle profile
r_d	BCJ-SNL model parameter
r_i	Inner radius of the gage section
r_s	BCJ-SNL model parameter
R	McDowell model parameter
R_d	BCJ-SNL model parameter
R_s	Static recovery parameter; BCJ-SNL model parameter
R_1	McDowell model parameter
R_2	McDowell model parameter

r_o	Outer radius of the gage section
σ	Flow stress
σ_a	Engineering stress
σ_0	YJ/C model parameter, yield stress
σ_t	True stress
$\sigma_n(\epsilon)_{data}$	Experimental data stress value at strain increment, n
$\sigma_n(\epsilon)_{predicted}$	Predicted stress value at strain increment, n
$\hat{\sigma}$	Mechanical threshold stress (MTS)
$\hat{\sigma}_a$	Athermal component of MTS
$\hat{\sigma}_s$	Saturation threshold stress
$\hat{\sigma}_{s0}$	MTC model parameter
$\hat{\sigma}_t$	Thermal component of MTS
$\Delta\sigma_h$	Change in flow stress due to history effects
$\Delta\sigma_s$	Instantaneous change in flow stress
s	MTS parameter - defines the glide kinetics
Σ_v	Viscous stress
\dot{T}	Temperature rate
T	Torque; temperature
T_M	Melting point temperature
T_O	Reference temperature

T_r	Reference temperature
τ	Applied shear stress
τ_A	Measure of the long range stresses
V	BCJ-SNL model parameter; Activation volume
W_n	Weighting factor in objective function
χ	McDowell model parameter
$\hat{\chi}_1$	McDowell model parameter
$\hat{\chi}_2$	McDowell model parameter
$\bar{\chi}_1$	McDowell model parameter
Ψ_α	McDowell model parameter
Ψ_χ	McDowell model parameter
Y	BCJ-SNL model parameter

SUMMARY

Accurate material behavior prediction during large deformations is essential. For the U.S. Army, explosively formed projectiles (EFP), penetrators, and vehicle armor are applications which will benefit from a better understanding of and ability to predict material behavior when subjected to high and varying strain rates and temperatures. Linking macro-scale material behavior with the evolution of microstructure has proven effective in obtaining an appropriate mathematical structure for constitutive relationships. Incorporation of strain rate, temperature, and deformation path history effects are especially critical to accurately predict material responses for arbitrary nonisothermal, variable strain rate conditions. Material constitutive equations contain numerous parameters which must be determined experimentally, and often are not fully optimized.

The goal of this research was to develop more physically descriptive kinematics and kinetics models for large strain deformation based on internal state variable (ISV) evolution laws which include strain rate and temperature *history* dependence. A unique and comprehensive set of experiments involving sequences of different strain rates, temperatures, and deformation paths, as well as, constant strain rate, isothermal and experiments characterizing restoration processes, were conducted on OFHC Cu. Microstructural examinations found that recrystallization occurs and has a significant influence on the flow stress. The performance of various models, including state-of-the-art

models such as the BCJ (Sandia), MTS (Los Alamos), and McDowell models were correlated and compared to experimental data. A novel hybrid optimization strategy was used to obtain the optimum parameter set possible corresponding to each model form. To account for the observed flow stress softening, an internal state variable representing the “softened” recrystallized state was incorporated into the hardening evolution equations in the BCJ and McDowell models. The temperature dependent behavior at very high strain rates (10^6 s^{-1}) was investigated. A term, representing this high strain rate regime, added to the evolution equations was found to greatly improve the correlation to data.

CHAPTER I

INTRODUCTION

Accounting for complex paths of deformation, temperature, and strain rate is an important requirement of constitutive laws for many engineering applications. Large deformations are essential to many applications involving large strain such as high speed machining, impact, and various primary metal forming operations. These applications involve a great range of deformation conditions, including changing strain rates, temperatures, and deformation path. Current material characterization processes do not capture the effects of these changing conditions. An understanding of deformation behavior over a wide range of temperatures and strain rates is necessary for accurately predicting material behavior. In general, sequence experiments reveal more sophisticated phenomena of path history dependence than do constant strain rate, isothermal, monotonic deformation experiments such as compression tests. The development of new dynamic mechanical property tests and an improved ability to detect microstructural changes have resulted in an enhanced capability of examining and understanding actual material responses. Computational improvements now allow more complex models to be incorporated with a closer link to actual physics of the deformation process. Improvements in understanding the mechanisms involved at various strain rates and temperatures will result in an ability to develop improved design procedures, allow for effective designs, and reduce development

costs.

Strain rate and temperature history effects were first demonstrated by Dorn, Goldberg, and Tietz (1949). Consequently, the mechanical equation of state, $\sigma = \sigma(\epsilon, \dot{\epsilon}, T)$ (Ludwick, 1909), is invalid since it assumes that the material flow stress is only dependent upon instantaneous values of strain, strain rate, and temperature. The incorporation of history effects necessitates the consideration of internal state variable models to supersede mechanical equation of state models (cf. McDowell and Voorhees, 1995).

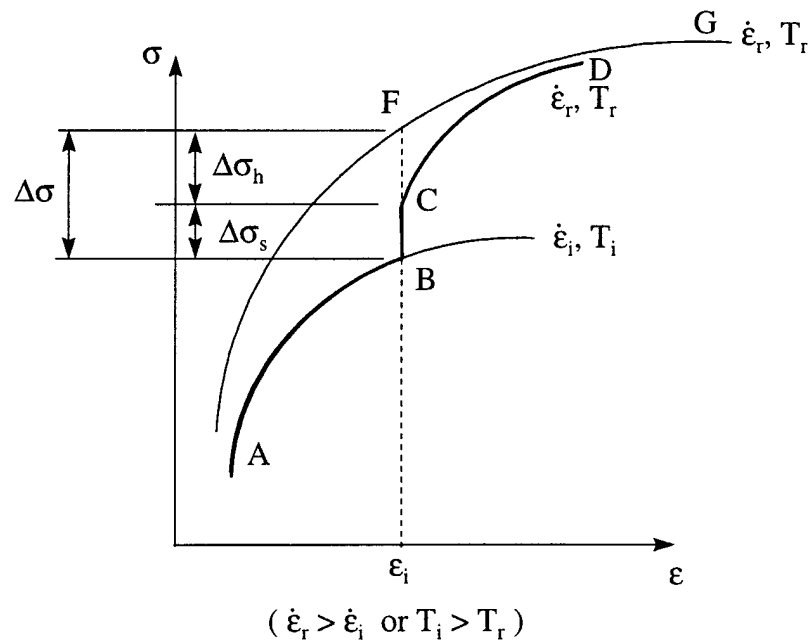


Figure: I.1: Strain rate and temperature history effects of f.c.c. metals (Klepaczko, 1975 and Duffy, 1979).

Strain rate and temperature history effects for f.c.c. metals are shown schematically in Fig. I.1 (Klepaczko, 1975 and Duffy, 1979). Stress-strain curves are plotted for two strain rates and temperatures. The lowest curve represents the stress-strain relation for a f.c.c. metal measured during loading at a relatively low constant strain rate, $\dot{\epsilon}_l$. The upper curve pertains to a high constant strain rate, $\dot{\epsilon}_r$. During a strain rate jump test, the stress-strain curve follows the path ABCD, where point B corresponds to the strain, ϵ_i , at which the strain rate is changed abruptly from $\dot{\epsilon}_l$ to $\dot{\epsilon}_r$. If the mechanical equation of state were valid, there would be no strain rate history effect; the response to the strain rate jump would be along path ABFG. The abrupt change in flow stress is identified as $\Delta\sigma_s$. At points C and F, the strain and strain rate are identical, while the stress differs. Therefore, material behavior depends on the strain rate history. $\Delta\sigma_h$ is viewed as reflective of the history dependence on strain rate effects, while $\Delta\sigma_s$ is related to the instantaneous strain rate sensitivity. Curve segment B-C is interpreted as due to the kinetics of the deformation, dependent upon the deformation conditions, while the segment, C-D, depends upon the internal structure which has been developed during the prior deformation. Beyond ϵ_i , the difference in stress levels, especially for f.c.c. metals, diminishes as the deformation continues. This is referred to as fading memory. In some instances, the difference reduces to zero. Analogous results are obtained whether a sharp decrease in temperature or increase in strain rate is imposed. Similar strain rate and temperature history effects occur in b.c.c. metals. The primary difference is the response after a change, curve B-C and C-D in Fig. I.1, reaches a level

above the high constant strain rate curve and then approaches from the top.

In this research, significant contributions are made in terms of both new experimental data and modeling of sequence effects. The experimental research program supports the development of principles for determining optimized internal state variable (ISV) evolution equations and associated parameters, and facilitates the assessment of the capability to model strain rate history and temperature history effects in current constitutive models. Chapter III contains the results of a comprehensive set of experimental data on Oxygen-Free High Conductivity (OFHC) Copper. These experiments include the characterization of restoration, the relaxation of internal stored energy through both recovery and recrystallization processes, both statically and dynamically, strain rate and temperature characterization, and a comprehensive set of sequence experiments involving changes of strain rate, temperature and deformation path. In Chapter IV, a microstructural analysis is described which investigates the changes in grains due to recrystallization. Chapter V shows that equations of state based on isothermal, constant strain rate data from monotonic loading paths are insufficient to describe mechanical behavior and examines applicability of state-of-the-art ISV models. Three ISV viscoplasticity models which are representative of a broad class of such models, the BCJ-SNL model, (Bammann *et al.*, 1990), the Mechanical Threshold Stress model, (Klepaczko and Chiem, 1986, Follansbee and Kocks, 1988, and Klepaczko, 1988), and the McDowell model (Moosbrugger and McDowell, 1990 and McDowell, 1992), are fit to isothermal, constant true strain rate data for compression and then compared to the experimental results for various deformation condition sequence experiments. Chapter VI

investigates the use of advanced algorithms for the development of improved constitutive models. A statistical design of experiment approach for the evaluation of numerous competing factors is one approach. Another is the use of the pattern recognition capabilities of artificial neural networks. The addition of an auxiliary internal state variable with a static and dynamic softening term to capture the effects of recrystallization is implemented as well as a term for unique hardening effects at very high strain rates. Implications for the representation of history effects through the hardening, static and dynamic recovery functions are considered. Other approaches based on temperature and strain rate kinetics are discussed in terms of potential contribution to the ISV model framework.

CHAPTER 2

INELASTIC DEFORMATION MECHANISMS

II.1 Introduction

The accuracy and generality of any material model are dependent on the link established between the model and the actual physical processes. The small size and great number of elements at the atomic level are such that individual atomic elements cannot be modeled to predict macroscopic behavior, rather, the effects of atomic length scales must be modeled through an averaging process. An understanding of the microstructural processes of large strain deformation is necessary for proper macroscopic constitutive modeling. These linkages to actual physical deformation mechanisms create physically based constitutive models which have the structure and evolution of actual material.

Metals are crystalline and contain atoms which are arranged in a pattern which repeats itself periodically in three dimensions. The density of atoms in polycrystalline structures is high, $O(10^{23})$ atoms/cc, and they contain defects which have significant effects on their behavior as engineering materials. The theoretical strength of a perfect crystal, determined by the atomic bonding between atoms, and the strength of a polycrystalline material differ by many orders of magnitude. The reduced strength of actual materials is due to the presence of defects in the lattice structures. Defects may occur in several different

forms, including single atoms (point defects) which include vacancy sites or interstitial atoms, rows of atoms (linear defects), planes of atoms (planar defects), and small three-dimensional clusters of atoms (column defects).

The linear defect, the dislocation, is the most common mechanism for inelastic deformation of ductile materials. Microstructural studies concentrate on the ordered crystalline state, where deformation is viewed as due to the movement, generation, and annihilation of dislocations. Dislocations move through the crystalline material and encounter obstacles to subsequent motion. Obstacles to dislocation motion, such as other defects, inhibit motion, requiring increased applied stress for continued motion. The relation between applied loading and plastic strain rate is largely determined by how these obstacles are overcome. Dislocation motion past obstacles is affected by the deformation conditions, including strain rate and temperature. Obstacles range from small, such as point and line defects, interstitial or solute atoms, to large grain boundaries or other high angle boundaries. The classification of obstacles is generally based on the ability of the obstacle to be passed with thermal assistance. Dislocation motion results from both applied stress and statistical fluctuations due to thermal vibrations. Long range obstacles cannot be thermally assisted while short range obstacles can be overcome with thermal assistance (Fig. II.1).

At equilibrium and 0K, the force required for a dislocation to proceed past a set of obstacles is called the mechanical threshold stress, σ_0 , (Fig. II.1) and is a measure of the resulting strength due to the particular obstacle configuration. Dislocations that overcome

one set of obstacles will then move until another obstacle array is encountered. At temperatures above 0K, thermal activation assists the dislocation in proceeding past obstacles. As temperature increases above 0K, the stress required decreases. Dislocations are thermally assisted past short-range obstacles until the athermal, $\hat{\sigma}_a$, stress level is reached. Athermal stress is the measure of the long range obstacle strength. Increasing the strain rate reduces the time available for thermal assistance resulting in increased stress levels.

The investigation and understanding of microstructure are necessary for the development of ISV models which have linkages to physical deformation processes. Dislocation substructures develop differently under various deformation conditions. At low, quasi-static, strain rates, dislocations form tangled, dense dislocation walls, forming cell boundaries enclosing relatively dislocation free zones. At high, dynamic strain rates, a more homogenous substructure is developed. The remaining sections in this chapter will discuss characteristics of microstructures which influence deformation in OFHC Cu.

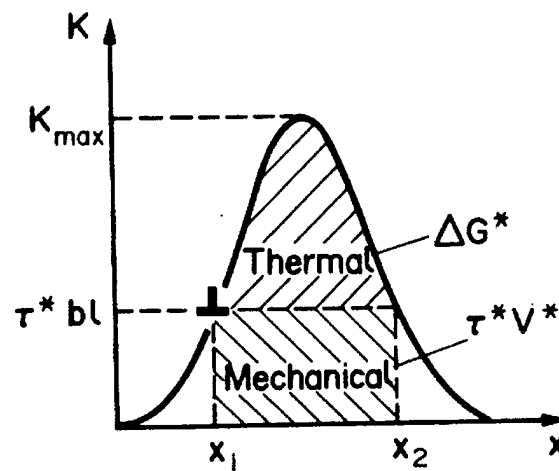
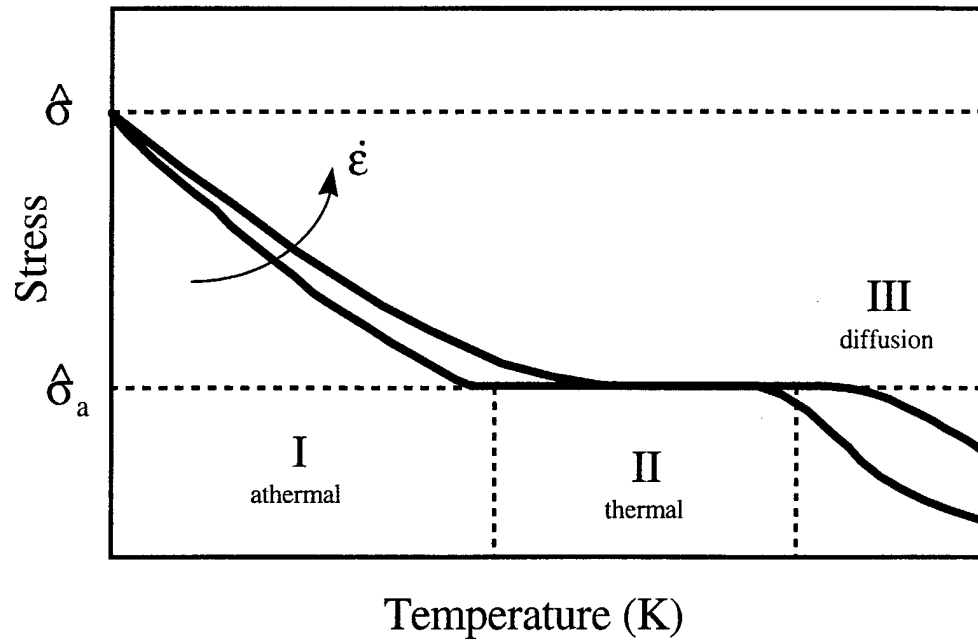


Figure II.1: Influence of thermal assistance on dislocation motion past obstacles.

II.2 Dislocation Substructures

OFHC Cu has been extensively studied (Kocks and Mecking, 1980; Shume *et al.*, 1989; and Hansen, 1992). Microstructures have been explored with details of grains and even individual dislocations observed. These capabilities improve the knowledge, understanding, and resultant descriptions of the internal structure. Deformation causes changes in microstructure, which vary depending upon the deformation conditions of strain rate, loading path, and temperature. Subsequent deformation, under different conditions, results in the transient behavior as the microstructure adjusts to the new conditions. At higher strain rates, the dislocation substructures maintain a more homogeneous distribution than that observed during low strain rate deformation. A well defined cell substructure which develops at low strain rates is a relaxation phenomenon which is not achieved during the reduced times at dynamic straining (Cheval and Priester, 1989). The differences in dislocation structures that develop between tension and torsion deformation was investigated by Doner, *et al.*, (1974), Ungar, *et al.*, (1986), and Bassion and Liu (1993). The latter determined a major difference in dislocation configuration may explain the work hardening differences of copper in tension and torsion. In torsion, the dislocation structures evolve from a random, checkerboard pattern to paired sheets which become two sets of walls. During tension, the presence of three sets of dislocation walls were observed, resulting in a larger obstacle and a higher hardening rate. A brief description of important microstructural features to strain rate and temperature history effects follow in subsequent sections.

II.2.1 Dislocation Obstacles

Internal stresses result from the non-uniform distribution of dislocation motion. This distribution of obstacles is typically categorized as having a long range or short range character. Long range obstacles are distinguished by not being passed by dislocations with thermal assistance while short range obstacles can be overcome. Plastic deformation is the result of many displacements of many dislocations in the lattice. The categorization of the obstacles reflects an averaging process which allows the modeling of these physical processes. Subgrains and grain boundaries are physically larger than individual dislocations and are separated by distances large relative individual dislocations. They form a heterogeneous distribution to the motion of dislocations. These substructure and grain boundaries are the dominant large obstacles to dislocation motion and remain relatively stable through time. Short range obstacles consist of forest dislocations, dislocation tangles, point defects, and sessile dislocation structures and are relatively homogeneous. The effects of long and short range obstacles can be characterized by their respective slow and fast kinetics.

Crystalline materials usually consist of randomly oriented grains which contain crystals with the same orientation. The grains are separated by grain boundaries which consist of an array of dislocations. Grain size has an important role in influencing flow stress levels due to the interaction between grain boundaries and dislocation motion. Grain size, shape, and orientation determine the amount of boundary length which will interfere with dislocation motion. Stresses result from dislocation pileups at grain boundaries, which are

obstacles to dislocation slip, and can also result in the generation of dislocations at boundaries. Hansen (1985) determined the influence of grain size on flow stress. At low, strain levels, the flow stress increases with decrease in grain size. Gourdin and Lassila (1991) and Domeral and Stelly (1979) determined that copper flow stress follows a Hall-Petch relationship, with the flow stress being dependent on the average grain size, d , of the material. For several strain levels, they determined the relationship to be

$$\hat{\sigma}_a = \frac{2.78 \times 10^{-4}}{\sqrt{d}} \text{ GPa} \quad (\text{II.1})$$

which is independent of strain and strain rate.

As deformation occurs in Cu, the substructure evolves. Areas of sparse dislocation population are interspersed with densely packed dislocation arrays. The substructure develops with increasing strain from a tangled dislocation structure to a structure consisting of equilaxed cells. Within the cells, dense dislocation walls (DDW's) are formed as the grains are subdivided into cell blocks (Barlow *et al.*, 1985, Hansen and Kuhlmann-Wilsdorf, 1986, Bay and Hansen, 1988, and Bay *et al.*, 1992). During deformation, grains divide and subdivide into volume elements. Such elements are termed cell blocks (CB's) and are composed of ordinary cells. Cells are the dominate structure during the Stage II hardening regime. Between CB's, dislocation boundaries form which are much longer and which have

larger misorientations across them. These boundaries are geometrically necessary boundaries and are DDW's. The evolution of certain cell walls into these geometrically necessary boundaries signals the onset of the nonlinear Stage III strain-hardening regime. At increasing deformation, DDW's develop into characteristic dislocation bands called microbands (MB's) (Hansen, 1992). This microstructural evolution with increasing strain consists of a continuous subdivision on a smaller and smaller scale by geometrically necessary boundaries. The subdivision into CB's defines the strain hardening rate during the larger strain Stage IV regime. These boundaries form additional obstacles to dislocation motion and determine the amount and distribution of internal energy available for restoration processes. The description of barriers to dislocation motion as short and long range supports the use of multiple ISV's which have the corresponding characteristic slow and rapid kinetics. This concept will be investigated in Chapter VI.

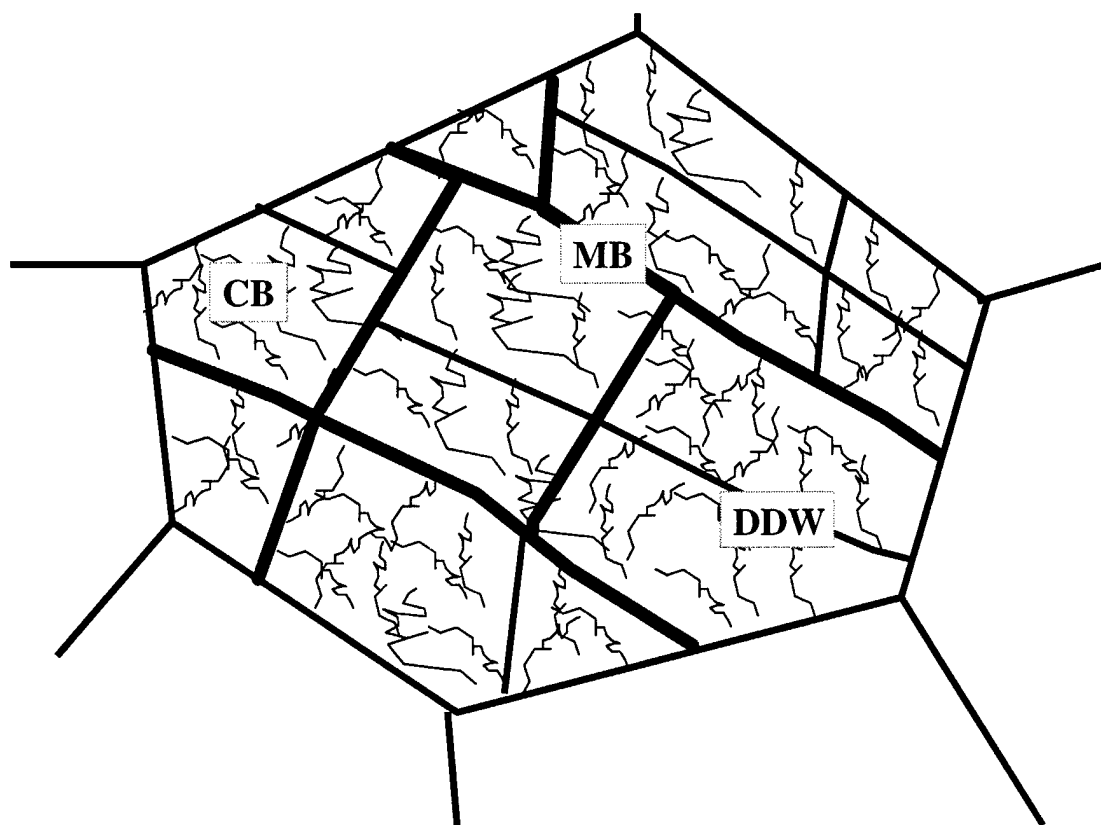


Figure II.2: Diagram of microstructure. Grain subdivision into geometrically necessary boundaries including dense dislocation walls (DDW's) and microbands (MB's) which delineate cell blocks (CB's) containing incidental dislocation boundaries in the form of cell walls (Bay *et al.*, 1992)

II.2.2 Stacking Faults

Stacking faults are planar defects in the crystalline structure where the stacking sequence has been disrupted by the removal or addition of part of the stacking layer. Stacking fault energy (SFE) is the corresponding energy per unit area of stacking fault. The SFE of metals controls the relative rates of dislocation cross-slip and ability to form sub-boundaries. Cu is considered to be a low to medium SFE material while aluminum has high SFE. During the deformation of low to medium SFE materials, dislocations are unable to cross-slip and recovery processes are partially inhibited. Metals of low SFE (e.g. copper and nickel) do not polygonize readily and this creates the conditions suitable for recrystallization. Dislocations are stopped at obstacles and provide the stored internal energy to drive the nucleation of new grains and subsequent grain growth associated with recrystallization. This makes materials with low to medium SFE more susceptible to recrystallization, both static and dynamic (McQueen and Jonas, 1975), since recrystallization is likely to occur before significant recovery. In metals of high SFE (e.g. aluminum), polygonization is so rapid that conditions are not suitable for recrystallization to be initiated. In high SFE materials, dislocations easily cross-slip onto different gliding planes which allows dynamic recovery processes to proceed, continuously reducing the internal energy.

II.3 Strain Hardening Processes

The initial dislocation distribution is random with relatively uniform distribution. At the beginning of plastic deformation, the dislocation density is at its lowest. During deformation, dislocations are continuously created and as dislocations move through material, they continuously encounter obstacles to their movement. This interaction between dislocations and obstacles to their motion causes the hardening behavior. At low strains, hardening is essentially a geometrical process. The dislocation density increases rapidly with strain and the dislocations arrange in a random pattern with a continuously decreasing average dislocation spacing. For well-annealed material, the initial hardening is presumably dominated by interactions between mobile and sessile dislocations. The initial slope of flow stress curves is strongly affected by the athermal dislocation accumulation rate. The initial strain hardening rate (initial slope of flow stress) increases with increasing strain rate. With increasing strain, the dislocation structure develops from tangles to a cellular structure with an arrangement of dislocation cells or subgrains. At high strain rates, the dislocation immobilization distance is the length a dislocation can move during the imposed time duration of the deformation. At large strain, the flow stress is strongly affected by dislocation rearrangement which leads to a saturation flow stress behavior.

There is evidence that at higher strain rates, the dislocation accumulation rate in copper becomes rapid. Edington (1969) reported slightly increased dislocation densities in a copper single crystal deformed at strain rates up to $4 \times 10^3 \text{ s}^{-1}$ than in samples deformed at quasi-static strain rates to the same strain levels. Dislocation density measurements reported

by Murr (1981) and Follansbee and Gray (1986), showed significantly increased dislocation densities in shock deformed copper. Increased rate sensitivity is due to the rate sensitivity of the structure evolution and not on the contribution of another deformation mechanism such as viscous drag.

II.4 Restoration Processes

When crystalline materials are deformed at elevated temperatures, the accumulated dislocations are continuously destroyed by restoration processes. Recovery and recrystallization are the restoration processes that result in the release of the internal energy stored during deformation. These restoration processes returns the material, partially or completely, to its condition prior to deformation. When these changes occur concurrent with straining under stress, they are termed dynamic, and static in the absence of stress. The SFE of a material controls the ability of dislocations to cross-slip onto different slip planes. In high SFE materials, dislocations cross-slip and recovery occurs readily, reducing the internal strain energy. During the deformation of low to medium SFE materials, dislocations are unable to cross-slip and recovery processes are partially inhibited . Due to the weak recovery in OFHC Cu, the density of local dislocations continuously increases, which creates instabilities in the substructure and recrystallization processes become possible.

II.4.1 Dynamic Restoration

Dynamic restoration processes include dynamic recovery and dynamic recrystallization. Dynamic recovery is the annihilation of dislocation pairs and the formation of sub-grains and regular sub-boundaries. These dynamic restoration processes eventually result in completely balancing the effects of strain hardening and work hardening which leads to the establishment of a steady state flow stress. Dynamic recrystallization occurs through the migration of high angle boundaries which eliminate large numbers of dislocations. The relative amount of energy released during recovery is small compared to the amount released after the onset of recrystallization. This relative amount decreases with increased pre-strain.

In materials of moderate to low SFE, the dislocation density increases and eventually the local differences in density are great enough for the nucleation of recrystallization during deformation. Dynamic recrystallization was first reported in Pb during creep (Greenwood and Worner 1939). The first investigation of recrystallization in metals under constant strain rate conditions was reported by Rossard and Blain (1959). Recrystallization is the process of new grains forming and growing through the material resulting in new regions of low dislocation density. Large numbers of dislocations are eliminated during recrystallization. Dynamic recrystallization occurs when the nucleation and growth occurs concurrent with straining under stress.

A portion of the work done by external forces during plastic deformation is retained in the material as stored energy. This stored energy can be released through the rearrangement of dislocations into lower energy configurations. In metals with low SFE,

dislocations accumulate in planar arrays which have high stored energy. This energy creates a strong driving force for recrystallization which is likely to occur before recovery progresses significantly (Cahn 1965; Byrne, 1965). Flow stress, and hence microstructure, evolve toward a quasi-steady state after recrystallization.

In annealed material, individual dislocations are initially randomly distributed and the dislocation density is low (Fig. II.3A). As deformation occurs, dislocations are created, move, and rearrange. Dislocation motion is impeded by obstacles which results in the strain hardening observed on the macroscopic scale. Dislocations begin to form a cellular structure as dislocations move and encounter obstacles. At strains of 0.5, the cell structure becomes more defined, and the cell size decreases as additional deformation occurs (Figs. II.3B and II.3C) (McQueen and Jonas, 1975). The walls become thicker as additional dislocations are trapped (Fig. II.3D). The cell walls, in low SFE metals, develop high misorientations, which become subsequent nucleation sites due to the high gradient of internal energy.

Dynamic recovery occurs during deformation when dislocations meet and annihilate each other. The ability of dislocations to change slip planes, through climb, enhances the recovery rate. Eventually, a dynamic balance between the creation of new dislocations, hardening, and the annihilation of dislocations, recovery, results in steady state flow. The strain hardening rate approaches zero.

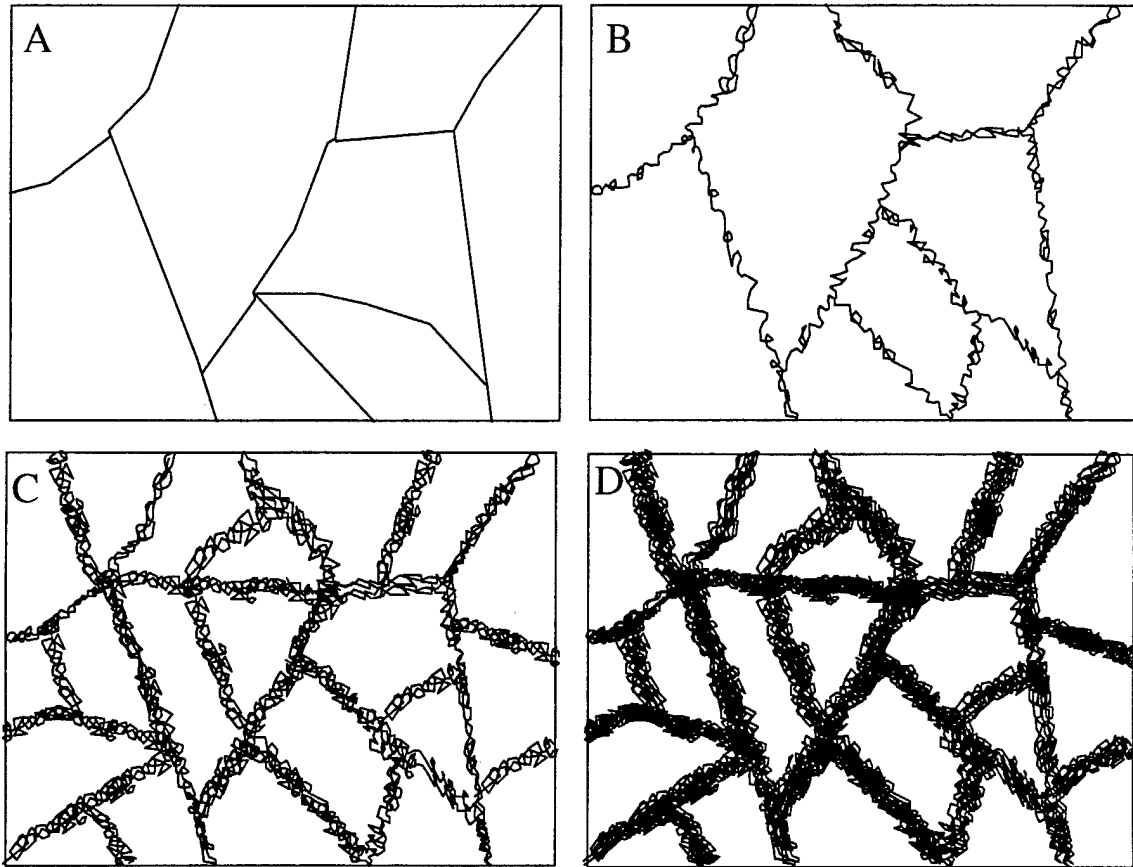


Figure II.3(A - D): Microstructure changes during deformation. (A) During deformation, a cellular substructure develops as the strain increases, (B and C) the cells become smaller and the walls more dense, achieving a limit in cell size (D) (McQueen and Jonas, 1975). At increasing strain, some dense dislocation walls develop into microbands (Bay *et al.*, 1992).

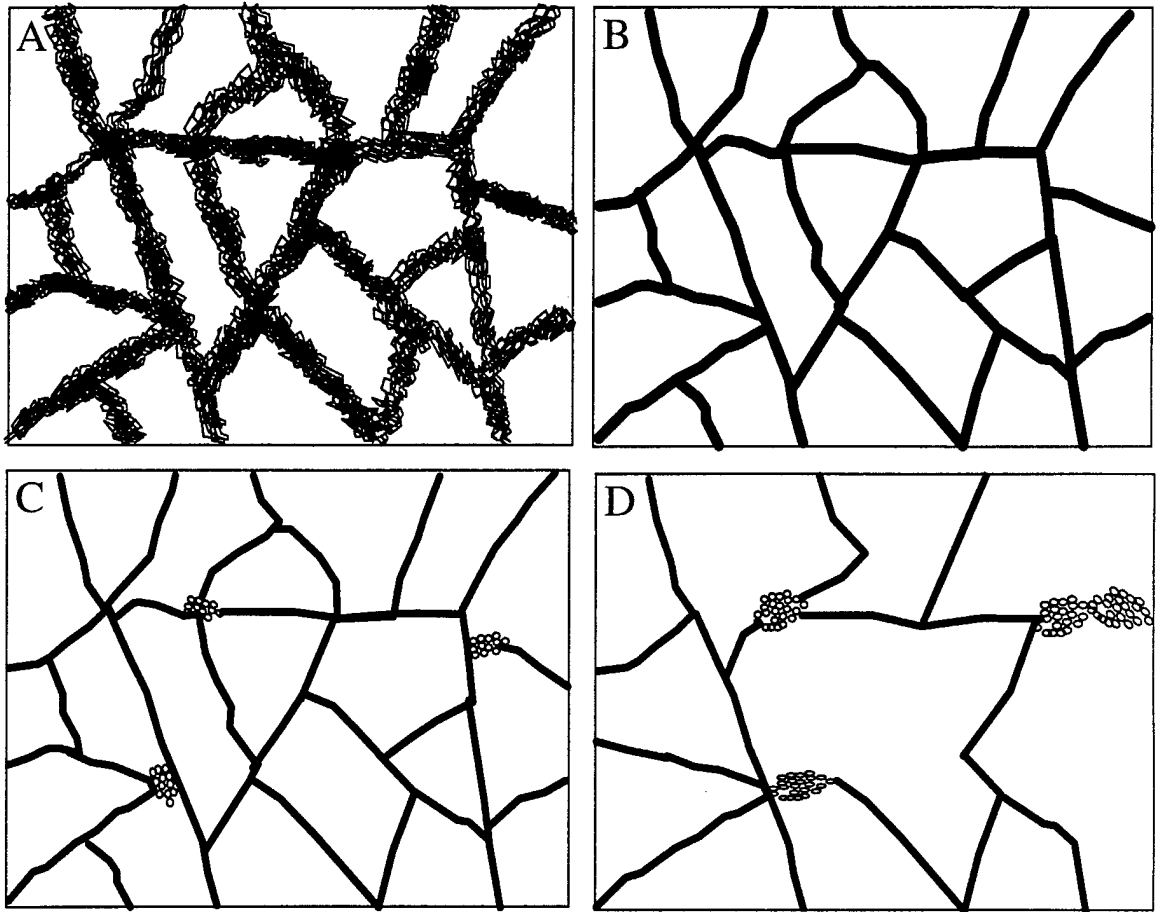


Figure II.4 (A - D): Recovery process. Recovery begins with the annihilation of dislocations in the cell walls which become subboundaries (A - B). As recovery continues, the subgrains grow in diameter and the overall dislocation density decreases (C - D) (McQueen and Jonas, 1975).

II.4.2 Static Restoration

Static restoration processes take place by the operation of three distinct mechanisms, static recovery, static recrystallization, and meta-dynamic recrystallization. Static recrystallization occurs when the nucleation and growth of new grains occurs in the absence of straining and stress. Meta-dynamic recrystallization occurs when the nucleation of new grains is initiated dynamically and the subsequent new grain growth occurs statically. During meta-dynamic recrystallization, nuclei are formed during deformation from the strain energy stored during the pre-strain. After deformation, the stored energy is sufficient to drive the continued growth of the new grains. Static recovery is described using Figs. II.3(A - D) and II.4(A-D) from (McQueen and Jonas, 1975). The first sequence of diagrams show the dislocation accumulation during cold-work, deformation at low temperatures. The second sequence of diagrams demonstrates how recovery progresses. Dislocations within cells are attracted into the cell walls and the redundant dislocations annihilate each other. This results in dislocation networks separating the polygonal crystallites, called polygonization. The result of the polygonization phase is a neat dislocation network separating the polygonal crystallites (Leslie *et al.*, 1963 and Vandermeer and Gordon, 1963). The subgrains grow larger as the shared subboundary separating neighboring subgrains is unraveled and the individual dislocations move away and are incorporated into other boundaries (Hu, 1963 and Weissmann *et al.*, 1963). The dislocation walls essentially dissolve with dislocations moving and being incorporated into other boundaries. The macroscopic softening associated with recovery is attributed to the loss of dislocations which were generated and trapped by

obstacles during deformation. The effect of pre-strain in a material increases the kinetics of static recovery (Kwon and DeArdo, 1990). They observed a significant increase in the amount of static recovery which occurs when the pre-strain is increased. The overall activation energy for recovery is often lower than for recrystallization. At low temperatures, recovery occurs as a separate process since the incubation time for recrystallization can be fairly long.

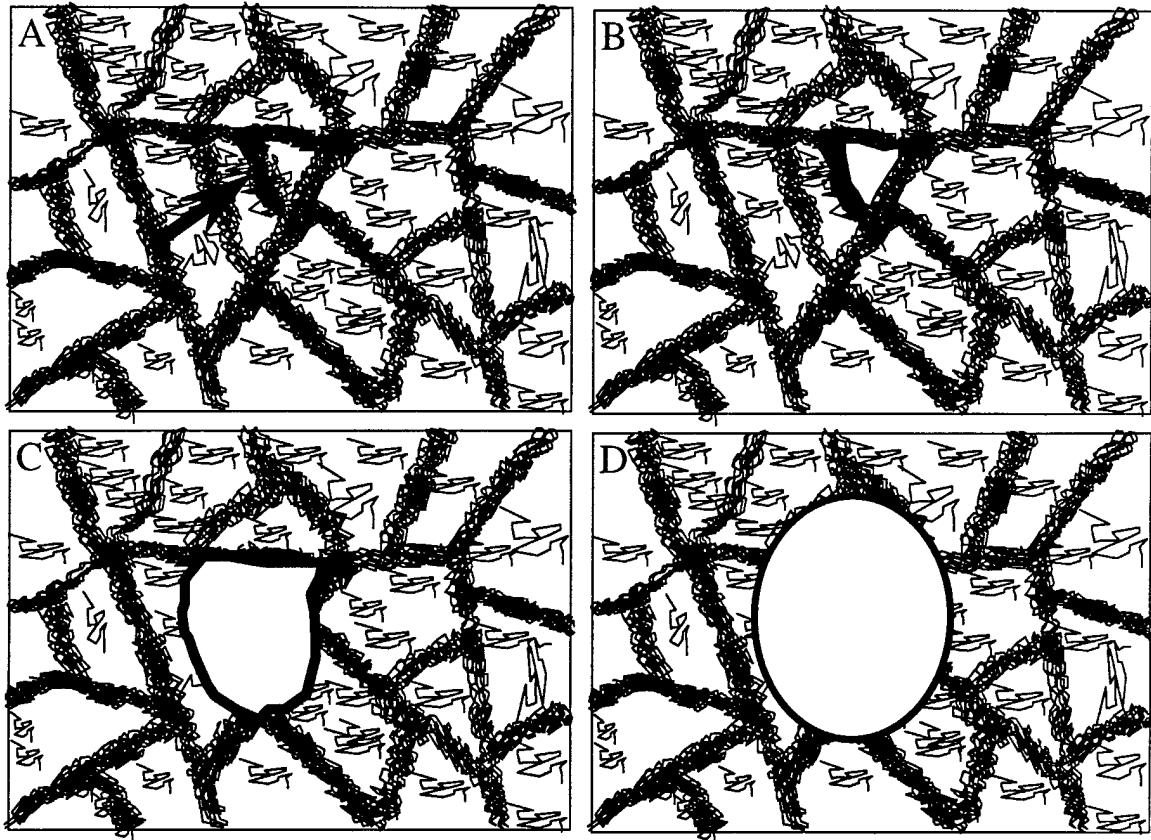


Figure II.5(A - D): Recrystallization. In metals of low SFE, straining creates localized high densities of dislocations. The high misorientation of the cell walls become capable of migrating. The driving force for the migration is provided by the difference in dislocation density between the interior of the new grain and the surrounding worked area (McQueen and Jonas, 1975).

After static recovery has occurred, another and often greater decrease in strength occurs through static recrystallization. Recrystallization results in the formation and growth of new grains which have lower dislocation densities than the worked grains they replace. In low SFE metals, the concentration of dislocations in tangles formed during deformation is high and the cell walls appear to develop high misorientations which promotes the

nucleation sites for new grains. Once nuclei are formed, the new grains grow into the deformed material by the migration of their boundaries. The driving force for the grain growth is provided by the difference in dislocation density between the interior of the new grain and the surrounding deformed material. As the new grains grow, the driving force decreases. The dislocation density in the deformed material has continued to decrease through recovery while the dislocation density in the new grains continue to increase.

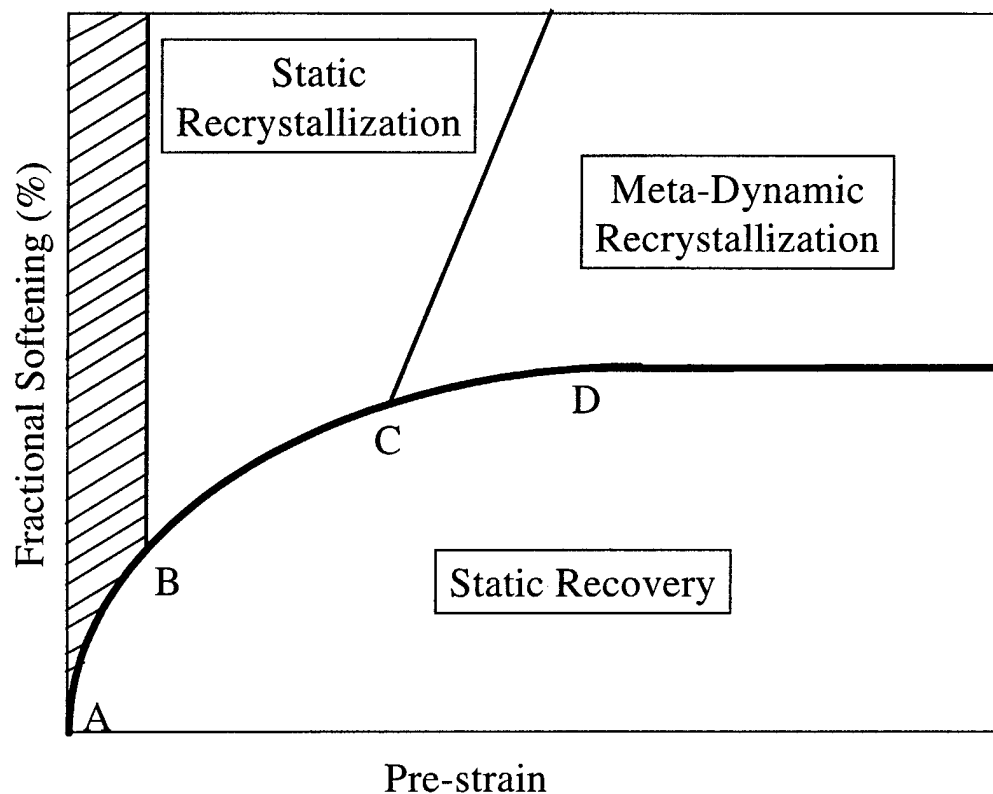


Figure II.6: Categories of static restoration. The proportions of each softening mechanism are shown. On initial straining (A - B), static recovery can occur. At strains above B, which reflects the critical strain for recrystallization, both recovery and recrystallization occurs. C is the strain associated with the peak stress. Between C and D, both meta-dynamic and static recrystallization along with recovery occurs.

McQueen and Vazquez (1986) found that the reload yield stress, after both stress relaxation and unload experiments, drops with time and ultimately becomes as low as the initial yield stress. The relaxation rate was higher during stress relaxation tests than during the unloading tests. They also determined that static recrystallization occurred and coincided with full softening. Static restoration during holding may enhance the rate of dynamic recrystallization during subsequent deformation. Specimens deformed close to the critical strain for the initiation of dynamic recrystallization were then subjected to stress relaxation at various stress levels. At the highest stress levels, the substructure continued to evolve and create nuclei. The resulting recovery in stress relaxation was slower as a result of further hardening events associated with continued forward plastic flow as the stress gradually decreased. The slower decrease in strain energy leads to earlier nucleation and more rapid progress of recrystallization.

II.5 Thermal Activation

Deformation during relatively low temperature and low strain rates is typically dominated by a series of thermally activated mechanisms. These mechanisms are characterized by the rapid decrease in flow stress with increasing temperatures. The motion of dislocations past barriers occur by the nucleation of slip resulting from the bowing out of short dislocation segments resulting from thermal activation.

The rate controlling mechanism for the thermally-assisted motion of dislocations past obstacles is given by the relationship

$$Q = Q_0 - (\tau - \tau_A) V \quad (\text{II.2})$$

where Q_0 is the total energy barrier, τ is the applied shear stress, τ_A is a measure of the long range stresses and V is the activation volume. Figure II.1 shows a profile of the force required to overcome an obstacle. Part of the energy can be provided through the mechanical work done by the applied load. The remainder of the energy can be obtained through thermal activation. At temperatures above 0K, thermal activation assists in the motion of dislocations past obstacles. The value of the applied stress is temperature dependent, given by an Arrhenius expression. Arrhenius processes are very common in the study of materials and is used to model a wide variety of processes.

$$\text{Reaction Rate} = C \exp\left(-\frac{Q}{k T}\right) \quad (\text{II.3})$$

where Q is the activation energy and is the amount of energy that must be supplied to a system in order for the reaction to proceed. The parameter k is Boltzmann's constant, and T is absolute temperature. Activation energy changes during deformation, and is dependent on stress and temperature. During deformation, different mechanisms become dominant under different conditions which forms the basis for the development of deformation mechanism maps (Ashby, 1972 and 1983). Normalized activation energy has been observed

to vary (Follansbee and Kocks, 1988). They conclude that variations of activation energy should be incorporated for best predictions in models. The variation of activation energy will be considered during modeling in Chapter VI.

CHAPTER III

OFHC COPPER EXPERIMENTS

III.1 Introduction

The dependence of flow stress on temperature history was investigated much earlier than either strain rate or deformation path history effects. The range of temperatures required for the observation of temperature history effects was well within the capability of standard laboratory techniques, whereas the variation of strain rates required specialized apparatuses. While temperature sequence experiments were initially conducted, a greater number of experiments are now conducted using sequences of strain rates.

The first sequence experiments involved temperature changes on polycrystalline aluminum loaded in tension at a low constant strain rate (Dorn *et al.*, 1949). Additional temperature sequence experiments were conducted on many f.c.c. metals: Al and Cu by Sylwestrowicz (1958), Al by Hartley and Duffy (1984), and Ni-30%wt Co by Hughes (1986). The transient flow stress, for these temperature sequence experiments, remains between the constant temperature curves. The sequence flow stress does not exhibit a fading memory over the limited subsequent straining of approximately 25%. Temperature sequence experiments were also conducted on these b.c.c. alloys: low carbon steel by Lindley (1965), 1020 HRS by Hartley (1984), and 4340 steel by Tanimura and Duffy (1986).

The b.c.c. alloy transient flow stress reaches a level above the constant lower temperature curve, for a sequence involving a decrease of temperature, and remains above the constant temperature flow stress.

A greater number of experiments have now been conducted involving sequences of strain rates. An advantage of strain rate sequence experiments is the capability of imposing a strain rate change within a short time interval. Temperature sequence experiments necessitate a finite time to achieve changes in temperature. The first experiments involving dynamic strain rates were conducted in compression on aluminum by Lindholm (1964 and 1968). The transient flow stress remains between the two constant strain rate curves and approaches the higher rate curve during low to high strain rate sequences. Numerous investigations have been conducted using the torsional split Hopkinson pressure bar apparatus: Al and Cu by Campbell and Dowling (1970), Al-1100 and 1199 by Nicholas and Whitmire (1970), Al-1100 by Frantz and Duffy (1972), Ni by Gulec and Baldwin (1973), OFHC Cu by Eleiche and Campbell (1974 and 1976), Pb and Cu by Klepaczko and Duffy (1974), OFHC Cu and Al-1100 by Senseny (1977), Cu by Stelly and Dormeval (1977), AISI 316 by Albertini *et al.* (1985), and on OFHC Cu by Follansbee and Gray (1991) and Gourdin and Lassila (1992). The advantage of the torsional split Hopkinson pressure bar test procedure, is the ability to rapidly impose a strain rate change on a specimen. Rise times of about 5 μ seconds have been achieved (Duffy *et al.*, 1971). A low strain rate is applied to one end of the apparatus and a higher strain rate can then be suddenly applied to the other. Another advantage is the avoidance of the radial inertia effects and the geometrical non-

uniformity of straining associated with compression testing. The transient flow stress typically exhibits an initial sharp increase and then gradually approaches the higher rate constant curve. The actual approach to the upper curve is based on extrapolation due to limited subsequent straining after the strain rate sequence.

Experiments which have been conducted on OFHC Cu include strain rate increases from $\dot{\gamma} = 0.0017 \text{ s}^{-1}$ to 520 s^{-1} , at 25°C , 200°C and 400°C in torsion with polycrystalline material with an initial grain size of $53\mu\text{m}$ (Eleiche and Campbell, 1974) and single crystal (Eleiche and Campbell, 1976). Additional torsional experiments have been completed with strain rate increases from $\dot{\gamma} = 0.0001 \text{ s}^{-1}$ to 520 s^{-1} , at -196°C , -125°C , 25°C and 250°C using material with an initial grain size of $35\mu\text{m}$ (Senseney, 1977) and strain rate decreases from $\dot{\gamma} = 460 \text{ s}^{-1}$ to 115 s^{-1} and 690 s^{-1} to 175 s^{-1} at 25°C using material with an initial grain size of $80\mu\text{m}$ (Lipkin *et al.*, 1978). The most extensive experimental program investigating strain rate sequences were conducted using OFHC Cu at room temperature and represented about 600 compression experiments (Follansbee and Kocks, 1988). It was found that the transient flow stress, following a strain rate sequence, exhibits an instantaneous jump, less than half of the difference between the two constant rate curves, and then gradually approaches the constant rate curve.

During the past decade, there have been numerous investigations at strain rates above 10^4 s^{-1} . These high strain rates are achieved through shock loading and pressure-shear experiments (Clifton, 1990, Tong, 1991, Follansbee and Gray, 1991, Sakino and Shioiri, 1991, Gourdin and Lassila, 1992, Tong and Clifton, 1992, Klepaczko *et al.*, 1993, Shioiri *et*

al., 1994, Sakino and Shioiri, 1996, and Frutschy and Clifton, 1998).

The experimental program reported here is believed to be the most comprehensive involving sequences of temperature, strain rate, and deformation paths, using the same material and initial microstructure. This same material was also used for sequences of deformation path experiments conducted by Graham (1995) and reported by Horstemeyer (1995). The experimental results presented here are organized as follows. Experimental procedures are first described, including techniques for sequencing path, strain rate, and temperature. Next, experimental results are presented for a wide range of conditions. Finally, implications are discussed.

III.2 Experimental Procedures

Compression and free-end torsion experiments were conducted on initially annealed OFHC Cu across a range of temperatures (25°C to 676°C) and constant true strain rates (quasi-static - 0.0004 s^{-1} to dynamic - 6000 s^{-1}), along with sequences involving different temperatures, strain rates, and deformation paths. The purpose of these experiments was to obtain a comprehensive experimental data set for the evaluation of current modeling approaches and the subsequent development of improved constitutive relations for predicting strain rate and temperature history effects. OFHC Cu was selected for this research due to previous experimental data obtained on similar OFHC Cu, which this data set supplements, and the importance of this material as a shaped charge liner for explosively formed projectiles.

III.2.1 Material

Oxygen-free high conductivity (OFHC) f.c.c. copper (99.99 % pure) was selected for this investigation. It has been rather widely studied under isothermal, constant strain rate deformation. Copper has a low to moderate stacking fault energy that serves to reduce the rate of dynamic recovery which creates the conditions necessary for recrystallization (McQueen, 1975 and Sellars, 1979). The melting point of copper is $T_m = 1356\text{K}$. The material was furnished in 51 and 76mm diameter extruded bar stock. The large specimens, 50.8 mm Lindholm and 70.8 mm diameter compression, were machined from the larger stock. The remaining specimens were machined from the small stock. All specimens were machined such that their axis of symmetry was parallel to the axis of the bar. Initial specimen configurations are given in Table III.1. All references herein to specimen "type" will refer to this table.

After initial machining, the copper was annealed at 600°C for four hours in vacuo and then quick cooled at room temperature. This is the same annealing schedule as the copper used in experiments reported by Graham (1995) and Horstemeyer (1995) (Fig. III.1). The resulting grain size was measured. An annealed specimen was cut to reveal a circumferential cross-section. The material was mounted in epoxy, polished, and etched. The average grain diameter was then determined optically using the average grain intercept method (Underwood, 1970). This heat treatment resulted in an average grain diameter of $62\text{ }\mu\text{m}$ with a standard deviation of $4\text{ }\mu\text{m}$. Figure III.2 shows sample regions magnified 50X and 100X. The initial material texture is shown in Fig. III.3 for a surface normal to the

compression specimen axis. The texture is essentially random, with the maximum intensity of 4.74 (times random, normalized to a random intensity of 1.0). Ideally, the intensity of an initially untextured, random sample would be 1.0 and uniform, but small intensity peaks with a maximum intensity of 5.25 are common (cf. Bronkhorst *et al.*, 1992).

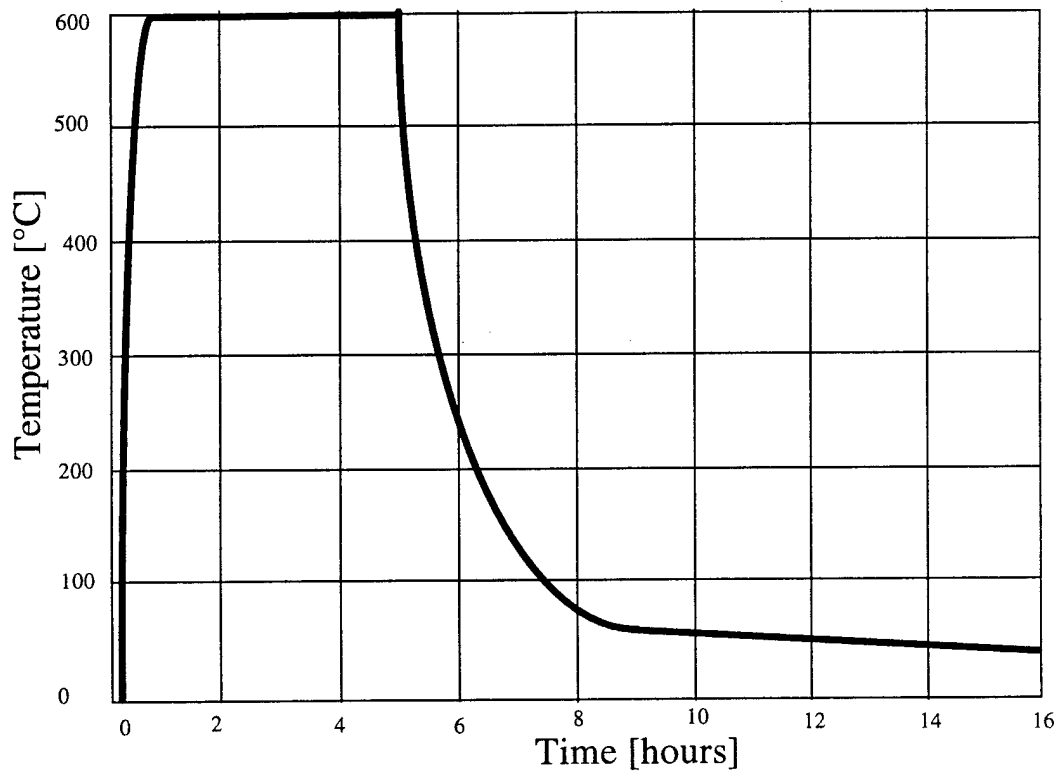


Figure III.1: Annealing schedule for OFHC copper.

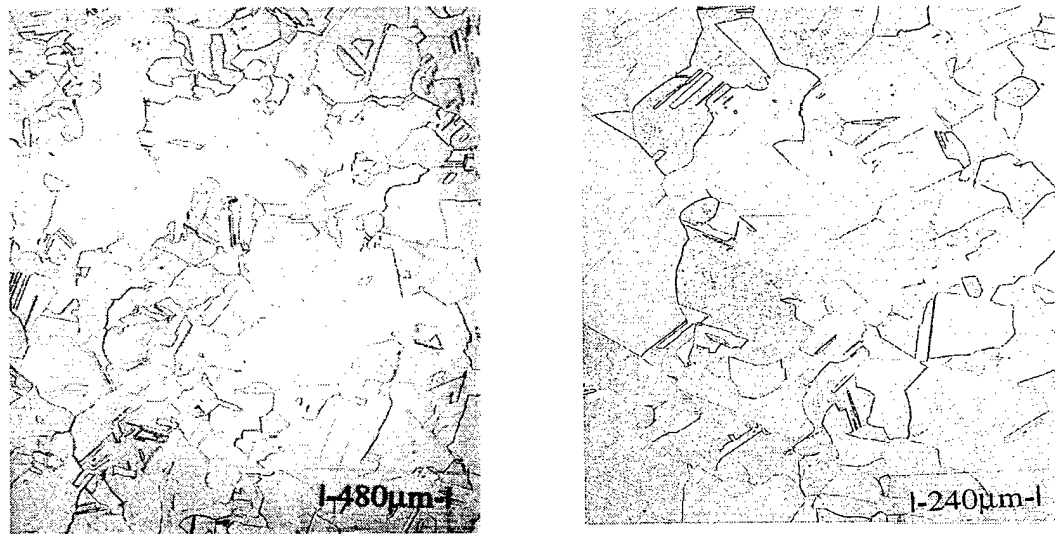


Figure III.2a,b: Micrographs of the initial grain structure of annealed OFHC Cu material (50 and 100 magnification).

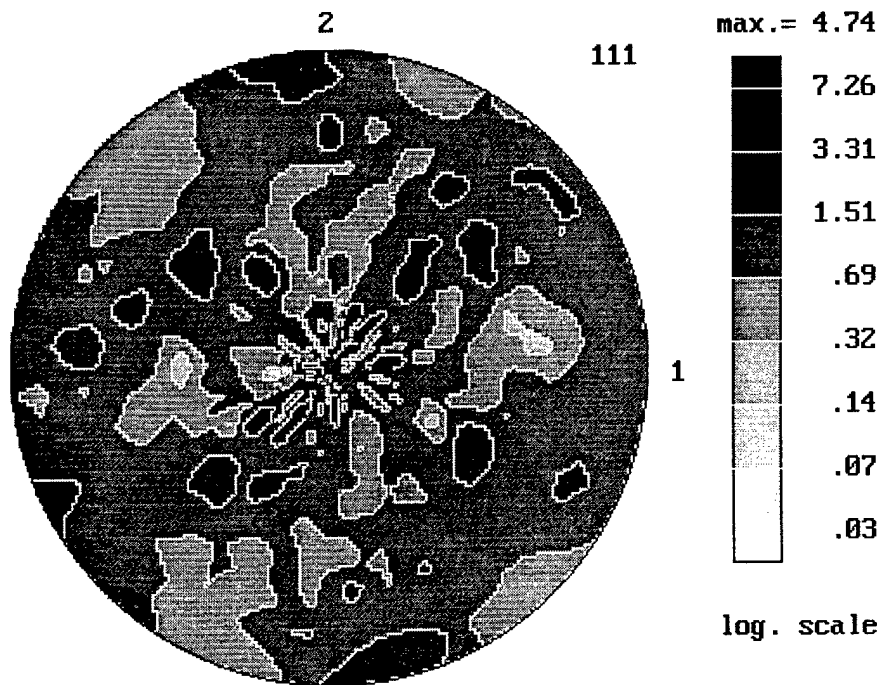


Figure III.3: Initial texture of annealed OFHC Cu material. Pole figure for (111) orientation.

Table III.1: SPECIMEN CONFIGURATION

Type	Test	Size (mm)	Ends	Type	Sequence Test	Sequence Size (mm)
1	High	8.89 x 4.45	Polished	1a	Comp	7.62 x 7.62
				1b	Double Shear	2.54 x 7.62
2	Comp	10.16 x 15.24	Grooved			
3	Comp	30.48 x 45.72	Grooved	3a	Comp	10.16 x 15.24
				3b	Shear	25.4 x 27.94
4	Comp	71.12 x 106.68	Grooved	4a	Comp	10.16 x 15.24
				4b	Shear	50.8 x 63.5
				4c	Rev C/T	6.78
5	Shear	50.8 x 203.2				
6	Rev C/T	6.78				

III.2.2 Test Matrices

A series of experiments was conducted to fully characterize OFHC Cu. These comprehensive experimental matrices were developed to obtain material behavior over a range of conditions including different temperatures, strain rates, and sequences of temperature, strain rate, and path. The completed experiments are shown in the following tables. They include isothermal and constant true strain rate tests, restoration experiments characterizing both static recovery and recrystallization, as well as, dynamic recovery and

recrystallization, and experiments involving various sequences of deformation paths, temperatures, and strain rates.

III.2.2.1 Constant True Strain Rate and Isothermal Experiments

Table III.2: COMPRESSION: STRAIN, STRAIN RATE AND TEMPERATURE EFFECTS

Trial #	Specimen Type	Loading	Constant True Strain Rate (s^{-1})	Temperature ($^{\circ}C$)	True Strain
A1	2	Compression	0.0004	25	0.5
A2	2	Compression	0.0004	25	1.0
A3	2	Compression	0.0004	134	1.0
A4	2	Compression	0.0004	202	1.0
A5	2	Compression	0.0004	236	1.0
A6	2	Compression	0.0004	269	0.5
A7	2	Compression	0.0004	269	1.0
A8	2	Compression	0.0004	286	1.0
A9	2	Compression	0.0004	303	1.0
A10	2	Compression	0.0004	337	1.0
A11	2	Compression	0.0004	405	1.0
A12	2	Compression	0.0004	541	0.5
A13	2	Compression	0.0004	541	1.0
A14	2	Compression	0.01	25	1.0
A15	2	Compression	0.01	269	1.0
A16	2	Compression	0.01	541	1.0
A17	2	Compression	1.0	25	1.0
A18	2	Compression	1.0	269	1.0
A19	2	Compression	1.0	541	1.0
A20	1	Compression	6000	25	0.4
A21	1	Compression	5200	269	0.4

Table III.3: TORSION EXPERIMENTS: STRAIN AND TEMPERATURE EFFECT
(von Mises equivalent true strain rate and true strain are shown).

Trial #	Specimen Type	Path	Strain Rate (s⁻¹)	Temperature (°C)	Strain
T1	5	Torsion	0.0004	25	1.0
T2	5	Torsion	0.0004	100	1.0
T3	5	Torsion	0.0004	269	1.0
T4	5	Torsion	0.0004	405	1.0

III.2.2.2 Restoration Experiments

Table III.4: STATIC RESTORATION: LOAD, UNLOAD, HOLD, RELOAD
EXPERIMENTS

(Conducted in compression at 0.0004 s^{-1} . Hold time after pre-strain.)

Trial #	Specimen Type	Constant True Strain Rate (s^{-1})	Temperature ($^{\circ}\text{C}$)	Hold Time (seconds)
D1	2	0.0004	269	30
D2	2	0.0004	269	120
D3	2	0.0004	269	600
D4	2	0.0004	541	30
D5	2	0.0004	541	120
D6	2	0.0004	541	600
D7	2	0.0004	676	30
D8	2	0.0004	676	120
D9	2	0.0004	676	600

Table III.5: DYNAMIC RESTORATION: LOAD, HOLD, AND RELOAD
EXPERIMENTS
(Conducted in compression at 0.0004 s^{-1}).

Trial #	Temp (°C)	Hold Control	# of Increments	Hold Time (min)	True Strain Levels
E1	25	Load	1	20	0.5
E2	25	Load	1	20	1.0
E3	25	Stroke	1	20	
E4	25	Load	4	10	0.3, 0.5, 0.7, 1.0
E5	25	Stroke	3	10	0.3, 0.5, 0.7
E6	269	Load	1	20	
E7	269	Stroke	2	60	0.5, 1.0
E8	269	Load	2	60	0.5, 1.0
E9	269	Stroke	4	10	0.3, 0.5, 0.7, 1.0
E10	405	Stroke	3	50	0.1, 0.2, 0.3
E11	405	Stroke	4	17	0.3, 0.5, 0.7, 1.0
E12	405	Stroke	2	15	0.3, 0.5

III.2.2.3 Sequence Experiments

Table III.6: QUASI-STATIC (0.0004 s^{-1}) TWO STEP TEMPERATURE SEQUENCE
(von Mises equivalent true strain rate and true strain are shown).

Trial #	Initial Loading	Type	Initial Temp °C	Initial Strain	Final Loading	Final Temp °C	Final Strain
B1	Compression	4	25	0.5	Compression	269	1.0
B2	Compression	4	25	0.5	Torsion	269	1.0
B3	Compression	3	269	0.5	Compression	25	1.0
B4	Compression	3	269	0.5	Torsion	25	1.0

Table III.7: HIGH RATE (1000 s^{-1}), FOLLOWED BY QUASI-STATIC (0.0004 s^{-1})
TWO STEP STRAIN RATE SEQUENCE
(von Mises equivalent true strain rate and true strain are shown).

Trial #	Initial Loading	Type	Initial Temp °C	Initial Strain	Final Loading	Final Temp °C	Final Strain
C1	Comp	1	25	0.4	Comp	25	1.0
C2	Comp	1	25	0.4	Shear	25	1.0
C3	Comp	1	25	0.4	Comp	269	1.0
C4	Comp	1	25	0.4	Shear	269	1.0
C5	Comp	1	269	0.4	Comp	25	1.0

Table III.8: STRAIN RATE CHANGE SEQUENCE EXPERIMENTS
(Compression at 269C.)

Trial #	Constant True Strain Rate (s^{-1})	Specimen Type	True Strain	Constant True Strain Rate (s^{-1})	Specimen Type	Total True Strain
S1	0.0004	3	0.5	0.1	2	1.0

Table III.9: REVERSE PATH EXPERIMENTS
(von Mises equivalent constant true strain rate and true strain are shown.
All strain rates were $0.0004 s^{-1}$.)

Trial #	Initial Path	Type	Temp ($^{\circ}C$)	Strain	Final Path	Type	Temp ($^{\circ}C$)	Strain
R1	Comp	4	25	0.3	Torsion	5	25	1.0
R2	Comp	4	25	0.5	Torsion	5	25	1.0
R3	Comp	4	25	0.5	Torsion	5	100	1.5
R4	Comp	4	25	0.5	Torsion	5	269	1.5
R5	Torsion	5	25	0.5	Torsion	5	25	-0.5
R6	Torsion	5	25	1.0	Torsion	5	25	-1.0
R7	Torsion	5	269	1.0	Torsion	5	269	-1.0
R8	Torsion	5	405	1.0	Torsion	5	405	-1.0
R9	Tension	6	25	0.1	Comp	6	25	-0.1
R10	Tension	6	25	0.25	Comp	6	25	-0.25
R11	Comp	6	25	0.1	Tension	6	25	-0.1
R12	Comp	6	25	0.13	Tension	6	25	-0.13
R13	Comp	6	25	0.17	Tension	6	25	-0.17
R14	Comp	4	25	0.5	Comp	6	25	0.55

Table III.10: CONTINUOUSLY VARYING TEMPERATURE AND/OR STRAIN RATE EXPERIMENTS.

(All experiments were conducted in compression to a true strain of 1.0).

Trial #	Initial Temperature (°C)	Final Temperature (°C)	Initial Strain Rate (s ⁻¹)	Final Strain rate (s ⁻¹)
V1	25	25	0.0004	0.1
V2	25	25	0.1	0.0004
V3	405	405	0.0004	0.1
V4	405	405	0.1	0.0004
V5	405	350	0.1	0.0004
V6	405	250	0.0004	0.1
V7	405	50	0.0004	0.0004
V8	25	450	0.0004	0.0004

III.2.3 Experimental Procedures

Experiments were performed at the Georgia Institute of Technology's, Mechanical Properties Research Laboratory (MPRL) and at Sandia National Laboratory (SNL) in Livermore, California. All compression specimen design, fabrication, and experiments were performed at SNL, and all torsional tests were conducted in the MPRL. Two different compression test apparatuses were used at SNL. Quasi-static strain rate experiments for $\dot{\epsilon}$ ranging from 0.0004 s⁻¹ to 1.0 s⁻¹ were performed using high capacity MTS closed-loop servo-hydraulic test machines. High strain rate experiments were obtained using a modified

split Hopkinson pressure bar apparatus. The experimental set-up for low and then high strain rate experiments are described, followed by that utilized for torsion experiments. Temperature control apparatuses are also described.

III.2.3.1 Compression Experiments

The advantages and difficulties of the compression test are well established (ASTM STP 808, 1983, ASTM Standard E209-65, 1983, and Miller, 1993). As compared to tension tests, larger strains can be achieved in compression due to the absence of necking. Another advantage is the simplicity of fixtures and specimens for compression tests. The main disadvantage is the difficulty of accomplishing homogeneous deformation. Uniform deformation is achieved by reducing the effects of friction between the specimen and the compression platens.

III.2.3.1.1 Quasi-static (Low) Strain Rate Experiments

III.2.3.1.1.1 Quasi-static (Low) Strain Rate Test Apparatuses

The low constant true strain rate and isothermal (Table III.2), as well as, the static thermal restoration (Table III.4) experiments, were conducted using a MTS Model 309.40 (110 kip) servo-hydraulic test machine (Fig. III.4). The actuator was controlled using displacement feedback using signals generated from a MTS Micro console 458.20, which resulted in a constant true strain rate compression test. Load, stroke, temperature, and

extensometer data were collected using a Nicolet 440 digital oscilloscope. Load and displacement data were converted into engineering stress (σ_a) and axial engineering strain (ϵ_a). True axial strain (ϵ_t) and true axial stress (σ_t) were then calculated as

$$\epsilon_t = \ln(1 + \epsilon_a) \quad \text{and} \quad \sigma_t = \sigma_a(1 + \epsilon_a) \quad (\text{III.1})$$

Strain was determined using the stroke data from the MTS machine. These stroke data were corrected for test machine compliance. A correction factor was determined for each of the test temperatures. The actual strain was calculated by subtracting the test machine compliance from the displacement of the actuator. A MTS extensometer, modified for use within the three-zone furnace during elevated temperature tests, was used to verify the accuracy of this correction (Fig. III.5). The corrected strain data compared precisely with the data obtained using the extensometer.

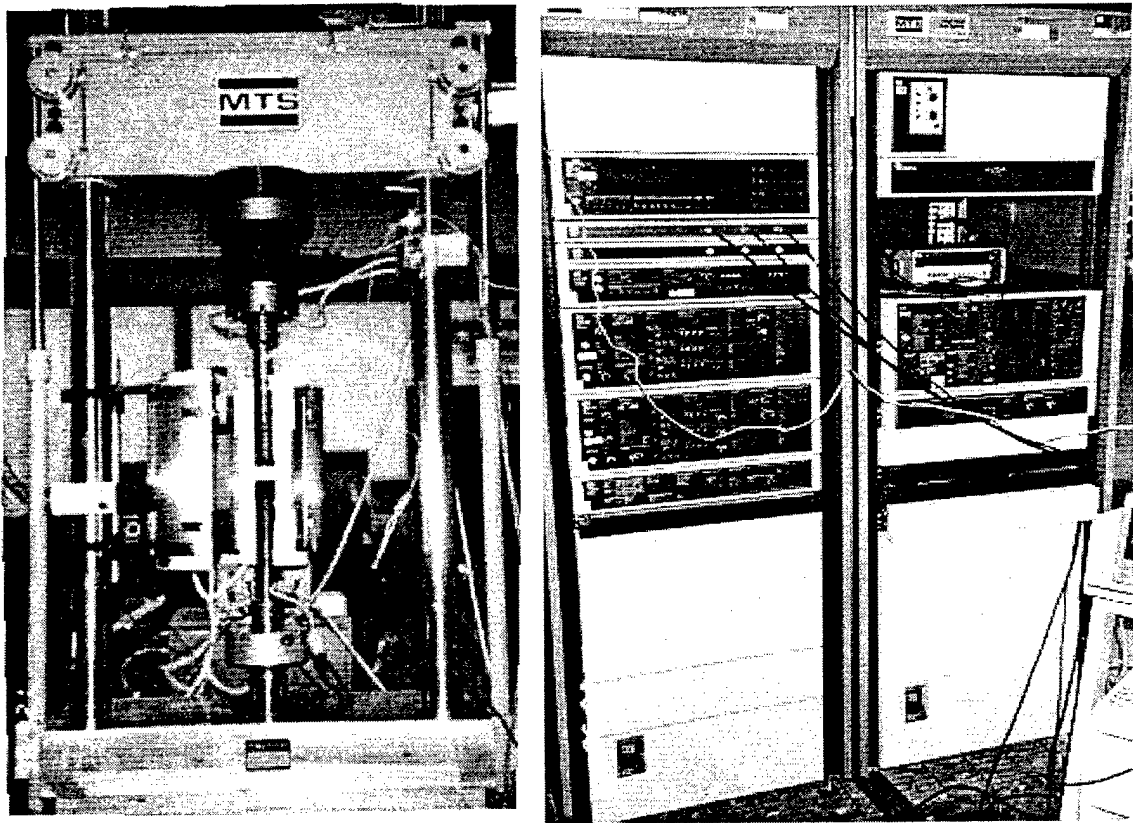


Figure III.4: MTS servo-hydraulic test machine and controller at SNL.

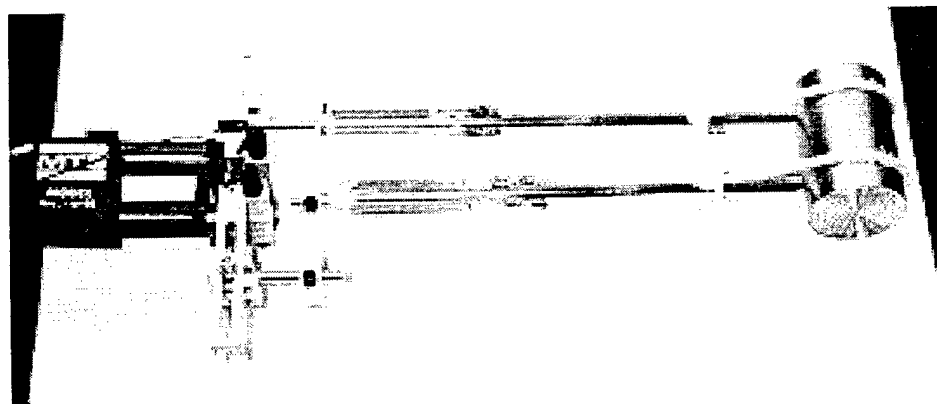


Figure III.5: MTS extensometer modified for use within a three-zone furnace.

Continuously varying temperature and/or strain rate experiments (Table III.10) were conducted on a MTS 810 200 kip test frame with a 20 kip load cell and controlled with a MTS 880 controller under computer control (Fig. III.6). The actuator was controlled in displacement control using a file playback procedure which incremented the displacement position command every second. This resulted in a constant true strain rate compression experiment. Type 2 compression specimens were used. The series of temperature and strain rate sequence experiments included sequences of constant variation in either temperature or strain rate and combinations of variation in both temperature and strain rate. Strain rate changes were accomplished by incrementing the true strain rate every 0.05 of true strain. The resulting increasing strain rate is shown in Figs. III.7 and III.8. The greatest temperature changes were achieved by preheating the furnace and specimen to the higher temperature, 405°C. The specimen temperature was then varied by cooling the apparatus using forced air. Only large temperature decreases were accomplished due to the thermal mass of the system. Temperature increase experiments were completed, but the amount of increase was less than the amount of change achieved during temperature decreases. Temperatures were recorded during all temperature change experiments using a digital recorder. Thermal expansion of the test apparatus, including primarily the changes in the push rod lengths, was measured and used to correct the recorded stroke data. Additionally, a machine compliance correction was measured at each temperature and the appropriate correction also made.

A series of load, hold and reload experiments (Table III.5) were also completed using the 200 kip MTS test frame. Compression specimens, type 2, were utilized for these

experiments. Two different control procedures were utilized during the hold periods to observe the effects. Hold times were enforced under either load control, during which the load was maintained at a constant value, or stroke control, during which the crosshead stroke position was held constant.

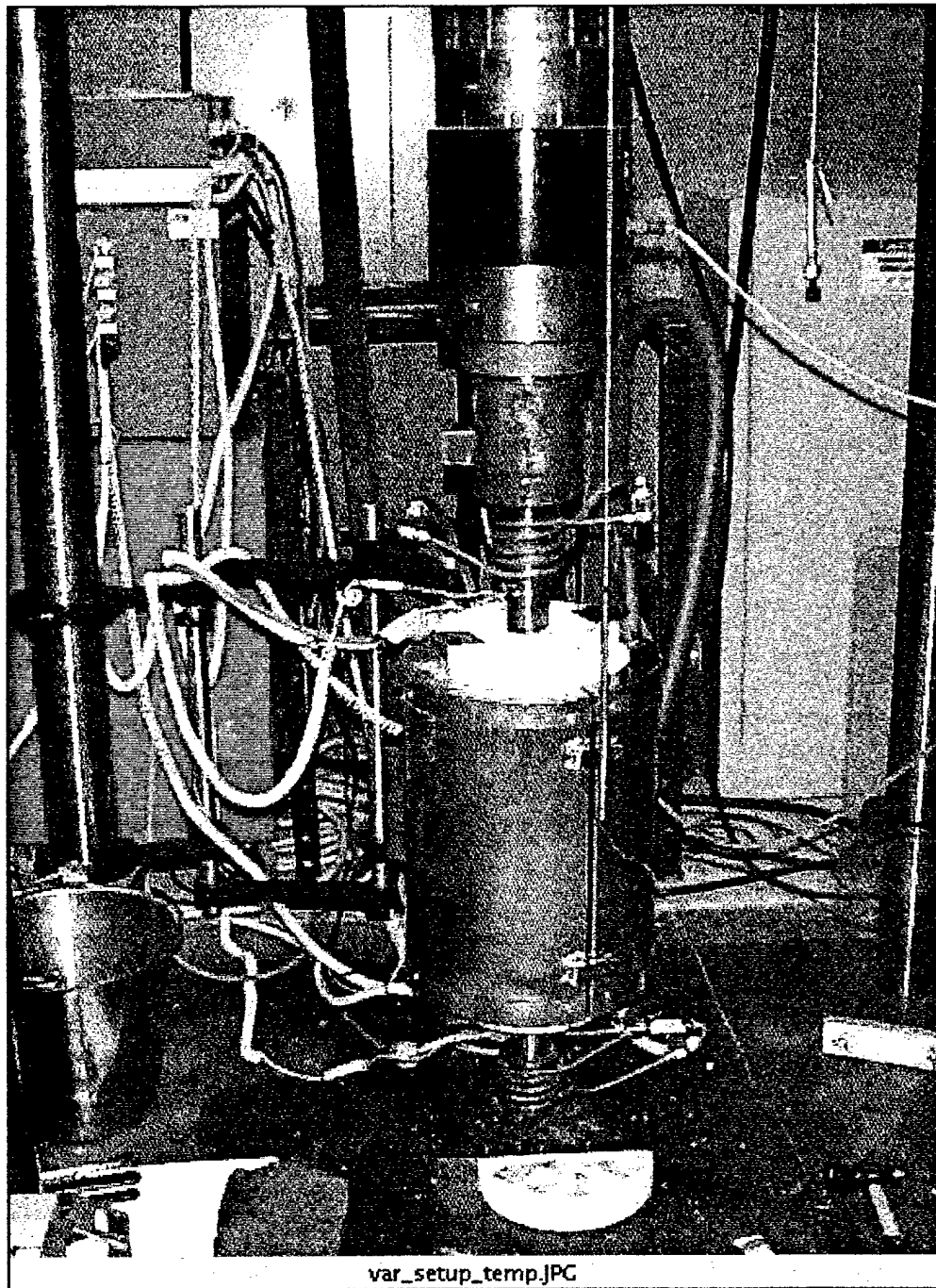


Figure III.6: MTS 810 Test machine at SNL used for continuously varying temperature and strain rate experiments and load, hold, and reload experiments. Three-zone furnace used for elevated temperature experiments is shown mounted.

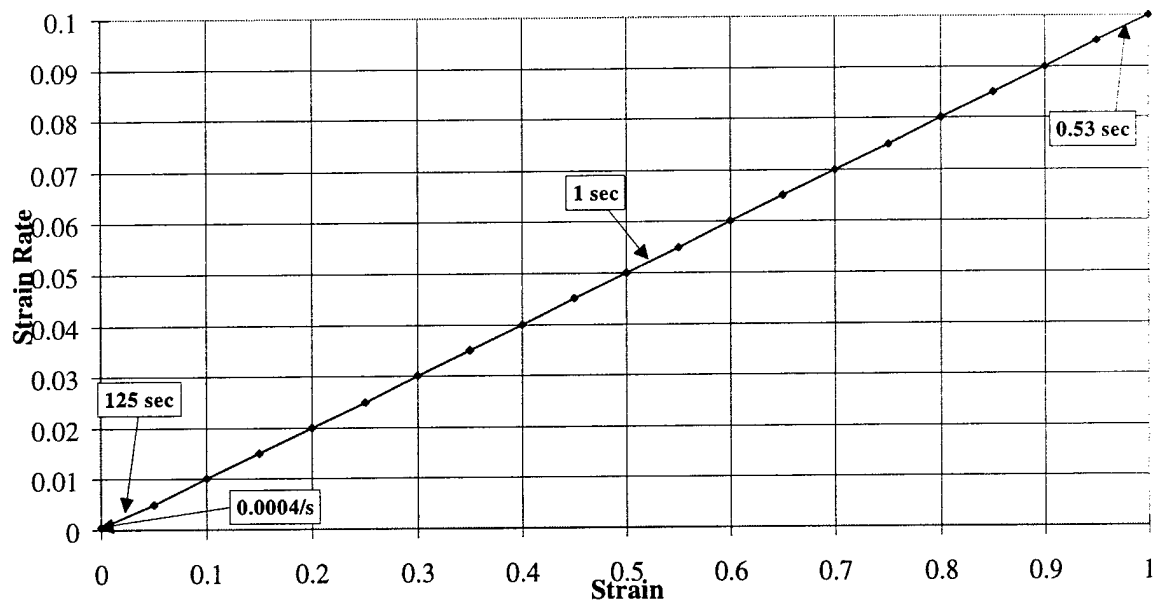


Figure III.7: True strain rate for strain rate variation sequences in compression (vs strain).

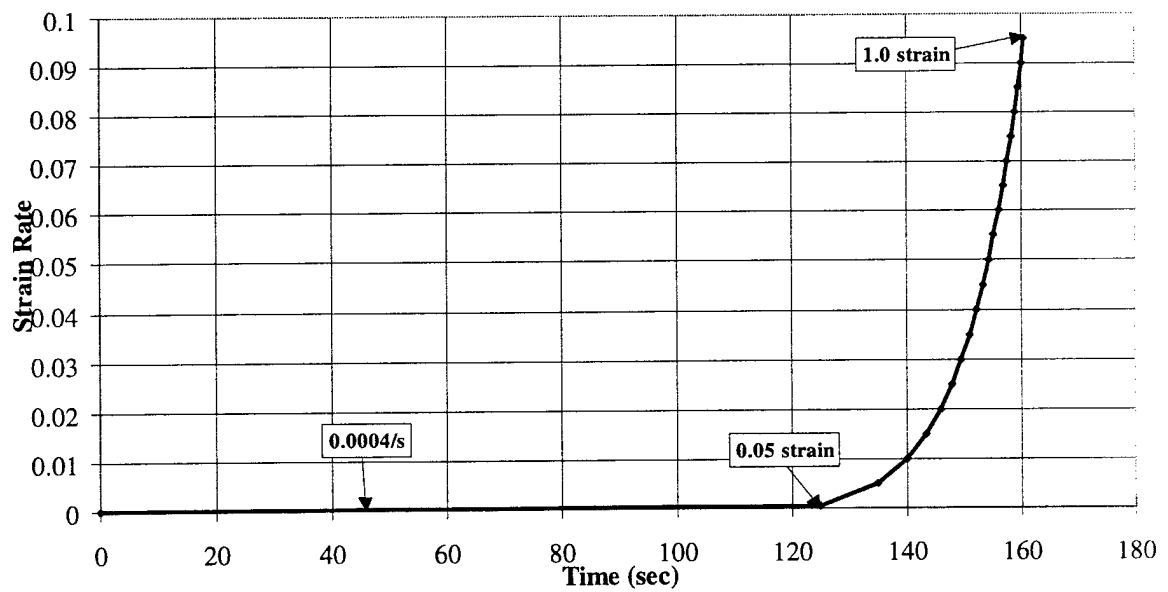


Figure III.8: True strain rate for strain rate variation sequences in compression (vs time).

III.2.3.1.1.2 Quasi-static (Low) Strain Rate Specimens

Type 2 compression specimens were used for these experiments. All low strain rate compression specimens had a height-to-diameter ratio of 1:1.5. Uniform material deformation was obtained by reducing the friction between the specimen and the compression platens. Hastelloy and Kennometal, part number K313, lapped to a mirror finish were used for the compression platen material since they could be easily polished to maintain a smooth compression surface and to distribute the specimen contact load evenly over the cross section of the push rods. Concentric grooves were machined into the ends of the specimens to hold special lubricants, depending upon the strain rate and temperature as shown in Figs. III.9 and III.10. At low strain rates, an oil-based molybdenum disulfide lubricant was used from 25°C to 134°C, an oil-based silver lubricant was effective from 200° to 300°C, and a powdered glass with boron nitrate was used above 300°C. The particular lubricants used at different test temperatures are listed in Table III.11. Lubricant was placed in the grooves on the specimen ends. The center three grooves were not lubricated on the larger specimens, types 3 and 4, to provide an "anchor" point at the specimen center. The specimen sides were coated to prevent oxidation during elevated temperature tests. The grooves retain lubricant during compression and release it as the hydrostatic pressure in the grooves increases allowing the specimen ends to radially expand. This specimen configuration works well in promoting homogenous deformation in compression. Typical copper compression specimens before and after an isothermal, constant true strain rate compression to a true strain of 0.5 and 1.0 are shown in Fig. III.11. The deformed specimens

are still cylindrical, with no barreling resulting from side roll-over which would occur if there were significant friction between the specimen ends and the compression platens. Homogenous deformation is obtained using this method.

Table III.11: COMPRESSION SPECIMEN LUBRICANT

Temp ° C	0.0004 s ⁻¹	0.01 s ⁻¹	1.0 s ⁻¹	1000 s ⁻¹
25	Molykote GN paste	Molykote GN paste	Silver Goop	Molykote GN paste
202	Silver Goop			
269	Silver Goop	Silver Goop	Molykote GN paste	Molykote GN Paste
303	Silver Goop			
337	Silver Goop			
541	.5m/.5BN/side	.5m/.5BN/side	.5m/.5BN/side	Silver Goop
676	.25m/.375h/.375BN/side			

Where: m = CF 7570 Ferro Electronic Glass

h = F 3227 Ferro Electronic Glass

BN = boron nitride (mixed into paste with isopropyl alcohol)

side = coating of the specimen sides with Delta Glaze 153

Molykote = oil-based molybdenum disulfide lubricant

Silver Goop = oil-based silver lubricant

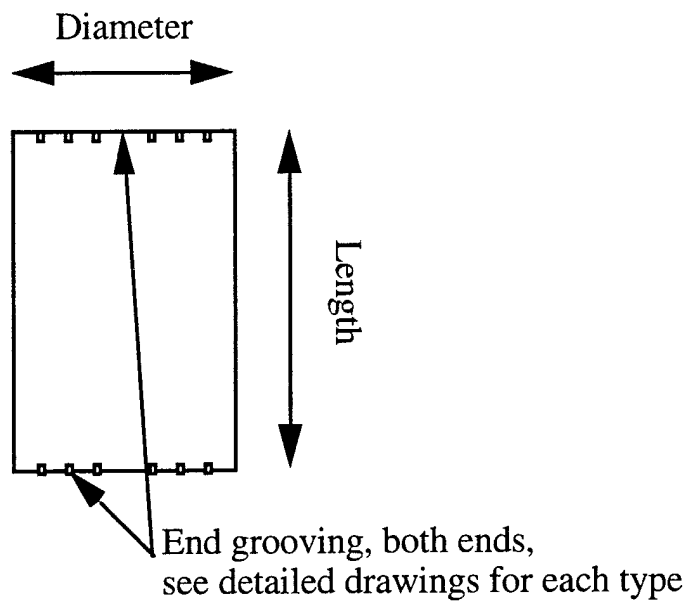


Figure III.9: Compression specimen detail.

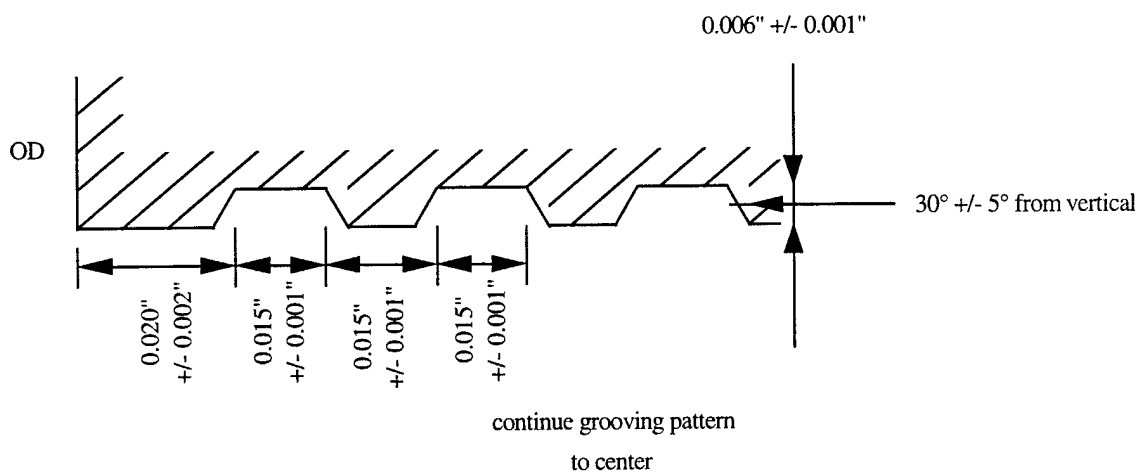


Figure III.10: Compression specimen end grooving details.

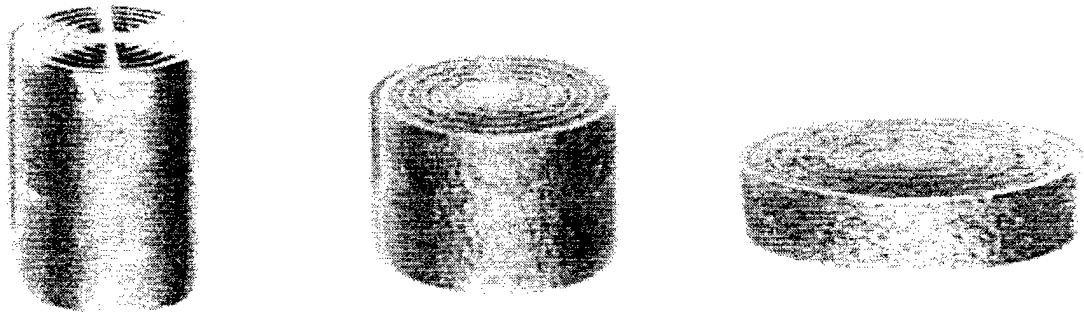


Figure III.11: Typical compression specimens (true strain):
 (left - no strain middle - 0.5 strain right - 1.0 strain).

III.2.3.1.1.3 Homogeneous Compression

Achieving uniform specimen deformation during compression experiments is difficult. Friction between the specimen ends and platens cause barreling (Hockett, 1959), when specimen side roll over occurs, and hour-glassing, when specimen ends deform more than the middle. Two measures of nonuniform deformation are the percent barreling and barreling rate. These measures use the diameter of the specimen and are defined as follows:

$$\begin{aligned} \% \text{ barreling} &= \frac{D_{\text{middle}} - D_{\text{end}}}{D_{\text{middle}}} \\ \text{barreling rate} &= \frac{D_{\text{middle}} - D_{\text{end}}}{D_{\text{middle}} - D_{\text{initial}}} \end{aligned} \quad (\text{III.2})$$

Examples of barreling and hour-glassing are shown in Fig. III.12. These specimens were obtained while determining the optimal lubricant and specimen groove details for each temperature and strain rate combination. Figure III.13 shows the material response for different non-uniform deformations. The barreling measurements were calculated after each experiment. Only the results of those specimens with deformations of % barreling less than 2.0 and barreling rates less than 5.0 are presented in this thesis.

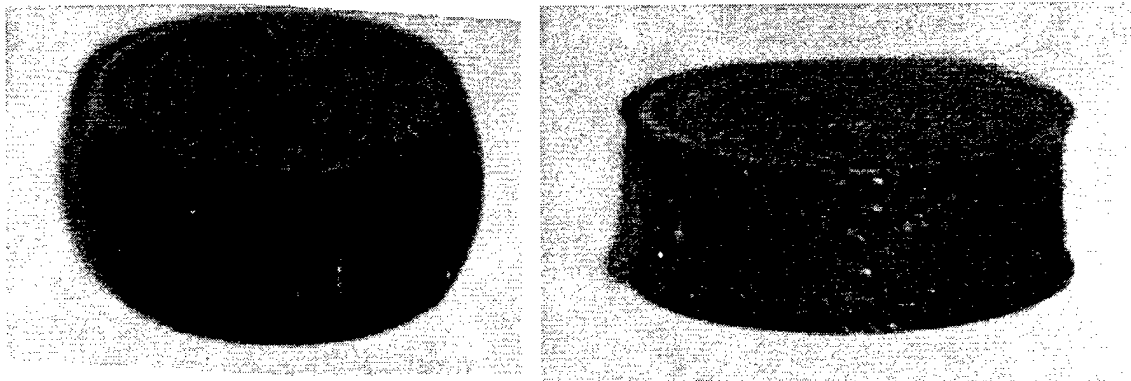


Figure III.12: Examples of non-uniform deformation: Barreling (left) and hour-glassing (right).

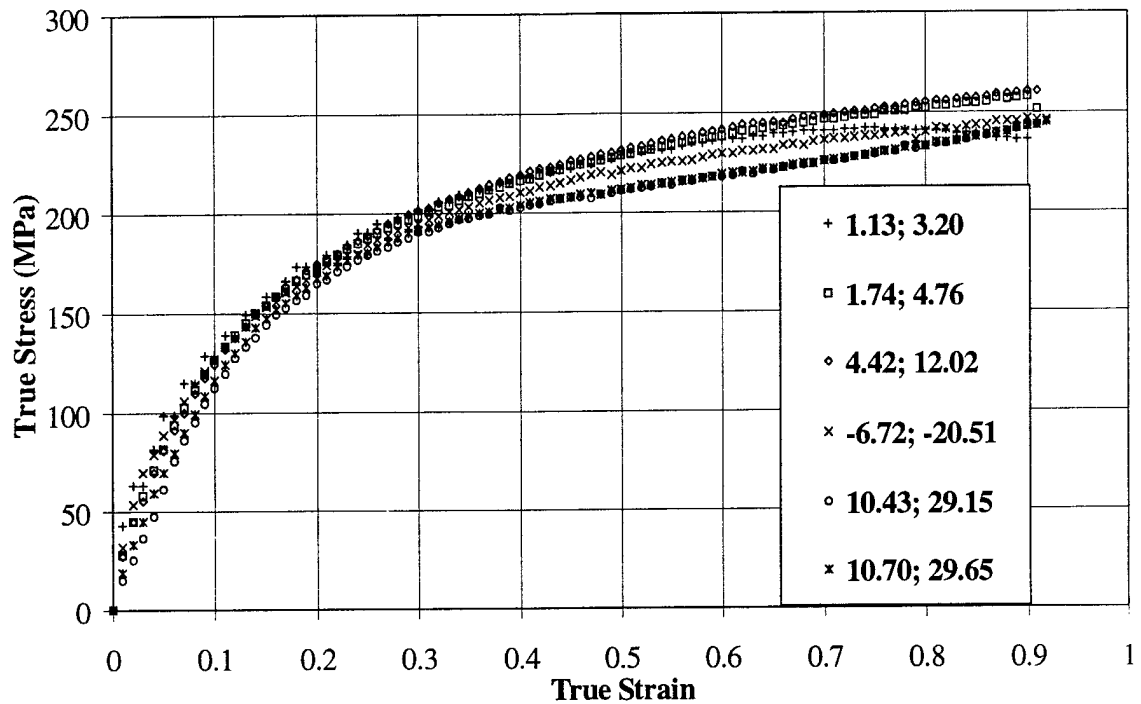


Figure III.13: Effect of barrelling on flow stress of copper. The % barrelling and barrelling rates are given in the legend.

III.2.3.1.2 High Strain Rate Experiments

High strain rate uniaxial compression experiments were conducted using a modified split Hopkinson pressure bar apparatus. The specimen was placed between the two, 76.2 cm long, elastic pressure bars which were instrumented with strain gages. A schematic of the apparatus is shown in Fig. III.14, and is pictured in Fig. III.16. The incident wave was generated by propelling the striker bar using compressed gas. Strain rate within the specimen is directly proportional to the amplitude of the reflected wave in the incident bar which is measured by strain gage A. Stress in the specimen is directly proportional to the

amplitude of the transmitted wave, measured by strain gage B. Figure III.17 shows a sample result. Both the incident and transmitted signal from the strain gages are shown. Data were reduced from the strain gage voltages using the procedures described by Follansbee and Frantz, 1983, Frantz *et al.*, 1985, and Davies and Hunter, 1963. Strain rates of magnitude 10^3 were obtained. Friction between the specimen and bars was reduced by using polished specimens and lubrication. At low temperatures, an oil-based molybdenum disulfide lubricant was used. At temperatures between 200°C and 350°C, an oil-based silver lubricant was used. Errors due to radial and axial constraint in a rapidly deforming solid cylinder are minimized if the aspect ratio of the specimen is chosen such that

$$\frac{L}{d} = \left(\frac{3\nu_s}{4} \right)^{\frac{1}{2}} \quad (\text{III.3})$$

where L and d are the specimen length and diameter respectively (Follansbee, 1985). When a Poisson ratio of 1/3 is used, a L/d aspect ratio of 1/2 results, which is the value utilized for the Hopkinson bar specimens used in this research.

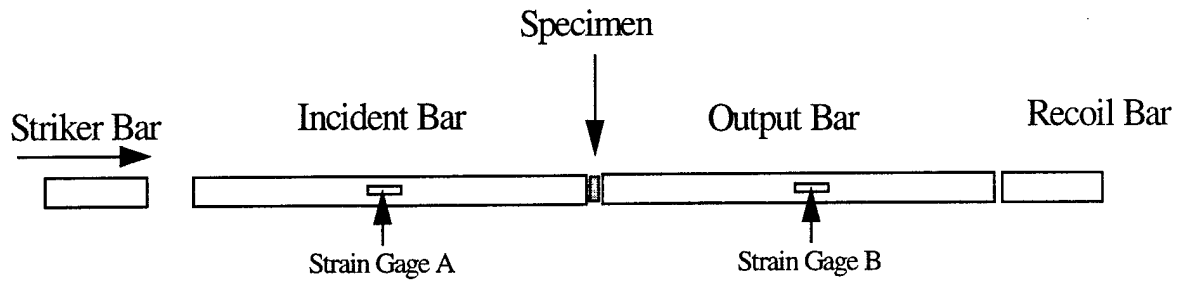


Figure III.14: Configuration of the Hopkinson Bar.

Elevated temperature experiments were conducted using a 5.0 kW Ameritherm induction heater. Specimen temperature was controlled using a thermocouple placed between the specimen and the pressure bar. Details of the actual test setup are shown in Fig. III.15. The pressure bars are maintained at low temperature by using a water cooling system.

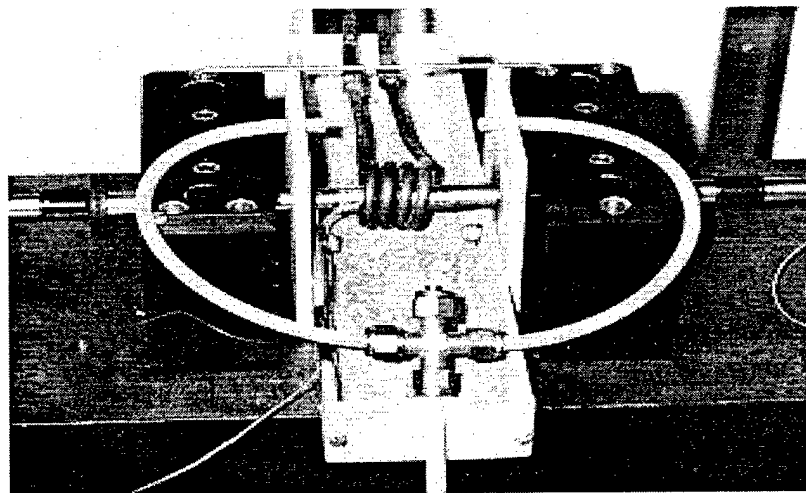


Figure III.15: Hopkinson bar experimental setup. Induction heater coil and water cooling system are shown.

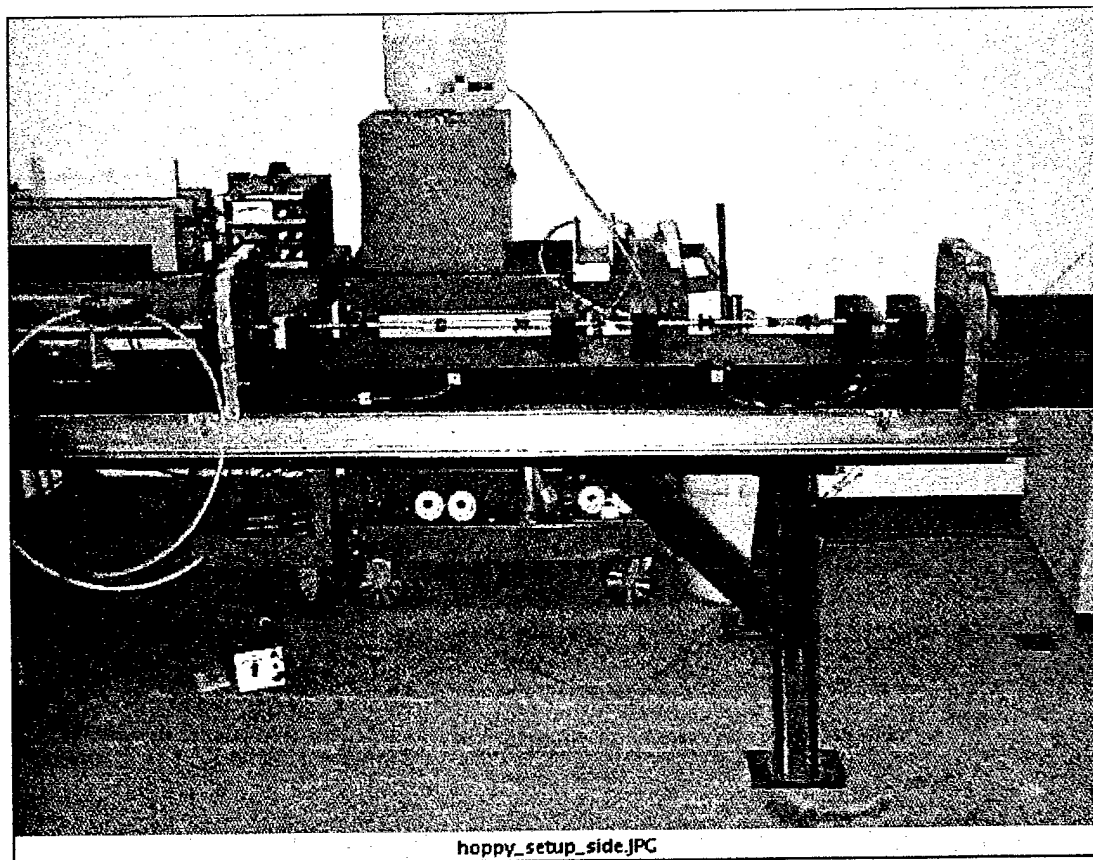


Figure III.16: Configuration of the modified split Hopkinson pressure bar apparatus at SNL.

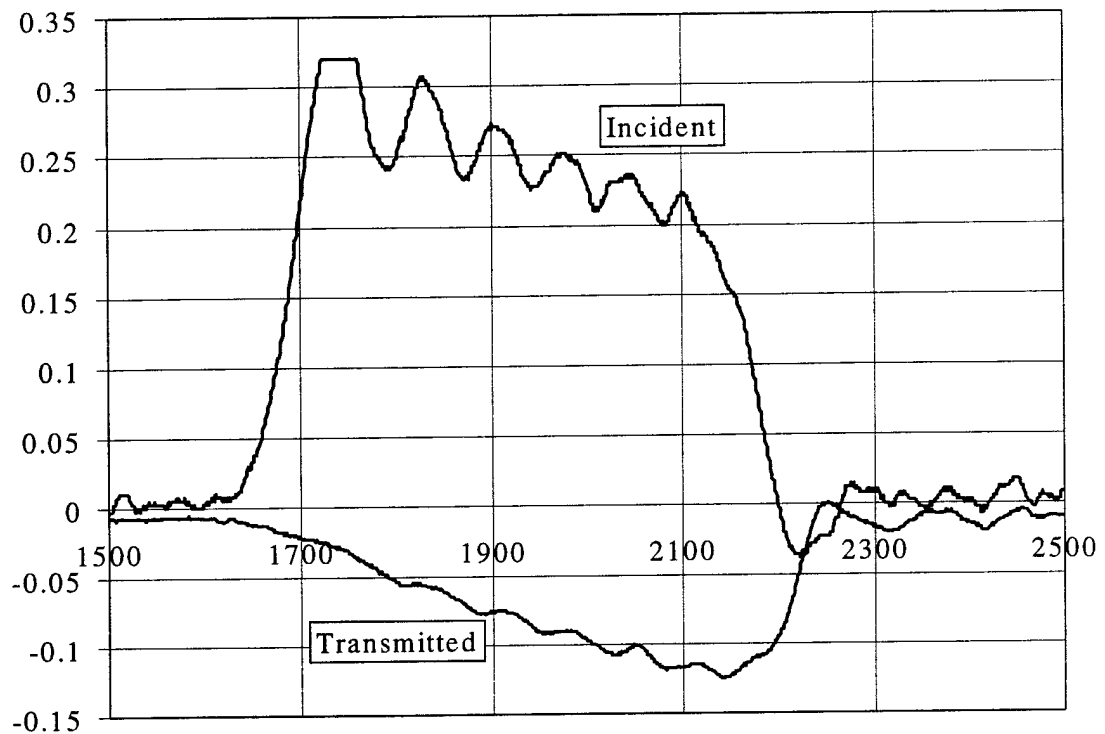


Figure III.17: Sample Hopkinson bar experimental results showing the strain gage measurements from the incident and transmitted bars.

III.2.3.2 Quasi-static Torsion Experiments

Quasi-static torsional experiments were all conducted at the MPRL and are listed in Table III.3. Experiments were performed at various temperatures to determine the temperature dependencies and for comparison with compression experimental results. Experiments were performed using an MTS closed loop axial-torsional servo-hydraulic test machine with simultaneous axial and torsional control. Specimens were gripped with a

hydraulic grip system using either 25.4 mm or 50.8 mm collets. All torsional experiments were conducted free-end, the axial load was maintained at zero. The rotation angle, θ , and the torque, T , were measured using the servo-hydraulic ram's rotary variable differential transformer (RVDT) and a torsional load cell. The experiments were controlled and the data collected using an MTS Test Star controller.

The design of the thin walled torsion specimens was adapted from a design developed by Lindholm (Lindholm *et al.*, 1980). These specimens, type 5, limit the deformation to the gage section even at large strains. A high degree of uniformity of shear strain is maintained in the gage section. Figures III.18 and III.19 show a drawing and picture of a 50.8 mm diameter Lindholm specimen. Since the specimens were hollow, the ends of the specimens were plugged with stainless steel, using a weak interference fit, to resist significant inelastic deformation during gripping. A gripping pressure of 24 MPa (3500 psi) was used. The inserts extended from the specimen ends to the beginning of the beveled shoulder region. The resulting gage section is 6.35 mm in length and 2 mm thick. A line spanning the thickness of the gage section wall would intercept an average of thirty grains. The usual assumption when using a short, thin-walled gage section is that the shear strain is confined to the gage section of the specimen, and the shoulder and bevel region of the specimen are assumed rigid. A three-dimensional finite element analysis conducted by Miller (1993) showed that no obvious rotational deformation occurred within the bevel regions of the specimen at the strain levels of interest here. This observation was verified using scribed lines, parallel to the specimen axis, on the specimen gage section and bevel region. The

assumption of homogenous deformation in the gage section permits definition of the engineering shear strain γ , according to

$$\gamma = \frac{\frac{1}{2}(r_o + r_i)\theta_g}{g_o} \quad (\text{III.4})$$

where θ_g is the angle of rotation of the top of the gage section relative to the bottom, g_o is the initial gage length of the specimen, r_i is the inner radius of the gage section, and r_o is the outer radius. The shear stress, assumed uniform, is given by

$$\tau = \frac{3T}{2\pi(r_o^3 - r_i^3)} \quad (\text{III.5})$$

where T is the torque.

A machine compliance correction was made for the shear strain measurements, since the angle of twist between the grips, not within the actual gage section, was measured by the RVDT. The beveled region of the specimen was assumed to remain elastic and to be the main contributor to the additional strain outside of the gage section. The compliance correction, as determined by Graham (1995), was applied to all torsional experiments.

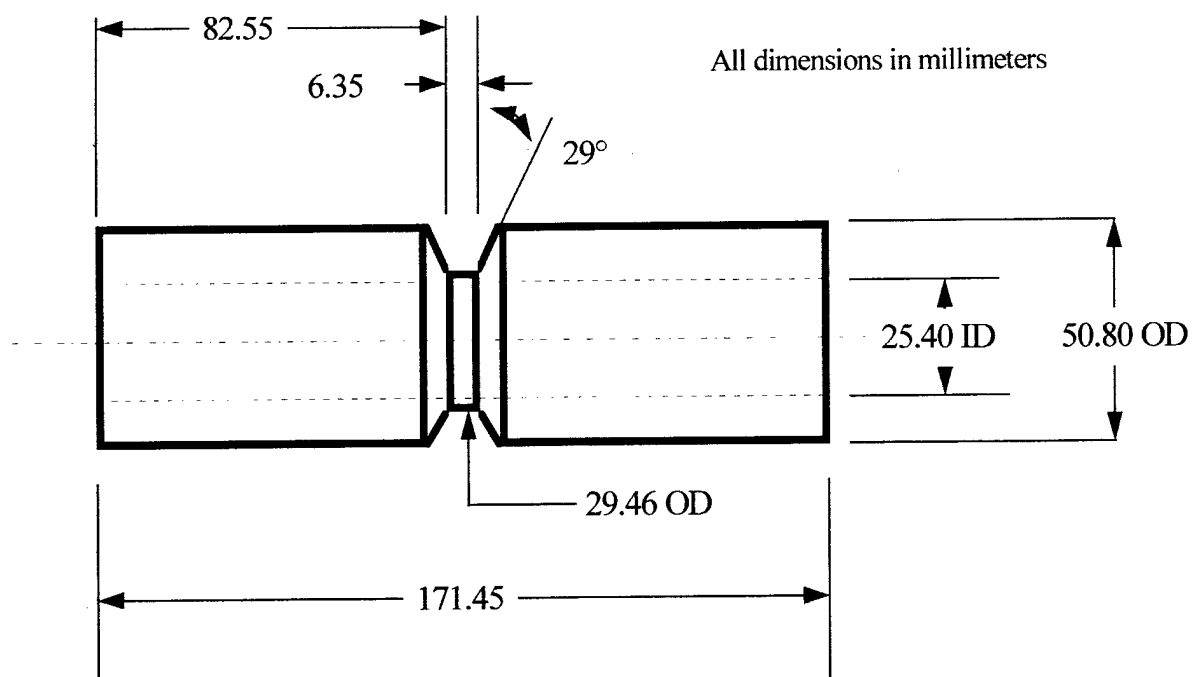


Figure III.18: Drawing of a 50.8 mm diameter Lindholm specimen. All dimensions are in mm.

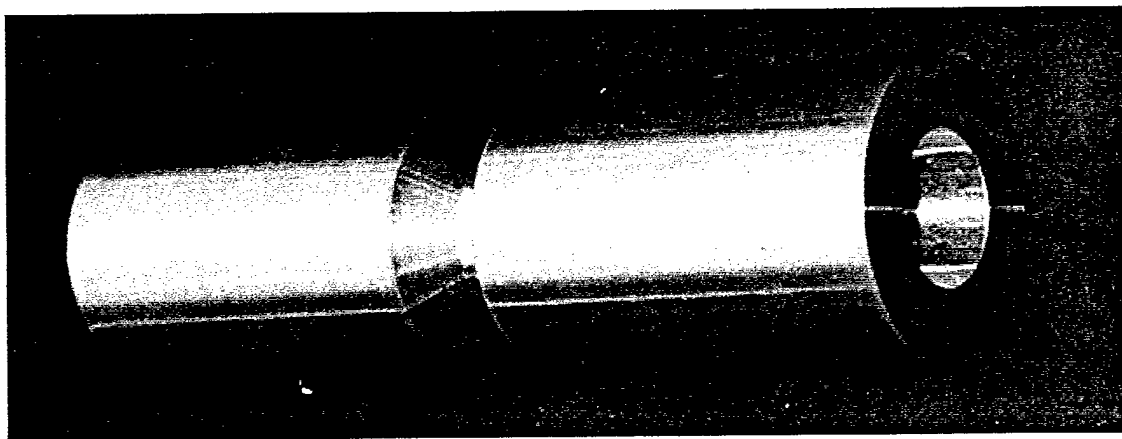


Figure III.19: 50.8 mm diameter Lindholm specimen before deformation.

III.2.3.3 Specimen Temperature Histories

Many experiments were conducted above room temperature. Three-zone furnaces and induction heaters were used to heat the specimens to the desired temperature. At lower strain rates (0.0004 s^{-1} to 1.0 s^{-1}) in compression, elevated temperature experiments were achieved with a three-zone furnace capable of heating to 1100°C . Additionally, heaters were installed in the 50.8 mm diameter Inconel push-rods and controlled using a digital temperature controller. Temperature was controlled to $\pm 1^{\circ}\text{C}$ using three thermocouples mounted in the furnace and two in each push rod. Specimen temperature was monitored and recorded during compression using a spring-loaded contact thermocouple. Elevated temperature split Hopkinson pressure bar experiments were conducted using a 5.0 kW induction heater. Specimen temperature was controlled using a thermocouple placed between the specimen and the pressure bar. The pressure bars are maintained at low temperature by using a water cooling system. Elevated temperature torsion experiments were conducted using either a 2.5 kW induction heater (Fig. III.21) or a three-zone furnace. Due to the high conductance of OFHC copper, steel susceptors (Fig. III.22) were used along with the induction heater to raise the temperature of the specimens. Elevated temperature experiments using a three-zone furnace required the creation of grip extensions, such that only the specimen was inside the furnace, allowing the hydraulic grips to be outside the furnace. These grip extensions were machined using 70.8 mm 1020 HRS bar stock. Temperature was controlled using thermocouples attached to the specimen gage section. Specimen gage section temperature was maintained to $\pm 3^{\circ}\text{C}$ during constant temperature

tests. During elevated temperature sequence testing, specimens were heated until they reached the desired uniform temperature. The amount of time spent at elevated temperature increased the amount of static restoration; therefore the time was minimized, and was just long enough for the specimen to reach uniform temperature. Figure III.20 shows the average specimen temperature history during increases to 269°C from the time it was inserted into the furnace and the decreases from 269°C after removal from the furnace. The initial temperature increase is primarily radiative heat transfer, while the steep slope beginning at 30 seconds includes the effects of conduction resulting from the specimen ends being in contact with both push rods. Specimen temperature was recorded during *all* tests for purposes of thermomechanical modeling.

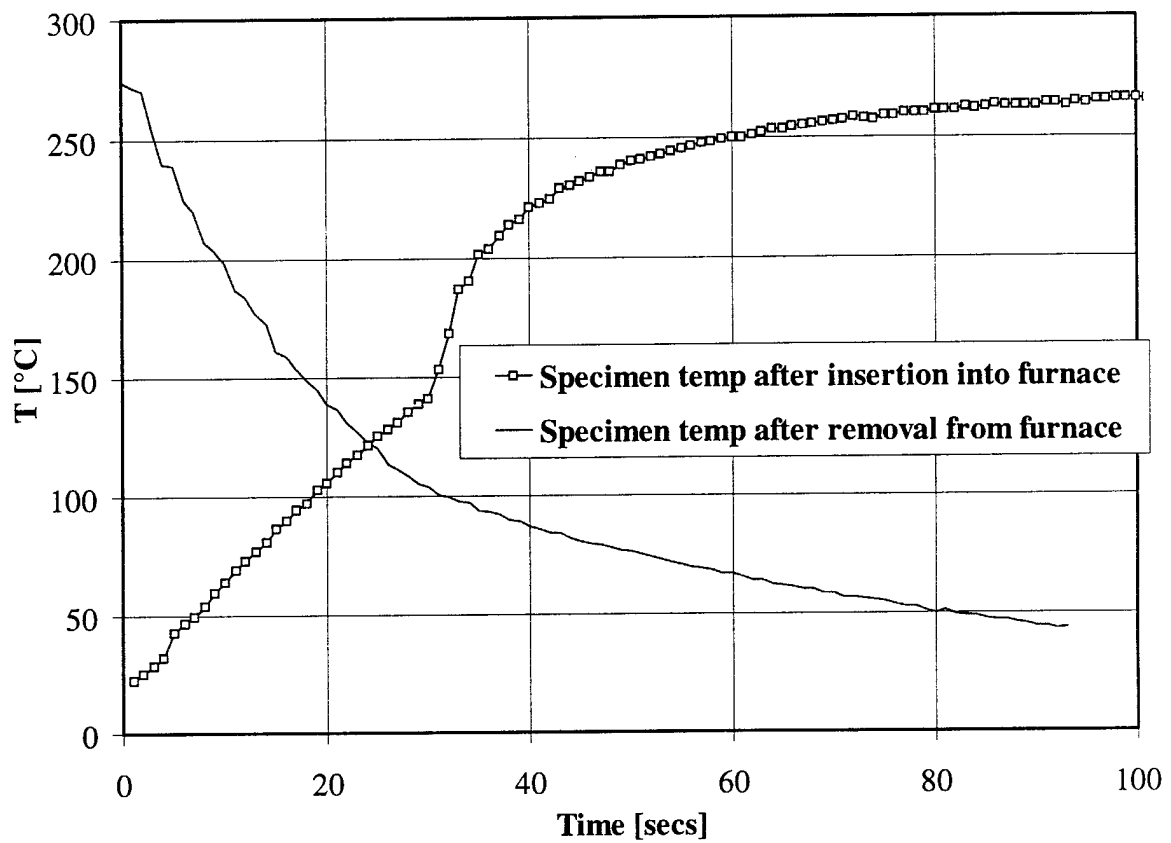


Figure III.20: Specimen temperature response after insertion into three-zone furnace at 269°C and after removal from three-zone furnace at 269°C.

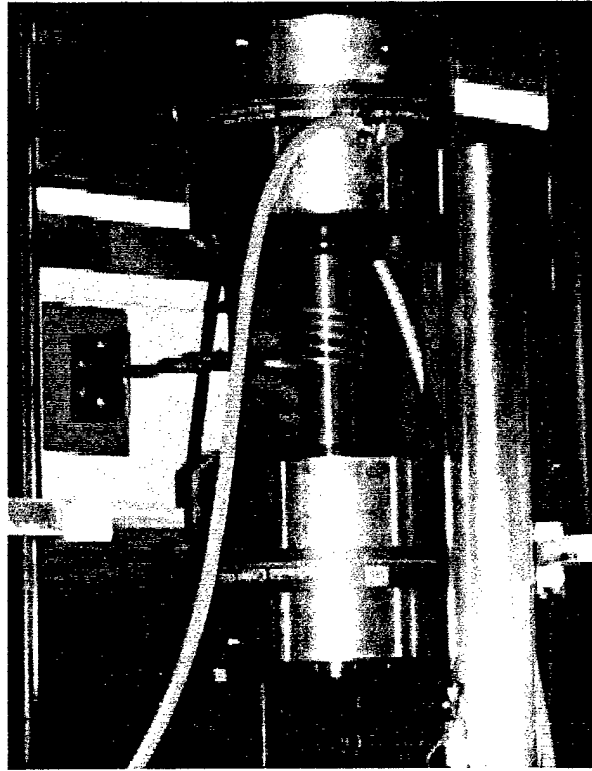


Figure III.21: MTS Servo-Hydraulic test machine with 2.5kW induction heater at MPRL.

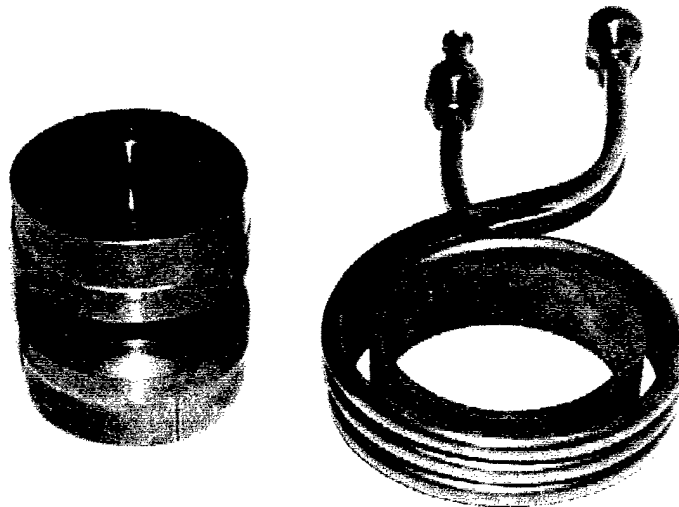


Figure III.22: 50.8 mm Lindholm copper specimen with induction heater coil and steel susceptor.

III.2.3.4 Sequence Experiments

A series of sequence experiments was conducted (Table III.6 - III.10). These sequence experiments were completed to identify the transients in flow stress curves which result from the history effects due to prior deformation. A series of strain rate change experiments was completed. These included sequences of high rate deformation followed by low rate at various temperatures, and from quasi-static strain rate to higher rates also at various temperatures (Table III.7). The initial deformation at high strain rate was applied using a split Hopkinson pressure bar apparatus at SNL. The results for the isothermal, constant high strain rate reflects an average of approximately fifteen different experiments. Subsequent sequence experiments involving quasi-static strain rates and both 25°C and 269°C were conducted using a MTS servo-hydraulic machine. These second sequence specimens were obtained using three split Hopkinson pressure bar specimens (Type 1). Each split Hopkinson pressure bar specimen surface was machined flat with grooves added to the outside ends. The three specimens were then bonded together using a ceramic glue (Fig. III.23). The glued specimen was pressed while drying so that the glue thickness was less than 25.4 μm . The bonded specimen was then machined such that the final diameter was equal to the final height. Machining was accomplished slowly, so that the specimen temperature did not increase, with material removal during the last three passes at a rate of less than 76.2 μm per turn to prevent additional work hardening. Completed specimens are shown in Fig. III.24.

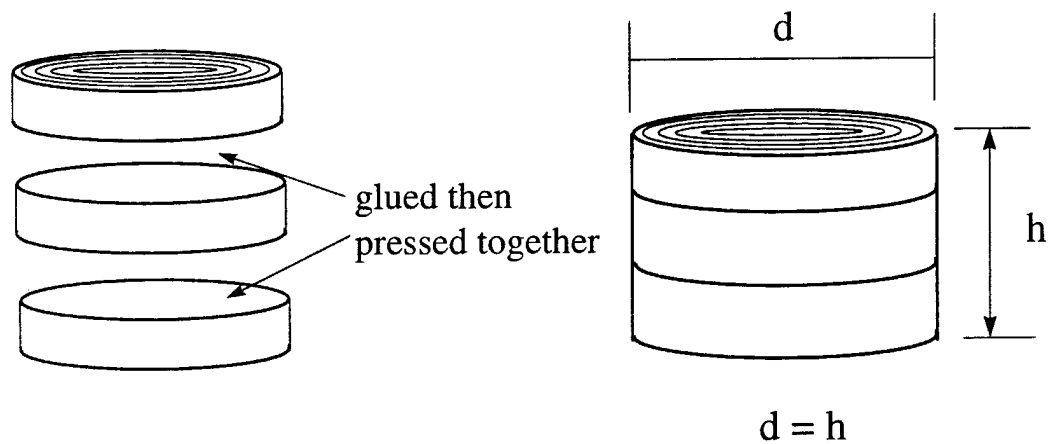


Figure III.23: Diagram of the second phase sequence specimens (quasi-static following high strain rate).

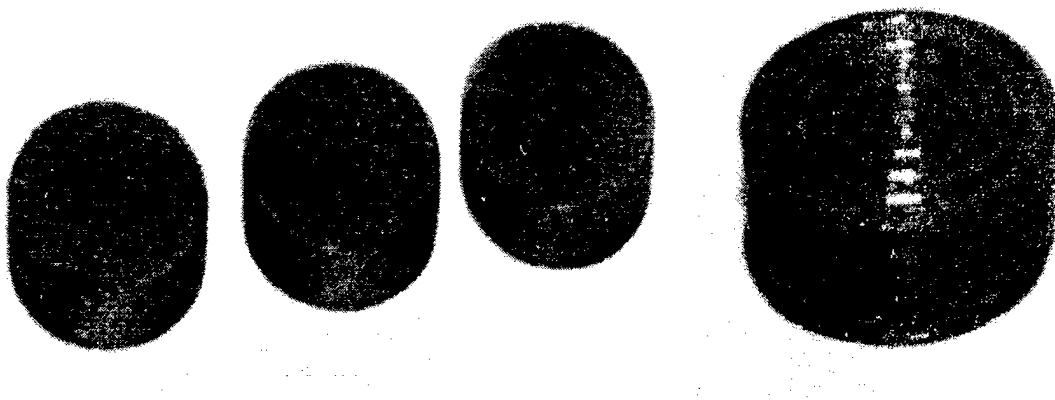


Figure III.24: Picture of three pre-strained Hopkinson bar specimens (left) which are then made into the quasi-static compression specimen (right - shown after compression).

Reverse path experiments were completed in torsion and compression/tension (Table III.9). Torsion (type 5) specimens were used. The torsion path direction reversal was accomplished without removing the specimen from the test machine apparatus. The reverse path compression/tension specimen design is shown in Fig. III.25. Path sequence experiments were conducted using two different procedures. The first process used a large compression specimen, type 4, (71.12 mm x 106.68 mm) which was compressed at 25°C with a strain rate of 0.0004 s^{-1} to 0.5 strain using a 10M pound MTS test frame (Fig. III.27). Reverse path specimens, type 6, were then machined out of this material using electro-discharge machining (EDM) and subsequently tested in both tension and compression. The second process utilized the specimen, type 6, design shown in Fig. III.25. The specimens were annealed after initial machining. These specimens were tested using sequences of compression and tension without removal from the test machine. Reverse path compression experiments were conducted on a MTS 880 test frame (Fig. III.28) controlled using a Test Star controller.

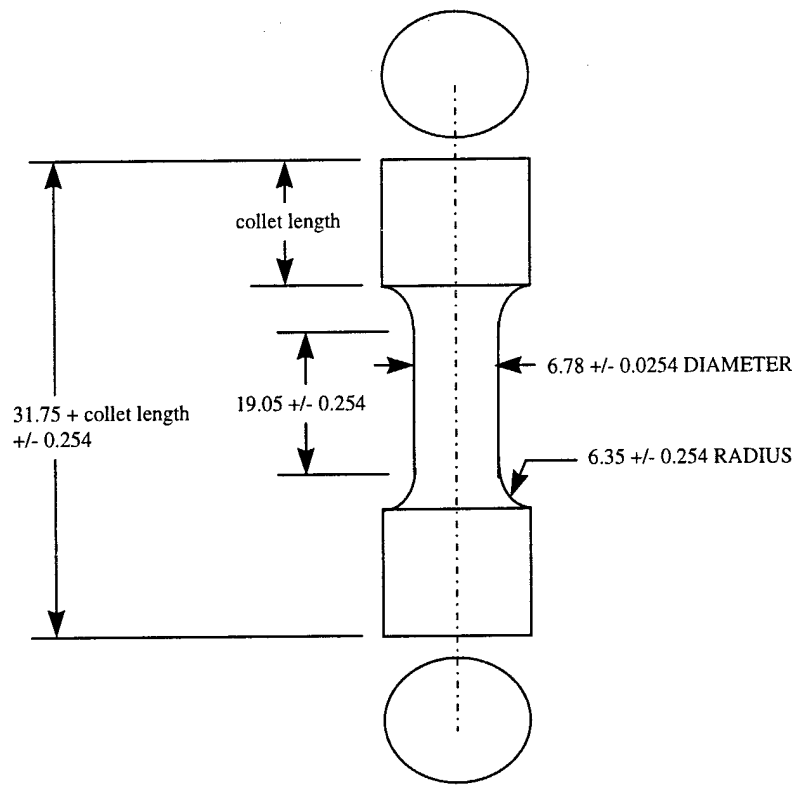


Figure III.25: Specimen design for path sequence; compression/tension and tension/compression (all dimensions are in mm).

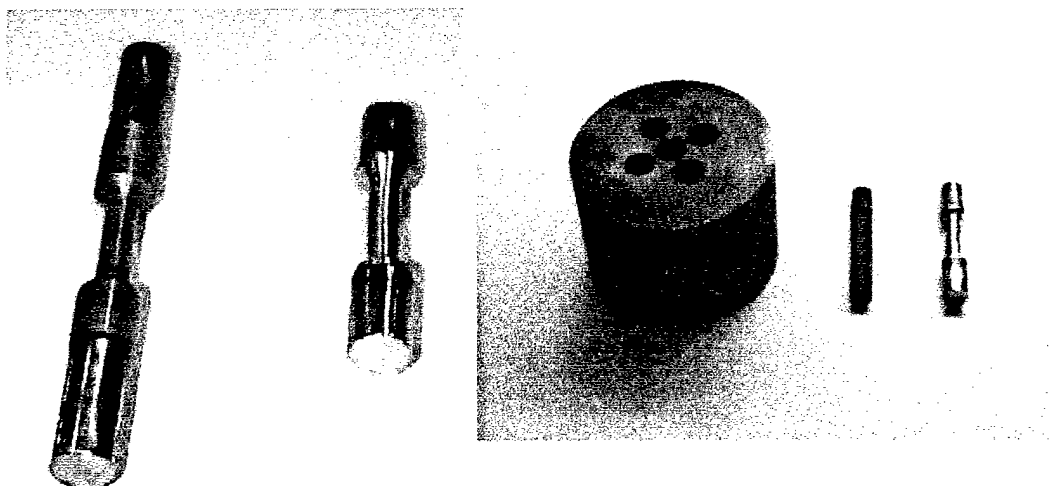
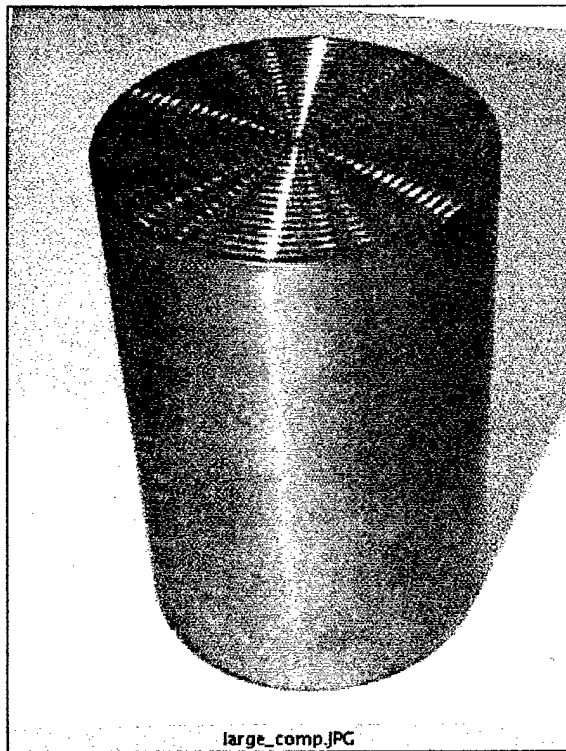


Figure III.26: Top: large compression specimen (type 4) before deformation. Bottom: picture of reverse path (compression/tension) specimens, (left) machined from virgin material then annealed, (right) machined from pre-strained compression specimen.

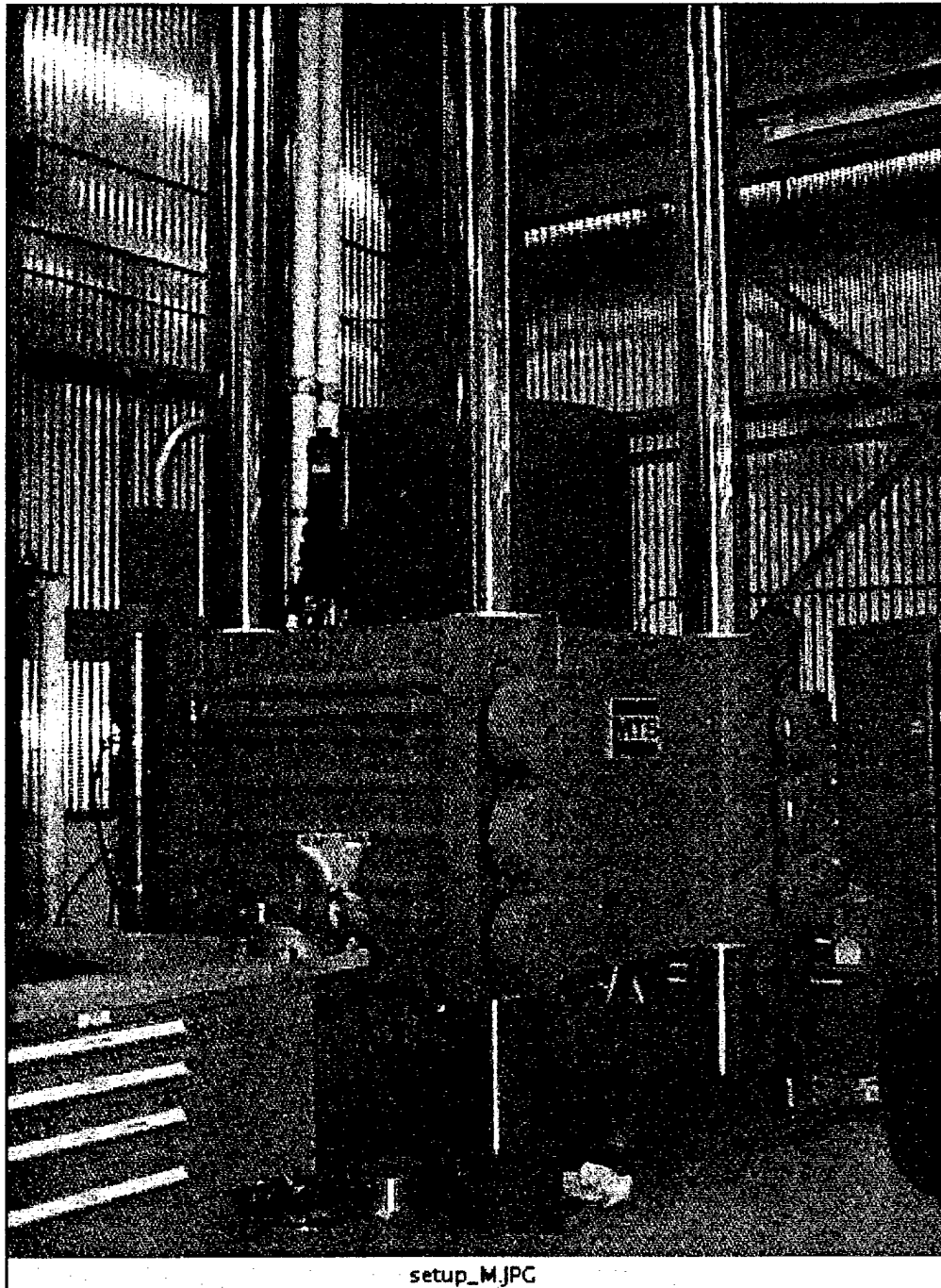


Figure III.27: 10M pound MTS test frame at SNL. Used for compression of large (type 4) specimens.

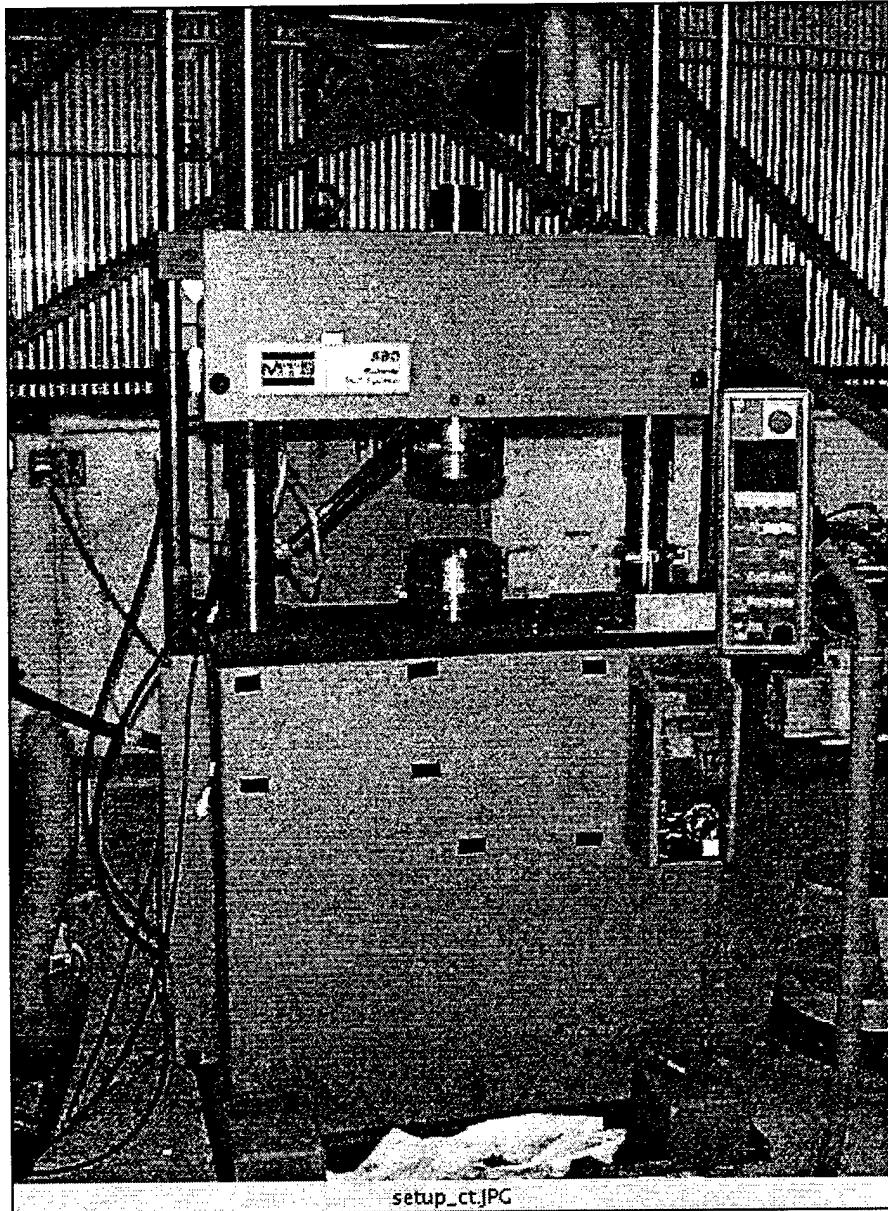


Figure III.28: MTS 880 Test machine at SNL used for reverse path compression/tension experiments.

A series of experiments was conducted with changes in temperature between 25°C and 269°C (Table III.6) and strain rate (0.0004 s^{-1} and 0.1 s^{-1}) (Table III.8). The initial deformation was conducted with larger compression specimens (Types 3 and 4). Type 2 compression specimens (10.16 x 15.24 mm) were then obtained from the pre-strained material. The material was removed using EDM and then machined to the final configuration, removing material at the rate of less than 76.2 μm per turn, to prevent alteration of the internal structure (Fig. III.29).

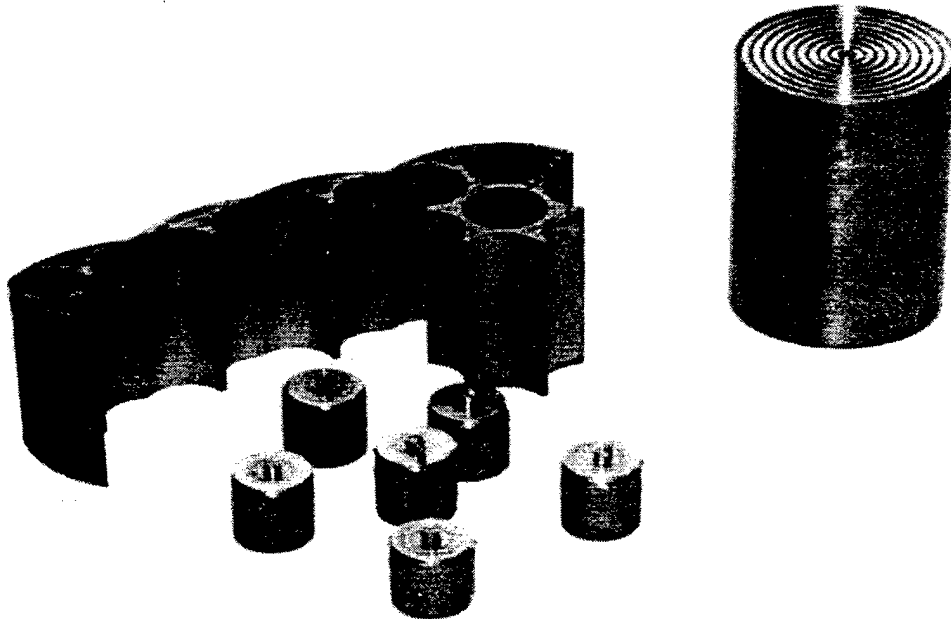
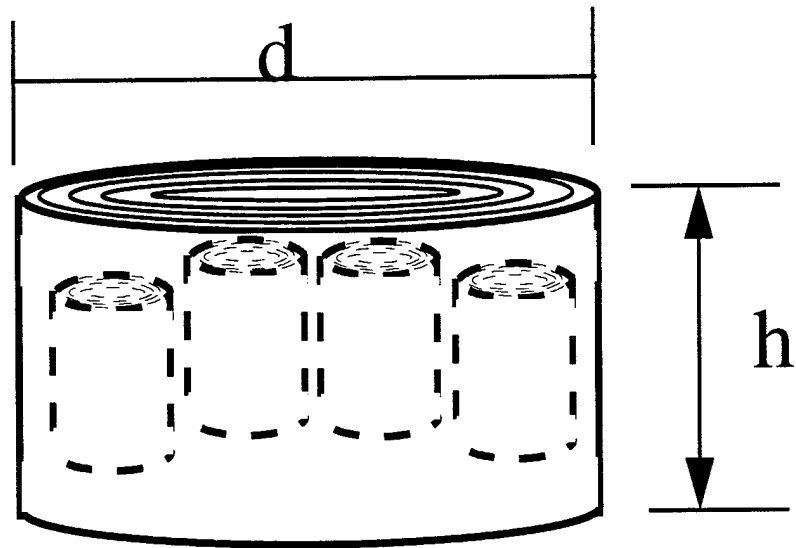


Figure III.29: Diagram and picture of preparation of the second sequence specimens from pre-strained material.

Deformation path change experiments were conducted with compression pre-strain to subsequent torsion deformation. These included high rate (10^3 s^{-1}) compression at 25°C and 269°C followed by quasi-static (0.0004 s^{-1}) shear at 25°C and 269°C (Table III.7). Additionally, quasi-static compression experiments were followed by quasi-static shear at combinations of 25°C and 269°C (Table III.9).

The high rate compression specimen was approximately 3.61 mm in length and 10.16 mm in diameter after a deformation of 0.4 true strain. A novel double shear specimen was designed to conduct the subsequent shear experiments on the small volume of material available (Figs. III.30 and III.31). Quasi-static path sequence experiments were conducted by first compressing material to 0.5 true strain and then machining a Lindholm specimen from the pre-strained material (Fig. III.32). The Lindholm specimen was electro-discharge machined to avoid evolving the internal structure of the material.

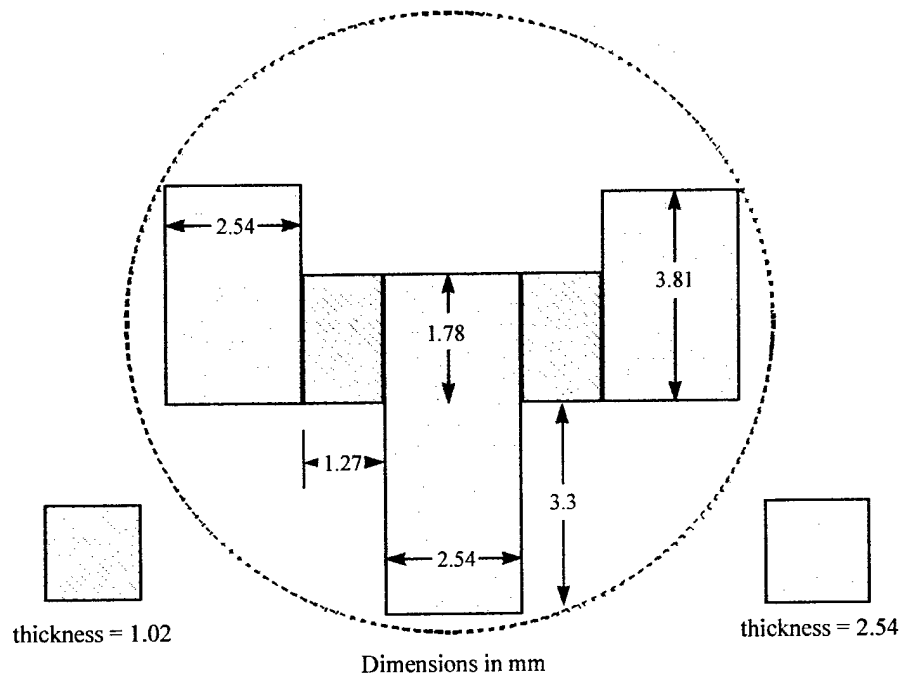


Figure III.30: Double shear specimen design for path and strain rate sequence experiments.

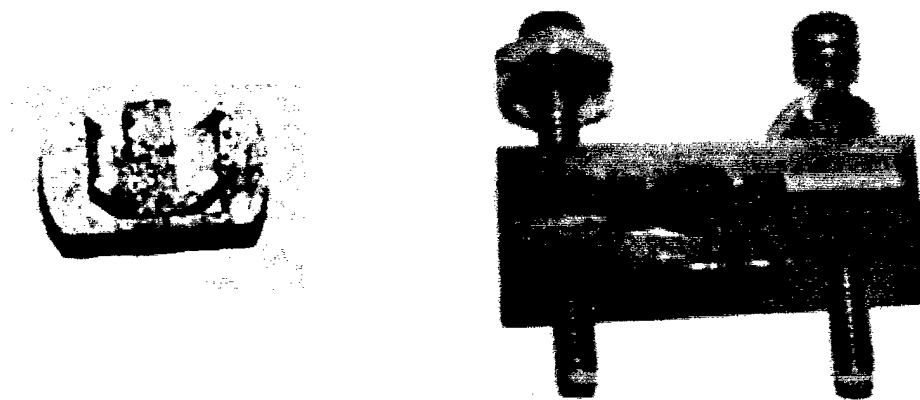


Figure III.31: Double shear specimen for path and strain rate sequence experiments, shown after deformation, and bracket used to maintain alignment.

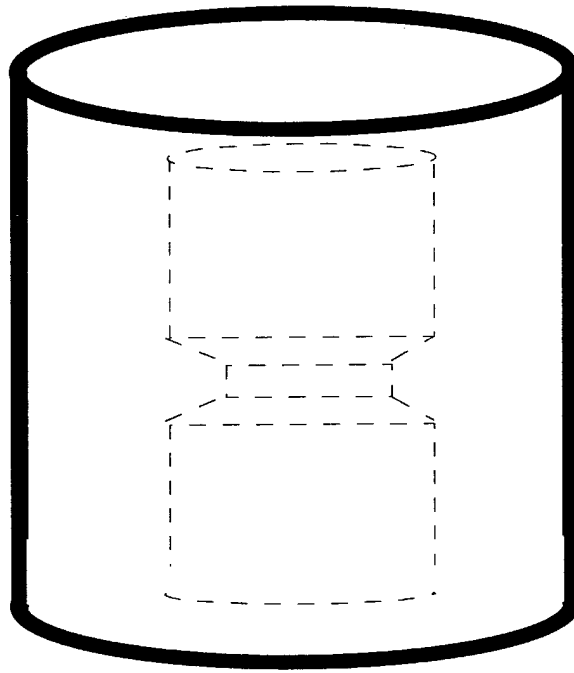


Figure III.32: Diagram showing the removal of a Lindholm specimen from a pre-strained compression specimen.

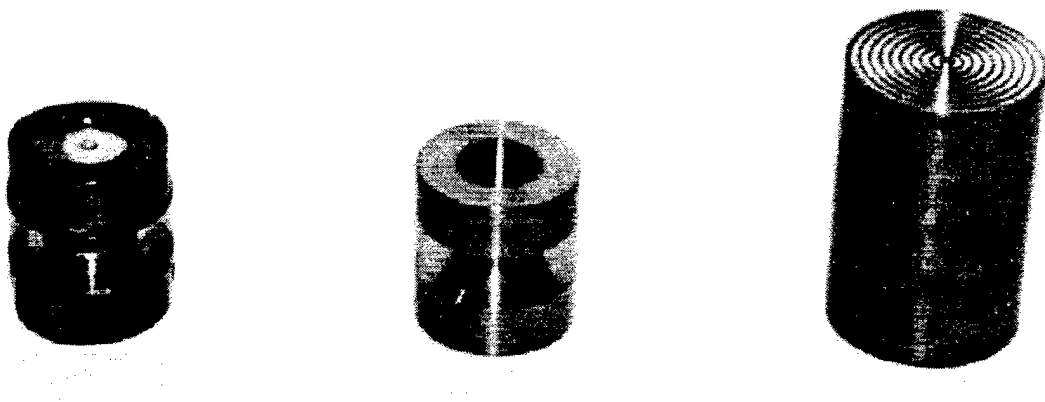


Figure III.33: Picture of one inch diameter Lindholm specimen removed from a 30.48 mm (1.2 inch) diameter compression specimen (shown before deformation).

III.2.3.5 Experimental Consistency

Several experiments were conducted under the same deformation conditions of deformation path, temperature, and strain rate to verify the repeatability of the experimental results. Figure III.34 shows the results for five experiments conducted under the same deformation conditions, of a strain rate at 0.0004 s^{-1} and temperature of 25°C . The results are very repeatable and indicate that the testing procedure and material response were consistent.

Many of the sequence experiments required a change in specimen type. These changes were needed to accomplish the large changes in strain rate and deformation path. The specimen change necessitated a remachining process. Experiments were conducted to determine the effect that the unload, remachine, and reload process had on the internal structure of the specimen. The remachining process was accomplished to minimize internal structural changes. EDM was used initially to remove the bulk of material and then the final specimen configuration was achieved by removing only a small amount of material during each lathe turn. This maintained a low material temperature and prevented significant changes in internal microstructure.

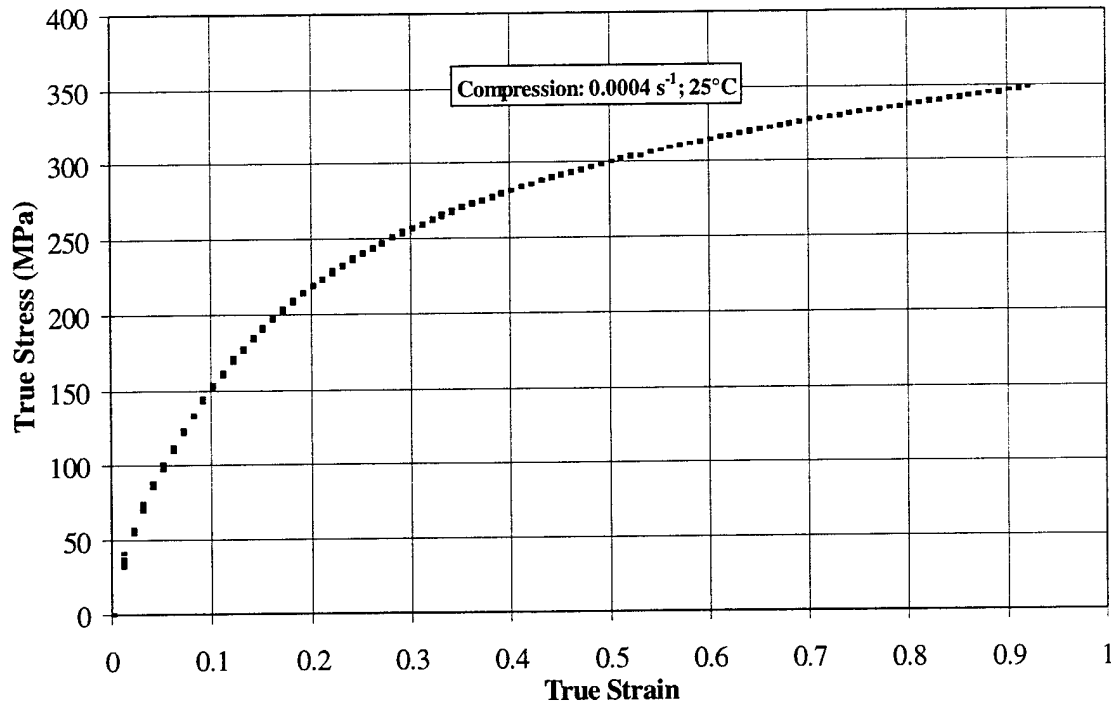


Figure III.34: Repeatability of compression tests. Five experimental tests are shown.

Figure III.35 shows the sequence of loading at either 25°C at 0.0004 s⁻¹ or 269°C at 0.0004 s⁻¹, unloading and remachining the specimen, and then reloading at the same strain rate and temperature. The results show that the reload response is the same as the constant strain rate and temperature response. This demonstrates that the test procedure is consistent, and the remachining process has not altered the subsequent material behavior. At 269°C, the reload curve (after remachining) shows that the mechanical behavior is not significantly affected by neither the cool down and subsequent heat up, nor the remachining events. The similar effects of the unload and remachining process are shown in Fig. III.35 for the compression/tension specimens. A compression/tension specimen remachined from the

compressed material is subsequently tested in compression. The flow stress from the remachined specimen fits smoothly with the data from the initial compression flow stress curve, indicating no material effects resulted from the remachining protocol.

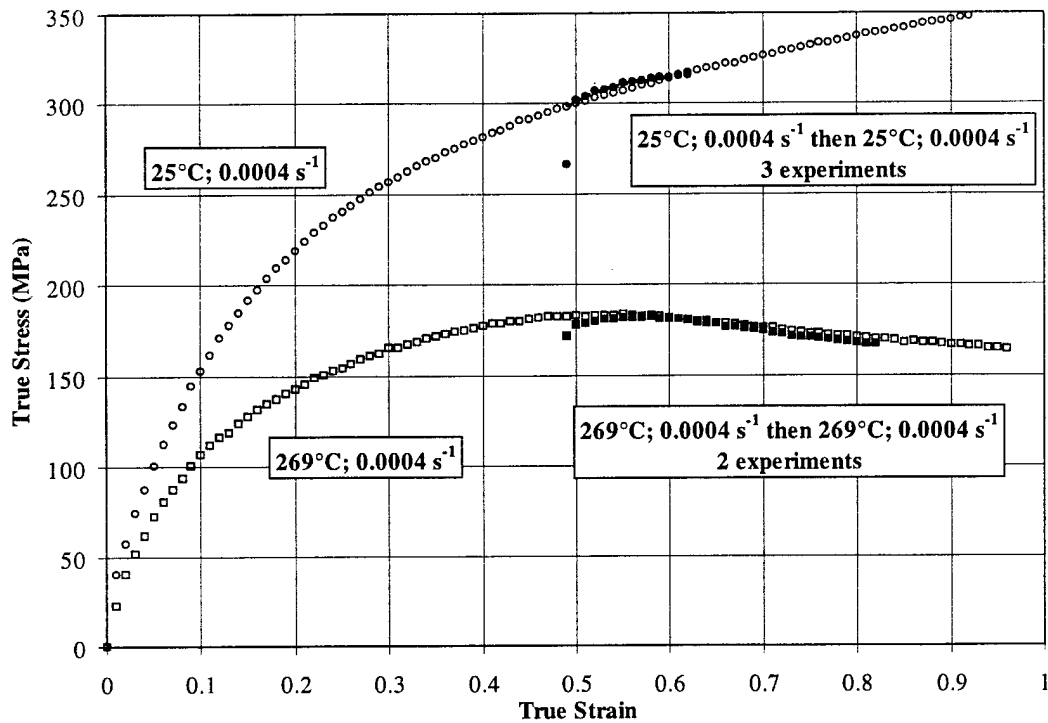


Figure III.35: Load, unload and remachine, and reload at same temperature and strain rate conditions. Both 25°C at 0.0004 s⁻¹ and 269°C at 0.0004 s⁻¹ are shown.

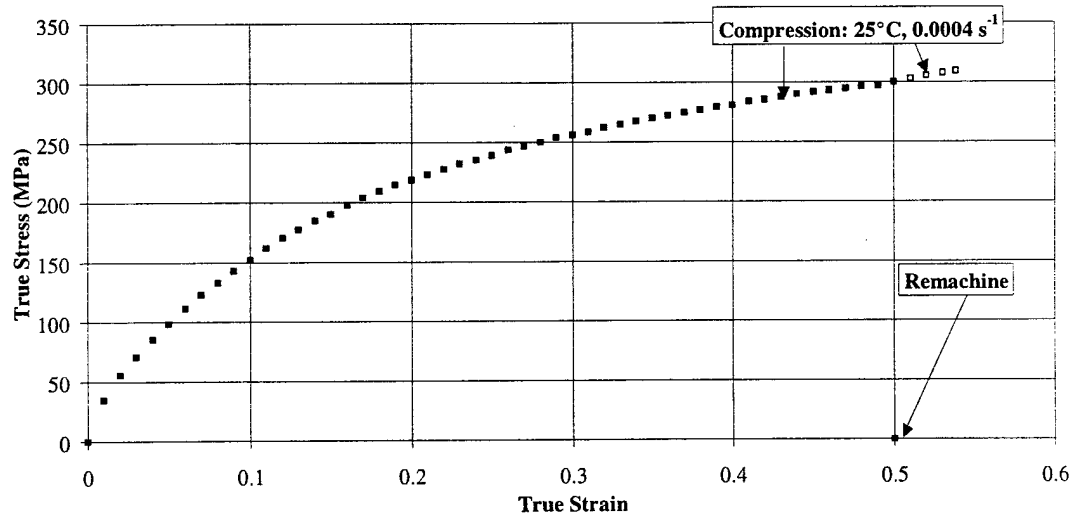


Figure III.36: Effects of unload and remachining on material response. Experimental data for compression at 25°C and 0.0004 s⁻¹ strain; unload and remachine into specimen type 6; then reload in compression at 25°C and 0.0004s⁻¹.

III.3 Experimental Results

All of the data presented for compression experiments corresponded to low barreling (less than 2.0 %), confirming uniform deformation. All stress-strain curves are plotted using true strain and true stress (in MPa). Shear results are plotted using the uniaxial normalized von Mises equivalent strain and stress, i.e.

$$\bar{\epsilon} = \frac{\gamma}{\sqrt{3}} \quad \text{and} \quad \bar{\sigma} = \sqrt{3}\tau. \quad (\text{III.6})$$

III.3.1 Restoration Experimental Results

A series of restoration experiments were conducted to evaluate the amount of recovery and recrystallization which occurs in OFHC Cu. These experiments were conducted both statically (unloaded to zero load) and dynamically (under a constant load or crosshead position).

III.3.1.1 Static Restoration Experimental Results

Load-unload-hold-reload experiments (Table III.4) were performed under isothermal, constant true strain rate conditions to evaluate the amount of static thermal recovery and static recrystallization. This experimental technique does not distinguish between restoration

softening which results from recovery or recrystallization. OFHC Cu, a low to moderate SFE material, has been found to both statically recover and recrystallize (McQueen and Jonas, 1975, Jonas and Sakai, 1984, Sakai and Jonas, 1984, and Blaz *et al.*, 1983). In these experiments, the stress was reduced to zero during hold periods applied after initial straining. The difference between the stress just before unloading and the yield stress upon reloading represents the change in state due only to diffusionally-governed static restoration processes. Increasing the hold time increases the cumulative effect of static restoration.

At 269°C, the stress upon reloading at 0.3 strain is not significantly different from that measured just before unloading at 0.3 strain, even for relatively long hold periods, (Fig. III.37). Conversely, there are significant differences in reload stress after holding at 0.5 strain. The reload stress decreases with increasing length of hold time (Fig. III.38). These results show that static restoration is pre-strain dependent, being much more strongly activated with 0.5 compressive pre-strain than a 0.3 pre-strain.

At 541°C and 676°C ($T/T_m = 0.6$ and 0.7 , respectively), the amount of restoration, as evidenced by the change in flow stress before and after unloading, is very similar for the various hold times, (Figs. III.38 to III.40). It is interesting to note that the influence of hold time is indiscernible at 541°C and 676°C, likely because the kinetics of recovery are so rapid that hardening and recovery processes are nearly equilibrated. At 541°C and following the 600-second hold time, the flow stress has an increase in the amplitude of oscillations. This increase is similar, but of lower magnitude, to those which occur immediately upon loading of the annealed material. This is likely due to occurrence of static recrystallization during

the hold period and will be further examined in Chapter IV.

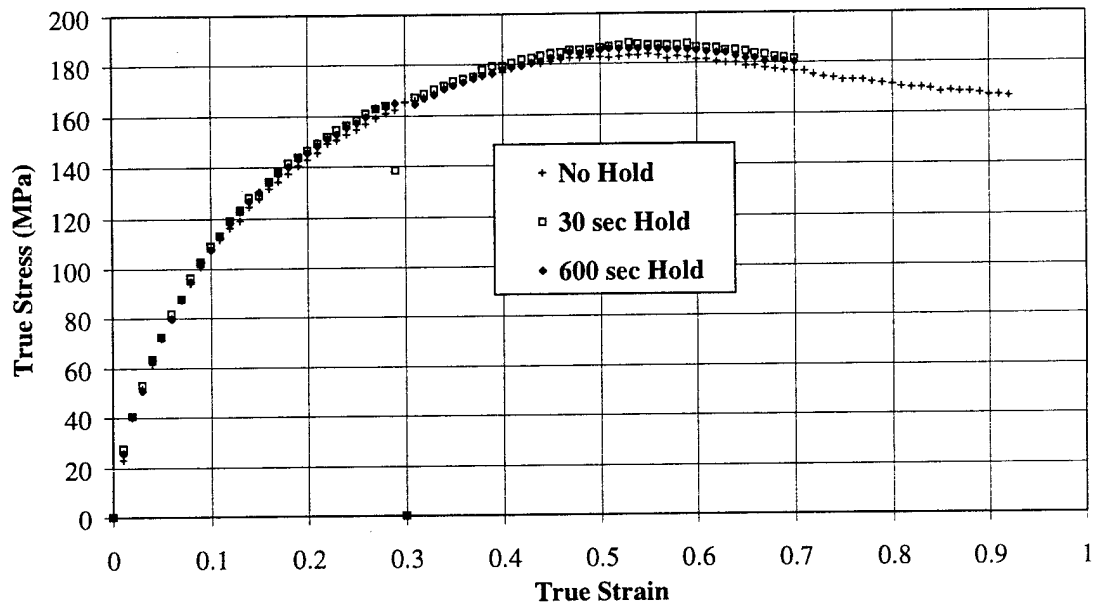


Figure III.37: Static restoration results for compression at 269°C, 0.0004 s⁻¹ and different hold times at 0.5 strain.

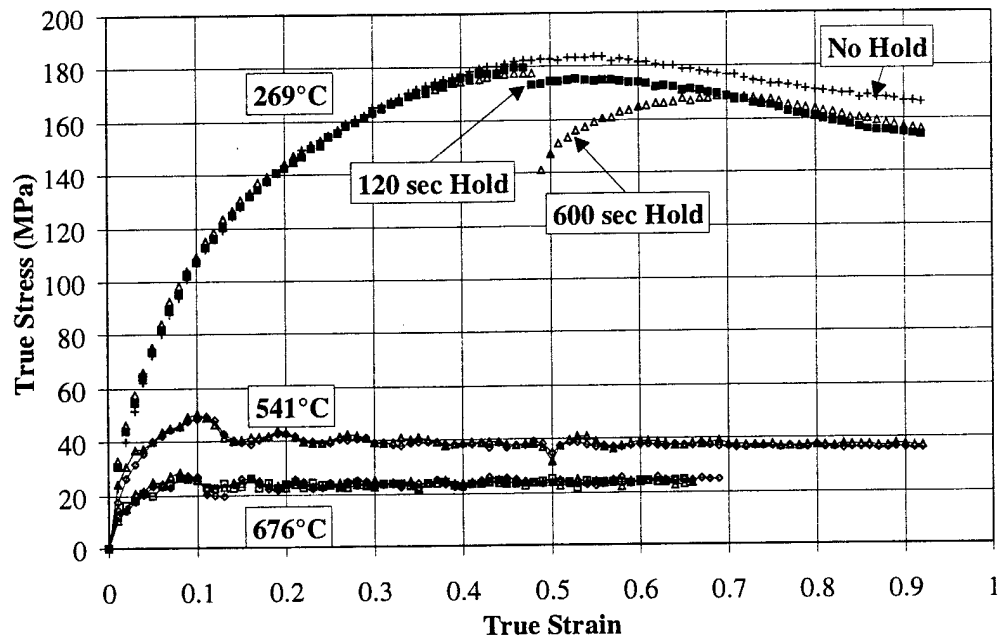


Figure III.38: Static restoration results for OFHC Cu in compression at 0.0004 s^{-1} , 269°C, 541°C and 676°C for different hold times at 0.5 strain.

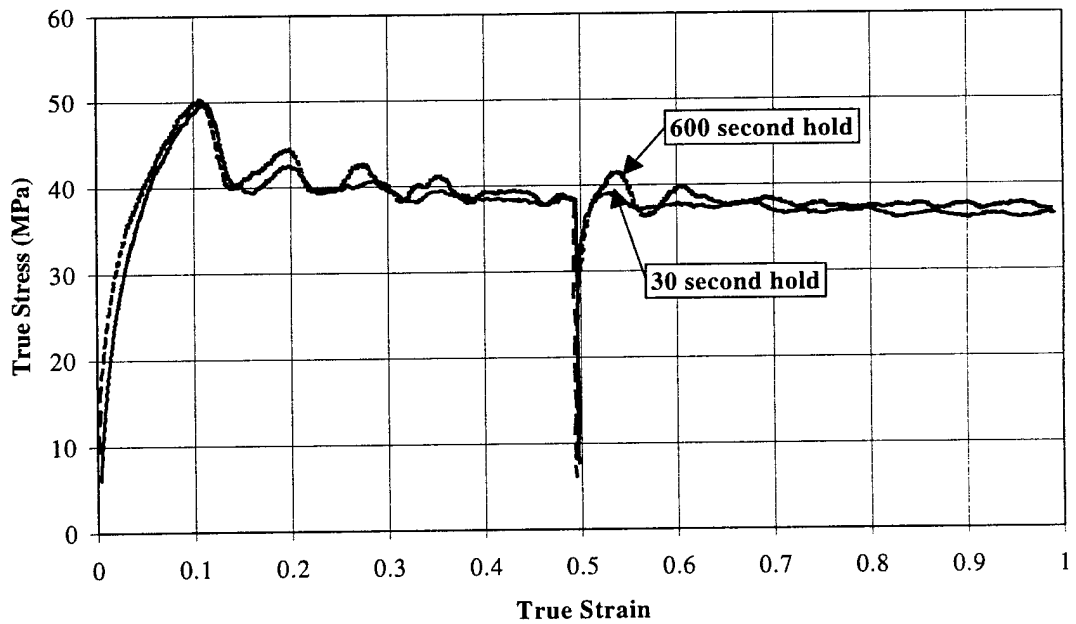


Figure III.39: Static restoration results for OFHC Cu in compression at 541°C, 0.0004 s^{-1} , and different hold times at 0.5 strain.

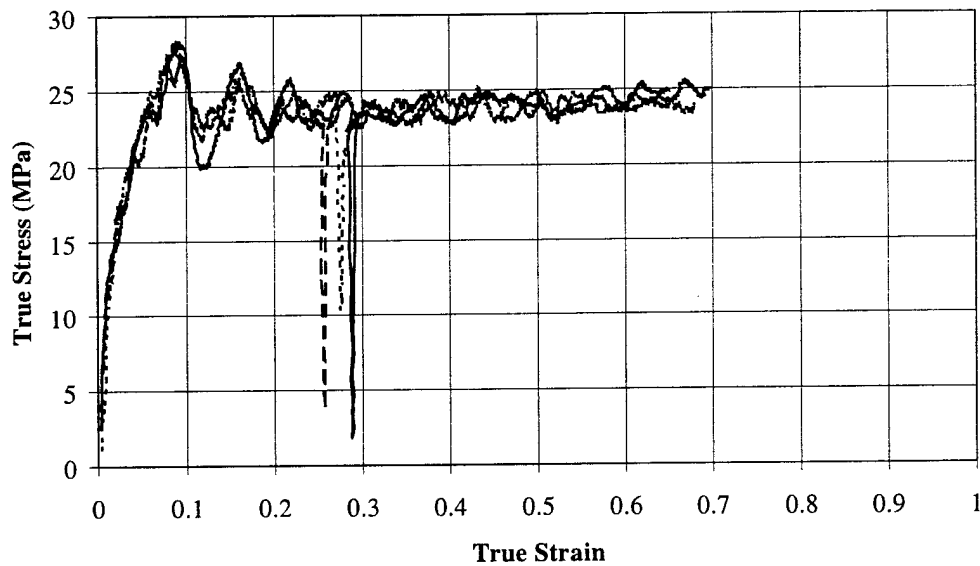


Figure III.40: Static restoration results for OFHC Cu in compression at 676°C, 0.0004 s⁻¹, and different hold times at 0.3 strain.

Oscillations are seen to occur in the flow stress at strains of about 0.1, and are highly repeatable. When crystalline materials are deformed at elevated temperatures, the accumulated dislocations are continuously annihilated by two separate processes, dynamic recovery and dynamic recrystallization, which both result in the release of the internal energy stored during deformation. At temperatures above about 0.3 T_m and at low strain rates, oscillations in OFHC Cu flow stress have been attributed to cycles of dynamic recrystallization (Sellars and Tegart, 1966, Blaz *et al.*, 1983, Derby and Ashby, 1987, and Chen and Kocks, 1992), similar to those reported in Figs. III.38 to III.40. During deformation, the dislocation density and the stored energy increase. When the stored energy

becomes high enough, dynamic recrystallization is observed to nucleate at prior grain boundaries (Derby and Ashby, 1987 and McQueen and Jonas, 1975). The nucleation and growth of new grains eliminate dislocations and reduce the stored energy, resulting in a reduction in flow stress. These new grains continue to undergo deformation, experience an increase in the local dislocation density, and cause macroscopic strain hardening. The stored internal energy increases until nucleation occurs in these recrystallized grains resulting in another cycle of local recrystallization. The resulting behavior causes the cyclical variation of the flow stress. Moreover, the frequency and amplitude of oscillations are very repeatable, and are largely unaffected by the hold time. These oscillations tend to die out with the flow stress reaching a steady state value. At lower temperatures or higher strain rates, the flow stress passes through a single peak before decreasing to a steady state value, similar to the flow stress at 269°C in Fig. III.38. This steady state stress is associated with a new, constant mean grain size within the material, and reflects a dynamic balance between nucleation and growth (Blaz *et al.*, 1983 and Sakai and Jonas, 1984). Single peak behavior is associated with grain refinement while multiple peaks occur with discrete cycles of grain coarsening (Saki and Jonas, 1984).

III.3.1.2 Dynamic Restoration Experimental Results

Load, hold, then reload experiments were conducted in compression (Table III.5). These experiments were conducted to obtain information about the creep behavior of OFHC Cu. Experiments were conducted at 25°C, 269°C and 405°C with different hold times,

strains, and holding conditions. Results are plotted with flow stress versus true strain, and also, flow stress versus time to observe the effect of the hold time.

Experiments at 25°C show little change in flow stress when held after a compressive pre-strain. There is no difference whether held in load or stroke control. Figures III.41 and III.42 show the results for different strain levels and Figs. III.43 and III.44 compare the results for stroke and load hold times of 20 minutes after compression to 1.0. The amount of restoration at 25°C is insignificant. The activation energy at 25°C is low and the microstructure does not change significantly.

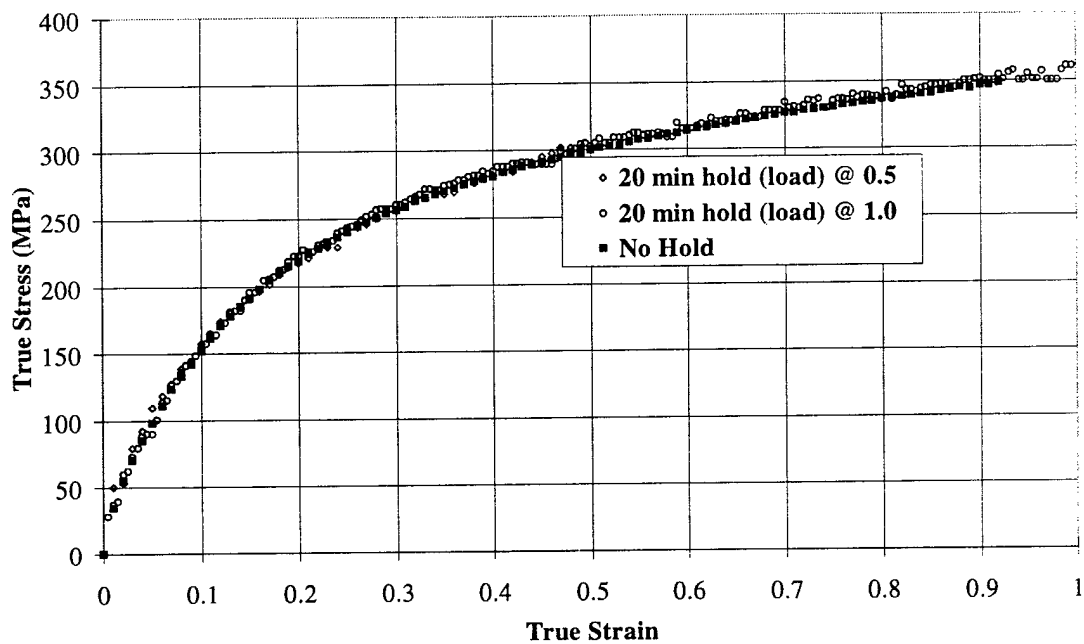


Figure III.41: Experimental results for OFHC Cu in compression at 0.0004 s^{-1} , 25°C , and hold under load control for 20 minutes at 0.5 strain compared to 1.0 strain.

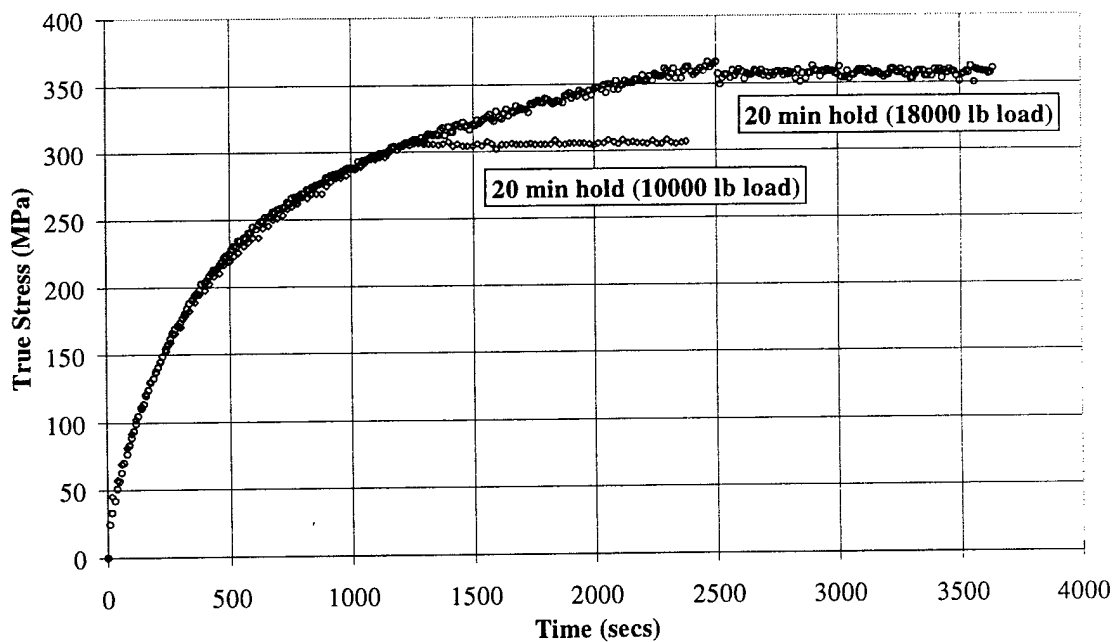


Figure III.42: Experimental results for OFHC Cu in compression at 0.0004 s^{-1} , 25°C , and hold under load control for 20 minutes at 0.5 strain compared to 1.0 strain.

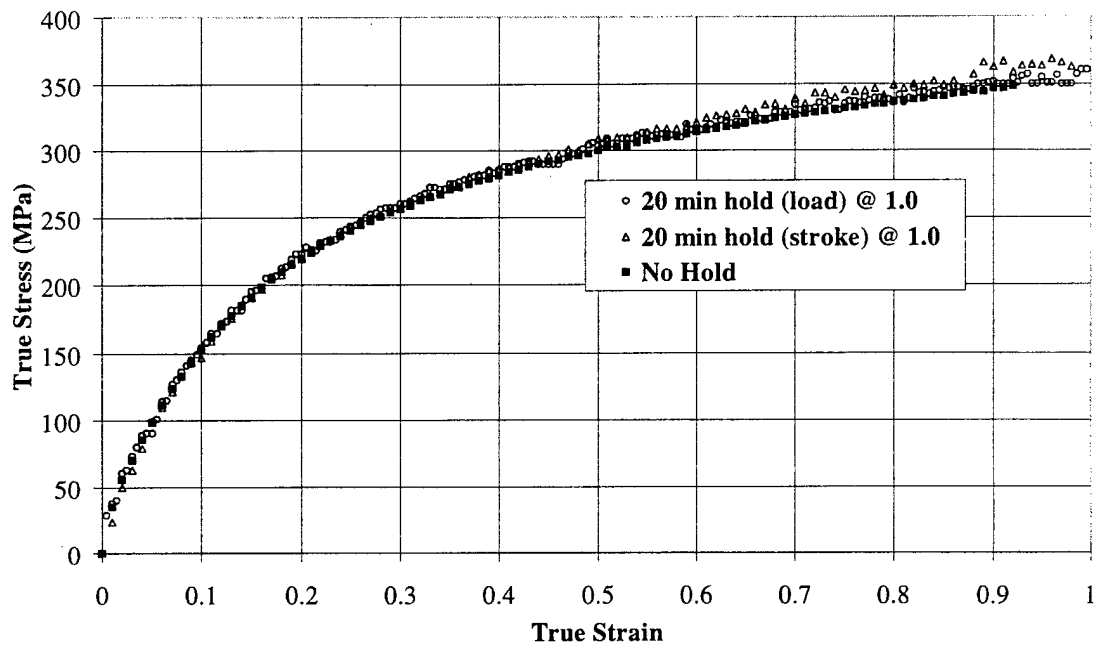


Figure III.43: Experimental results for OFHC Cu in compression at 0.0004 s^{-1} , 25°C , and hold under load control for 20 minutes at 1.0 strain compared to hold under stroke control.

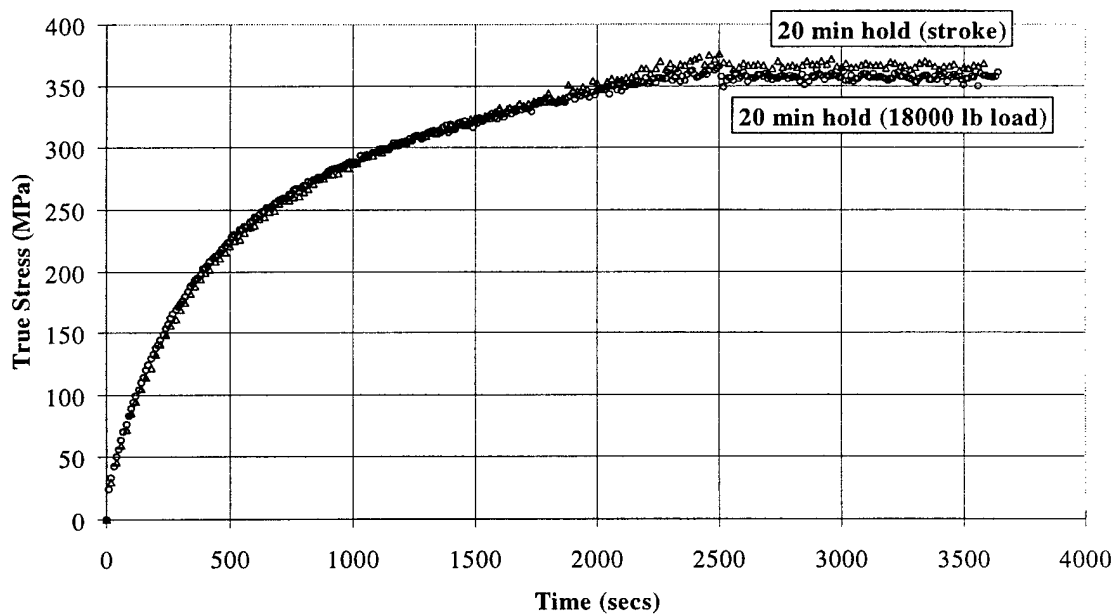


Figure III.44: Experimental results for OFHC Cu in compression at 0.0004 s^{-1} , 25°C , and hold under load control for 20 minutes at 1.0 strain compared to hold under stroke control.

The effect of a sequence of straining followed by 10 minute hold periods is shown in Figs. III.45 and III.46. A greater strain hardening rate is observed following each hold period than the constant strain rate curve. As strain increases, after holding under either stroke or load control, the strain hardening rate is higher than for annealed material at the same strain level. While holding, dislocation bowing occurs (Follansbee, 1985 and Kocks and Mecking, 1980) which may be the cause for the increased hardening rate.

Similar dynamic restoration experiments were completed at 269°C. These results are shown in Figs. III.47 - 57. Figures III.47 and III.48 plot the results of deformation at 269°C and a strain rate of 0.0004 s^{-1} to a strain of 1.0 followed by a 20 minute hold under load control. Figure III.47 shows the comparison of the results for material without hold with material held under load control. The two flow stresses are consistent. A large amount of additional straining occurred during the hold under load control hold (Fig. III.48). The decreasing flow stress is the result of the increased surface area while the specimen continued to deform. The decrease in flow stress is initially rapid and then appears to approach a steady state value.

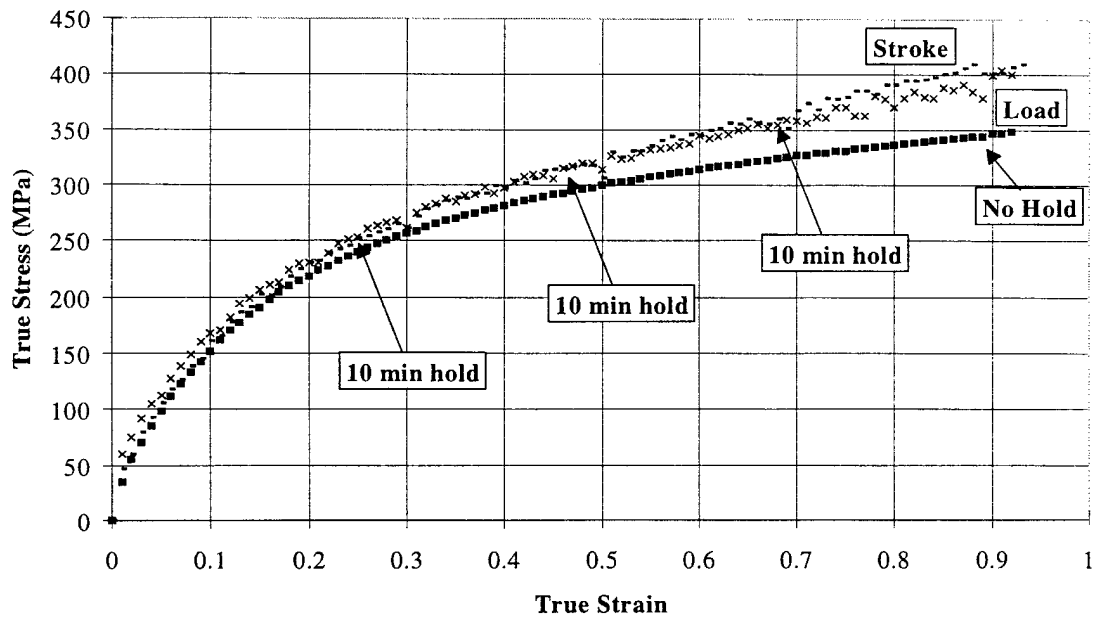


Figure III.45: Experimental results for OFHC Cu in compression at 0.0004 s^{-1} , 25°C , load and hold sequences to 0.3, 0.5, 0.7, and 1.0 strain, and hold for 10 minutes under load control compared to hold under stroke control.

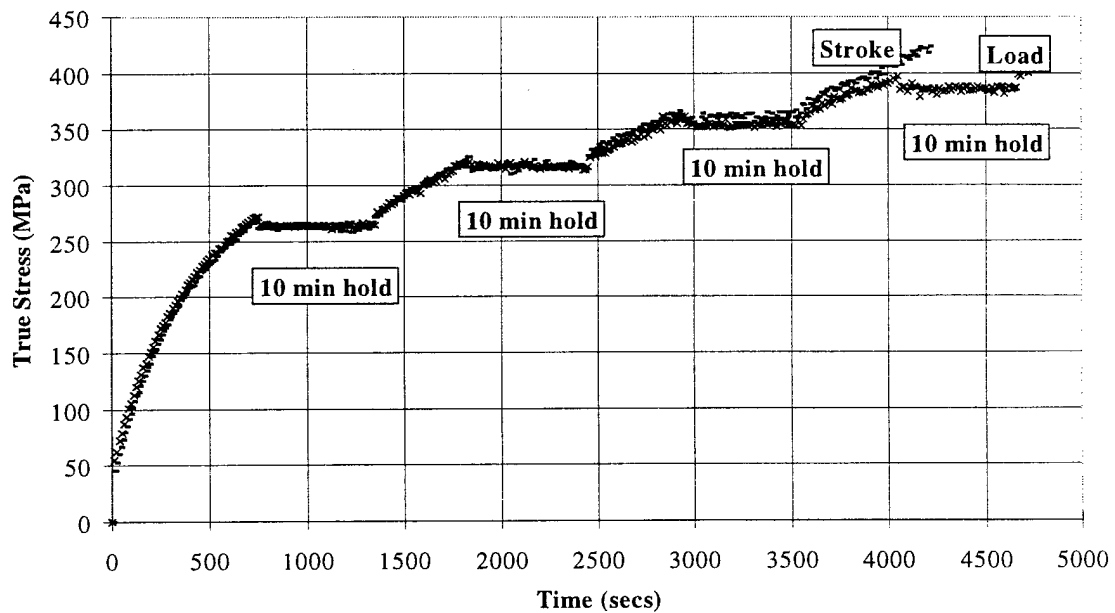


Figure III.46: Experimental results for OFHC Cu in compression at 0.0004 s^{-1} , 25°C , load and hold sequences to 0.3, 0.5, 0.7, and 1.0 strain, and hold for 10 minutes under load control compared to hold under stroke control.

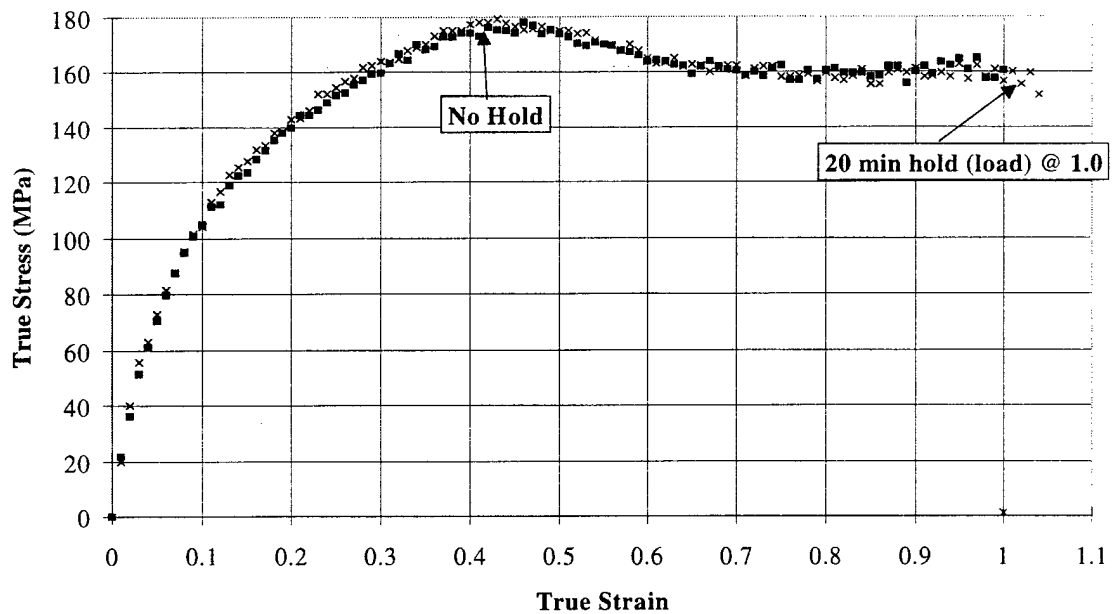


Figure III.47: Experimental results for OFHC Cu in compression at 0.0004 s^{-1} , 269°C , and hold under load control for 20 minutes at 1.0 strain compared to a no hold experiment, shown in solid symbols.

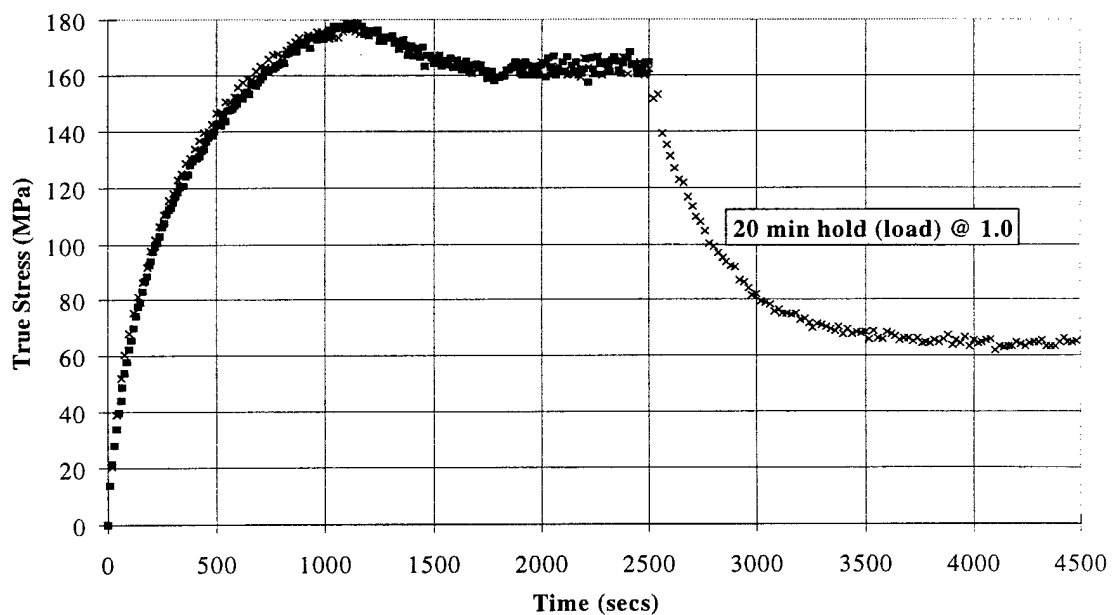


Figure III.48: Experimental results for OFHC Cu in compression at 0.0004 s^{-1} , 269°C , and hold under load control for 20 minutes at 1.0 strain compared to a no hold experiment, shown in solid symbols.

Figures III.49 through III.55 show the experimental results for compression at 269°C and 0.0004 s⁻¹ strain rate to a strain of 0.5, followed by holding under either load or stroke control, then an additional 0.5 strain followed by another hold period. Hold times at each strain level were 60 minutes. Results for holding under stroke control are shown in Figs. III.49 to III.51, while results for holding under load control are shown in Figs. III.52 and III.53. Dynamic restoration processes, which occur while stroke is held constant, result in a large amount of softening. The flow stress essentially reaches zero stress during the first hold period of 60 minutes (Fig. III.53). The reload flow stress is similar to that of an initially annealed material. Figure III.51 compares the flow stress after hold to the initial flow stress of annealed material. The strain hardening rate after a 60 minute hold is consistent with that of annealed material. Additional straining occurs, approximately 0.35 more strain, during the hold period while under load control. A comparison of the differences in flow stress which occur during dynamic restoration under both stroke and load control are shown in Figs. III.54 and III.55. Figures III.56 and III.57 display the results for an experiment at 269°C with various holds under stroke control. The effect of pre-strain is apparent. At 0.3 strain, there is little effect on the reload flow stress. A large and comparable amount of softening occurs at 0.5, 0.7 and 1.0 strain. This indicates that the restoration mechanism is strain dependent and once activated is similar at all higher strain levels.

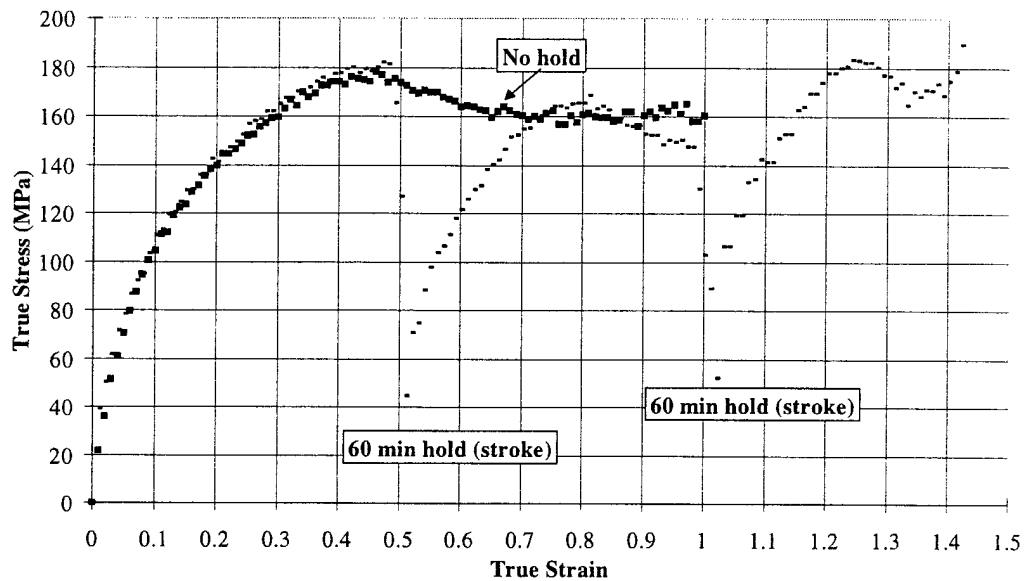


Figure III.49: Experimental results for OFHC Cu in compression at 0.0004 s^{-1} , 269°C , load and hold sequences to 0.5 and 1.0 strain, with hold for 60 minutes under stroke control compared to a no hold experiment, which is shown in solid symbols.

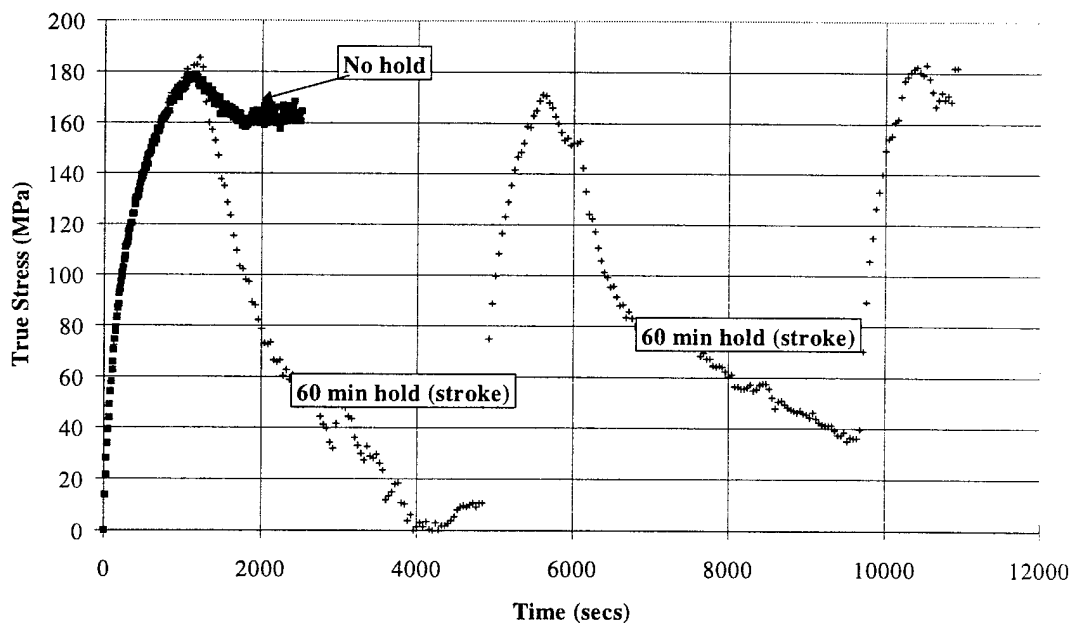


Figure III.50: Experimental results for OFHC Cu in compression at 0.0004 s^{-1} , 269°C , load and hold sequences to 0.5 and 1.0 strain, with hold for 60 minutes under stroke control compared to a no hold experiment, which is shown in solid symbols.

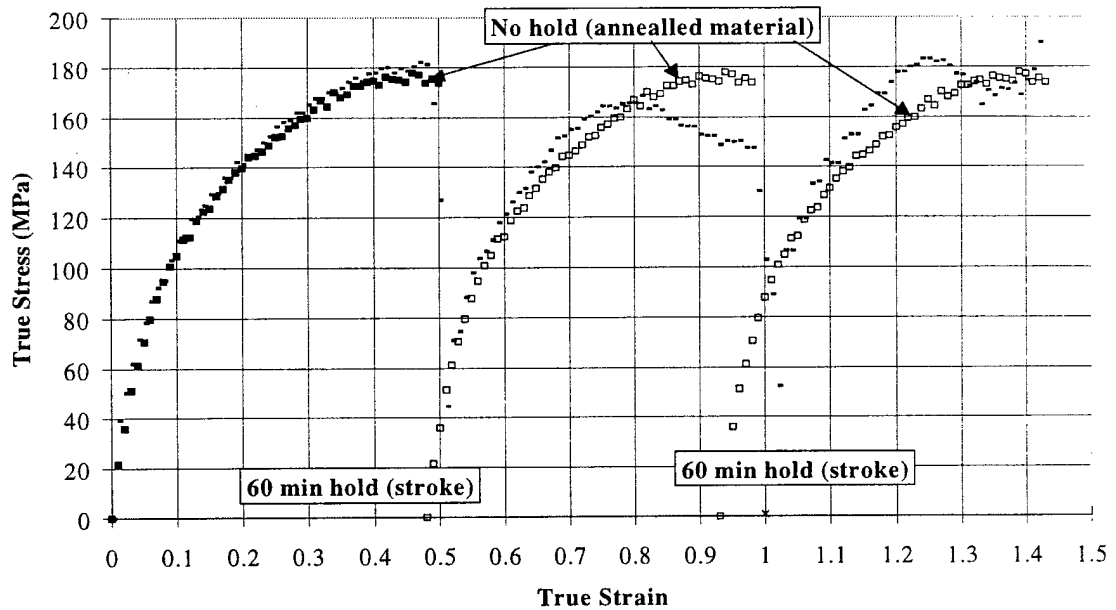


Figure III.51: Experimental results for OFHC Cu in compression at 0.0004 s^{-1} , 269°C , load and hold sequences to 0.5 and 1.0 strain, and hold for 60 minutes under load control compared to a no hold experiment. Reload curves are compared with annealed material, shown shifted to the reload strain with open symbols.

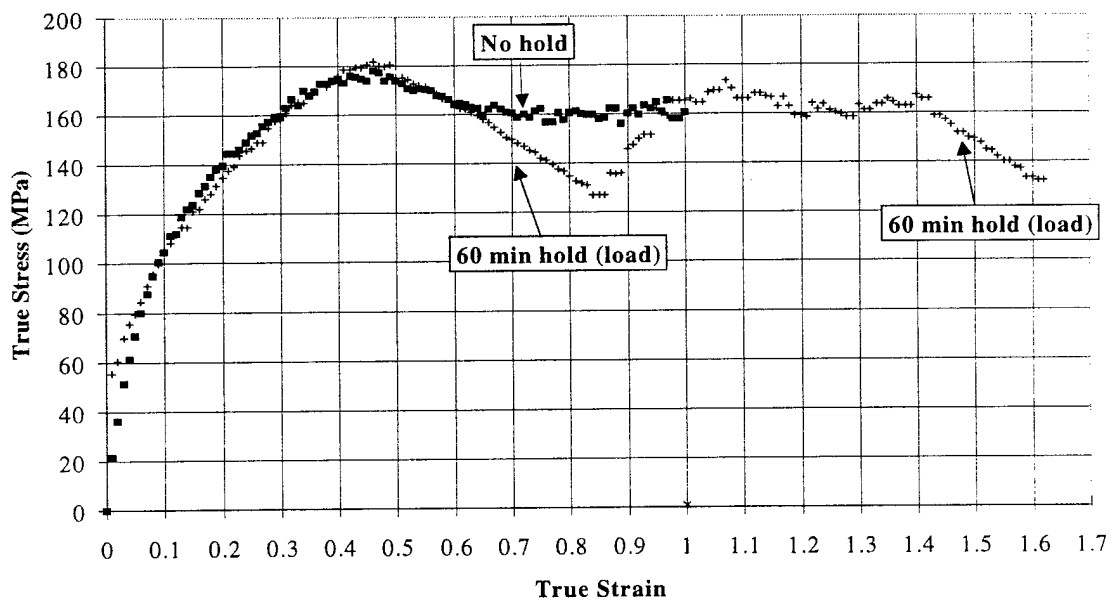


Figure III.52: Experimental results for OFHC Cu in compression at 0.0004 s^{-1} , 269°C , load and hold sequences to 0.5 and 1.0 strain, and hold for 60 minutes under load control compared to a no hold experiment, shown with solid symbols.

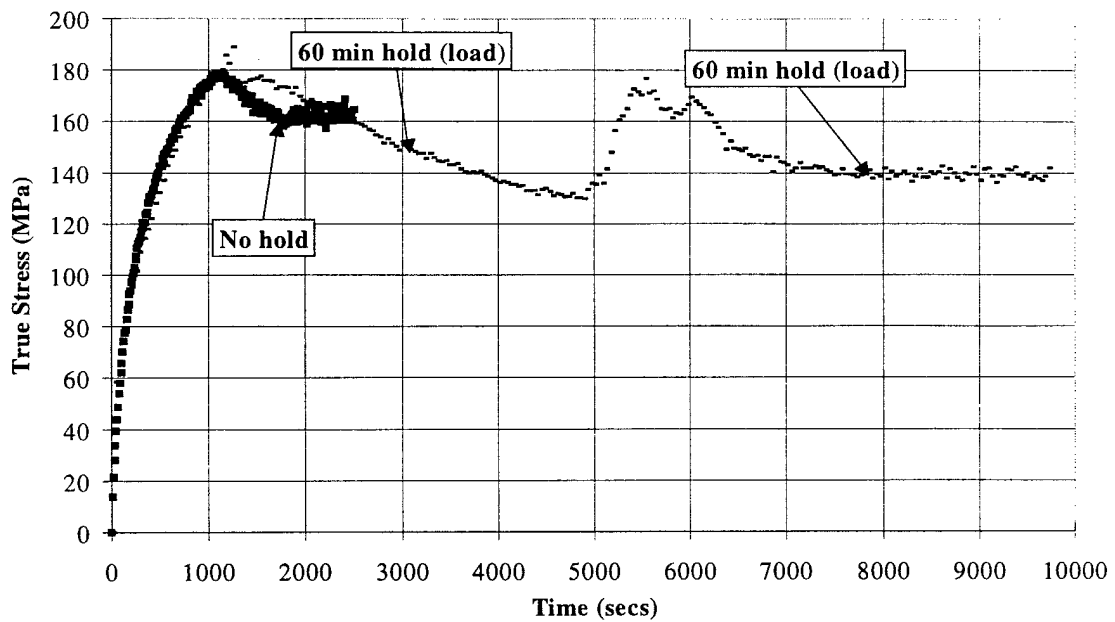


Figure III.53: Experimental results for OFHC Cu in compression at 0.0004 s^{-1} , 269°C , load and hold sequences to 0.5 and 1.0 strain, and hold for 60 minutes under load control compared to a no hold experiment, shown with solid symbols.

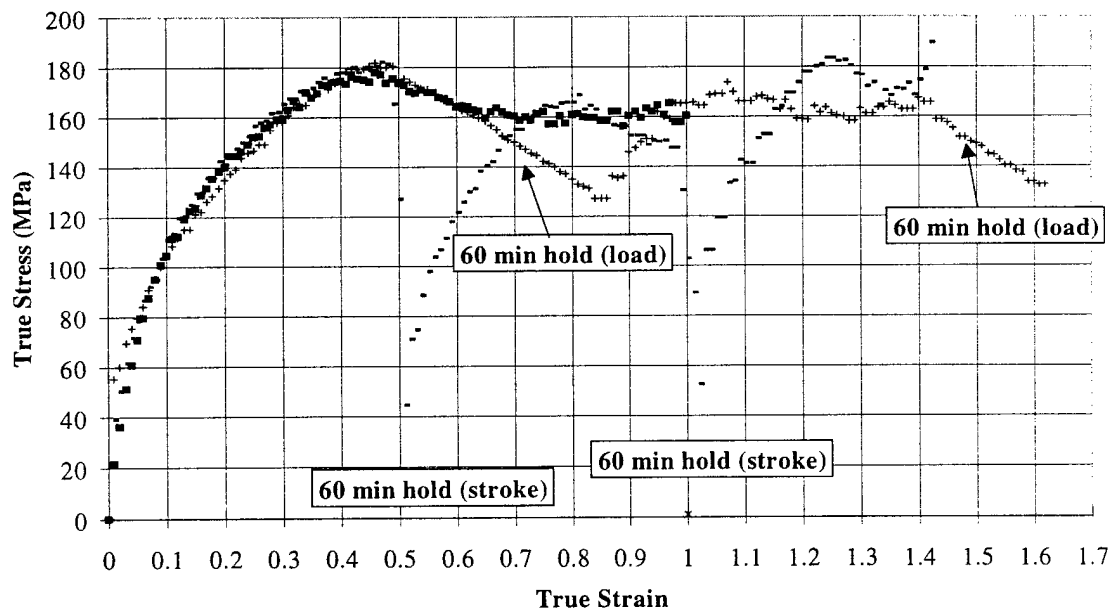


Figure III.54: Experimental results for OFHC Cu in compression at 0.0004 s^{-1} , 269°C , load and hold sequences to 0.5 and 1.0 strain, and hold for 60 minutes under stroke control compared to a no hold experiment and to the response to hold under load control.

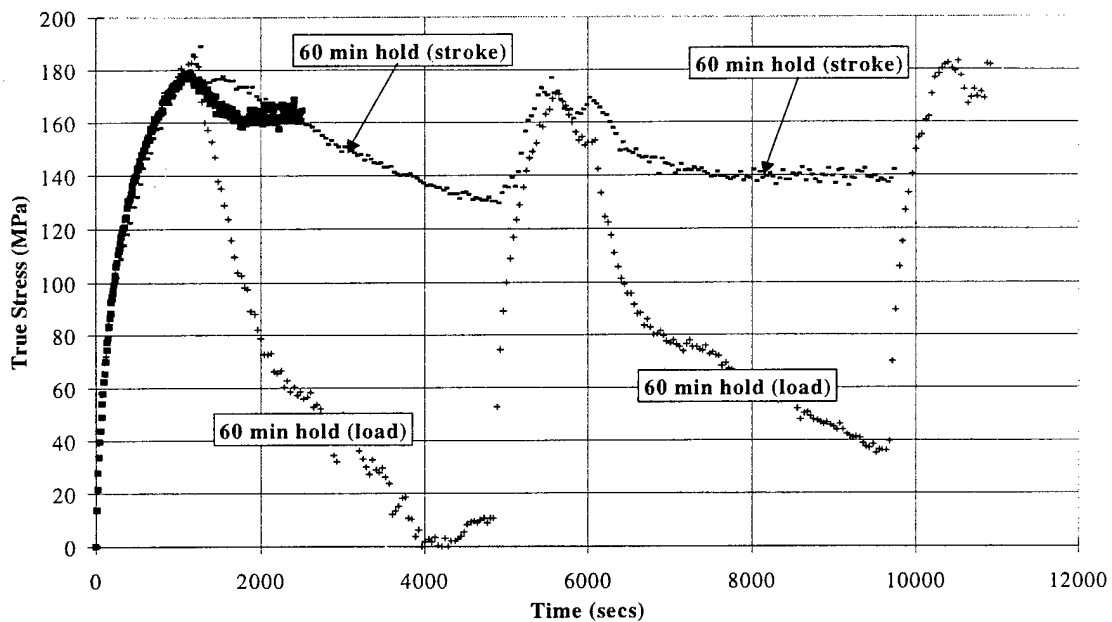


Figure III.55: Experimental results for OFHC Cu in compression at 0.0004 s^{-1} , 269°C , load and hold sequences to 0.5 and 1.0 strain, and hold for 60 minutes under stroke control compared to a no hold experiment and to the response to hold under load control.

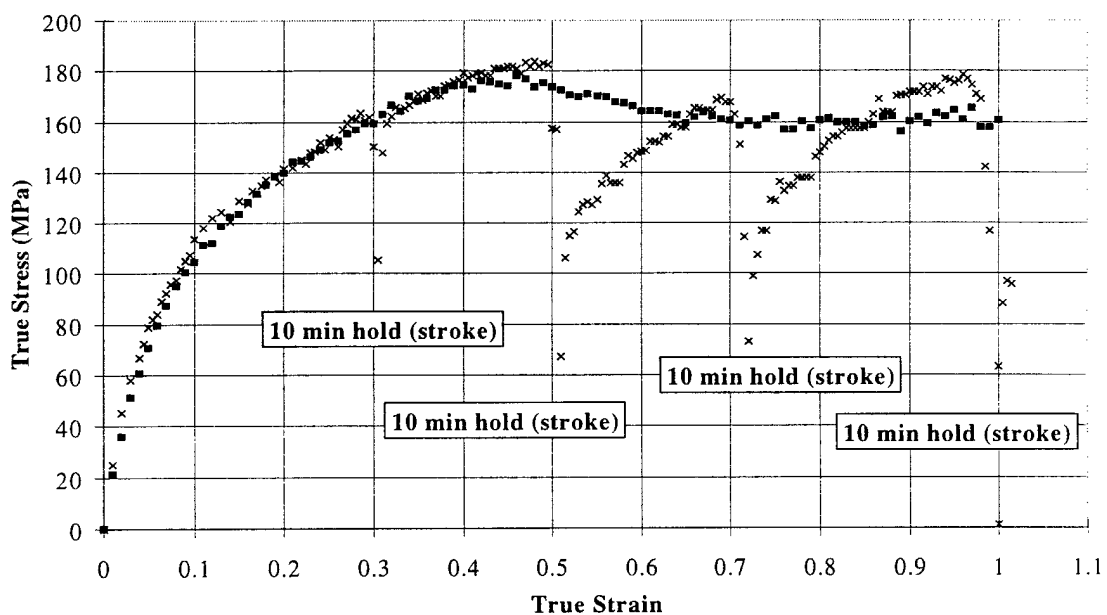


Figure III.56: Experimental results for OFHC Cu in compression at 0.0004 s^{-1} , 269°C , load and hold sequences to 0.3, 0.5, 0.7, and 1.0 strain, and hold for 10 minutes under stroke control compared to a no hold experiment.

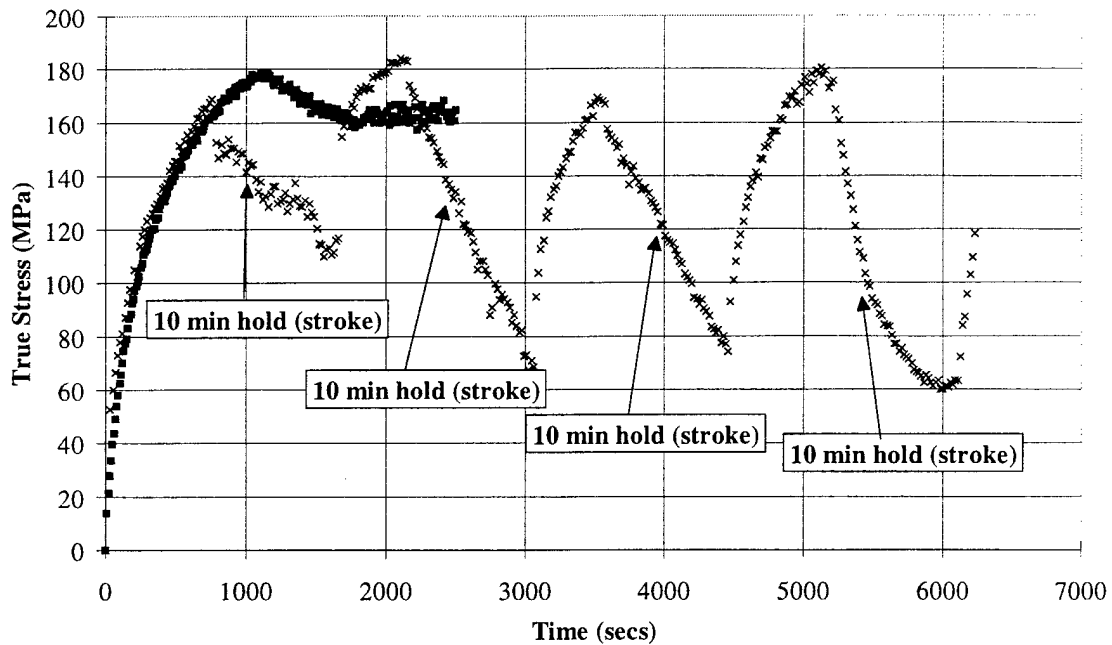


Figure III.57: Experimental results for OFHC Cu in compression at 0.0004 s^{-1} , 269°C , load and hold sequences to 0.3, 0.5, 0.7, and 1.0 strain, and hold for 10 minutes under stroke control compared to a no hold experiment, shown with solid symbols.

Similar dynamic restoration experiments were completed at 405°C ($0.5 T_m$) as were conducted at 269°C (Figs. III.58 - III.65). The results of three different experiments conducted at 405°C and 0.0004 s^{-1} conditions are compared (Fig. III.58). The results show slight variations but all demonstrate oscillations with comparable period and amplitude. The initial peak stress is larger than subsequent peaks after holds (Fig. III.65). The subsequent peak stresses, after holds at 0.3, 0.5, and 0.7, are very similar also demonstrating similar periods and amplitudes of oscillations.

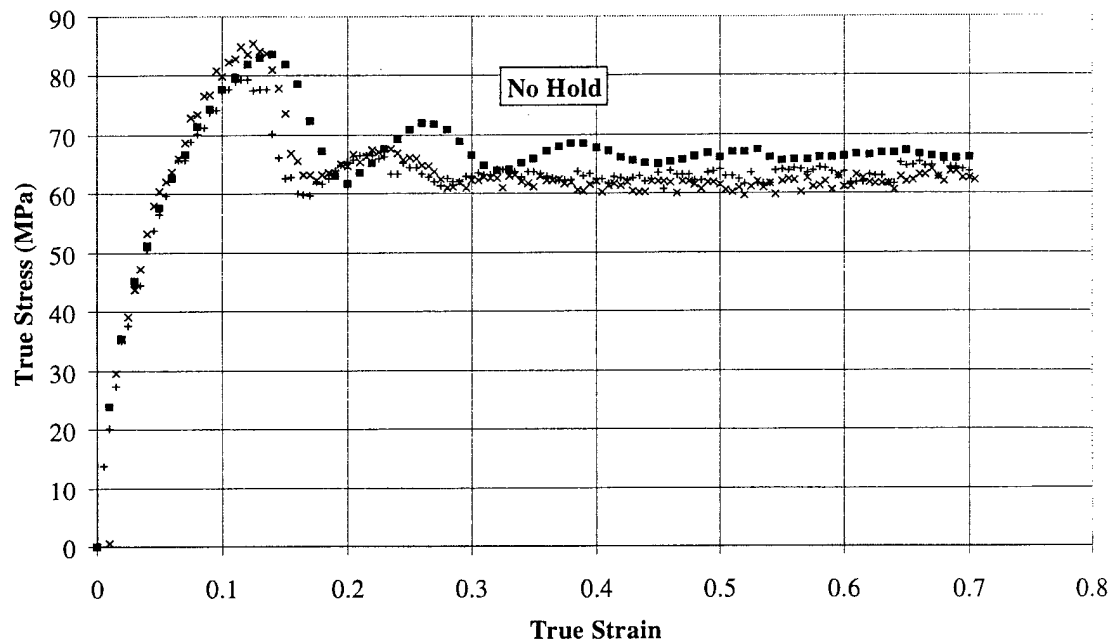


Figure III.58: Experimental results for OFHC Cu in compression at 0.0004 s⁻¹ and 405°C. Four experiments are shown.

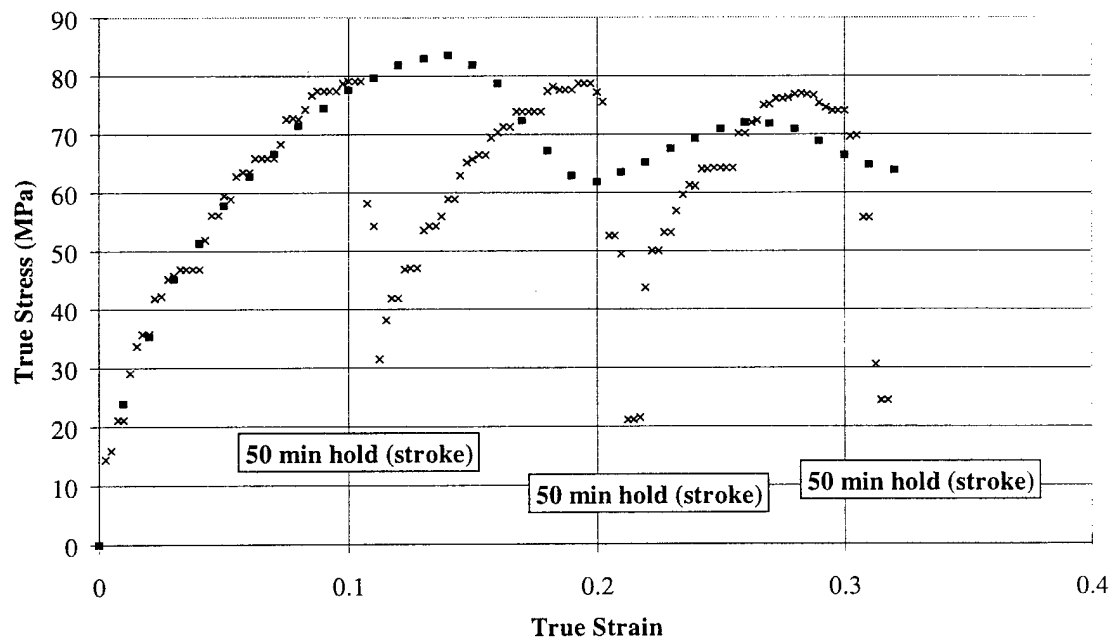


Figure III.59: Experimental results for OFHC Cu in compression at 0.0004 s⁻¹, 405°C, load and hold sequences to 0.1, 0.2, and 0.3 strain, and hold for 50 minutes under stroke control compared to a no hold experiment, shown with solid symbols.

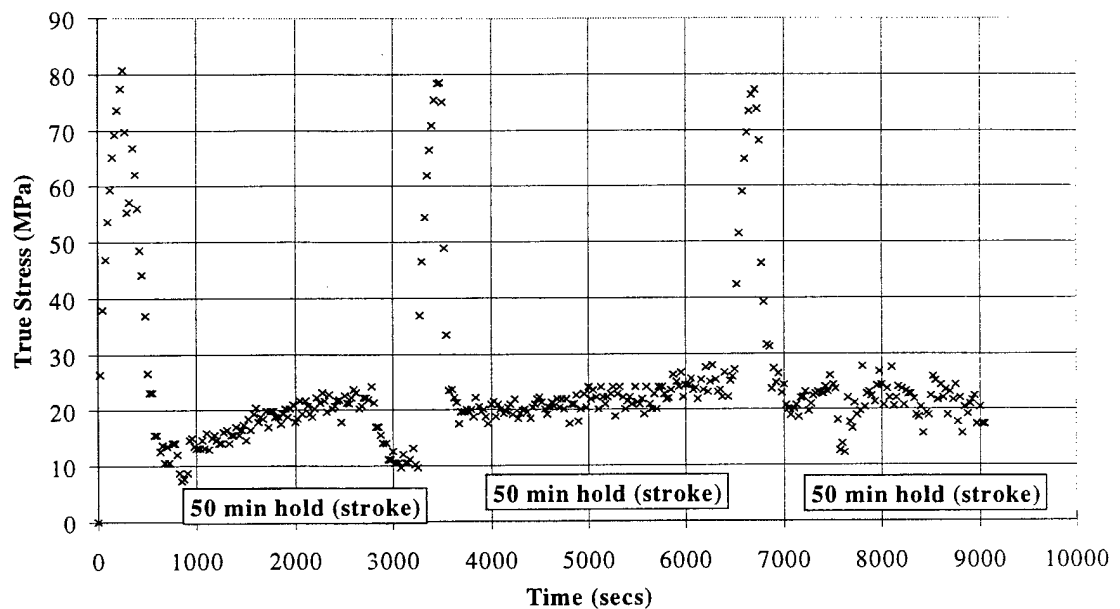


Figure III.60: Experimental results for OFHC Cu in compression at 0.0004 s^{-1} , 405°C , load and hold sequences to 0.1, 0.2, and 0.3 strain, and hold for 50 minutes under stroke control.

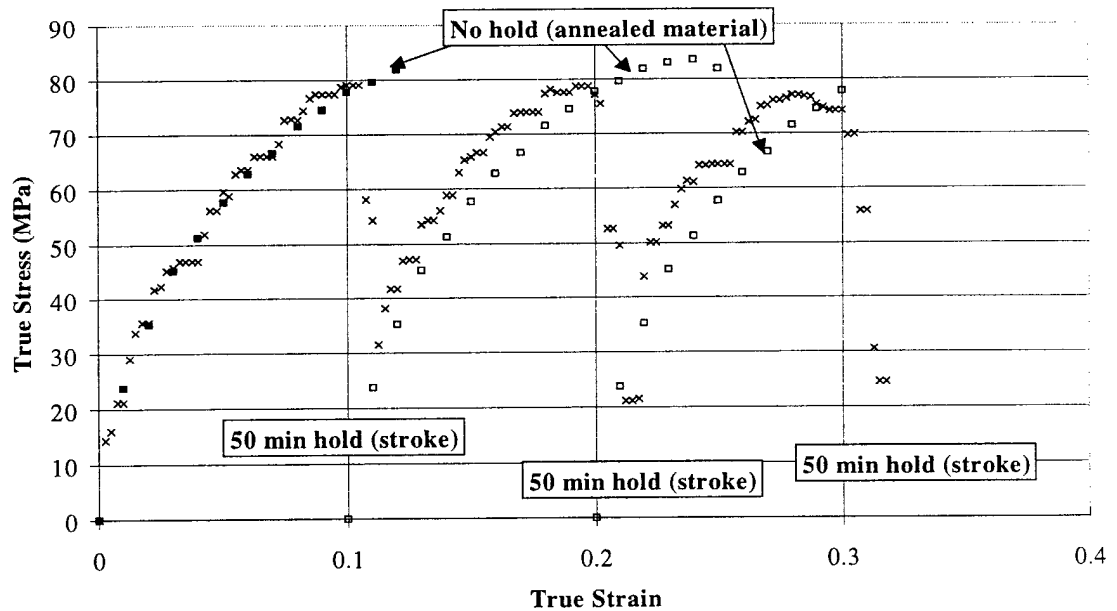


Figure III.61: Experimental results for OFHC Cu in compression at 0.0004 s^{-1} , 405°C , load and hold sequences to 0.1, 0.2, and 0.3 strain, and hold for 50 minutes under stroke control compared to a no hold experiment. Reload curves are compared with annealed material, shown shifted to the reload strain using open symbols.

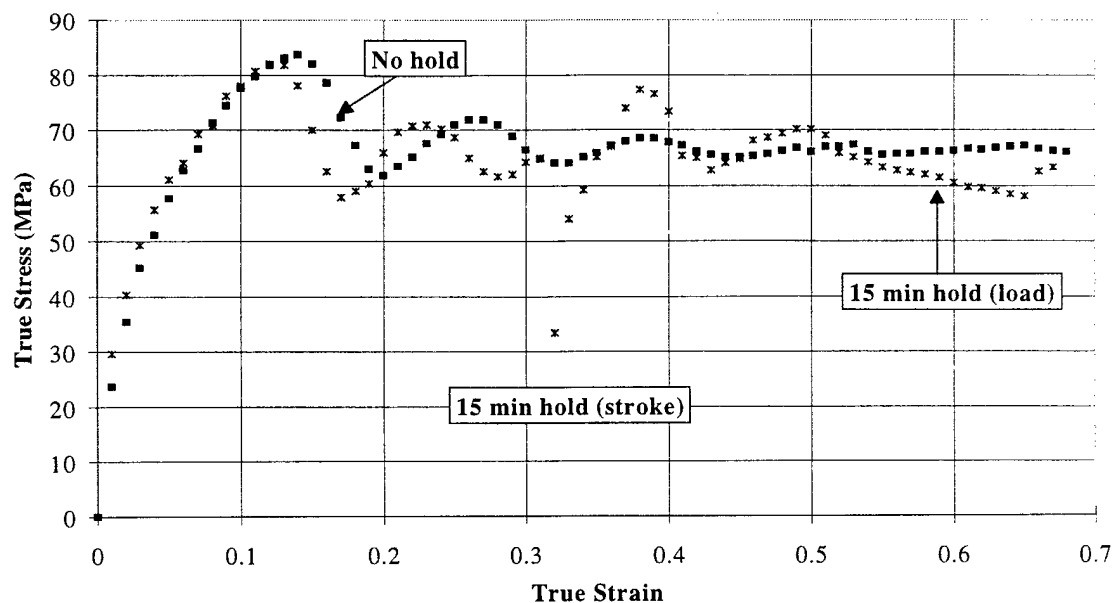


Figure III.62: Experimental results for OFHC Cu in compression at 0.0004 s^{-1} , 405°C , load and hold sequences to 0.3 strain and hold for 15 minutes under stroke control and 0.5 strain and hold for 15 minutes under load control compared to a no hold experiment, shown with solid symbols.

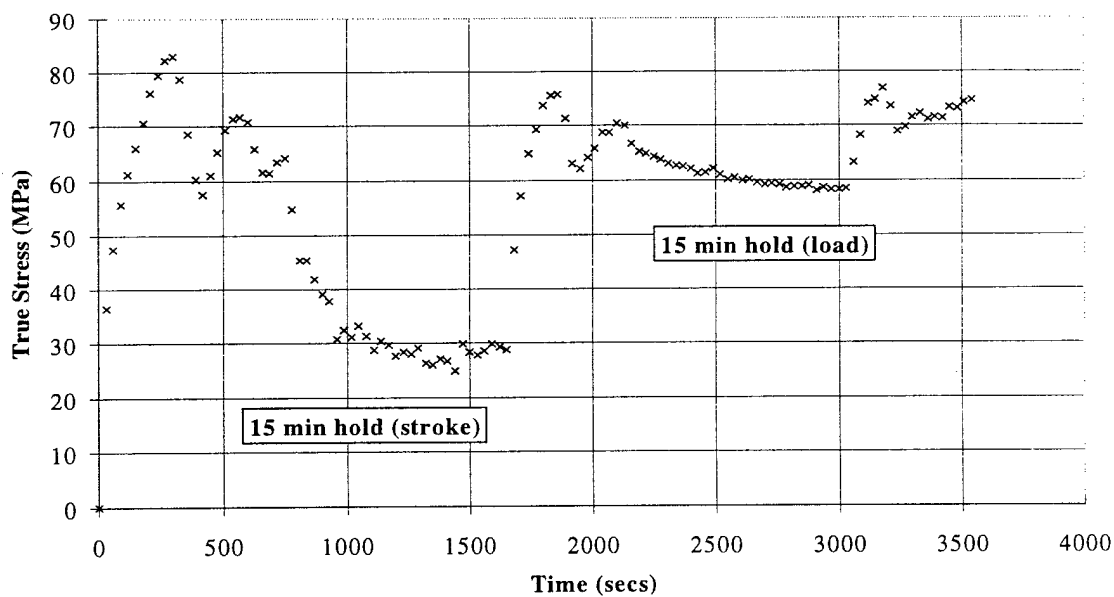


Figure III.63: Experimental results for OFHC Cu in compression at 0.0004 s^{-1} , 405°C , load and hold sequences to 0.3 strain and hold for 15 minutes under stroke control and 0.5 strain and hold for 15 minutes under load control.

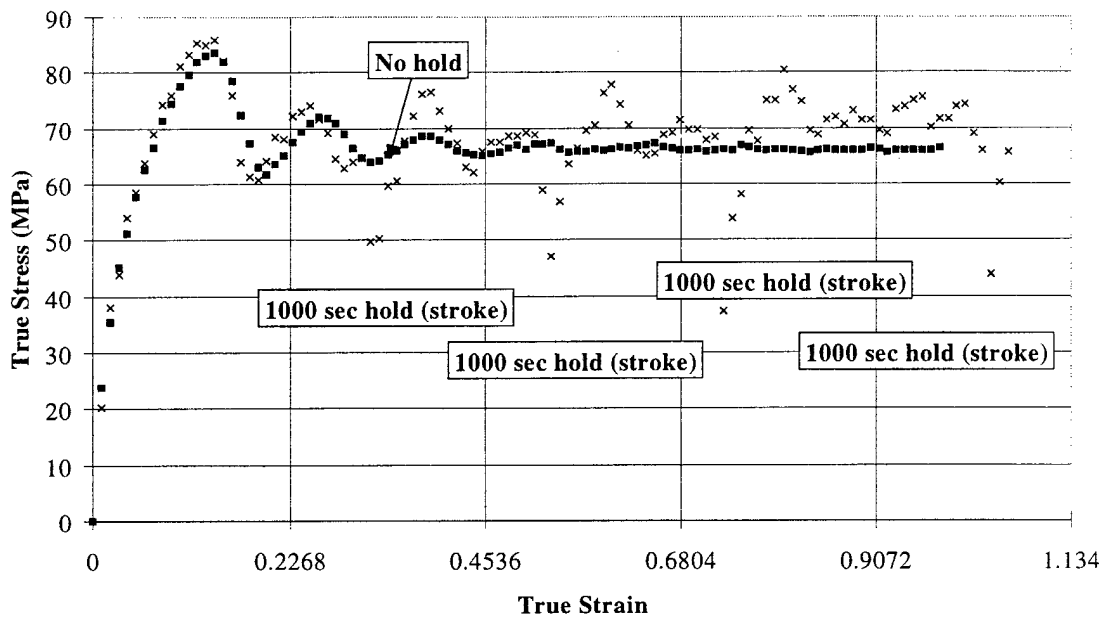


Figure III.64: Experimental results for OFHC Cu in compression at 0.0004 s^{-1} , 405°C , load and hold sequences to 0.3, 0.5, 0.7, and 1.0 strain, and hold for 1000 seconds under stroke control compared to a no hold experiment (solid symbols).

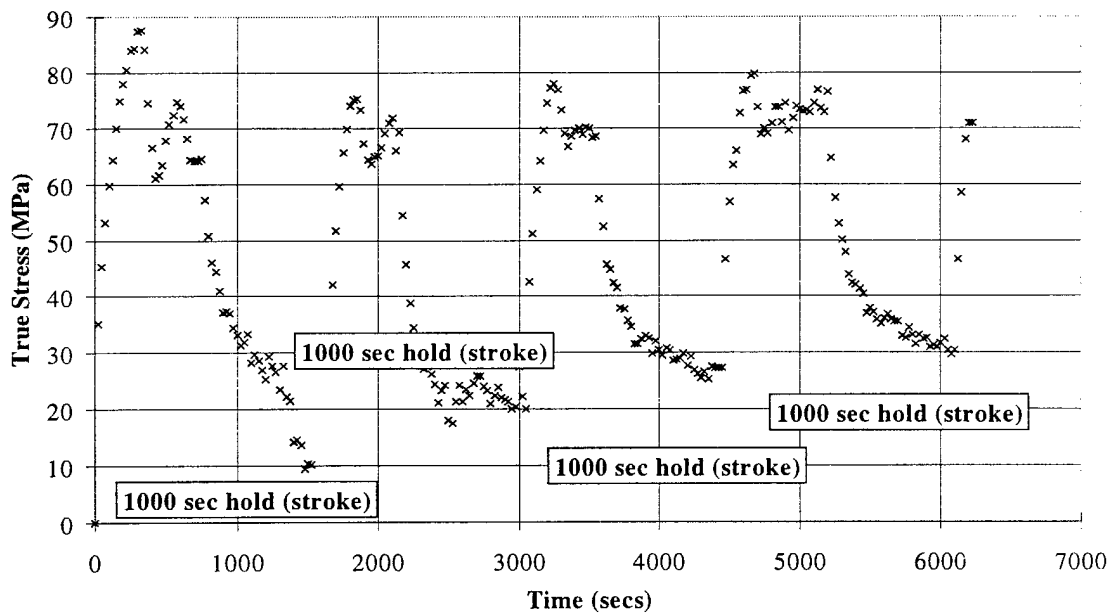


Figure III.65: Experimental results for OFHC Cu in compression at 0.0004 s^{-1} , 405°C , load and hold sequences to 0.3, 0.5, 0.7, and 1.0 strain, and hold for 1000 seconds under stroke control.

III.3.2 Constant True Strain Rate, Isothermal Experimental Results

III.3.2.1 Compression

Compression experiments were conducted at constant true strain rates of 10^3 s^{-1} , 1.0 s^{-1} , 0.1 s^{-1} , 0.01 s^{-1} and 0.0004 s^{-1} and at various temperatures ranging from room temperature 25°C to 676°C ($0.7 T_m$) (Table III.2). Both strain rate and temperature dependence of flow stress are clearly shown in Figs. III.66 - III.68 and Figs. III.69 to III.72, respectively. At strain levels on the order of 0.02, the flow stresses at all temperatures nearly coincide, indicating a range of athermal hardening or resistance to dislocation motion (Mecking, 1980). At medium to high strains, the curves exhibit a temperature dependence. The transition between single and multiple peak oscillations associated with dynamic recrystallization occurred between 303°C and 337°C for a strain rate of 0.0004 s^{-1} . Blaz *et al.*, 1983 determined this transition, for OFHC copper, with an initial grain size of $78 \mu\text{m}$ and strain rate 0.002 s^{-1} , to be about 550°C . Chen and Kocks, 1992 determined that the transition for Cu occurred at 400°C for a strain rate of 0.01 s^{-1} . The transition from single peak to multiple peak oscillations, indicating dynamic recrystallization, in this set of experiments, occurred at a lower temperature, but, also at a slower strain rate which increases the ability for material to recrystallize.

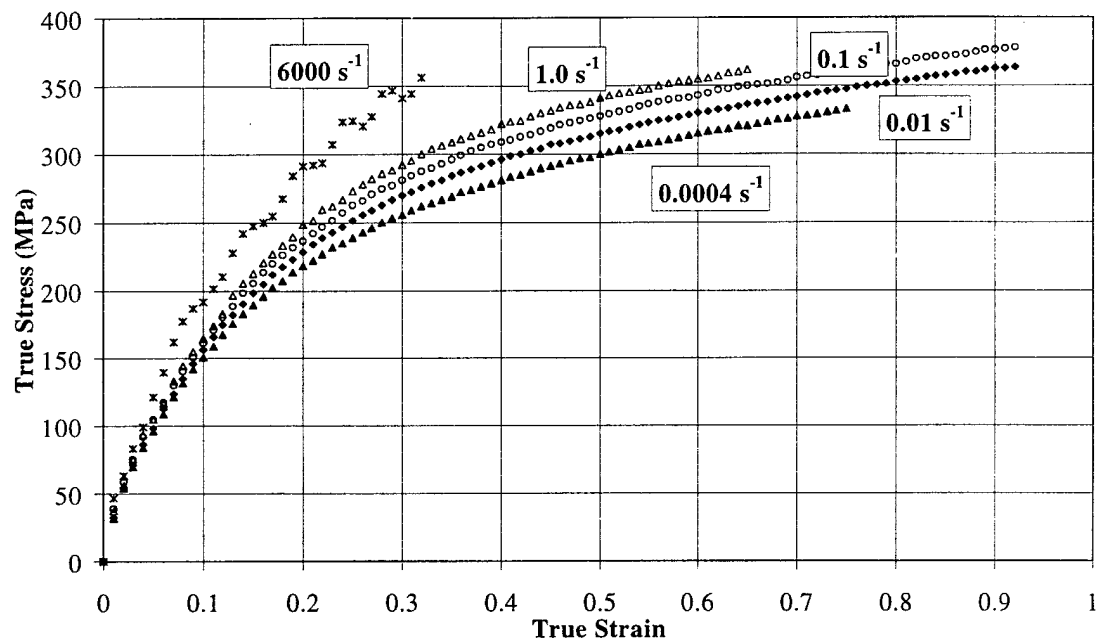


Figure III.66: Strain rate dependence of OFHC Cu in compression at 25°C.

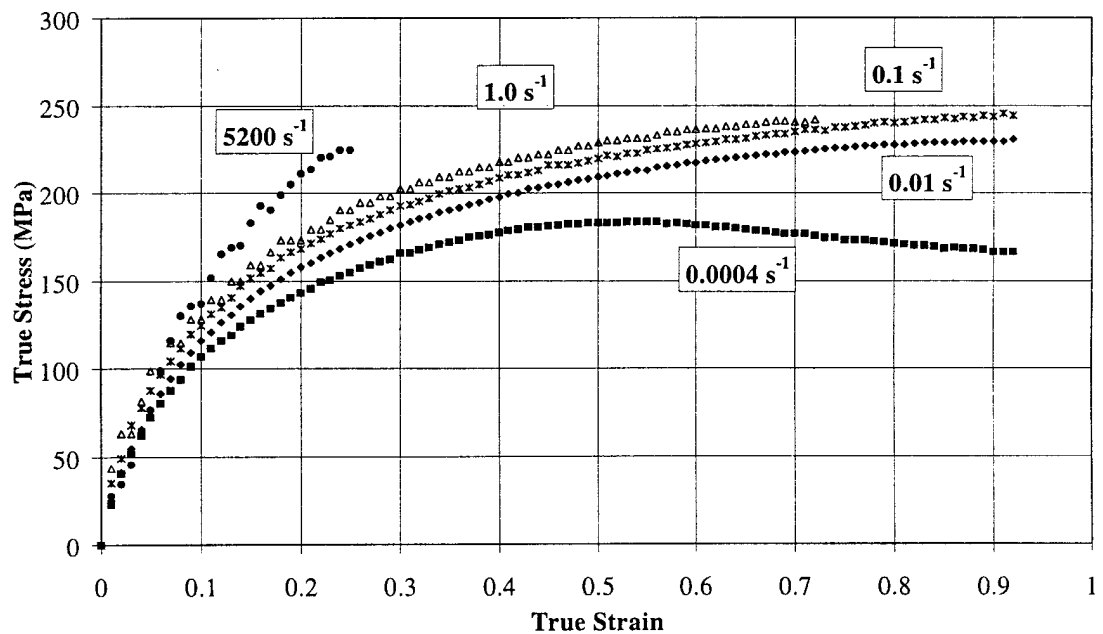


Figure III.67: Strain rate dependence of OFHC Cu in compression at 269°C.

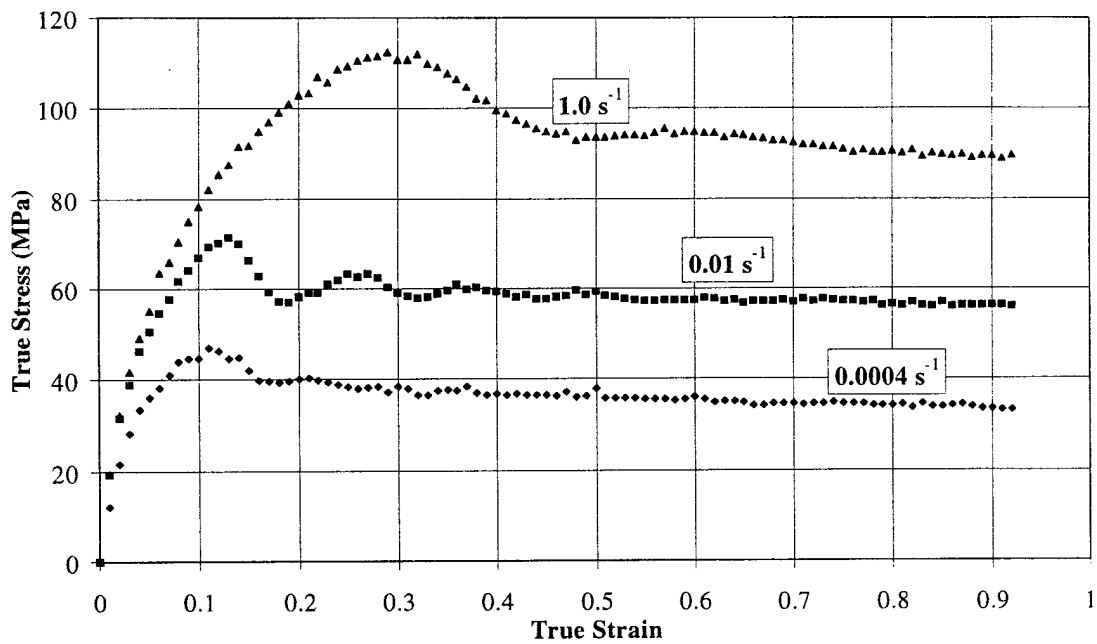


Figure III.68: Strain rate dependence of OFHC Cu in compression at 541°C.

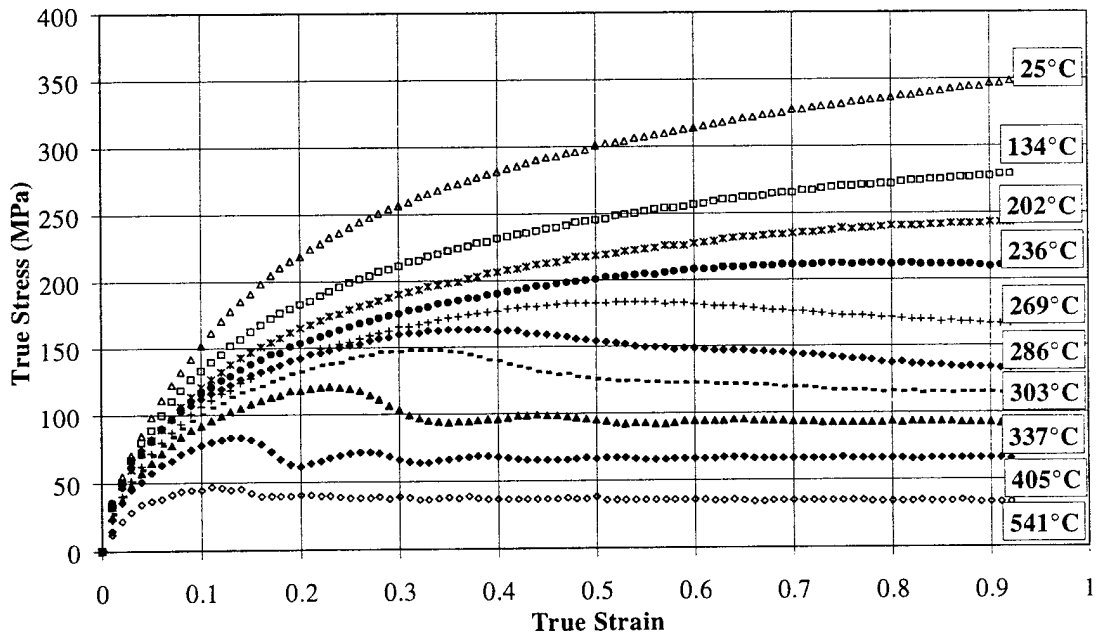


Figure III.69: Temperature dependence of OFHC Cu in compression at $\dot{\epsilon} = 0.0004 \text{ s}^{-1}$.

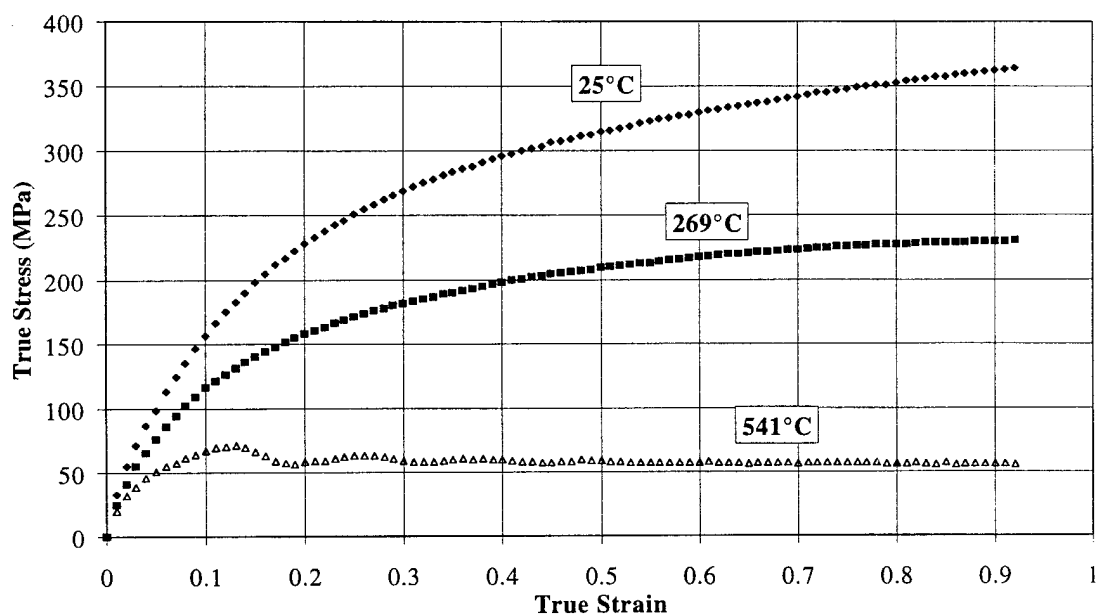


Figure III.70: Temperature dependence at $\dot{\epsilon} = 0.01 \text{ s}^{-1}$.

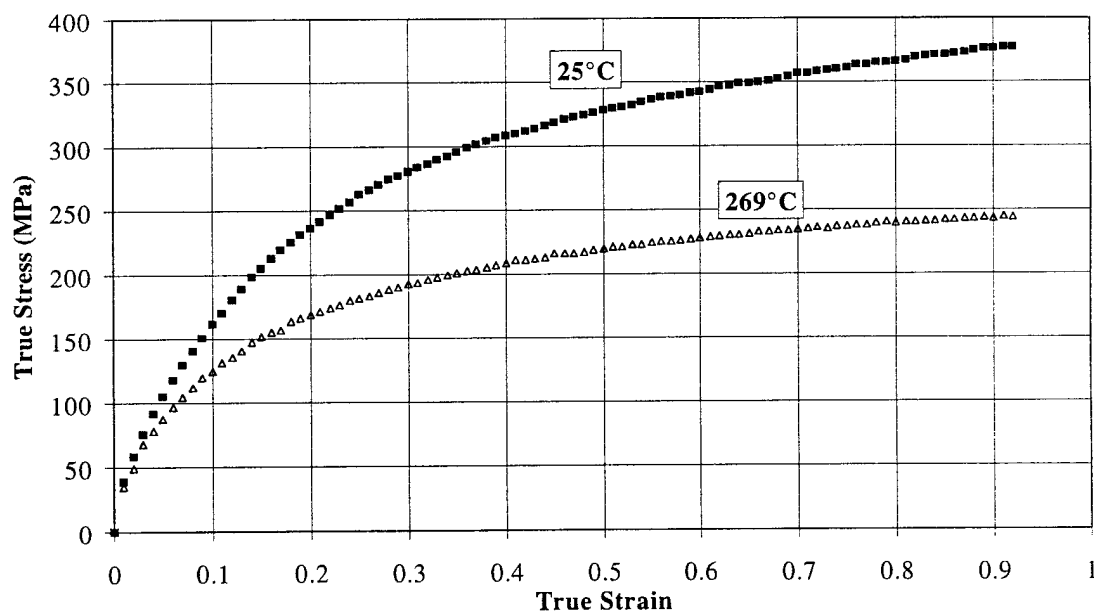


Figure III.71: Temperature dependence at $\dot{\epsilon} = 0.1 \text{ s}^{-1}$.

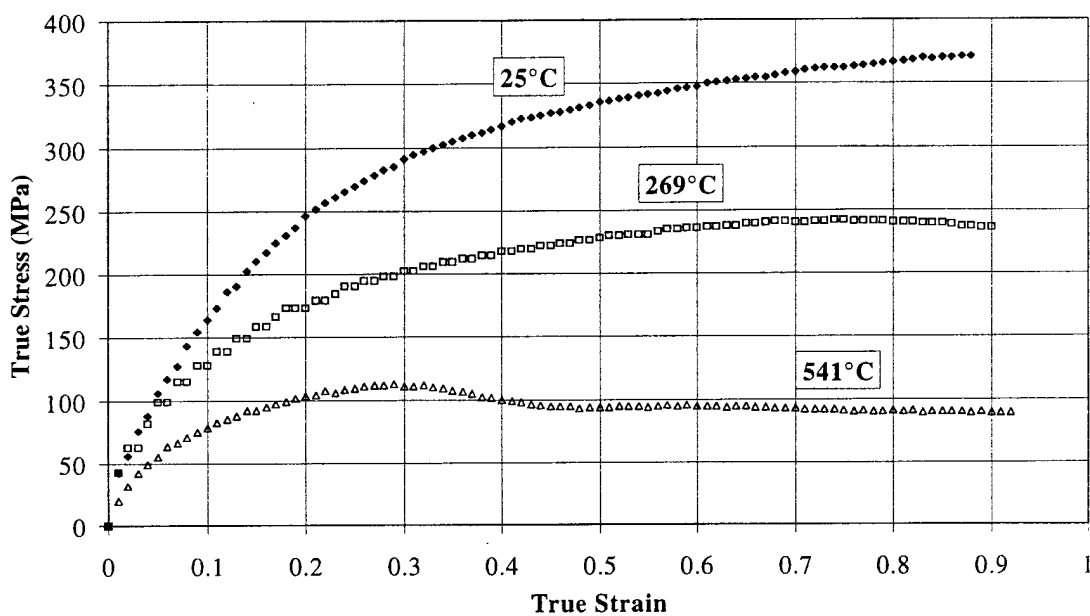


Figure III.72: Temperature dependence at $\dot{\epsilon} = 1.0 \text{ s}^{-1}$.

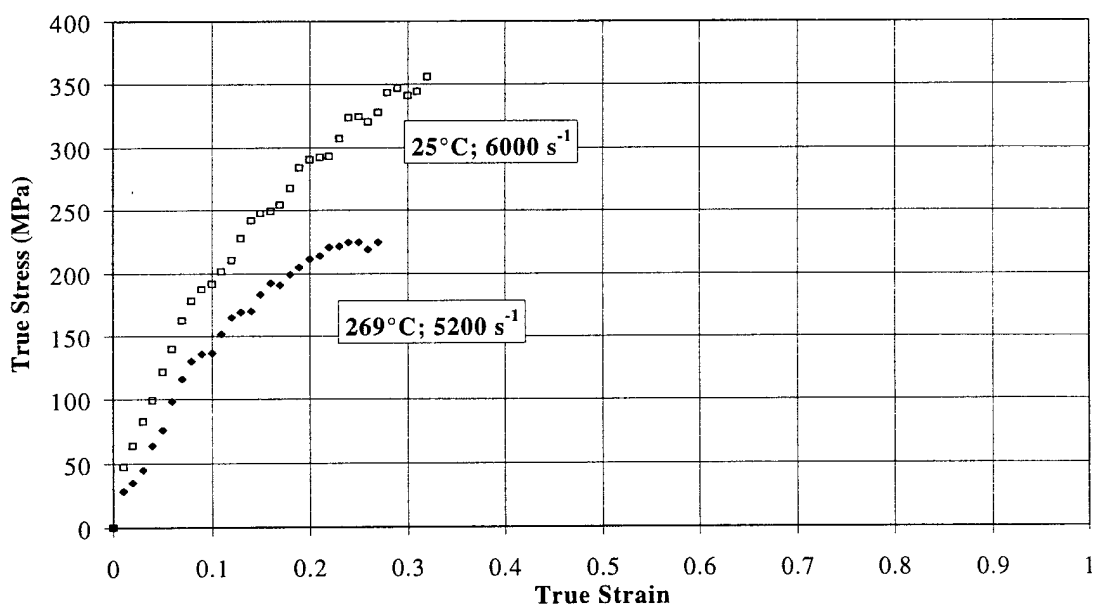


Figure III.73: Temperature dependence at $\dot{\epsilon} = 1000 \text{ s}^{-1}$.

II.3.2.2 Torsion Experiments

Torsion experiments were conducted at a constant true von Mises equivalent strain rate of 0.0004 s^{-1} (0.00069 s^{-1} shear strain rate) and at various temperatures ranging from room temperature 25°C to 405°C ($0.5 T_m$). Table III.3 identifies the free-end torsion experiments which were conducted (Fig. III.73). At 269°C and 405°C the flow stress exhibits a dynamic softening which results in a reduction in flow stress. The flow stress at 405°C exhibits a series of oscillations indicating periods of dynamic recrystallization. Figure III.75 compares torsion experimental data with compression data at the same temperatures. Torsional data exhibit softening relative to compression at all temperatures. The von Mises equivalent torsional flow stress is considerably below that of compression at room temperature, but this difference significantly decreases as the temperature approaches 405°C . Reduction of slip constraint, due to both texture development and formation of different dislocation substructures, have been identified as the main contributors to the torsional softening effect (cf. Miller, 1993; Miller and McDowell, 1996). The difference in the magnitude of compression and von Mises equivalent torsional flow stress decreases as temperature increases, suggesting that the difference in stress state and substructure is temperature dependent. At 25°C , the compression data is significantly above that for torsion. This difference between compression and torsion at 25°C decreases at 269°C , and at 405°C the same saturation flow stress level is reached. The strain to the peak stress at 269°C and 405°C is slightly greater for torsion than compression.

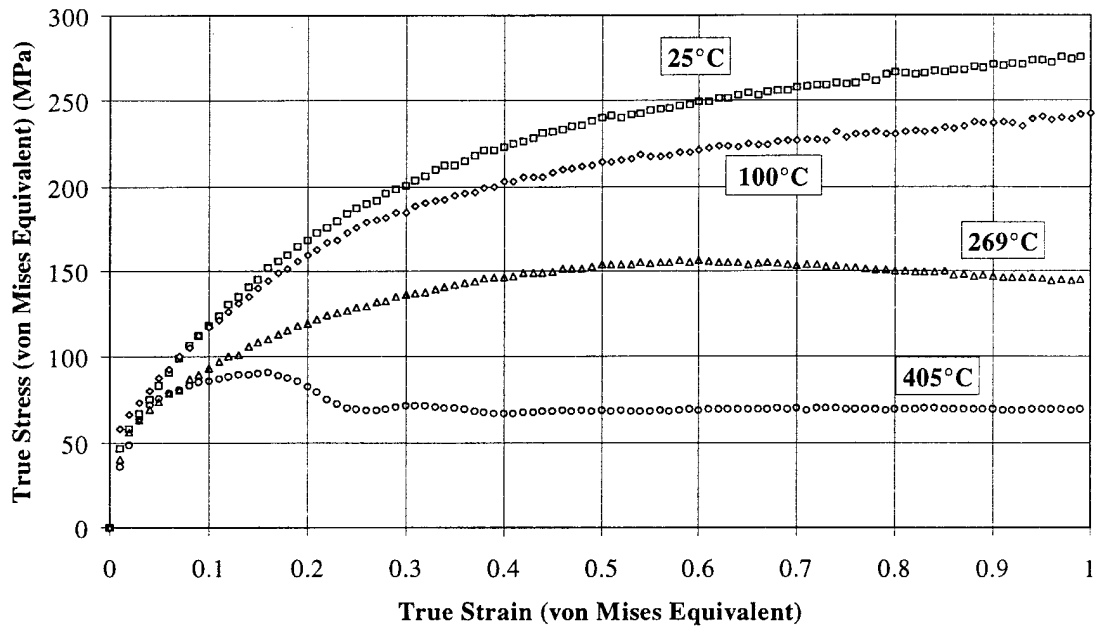


Figure III.74: Torsion experimental data at elevated temperatures and a von Mises equivalent strain rate of 0.0004 s^{-1} .

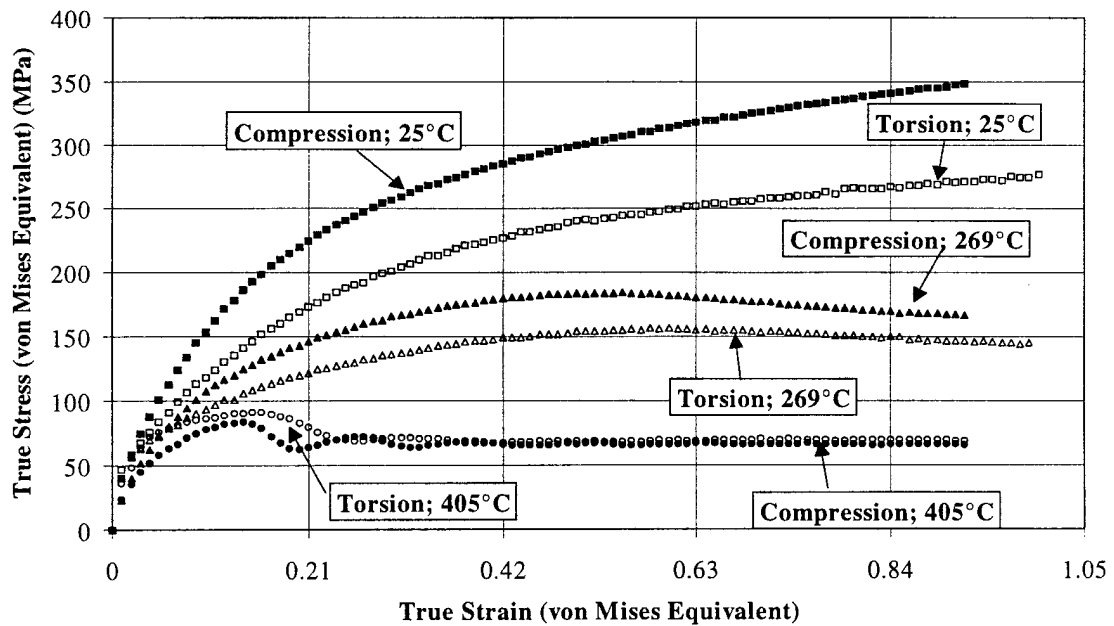


Figure III.75: Compression experimental results compared to torsion experimental results for OFHC Cu at elevated temperatures and a von Mises equivalent strain rate of 0.0004 s^{-1} .

III.3.3 Results of Sequence Experiments

Several series of experiments were completed involving sequences of strain rate, temperature, and deformation path. The purpose of these experiments was to identify the various strain rate, temperature, and deformation path history effects. Continuously varying temperature and strain rate experiments were also conducted (Table III.10). These experiments were conducted to obtain a data set which could be used for model validation. Continuously varying temperature and strain rate conditions are difficult to accurately model, but are more representative of the actual deformation conditions which exist during many applications. Temperatures ranged from 25°C to 450°C and true strain rates from 0.0004 s⁻¹ to 0.1 s⁻¹.

III.3.3.1 Strain Rate Sequence Results

Strain rate incremental change experiments were completed at various strain rates (Tables III.7 and III.8). A specimen is initially deformed in compression at a high strain rate (6000 s⁻¹) and at room temperature (25°C) to a pre-strain of 0.34 (Fig. III.76). After remachining, the specimen is deformed quasi-statically (0.0004 s⁻¹) in compression to a total true strain of 0.84. Upon reloading, the flow stress reaches a level between the two constant strain rate curves, and then, approaches the quasi-static curve as the total strain increases. Figure III.77 shows similar results for a strain rate change from 0.0004 s⁻¹ to 0.1 s⁻¹ after a pre-strain of 0.5. After remachining, the flow stress is initially between the two constant

strain rate curves, and then moves toward the constant strain rate curve corresponding to the new conditions.

Figures III.78 to III.80 and III.81 to III.83 show the results of experiments with continuously varying strain rates at 25°C and 405°C respectively. Strain rate decrease experiments are shown first followed by strain rate increase. The third plot combines both strain rate decrease and increase results for comparison at each temperature. The flow stress initially follows the initial constant strain rate values, and then, gradually approaches the final constant strain rate curve.

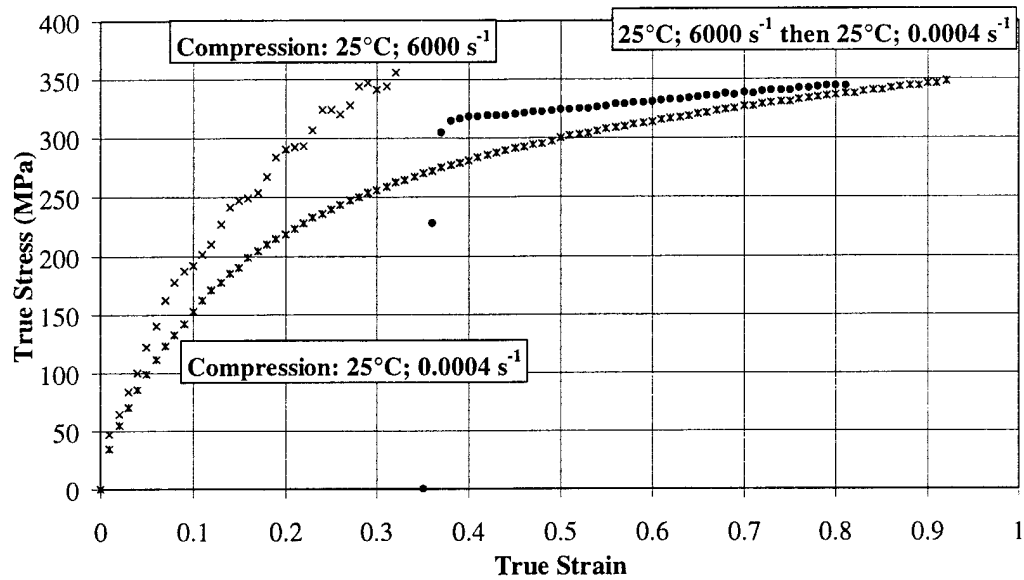


Figure III.76: Compression strain rate history effects at 25°C from high strain rate (6000 s^{-1}) to quasi-static (0.0004 s^{-1}).

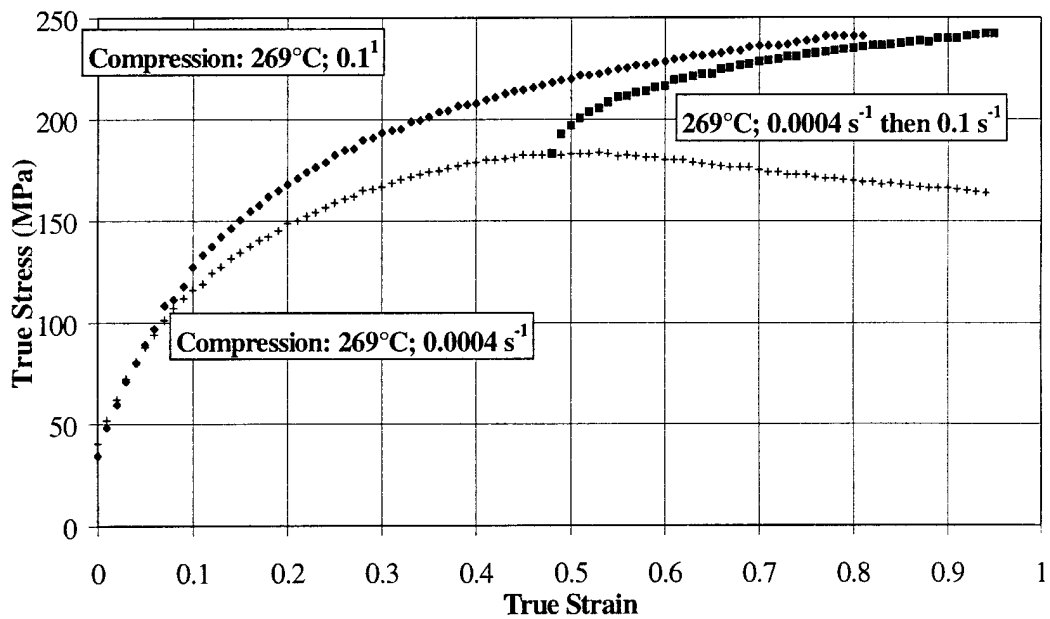


Figure III.77: Compression strain rate history effects at 269°C from 0.0004 s^{-1} to 0.1 s^{-1} .

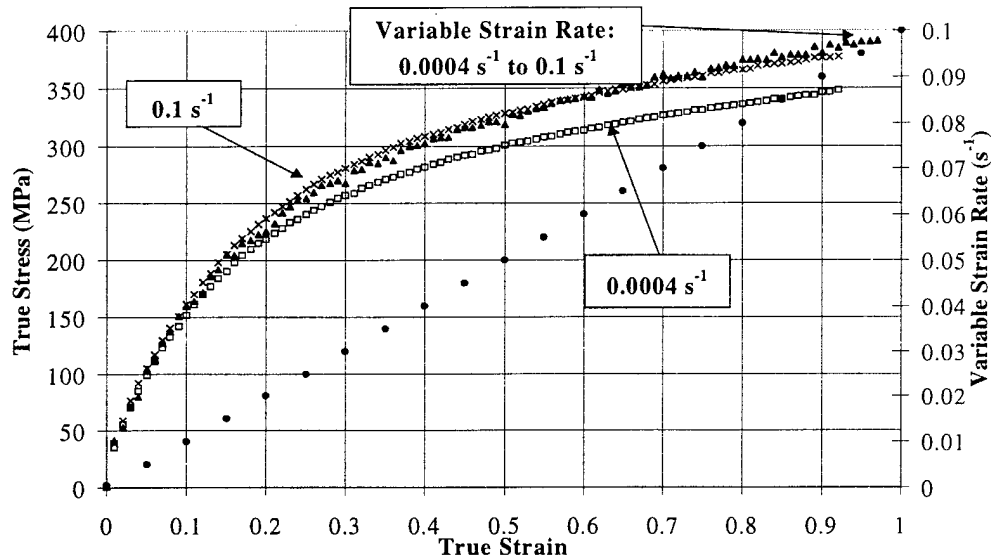


Figure III.78: Experimental results for OFHC Cu compressed at 25°C while strain rate continuously varied from 0.0004 s^{-1} to 0.1 s^{-1} .

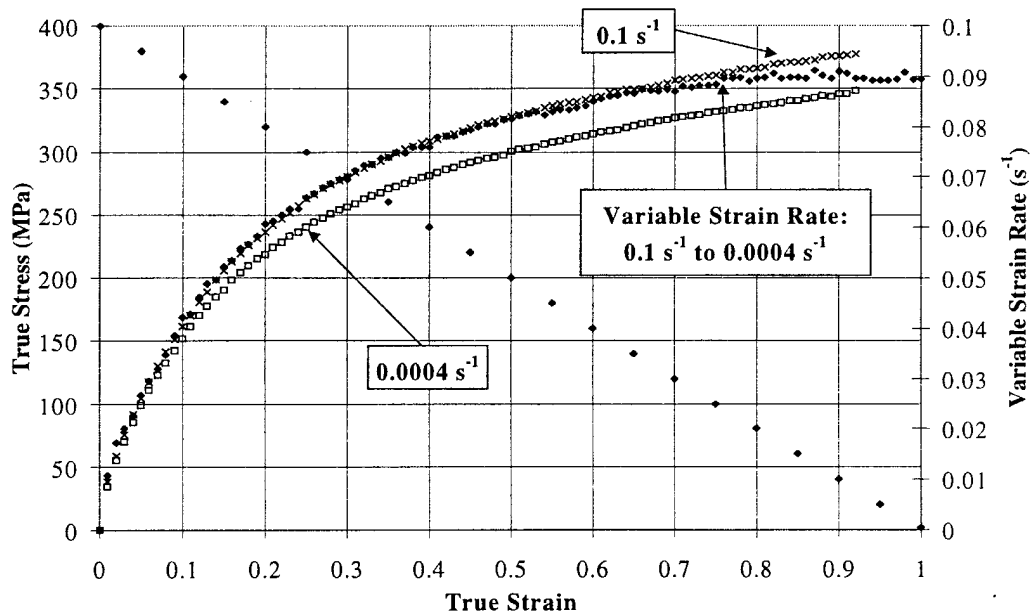


Figure III.79: Experimental results for OFHC Cu compressed at 25°C while strain rate continuously varied from 0.1 s^{-1} to 0.0004 s^{-1} .

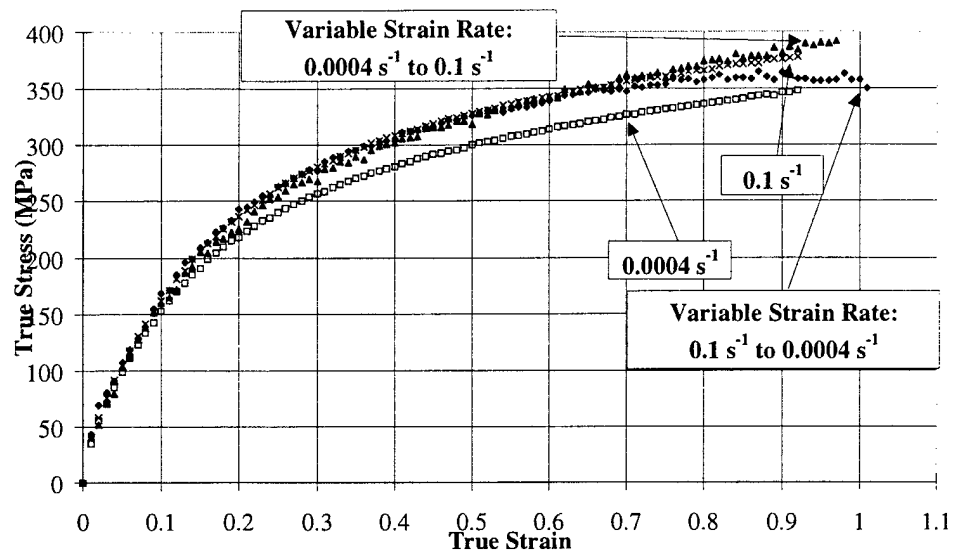


Figure III.80: Experimental results for OFHC Cu compressed at 25°C while strain rate continuously increased from (0.0004 s⁻¹ to 0.1 s⁻¹) is compared to results while the strain rate continuously decreased from (0.1 s⁻¹ to 0.0004 s⁻¹).

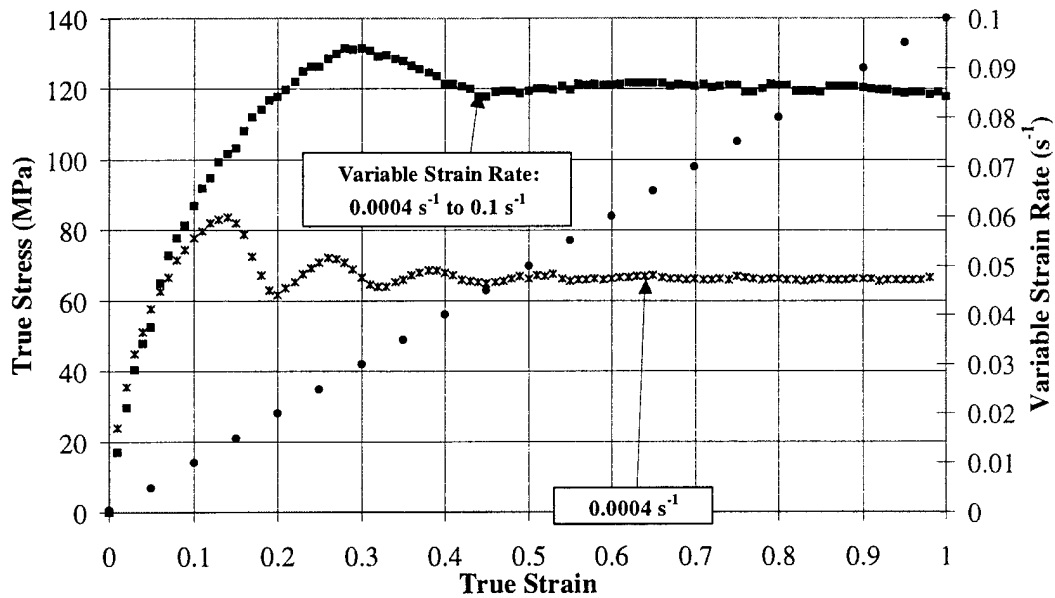


Figure III.81: Experimental results for OFHC Cu compressed at 405°C while strain rate is continuously varied, from 0.0004 s⁻¹ to 0.1 s⁻¹.

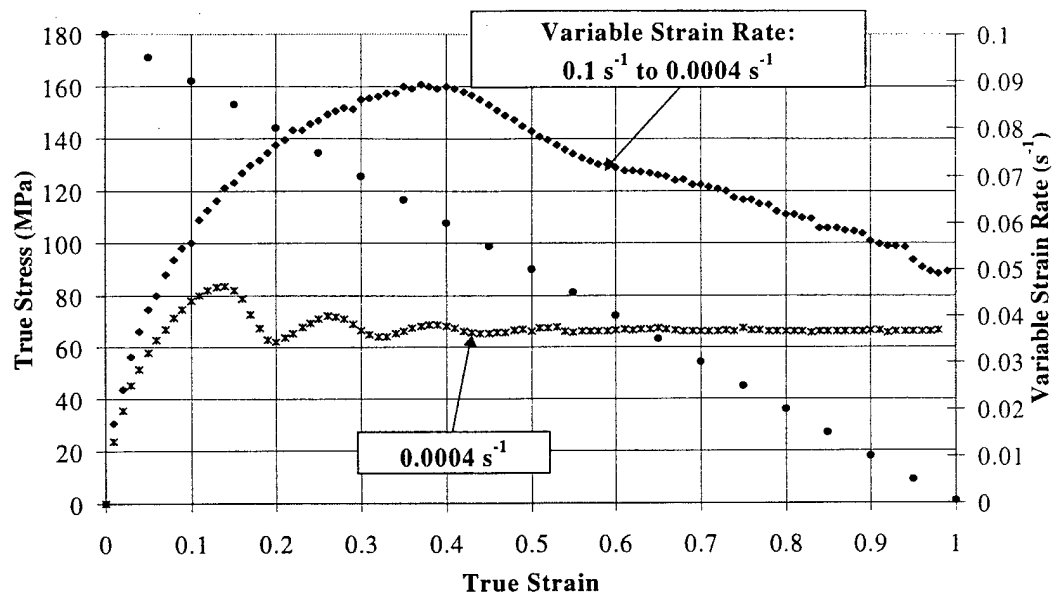


Figure III.82: Experimental results for OFHC Cu compressed at 405°C while strain rate is continuously decreased from 0.1 s^{-1} to 0.0004 s^{-1} .

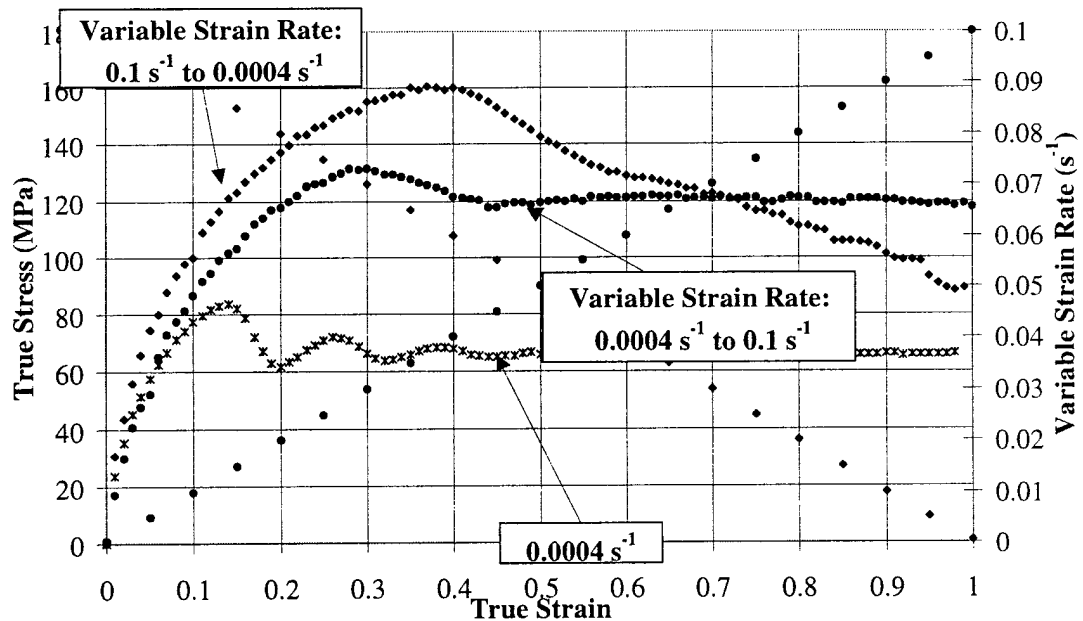


Figure III.83: Experimental results for OFHC Cu compressed at 405°C while strain rate continuously increased from (0.0004 s^{-1} to 0.1 s^{-1}) is compared to results while the strain rate continuously decreased from (0.1 s^{-1} to 0.0004 s^{-1}).

III.3.3.2 Temperature Sequence Results

During temperature sequence experiments at 269°C, the specimen is rapidly heated, remaining in the furnace for 45 seconds before imposing the quasi-static deformation. This time was necessary to achieve uniform temperature throughout the specimen. Upon reloading, the flow stress rapidly rises somewhat above the constant strain rate curve, and then displays accentuated softening. Figures III.84 and III.85 show the OFHC copper response to temperature sequences. Figure III.84 shows the stress-strain behavior of material initially deformed at 269°C, and then, reloaded at 25°C. Figure III.85 shows the response for copper initially deformed at 25°C, and then, reloaded at 269°C. The material is strained to 0.5, unloaded, remachined, and then, reloaded at 269°C to a total strain of 1.0. Initial material response after reloading is clearly dependent upon the amount of time spent in the furnace before the start of the experiment; the longer the time, the greater the amount of restoration that occurs. The initial reload response for material held at zero stress for 20 minutes in the furnace at 269°C is similar to that of an annealed material subjected to a strain level of about 0.3 (Fig. III.86).

Continuously varying temperature experiments are shown in Figs. III.87 to III.89. Temperature decrease results are shown in Fig. III.87. The temperature rapidly falls initially and then gradually decreases to about room temperature. Figures III.88 and III.89 are results for two different temperature increase experiments. The temperature increase profile is different, being initially more rapid in Fig. III.89. The resulting flow stress reflects this difference. The flow stress initially corresponds to the constant 25°C temperature curve

when the temperature increase is delayed (Fig. III.88). When the temperature increases more rapidly, the flow stress rapidly departs from the constant 25°C curve. The flow stress then approaches, but may not actually reach, the higher constant temperature curve.

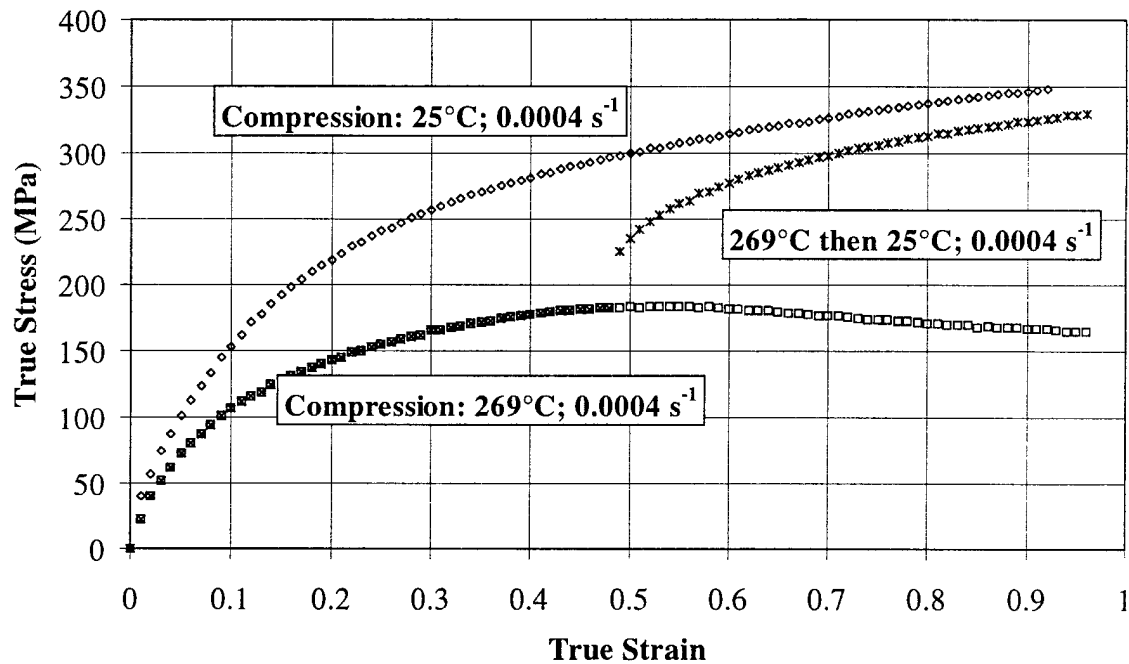


Figure III.84: Temperature history effects of OFHC Cu in compression at 269°C and 0.0004 s⁻¹ pre-strained to 0.5 and then in compression at 25°C and 0.0004 s⁻¹.

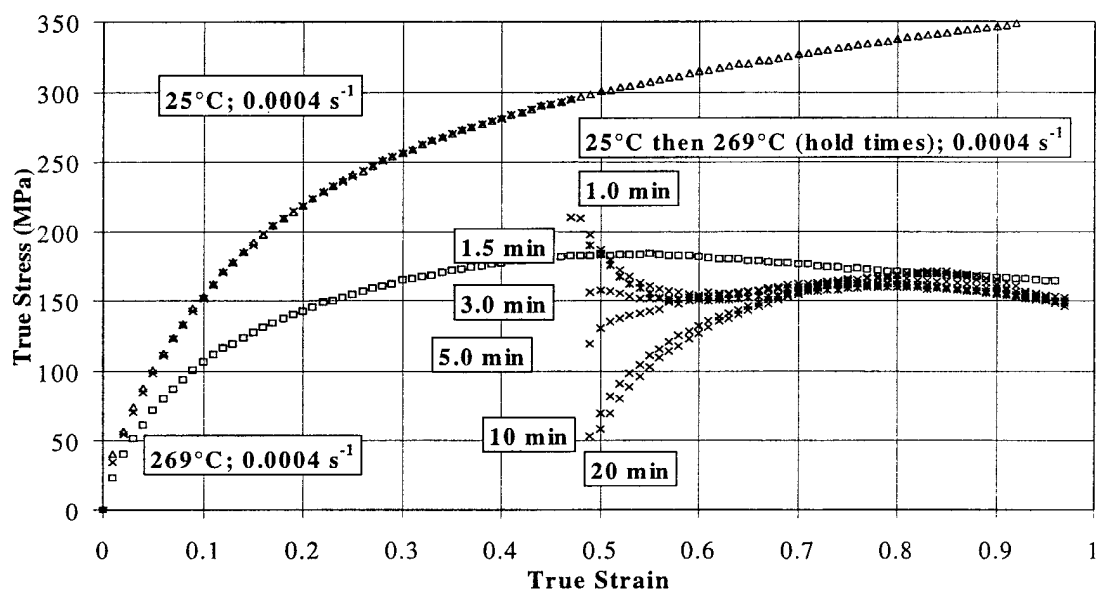


Figure III.85: Temperature history effects of OFHC Cu in compression at 25°C and 0.0004 s^{-1} pre-strained to 0.5 and then in compression at 269°C and 0.0004 s^{-1} .

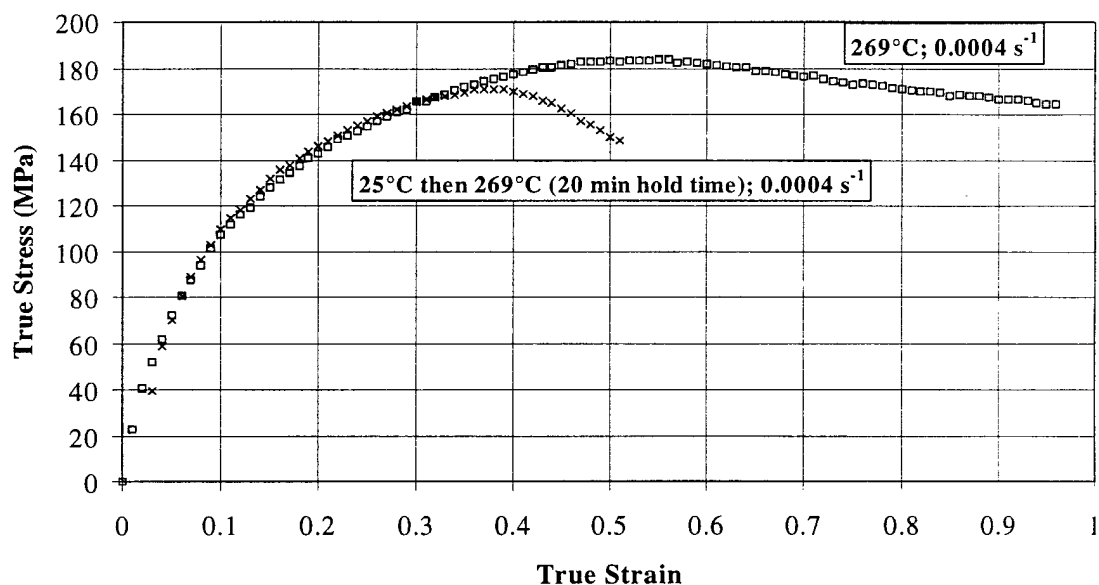


Figure III.86: Temperature history effects of OFHC Cu in compression at 25°C and 0.0004 s^{-1} pre-strained to 0.5 and then in compression at 269°C and 0.0004 s^{-1} after 20 minutes in furnace (axis transformed to zero strain) compared to initial response of annealed material.

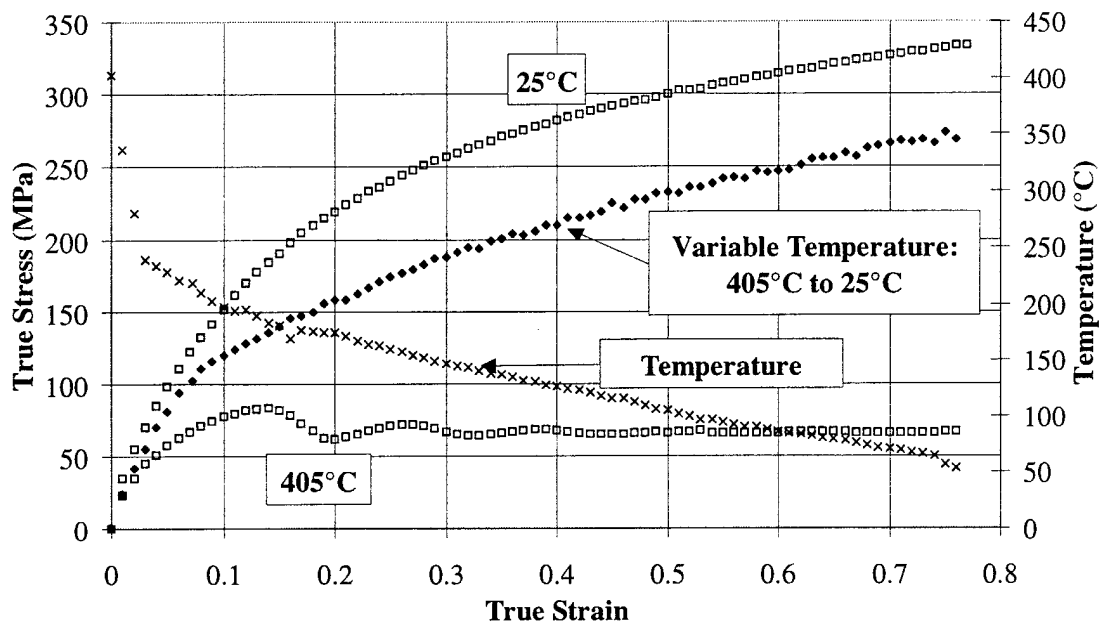


Figure III.87: Experimental results for OFHC Cu compressed at 0.0004 s^{-1} while temperature was continuously reduced from 405°C .

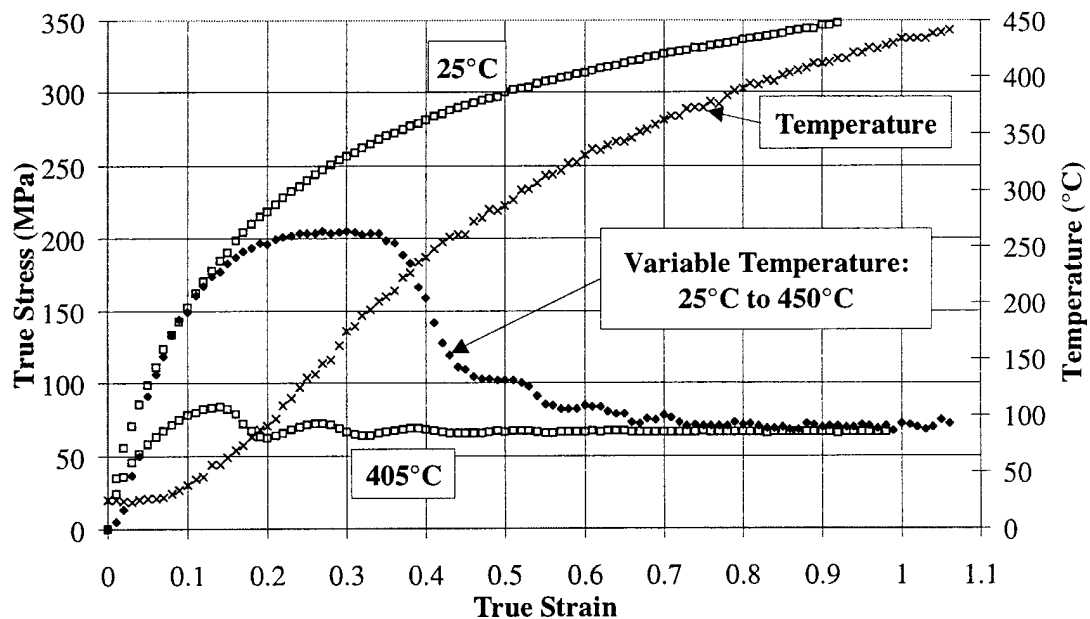


Figure III.88: Experimental results for OFHC Cu compressed at 0.0004 s^{-1} while temperature was continuously increased from 25°C .

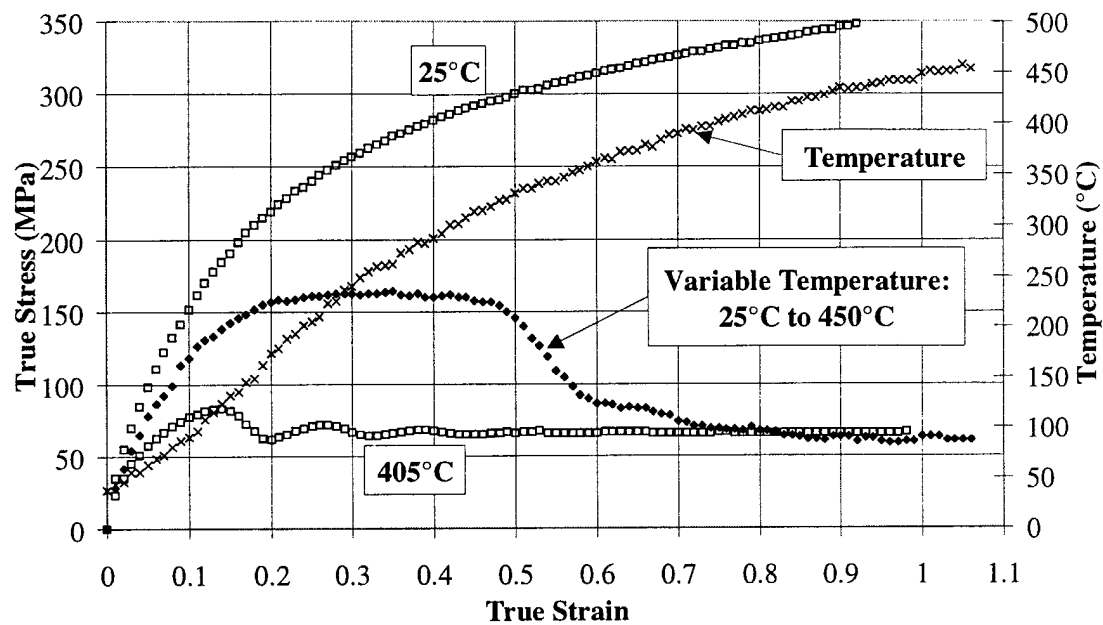


Figure III.89: Experimental results for OFHC Cu compressed at 0.0004 s^{-1} while temperature was continuously increased from 25°C .

II.3.3.3 Deformation Path Sequence Results

Deformation path change experiments were conducted involving sequences of compression followed by torsion or shear (Tables III.6 and III.7) and reverse deformation path (Table III.9). These included high rate (10^3 s^{-1}) compression at 25°C and 269°C followed by quasi-static (0.0004 s^{-1}) shear at 25°C and 269°C . Additionally, experiments at quasi-static compression were followed by quasi-static torsion at temperatures of 25°C , 100°C , and 269°C .

III.3.3.3.1 Compression/Torsion Deformation Path Sequence Results

The high strain rate compression specimens were approximately 3.61 mm in length and 10.16 mm in diameter after deformation using the Hopkinson bar apparatus. Using the double shear specimen design described in section III.2, shear results were obtained from the small volume of material available. Figure III.90 shows the flow stress results from the high rate compression experiment at 25°C followed by quasi-static shear at 25°C and 269°C . The subsequent equivalent flow stress in shear persists well above the level for pure torsion experiments at the same $\bar{\epsilon}$ level due to prior formation of a different texture and dislocation substructure in compression.

Material was also tested in sequences of compression followed by torsion at quasi-static strain rates. OFHC Cu was first compressed to a pre-strain of 0.3 and 0.5 at 25°C and 0.0004 s^{-1} . The material was then unloaded and remachined into Lindholm torsion

specimens. An EDM process was used to prevent significant changes to the microstructure. Figure III.91 shows the results of the deformation path change from compression to torsion at 25°C for two levels of pre-strain (Graham, 1995). After reloading in torsion, the flow stress stays approximately parallel to the constant torsion curve, maintaining a similar strain hardening rate. Figure III.92 compares similar deformation path sequence results for reload temperatures of 25°C, 100°C, and 269°C. Consistent with the previous results, the flow stress stays between the compression and torsion curves. At 269°C, the flow stress rapidly decreases to a level below that for the constant torsion curve at 269°C. This result is significantly different from the previous. Figure III.93 compares the torsion reload flow stress with data from annealed material. An OFHC Cu material specimen that is initially deformed in compression at 269°C and a strain rate of 0.0004 s^{-1} , and then, subsequently deformed in torsion at 25°C, is shown in Figure III.94. The flow curve quickly rises to a level *above* the pure torsion curve and then maintains a similar hardening rate.

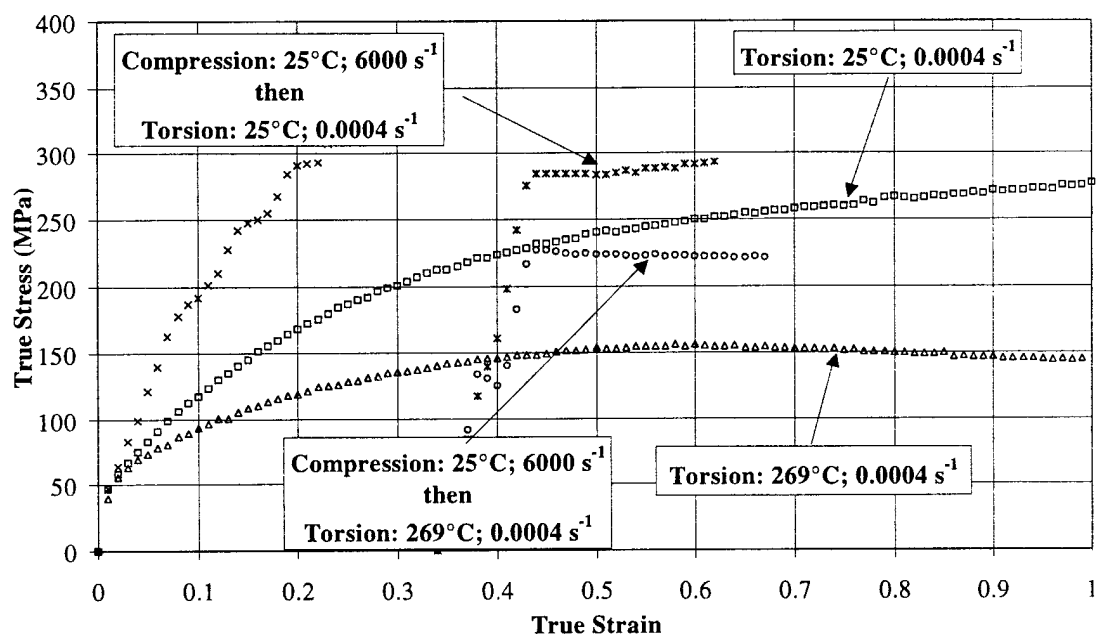


Figure III.90: Deformation path sequence experiments on OFHC Cu conducted in high rate compression followed by quasi-static shear (von Mises equivalent responses are shown).

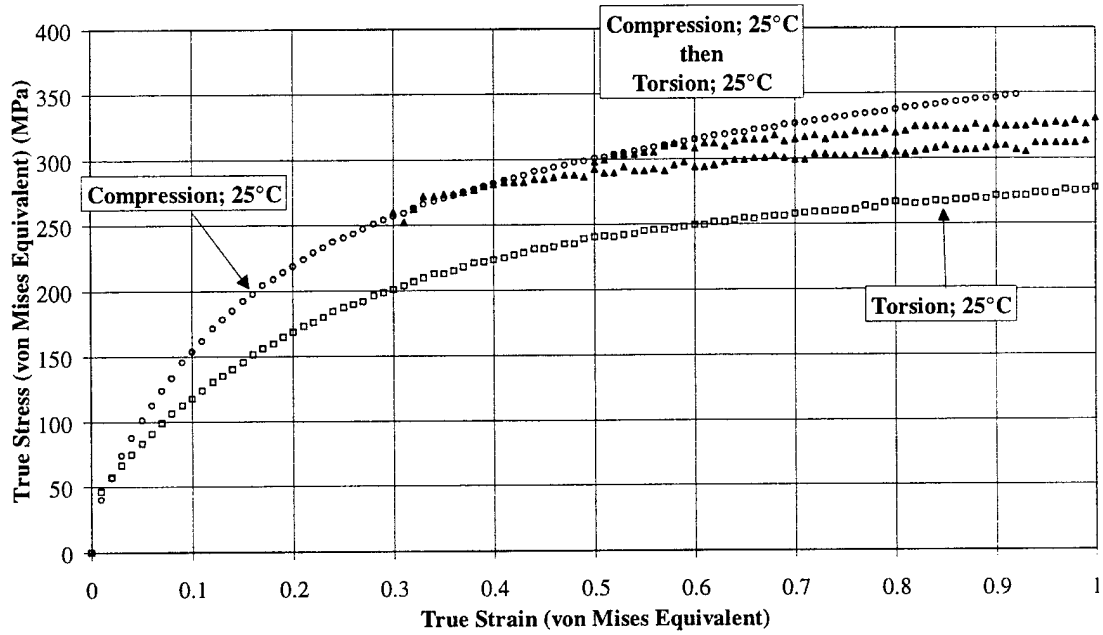


Figure III.91: Deformation path sequence experiments on OFHC Cu conducted in quasi-static compression and 25°C to 0.3 and 0.5 strain followed by quasi-static shear to 1.0 strain (von Mises equivalent responses are shown). The von Mises equivalent strain rate was 0.0004 s^{-1} .

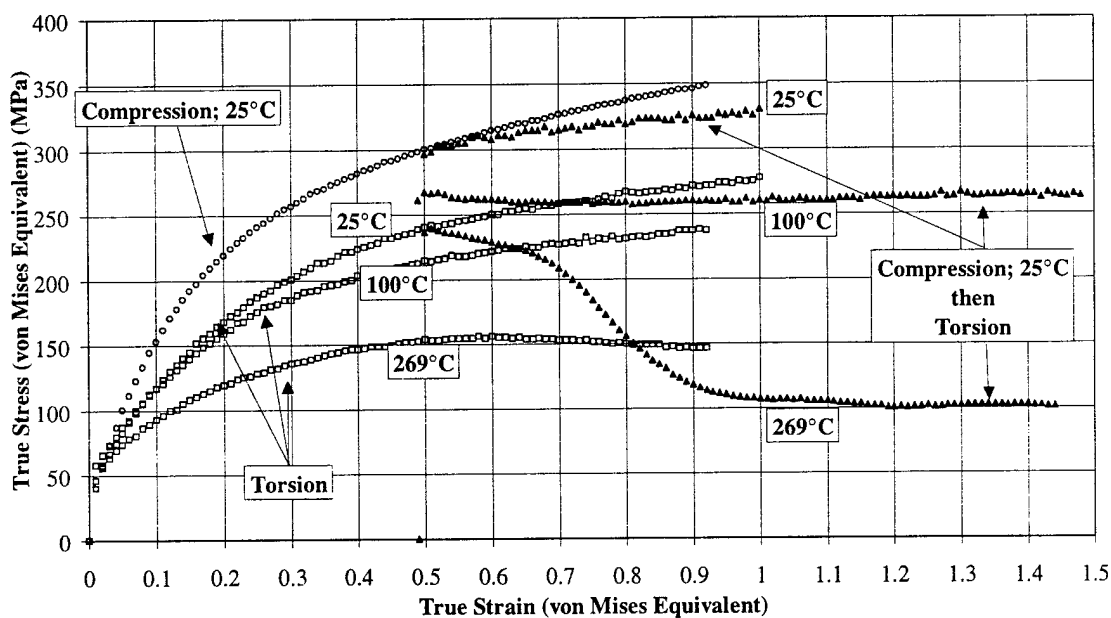


Figure III.92: Deformation path sequence experiments on OFHC Cu conducted in quasi-static compression to 0.5 strain followed by quasi-static shear to 1.0+ strain are compared for various temperatures (von Mises equivalent responses are shown). The von Mises equivalent strain rate was 0.0004 s^{-1} .

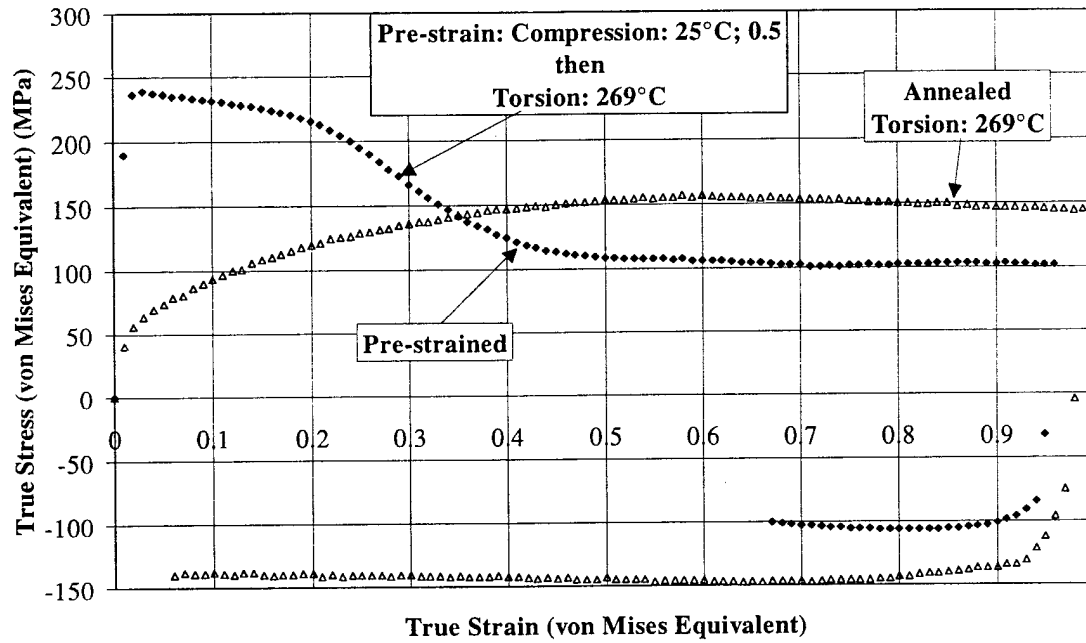


Figure III.93: Deformation path sequence experiments on OFHC Cu conducted in quasi-static compression to 0.5 strain followed by quasi-static shear to 1.5 strain are compared to the shear response of initially annealed material (von Mises equivalent responses are shown). The equivalent strain rate was 0.0004 s^{-1} .

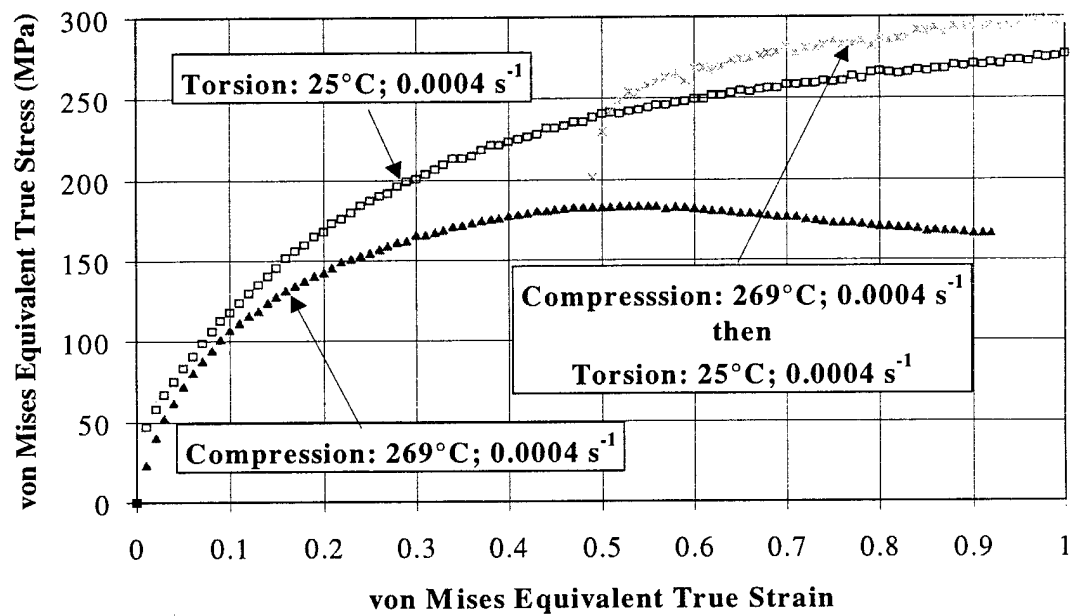


Figure III.94: Deformation path sequence experiments on OFHC Cu conducted in quasi-static compression and 269°C to 0.5 strain followed by quasi-static shear to 1.0 strain (von Mises equivalent responses are shown). The von Mises equivalent strain rate was 0.0004 s⁻¹.

III.3.3.3.2 Reverse Compression/Tension Deformation Path Sequence Results

Reverse deformation path sequence experiments involving compression and tension were conducted. When both tension and compression are displayed on the same graph, compression is shown as negative and tension as positive. Figure III.95 shows the results of deformation path sequences, tension followed by compression. Experiments were conducted using specimen type 6. Data for compression after a pre-strain of 0.25 in tension were limited due to the onset of buckling. The test was halted at any indication of buckling in compression or necking in tension. Figure III.96 compares the data obtained for annealed material, tension followed by compression, with similar data after a compressive pre-strain of 0.5.

Figure III.97 shows the flow stress results of deformation path sequence experiments for compression followed by tension. The strains are limited to amounts which did not exhibit any buckling in compression. The reverse tension flow stress is greater for increasing compressive pre-strain. The test procedure for large compressive pre-strains required remachining specimens. The effect of this unload, remachining, and different specimen configuration is seen in Fig. III.98. The material is given a compressive pre-strain at 25°C and 0.0004 s^{-1} to a strain of 0.5. The material was then remachined into a reverse tension/compression specimen and tested in compression followed by tension. The compressive flow stress for the pre-strain and subsequent compression experiment is smooth and continuous, indicating that the test procedure is consistent, and has not resulted in any anomalies. The comparison data for material after a compressive pre-strain with annealed

material is shown in Fig. III.99. The pre-strained material has a much higher work hardened state, but exhibits the same curve shape as the annealed material. The flow stress in tension after a compressive pre-strain of 0.5 is shown in Figure III.100. The data are limited due to the initiation of necking.

Figures III.101 through III.102 show the flow stress from the results of cyclic experiments conducted on stroke control. Figure III.100 shows the results of annealed material undergoing 20 cycles of compression/tension at 25°C and 0.0004 s^{-1} to a ± 0.01 strain followed by 5 cycles to a strain of ± 0.03 . Figure III.102 shows the results of an experiment conducted using pre-strained material undergoing 20 cycles of compression/tension at 25°C and 0.0004 s^{-1} to a strain of ± 0.01 . Pre-strain was conducted at 25°C and 0.0004 s^{-1} to 0.5 strain. The actual deformation path sequence is shown in Fig. III.103. A comparison of the flow stress resulting from annealed and pre-strained material is shown in Fig. III.104. Experimental results of pre-strained material are overlaid on the annealed material results. The pre-strained material appears to cyclically soften, decreasing approximately 50 MPa during the 20 cycles.

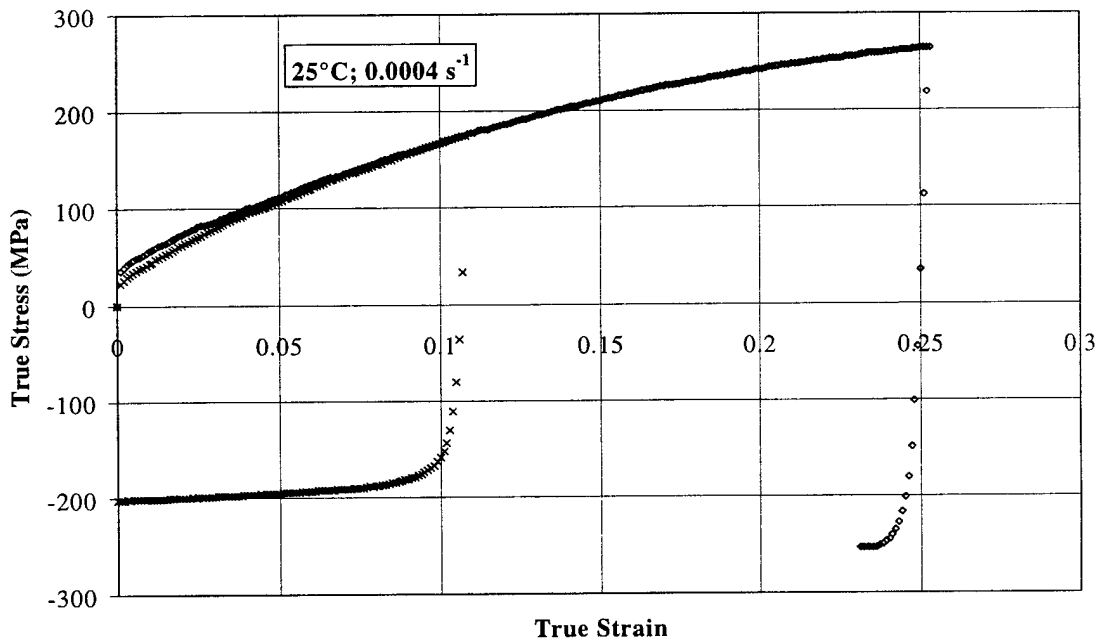


Figure III.95: Deformation path sequence experiments on OFHC Cu conducted in quasi-static tension and 25°C followed by quasi-static compression. The specimen remained in the test machine during the deformation path sequences.

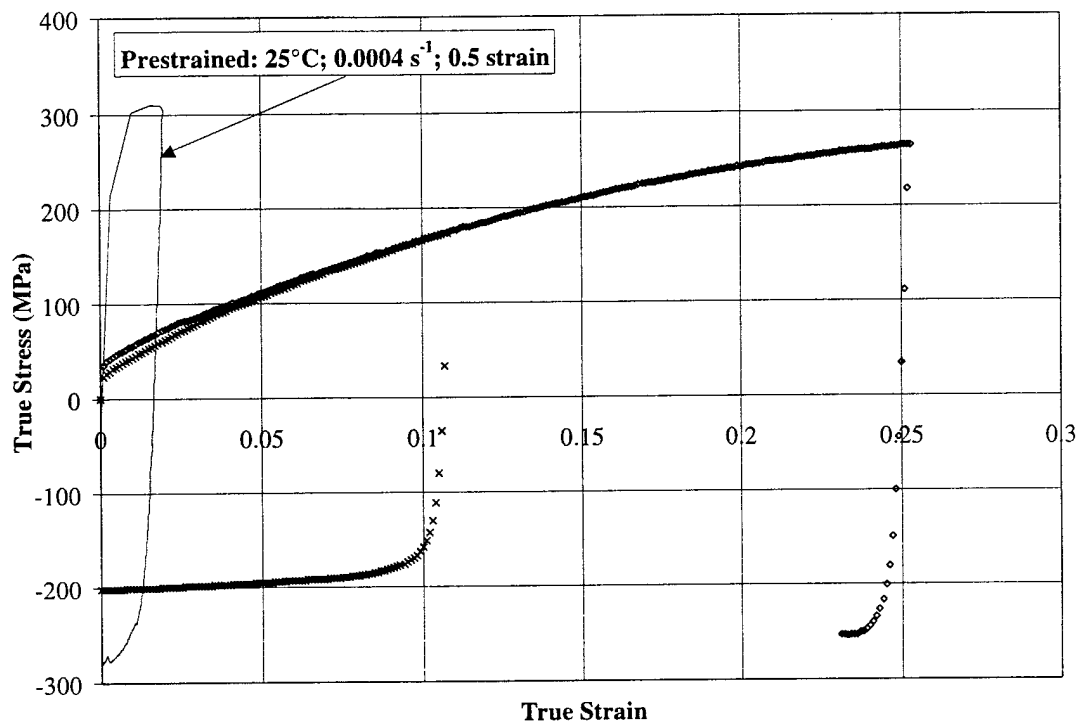


Figure III.96: Deformation path sequence experiments on annealed OFHC Cu conducted in quasi-static tension and 25°C followed by quasi-static compression is compared to material after a compressive, quasi-static pre-strain of 0.5.

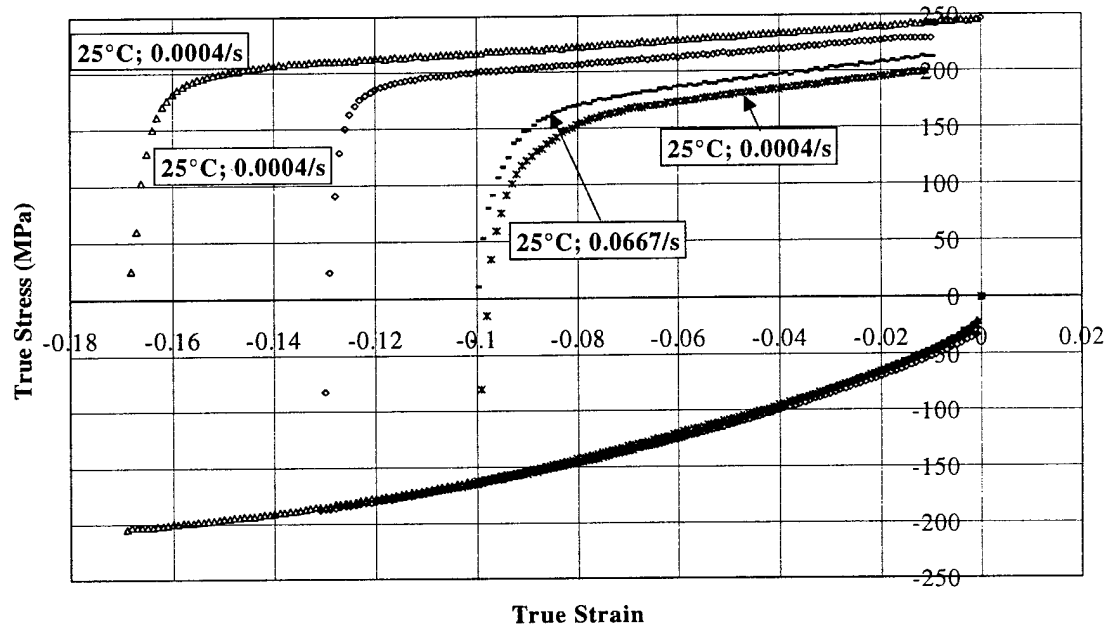


Figure III.97: Deformation path sequence experiments on OFHC Cu conducted in quasi-static compression and 25°C followed by tension. The specimen remained in the test machine during the deformation path sequences.

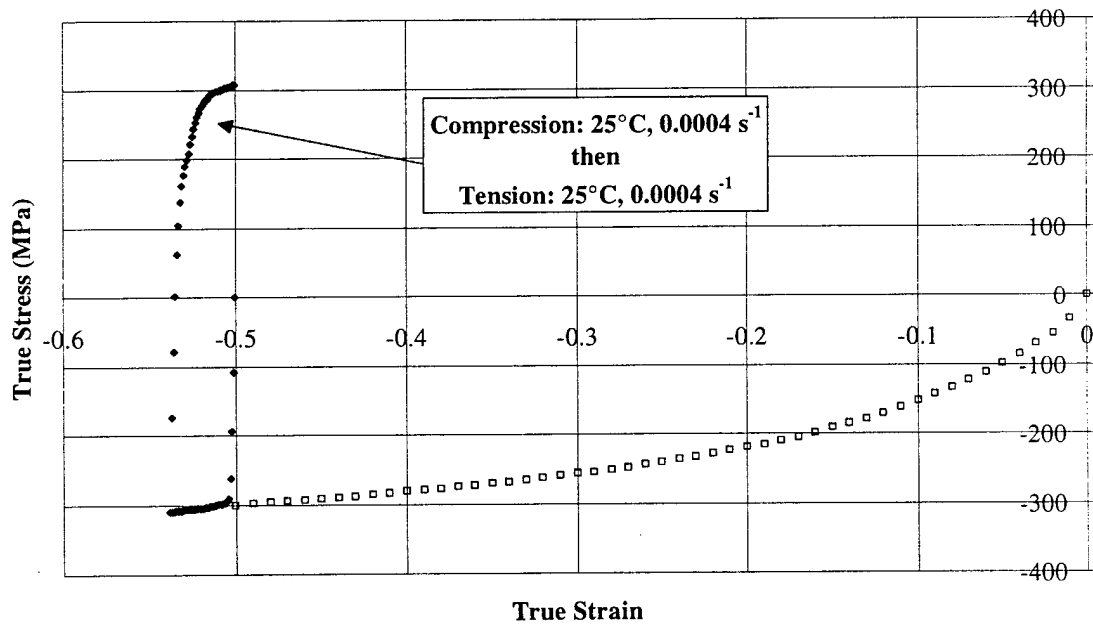


Figure III.98: Deformation path sequence experiments on OFHC Cu conducted in quasi-static compression at 25°C to 0.5 strain followed by compression at 25°C then tension.

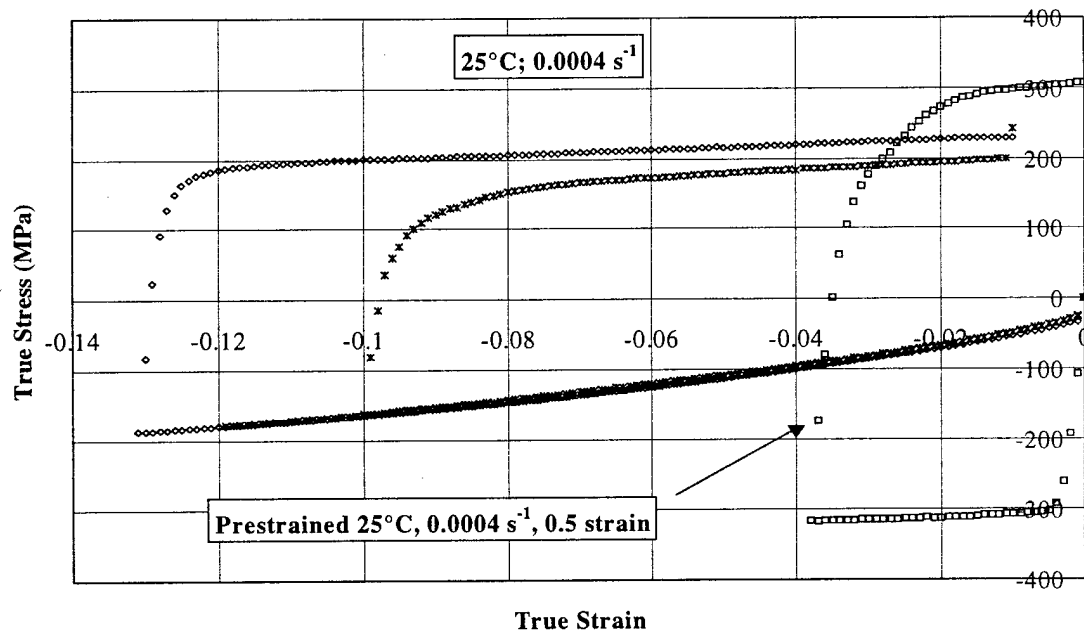


Figure III.99: Deformation path sequence experiments on OFHC Cu conducted in quasi-static compression and 25°C followed by tension is compared to the response after a compression pre-strain at 25°C to 0.5 strain.

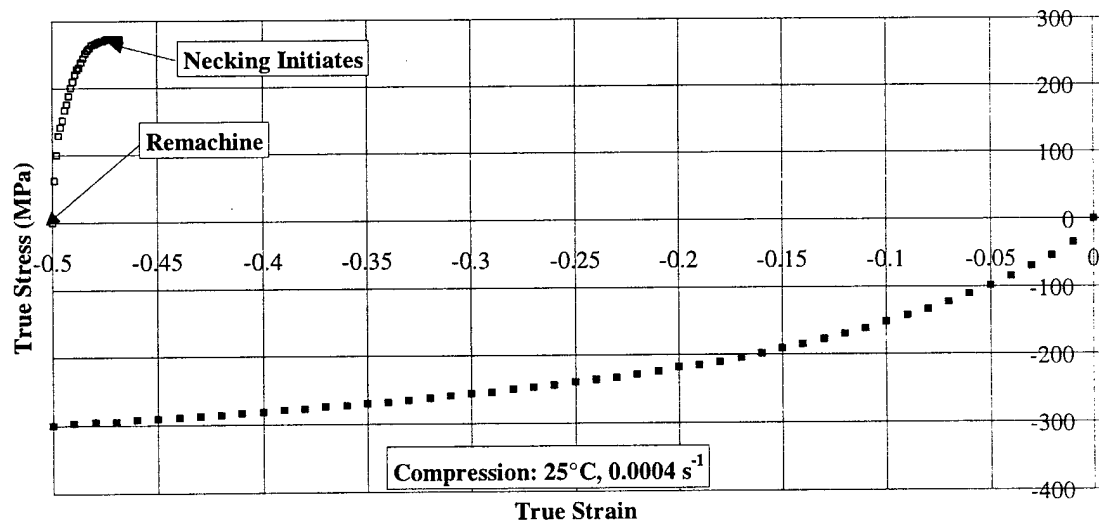


Figure III.100: Deformation path sequence experiments on OFHC Cu conducted in compression, 25°C, and 0.0004 s⁻¹ to 0.5 strain followed by tension until necking initiated.

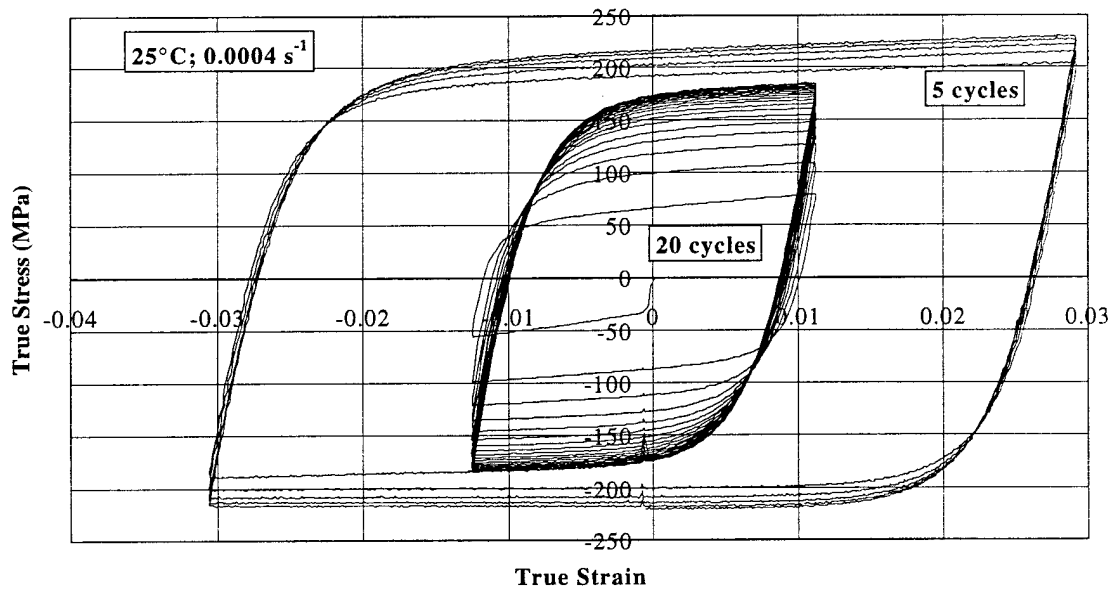


Figure III.101: Cyclic deformation path sequence experiments on annealed OFHC Cu conducted in compression, 25°C , and 0.0004 s^{-1} followed by tension under stroke control.

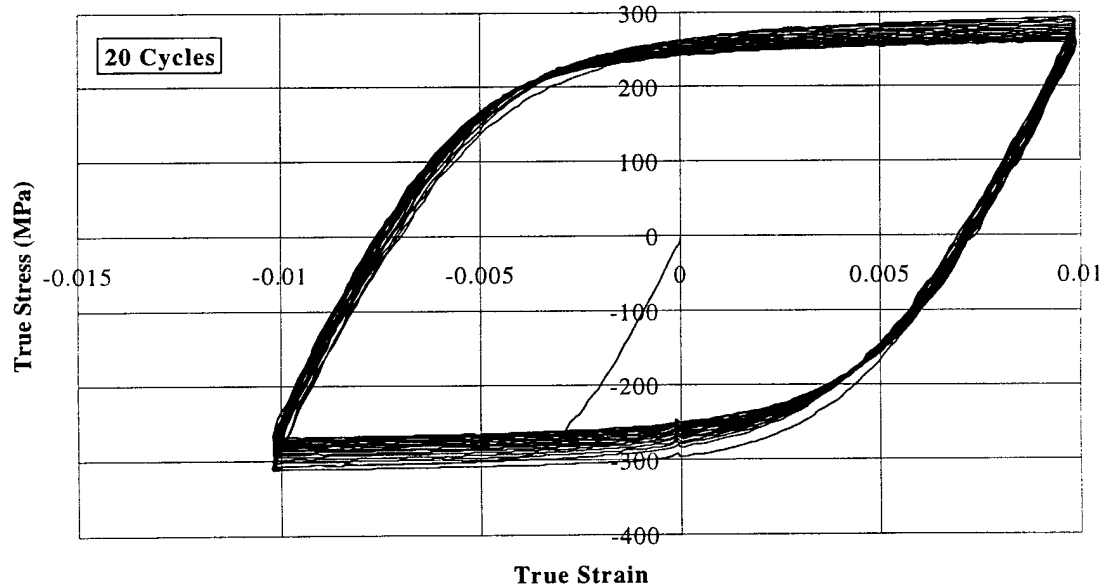


Figure III.102: Cyclic deformation path sequence experiments on pre-strained (0.5 compression at 25°C and 0.0004 s^{-1}) OFHC Cu conducted in compression, 25°C , and 0.0004 s^{-1} followed by tension under stroke control. Twenty complete cycles are shown.

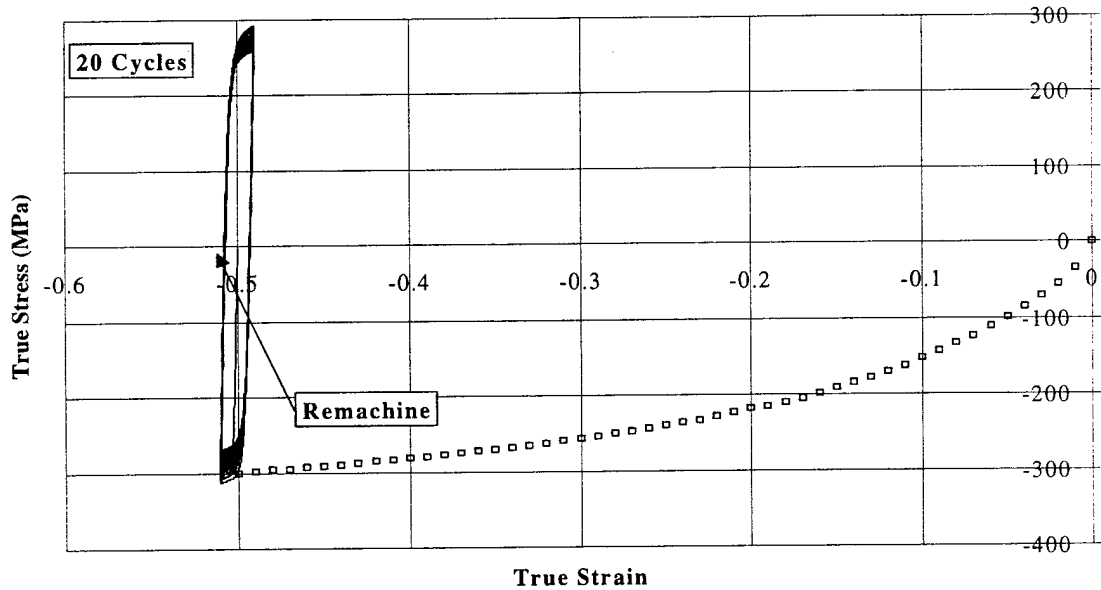


Figure III.103: Cyclic deformation path sequence experiments on pre-strained (0.5 compression at 25°C and 0.0004 s⁻¹) OFHC Cu conducted in compression, 25°C, and 0.0004 s⁻¹ followed by tension under stroke control. Twenty complete cycles are shown relative to the initial compressive pre-strain.

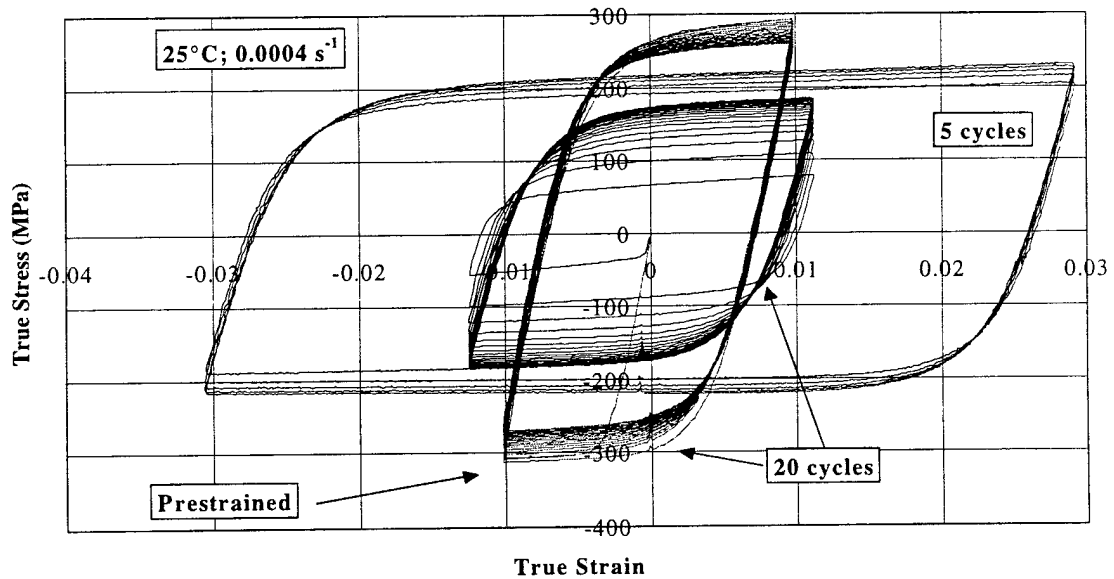


Figure III.104: Cyclic deformation path sequence experiments on pre-strained (0.5 compression at 25°C and 0.0004 s⁻¹) OFHC Cu conducted in compression, 25°C, and 0.0004 s⁻¹ followed by tension under stroke control is compared to annealed material under the same deformation conditions.

III.3.3.3 Reverse Torsion Deformation Path Sequence Results

Figures III.105 and III.106 show the dependencies of temperature and strain, respectively, on the reverse torsion flow stress of OFHC Cu. The flow stress is lower for increasing temperature. At 269°C, a softening of the flow stress is evident during both deformation path directions. Oscillations in the flow stress are observed in both deformation path directions at 405°C.

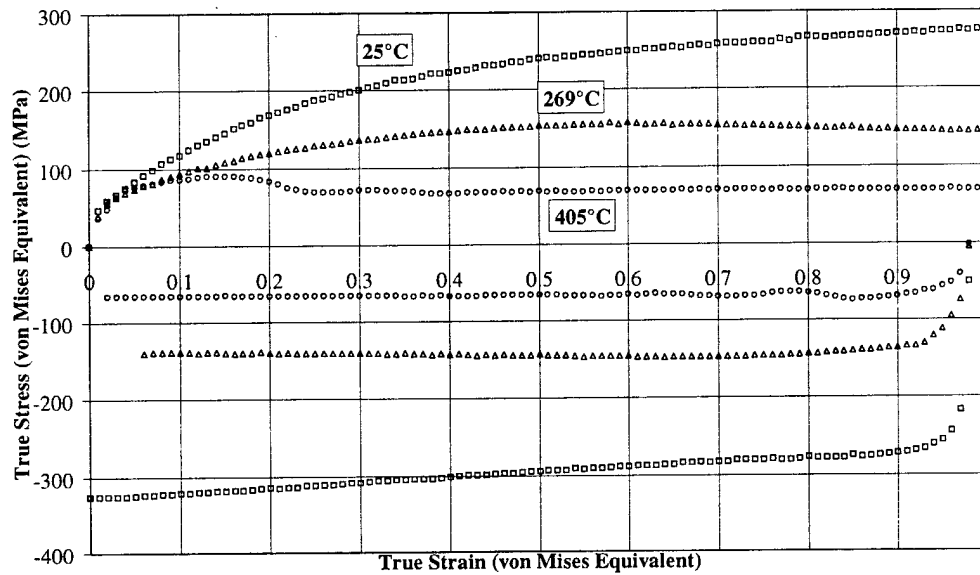


Figure III.105: Reverse deformation path sequence experiments on annealed OFHC Cu conducted in torsion at various temperatures. The von Mises equivalent strain rate was 0.0004 s^{-1} .

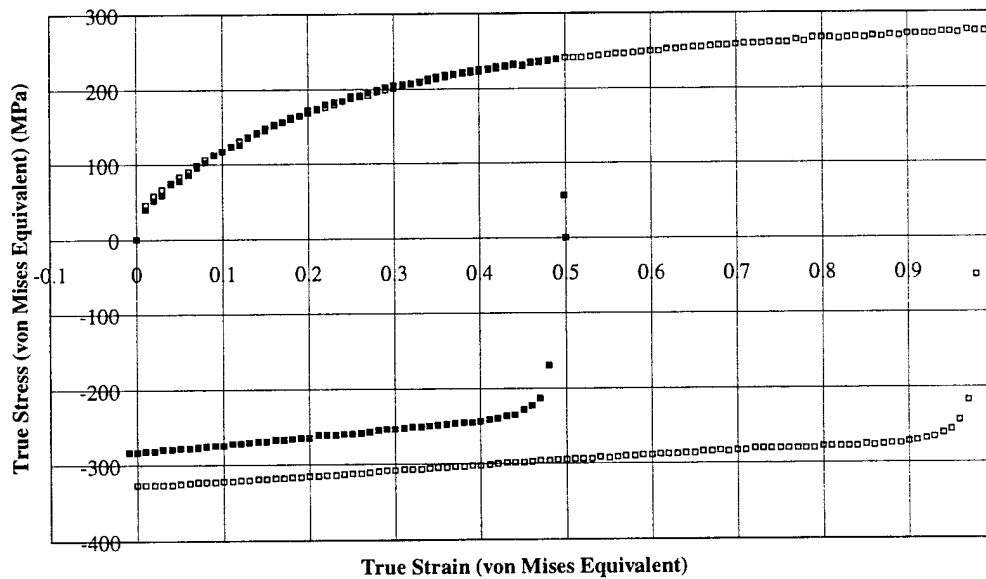


Figure III.106: Reverse deformation path sequence experiments on annealed OFHC Cu conducted in torsion at 25°C is compared for two strain levels, 0.5 and 1.0. The von Mises equivalent strain rate was 0.0004 s^{-1} .

III.3.3.4 Combined Strain Rate, Temperature and/or Deformation Path Sequence Results

Combined strain rate incremental change and temperature change experiments were performed at various strain rates (Table III.7). A specimen was initially deformed in compression at a high strain rate (6000 s^{-1}), and at room temperature (25°C), to a pre-strain of 0.34 (Fig. III.107). After remachining, the specimen was deformed quasi-statically (0.0004 s^{-1}) in compression at 269°C to a total true strain of 0.84. Upon reloading, the flow stress reached a level between the two constant strain rate curves, and then rapidly approached the quasi-static curve as the total strain increased. Figure III.108 shows the results for a material initially deformed at high strain rate (5200 s^{-1}) and at 269°C . A pre-strain of 0.28 was achieved at the high rate. After remachining, the specimen was deformed quasi-statically (0.0004 s^{-1}) at 25°C . The flow stress rises somewhat above the constant strain rate curve, but then eventually coincides.

Continuously varying temperature and strain rate experiments were conducted in compression. Decreasing temperature and strain rate results are shown in Fig. III.109, increasing temperature and strain rate results are shown in Fig. III.110, and decreasing temperature while strain rate increased is shown in Fig. III.111. The time required for a significant temperature increase was too great for the amount of time available during strain rate change experiments.

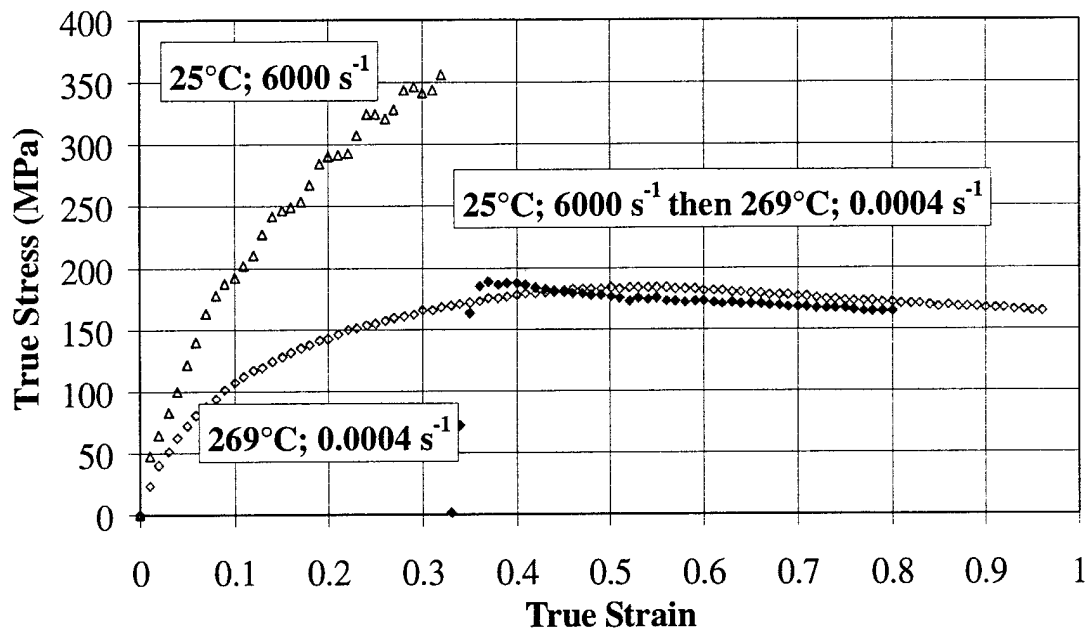


Figure III.107: Strain rate and temperature history effects for OFHC Cu in compression from 25°C and 6000 s⁻¹ followed by 269°C and 0.0004 s⁻¹.

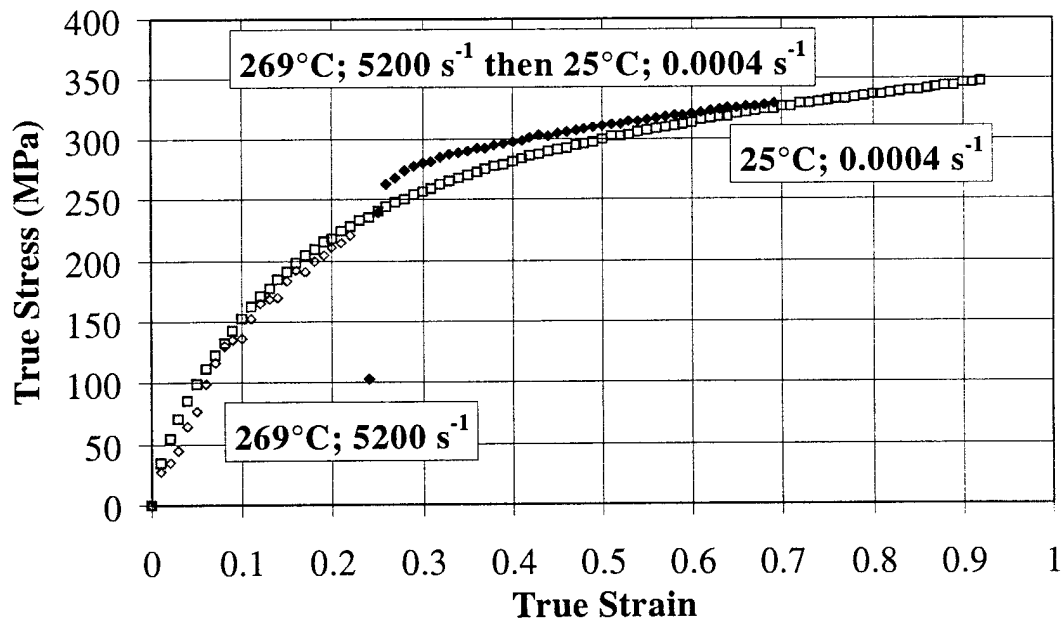


Figure III.108: Strain rate and temperature history effects for OFHC Cu in compression from 269°C and 5200 s⁻¹ followed by 25°C and 0.0004 s⁻¹.

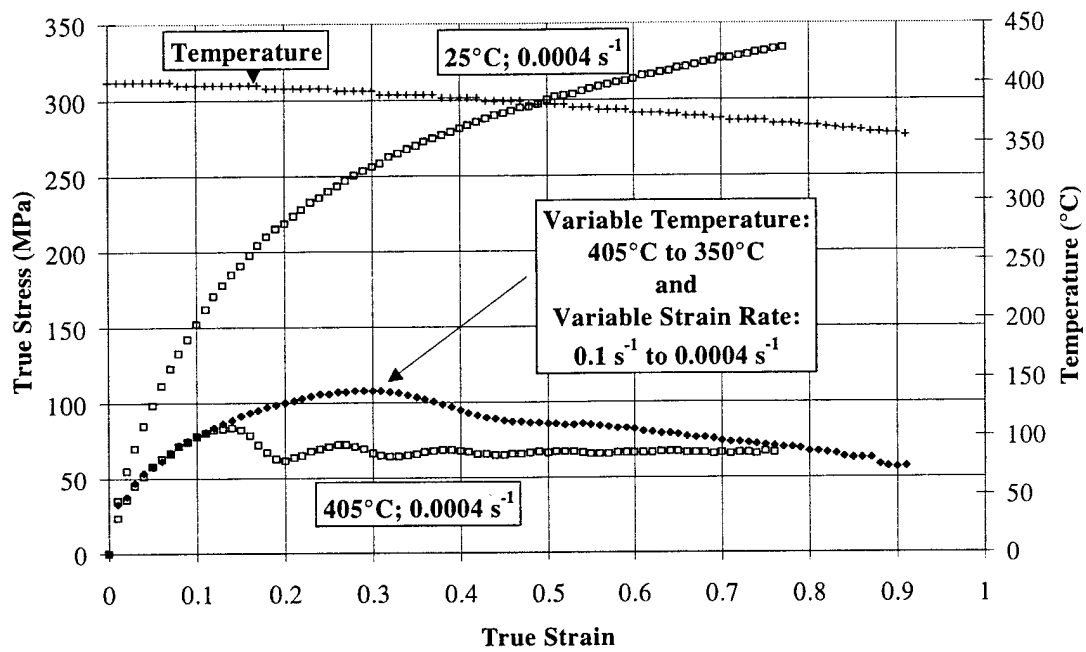


Figure III.109: Strain rate and temperature history effects for OFHC Cu in compression. The deformation conditions continuously changed from 405°C and 0.1 s⁻¹ to 350°C and 0.0004 s⁻¹.

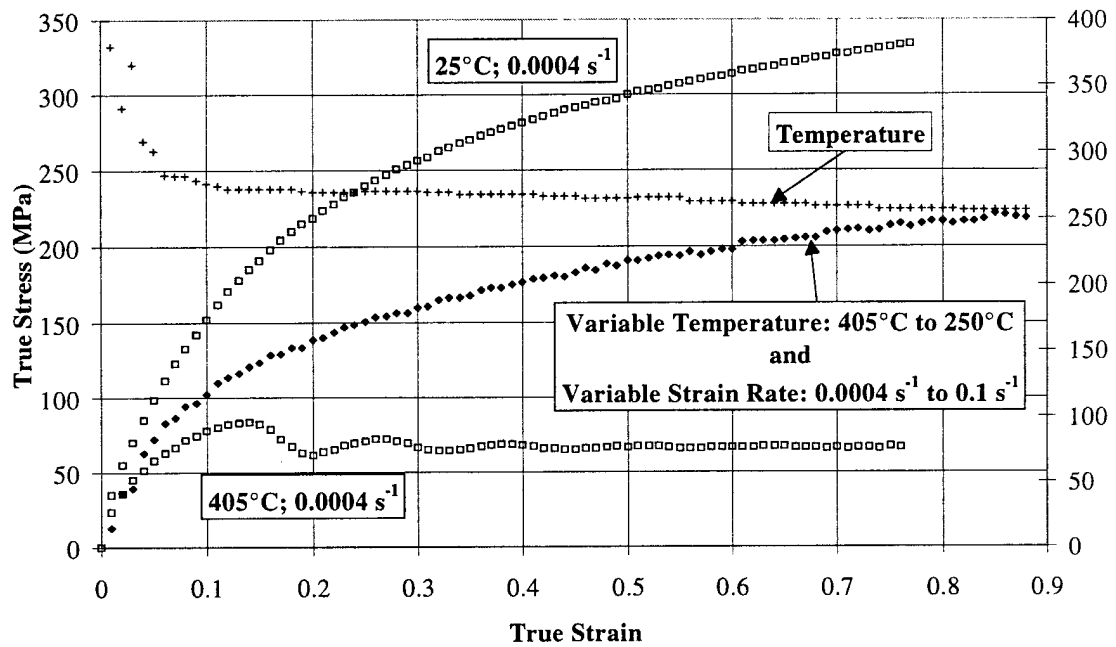


Figure III.110: Strain rate and temperature history effects for OFHC Cu in compression. The deformation conditions continuously changed from 405°C and 0.0004 s⁻¹ to 250°C and 0.1 s⁻¹.

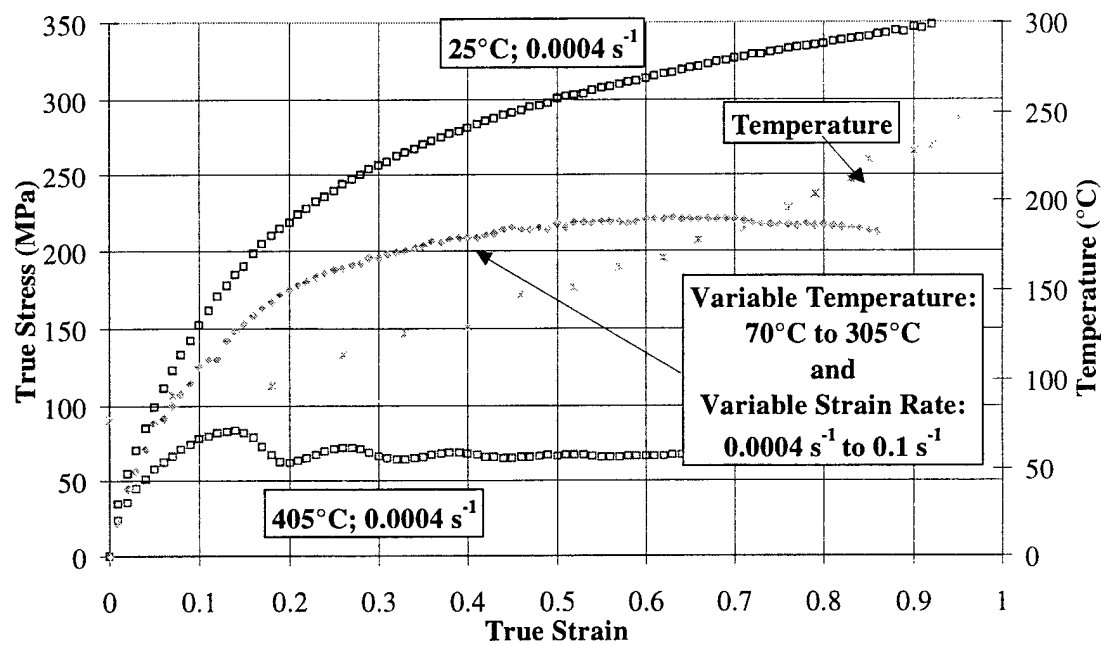


Figure III.111: Strain rate and temperature history effects for OFHC Cu in compression. The deformation conditions continuously changed from 70°C and 0.0004 s⁻¹ to 305°C and 0.1 s⁻¹.

III.4 Data Analysis

This section includes some of the analysis used for traditional parameter determination. These traditional approaches attempt to isolate certain parameters through specialized tests or data analysis. The principle challenge in the use of constitutive models has been the experimental evaluation of the resulting material parameters. Plots of stress versus logarithmic strain rate, for different temperatures and strains are often used to obtain the strain rate hardening. The change in strain hardening versus strain is used to obtain relationships for the dynamic recovery function.

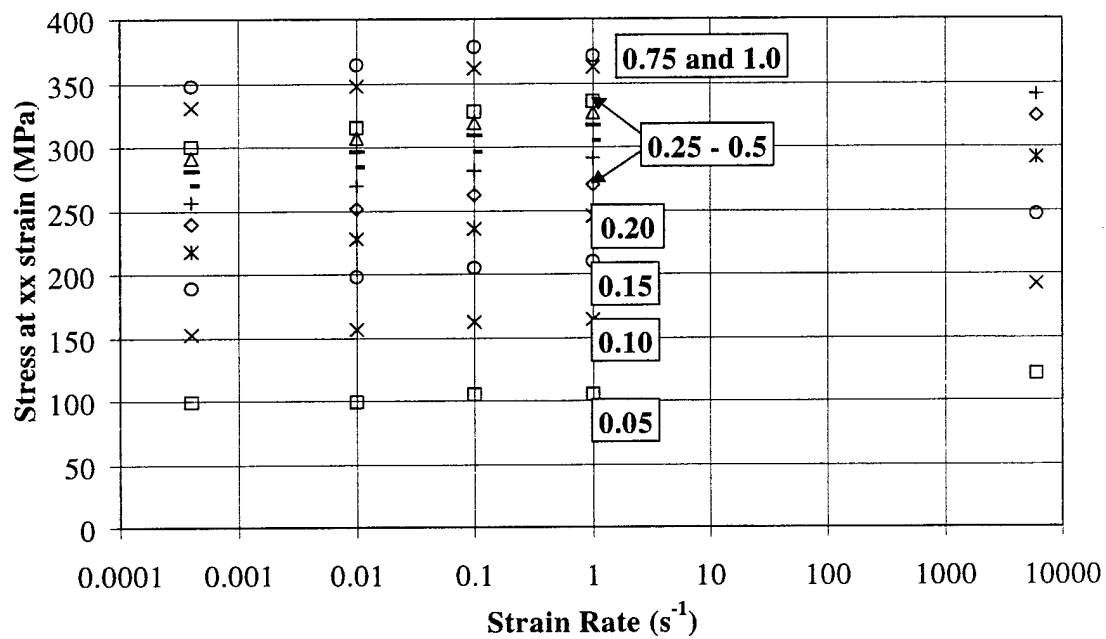


Figure III.112: Strain rate sensitivity for OFHC Cu deformed in compression at 25°C. The stress was measured at the indicated (in boxes) strain levels, ranging from 0.05 to 1.0.

The strain rate sensitivity remains essentially linear, on the stress versus logarithmic strain rate plot (Fig. III.112), over all levels of strain. The slopes remain fairly consistent. The large increase in sensitivity typically observed at rate above 10^3 to 10^4 , is not observed here. The highest strain rate, 6000 s^{-1} , is just at the point where the dramatic increase occurs (Follansbee and Kocks, 1988) (Fig. III.113). The strain rate sensitivity of this material is consistent with other data.

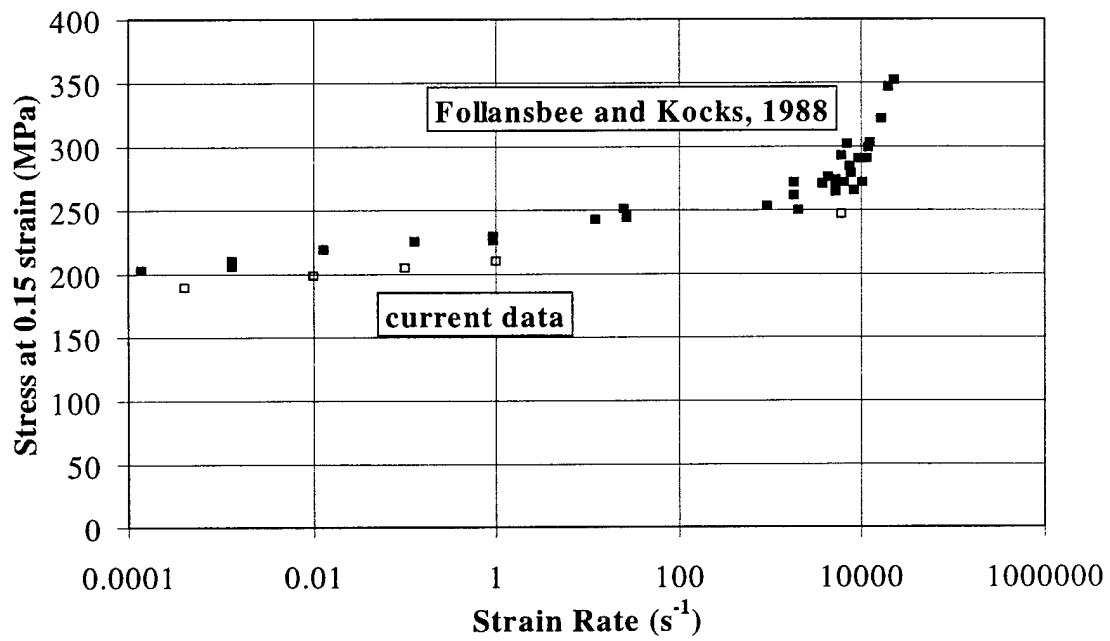


Figure III.113: Strain rate sensitivity for copper deformed in compression at 25°C to a strain of 0.15. Data from Follansbee and Kocks, 1988, shown in close symbols, is compared to the current experimental data, open symbols.

The strain rate sensitivity at 269°C and 541°C remains fairly linear, except for the softening which occurs (Figs. III.114 and III.115). The stress decreases at higher strain levels, above 0.5 at 269°C and 0.3 at 541°C.

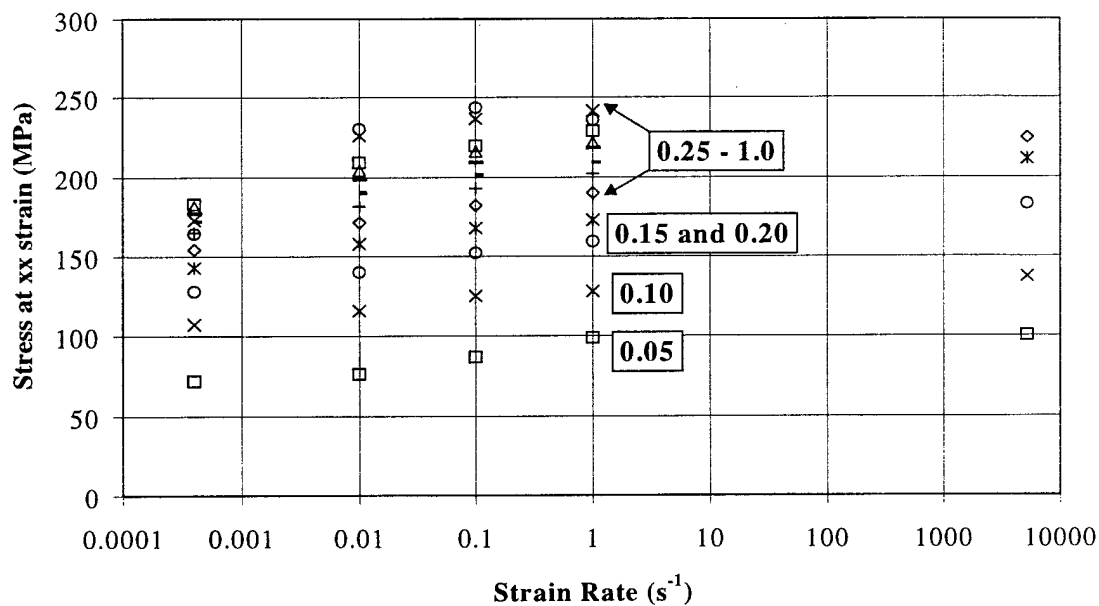


Figure III.114: Strain rate sensitivity for OFHC Cu deformed in compression at 269°C. The stress was measured at the indicated (in boxes) strain levels, ranging from 0.05 to 1.0.

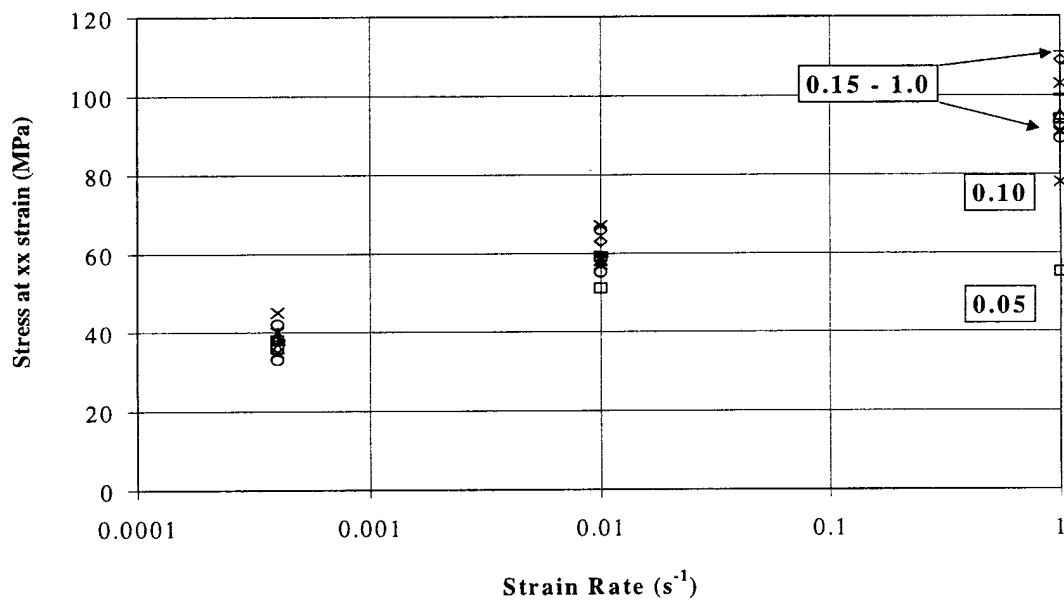


Figure III.115: Strain rate sensitivity for OFHC Cu deformed in compression at 541°C. The stress was measured at the indicated (in boxes) strain levels, ranging from 0.05 to 1.0.

Dynamic recovery reduces the strain hardening during deformation. Hardening occurs as the result of the increase in dislocation density and the additional stress required to move dislocations past obstacles. When redundant dislocations meet, they annihilate each other resulting in dynamic recovery. Recovery, as well as recrystallization, are restoration processes that are both thermally activated. Recovery is facilitated by the ability of dislocations to climb to different slip planes which increases the likelihood for meeting a redundant dislocation and for annihilation. The change in slope during deformation is a measure of the amount of dynamic recovery which occurs. The strain hardening rate from the current data set are shown in Figs. III.116, III.117, and III.120 for quasi-static, 0.0004 s^{-1} , compression at 25°C , 269°C , and 541°C respectively. The curves demonstrate the typical shape, initially a rapid reduction and then gradual approach to zero. The softening at 269°C and 541°C result in negative values. A comparison of the hardening rates at various strain rates is made in Figs. III.118, III.119, and III.121 for 25°C , 269°C , and 541°C respectively. The strain rate hardening for compression and torsion for quasi-static, 0.0004 s^{-1} , over a range of temperatures are shown in Figs. III.122 and III.123 respectively.

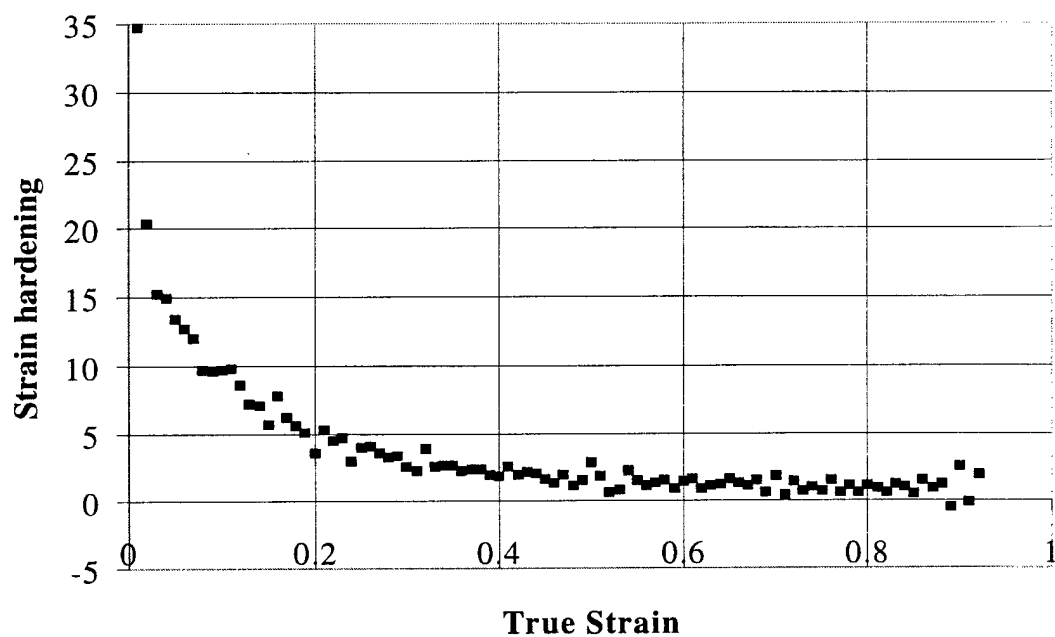


Figure III.116: Strain hardening for OFHC Cu in compression at 25°C and 0.0004 s⁻¹.

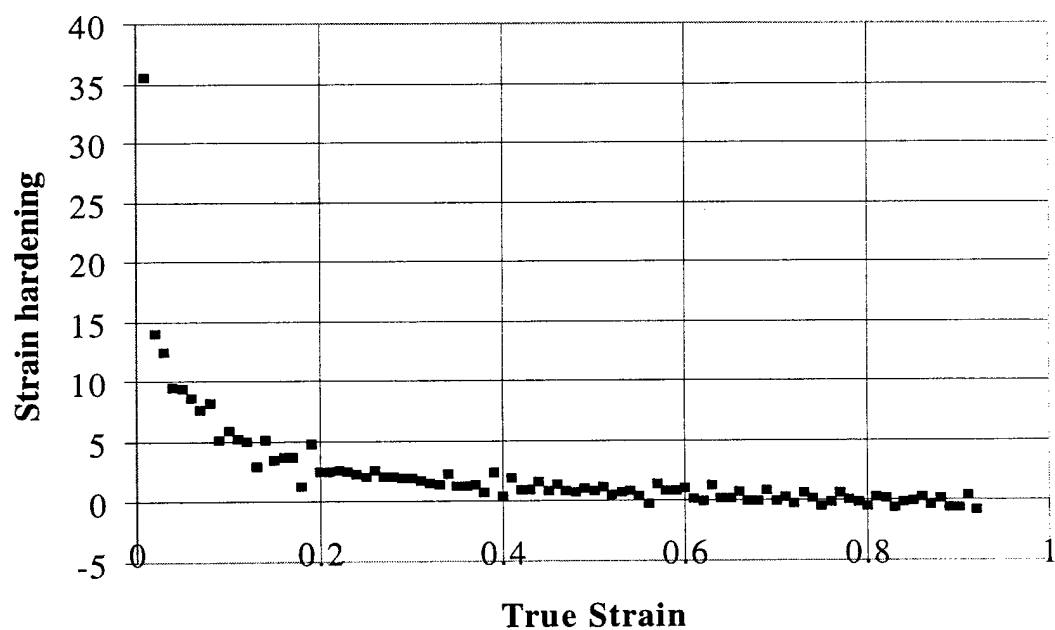


Figure III.117: Strain hardening for OFHC Cu in compression at 269°C and 0.0004 s⁻¹.

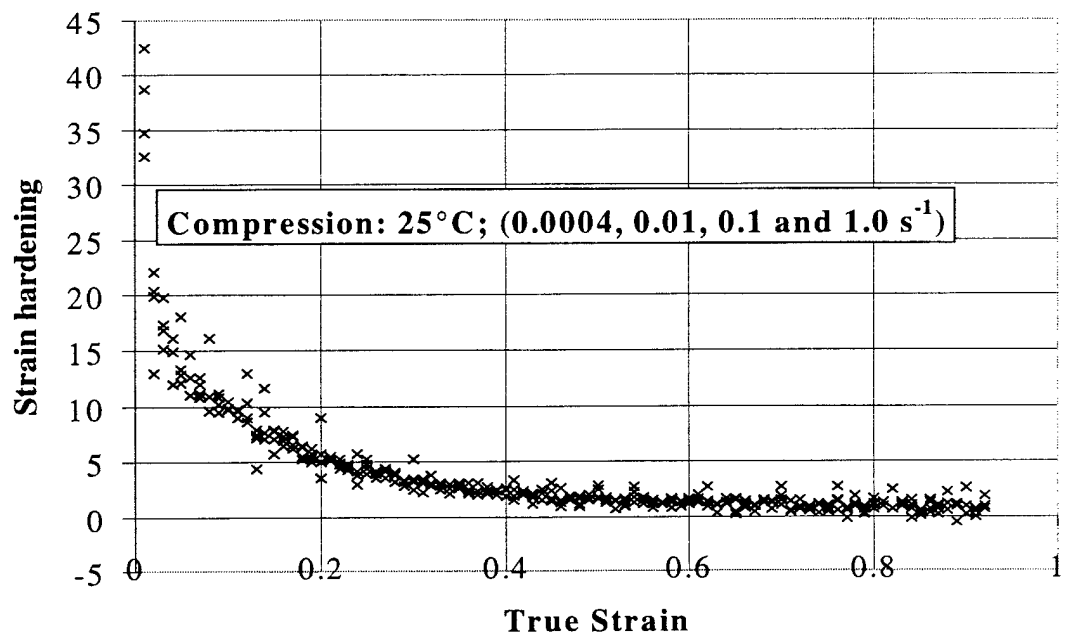


Figure III.118: Strain hardening for OFHC Cu in compression at 25°C and various strain rates (0.0004, 0.01, 0.1 and 1.0) s⁻¹.

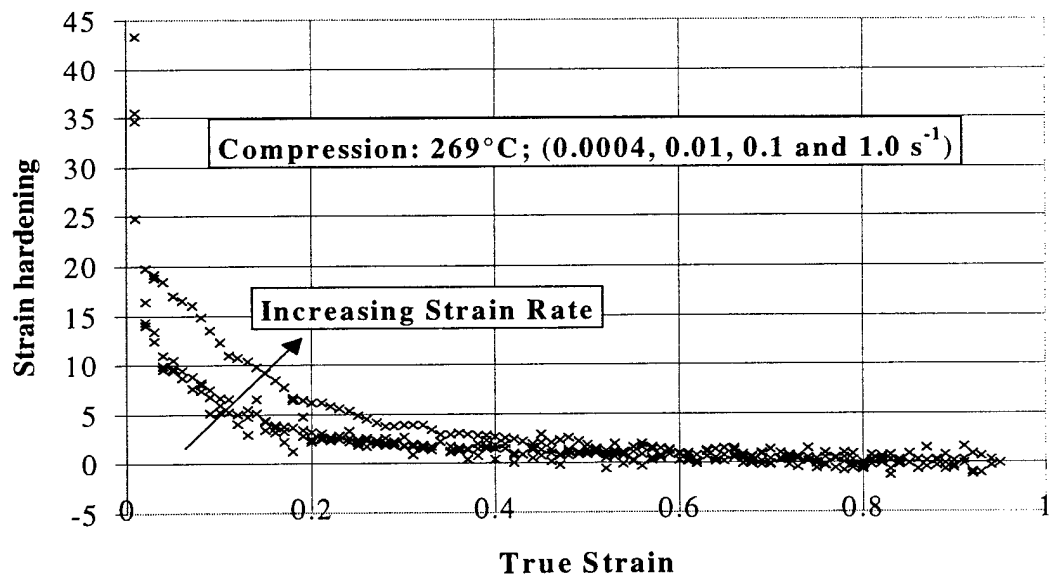


Figure III.119: Strain hardening for OFHC Cu in compression at 269°C and various strain rates (0.0004, 0.01, 0.1 and 1.0) s⁻¹.

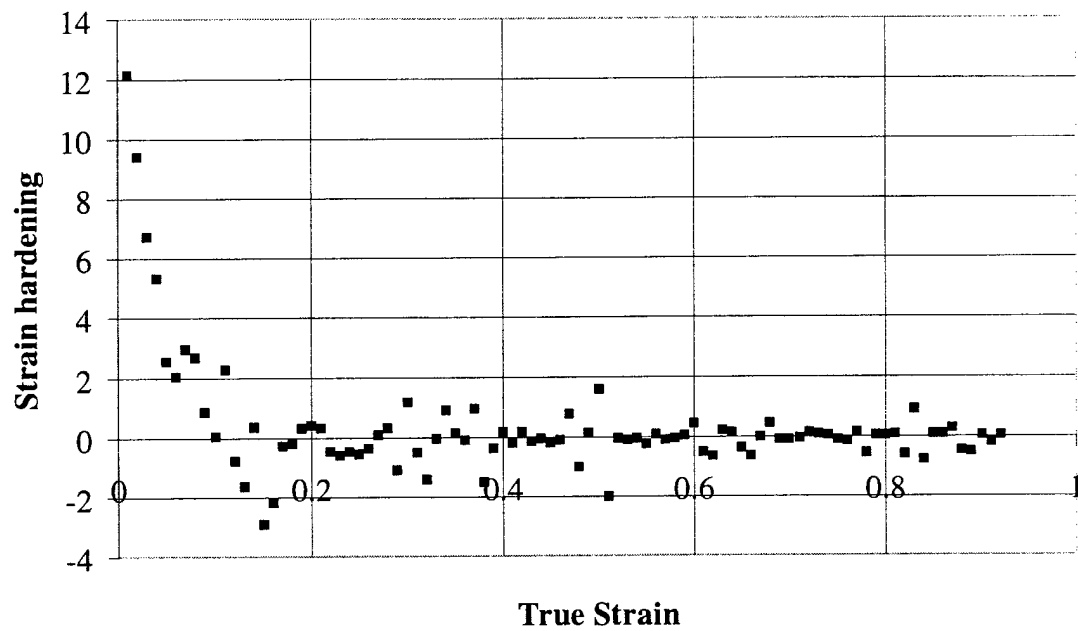


Figure III.120: Strain hardening for OFHC Cu in compression at 541°C and 0.0004 s^{-1} .

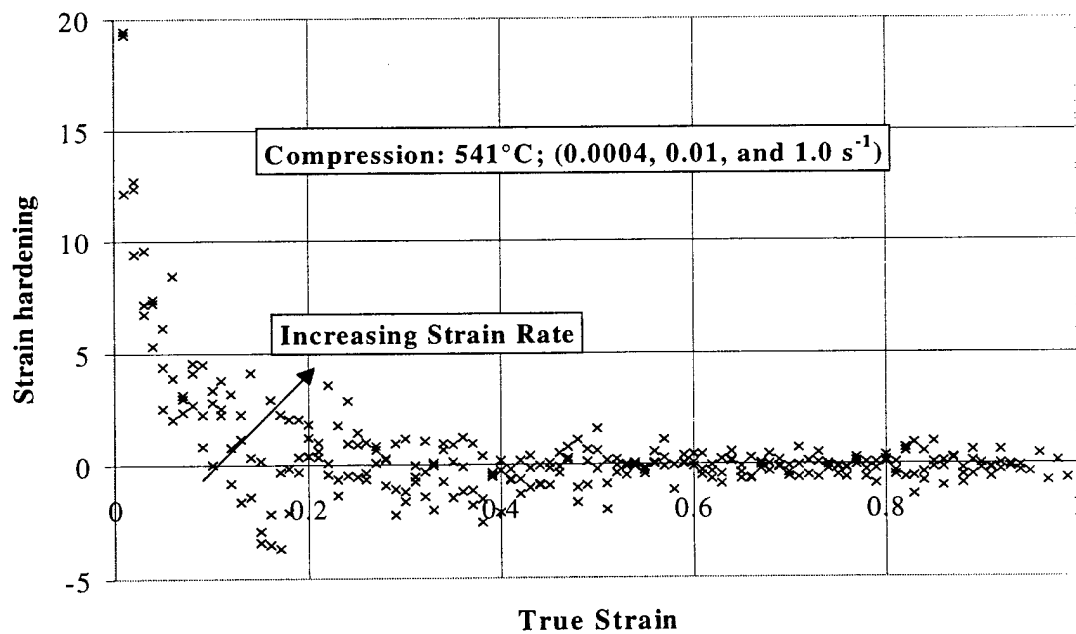


Figure III.121: Strain hardening for OFHC Cu in compression at 541°C and various strain rates (0.0004, 0.01, 0.1 and 1.0 s^{-1}).

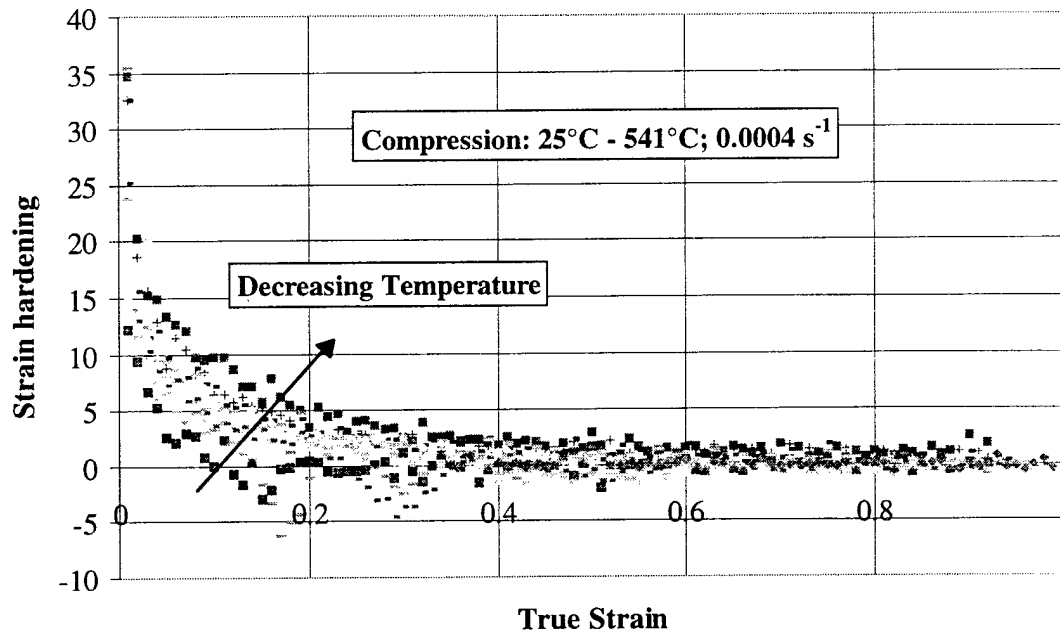


Figure III.122: Strain hardening for OFHC Cu in compression at 0.0004 s⁻¹ and various temperatures (25°C - 541°C).

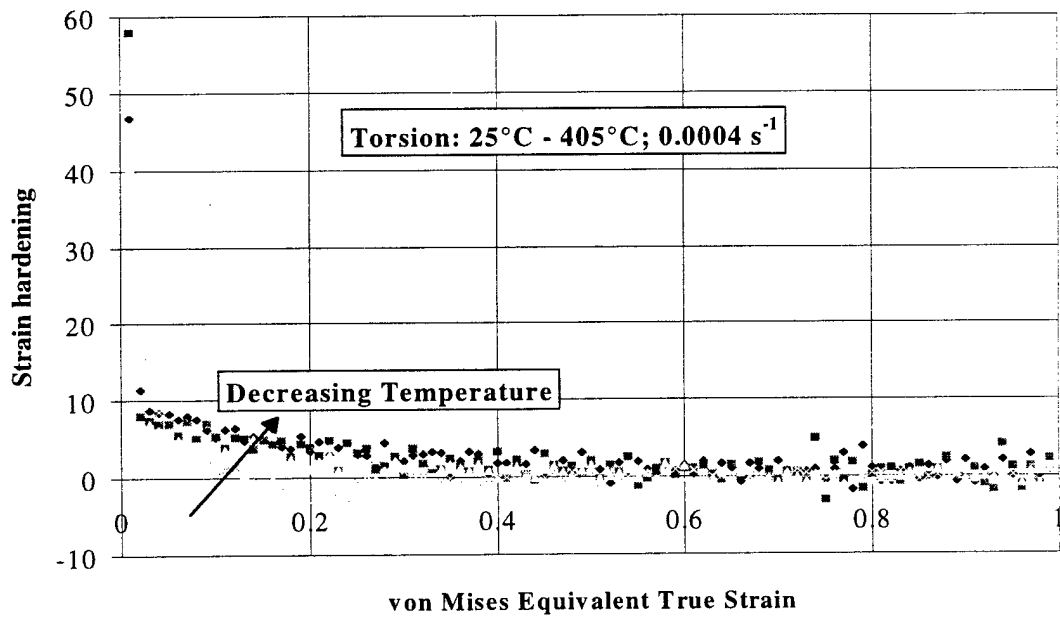


Figure III.123: Strain hardening for OFHC Cu in torsion at 0.0004 s⁻¹ and various temperatures (25°C - 405°C). (The von Mises equivalent strain levels are shown).

III.5 Comparison With Other Experimental Data

This section compares copper data obtained from other authors with the experimental data obtained during this research. Oxygen-free-electronic (OFE) copper with an initial grain size between 30 μm and 50 μm was tested in compression at room temperature and various strain rates. The high strain rates were obtained with a Hopkinson bar apparatus while the lower strain rates with a servo-hydraulic test machine (Follansbee, 1985) (Fig. III.124). The data compare precisely with the current experimental data at quasi-static, 0.0001 and 0.0004 s^{-1} , and 6000 s^{-1} strain rates (Fig. III.125). The data at 1.0 s^{-1} differ. OFHC Cu with an initial grain size of 20 μm was tested in tension at room temperature and various constant true strain rates (Christodoulou, et al., 1982) (Fig. III.126). The tension data exhibit a higher hardening rate than the compression data. The initial curves are similar for comparable strain rates (Fig. III.127). OFE Cu with an initial grain size of 40 μm was tested in compression at room temperature (Follansbee and Kocks, 1988) (Fig. III.128). The large strain, 1.0, measurements were obtained by incrementally loading in 0.25 strain steps, followed by relubrication and/or remachining. The flow stress at all strain rates exceeds that of the current data (Fig. III.129). This may be due to the smaller initial average grain size, 40 μm versus 62 μm . The effect of the initial average grain size was investigated on OFHC Cu at dynamic, 3000 s^{-1} , and quasi-static, 0.001 s^{-1} , strain rates (Meyers, et al., 1995) (Fig. III.130 and III.132 respectively). The data were obtained using a hat-shaped specimen which creates a shear zone of deformation. The zone size was determined by transmission electron

microscopy. The current experimental data, with an initial average grain size of 62 μm , are comparable, but corresponds to a level between the curves for 117 μm and 315 μm grain sizes (Figs. III.131 and III.133). These data demonstrate the increase in flow stress with decreasing grain size.

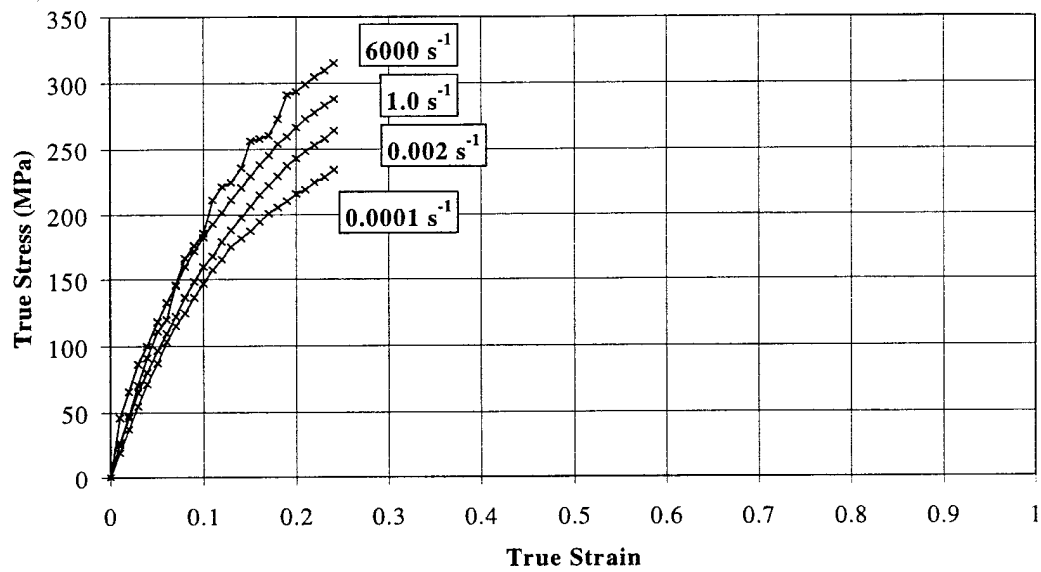


Figure III.124: Oxygen-free-electronic (OFE) copper (0.9999 Cu) with an initial average grain size of 30 - 50 μm deformed in compression at room temperature, 25°C (Follansbee, 1985).

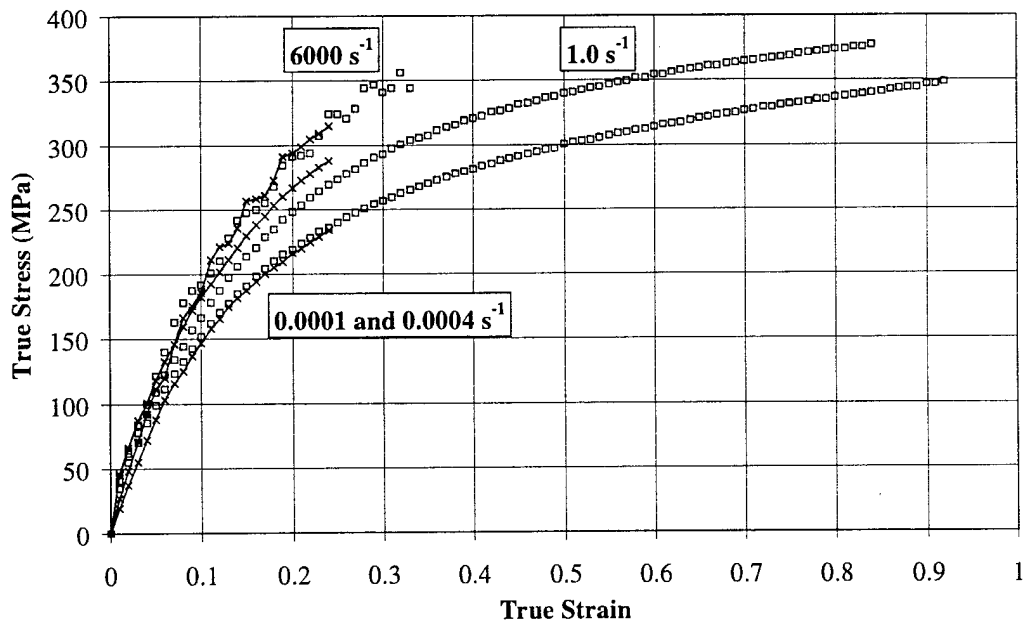


Figure III.125: Compression data from Follansbee, 1985, are shown with lines, and the current experimental data are shown with open symbols.

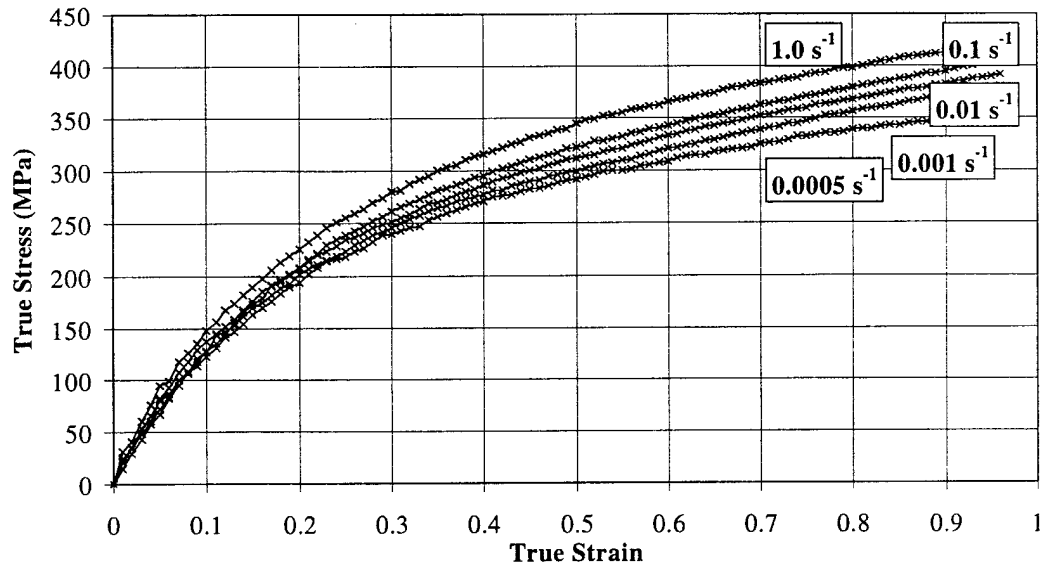


Figure III.126: OFHC Cu (0.9995) with an initial average grain size of $20 \mu\text{m}$ deformed in tension at room temperature, 25°C (Christodoulou, *et al.*, 1982).

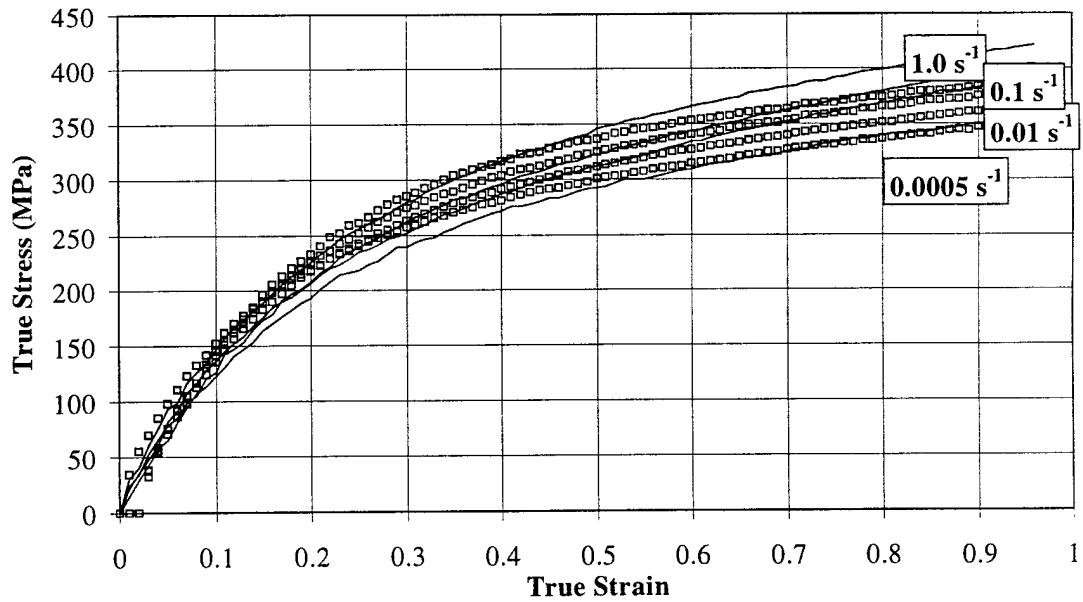


Figure III.127: Compression data from Christodoulou, *et al.*, 1982, are shown with lines, and the current experimental data are shown with open symbols.

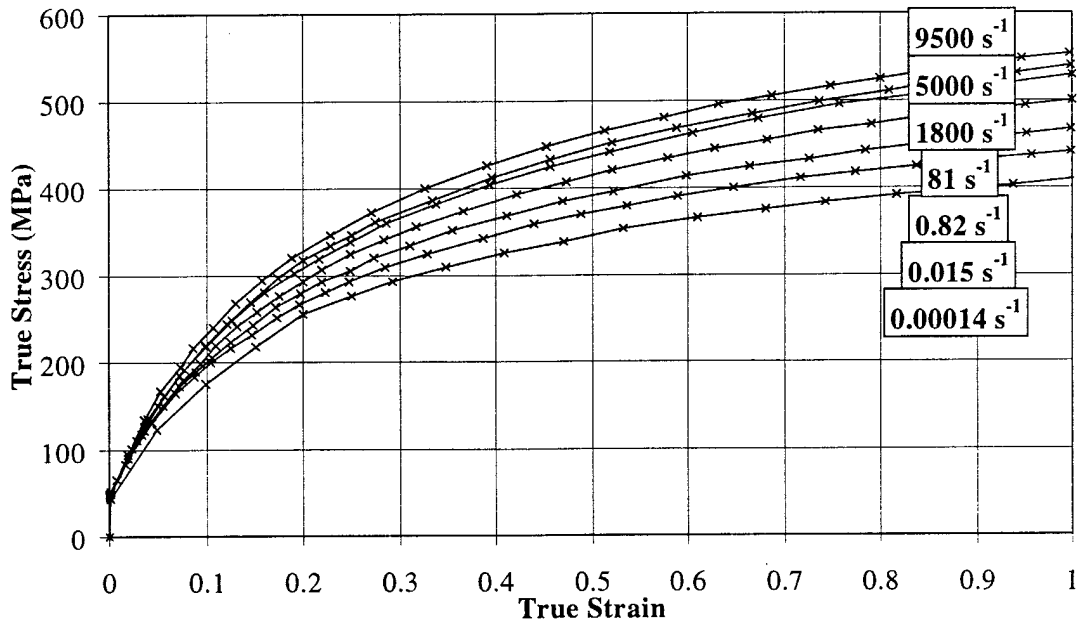


Figure III.128: OFE Cu (0.9999) with an initial average grain size of 40 μm deformed in compression at room temperature, 25°C (Follansbee and Kocks, 1988).

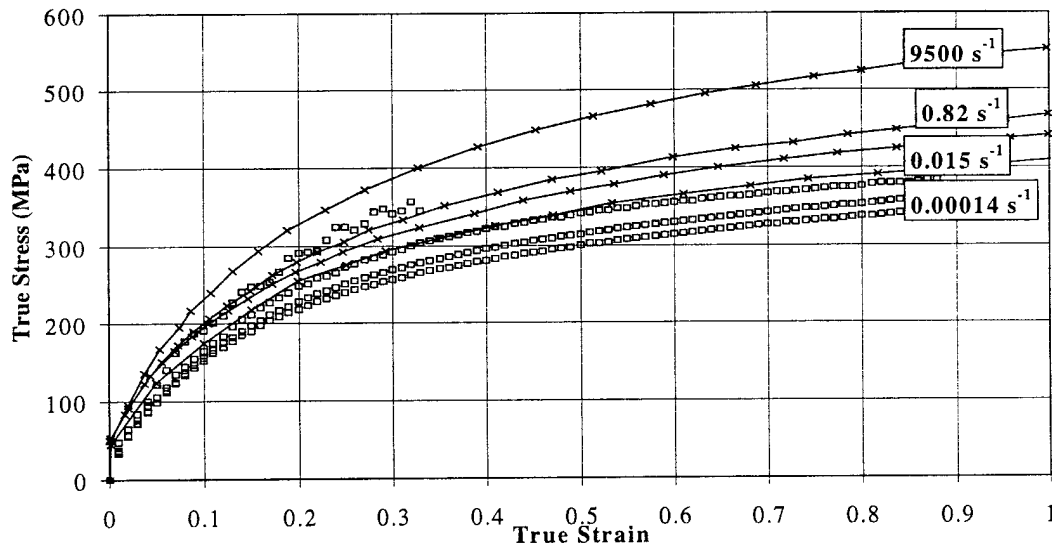


Figure III.129: Compression data from Follansbee and Kocks, 1988, are shown with lines, and the current experimental data are shown with open symbols.

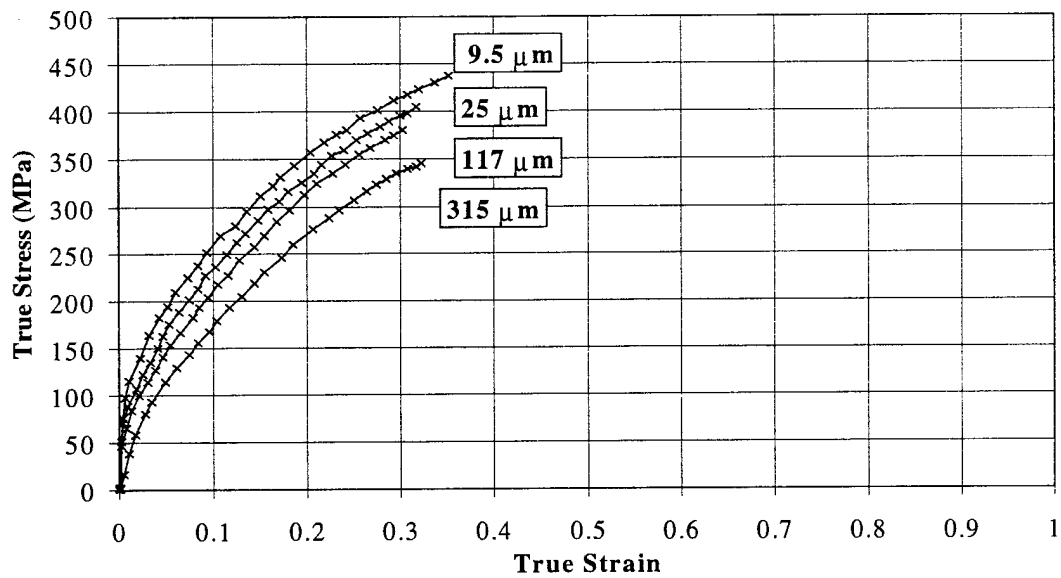


Figure III.130: OFHC Cu (0.9999) with varying initial average grain sizes deformed in shear at room temperature, 25°C, and 3000 s⁻¹ (Meyers, *et al.*, 1995). The von Mises equivalent stress and strain are shown.

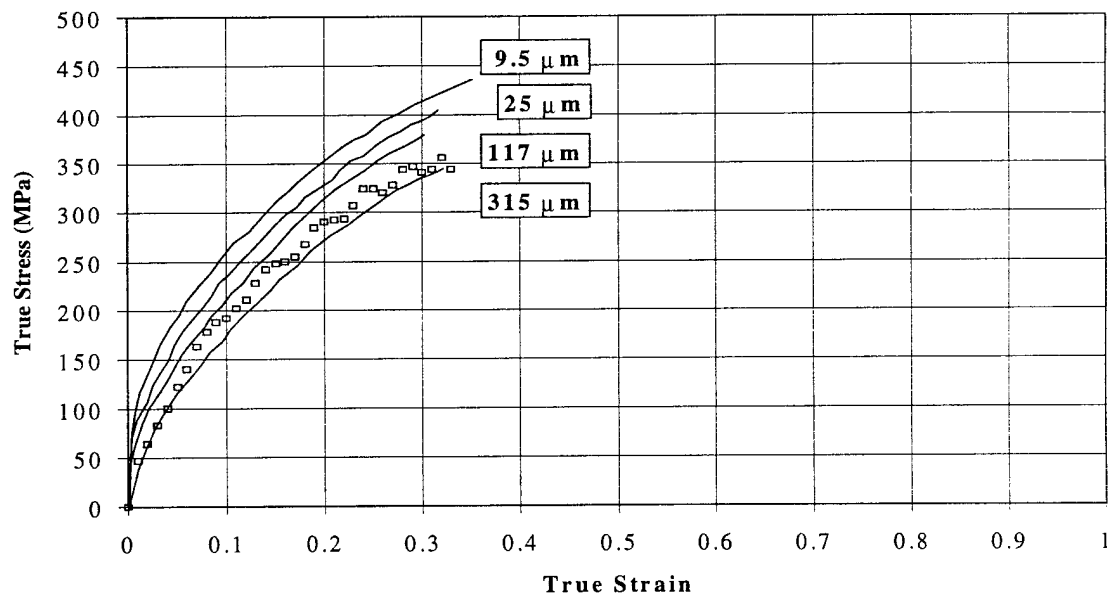


Figure III.131: Compression data from Meyers, *et al.*, 1995, are shown with lines, and the current experimental data at 6000 s⁻¹, are shown with open symbols. The von Mises equivalent stress and strain are shown.

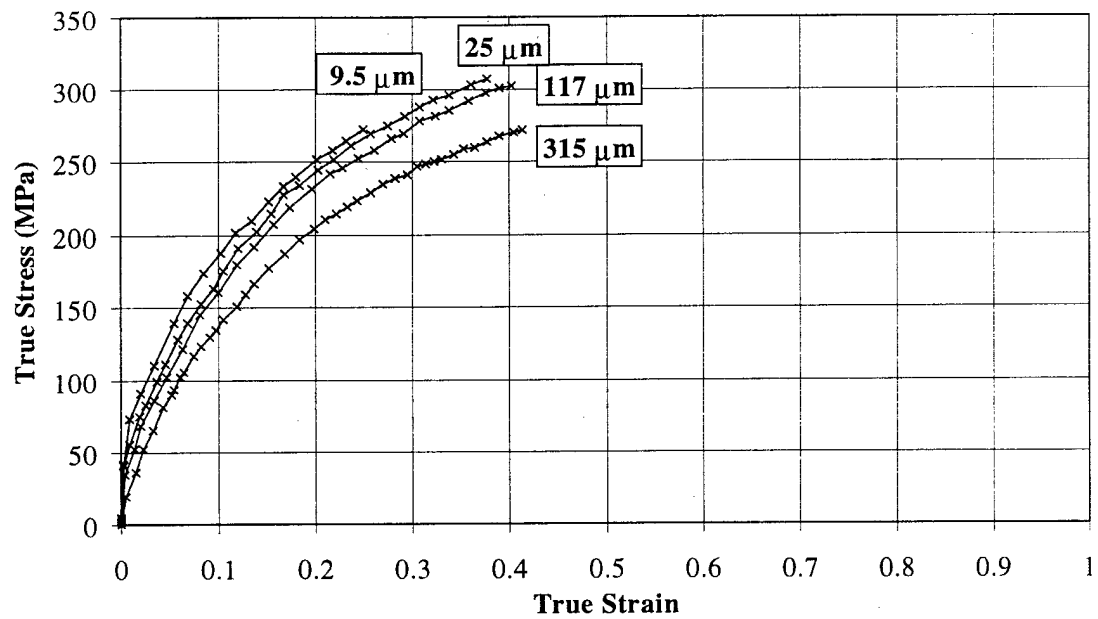


Figure III.132: OFHC Cu (0.9999) with varying initial average grain sizes deformed in shear at room temperature, 25°C, and 0.001 s^{-1} (Meyers, *et al.*, 1995). The von Mises equivalent stress and strain are shown.

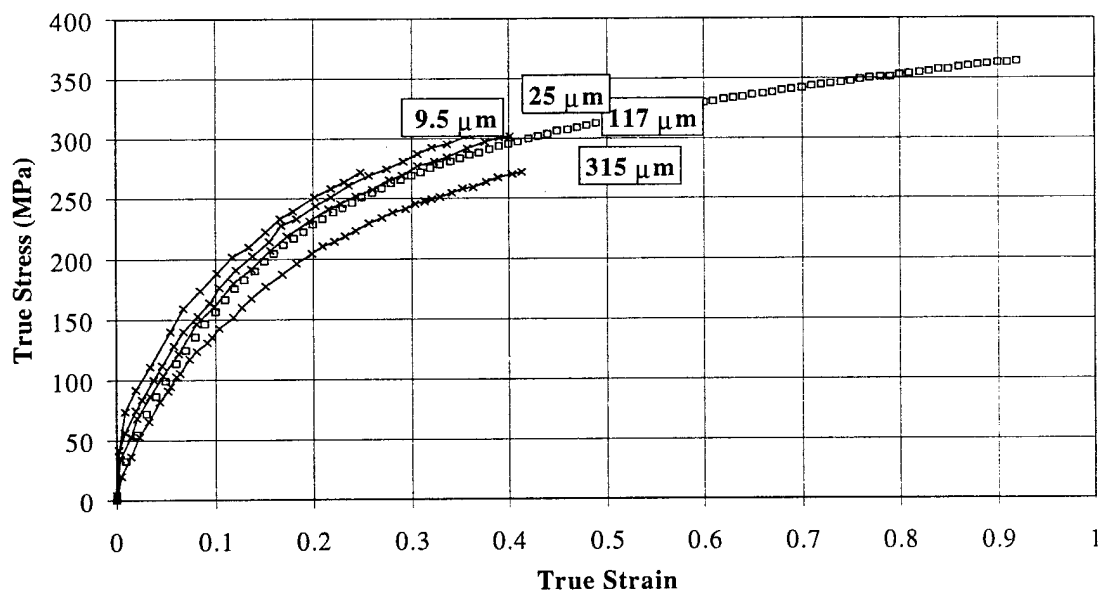


Figure III.133: Compression data from Meyers, *et al.*, 1995, are shown with lines, and the current experimental data, 0.01 s^{-1} , are shown with open symbols. The von Mises equivalent stress and strain are shown.

III.6 Very High Strain Rate Data

Many applications (e.g. shaped charges, explosively formed projectiles, armor defeat, explosive welding, and explosive compaction) involve large (finite) deformations at extremely high strain rates. Research on high rate deformation of materials has been directed primarily towards the development of suitable constitutive models. Pressure-shear impact experiments have been used to study the plastic flow of metals at strain rates of 10^5 s^{-1} to 10^7 s^{-1} . In this way, the flow stress of pure metals have been shown to increase rapidly with increasing strain rate at strain rates of approximately 10^5 s^{-1} and higher (Klopp, Clifton, and Shawki, 1985 and Huang and Clifton, 1985). Very thin OFHC Cu foils with an initial grain size of approximately 40 to 50 μm were used to obtain elevated, high strain rate data (Frutschy and Clifton, 1998) (Figs. III.134 - III.137).

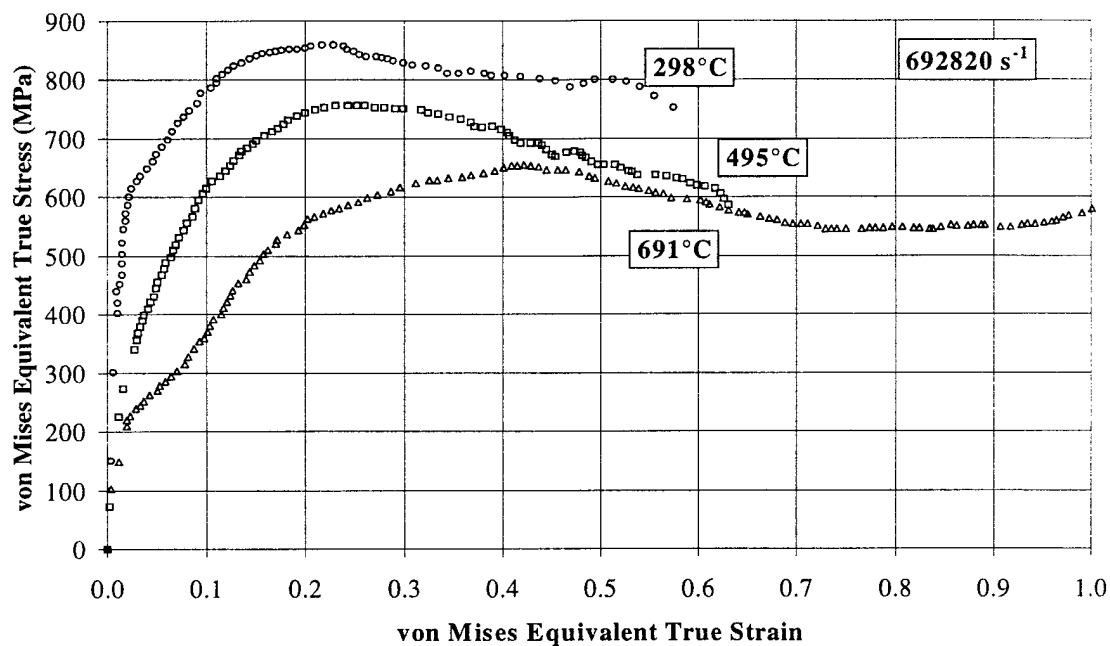


Figure III.134: Pressure-shear OFHC Cu data (Frutschy and Clifton, 1998).

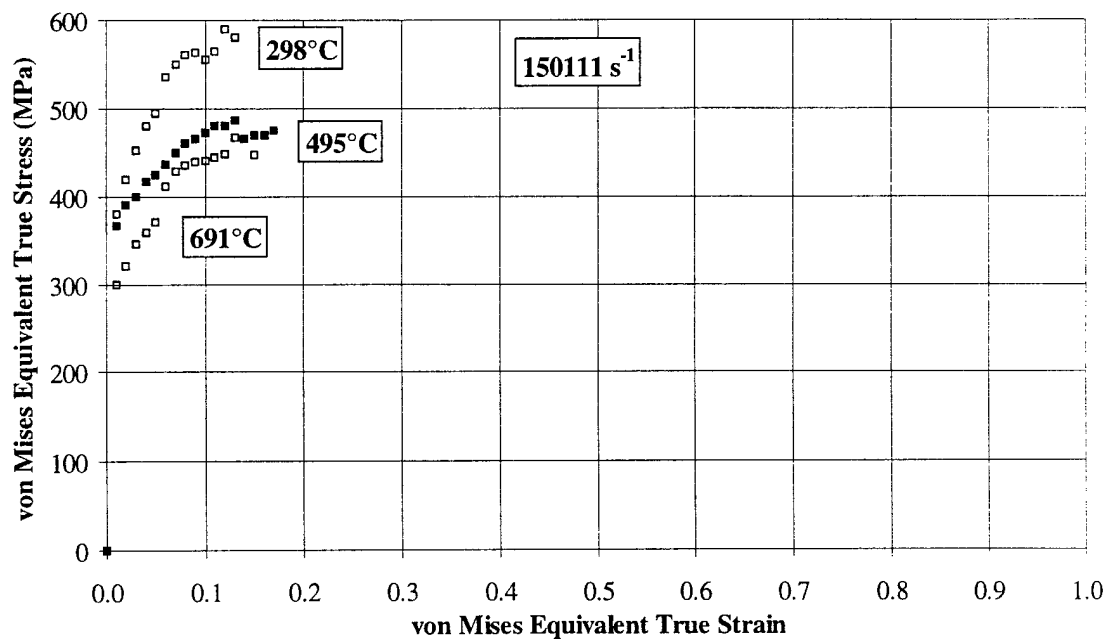


Figure III.135: Pressure-shear OFHC Cu data (Frutschy and Clifton, 1998).

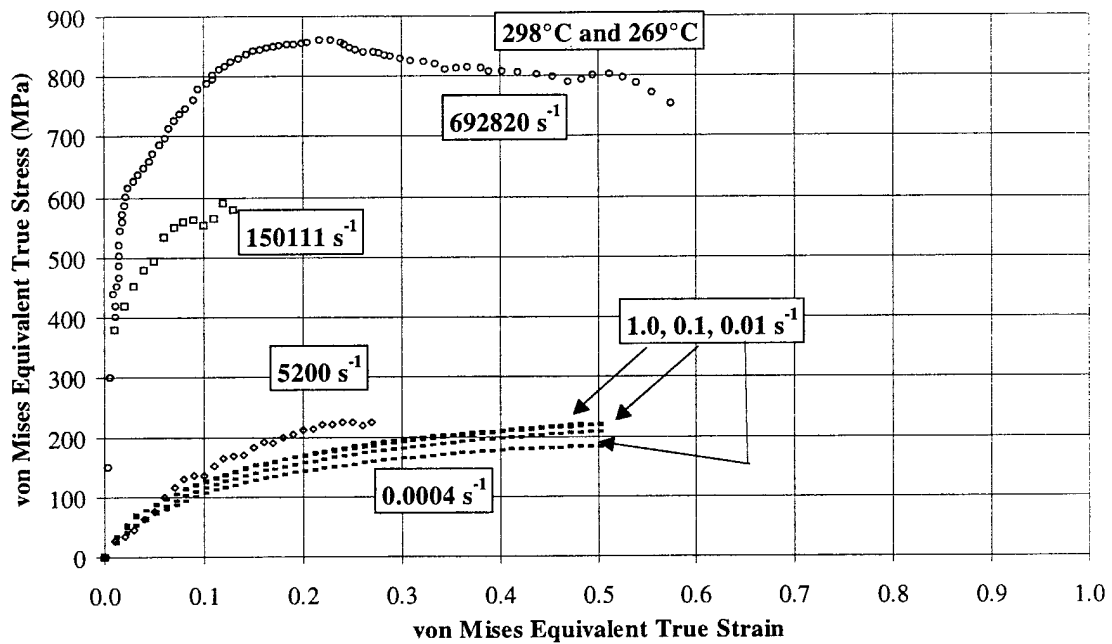


Figure III.136: Comparison of OFHC Cu data near 269°C (Frutschy and Clifton, 1998). The von Mises equivalent stress and strain are shown.

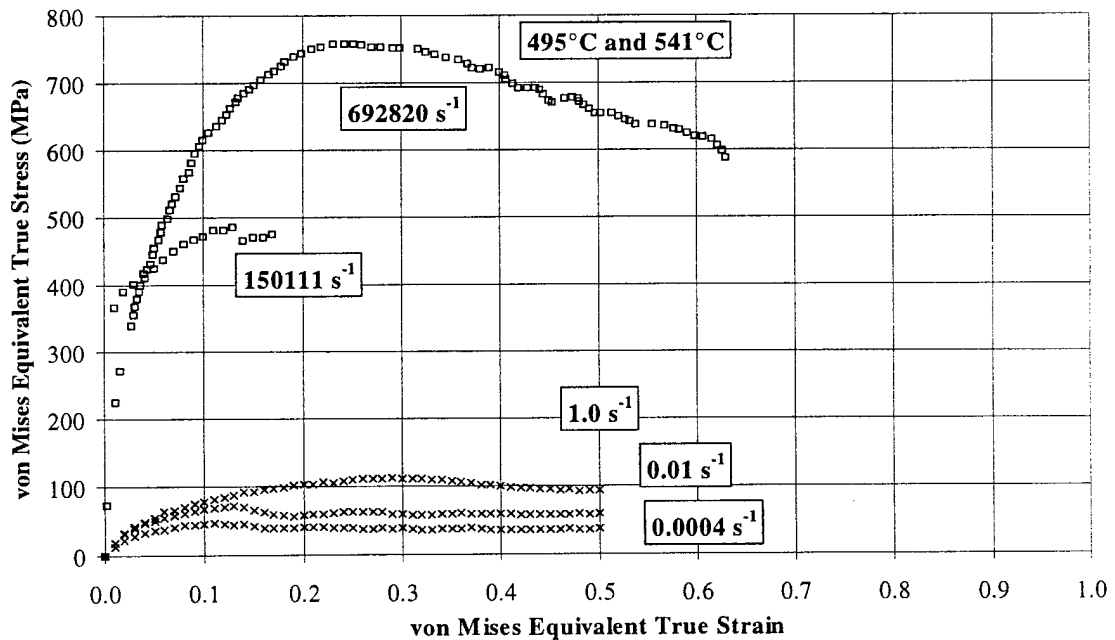


Figure III.137: Comparison of OFHC Cu data 495 - 541°C (Frutschy and Clifton, 1998). The von Mises equivalent stress and strain are shown.

III.7 Discussion

These experiments reinforce that a mechanical equation of state (Ludwick, 1909), does not exist for OFHC Cu. The sequence experiments clearly show that the flow stress is not only a function of instantaneous values of strain, strain rate, and temperature, but contain transients and in some cases, different asymptotic flow stress levels, representing history effects resulting from sequences of temperature, strain rate, and/or deformation path. There are multiple values of flow stress for the same strain, strain rate, and temperature with different preceding histories.

OFHC Cu demonstrates softening due to static and dynamic restoration processes. Static thermal recovery and recrystallization (Figs. III.36 and III.37) are strain level dependent. Little restoration occurs at strains of 0.3 or less, but is significant at strains of 0.5 at a temperature of 269°C. Static restoration is strongly temperature dependent, increasing in rate with temperature. Dynamic recrystallization is evident (Figs. III.38 - III.39 and III.68) at temperatures above 236°C. At 202°C and below, the flow stress continues to increase at quasi-static strain rate and at a strain of unity. As temperature increases above 236°C, the flow stress attains a peak stress and then decreases toward a steady state value. The strain to the peak stress decreases with increasing temperature: from 0.75 for 236°C to 0.38 for 286°C and 0.12 for 541°C. Additionally, as the strain rate increases, the strain corresponding to the peak stress also increases. Oscillations in flow stress occur at temperatures above 337°C. The steady state stress level decreases with increasing temperature. During finite deformation, the internal structure changes, strain hardening occurs due to an increasing

dislocation density and softening occurs due to recovery and recrystallization processes. These experiments indicate the requirement for constitutive models to have an evolutionary relation which results in a balance between hardening and recovery of various forms, and the capability of compensatory softening at increasing temperature to account for the peak stress behavior and dynamic recrystallization effects.

Strain rate, temperature, and deformation path history effects are evident from the sequence experiments (Figs. III.75 to III.110). Strain rate sequences, both high to low and low to high, result in a transient flow stress that stays between the constant rate curves and gradually approaches the subsequent constant strain rate curve, indicating that the effect of the pre-strain is eliminated with additional strain on the order of the pre-strain. The initial response upon reloading is intermediate to the two curves which correspond to each of the strain rate and temperature conditions. The work hardening rate is higher for the transient curve for lower to higher strain rate sequences than for the constant strain rate and temperature curve. This greater slope results in the transient curve approaching the constant curve with additional strain on the order of the pre-strain. For sequences from higher strain rates to lower, the reverse phenomenon occurs. Temperature sequence experiments also result in transients in flow stress (Figs. III.83 to III.88). The flow stress remains between the two constant temperature curves during temperature sequences from 269°C to 25°C, but does not ultimately reach the lower temperature curve; a permanent offset is evident which is not erased by further strain. The transient flow stress is strongly dependent on static thermal recovery for pre-straining at 25°C, at both high and low strain rates, and then straining quasi-

statically at 269°C. The internal structure resulting from the 25°C pre-strain recovers with time but, while this recovery is significant, it is not complete; a small offset below the constant temperature curve remains.

All deformation path changes (e.g. compression to torsion) result in a significant permanent offset of the flow stress; the stress following the deformation path change remains between the two constant stress levels. The subsequent equivalent flow stress in shear persists well above the level for pure torsion experiments at the same $\bar{\epsilon}$ level due to prior formation of texture and dislocation substructure in compression.

The experimental results presented were consistent with other sequence experimental results. The flow stress after a temperature sequence remains between the constant temperature curves and does not completely achieve the constant temperature curve corresponding to the new temperature (Sylwestrowicz, 1958), Ni-30%wt Co (Hughes, 1986) and Al (Hartley and Duffy, 1984). The transient flow stress after a strain rate sequence remains between the two constant strain rate curves and approaches the higher rate curve during low to high strain rate sequences (Campbell and Dowling, 1970), (Lindholm, 1964 and 1968), (Nicholas and Whitmire, 1970), (Frantz and Duffy, 1972), (Gulec and Baldwin, 1973), (Eleiche and Campbell, 1974 and 1976), (Klepaczko and Duffy, 1974), (Senseny, 1977), (Stelly and Dormeval, 1977), (Follansbee and Gray, 1991) and (Gourdin and Lassila, 1992). The transient flow stress typically exhibits an initial sharp increase, and then, gradually approaches the higher strain rate constant curve.

III.8 Experimental Results Summary

This chapter presents results of isothermal, constant true strain rate experiments, recovery experiments, and experiments involving sequences of strain rate, temperature, and deformation path. These OFHC Cu experiments form a comprehensive set of data for assessing model features necessary for describing thermomechanical finite strain material behavior, including strain rate, temperature, and deformation path history effects. Including these history effects in predictive models is necessary to accurately describe the response to arbitrary strain and temperature events. This is especially evident during multiple changes in loading conditions and when there are continuously varying conditions of deformation path, temperature, and strain rate as in various metal forming applications.

The dislocation structures created during high strain rate deformation persist upon unloading and reloading at quasi-static strain rates, suggesting significant differences of dislocation substructures. The rate of microstructural evolution at a given level of plastic strain and a given temperature also depends on strain rate. The strain rate and temperature history effects are due to the fact that the existing microstructure at the current temperature depends on strain rate, strain level, and the history of formation of that microstructure. The strain rate sensitivity of the flow stress comprises two components, the rate sensitivity at fixed structure and the sensitivity of the evolution of the structure. Strain rate hardening within the structure of the evolution equations of internal structure variables is, therefore, an important aspect (cf. Klepaczko and Chiem, 1986; Estrin and Mecking, 1986 and 1991; Moosbrugger and McDowell, 1990).

CHAPTER IV

MICROSTRUCTURAL ANALYSIS

IV.1 Specimen Preparation

The microstructures of many specimens were analyzed using an optical microscope to determine the microstructural evolution associated with various strain rate and temperature conditions. Specimens were mounted in epoxy and polished using the steps identified in Table IV.1. All compression specimens were mounted such that the surface examined was perpendicular to the axis of compression.

Table IV.1: GRINDING AND POLISHING PROCEDURE

Wheel	Speed (RPM)	Force (N)	Time (min)	Lubricant
220 grit sandpaper	300	25	4	water
1200 grit sandpaper	150	30	3.5	water
9 μm	150	25	5	ethanol
3 μm	150	25	4	ethanol
OP-S (oxide)	150	10	5	70% SiO_2

NOTE: A Struers Rotapol polishing machine was used.

The specimens were then etched to reveal the grain structure using the procedures described in Table IV.2.

Table IV.2: ETCHING PROCEDURE

Solution	Temperature (°C)	Time (sec)
5% (by vol) Sulfuric Acid (with distilled water)	65	60
rinse with distilled water	20	10
25% (by vol) Ammonium Persulfate (with distilled water)	20	60
rinse with distilled water	20	10
5% (by vol) Sulfuric Acid (with distilled water)	20	60
rinse (with distilled water and ethanol)	20	10
dry with heat gun	70	10

Specimens were examined using the Reichert MeF3A optical microscope in the School of Materials Science and Engineering at the Georgia Institute of Technology and micrographs were taken using a 35 mm camera. Quantitative analysis of the microstructure was accomplished by means of the linear intercept method (Underwood, 1970). The mean grain intercept, $\bar{\lambda}$, is given as:

$$\bar{\lambda} = \frac{1}{P_L} \quad (\text{IV.1})$$

where P_L is the number of intercepts with grain boundaries per unit length of a test line (Gokhale 1982). This number is determined by overlaying a line on the microstructure and counting the number of grain boundaries crossed. Fields of view were randomly chosen throughout the specimen surface with approximately twenty counts made per specimen.

Table IV.3: SPECIMEN GRAIN SIZES

Specimen # (Test Matrix)	average P_L	Average Grain Size λ (μm)
Annealed	18.3	58
A6	24.2	41.3
B1A	44.1	22.7
B1B	46.4	21.5
B1C	49.4	20.3
B1D	54.4	18.4
B1E	48.9	20.5
B1F	35.2	28.4
A2	13.8	72.7
A1	15.6	64.2
A7	31.9	31.3
A5	26.7	37.4
A8	37.6	26.6
A4	23.8	42.1
A9	34.5	28.9
A3	17.2	58

A10	18.2	55.1
A11	16.1	62.3
A13	14.1	71
D7	12.3	81
E8	43.3	23.1
D1	29.5	33.8
D2	21	47.7
D3	10.6	94.1
A15	10.6	41.1
A16	24.3	45.8
A17	21.8	51.8
E7	39	25.6
E6	39.2	25.5

IV.2 Results

The average grain sizes for specimens deformed in compression under various deformation conditions were determined. The objective was to obtain confirmation that the observed flow stress behavior was the result of recrystallization. The softening in flow stress and transition from single peak to oscillations with multiple peaks often indicates the occurrence of recrystallization. The investigation of the average grain sizes also indicates that recrystallization occurred. Single peak softening, flow stress reduction after reaching a peak stress, is associated with grain refinement while multiple peak, oscillations in the flow stress, occurs during grain coarsening. This is substantiated from the average grain size calculations. The grain size decreases, from 59 μm at 25°C to 27 μm at 286°C and then starts to increase as the temperature rises further. This transition temperature also corresponds to the change from single peak to multiple peak flow stress behavior (Fig. IV.1).

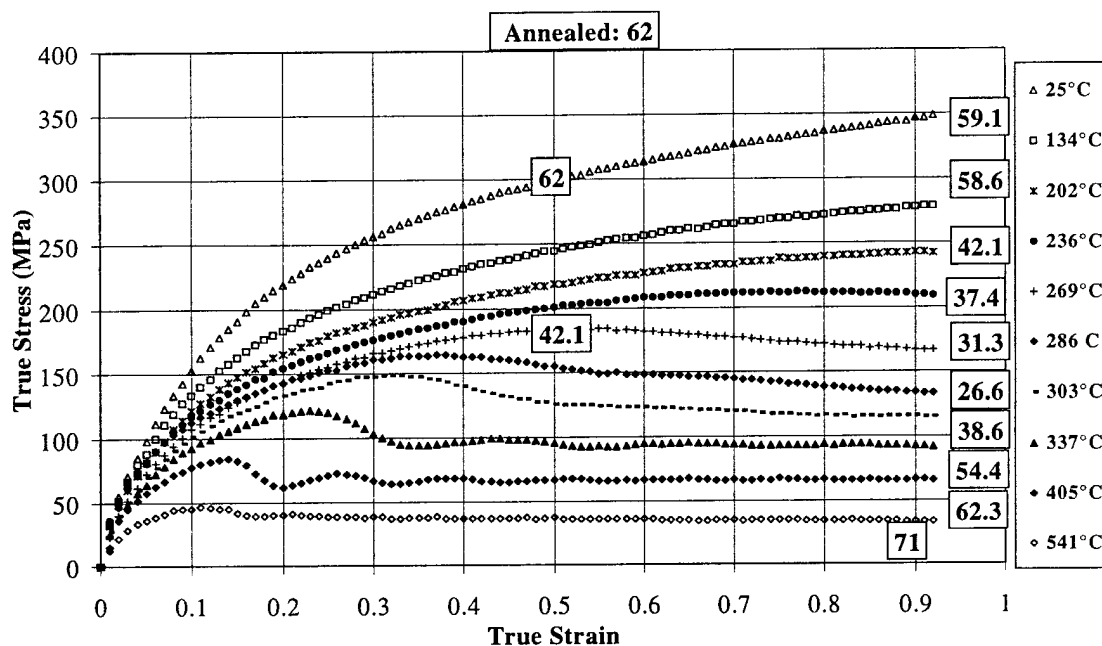


Figure IV.1: Average grain sizes for OFHC Cu from compression at constant strain rate, 0.0004 s^{-1} , isothermal experiments. The sizes (μm) are shown at the corresponding strain and temperature at completion of strain. Two values are shown at 0.5 strain, 25°C and 269°C , which were determined from separate experiments. The standard deviation on the measurements was $4 \text{ } (\mu\text{m})$.

The micrographs reveal grains which are equiaxed. The following sequence of figures detail the changes in microstructure resulting from the increasing temperature. The first two figures show the annealed state (Figs. IV.2 - IV.3). The smallest grains were observed after deformation at 286°C and 0.0004 s^{-1} to 1.0 strain (Fig. IV.7) and the largest after deformation at 676°C and 0.0004 s^{-1} . The differences in grain sizes are clearly observed.

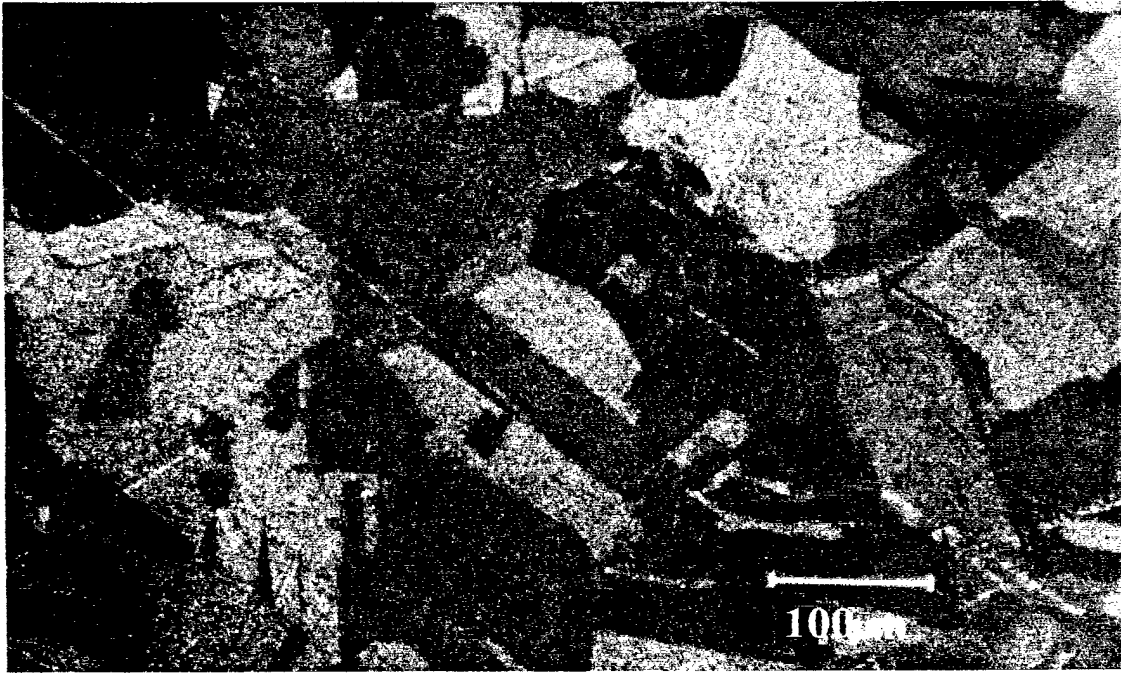


Figure IV.2: Micrograph of OFHC Cu annealed at 600°C for four hours. The micron bar corresponds to 20 μm and a magnification of 100 x.

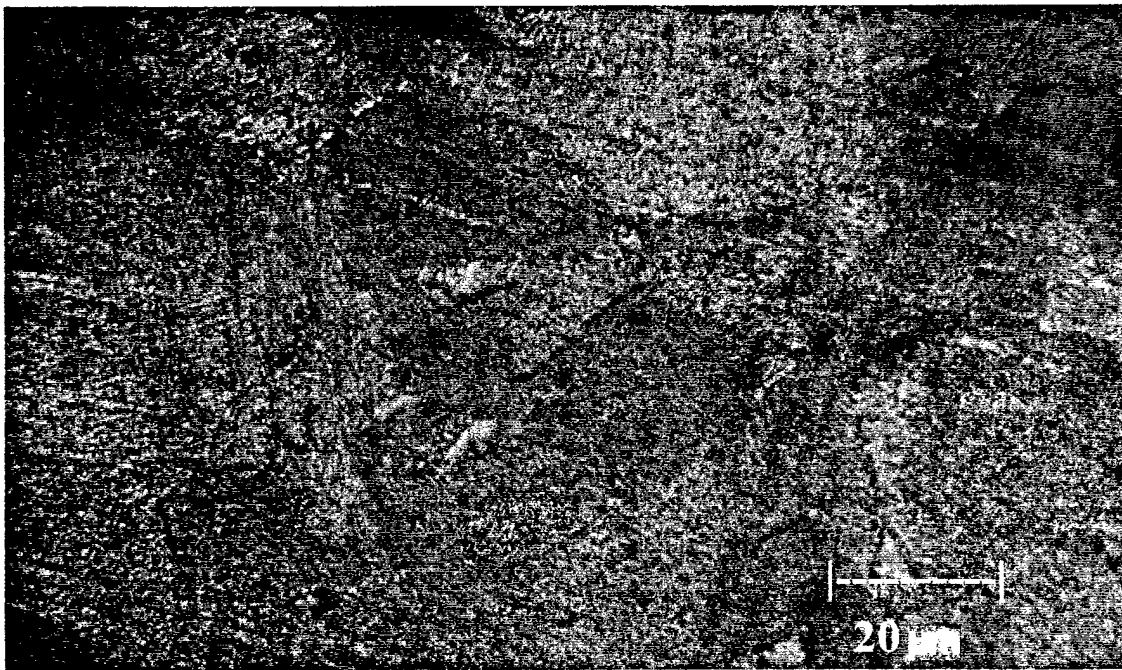


Figure IV.3: Micrograph of OFHC Cu annealed at 600°C for four hours. The micron bar corresponds to 20 μm and a magnification of 100 x.

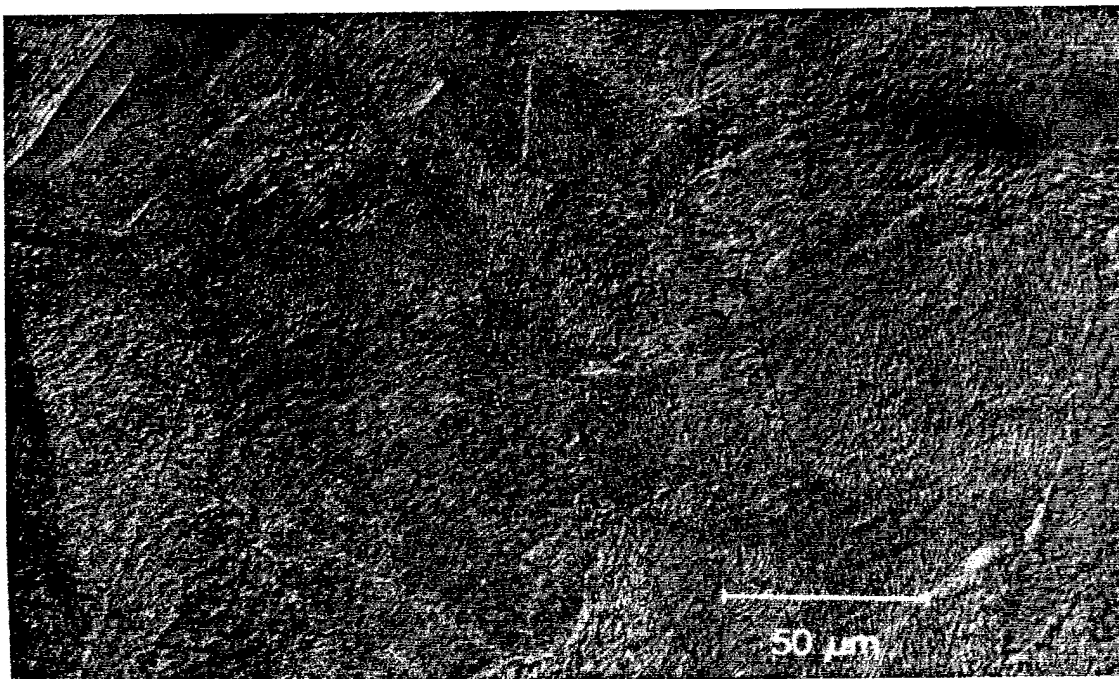


Figure IV.4: Micrograph of OFHC Cu compressed at 25°C and 0.0004 s^{-1} to a strain of 0.5. The micron bar corresponds to $50 \mu\text{m}$ and a magnification of 50 x.

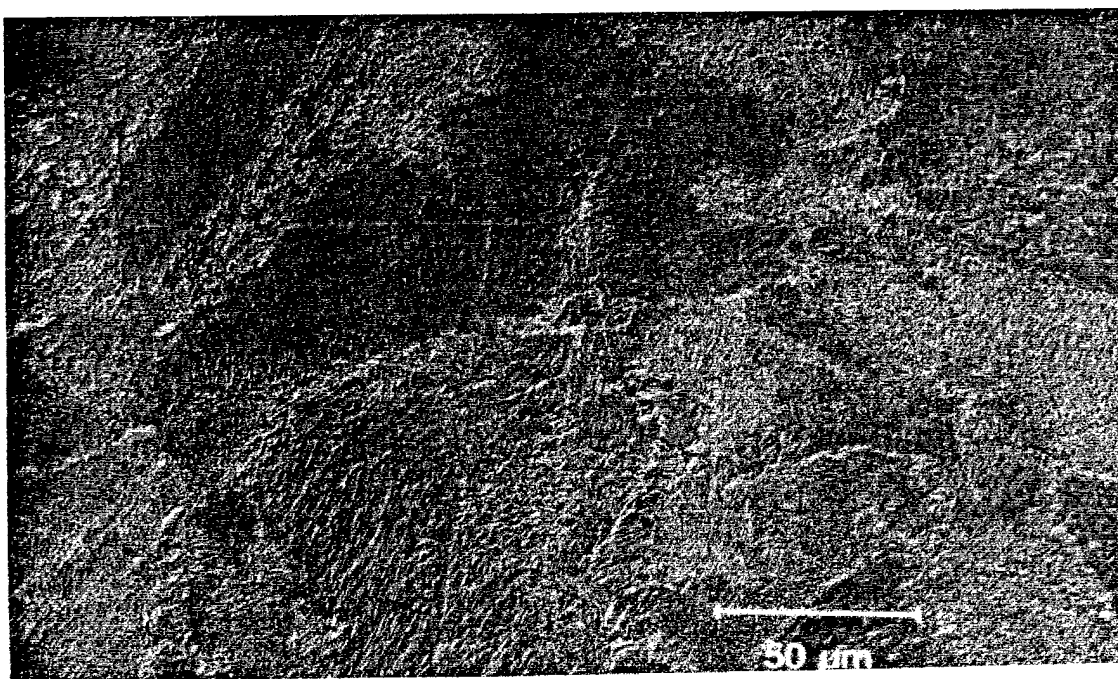


Figure IV.5: Micrograph of OFHC Cu compressed at 236°C and 0.0004 s^{-1} to a strain of 1.0. The micron bar corresponds to $50 \mu\text{m}$ and a magnification of 50 x.

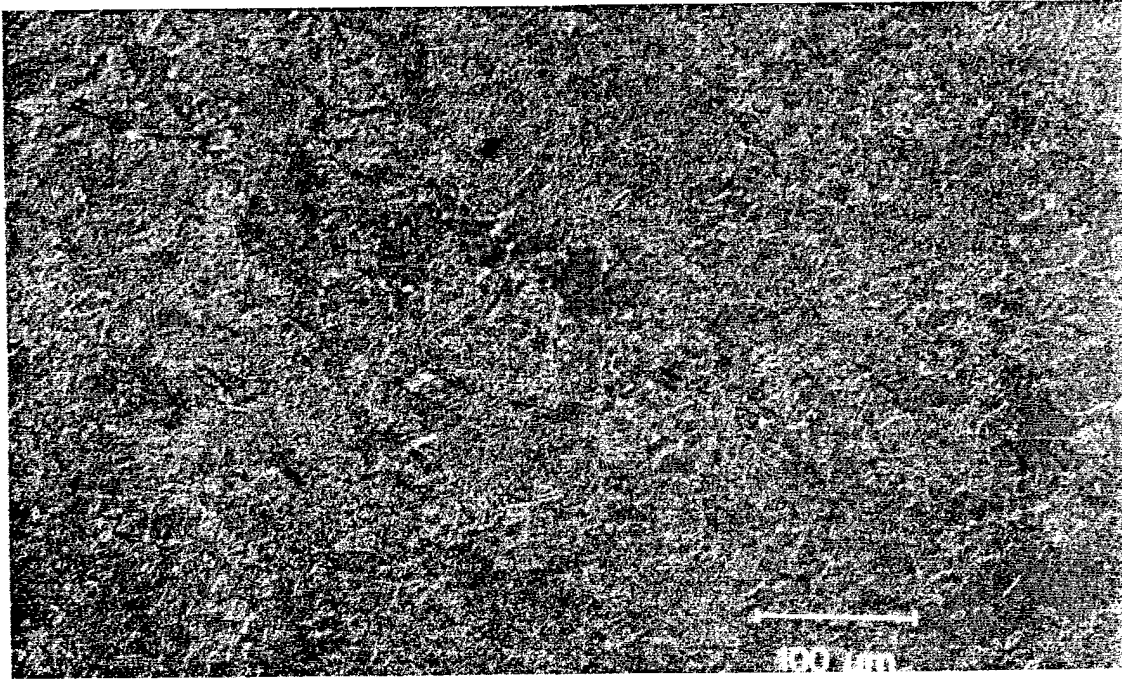


Figure IV.6: Micrograph of OFHC Cu compressed at 286°C and 0.0004 s^{-1} to a strain of 1.0. The micron bar corresponds to 100 μm and a magnification of 20 x.



Figure IV. 7: Micrograph of OFHC Cu compressed at 286°C and 0.0004 s^{-1} to a strain of 1.0. The micron bar corresponds to 50 μm and a magnification of 50x.

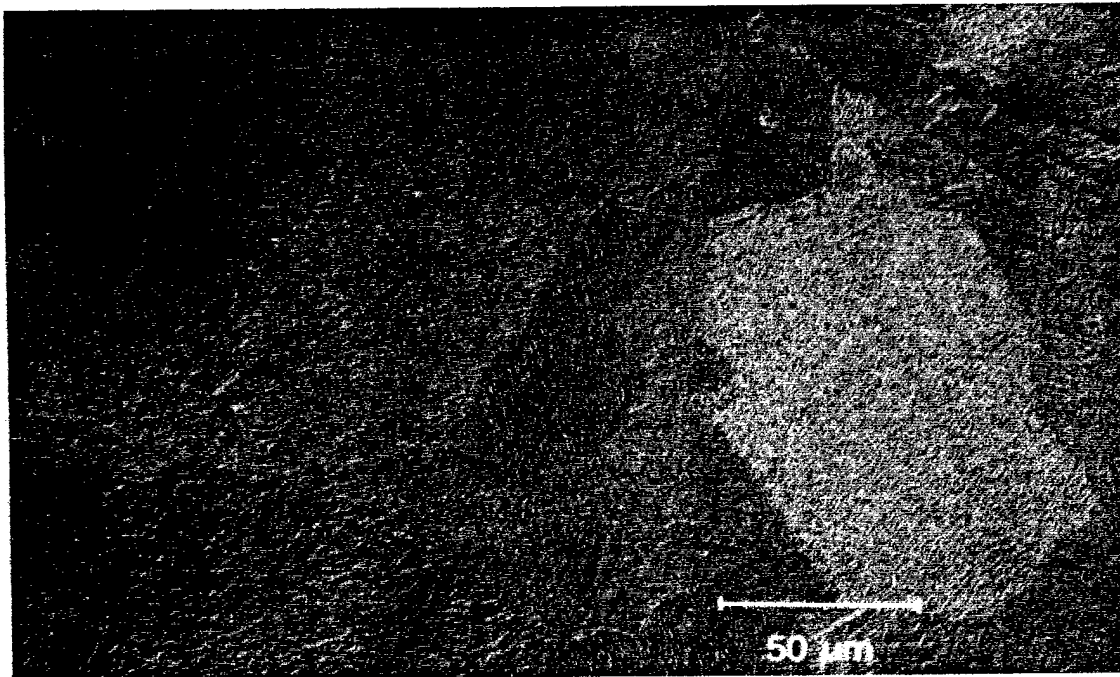


Figure IV.8: Micrograph of OFHC Cu compressed at 405°C and 0.0004 s^{-1} to a strain of 1.0. The micron bar corresponds to $50 \mu\text{m}$ and a magnification of 50 x.

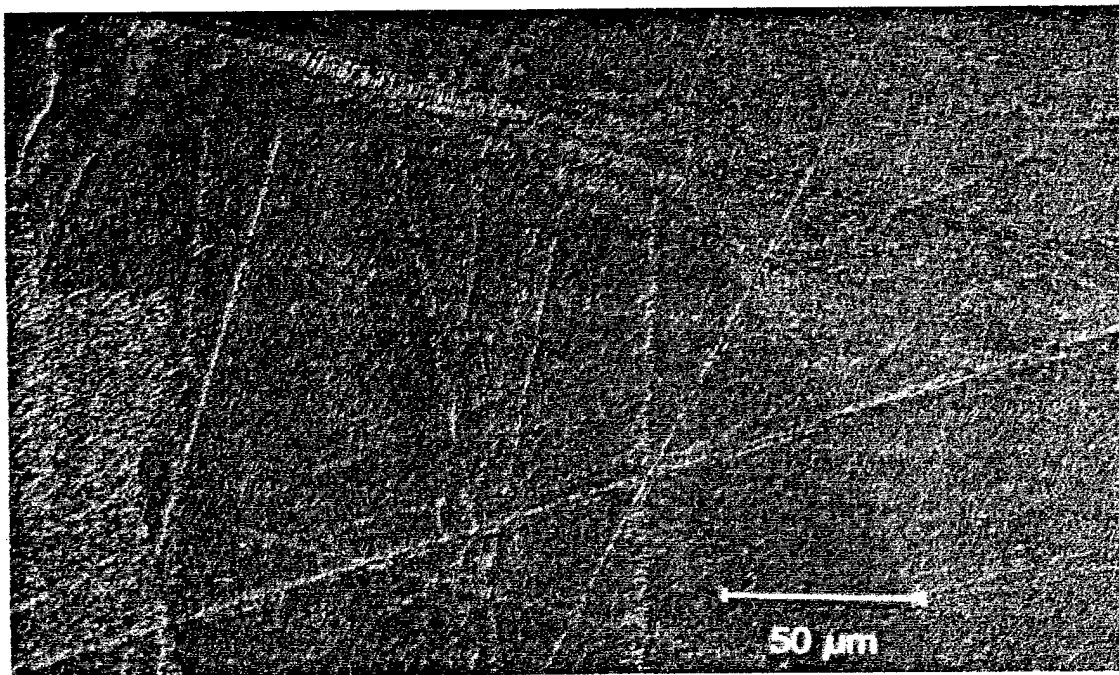


Figure IV. 9: Micrograph of OFHC Cu compressed at 676°C and 0.0004 s^{-1} to a strain of 1.0. The micron bar corresponds to $50 \mu\text{m}$ and a magnification of 50 x.

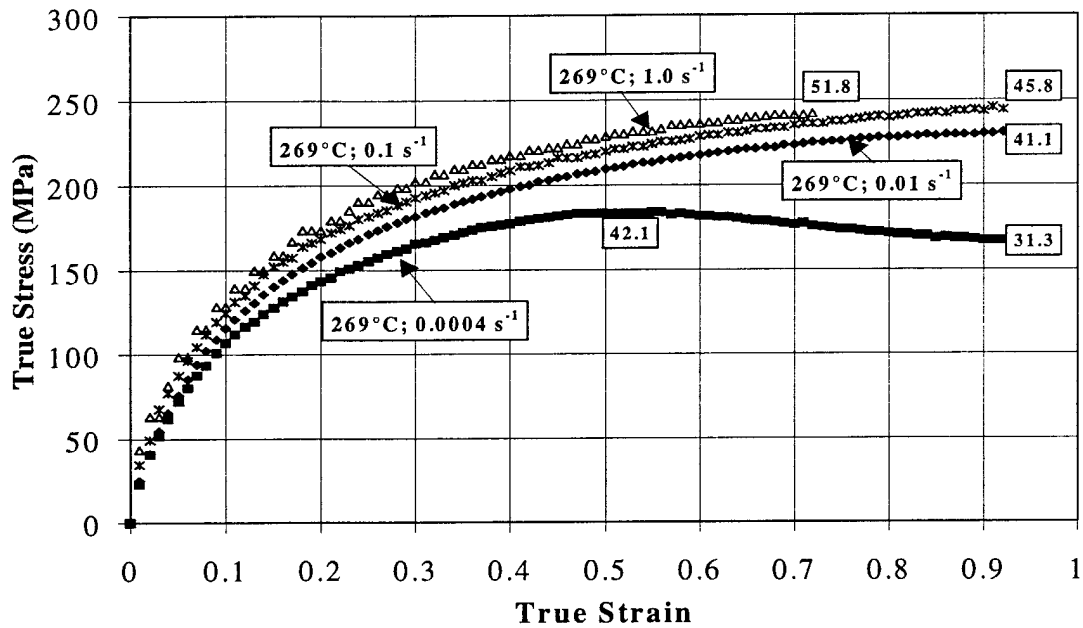


Figure IV.10: Average grain sizes for OFHC Cu from compression at 269°C and various constant strain rates, 0.0004 s⁻¹ experiments. The sizes (μm) are shown at the corresponding strain and temperature at completion of strain. The value shown at 0.5 strain was determined from a separate experiment. The standard deviation on the grain size measurements was 4 (μm).

The grain size decreases with decreasing strain rate during deformation in compression at 269°C. The average grain size decreases from 51.8 μm at 1.0 s⁻¹ to 31.3 μm at 0.0004 s⁻¹. The nucleation of grains is driven by the stored energy of dislocations and requires an incubation time. Lower strain rates permit the nucleation of new grains and their subsequent growth.

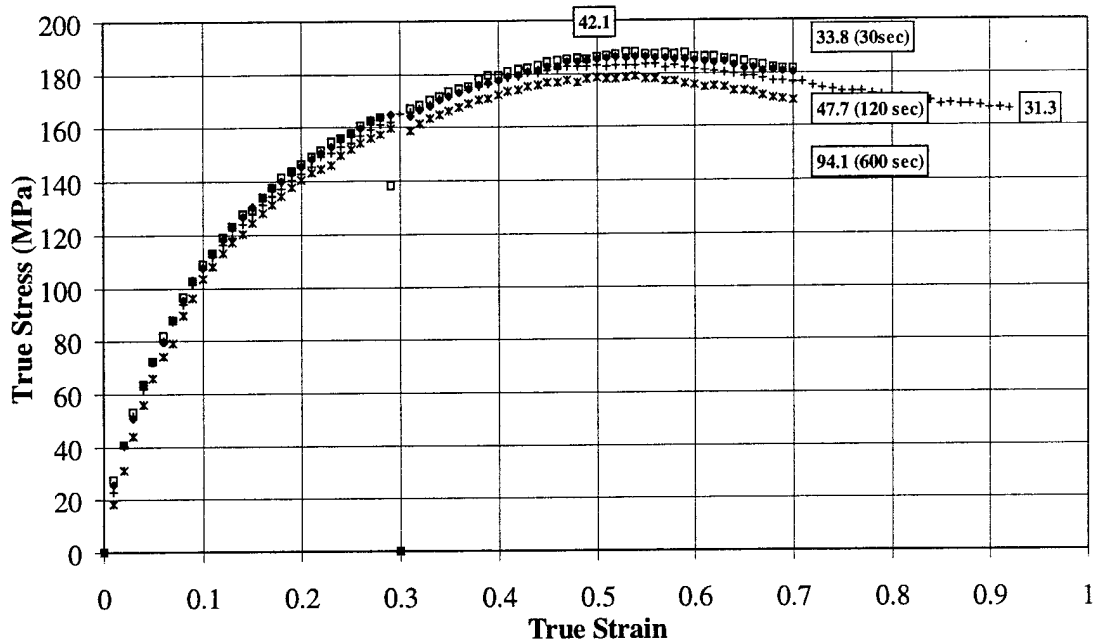


Figure IV.11: Average grain sizes for OFHC Cu from compression at constant strain rate, 0.0004 s^{-1} , isothermal experiments at 269°C with various hold times after unloading at 0.3 strain before reloading to a final strain level of 0.7 or 1.0. The sizes (μm) are shown at the corresponding strain and temperature at completion of strain. The value shown at 0.5 strain was determined from a separate experiment. The standard deviation on the grain size measurements was $4 \text{ }(\mu\text{m})$.

The average grain size increases with the length of the hold time. The specimens were compressed at 269°C to a strain of 0.3, unloaded and maintained at a constant temperature. After the indicated hold period of time, the specimens were again reloaded in compression to the final strain level. The grain size increases from $33 \text{ }(\mu\text{m})$ after a 30 second hold time to $94 \text{ }(\mu\text{m})$ after 600 seconds.

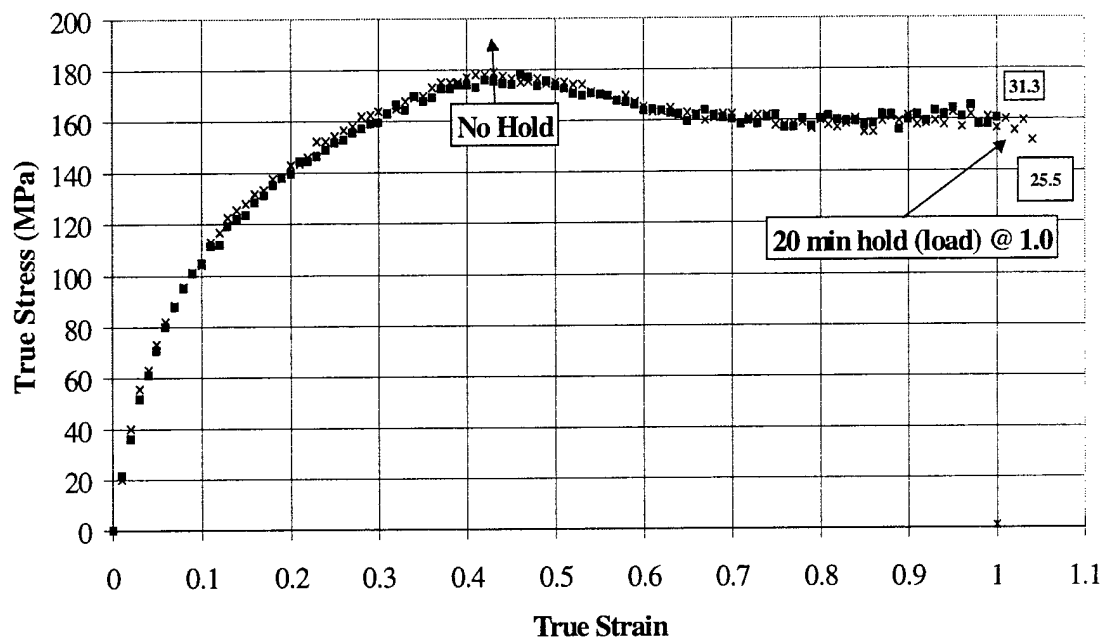


Figure IV.12: Average grain sizes for OFHC Cu from compression at constant strain rate, 0.0004 s^{-1} and 269°C isothermal experiments. The specimens were compressed to 1.0 strain and then held for 20 minutes while maintained under a constant load. The sizes (μm) are shown at the corresponding strain and temperature at completion of strain.

The average grain size decreased slightly when the specimen was held for an additional time under constant load. The grain size decreased from $31 \mu\text{m}$ when not held for any additional time to $26 \mu\text{m}$ when held for 20 minutes. The additional time spent at 269°C resulted in an additional grain refinement.

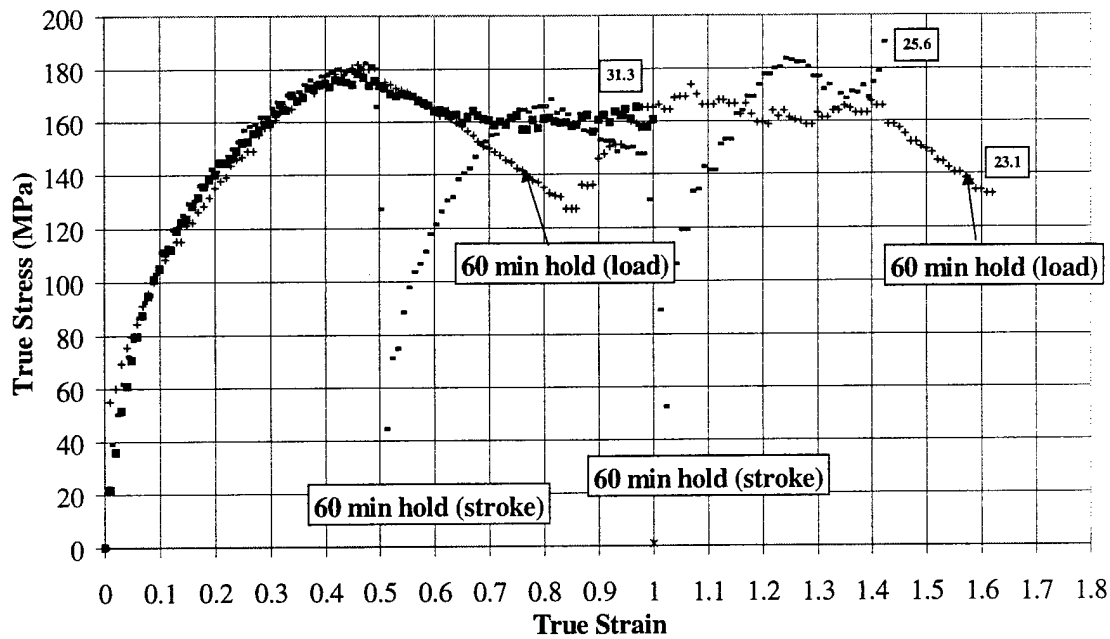


Figure IV.13: Average grain sizes for OFHC Cu from compression at constant strain rate, 0.0004 s^{-1} and 269°C isothermal experiments. The specimens were compressed to 0.5 strain and then held under constant temperature under either load or stroke control for 60 minutes and then reloaded for an additional 0.5 strain and held for another 60 minutes. The sizes (μm) are shown at the corresponding strain and temperature at completion of strain. The standard deviation on the grain size measurements was $4 \text{ } (\mu\text{m})$.

The average grain size does not vary much from the two conditions. The additional time spent at 269°C , 60 minutes, resulted in the grain size reduction corresponding to additional grain refinement. The loading condition, load or stroke control, had little effect.

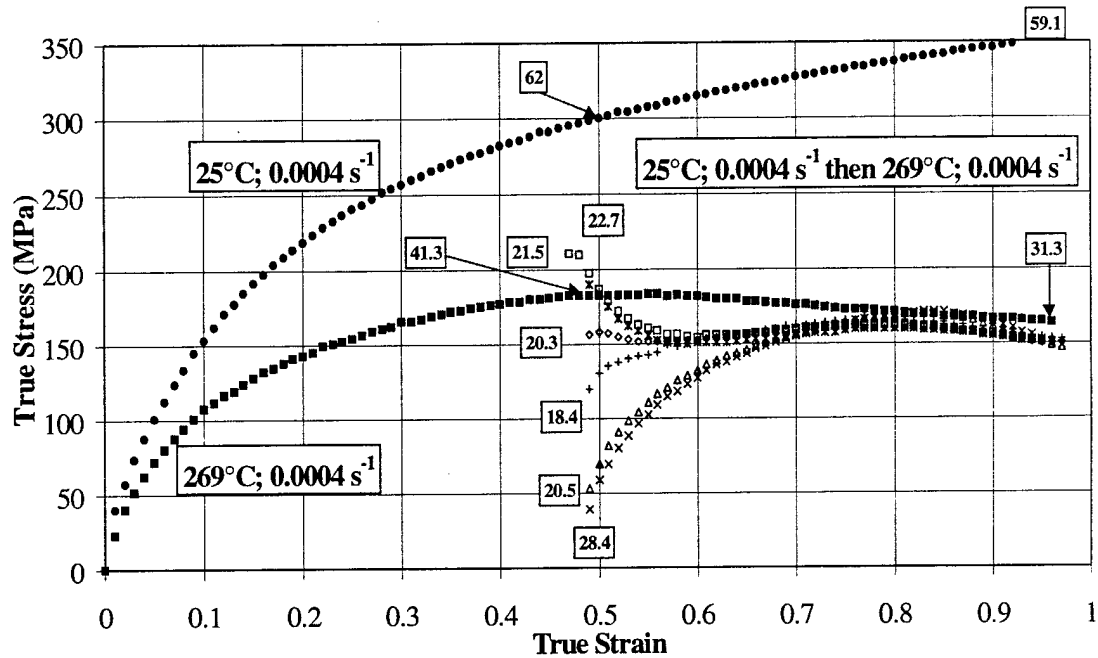


Figure IV.14: Average grain sizes for OFHC Cu from compression at constant strain rate, 0.0004 s^{-1} and sequences of temperature experiments. The specimens were first pre-strained at 25°C to 0.5 strain. The specimens were unloaded and subsequently reloaded at 269°C after the indicated periods at 269°C before deformation. The sizes (μm) are shown at the corresponding strain and temperature at completion of strain. Two values are shown at 0.5 strain, 25°C and 269°C , which were determined from separate tests. The standard deviation on the measurements was $4 \text{ } (\mu\text{m})$. Indicated sizes for the reloaded specimens correspond to the average grain size (μm) at 1.0 true strain.

The grain sizes were relatively constant, with all the values within one standard deviation. The grain size decreases with the additional time and compressive strain at 269°C from $62 \text{ } (\mu\text{m})$ after a compressive pre-strain to 0.5 strain to a grain size ranging from 18 to $23 \text{ } (\mu\text{m})$ after the temperature sequence to 269°C

IV.3 Discussion

The average grain sizes are consistent with the occurrence of recrystallization. The average grain size decreased during the deformation conditions when the flow stress exhibited a single peak, which is consistent with grain refinement. During the deformation conditions when oscillations in the flow stress occurred, the average grain size increased, consistent with grain coarsening. These observations indicate that the softening observed at temperatures above 269°C are due to the changes in grain structure resulting from recrystallization. The effect of recrystallization is to change the grain structure which results in the reduction of the steady state flow stress. The kinetics of recrystallization were described in Chapter 2. Grain refinement results in a single peak in the flow stress while grain coarsening causes multiple peaks. The initial peak strain, the strain corresponding to the peak in flow stress, decreases with increasing temperature at the same strain rate. The observed softening is consistent with the softening data shown in Fig. IV.15. A greater amount of softening occurs with increasing time. The kinetics of softening, and recrystallization, greatly increases with an increase in pre-strain. Modeling approaches for the prediction of this critical strain have been developed (Busso, 1998) based on a critical level of internal deformation resistance.

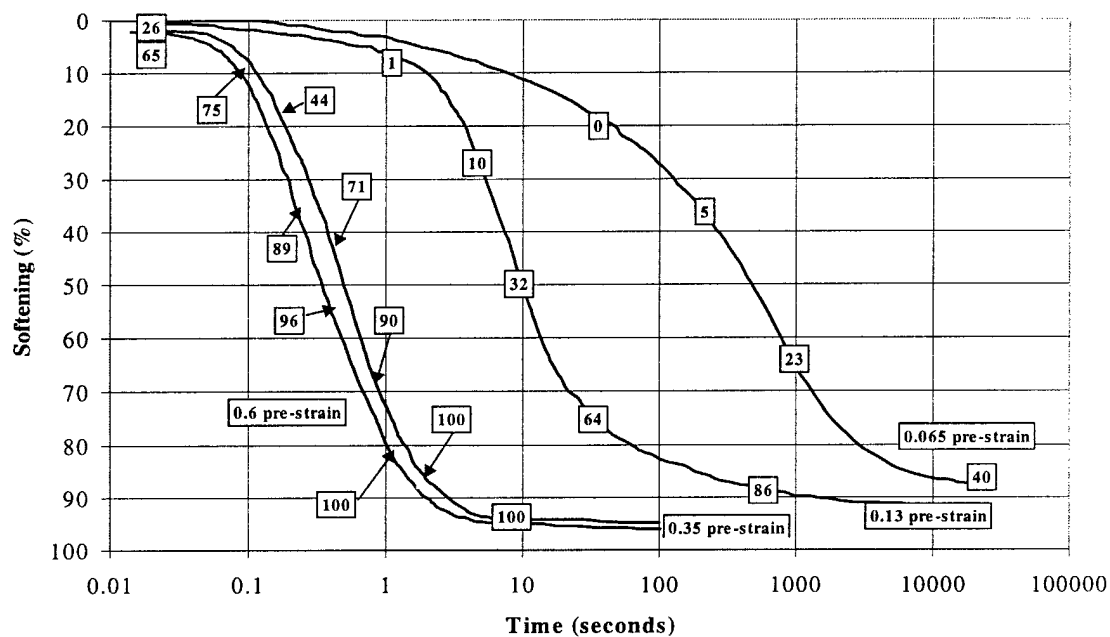


Figure IV.15: Relationship between softening and fractional amount of recrystallized grains in Cu (Kwon and DeArdo, 1990). Numbers in boxes represent the volume percentage of recrystallization.

CHAPTER V

CONSTITUTIVE MODELS

V.1 Introduction

Improved experimental capabilities have resulted in greater and more detailed information concerning material behavior. The understanding and characterization of material responses has been greatly enhanced through progress in both material test apparatuses, such as automatic controls, digital measurement systems and microprocessors, and the ability to detect and observe actual microstructure. These detailed, more accurate data permit improved state-of-the-art constitutive models to be developed which account for many of the observed material responses.

Constitutive models have evolved and become more complex as additional material responses are incorporated. Material behavior is included in internal state variable (ISV) constitutive models through the addition of appropriate internal variables, their evolutionary relationships, and their coupling with the kinetics of flow and hardening. Modern constitutive models do not currently incorporate all macroscopic behavior. Additional terms may be required to adequately predict such material behavior as dynamic restoration, including both single and multiple peak dynamic recrystallization, and static restoration, including both thermal recovery and recrystallization, and history effects resulting from

arbitrary sequences of temperature, strain rate and deformation path. Accounting for complex paths of deformation, temperature, and strain rate is an important requirement of constitutive laws for large strain problems such as high speed machining, impact, and various primary metal forming operations.

A prevalent paradigm for use of constitutive models is to correlate simple experiments and then predict more complex material behavior. The capability of a particular model is based on its predictive accuracy compared to actual measured experimental data which is obtained for the same temperature, strain rate and loading conditions. The utility of a particular model is also based on *robustness*, the ability to accurately provide predictions for conditions which have not been determined experimentally. The predictive accuracy of a given model is not the only important criterion for its usefulness; the effort required to determine the material parameters for the model also determines a model's utility. Difficulty in parameter identification is related to the number and uniqueness of these parameters, their relationship to actual, physically observed behavior and the types and amount of experimental data available or necessary.

Numerical calculations are conducted to obtain the flow stress predictions for each model. Evolution equations were time-stepped integrated using a second-order Runge-Kutta method. Time intervals were scaled to correspond to a strain increment of approximately 0.001.

This chapter reports on efforts to model history effects resulting from sequences of temperature and strain rate. The first section contains a description of a material parameter

optimization process which proves to be a powerful technique for determining parameters, functional forms, and the ability of a model structure to adequately predict behavior. Next, the constitutive models used in this analysis are discussed, and then, we determine an optimized parameter set using a range of isothermal, constant strain rate data. Sequence effects are then predicted. Additionally, the parameter sensitivity of each model is determined. The final section investigates different forms for improving the predictive capability for sequences of deformations at different temperatures and strain rates.

V.2 Parameter Optimization

A constitutive model's accuracy in predicting material behavior is not the only criterion in determining its usefulness. The practicality of using a particular model to describe material behavior also depends on the effort and skill required to determine the material parameters. Generally, a model which has physical foundations will have material parameters with a more direct interpretation than strictly empirical models. Parameters have traditionally been determined using mechanical test data combined with graphical procedures (Senseny and Fossum, 1993, Lindholm *et al.*, 1993 and Dave and Brown, 1994). Other methods include the use of expert systems such as BFIT, a program written to analyze and fit the Sandia BCJ-SNL model parameters to experimental data (Lathrop, 1996), and various optimization procedures (Braasch and Estrin, 1993 and Muller and Hartmann, 1989). Muller and Hartmann were the first to apply the evolution optimization strategy to the application of determining the optimal set of model parameters for constitutive modeling. They

determined the parameters for the Hart (1976) model for 25CrMo4 steel. Braasch and Estrin also used the evolution strategy and determined the parameters for the two ISV model of Estrin (1991) which included eleven parameters. Sensitivity to parameter variation is a related issue that pertains to the degree of “uniqueness.” The forms and parameters for non-linear, irreversible behavior are inherently non-unique, therefore, uniqueness, here, is concerned with any redundancies of parameters within the system of constitutive equations.

The typical approach to parameter evaluation is to perform a series of experiments which facilitate development of simplified assumptions about material behavior. These assumptions are usually: (i) the relationship between imposed stress and the inelastic strain rate can be measured, with the internal structure variables held constant; or (ii) for small inelastic strain increments, the isotropic hardness does not change appreciably. Parameters are then determined graphically using the slope or changes in the slope in cross plots of variables. Senseny and Fossum (1993) found that these assumptions cannot be considered valid during most material tests due to inaccuracies in testing and because load path changes cannot be applied instantaneously. The more robust approach is to integrate the constitutive model, simulating the actual loading histories, and then use an optimization approach to evaluate the model parameters.

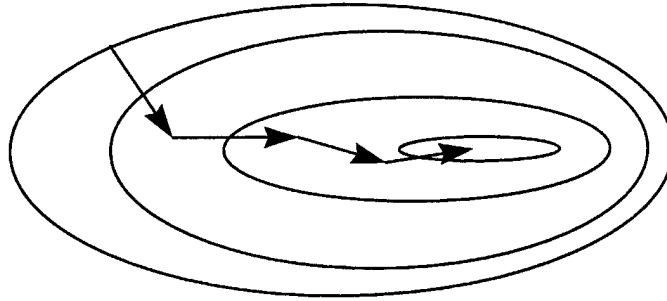
The optimum set of parameters necessary to describe a set of experimental data can be determined using a variety of optimization schemes. The particular constitutive model determines which of these methods will work the best in terms of accuracy and time. Gradient, downhill simplex, and genetic algorithms are three search methods to seek local

minima of a multivariate level function. Parameters of a model are evaluated by minimizing an objective function which employs an error measurement. The objective function is constructed from an error norm based on the difference of the predicted flow stress value for a particular strain level with measured data for the corresponding conditions. Different error norms can be used, such as the sum of the squares of the differences (L_2 norm) or the absolute value of the greatest difference between predicted and measured data. The optimization procedure must be robust enough to handle the topology of the objective function for a complicated constitutive model over a given set of deformation histories. Prevalent characteristics of ISV models for inelastic behavior include strong couplings among evolution equations, high parameter sensitivity, and high mathematical stiffness. In the parameter space, the model cannot be evaluated everywhere, and the objective function may be convex in some regions and concave in other.

The gradient method (Fig. V.1) follows the path of the steepest gradient to the local minimum of the objective function. Partial derivatives of the objective function with respect to the design parameters are calculated. This is a simple and effective method, but tends to get trapped in local minima (Pierre, 1969). A simplex is a body in n -dimensions consisting of $n+1$ vertices. Each vertex represents a point, consisting of a set of material parameters, in the design space. As the algorithm proceeds, the simplex makes its way downward toward the minimum location through a series of steps, called reflections, expansions, or contractions shown in Fig. V.1 (Belavendram, 1995). The vertex of the simplex with the largest (worst) objective function value is moved through the opposite face to a lower point.

Gradient

Follows steepest descent.



Uses partial derivatives of objective function w.r.t. design parameters

Downhill Simplex

Simplex:

Geometrical figure of n dimensions
and $n+1$ vertices

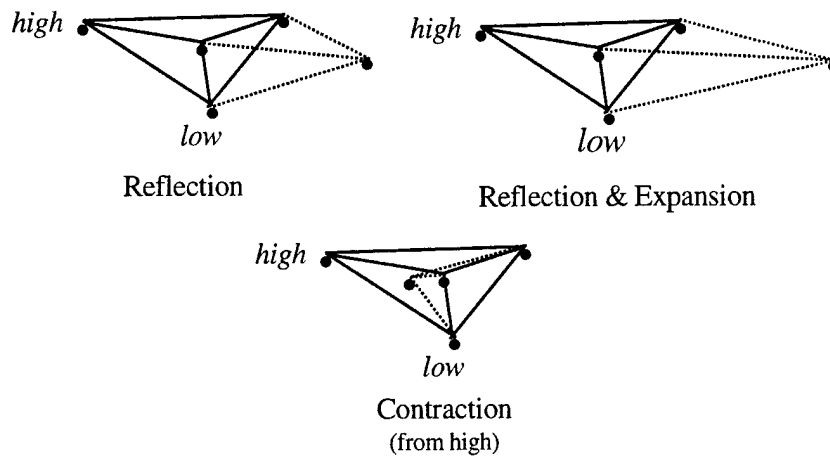


Figure V.1: Optimization schemes: Gradient and Downhill Simplex.

The genetic algorithm is useful for complex functions and large data sets and follows the mechanics of natural selection using a “generate and test” technique. A large number of points are randomly selected over the design space. Each of these points are “mutated,” given a random change, which produces a number of new points normally distributed around the original point. The point with the lowest objective value is then selected and is again randomly changed. Initially, this method converges rapidly and deals well with complex objective function topologies. Muller and Hartmann (1989) and Braasch and Estrin (1993) have used this evolution strategy to obtain parameters for the Hart (1976) model for 25-CrMo4 steel and Estrin (1991) model for Al-1100 aluminum, respectively.

The objective function topology determines which optimization process will be most effective in locating the global minimum and avoid getting trapped in local minima. A more powerful approach is a hybrid optimization scheme which employs combinations of the gradient, simplex, and evolution techniques. Pointer Optimization Software 1.2 (Van der Velden *et al.*, 1996) is a program which selectively uses all three optimization techniques based on evaluations of the objective function. The optimization programs links to the spreadsheet used to perform the numerical calculations for the model predictions. In this work, this optimization approach was used to determine the parameters corresponding to the Johnson/Cook (Johnson and Cook, 1983), Zerilli-Armstrong (Zerilli and Armstrong, 1987), MTS (Klepaczko and Chiem, 1986, Follansbee and Kocks, 1988, and Klepaczko, 1988), BCJ-SNL (Bammann, Chiesa, and Johnson, 1990, Bammann, 1990, and Bammann *et al.*, 1990), and McDowell (McDowell and Moosbrugger, 1987; Moosbrugger and McDowell,

1990; and McDowell, 1992) models. For each of these five models, the parameters were determined using five constant strain rate, isothermal conditions: 25°C, 6000 s⁻¹; 25°C, 0.0004 s⁻¹; 269°C, 5200 s⁻¹; 269°C, 0.1 s⁻¹ and 269°C, 0.0004 s⁻¹. These resulting parameters are then used to calculate sequence predictions which are then compared to experimental sequence data. The sensitivity of each model's parameters are then shown. The objective function which represents how well the model prediction fits the experiment data is defined as the weighted sum of the error, squared (L₂ norm) using

$$\text{error} = \sum_{n=1}^K W_n \left| \left(\sigma_n(\epsilon)_{\text{predicted}} - \sigma_n(\epsilon)_{\text{data}} \right) \right|^2 \quad (\text{V.1})$$

where $\sigma_n(\epsilon)_{\text{predicted}}$ is the predicted stress value and $\sigma_n(\epsilon)_{\text{data}}$ is the experimental data stress value respectively determined for each strain increment, n . A weighting factor, W_n , is necessary to provide equal weight for each data curve, even though the strain levels vary for the different deformation conditions. W_n is determined by the largest strain value for the n deformation conditions and the final strain for each condition

$$W_n = \frac{\epsilon_{\text{maximum}}}{\epsilon_n} \quad (\text{V.2})$$

The number of the deformation conditions, (eg. compression: 25°C, 0.0004 s⁻¹, etc.), is represented by K. The minimization of the objective function typically follows the progress shown in Fig. V.3. The progress is initially very rapid, achieving the majority of the reduction in 20% of the total time used.

Parameter sensitivity measures the effect each parameter has on the process of minimizing the objective function defined as the sum-square-errors between predicted and experimental data. The hybrid optimization scheme determines the parameter set which minimizes the objective function value, $OBJ_{\text{minimized}}$. After the optimal (minimum) objective function value has been calculated, an offset in the optimal parameters is assigned. This offset, $\pm 10\%$ of all optimized parameters, results in an objective function value, OBJ_{offset} , greater than the minimum value (Fig. V.2). Additional optimizations are then conducted with the offset parameters as the initial starting condition. When all parameters are allowed to vary, the optimal objective function value, $OBJ_{\text{minimized}}$, is again achieved. The relative importance of each parameter is determined by constraining a parameter to its initial offset value. The parameter sensitivity evaluation is then based on the ability of this constrained set of parameters to achieve the minimized objective function value from the offset initial conditions during subsequent optimizations, $OBJ_{\text{constrained}}$. Parameter sensitivity is defined as

$$\eta = \text{Parameter Sensitivity} = \frac{OBJ_{\text{offset}} - OBJ_{\text{constrained}}}{OBJ_{\text{offset}} - OBJ_{\text{minimized}}} \quad (V.3)$$

A value $\eta = 1$ results when $OBJ_{\text{constrained}} = OBJ_{\text{minimized}}$ which indicates the objective function is independent of the constrained parameter which has no effect on the objective function achieving the optimal value from that initial parameter offset starting location. This independence indicates the constrained parameter is not necessary to achieving the optimal objective function value and can, therefore, be considered redundant. A value $\eta = 0$ results when $OBJ_{\text{offset}} = OBJ_{\text{constrained}}$ which indicates the optimal objective function value is highly dependent on the constrained parameter. This mutual dependence indicates the constrained parameter is essential to achieving the optimal objective function value. Two sets of parameter sensitivity evaluations are made. The first measures the ability of one parameter to achieve the optimal objective function value with all other parameters constrained. Additionally, the sensitivity is determined from the ability of all the other parameters, without the single or set of parameters, to reach the minimized objective.

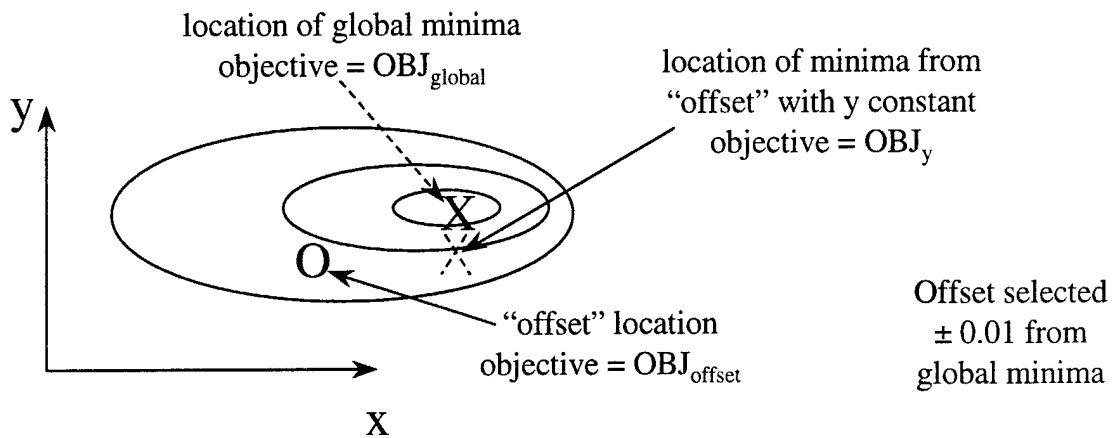


Figure V.2: Two dimension parameter sensitivity example. The global minima, OBJ_{global} , is the objective function value resulting from the optimization of the parameters. A consistent offset, OBJ_{offset} , is calculated using parameters adjusted ± 0.01 from the optimized parameter values. This offset objective function value is greater than OBJ_{global} . Another optimization is calculated using the offset parameters as the initial values and with certain parameters held fixed. The resulting objective function, OBJ_y , is a measure of the sensitivity of the objective function to that parameter set.

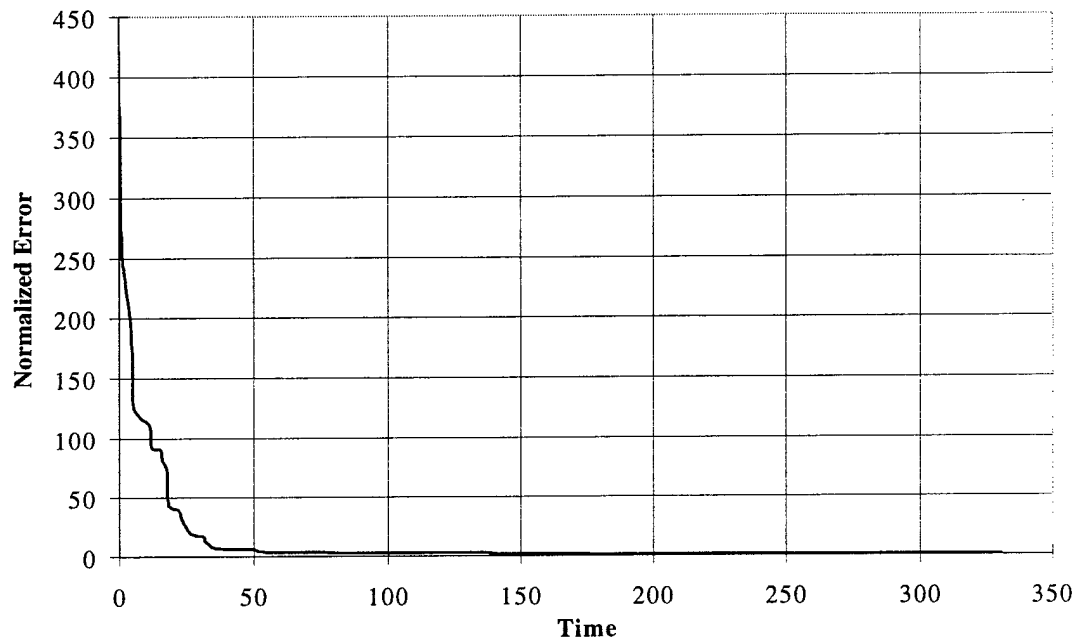


Figure V.3: Typical minimization of the objective function (shown normalized to the minimum value) using the Pointer Optimization software.

V.3 Constitutive Models

Even if experiments spanning the entire range of temperature and strain rates of interest have been performed, it is impossible to explore all the possible sequences and combinations of load paths that could occur in real applications. Hence, constitutive equations must extrapolate from simple and easily obtained test data to complex deformation histories which cannot be analyzed by controlled experiments.

Initially, mechanical equations of state were postulated with the stress dependent only on strain and temperature. As a greater level of understanding of the actual material processes was developed, especially with the linkage of deformation to the microstructural level, the complexity of equations grew. This results in a trade off between the simplicity of the model and the number of terms representing all of the identifiable deformation mechanisms. The closer the phenomenological description reflects the actual physical deformation mechanisms, the greater capability exists for the model to be extrapolated beyond the range of data used to obtain the initial model structure and material parameters. As the linkages to physical processes become more detailed, the number of material parameters also rises. The limiting effectiveness of a model has been the number of parameters and the tests necessary to determine them. From a practical standpoint, the number of parameters in a constitutive law is of less concern than the redundancy or relative dependence of parameters in the system of constitutive equations. Considering numerics, clearly it is only the number of variables that require constitutive update that is of concern.

The functional form for the ISV constitutive models to be considered here assumes

the deviatoric strain rate of deformation may be decomposed into elastic and inelastic components, i.e.

$$\dot{\epsilon}_{ij} = \dot{\epsilon}_{ij}^e + \dot{\epsilon}_{ij}^p \quad (V.4)$$

In this study, we consider classes of models for which the inelastic strain rate has the form

$$\dot{\epsilon}_{ij}^p = F(s_{ik} - \alpha_{ik})(s_{kj} - \alpha_{kj}) \quad (V.5)$$

where α_{ij} is the back stress and s_{ij} a measure of stress. The temperature dependent viscosity function, F , involves the state variables. Internal state variable (ISV) evolution equations are typically expressed in the Bailey-Orowan form of a hardening term minus recovery, i.e.

$$\dot{\xi}_i = \mu_i(\bar{\xi}_i - \xi_i) |\dot{\epsilon}^p| - R_s \xi_i \quad (V.6)$$

where each of the ξ_i 's represents a different ISV, in general, of potentially different tensorial rank. This evolutionary form (first order differential equation) has the following characteristics. When the ISV is initially zero, the hardening term dominates, causing the rate equation to be large until the recovery term grows. The ISV rate of evolution then

approaches zero (saturates) and the ISV reaches a saturation value. The first coefficient,

$\mu_1 \bar{\xi}_i$, affects the initial slope of the rate equation while the second coefficient couples to

establish the saturation value. Static recovery may be included through the R_s parameter.

Five constitutive models were selected to model the data in this experimental program, including, two equation-of-state models and three state-of-the-art ISV models. The Johnson/Cook model (Johnson and Cook, 1983 and Johnson *et al.*, 1983) and the Zerilli-Armstrong (Zerilli and Armstrong, 1987) model are empirical models designed for ease of computational implementation (Johnson, 1988). The Mechanical Threshold Stress (MTS) model (Klepaczko and Chiem, 1986), the Bammann, Chiesa, and Johnson (BCJ-SNL) model (Bammann *et al.*, 1990) and the McDowell (MCD) model (McDowell, 1992) were selected as ISV models possessing one, two, and multiple ISVs, respectively. The uniaxial form for each model is presented here. The temperature dependent shear modulus is given by

$$\mu = \mu_0 [1 - 0.00038(T - T_0)] \quad (V.7)$$

where μ_0 is the reference elastic shear modulus corresponding to the reference temperature, T_0 , and T is measured in °C (Bammann, 1988). Table V.1 compares the resulting elastic shear modulus values to a form proposed by Follansbee and Gray, 1991 given by

$$\mu = 1000 \left[47.093 - (0.1429 + 0.0002763 T^2)^{\frac{1}{2}} \right] \quad (\text{V.8})$$

where T is measured in Kelvin.

Table V.1 ELASTIC SHEAR MODULUS

Temperature (°C)	Bammann	Follansbee & Gray
25	42000	42130
269	38110	38080
405	35940	35820
541	33460	33560
691	31370	31070

V.3.1 Johnson and Cook Model

A well-characterized equation of state model was developed by Johnson and Cook (1983). The Johnson and Cook (1983) equation of state model has enjoyed much success due to its simplicity and the availability of parameters for various materials of interest. The uniaxial flow stress is given by

$$\sigma = (\sigma_0 + B \varepsilon^n) \left(1 + C \ln \frac{\dot{\varepsilon}}{\dot{\varepsilon}_0} \right) \left(1 - \left[\frac{T - T_r}{T_m - T_r} \right]^m \right) \quad (V.9)$$

where σ and ε are the true stress and true strain respectively. The first term provides for the dependence on strain, the second represents instantaneous strain rate sensitivity, and the last term represents the temperature-dependence of flow stress. The temperature term allows for the reduction in strength corresponding to the increase in temperature resulting from plastic work. This model contains a semi-logarithmic dependence of stress on strain rate. The yield stress is σ_0 , C is the slope of logarithmic strain versus stress, and m is related to the temperature dependence. This approach does not represent any thermal or strain rate history effects, but is simple to implement and the parameters are readily obtained from a limited number of experiments (Johnson, 1988). While this model is purely empirical, it is a widely used constitutive model (cf. Meyers, 1994). For purposes here, it provides a comparative basis between a history independent model and history dependent ISV constitutive models. The model is fully plastic, with no distinction of plastic strain and total strain.

V.3.2 Zerilli-Armstrong Model

The Zerilli-Armstrong model (Zerilli and Armstrong, 1987) is another empirical model which, like the Johnson-Cook model, has been successfully used, particularly for high

strain rate applications. This model has a physical basis linked to thermally activated dislocation motion (Andrade, *et al.*, 1994). This model was developed to be simple and easy to use for large scale predictive computations (Gray, *et al.*, 1994). Goldthorpe (1991) modified the Zerilli-Armstrong model (MZA) to include temperature dependence through the shear modulus. The resulting model for f.c.c. metals is given by

$$\sigma = C_0 + C_2 \varepsilon^n \exp\left(-C_3 T + C_4 T \ln \dot{\varepsilon}\right) \frac{\mu(T)}{\mu_{293}} \quad (\text{V.10})$$

where the temperature dependence for copper is given by

$$\frac{\mu(T)}{\mu_{293}} = 1.0842 - \frac{0.08634}{\exp\left(\frac{208}{T}\right) - 1} \quad (\text{V.11})$$

The first term, C_0 , is related to the average grain diameter and the athermal stress component of the initial material microstructure,

$$C_0 = \frac{k}{\sqrt{d}} + \sigma_a \quad (\text{V.12})$$

where k is the Hall-Petch strengthening parameter and σ_a is an athermal stress component. The next term, C_2 , provides the stress dependence on strain, while, C_3 and C_4 , represent the instantaneous strain rate sensitivity and the temperature-dependence of flow stress. This approach does not represent any thermal or strain rate history effects.

V.3.3 Mechanical Threshold Stress Model

The addition of history dependent parameters is necessary to represent material behavior. These parameters represent the current state of the material, which includes strain rate and temperature history effects as well as the coupling of rate- and temperature-dependence with material hardening. Klepaczko and Chiem (1986), Follansbee and Kocks (1988), and Klepaczko (1988) developed the MTS model which consists of a description of the material behavior at constant structure and a description of structure evolution during deformation. They attempted to establish a direct relation between dislocation behavior and macroscopic behavior. A reference threshold stress, $\hat{\sigma}$, is employed as the sole ISV representing a measure of the “hardness” of the material at its current dislocation structure. Physically, this variable represents an isotropic resistance to plastic flow which may be related to the dislocation density or dislocation substructure for single-phase, coarse-grained metals.

Deformation in a polycrystal occurs by the accumulation and motion of dislocations with the rate-controlling mechanism being the interaction of dislocations with defects, such as grain boundaries, forest dislocations, solute atoms, etc. The central basis of the MTS

approach is that the instantaneous flow stress depends on the instantaneous condition of the material, as determined by the structural state variable, as well as the strain rate and temperature. The structural state variable is characterized by the flow stress measured at ambient pressure and absolute zero temperature. This quantity, the mechanical threshold stress, is assumed to consist of two components: a thermal component, which is thermally activated, and an athermal component.

$$\hat{\sigma} = \hat{\sigma}_t + \hat{\sigma}_a \quad (\text{V.13})$$

where $\hat{\sigma}_a$, the athermal component, characterizes the rate independent interactions of dislocations with long range barriers such as grain boundaries, and $\hat{\sigma}_t$, the thermal component, characterizes the thermally activated, rate dependent interactions with short range obstacles such as other dislocations. The athermal stress, $\hat{\sigma}_a = \frac{0.278}{\sqrt{d}}$, depends on the

initial average grain size, d (Gourdin and Lassila, 1991). The flow stress is related to the mechanical threshold stress using

$$\sigma = \hat{\sigma}_a + s \hat{\sigma}_t \quad (\text{V.14})$$

where s defines the glide kinetics and is less than unity, since thermal activation energy reduces the stress needed to move dislocations past obstacles. The plastic strain rate is assumed to be controlled by the thermally activated interactions of dislocations with obstacles, e.g. interaction of mobile dislocations with forest dislocations. The thermal activated motion of dislocations over an obstacle is given by

$$\dot{\epsilon}^p = \dot{\epsilon}_0 \exp\left(-\frac{Q}{kT}\right) \quad (V.15)$$

where the constant $\dot{\epsilon}_0$ is limited to values $10^7 \leq \dot{\epsilon}_0 \leq 10^{10} \text{ s}^{-1}$ (Johnson, 1988). Here, Q is a modified activation energy which depends on both the applied stress and the current structure, and k is the Boltzmann constant. An empirical expression for Q is used which describes the statistically averaged shape of the obstacle profile

$$Q = Q_0 \left[1 - \left(\frac{\sigma_t}{\hat{\sigma}_t} \right)^p \right]^q \quad (V.16)$$

The constants p and q , which define the statistically averaged obstacle profile, are restricted to $0 \leq p \leq 1$ and $1 \leq q \leq 2$ (Kocks et al., 1975), and $Q_0 = g_0 \mu b^3$ is the activation energy,

assumed to remain constant and controlled by the short range obstacle kinetics. The thermal portion of the applied stress, σ_t , characterizes the rate dependent interactions with short range obstacles. The activation energy is determined using g_0 , a normalized activation energy; μ , the shear modulus; and b , Burger's vector. Combining Equations V.11 - V.14 results in the flow equation

$$\sigma = \hat{\sigma}_a + (\hat{\sigma} - \hat{\sigma}_a) \left(1 - \left[\frac{kT \ln \left(\frac{\dot{\epsilon}_0}{\dot{\epsilon}^p} \right) \right]^{\frac{1}{q}} \right)^{\frac{1}{p}} \quad (V.17)$$

The effect of the constants, p and q , and temperature on the activation energy is shown parametrically in Fig. V.4. For every 0.1 increment in p from 0 to 1.0, q is incremented by 0.1 from 1.0 to 2.0. Additionally, the temperature is incremented from 275°C to 350°C. The activation energy is reduced by the resulting value plotted in the figure.

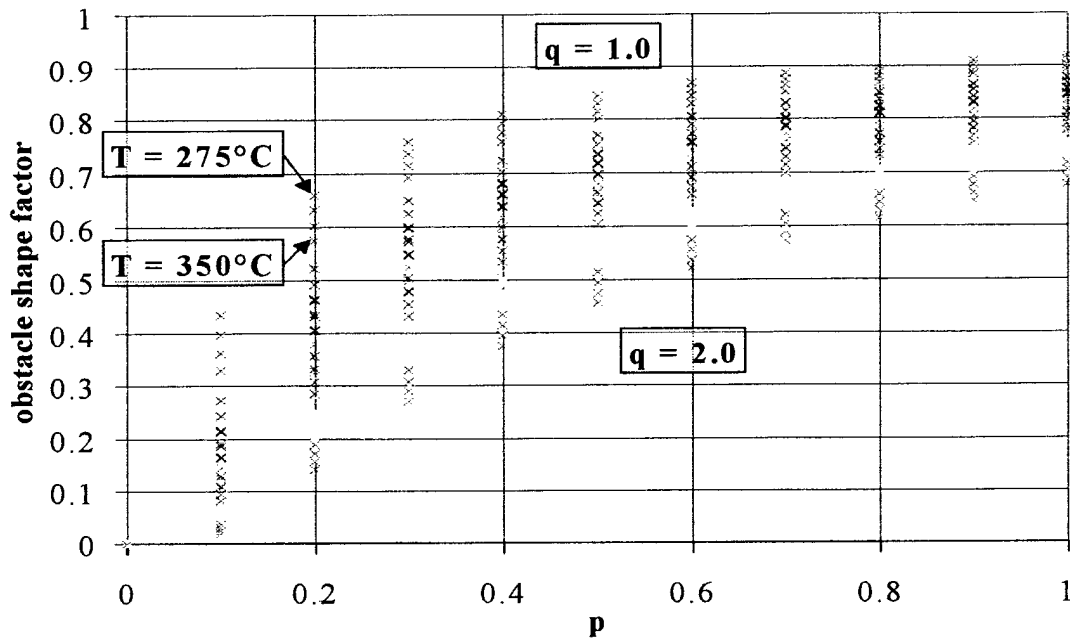


Figure V.4: Effect of temperature and variations in p and q on activation energy for the MTS model.

Evolution of microstructure is considered to be a balance between dislocation accumulation and dynamic recovery processes. Dynamic recovery processes occur by dislocation cross slip which is both thermally activated and stress assisted. The form chosen for the evolution of the mechanical threshold stress is

$$\Theta = \frac{d\hat{\sigma}}{d\varepsilon^p} = \Theta_0 \left[1 - \frac{\tanh\left(2 \frac{\hat{\sigma} - \hat{\sigma}_a}{\hat{\sigma}_s - \hat{\sigma}_a}\right)}{\tanh(2)} \right] \quad (\text{V.18})$$

which reflects the best fit to experimental data. The saturation threshold stress is $\hat{\sigma}_s$ and determines the stress level resulting in zero strain hardening. The differential evolution equation for $\hat{\sigma}$ incorporates work hardening and dynamic recovery, but does not include either static thermal recovery or dynamic recrystallization effects. The hyperbolic tangent form for the evolution equation was chosen to approximate the Voce law such that the strain hardening rate decreases with increasing strain and approaches saturation due to dynamic recovery. As dislocations move through the crystal, they become immobilized after traveling a distance proportional to the average saturation distance between dislocations.

The initial strain hardening rate, is observed to exhibit a dependence on strain rate which is due to dislocation accumulation. The initial strain hardening rate increases with increasing strain rate. The following relationship is an empirical fit to experimental data from OFHC Cu which suggests that the origin of the increased rate sensitivity of the flow stress at very high strain rates is a rapidly increasing dislocation accumulation rate:

$$\Theta_0 = C_1 + C_2 \ln(\dot{\varepsilon}) + C_3 \dot{\varepsilon} \quad (\text{V.19})$$

Gourdin and Lassila (1991) obtained the values: $C_1 = 2150$, $C_2 = 0$ and $C_3 = 0.034$ calculated from a curve fit to data for OFHC with a similar initial grain size to that used in this thesis. Assuming the activation energy depends logarithmically on stress, which is similar to the relation derived for cross slip by Schoeck and Seeger (Gottstein, et al., 1991), temperature and strain rate dependencies are incorporated through $\hat{\sigma}_s$, the saturation threshold stress, i.e.

$$\ln \left(\frac{\dot{\epsilon}}{\dot{\epsilon}_{s0}} \right) = \frac{\mu b^3 A}{kT} \ln \left(\frac{\hat{\sigma}_s}{\hat{\sigma}_{s0}} \right) \quad (\text{V.20})$$

where $\dot{\epsilon}_{s0}$, A , and $\hat{\sigma}_{s0}$ are constants. The flow rule for the uniaxial case is given by

$$\dot{\epsilon}^p = \dot{\epsilon}_0 \exp \left[\frac{\mu b^3 g_0}{kT} \left(1 - \left[\frac{|\sigma| - \hat{\sigma}_a}{\hat{\sigma} - \hat{\sigma}_a} \right]^p \right)^q \right] \text{sgn}(\sigma) \quad (\text{V.21})$$

and the ISV evolution equation is determined using Equation V.18. The eight resulting parameters are used to describe the behavior of a material, (g_0 , p , q , $\frac{k}{b^3}$, A , $\dot{\epsilon}_0$, $\dot{\epsilon}_{s0}$, and $\hat{\sigma}_{s0}$).

V.3.4 Bammann, Chiesa and Johnson Model

Bammann, Chiesa, and Johnson, 1990, Bammann, 1990, and Bammann *et al.*, 1990, developed the BCJ-SNL ISV constitutive model to correlate the large deformation behavior of metals. Two ISV's (a tensor kinematic hardening variable, α , and a scalar isotropic hardening variable, κ) account for the evolution of the yield surface with plastic deformation. The elastic behavior is assumed to be linear and isotropic. The flow rule and evolution equations for the uniaxial case are given by:

$$\dot{\epsilon}^p = f \sinh \left[\frac{\langle |\sigma - \alpha| - \kappa - Y \rangle}{V} \right] \text{sgn}(\sigma - \alpha) \quad (\text{V.22})$$

$$\dot{\alpha} = h \mu \dot{\epsilon}^p - \left[r_s + r_d |\dot{\epsilon}^p| \right] \alpha^2 \text{sgn}(\alpha) \quad (\text{V.23})$$

$$\dot{\kappa} = H \mu |\dot{\epsilon}^p| - \left[R_s + R_d |\dot{\epsilon}^p| \right] \kappa^2 \quad (\text{V.24})$$

where each of the parameters f , Y , V , r_d , r_s , R_d , and R_s potentially have an independent temperature dependence of the form

$$C_i \exp\left(\frac{C_j}{T}\right). \quad (\text{V.25})$$

Here, the parameters h , r_d and r_s , respectively, describe the hardening, dynamic and static recovery of the tensor or kinematic variable. Parameters H , R_d , and R_s , respectively, describe the hardening, dynamic, and static recovery of the scalar or isotropic variable. Parameters f , Y , and V specify the yield stress, and μ is the temperature dependent shear modulus. The evolutionary equations have the form of a hardening term minus effects of both dynamic recovery and static thermal recovery. The hardening term is analogous to that proposed by Prager (1955) and represents the increase in flow resistance due to dislocation density increase with plastic deformation. The dynamic recovery term represents dislocation annihilation, cross-slip, and organization into low energy structures. Note that complete recovery of state is indicated in Equations (V.22) and (V.23). Numerous ISV relations have been proposed analogous to this form (cf. Chaboche, 1989).

V.3.5 McDowell Model

The McDowell model was formulated to have more flexibility to address strain rate and temperature history dependence. The model admits multiple internal variables α_i , and χ_j , where α and χ are kinematic variables and isotropic auxiliary variables, respectively. The isotropic term accounts for transients resulting from long range obstacles while the kinematic variable evolves more rapidly. The flow law is given by

$$\dot{\epsilon}^p = \Theta \left(\sinh \left[B_0 \left(\frac{\Sigma_v}{D} \right)^{n_1} \right] \right)^{n_2} \text{sign}(\sigma - \alpha) \quad (\text{V.26})$$

where the viscous stress, Σ_v , is partitioned between the overstress and the isotropic hardening amplitudes (McDowell and Moosbrugger, 1987; Moosbrugger and McDowell, 1990; and McDowell, 1992). The viscous stress is given by

$$\Sigma_v = \left\langle \sqrt{\frac{3}{2}} |\sigma - \alpha| - R \right\rangle + R - \sqrt{\frac{3}{2}} \chi^0(T) - R_2 \quad (\text{V.27})$$

which is partitioned by η , the viscosity partitioning factor, between the viscous stress and the isotropic hardening, and is given by

$$\eta \Sigma_v = R - \sqrt{\frac{3}{2} \chi^0(T) - R_2} \quad (\text{V.28})$$

The viscosity partitioning factor is limited to values $0 \leq \eta < 1$. Combining Equations V.26 and V.28 results in

$$\Sigma_v = \frac{\left\langle \sqrt{\frac{3}{2}} |\sigma - \alpha| - R \right\rangle}{1 - \eta} \quad (\text{V.29})$$

where the Macauley brackets, $\langle \psi \rangle$, denote the function $\langle \psi \rangle = 0$ when $\psi < 0$, and $\langle \psi \rangle = \psi$ when $\psi \geq 0$. The drag stress, D , is given by

$$D = D_1 \left[\sqrt{\frac{3}{2} \chi^0(T) + R_{\text{iso}}} \right] + D_2 \quad (\text{V.30})$$

and Θ , the diffusivity parameter, accounts for an Arrhenius temperature dependence (Miller, 1975; Freed, 1988) given by

$$\Theta = \begin{cases} \exp\left(-\frac{Q}{kT}\right) & T > \frac{T_m}{2} \\ \exp\left[-\frac{2Q}{kT_m}\left(\ln\left(\frac{T_m}{2T}\right) + 1\right)\right] & T \leq \frac{T_m}{2} \end{cases} \quad (\text{V.31})$$

The diffusivity parameter varies with temperature and activation energy (Fig. V.5).

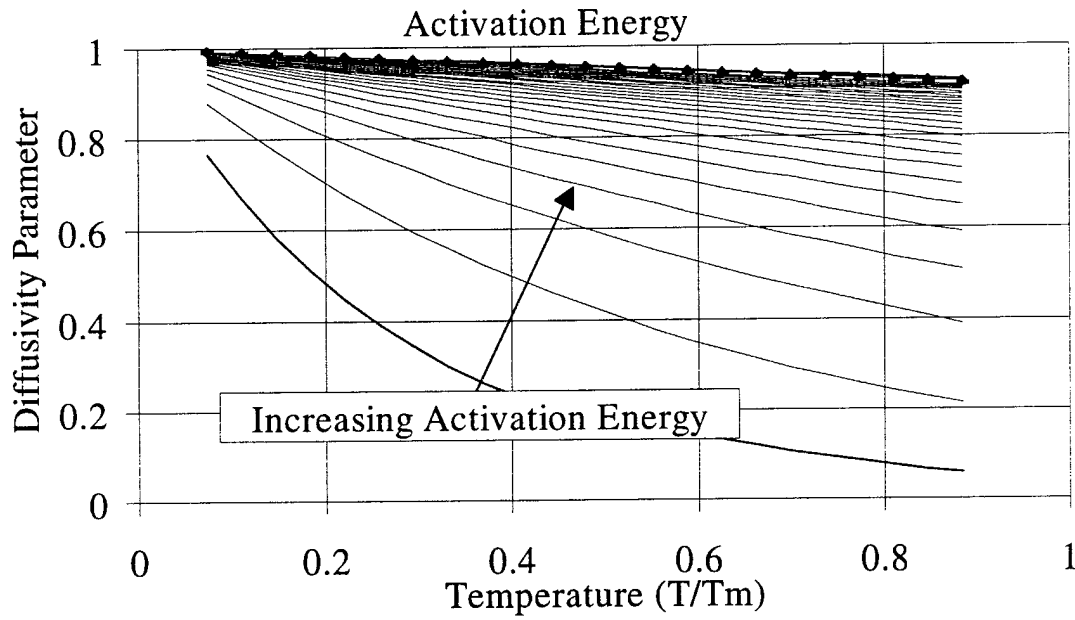


Figure V.5: Variation in diffusivity parameter with temperature and activation energy variations.

The yield surface radius, R , is composed of terms related to each isotropic variable. Two variables are considered to account for a categorization of obstacles into rapidly evolving short range and slowly evolving long range. The yield surface radius is given by

$$R = R_1 + R_2 \quad (V.32)$$

where R_1 depends only on the isotropic hardening

$$R_1 = \sqrt{\frac{3}{2}} \chi_1 = R_1^{\text{iso}} \quad (\text{V.33})$$

and R_2 is composed of an isotropic hardening independent component, which only depends on temperature, not on dislocation density or arrangement, and a component which is dependent on the degree of isotropic hardening.

$$R_2 = \sqrt{\frac{3}{2}} \chi^0(T) + R_2^{\text{iso}} \quad (\text{V.34})$$

The isotropic dependent term, R^{iso} , has two components given by

$$R^{\text{iso}} = R_1^{\text{iso}} + R_2^{\text{iso}} = \sqrt{\frac{3}{2}} \chi_1 + \sqrt{\frac{3}{2}} \chi_2 \quad (\text{V.35})$$

The evolution equations for the ISV's are given by a hardening minus recovery format, both dynamic and static, and a temperature rate term. The isotropic evolution form is given by

$$\dot{\chi}_i = \mu_{\chi_i} [\bar{\chi}_i - \chi_i] |\dot{\epsilon}^p| + \frac{\chi_i}{\mu_{\chi_i} \bar{\chi}_i} \frac{\partial(\mu_{\chi_i} \bar{\chi}_i)}{\partial T} \dot{T} - \mu_{\chi_i} \bar{\chi}_i (\chi_i)^{L_{\chi_i}} \psi_{\chi} \exp\left(-\frac{\Delta Q_{\chi}}{kT}\right) \quad (V.36)$$

for isotropic hardening variables, $i = 1, 2$. The first term includes hardening and dynamic recovery. The evolution rates for hardening are determined by the constants, μ_{χ_i} , and the saturation levels for χ_i are given by the coupling of the rate term and the constants, $\bar{\chi}_i$, which are given by

$$\bar{\chi}_2 = \chi^0(T) + \sqrt{\frac{2}{3}} \eta \Sigma_v \quad (V.37)$$

$$\bar{\chi}_1 = \hat{\chi}_1 \Sigma(T) \quad (V.38)$$

where $\hat{\chi}_1$ is a constant. Each isotropic saturation parameter has a temperature dependence with $\bar{\chi}_2$ also depending on the viscous stress. The temperature dependencies are given by

Equations V.39 and V.40. The second term in the evolution equation, Equation V.36, incorporates the changes in microstructure due to temperature changes. The last term is the static thermal recovery term, where ΔQ_χ is the activation energy and ψ_χ is a constant which provides a multiplicative factor to the thermal activation term. The exponential on χ_i , L_{χ_i} , is a constant. The temperature dependence for χ has two options, which will be evaluated in the next chapter, and are given by

$$\chi^0(T) = \begin{cases} [B_1 - B_2 T + B_3 \exp(-B_4 T)] \\ \text{or} \\ [B_1 - B_2 \tanh(B_3 (T - B_4))] \end{cases} \quad (V.39)$$

and

$$\Sigma(T) = \begin{cases} [A_1 - A_2 T + A_3 \exp(-A_4 T)] \\ \text{or} \\ [A_1 - A_2 \tanh(A_3 (T - A_4))] \end{cases} \quad (V.40)$$

The kinematic variable evolution has a form similar to that of the isotropic variables and is given by

$$\dot{\alpha} = C[v\mu \text{sign}(\sigma - \alpha) - \alpha]|\dot{\epsilon}^p| + \frac{\alpha}{Cv\mu} \frac{\partial(Cv\mu)}{\partial T} \dot{T} - Cv\mu |\alpha|^{L_\alpha} \psi_\alpha \exp\left(-\frac{\Delta Q_\alpha}{kT}\right) \quad (\text{V.41})$$

where the rate of evolution is determined by the constant C , while the saturation level is obtained through the coupling of the shear modulus and the two constants, C and v . The constants L_α , ψ_α , and ΔQ_α have similar functions as for the isotropic evolution equations. Different material responses are predicted with a variation on the relative magnitudes on the values for the rate and saturation amplitudes for χ_i and α . The possible combinations on rate of evolution and saturation of the ISV's are explored in Chapter VI.

V.4 Correlation to Experiment Data and Sequence Predictions

Constitutive models typically have more ability to extrapolate to conditions not included in the parameter determination process when there are closer linkages between the function forms and parameters in the model and to physical deformation processes involved. The complexity and difficulty of determining multiple parameters have limited the utility of these more complex models in the past, until the recent improvements in computational capabilities. The optimization routine described in Section V.2 was extremely powerful in obtaining the optimized correlations between the model predictions and the experiment data. This section describes the results from the optimization of the parameters for each model using the same five isothermal and constant true strain rate data: 25°C and 0.0004 s⁻¹; 25°C

and 6000 s^{-1} ; 269°C and 0.0004 s^{-1} ; 269°C and 0.1 s^{-1} ; and 269°C and 5200 s^{-1} . This set of experimental isothermal, constant true strain rate data were selected for the optimization process since they span the range of sequence data predictions used for model evaluation. Following the correlation to these data, the models were used to predict six different sequence experiments: 1) strain rate sequences of 269°C and 0.0004 s^{-1} followed by 269°C and 0.1 s^{-1} and 25°C and 6000 s^{-1} followed by 25°C and 0.0004 s^{-1} ; 2) temperature sequences of 25°C and 0.0004 s^{-1} followed by 269°C and 0.0004 s^{-1} and 269°C and 0.0004 s^{-1} followed by 25°C and 0.0004 s^{-1} ; and 3) combinations of strain rate and temperature sequences of 25°C and 6000 s^{-1} followed by 269°C and 0.0004 s^{-1} and 269°C and 5200 s^{-1} followed by 25°C and 0.0004 s^{-1} .

V.4.1 Johnson/Cook Model

V.4.1.1 Johnson/Cook Model Correlation to Experimental Data

The Johnson/Cook model has five parameters (σ_0 , B, C, n, and m) which were determined using data for large strain, isothermal, constant true strain rate compression experiments, resulting in the correlation shown in Fig. V.6. Temperature and strain rate dependence were predicted, but not the actual strain hardening or dynamic softening. The optimized parameter values are shown in Table V.2, and compared to other parameter sets calculated for OFHC Cu using traditional graphical procedures.

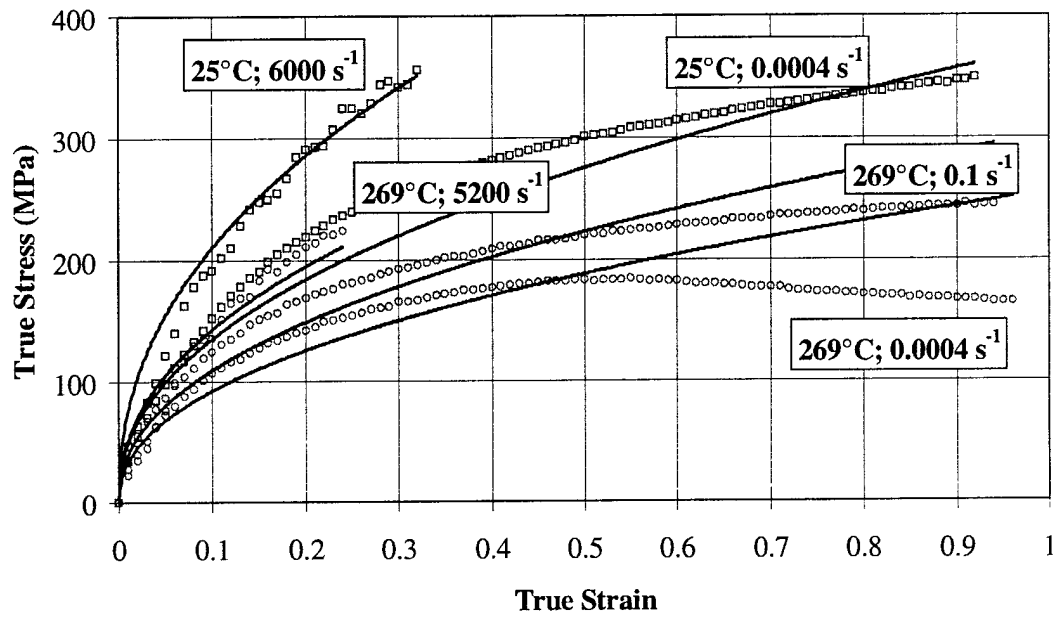


Figure V.6: Correlation to OFHC Cu data using Johnson/Cook model. The model correlations are shown using solid lines, while the experimental data are shown with open symbols.

Table V.2: JOHNSON/COOK MODEL PARAMETER COMPARISON FOR OFHC CU

Parameter	(Johnson and Cook, 1983)	(Andrade, <i>et al.</i> , 1994)	Optimized
Deformation Conditions	10^3 to 10^5 s ⁻¹		4×10^{-4} to 6×10^3 s ⁻¹ 25 to 269°C 62 μ m
σ_0 (MPa)	90	225	0
B (MPa)	292	178	470
C	0.025	0.027	0.027
n	0.31	0.67	0.44
m	1.09	0.97	0.78

V.4.1.2 Johnson/Cook Model Predictions

Predictions are calculated using the optimized parameters for the Johnson/Cook model for compression tests involving strain rate sequences (Figs. V.7 and V.8), temperature sequences (Figs. V.9 and V.10), and for combined strain rate and temperature sequences (Figs. V.11 and V.12). The solid lines represent the model prediction, while symbols represent experimental data. The Johnson/Cook model does not predict any history effects. During the predicted sequences, the flow stress changes instantaneously from the flow stress associated with the initial set of conditions to that associated with the next. No transition behavior is predicted.

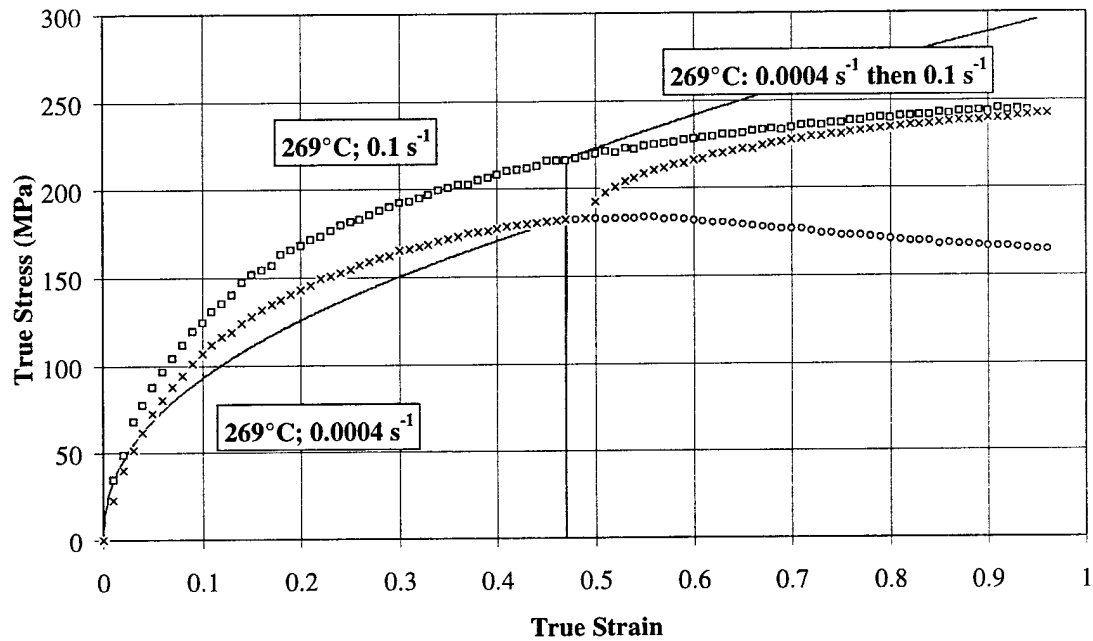


Figure V.7: Strain rate sequence prediction for OFHC Cu using the Johnson/Cook model. Solid lines represent the model prediction, while symbols represent data.

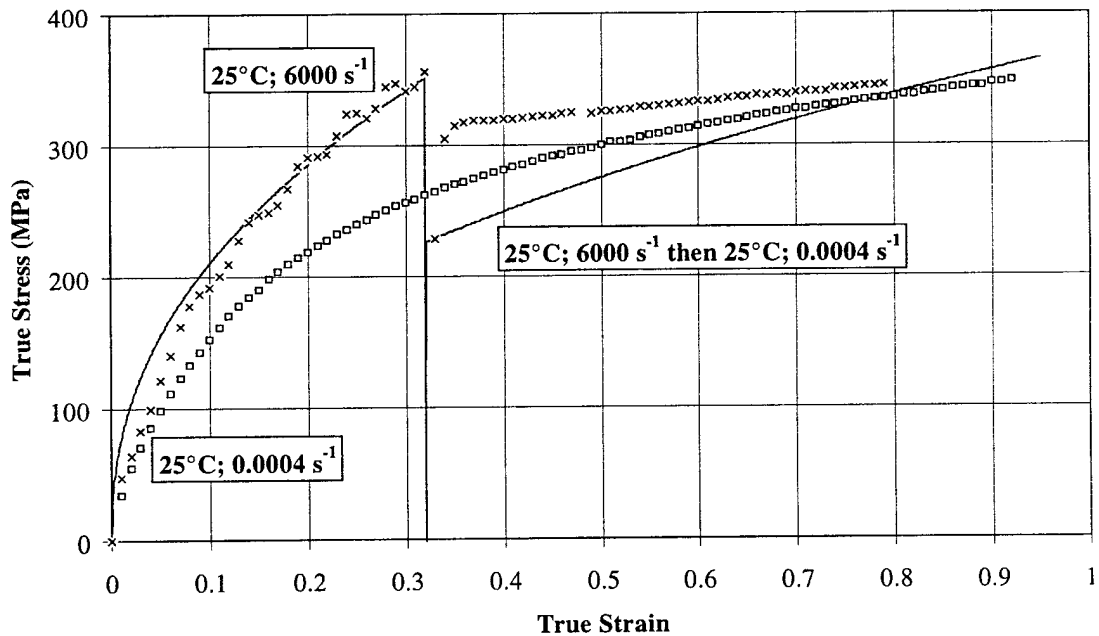


Figure V.8: Strain rate sequence prediction for OFHC Cu using the Johnson/Cook model. Solid lines represent the model prediction, while symbols represent data.

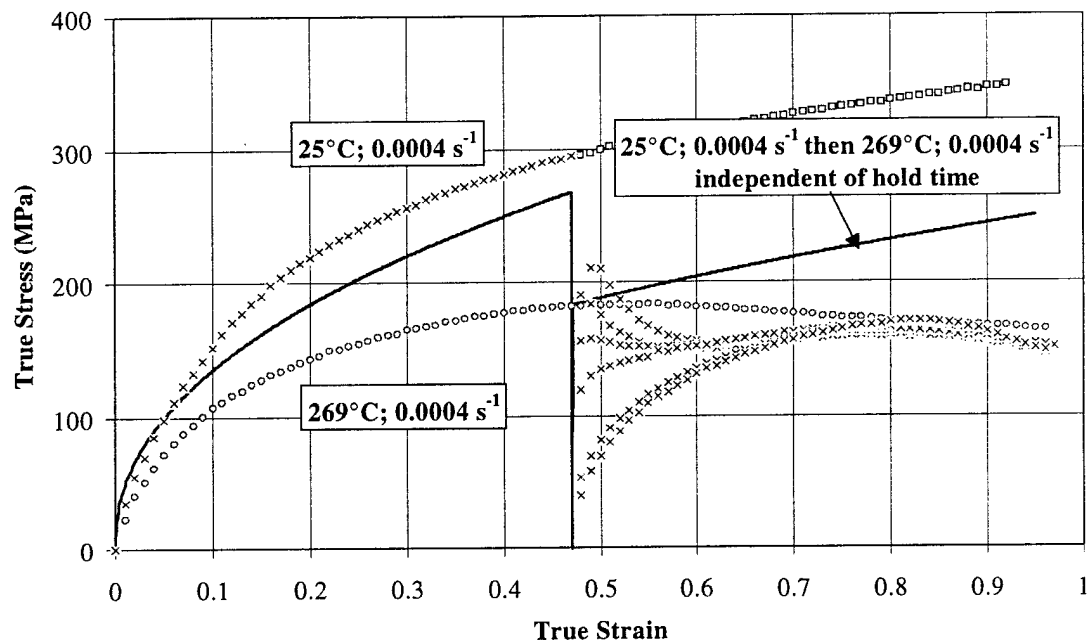


Figure V.9: Temperature sequence prediction for OFHC Cu using the Johnson/Cook model. Solid lines represent the model prediction, while symbols represent data.

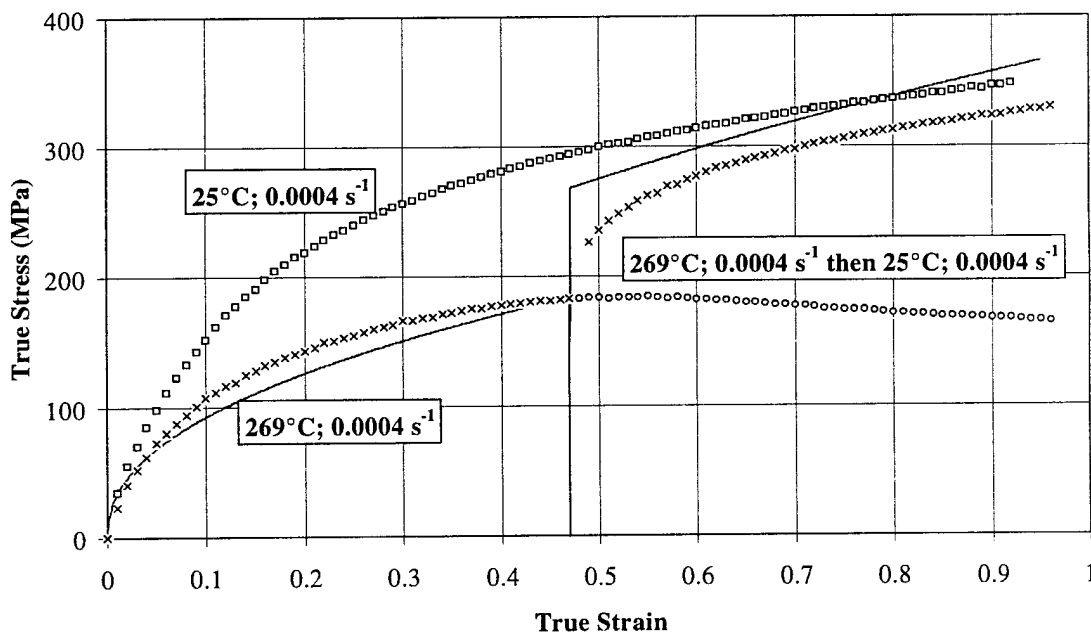


Figure V.10: Temperature sequence prediction for OFHC Cu using the Johnson/Cook model. Solid lines represent the model prediction, while symbols represent data.

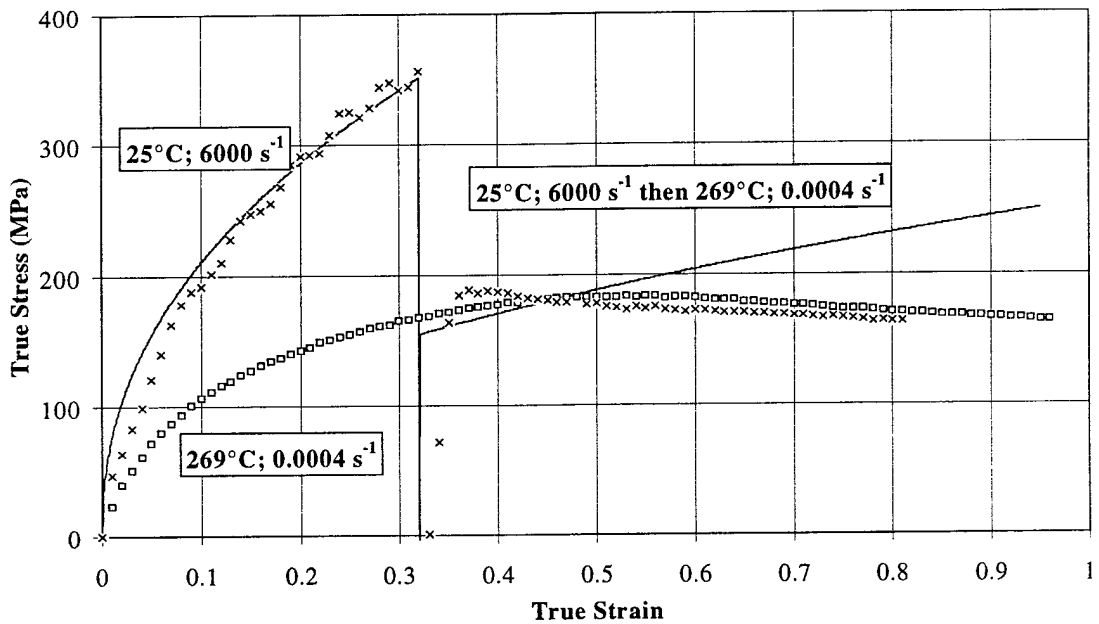


Figure V.11: Strain rate and temperature sequence prediction for OFHC Cu using the Johnson/Cook model. Solid lines represent the model prediction, while symbols represent data.

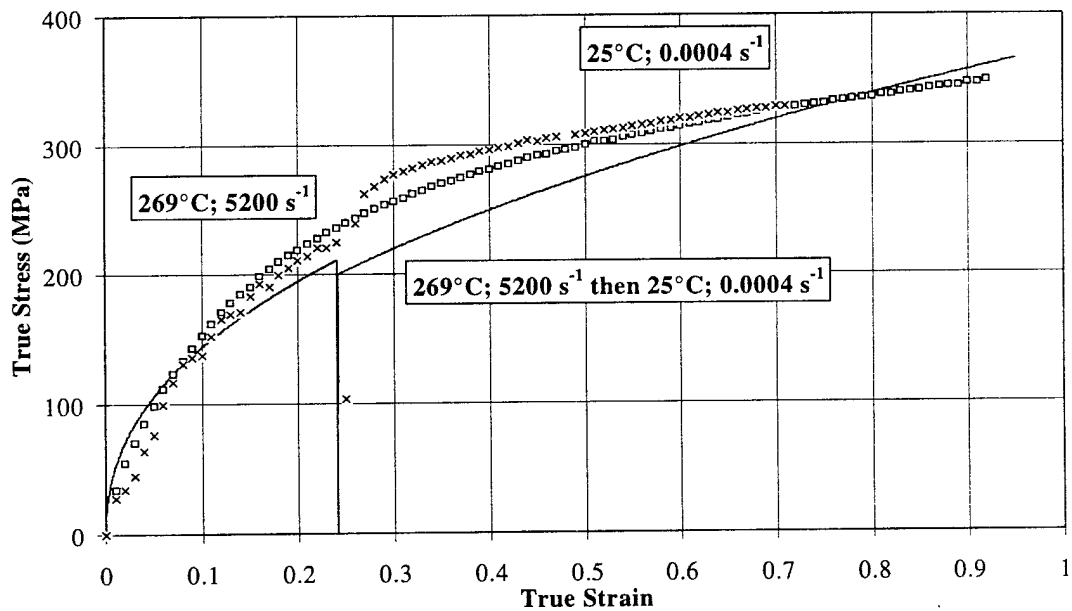


Figure V.12: Strain rate and temperature sequence prediction for OFHC Cu using the Johnson/Cook model. Solid lines represent the model prediction, while symbols represent data.

V.4.1.3 Johnson/Cook Model Parameter Sensitivity

A parameter sensitivity study was completed for the Johnson/Cook model using the optimized values shown in Table V.2. The light and dark bars in Fig. V.13 reflect $\pm 10\%$ offset from the optimized parameter values. The first two bars reflect the ability of the indicated parameter alone to achieve the global minimum while the second two bars show how the well the remaining parameters can reach the minimum with the indicated parameter held constant. This analysis shows that any one of the five parameters can be held constant and the optimized objective function value can still be achieved. The model's performance is most sensitive to the m parameter, which determines the temperature dependence.

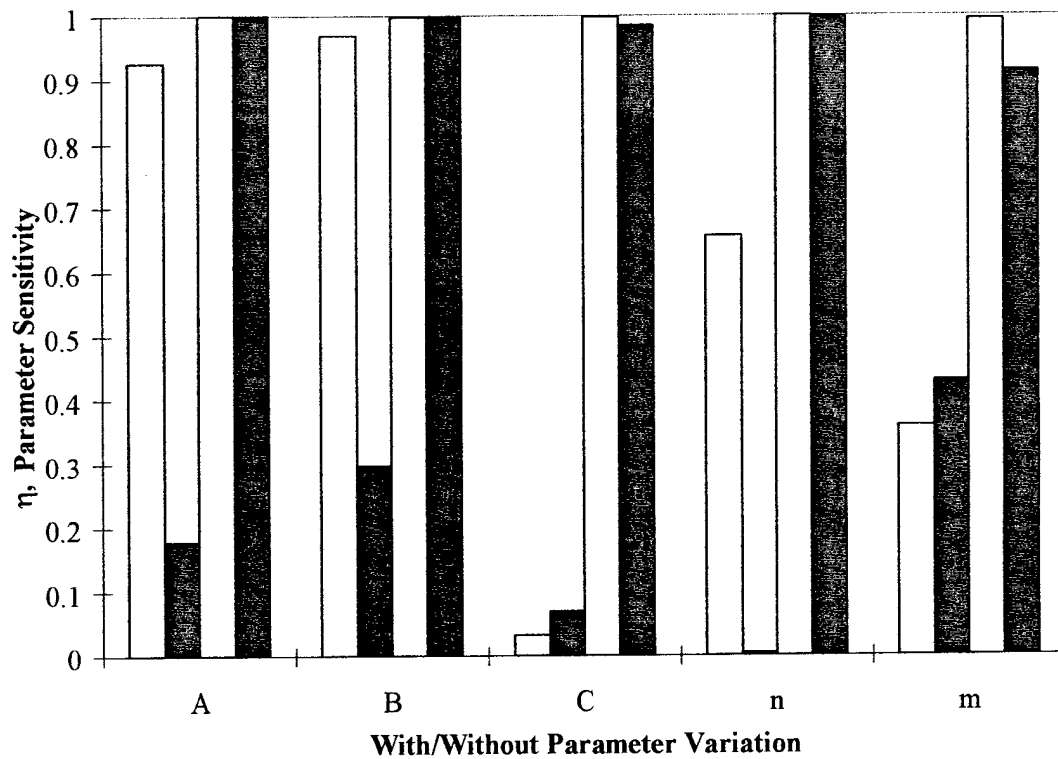


Figure V.13: Parameter sensitivity for OFHC Cu using the Johnson/Cook model. Light and dark bars reflect a $\pm 10\%$ offset from the optimized parameter values corresponding to a minimum of the objective function. First two bars show ability of indicated parameter, alone, to achieve the global minimum while the second two bars show ability of the remaining parameters, with the indicated parameter held constant, to reach the minimum.

V.4.2 Zerilli-Armstrong Model

V.4.2.1 Zerilli-Armstrong Model Correlation to Experimental Data

The Zerilli-Armstrong model has five parameters (C_0 , C_2 , n , C_3 , and C_4) which were determined using data for large strain, isothermal, constant true strain rate compression experiments, resulting in the correlation shown in Fig. V.14. Temperature and strain rate dependence were predicted, but not the actual strain hardening or dynamic softening. The optimized parameter values are shown in Table V.3, and are compared to another parameter set calculated for OFHC Cu.

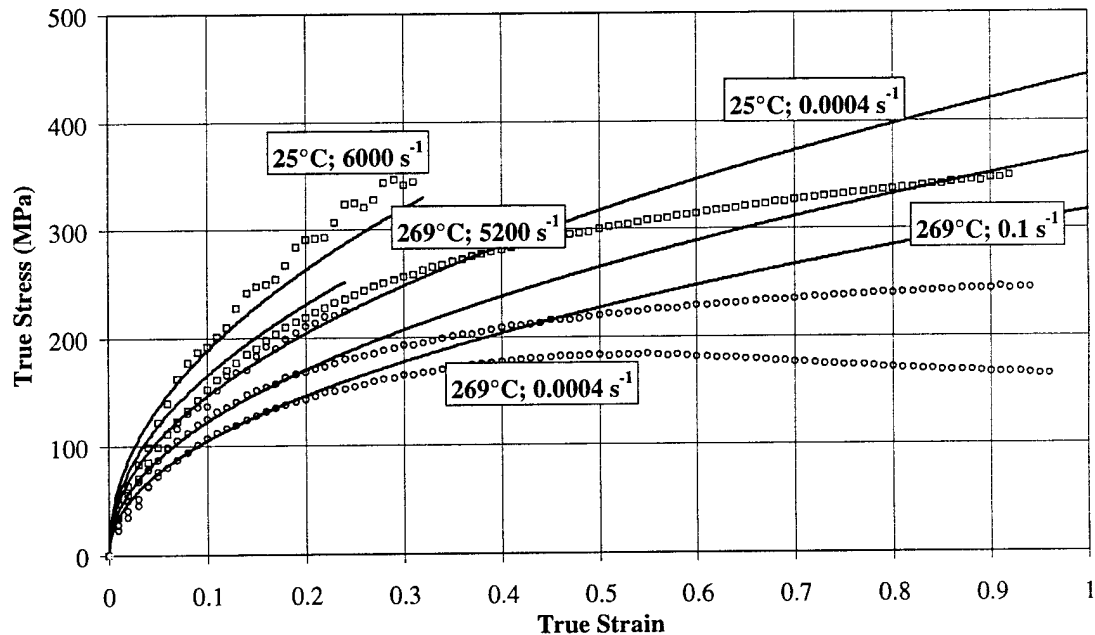


Figure V.14: Correlation to OFHC Cu data using the Zerilli-Armstrong model. The model correlations are shown using solid lines, while the experimental data are shown with open symbols.

Table V.3: ZERILLI-ARMSTRONG MODEL PARAMETER COMPARISON FOR OFHC CU

Parameter	Gray, et al. (1994)	Optimized
Deformation Conditions	2000 s ⁻¹ 25 to 800°C 50 μm	4x10 ⁻⁴ to 6x10 ³ s ⁻¹ 25 to 269°C 62 μm
C ₀ , [MPa]	8	0
C ₂ , [MPa]	1200	605
n	0.7	0.44
C ₃	.0005	.0009
C ₄	.000005	.00005

V.4.2.2 Zerilli-Armstrong Model Sequence Predictions

Predictions were calculated using the optimized parameters (Table V.3) for the Zerilli-Armstrong model for compression tests involving strain rate sequences (Figs. V.15 and V.16), temperature sequences (Figs. V.17 and V.18), and for combined strain rate and temperature sequences (Figs. V.19 and V.20). The solid lines represent the model prediction, while symbols represent experimental data. The Zerilli-Armstrong model does not predict any history effects. During the predicted sequences, the flow stress changes instantaneously from the flow stress associated with the initial set of conditions to that associated with the next. No transition behavior is predicted.

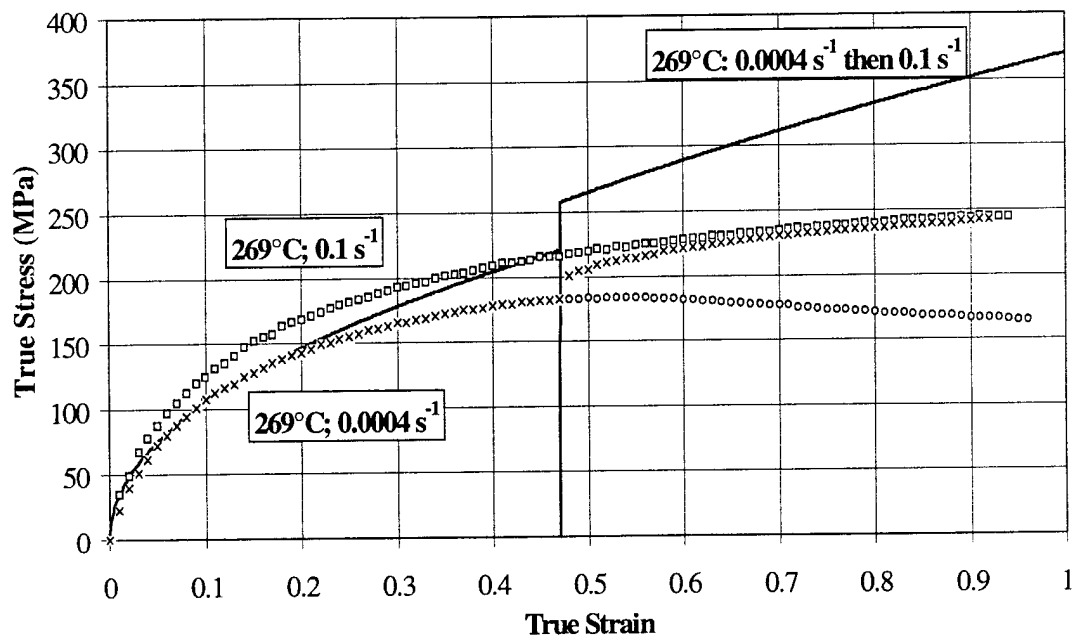


Figure V.15: Strain rate sequence prediction for OFHC Cu using the Zerilli-Armstrong model. Solid lines represent the model prediction, while symbols represent experimental data.

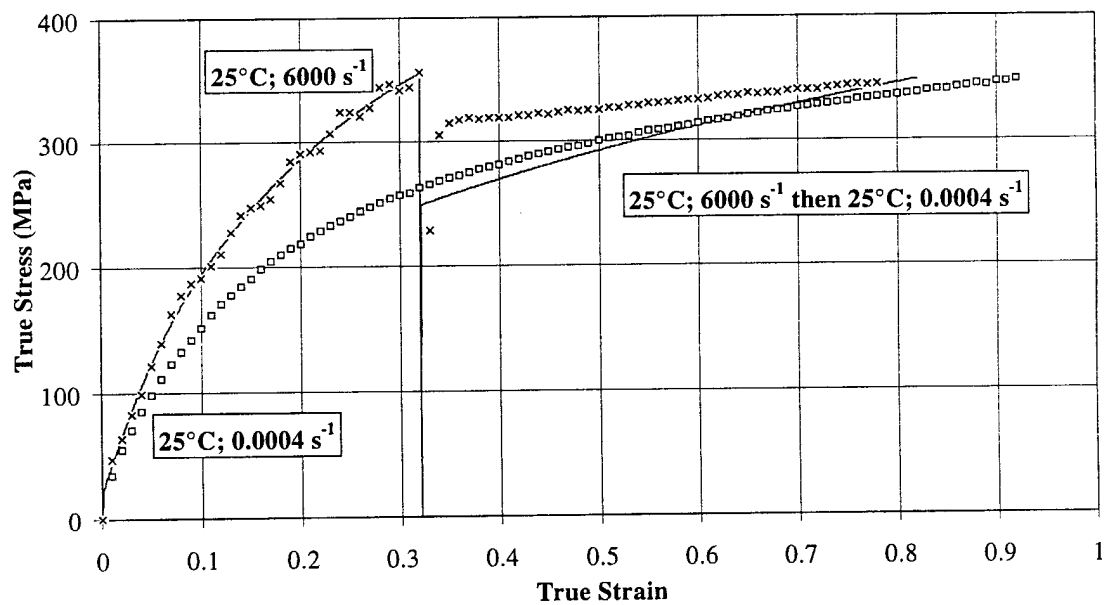


Figure V.16: Strain rate sequence prediction for OFHC Cu using the Zerilli-Armstrong model. Solid lines represent the model prediction, while symbols represent experimental data.

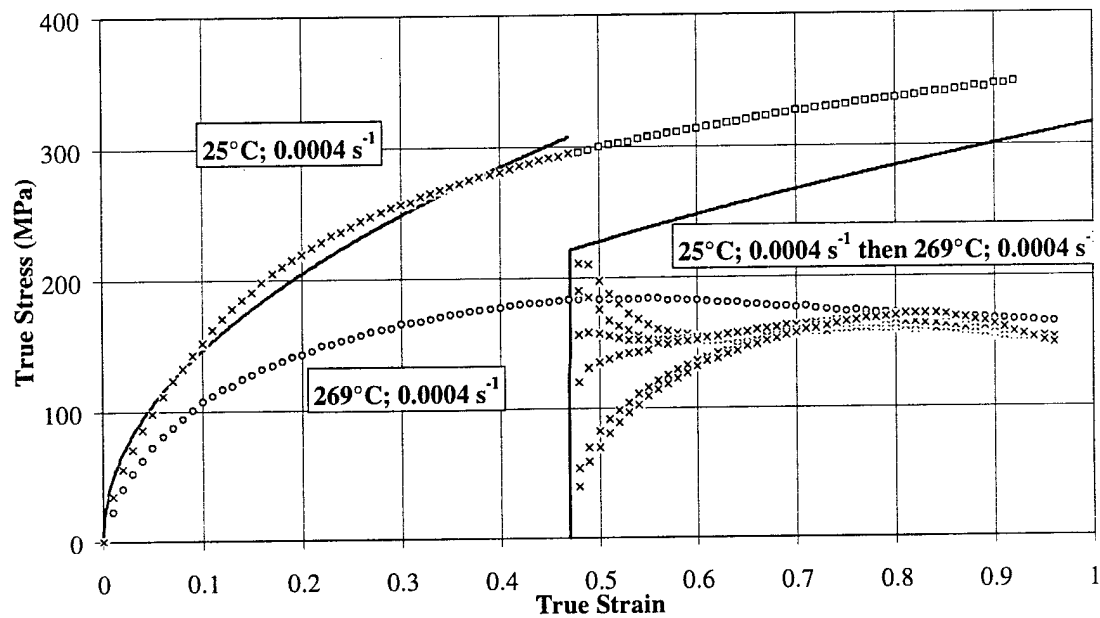


Figure V.17: Temperature sequence prediction for OFHC Cu using the Zerilli-Armstrong model. Solid lines represent the model prediction, while symbols represent experimental data.

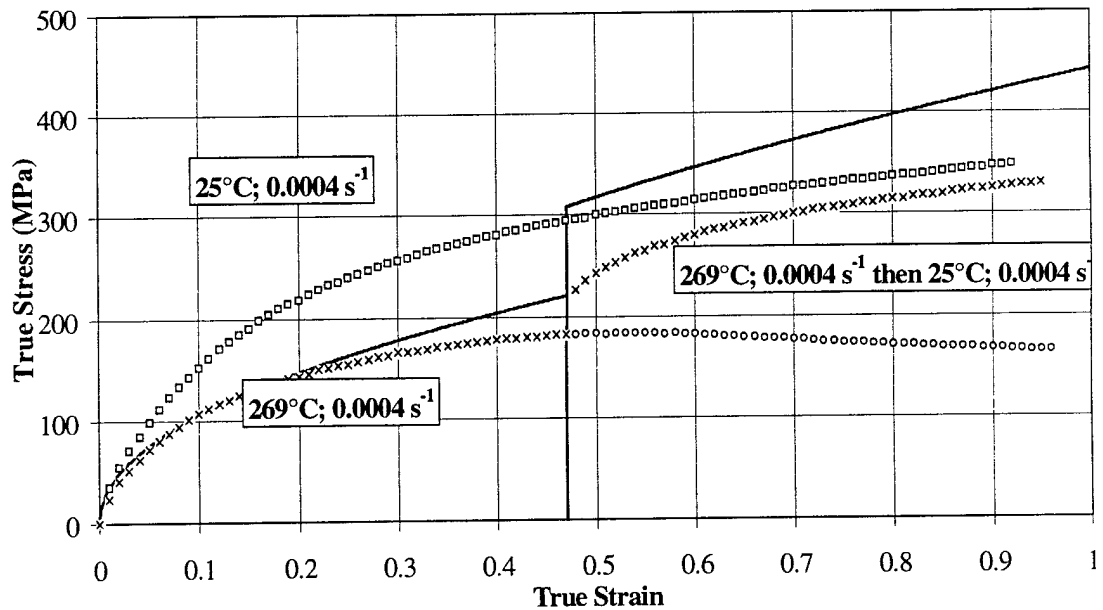


Figure V.18: Temperature sequence prediction for OFHC Cu using the Zerilli-Armstrong model. Solid lines represent the model prediction, while symbols represent experimental data.

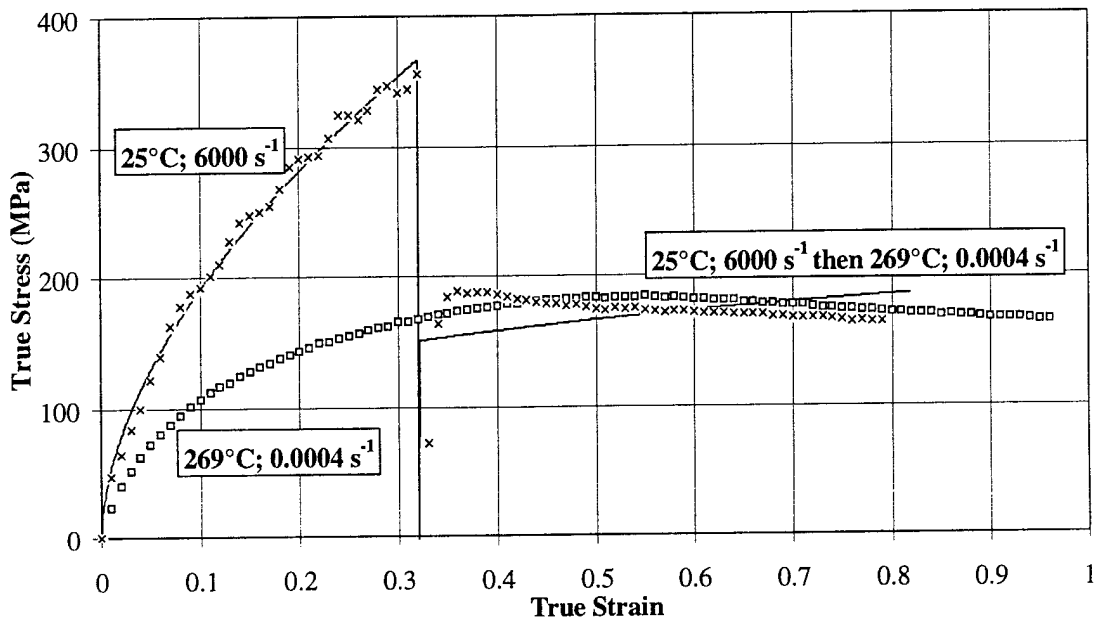


Figure V.19: Strain rate and temperature sequence prediction for OFHC Cu using the Zerilli-Armstrong model. Solid lines represent the model prediction, while symbols represent experimental data.

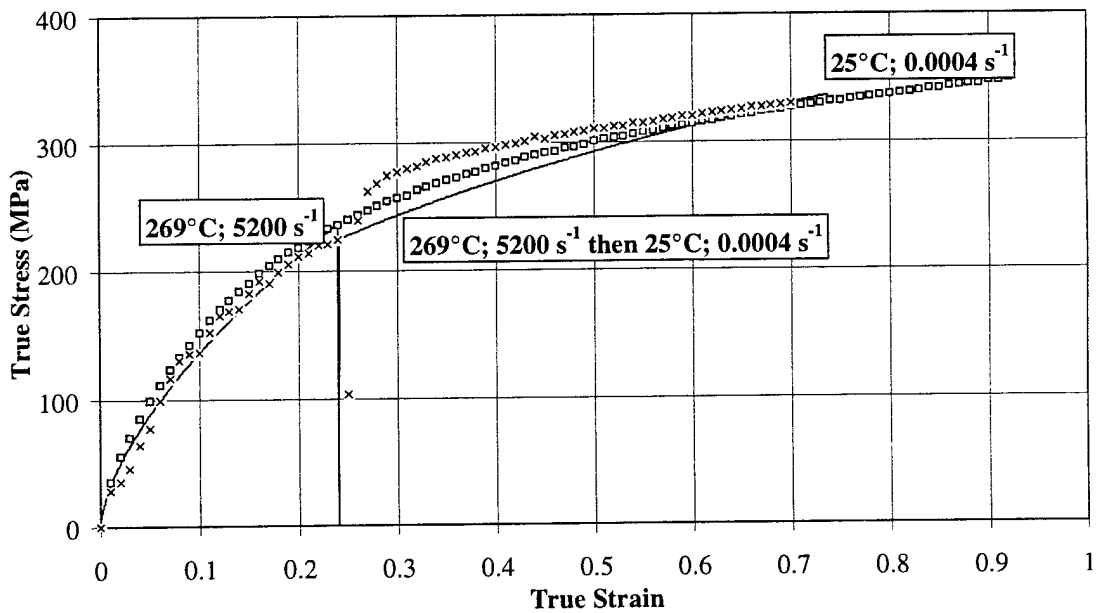


Figure V.20: Strain rate and temperature sequence prediction for OFHC Cu using the Zerilli-Armstrong model. Solid lines represent the model prediction, while symbols represent experimental data.

V.4.2.3 Zerilli-Armstrong Model Correlation to High Strain Rate Data

The Zerilli-Armstrong model has been successfully applied to high strain rate applications. The model was utilized here to obtain a basis for comparison for very high strain rate predictions. The five parameters were determined through optimization to the same isothermal, constant strain rate data as before, with the addition of the high strain rate data, 692820 s^{-1} at 298°C and 461°C (Frutschy and Clifton, 1988). The correlation with these data are shown in Fig. V.21. The model under predicts the sharp initial rise in flow stress and then over predicts the flow stress saturation level.

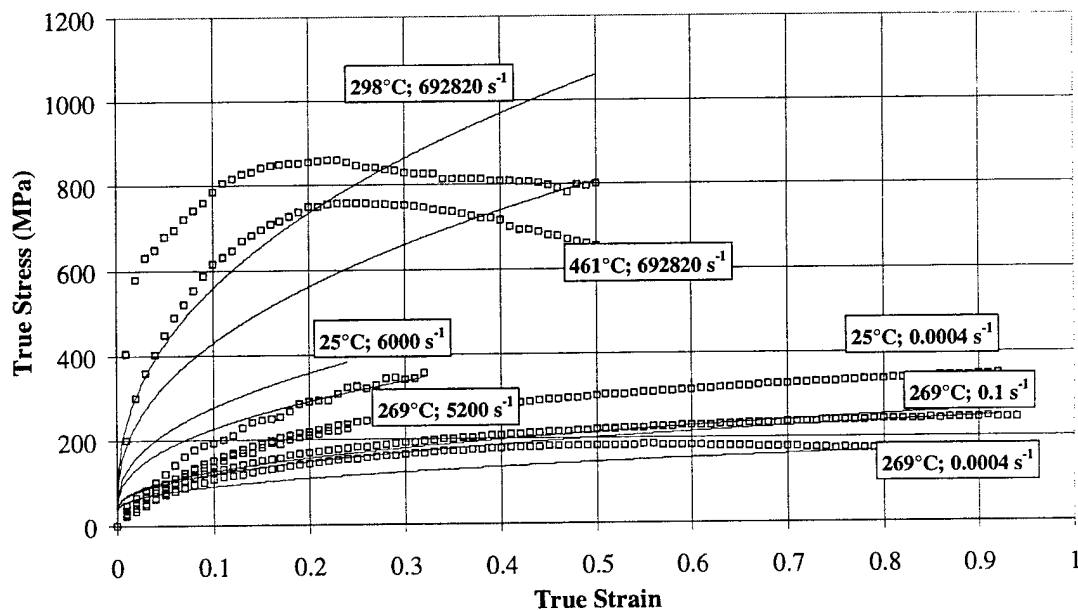


Figure V.21: Correlation to OFHC Cu data using Zerilli-Armstrong model. The model correlations are shown using solid lines, while the experimental data are shown with open symbols.

V.4.2.4 Zerilli-Armstrong Model Sequence Predictions (using parameters fit with very high strain rate data)

The parameters obtained during the correlation shown in Fig. V.21 were used for the sequence predictions shown in Figs. V.22 - V.27. The sequence predictions are similar to the ability shown using the parameters determined using the lower strain rate data. The transients associated with changes in strain rate or temperature are not predicted. The predicted flow stress instantaneously changes from the curve associated with the initial conditions to that due to the subsequent conditions. The addition of the very high strain rate data did influence the predictions on the lower strain rate sequence predictions significantly.

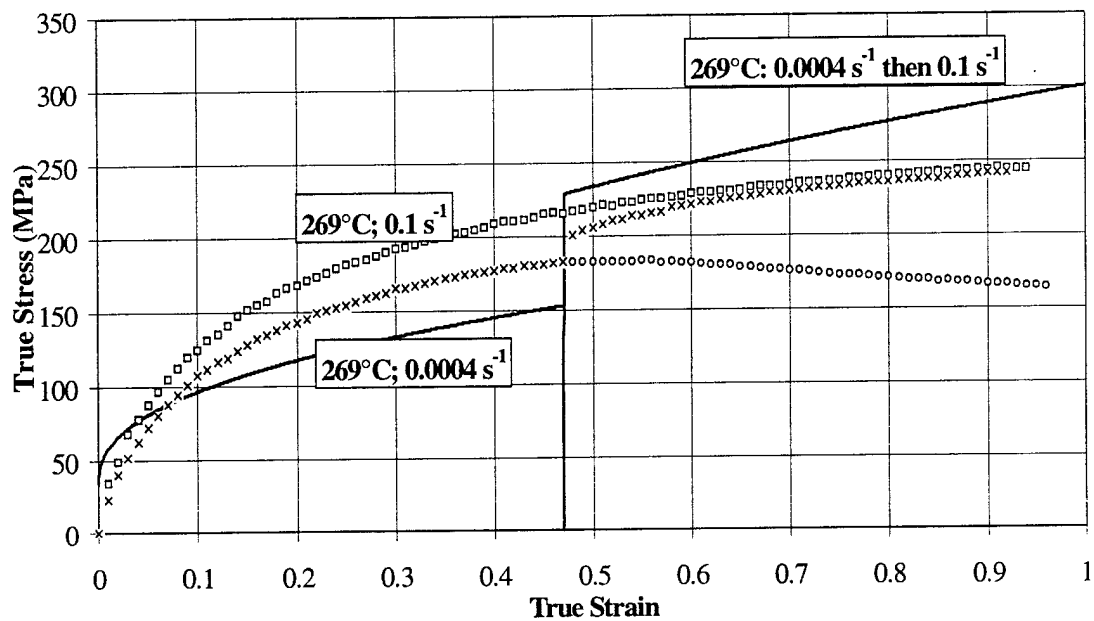


Figure V.22: Strain rate sequence prediction for OFHC Cu using the Zerilli-Armstrong model correlated with the additional high strain rate data. Solid lines represent the model prediction, while symbols represent experimental data.

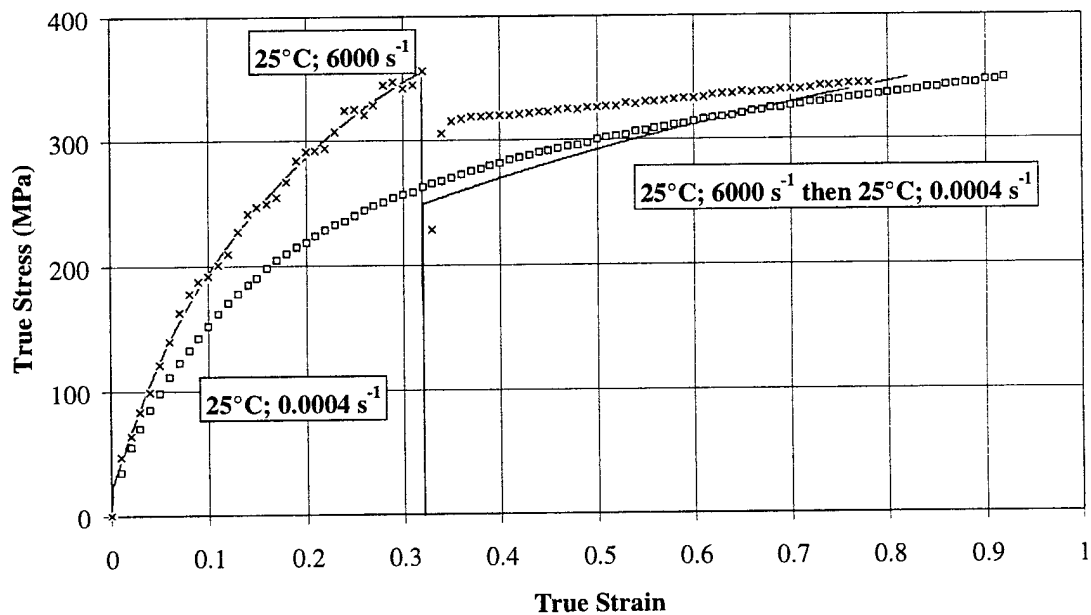


Figure V.23: Strain rate sequence prediction for OFHC Cu using the Zerilli-Armstrong model correlated with the additional high strain rate data. Solid lines represent the model prediction, while symbols represent experimental data.

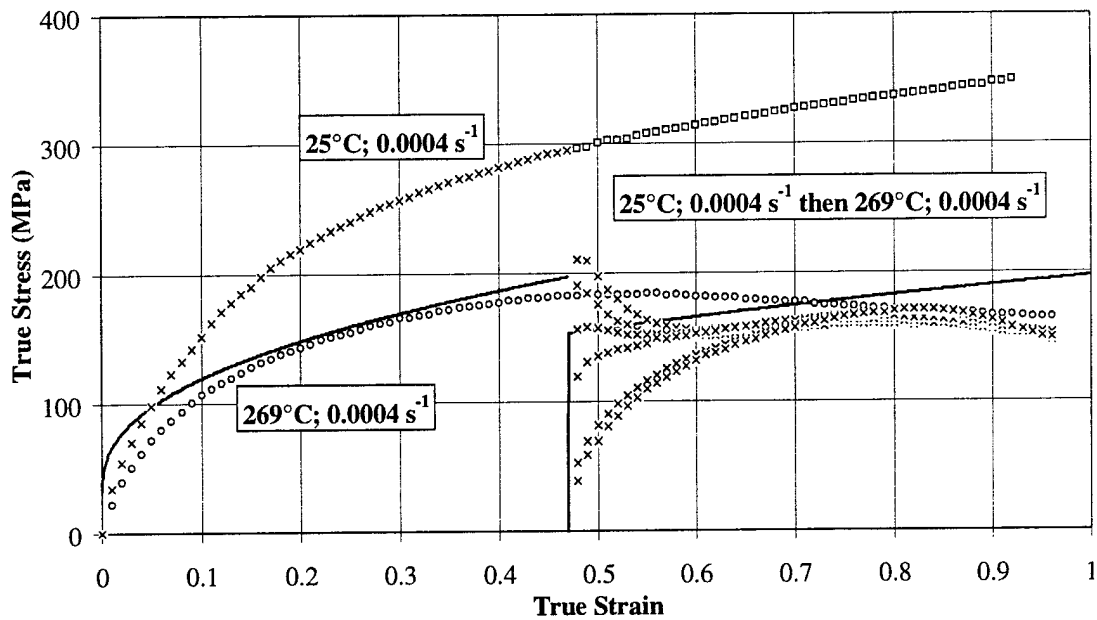


Figure V.24: Temperature sequence prediction for OFHC Cu using the Zerilli-Armstrong model correlated with the additional high strain rate data. Solid lines represent the model prediction, while symbols represent experimental data.

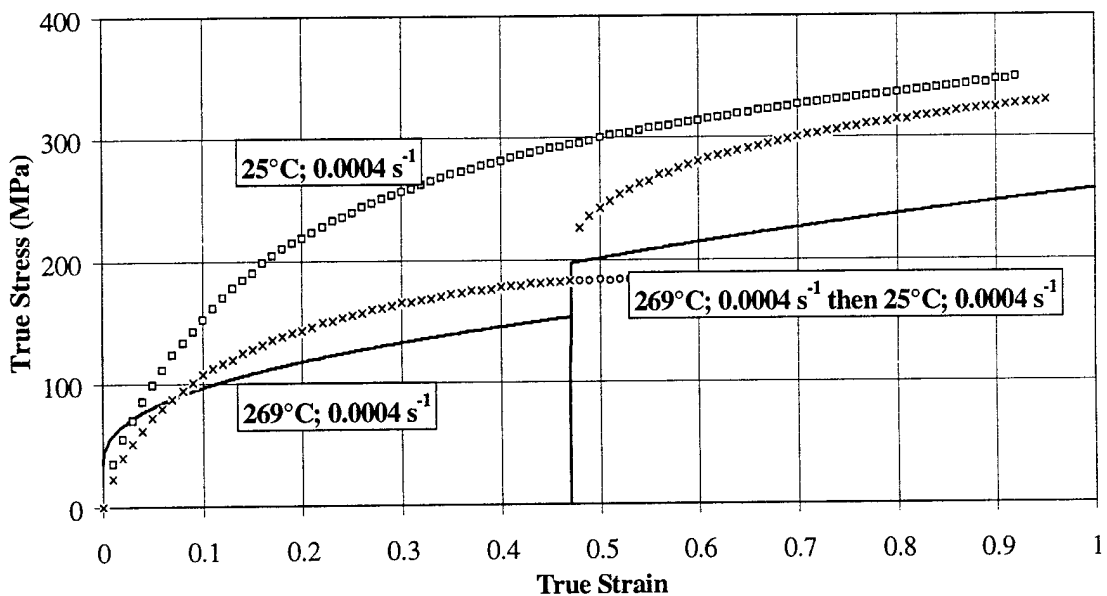


Figure V.25: Temperature sequence prediction for OFHC Cu using the Zerilli-Armstrong model correlated with the additional high strain rate data. Solid lines represent the model prediction, while symbols represent experimental data.

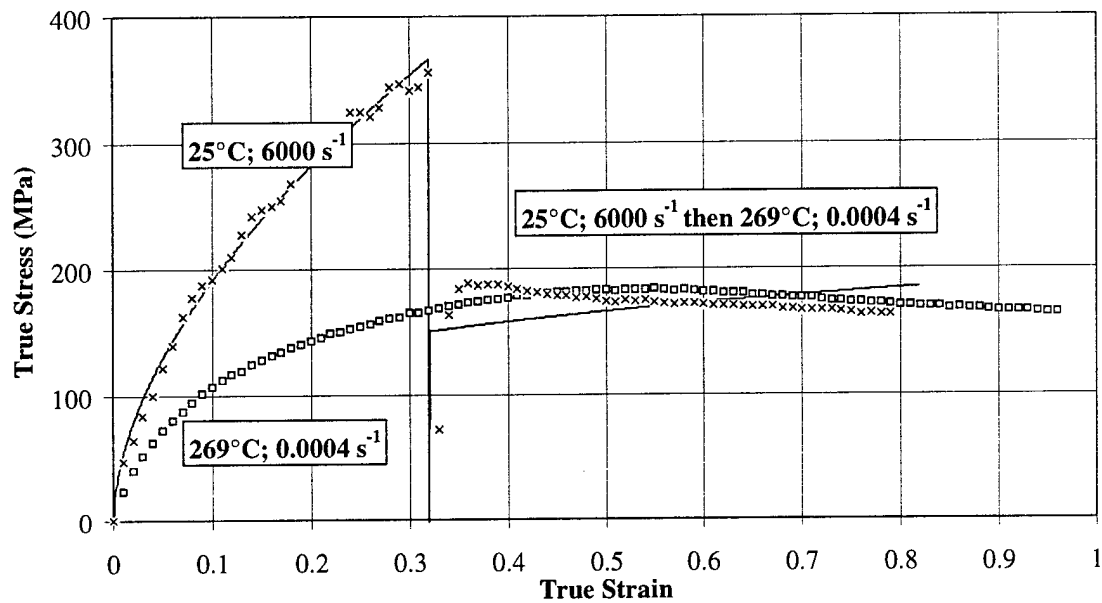


Figure V.26: Strain rate and temperature sequence prediction for OFHC Cu using the Zerilli-Armstrong model correlated with the additional high strain rate data. Solid lines represent the model prediction, while symbols represent experimental data.

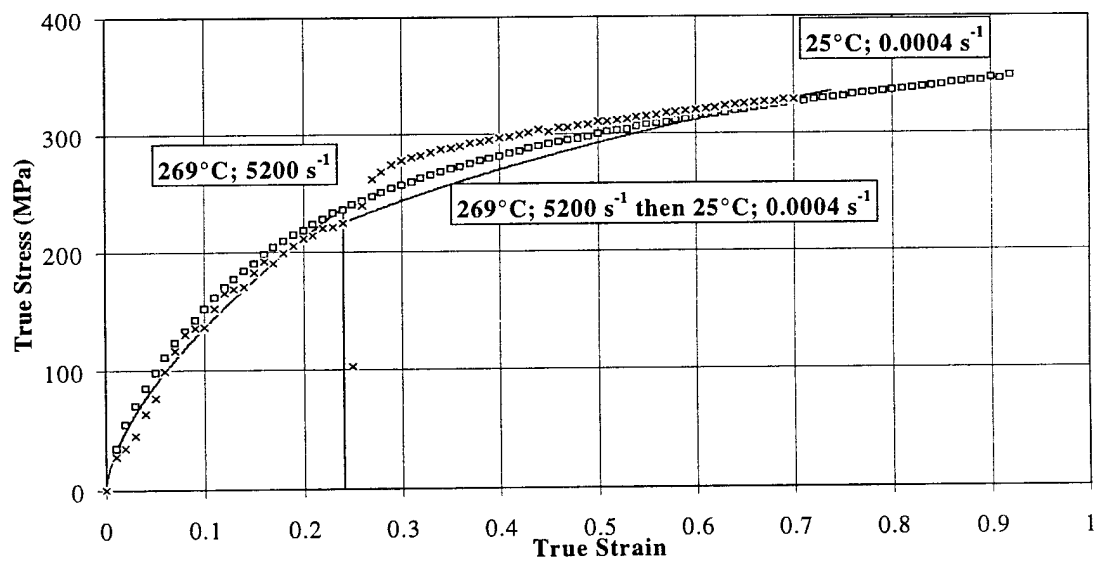


Figure V.27: Strain rate and temperature sequence prediction for OFHC Cu using the Zerilli-Armstrong model correlated with the additional high strain rate data. Solid lines represent the model prediction, while symbols represent experimental data.

V.4.2.5 Zerilli-Armstrong Model Parameter Sensitivity

A parameter sensitivity study was completed for the Zerilli-Armstrong model using the optimized values shown in Table V.3. The light and dark bars in Fig. V.28 reflect $\pm 10\%$ offset from the optimized parameter values. The first two bars for each parameter reflect the ability of the indicated parameter alone to achieve the global minimum while the second two bars show how well the remaining parameters can reach the minimum with the indicated parameter held constant. This analysis shows that parameters C_0 and C_3 have the least effect on achieving the optimized objective function value. The model's performance is most sensitive to the n parameter.

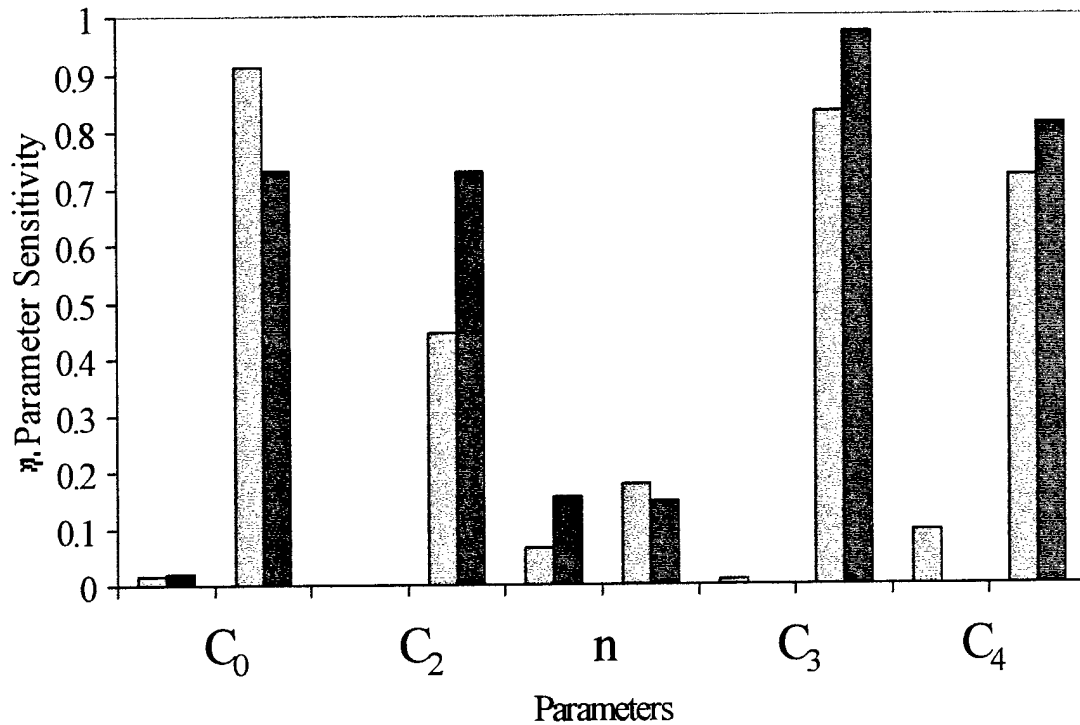


Figure V.28: Parameter sensitivity for OFHC Cu using the Zerilli-Armstrong model. Light and dark bars reflect a $\pm 10\%$ offset from the optimized parameter values corresponding to a minimum of the objective function. First two bars show ability of indicated parameter, alone, to achieve the global minimum while the second two bars show ability of the remaining parameters, with the indicated parameter held constant, to reach the minimum.

V.4.3 MTS Model

V.4.3.1 MTS Model Correlation to Experimental Data

The threshold stress, $\hat{\sigma}$, is the material yield stress for a given internal structure at 0K. The threshold stress, which characterizes the strength and density of obstacles, is typically determined experimentally. Multiple specimens are pre-strained at room temperature along the strain rate and strain path of interest and then unloaded. This pre-strain creates a structure which is characteristic of the strain, strain rate, and temperature imposed during the deformation. The pre-strained specimens are then reloaded at a low strain rate and various low temperatures, approaching 0K. The flow stress upon reloading is determined by back extrapolating, to eliminate any recovery, to the elastic line. The data is then plotted and the mechanical threshold stress determined through extrapolation to 0K. The eight parameters (g_0 , p , q , k/b^3 , A , $\dot{\epsilon}_0$, $\dot{\epsilon}_{s0}$, and σ_{s0}) used in the MTS model were obtained using the same five isothermal, constant true strain rate compression tests as before. Constraints were imposed on several parameters. The constants p and q , which define the average obstacle profile, were restricted to $0 \leq p \leq 1$ and $1 \leq q \leq 2$ (Kocks *et al.*, 1975) and the constant $\dot{\epsilon}_0$, was limited to values $10^7 \leq \dot{\epsilon}_0 \leq 10^{10} \text{ s}^{-1}$ (Johnson, 1988). The correlation to the five data sets are shown in Fig. V.29. The model correlates the data well, except for the strain softening observed at 269°C at a strain rate of 0.0004 s^{-1} .

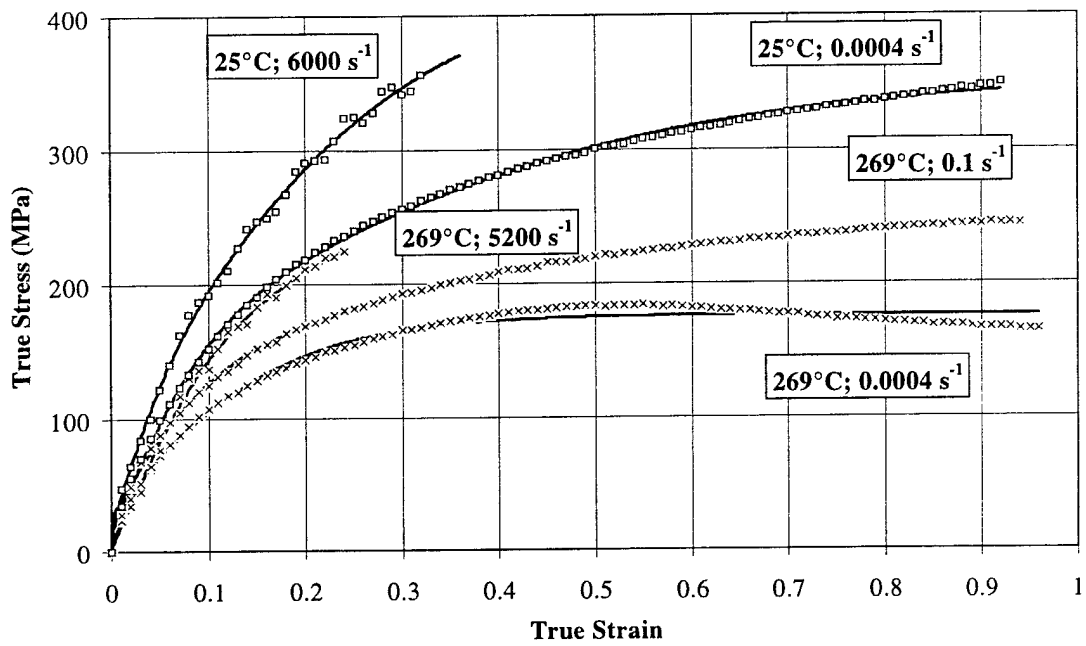


Figure V.29: Correlation to OFHC Cu compression data using the MTS model. The model correlations are shown using solid lines, while the experimental data are shown with open symbols.

Table V.4 shows a comparison of the optimized parameter values with other values determined using a graphical approach. The values are reasonably consistent, providing confidence that the physical interpretation of the parameters is valid. The parameter, $\dot{\epsilon}_{s0}$, is many orders of magnitude different than previously determined values. This term is used to obtain the saturation stress value in Equation (V.18). The parameter is embedded within a logarithmic term and is coupled with parameters A , k/b^3 and σ_{s0} , so is not necessary to determine a precise value (Johnson, 1988). $\dot{\epsilon}_0$ is proportional to the mobile dislocation density and the average spacing between obstacles.

Table V.4: MTS MODEL PARAMETER COMPARISON FOR OFHC CU

Parameter	Follansbee & Kocks (1988)	Gourdin & Lassila (1991)	Optimized
Deformation Conditions	10^{-4} to 10^4 s ⁻¹ 25°C 40 μ m	10^{-3} to 10^4 s ⁻¹ 25 to 400°C 10-200 μ m	4×10^{-4} to 6×10^3 s ⁻¹ 25 to 269°C 62 μ m
g_0	1.6	1.6	2.98
p	2/3	2/3	0.318
q	1.0	1.0	1.20
$\dot{\epsilon}_0$ (s ⁻¹)	10^7	10^7	10^7
k/b^3 (MPa K ⁻¹)	0.823	0.823	0.848
A	0.31	0.235	0.633
σ_{s0} (MPa)	900	1100	1070
$\dot{\epsilon}_{s0}$ (s ⁻¹)	6.2×10^{10}	5.66×10^{10}	4.0×10^{23}

V.4.3.2 MTS Model Sequence Predictions

Predictions using the optimized parameters for the MTS model are shown for the strain rate sequence results (Figs. V.30 and V.31), temperature sequence results (Figs. V.32 and V.33), and combined strain rate and temperature sequence results (Figs. V.34 and V.35). The correlation to experimental sequence data are much improved over those of the empirical models. The instantaneous change in flow stress during strain rate sequences is greater than that observed with the experimental data. The lack of a static thermal recovery term is obvious in the sequences involving reloads at elevated temperatures, 269°C. The flow stress after a pre-strain at 25°C and then reloaded at 269°C remains constant, whereas the experimental data exhibits significant softening (Fig. V.32). This same behavior is also observed after a higher strain rate, 6000 s⁻¹, pre-strain (Fig. V.34). The best predictions are achieved during temperature decrease sequences (Fig. V.33) and strain rate increases (Fig. V.30). The flow stress has the proper characteristics, with an instantaneous initial increase in the flow stress followed by a gradual approach to the higher curve, corresponding to the subsequent deformation conditions.

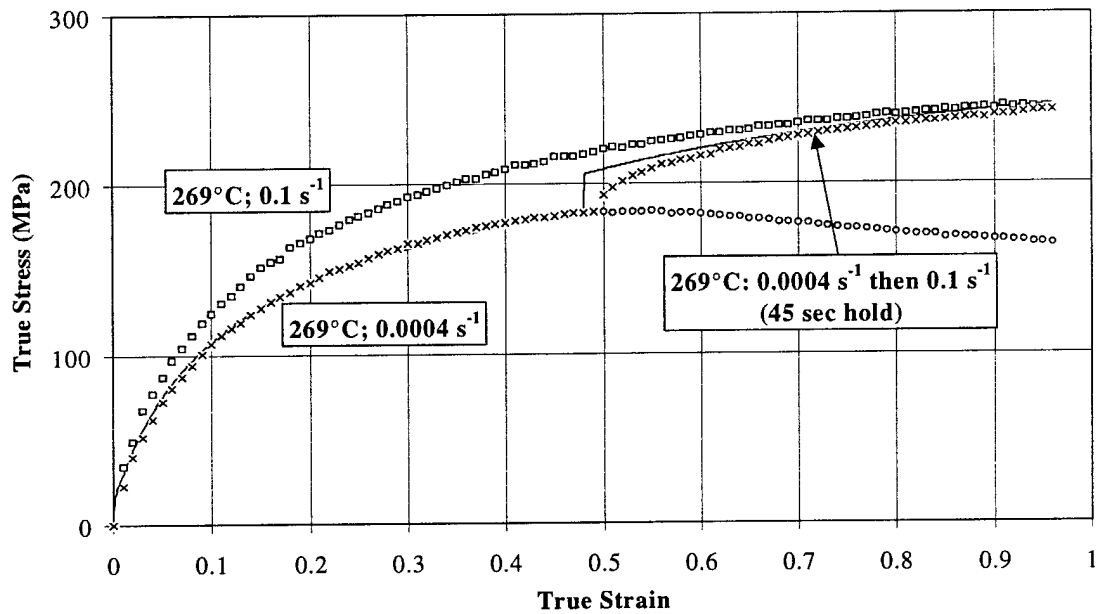


Figure V.30: Strain rate sequence prediction for OFHC Cu using the MTS model. Solid lines represent the model prediction, while symbols represent experimental data.

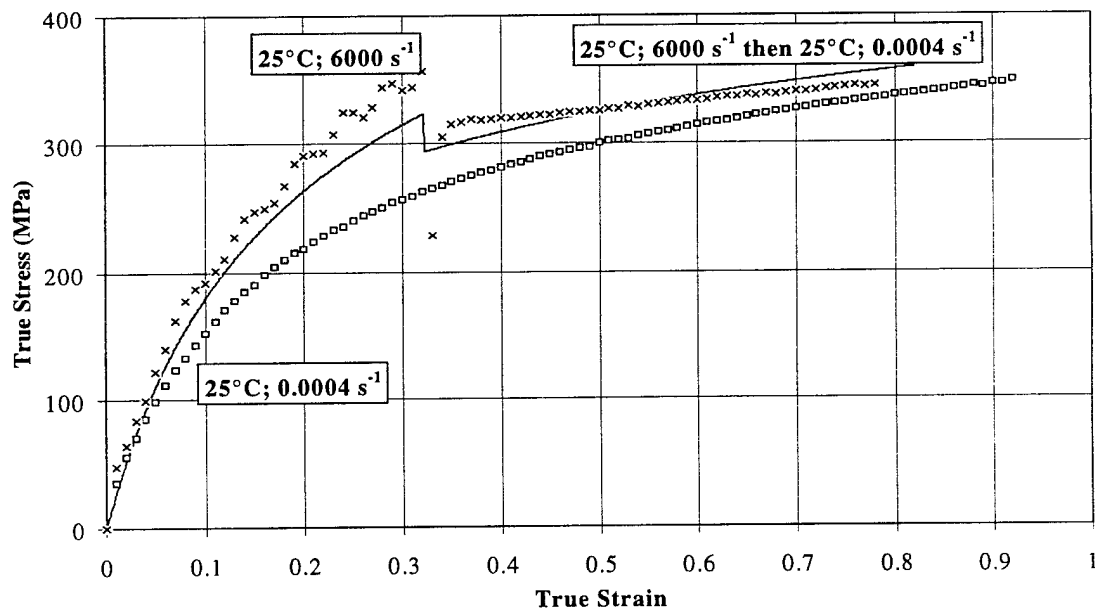


Figure V.31: Strain rate sequence prediction for OFHC Cu using the MTS model. Solid lines represent the model prediction, while symbols represent experimental data.

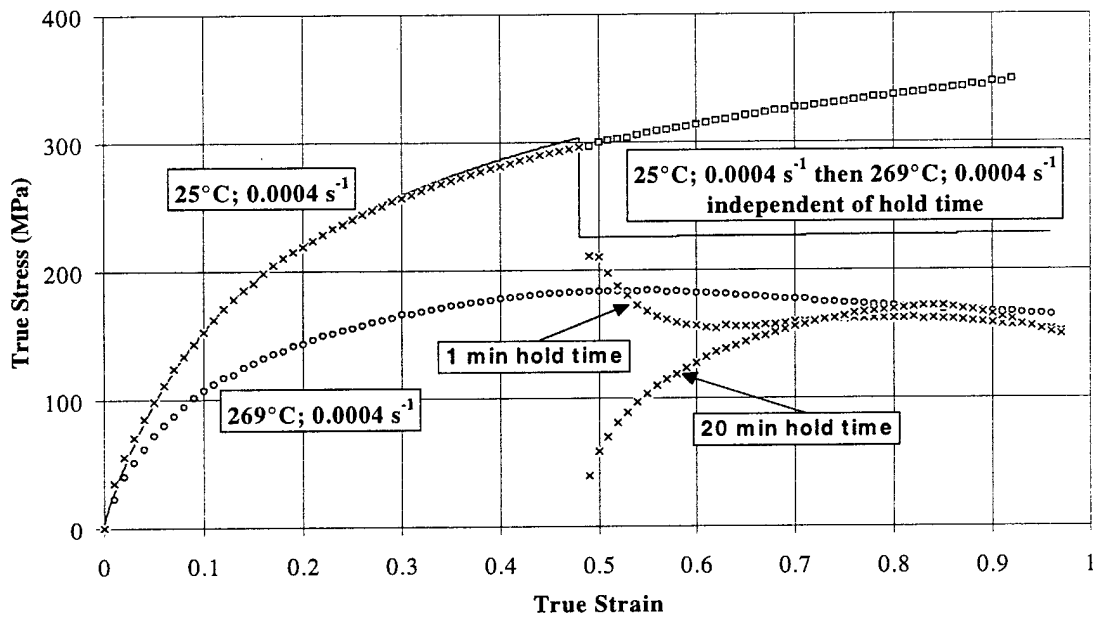


Figure V.32: Temperature sequence prediction for OFHC Cu using the MTS model. Solid lines represent the model prediction, while symbols represent experimental data.

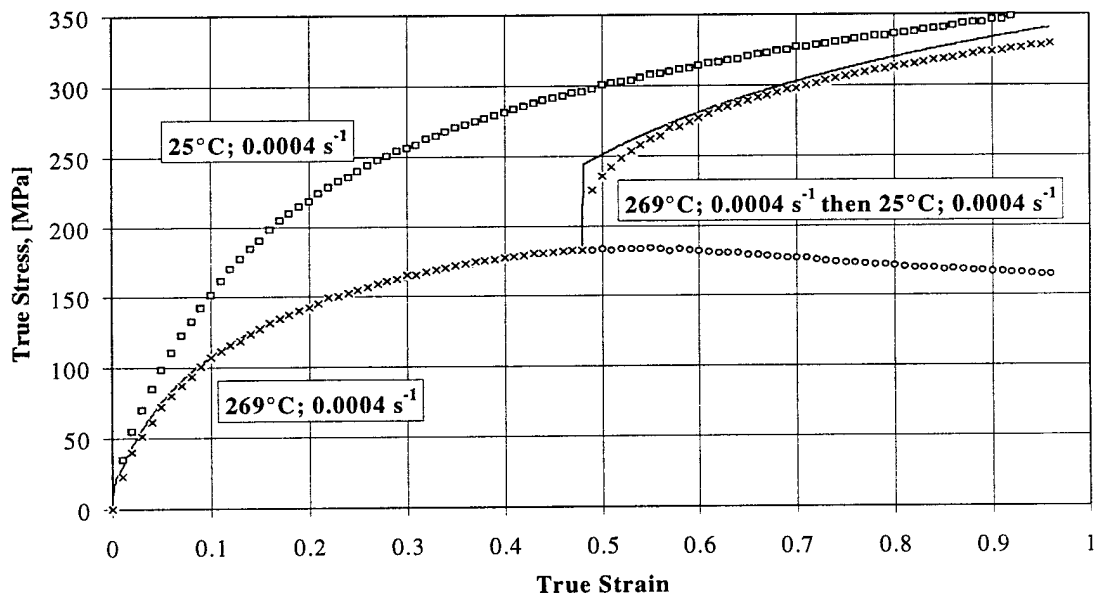


Figure V.33: Temperature sequence prediction for OFHC Cu using the MTS model. Solid lines represent the model prediction, while symbols represent experimental data.

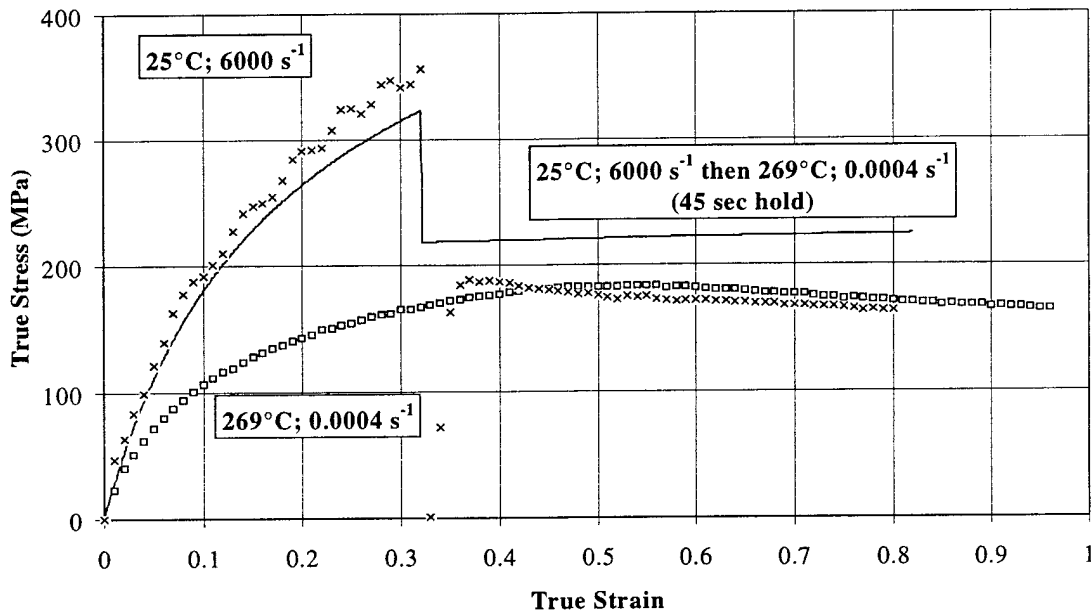


Figure V.34: Strain rate and temperature sequence prediction for OFHC Cu using the MTS model. Solid lines represent the model prediction, while symbols represent experimental data.

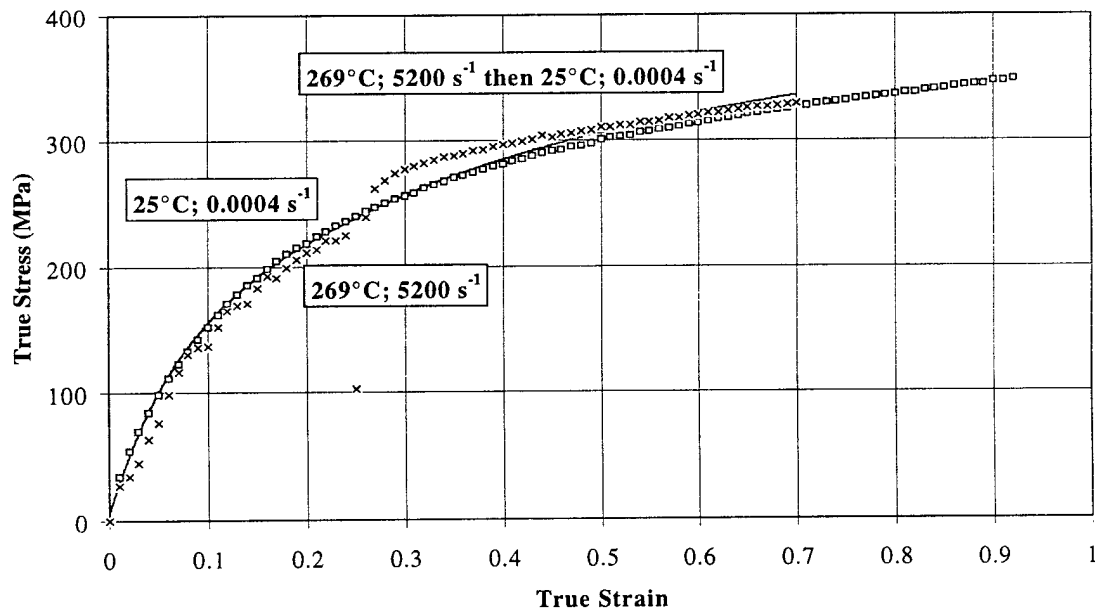


Figure V.35: Strain rate and temperature sequence prediction for OFHC Cu using the MTS model. Solid lines represent the model prediction, while symbols represent experimental data.

The MTS model lacks capability to describe static thermal recovery and strain softening (Figs. V.32 and V.34). It predicts rather well the strain rate and temperature sequences excluding static thermal recovery effects. Since it has no kinematic hardening and a single hardening variable, the MTS model is limited in ability to capture details of transients just after a change in loading condition. The single-parameter model is more successful in describing monotonic deformation than transient behavior. The addition of a term to account for the enhanced hardening following a strain rate change is required.

V.4.3.3 MTS Model Parameter Sensitivity

A parameter sensitivity study was conducted for the MTS model using the optimized values shown in Table V.4. The light and dark bars in Fig. 36 reflect a $\pm 10\%$ offset from the optimized parameter values. This analysis indicates that there is redundancy in the parameters, since any one of the eight parameters can be held constant and the optimized objective function value can still be practically achieved. Parameter σ_{so} is the only one which has much impact alone on achieving the minimum error. The parameter k/b^3 has the least capability to reduce the objective function, so it has the least sensitivity.

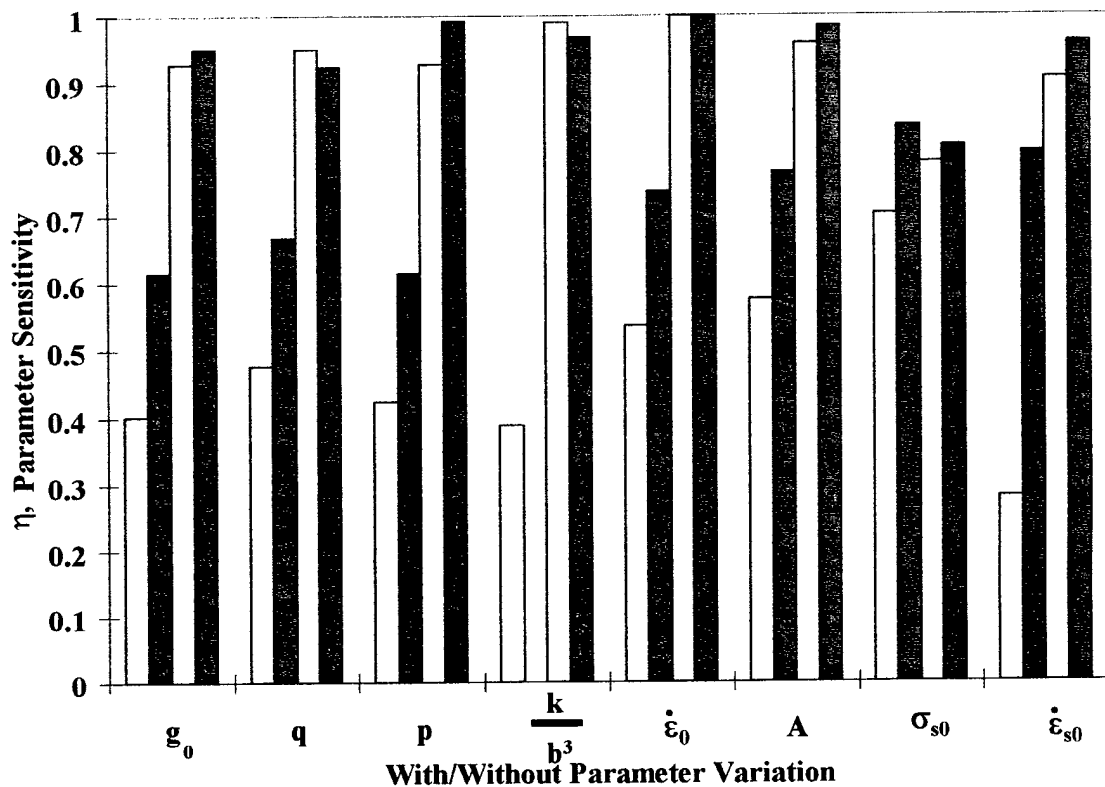


Figure V.36: Parameter sensitivity for OFHC Cu using the MTS model. Light and dark bars reflect a $\pm 10\%$ offset from the optimized parameter values corresponding to a minimum of the objective function. First two bars show ability of indicated parameter, alone, to achieve the global minimum while the second two bars show ability of the remaining parameters, with the indicated parameter held constant, to reach the minimum.

V.4.4 BCJ-SNL Model

V.4.4.1 BCJ-SNL Model Correlation to Experimental Data

The BCJ-SNL model employs nine parameters. The first three are V , Y and f which specify the flow stress relative to α , the kinematic hardening variable, with Y controlling the rate independent part, and V and f controlling the rate dependent part. Parameters h , r_d , and

r_s describe the evolution of α , including direct hardening, dynamic recovery, and static thermal recovery, respectively. Similarly, H , R_d and R_s govern the evolution of the isotropic variable, κ . The nine parameters all have a temperature dependence, V , f , Y , r_d , r_s , R_d , and R_s through a form as described in Equation (V.24) and h and H through a coupling with the elastic shear modulus defined in Equation V.6. The nine parameters (V , f , Y , r_d , h , r_s , R_d , H , and R_s) were obtained using the same five isothermal, constant strain rate conditions as for the other models. An initial value of zero was used for both α and κ for the initially annealed material. An apparent softening can be achieved when a negative initial value for κ is assumed. The correlations with the five data sets are shown in Fig. V.37. The data are well correlated with the experimental data, except for the strain softening observed at 269°C above 0.5 strain.

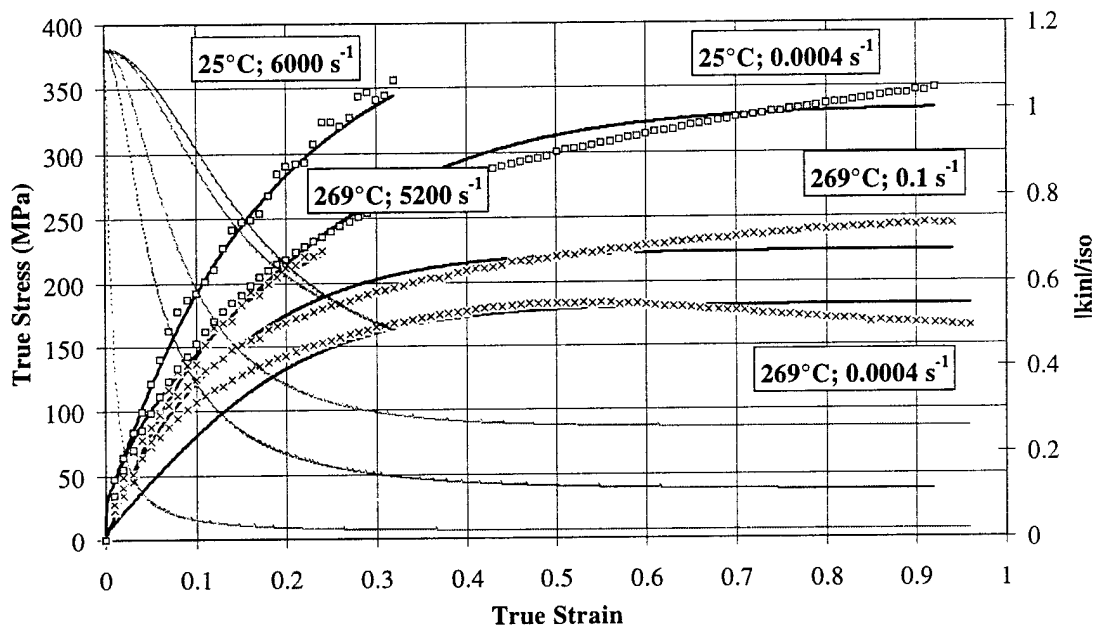


Figure V.37: Correlation to OFHC Cu compression data using the BCJ-SNL model. The model correlations are shown using solid lines, while the experimental data are shown with open symbols. The ratio $|k_{II}|/k$ are displayed using short dashed lines.

Table V.5: BCJ-SNL OPTIMIZED MODEL PARAMETERS FOR OFHC CU
(strain rates 4×10^{-4} to $6 \times 10^3 \text{ s}^{-1}$ and temperatures 25°C to 269°C).

Parameter	Optimized Value
Deformation Conditions	4×10^{-4} to $6 \times 10^3 \text{ s}^{-1}$ 25 to 269°C $62 \mu\text{m}$
V	10^{-6} (- 43)
Y	1.7 (70)
f	38 (- 15)
r_d	0.15 (- 12)
h	0.024
r_s	0.046 (- 120)
R_d	0.028 (- 22)
H	0.021
R_s	10^{-9} (- 130)

The temperature dependence parameter, C_j , is provided in ().

V.4.4.2 BCJ-SNL Model Sequence Predictions

The ratio of the magnitude of the kinematic to the isotropic hardening ISV's ($|\alpha|/\kappa$) are also shown on each plot for each case as short dashed curves. The saturation ratio of ($|\alpha|/\kappa$) at large strain was constrained in the optimization process to lie between 0.05 and 0.3. This range of values is consistent with experimentally determined values for OFHC Cu using reverse loading paths (cf. Jackson *et al.*, 1997). The kinematic hardening variable accounts for short range work hardening transients and the isotropic the longer range transients. This ratio is seen to increase for increasing strain rates. Predictions using the $|\alpha|/\kappa$ optimized parameters for the BCJ-SNL model are shown in Figs. V.38 and V.39 for strain rate sequence experiments, Figures V.40 and V.41 show the temperature sequence results, and Figs. V.42 and V.43 show combined strain rate and temperature sequence results. In all cases, the ratio of kinematic to isotropic hardening is plotted as a function of strain. The initial ratios are the same in all cases (1.13), corresponding to the ratio of direct hardening coefficients, h/H . It is clear that the description of transient history effects is enhanced by the introduction of the two ISVs.

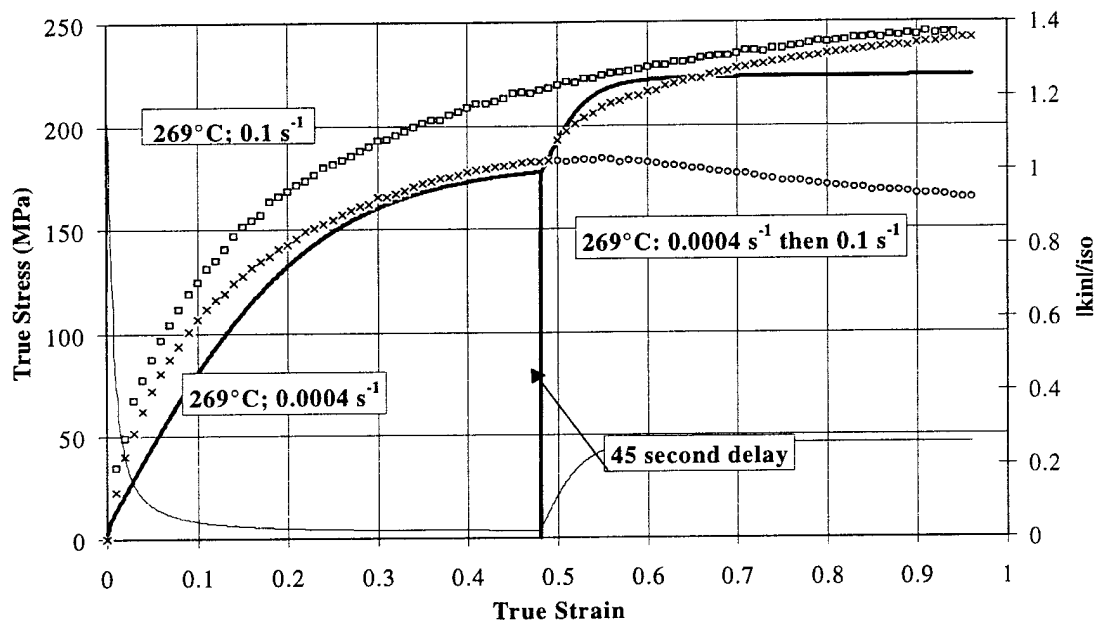


Figure V.38: Strain rate sequence prediction for OFHC Cu using the BCJ-SNL model. Solid lines represent the model prediction, while symbols represent experimental data.

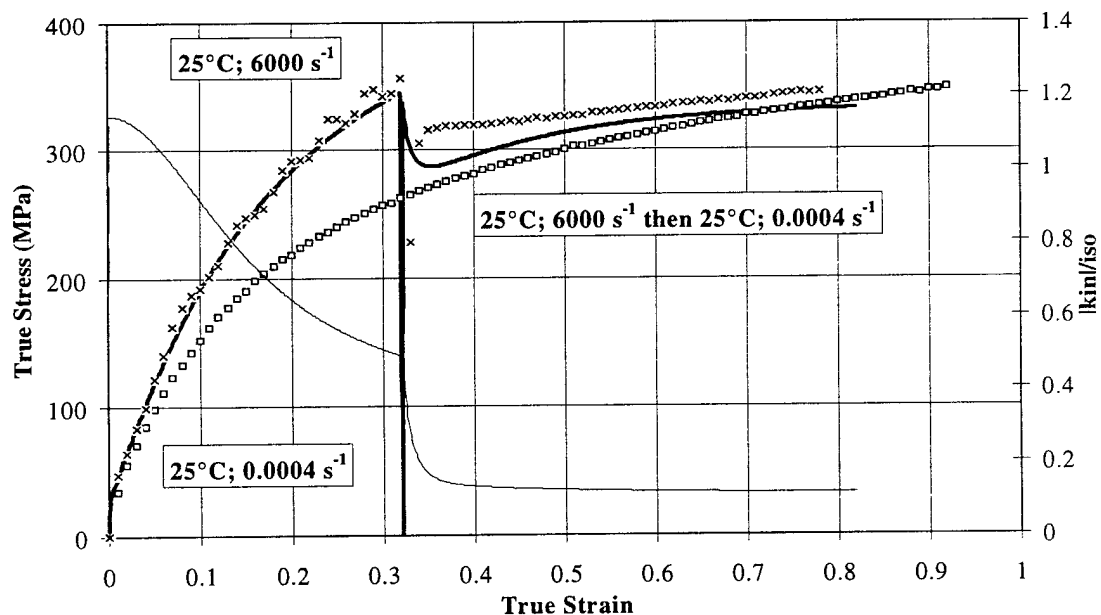


Figure V.39: Strain rate sequence prediction for OFHC Cu using the BCJ-SNL model. Solid lines represent the model prediction, while symbols represent experimental data.

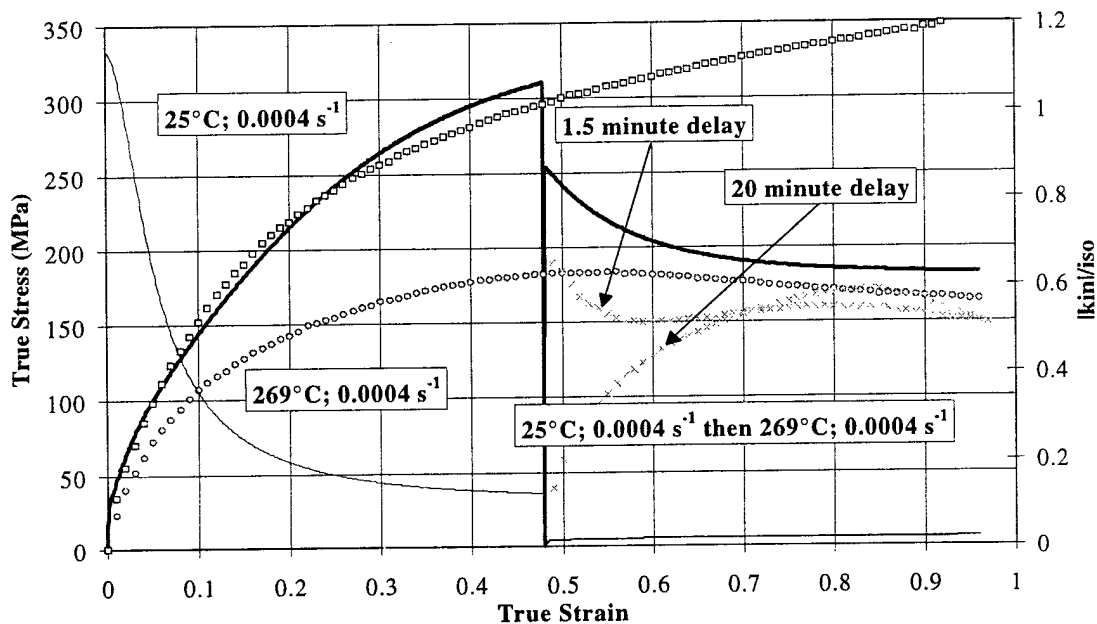


Figure V.40: Temperature sequence prediction for OFHC Cu using the BCJ-SNL model. Solid lines represent the model prediction, while symbols represent experimental data.

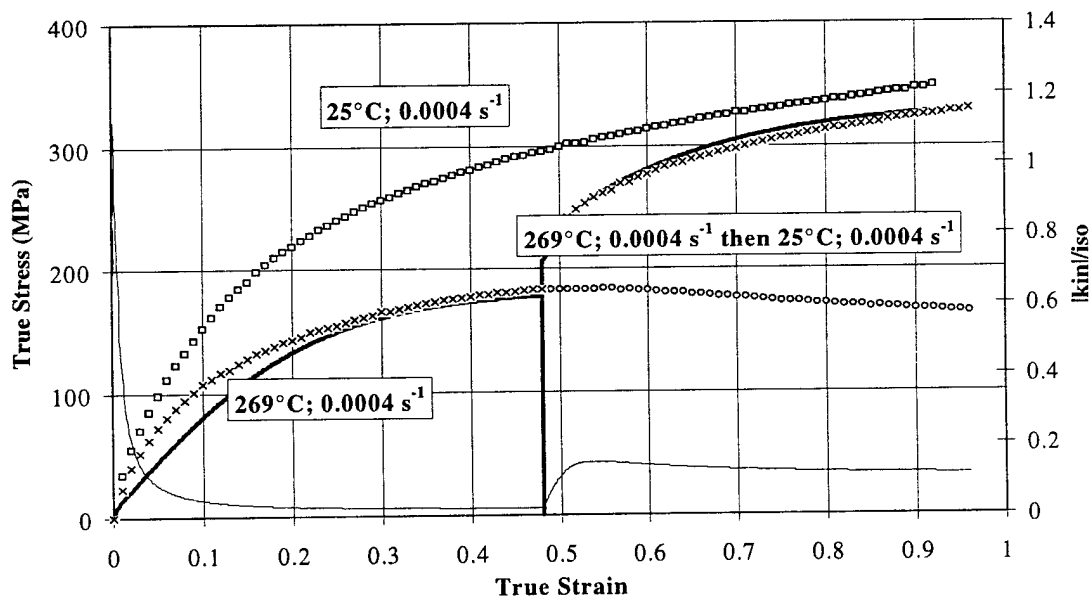


Figure V.41: Temperature sequence prediction for OFHC Cu using the BCJ-SNL model. Solid lines represent the model prediction, while symbols represent experimental data.

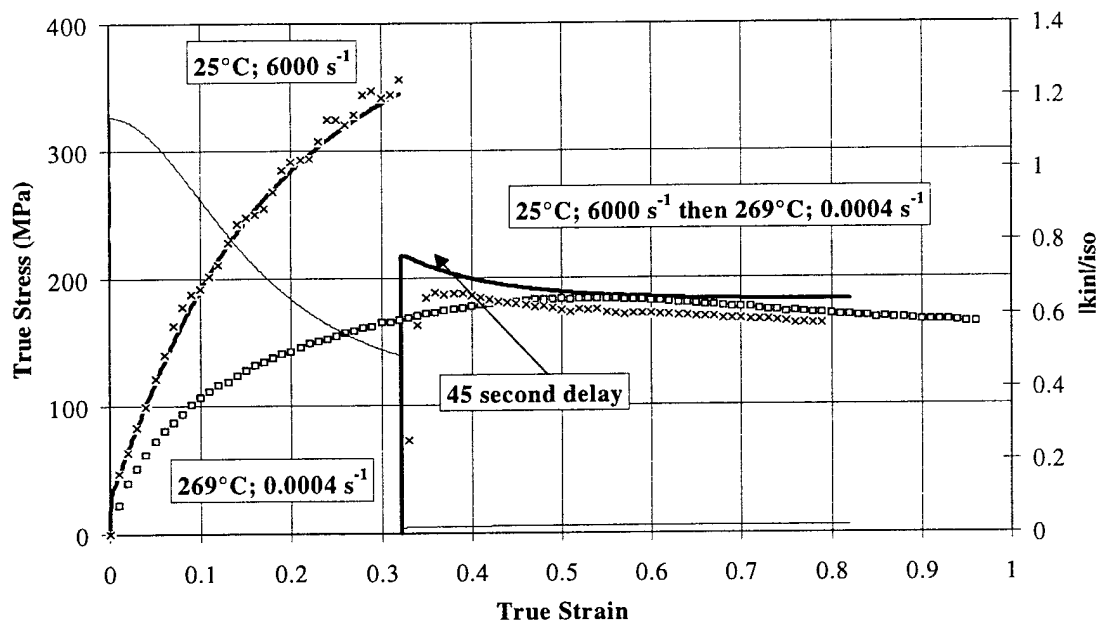


Figure V.42: Strain rate and temperature sequence prediction for OFHC Cu using the BCJ-SNL model. Solid lines represent the model prediction, while symbols represent experimental data.

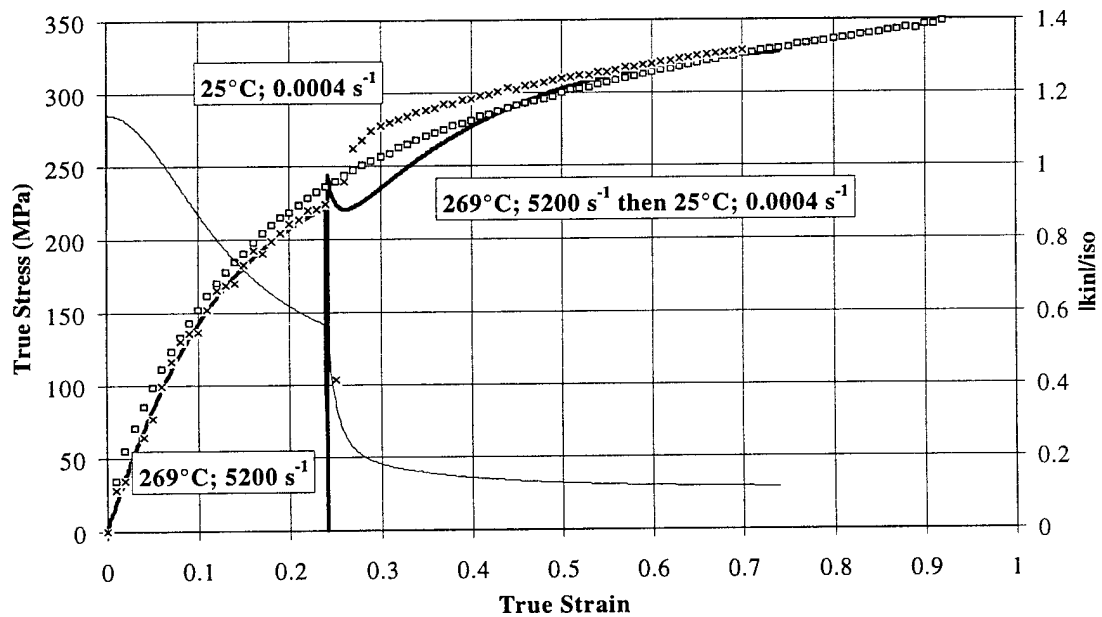


Figure V.43: Strain rate and temperature sequence prediction for OFHC Cu using the BCJ-SNL model. Solid lines represent the model prediction, while symbols represent experimental data.

The BCJ-SNL model incorporates many of the observed history effects. However, there is insufficient static thermal recovery while holding at zero stress at 269°C in-between loading events (Figs. V.38 and V.40). This arises from the fact that no stress relaxation or creep data were used in parameter estimation. Strain softening at 269°C following dynamic pre-strain is also not predicted (Fig. V.42); the model does not have this capability given its asymptotic saturation for a given temperature and strain rate.

V.4.4.3 BCJ-SNL Model Parameter Sensitivity

Figure V.44 shows the results of BCJ-SNL model parameter sensitivity study. The parameter sensitivity analysis shows that the hardening variables h and H are the most critical parameters to achieving the optimal objective (lowest error) function. It also indicates that there is redundancy in the three yield variables, V , f , and Y . Alone, none of these functions have much impact on achieving the minimum error (a zero value), but combined (yield), they are effective. To investigate the effect of groups of parameters, clusters were created of parameters with similar functions. These groups included, the yield parameters, V , f , and Y ; the kinematic variable parameters, H , R_d , and R_s ; the isotropic variable parameters, h , r_d , and r_s ; and the groupings of both hardening parameters, both dynamic recovery parameters, and both static recovery parameters. The analysis also shows that the recovery terms, both static and dynamic, are essential; the optimal error cannot be attained without them by varying other parameters.

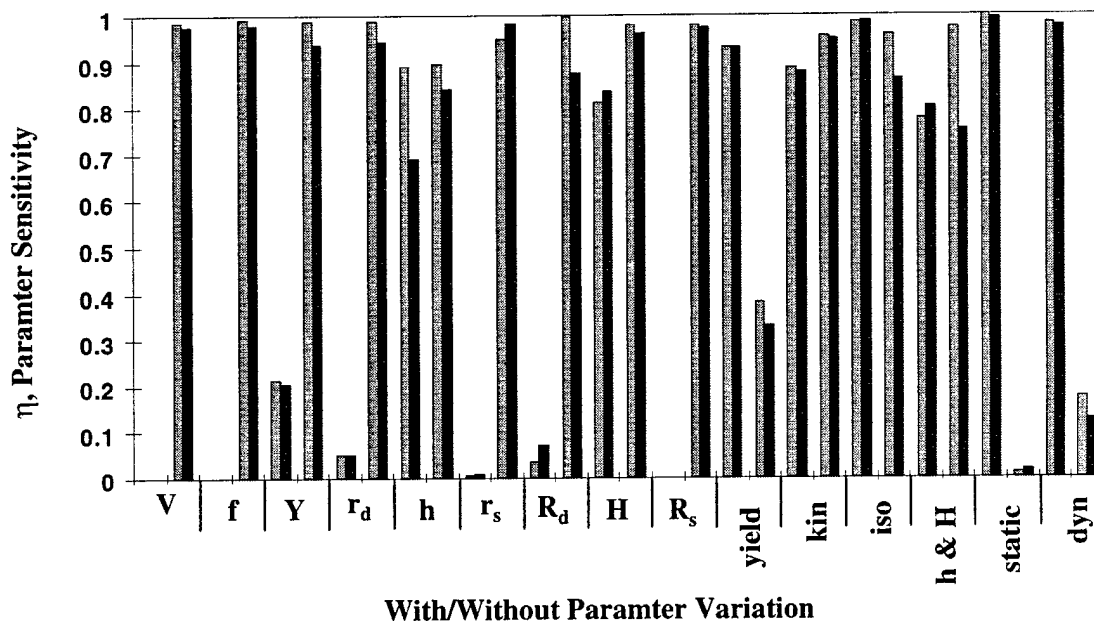


Figure V.44: Parameter sensitivity for OFHC Cu using the BCJ-SNL model. Light and dark bars reflect a $\pm 10\%$ offset from the optimized parameter values corresponding to a minimum of the objective function. First two bars show ability of indicated parameter, alone, to achieve the global minimum while the second two bars show ability of the remaining parameters, with the indicated parameter held constant, to reach the minimum.

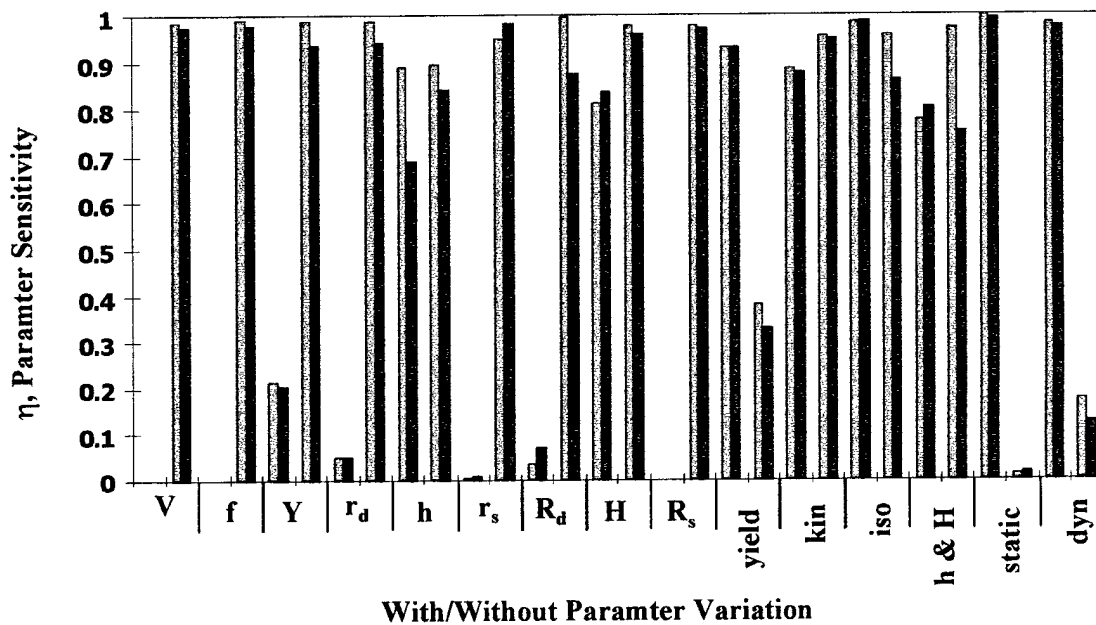


Figure V.44: Parameter sensitivity for OFHC Cu using the BCJ-SNL model. Light and dark bars reflect a $\pm 10\%$ offset from the optimized parameter values corresponding to a minimum of the objective function. First two bars show ability of indicated parameter, alone, to achieve the global minimum while the second two bars show ability of the remaining parameters, with the indicated parameter held constant, to reach the minimum.

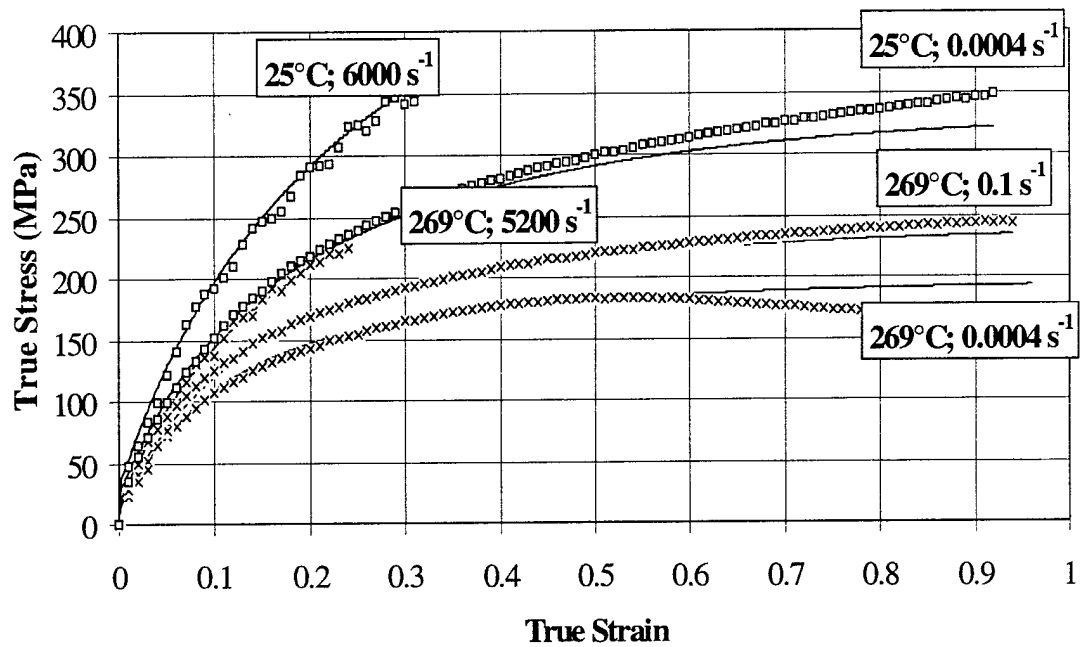


Figure V.45: Correlation to OFHC Cu compression data using the McDowell model. The model correlations are shown using solid lines, while the experimental data are shown with open symbols. The softening data, beginning at 269°C above 0.5 strain, was included in the calculation of the objective function during the optimization.

Table V.6: MCDOWELL MODEL PARAMETER COMPARISON FOR OFHC CU

Parameter	Optimized
Deformation Conditions	4×10^{-4} to $6 \times 10^3 \text{ s}^{-1}$ 25 to 269°C 62 μm
D_1	0.07
D_2	40
B_0	55
n_1	0.7
n_2	0.3
η	0.95
(Q/k)	16000
L_{χ_1}	2.0
L_{χ_2}	2.2
μ_{χ_1}	12.6
μ_{χ_2}	3.8
χ_{10}	6.6
χ_{20}	0.01
$\hat{\chi}_1$	56
A_1	2.3
A_2	14.4
A_3	0.00003
A_4	.005
B_1	17.5
B_2	76.5
B_3	0.009

B_4	87.4
$(Q/k)_\chi$	10800
ψ_χ	0
α_0	0
C	15
v	0.00009
L_α	2.3
$(Q/k)_\alpha$	10350
ψ_α	15

V.4.5.2 McDowell Model Sequence Predictions

Predictions were calculated using the optimized parameters for the McDowell model for compression tests involving strain rate sequences (Figs. V.46 and V.47), temperature sequences (Figs. V.48 and V.49), and for combined strain rate and temperature sequences (Figs. V.50 and V.51). The solid lines represent the model prediction, while symbols represent experimental data.

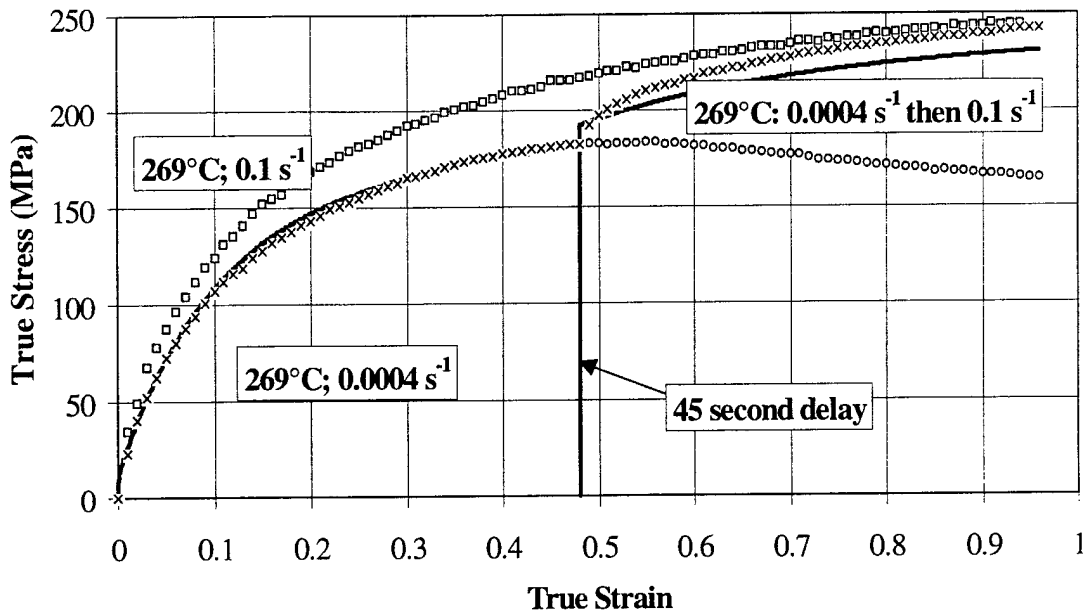


Figure V.46: Strain rate sequence prediction for OFHC Cu using the McDowell model. Model correlations are given by solid lines while symbols represent experimental data.

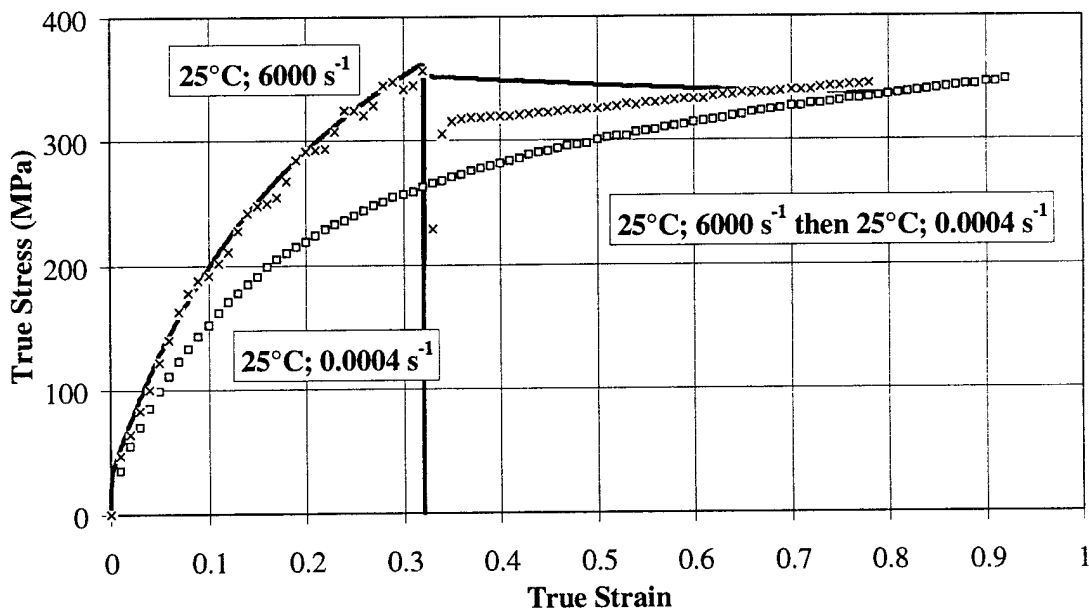


Figure V.47: Strain rate sequence prediction for OFHC Cu using the McDowell model. Model correlations are given by solid lines while symbols represent experimental data.

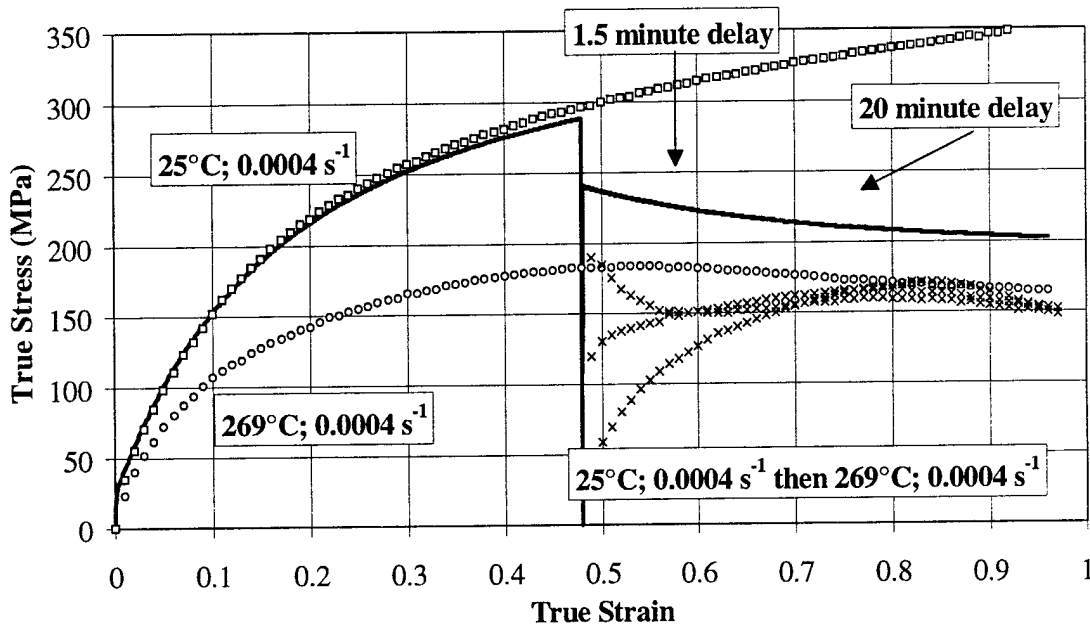


Figure V.48: Temperature sequence prediction for OFHC Cu using the McDowell model. Model correlations are given by solid lines while symbols represent experimental data.

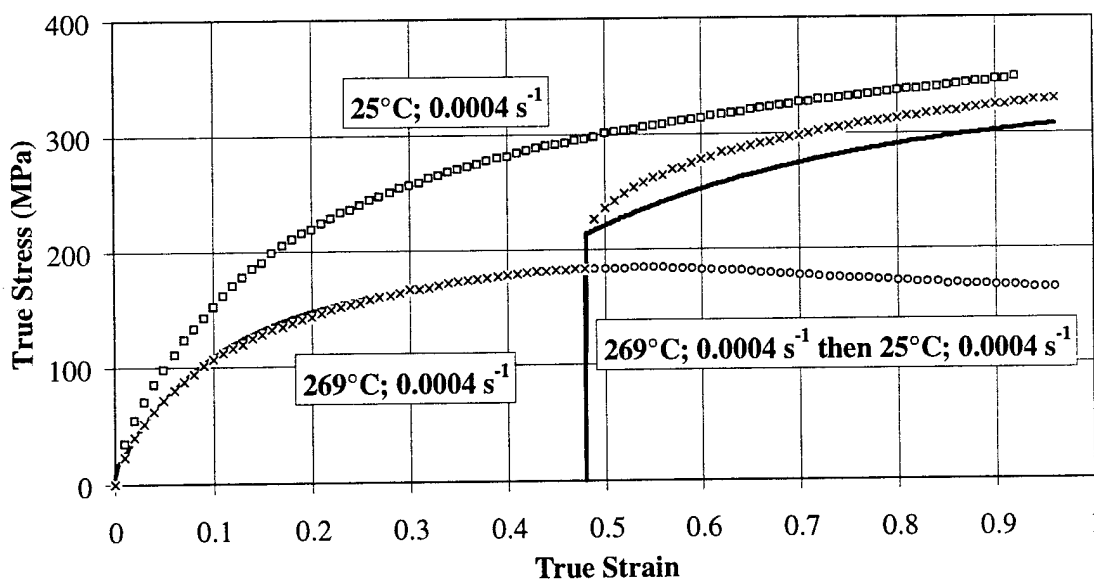


Figure V.49: Temperature sequence prediction for OFHC Cu using the McDowell model. Model correlations are given by solid lines while symbols represent experimental data.

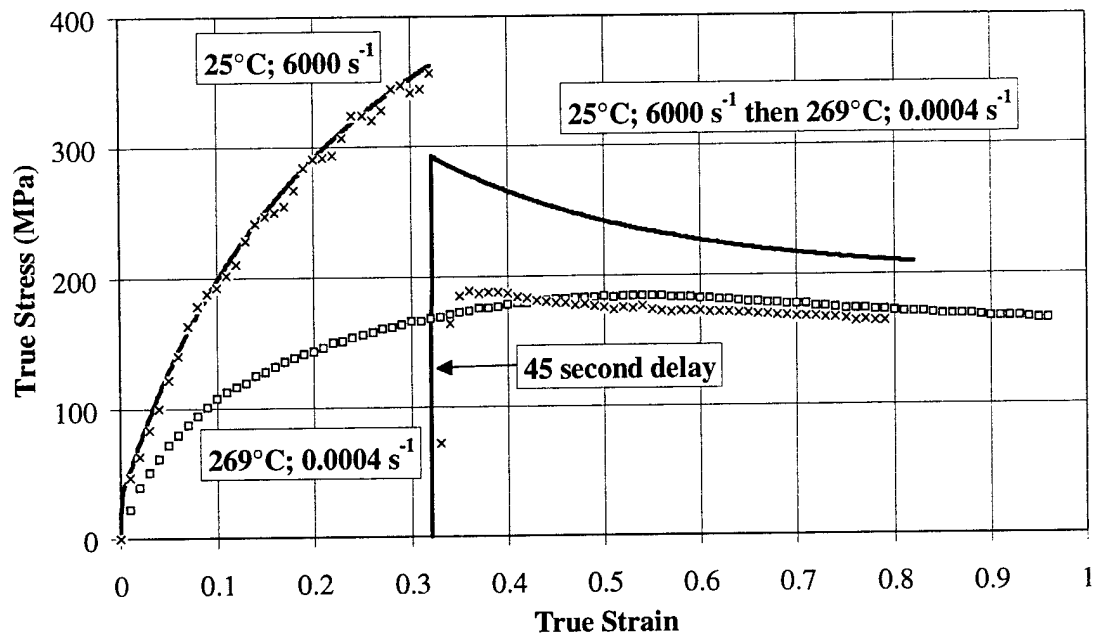


Figure V.50: Strain rate and temperature sequence prediction for OFHC Cu using the McDowell model. Model correlations are given by solid lines while symbols represent experimental data.

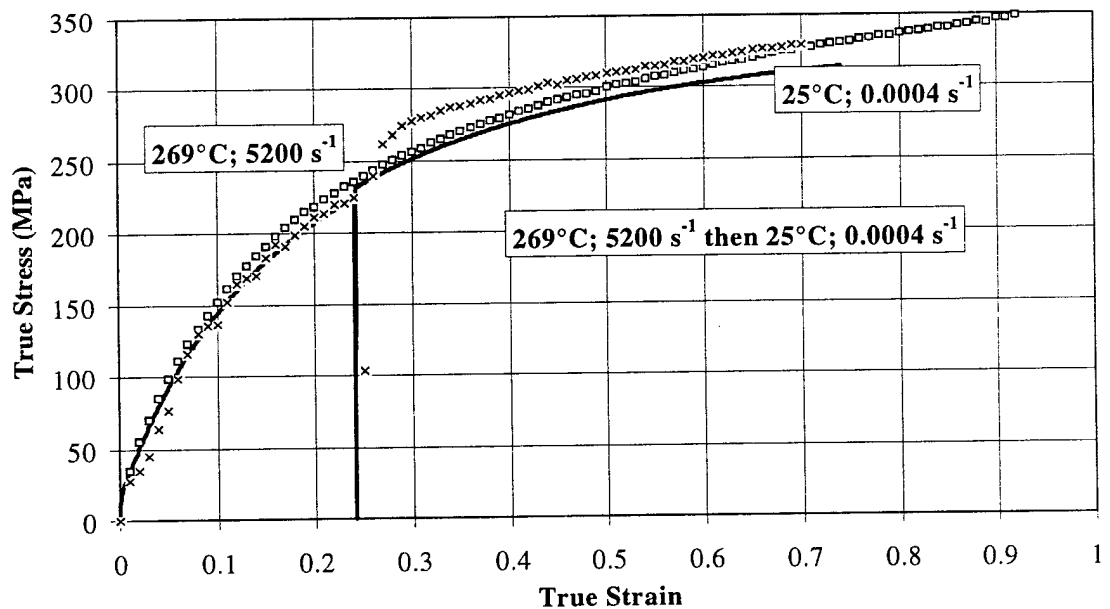


Figure V.51: Strain rate and temperature sequence prediction for OFHC Cu using the McDowell model. Model correlations are given by solid lines while symbols represent experimental data.

V.4.5.3 McDowell Model Parameter Sensitivity

A parameter sensitivity study was completed for the McDowell model using the optimized values shown in Table V.6. The light and dark bars in Figure V.51 reflect a $\pm 10\%$ offset from the optimized parameter values. The first two bars reflect the ability of the indicated parameter alone to achieve the global minimum while the second two bars show how well the remaining parameters can reach the minimum with the indicated parameter, or group of parameters, held constant. The parameters are grouped into “clusters” which are related and would provide information on the relative importance of the major terms within the McDowell model. The grouping, D’s, includes D_1 and D_2 which determines the drag stress in the flow equation. The isotropic hardening temperature dependencies are grouped into A’s and B’s. The “flow” group includes B_0 , n_1 , n_2 while the isotropic parameters are contained in χ_1 and χ_2 respectively. The kinematic variable parameters are grouped in α . The “temp” group contains all the temperature dependent parameters, $\left(\frac{Q}{k}\right)$, A_1 , A_2 , A_3 , A_4 , B_1 , B_2 , B_3 , B_4 , ψ_χ , and $\left(\frac{Q}{k}\right)_\chi$, ψ_α , and $\left(\frac{Q}{k}\right)_\alpha$. The recrystallization softening parameters are evaluated in the “soft” group and η is evaluated alone. The parameter sensitivity indicates a relative amount of redundancy in all groupings, but identifies χ_2 and η as being the most important parameters for achieving the lowest objective function value.

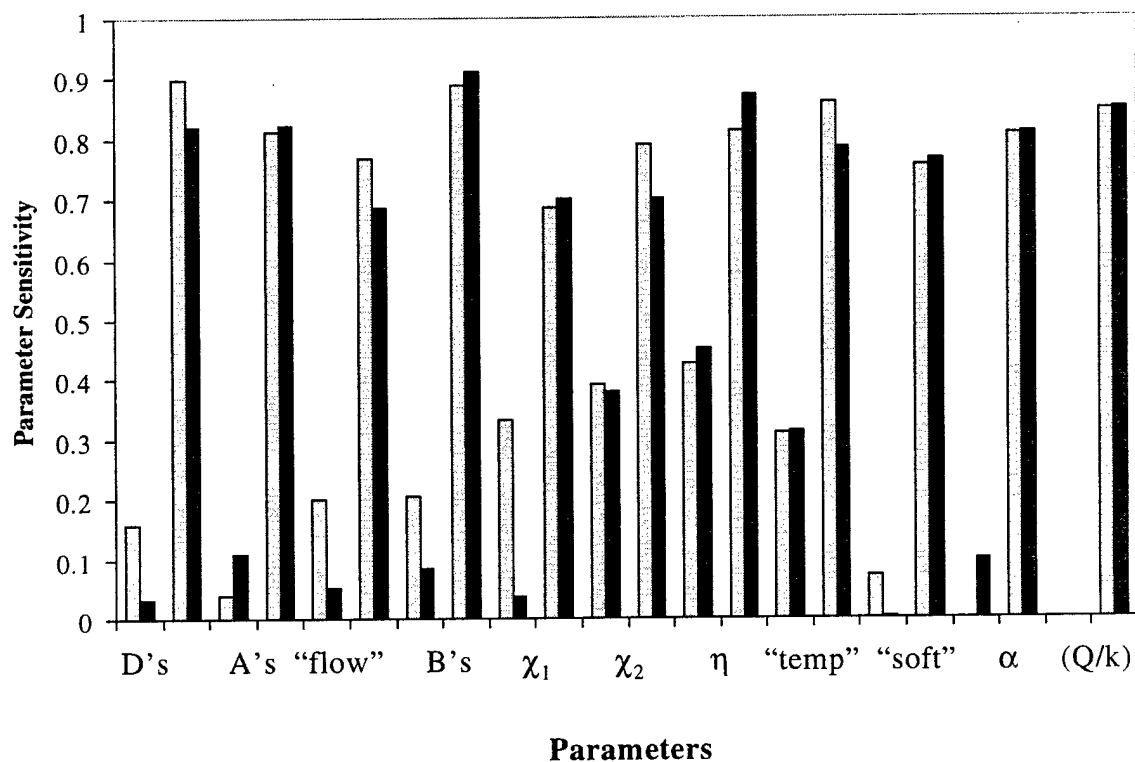


Figure V.52: Parameter sensitivity for OFHC Cu using the McDowell model. Light and dark bars reflect a $\pm 10\%$ offset from the optimized parameter values corresponding to a minimum of the objective function. First two bars show ability of indicated parameter, alone, to achieve the global minimum while the second two bars show ability of the remaining parameters, with the indicated parameter held constant, to reach the minimum.

V.4.5.4 McDowell Model Sequence Predictions (modified data set)

The procedure was repeated using the same constant strain rate, isothermal data without the strain about 0.5 at 269°C where flow softening was observed. The data correlations are shown in Fig. V.53. Predictions were calculated using the optimized parameters for the McDowell model for compression tests involving strain rate sequences (Figs. V.54 and V.55), temperature sequences (Figs. V.56 and V.57), and for combined strain rate and temperature sequences (Figs. V.58 and V.59). The solid lines represent the model prediction, while symbols represent experimental data.

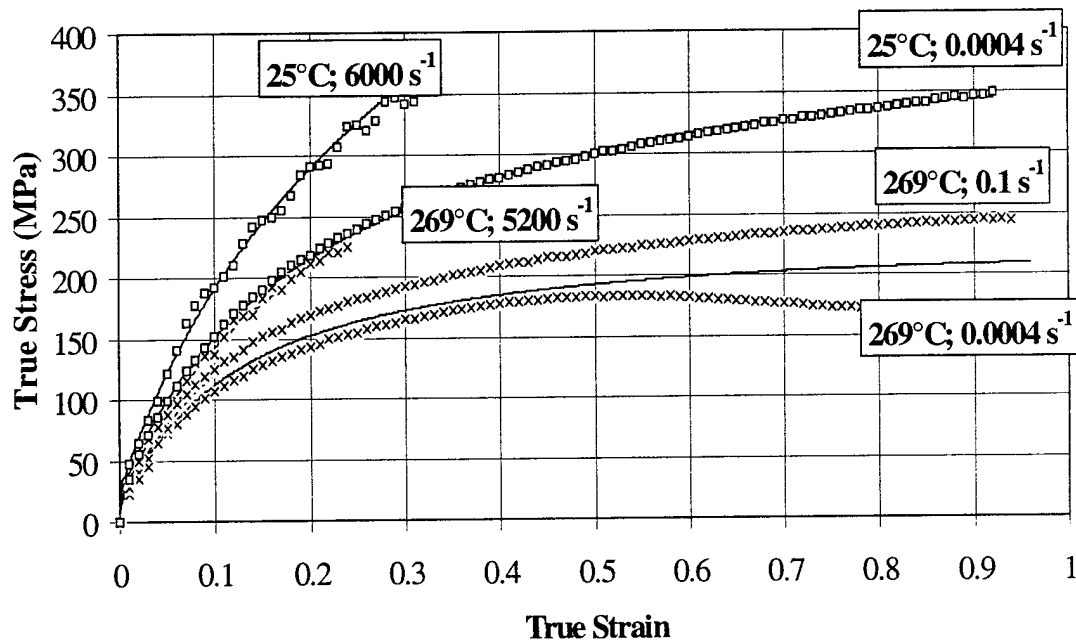


Figure V.53: Correlation to OFHC Cu compression data using the McDowell model. The model correlations are shown using solid lines, while the experimental data are shown with open symbols. The softening data, beginning at 269°C above 0.5 strain, were eliminated from the calculation of the objective function during the optimization.

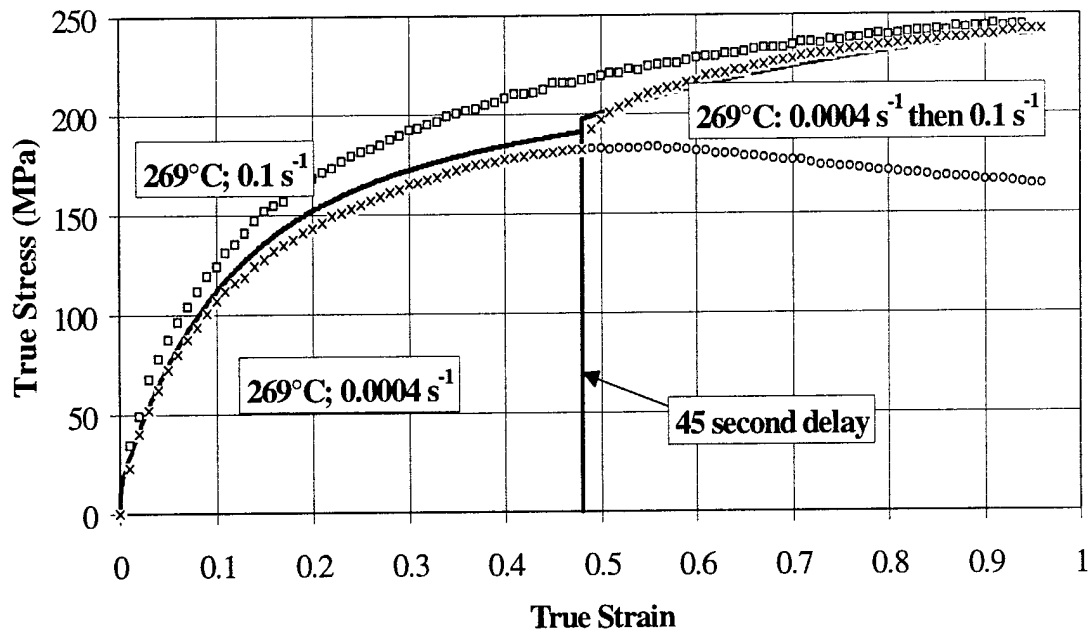


Figure V.54: Strain rate sequence predictions for OFHC Cu using the McDowell model. Solid lines represent the model predictions, while symbols represent experimental data.

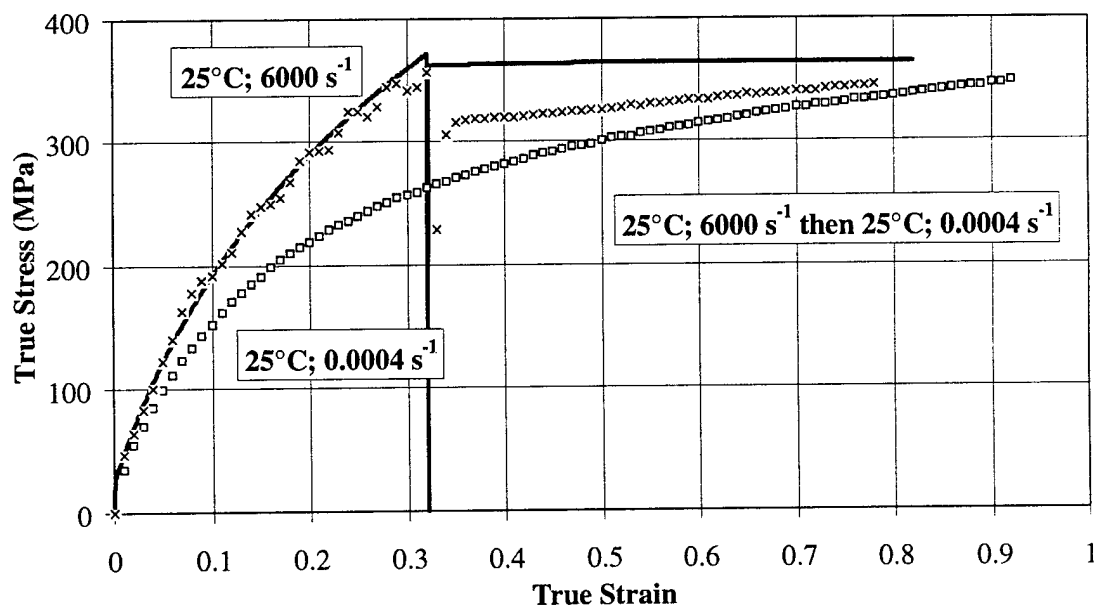


Figure V.55: Strain rate sequence predictions for OFHC Cu using the McDowell model. Solid lines represent the model predictions, while symbols represent experimental data.

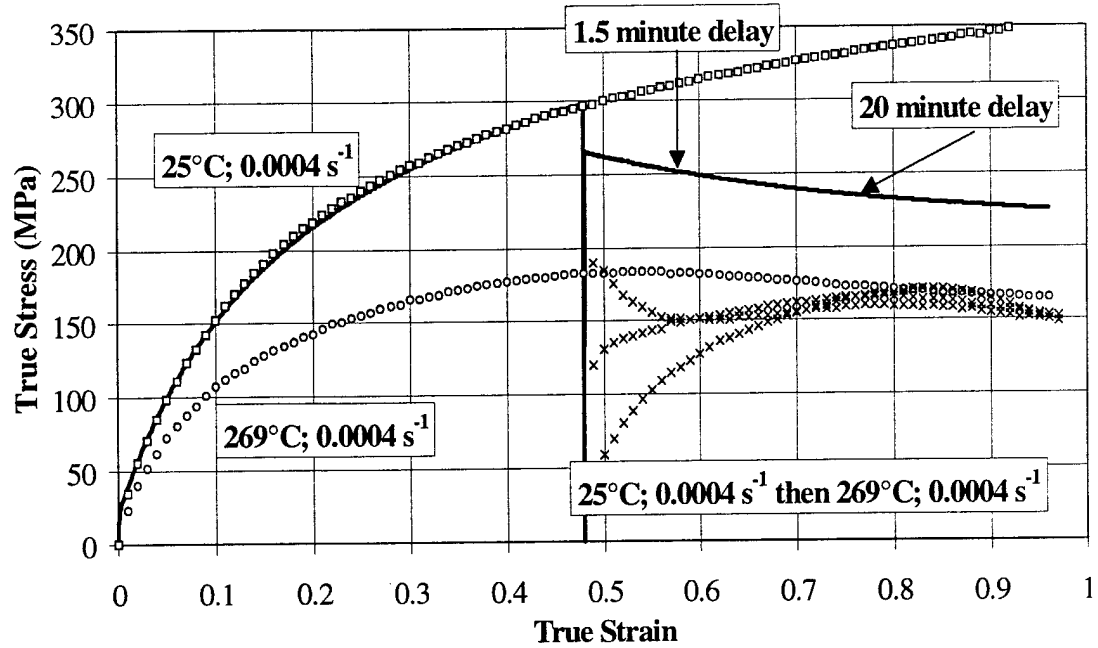


Figure V.56: Temperature sequence predictions for OFHC Cu using the McDowell model. Solid lines represent the model predictions, while symbols represent experimental data.

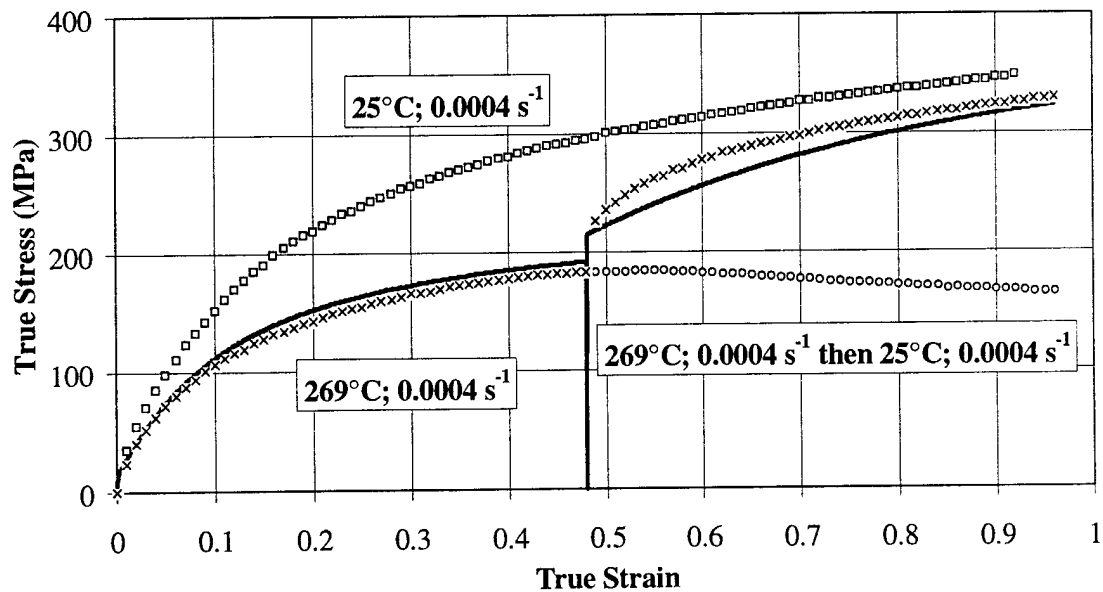


Figure V.57: Temperature sequence predictions for OFHC Cu using the McDowell model. Solid lines represent the model predictions, while symbols represent experimental data.

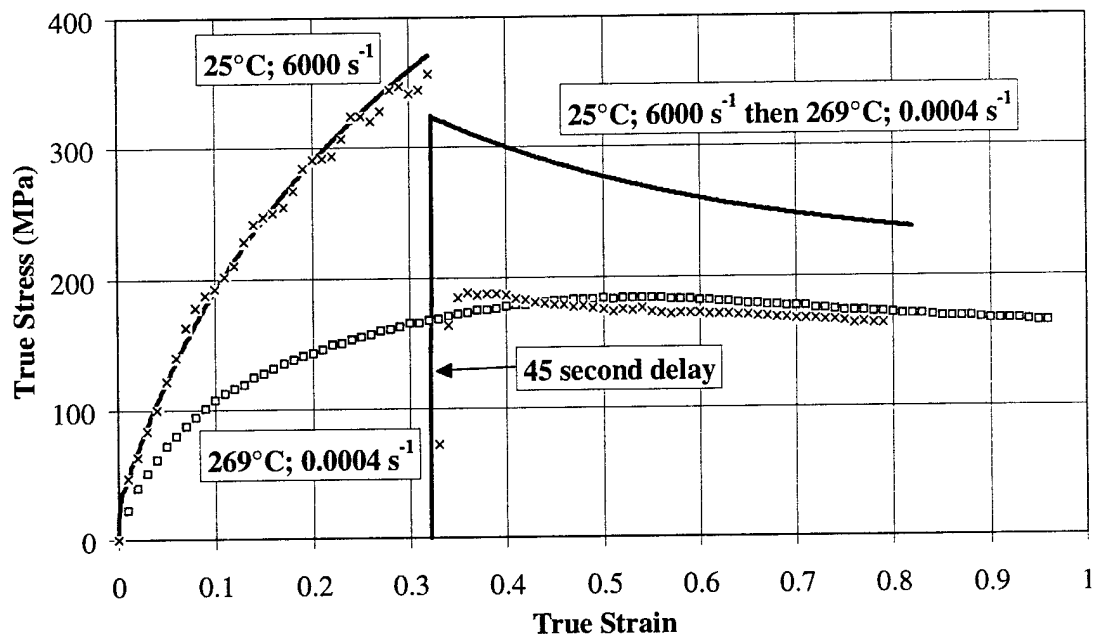


Figure V.58: Strain rate and temperature sequence predictions for OFHC Cu using the McDowell model. Solid lines represent the model predictions, while symbols represent experimental data.

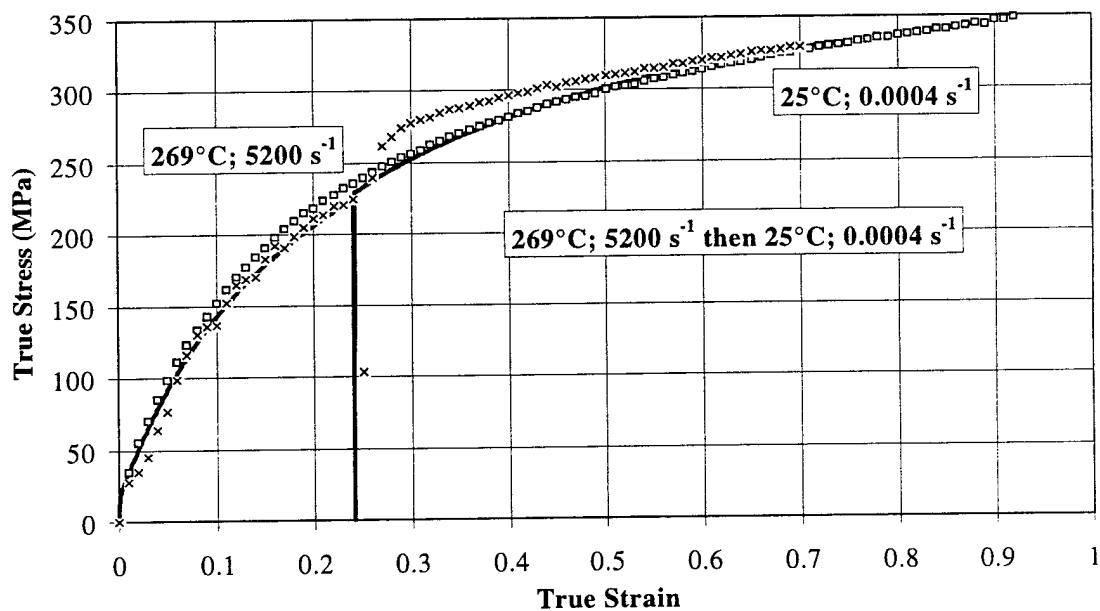


Figure V.59: Strain rate and temperature sequence predictions for OFHC Cu using the McDowell model. Solid lines represent the model predictions, while symbols represent experimental data.

V.4.5.5 McDowell Model Correlation to Data (high strain rate)

The McDowell model was correlated to the very high strain data to determine the ability of the model to correctly account for the extremely high strain rate hardening. The model parameters were determined through optimization to the same isothermal, constant strain rate data as before, with the addition of the high strain rate data, 692820 s^{-1} at 298°C and 461°C (Frutschy and Clifton, 1988). The correlation with these data are shown in Fig. V.21. The model under predicts the sharp initial rise in flow stress and then under predicts the flow stress saturation levels. The correlation to data indicates that the model lacks the correct form applicable for these higher strain rate mechanisms.

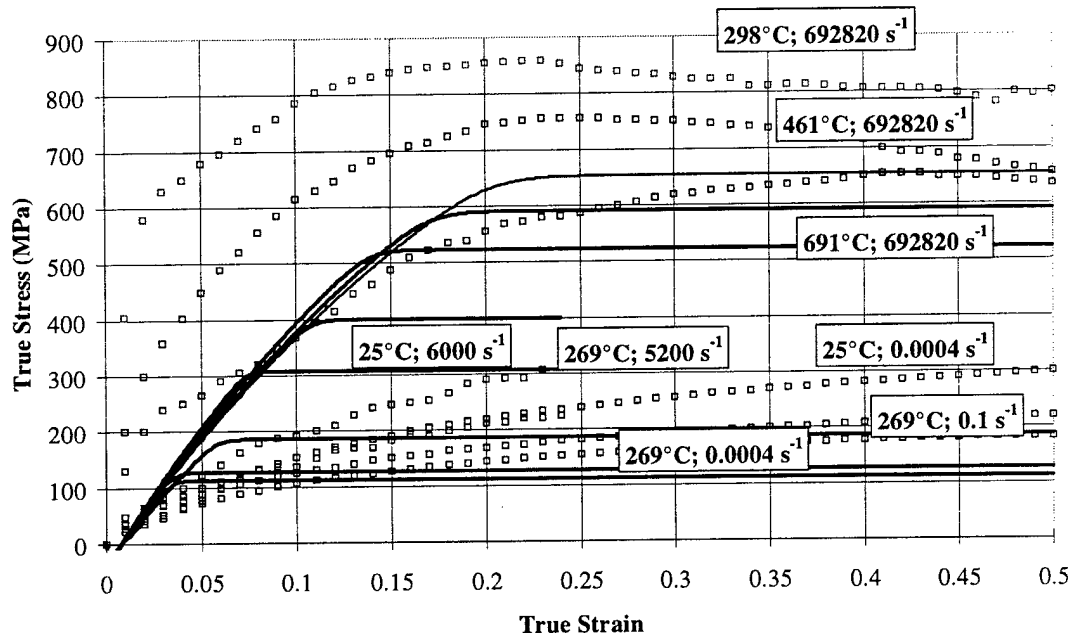


Figure V.60: Correlation to OFHC Cu compression data including the very high strain rate data 692820 s^{-1} at 298°C and 461°C (Frutschy and Clifton, 1988). The model correlations are shown using solid lines, while the experimental data are shown with open symbols. The optimization was conducted only using the data to a strain of 0.5.

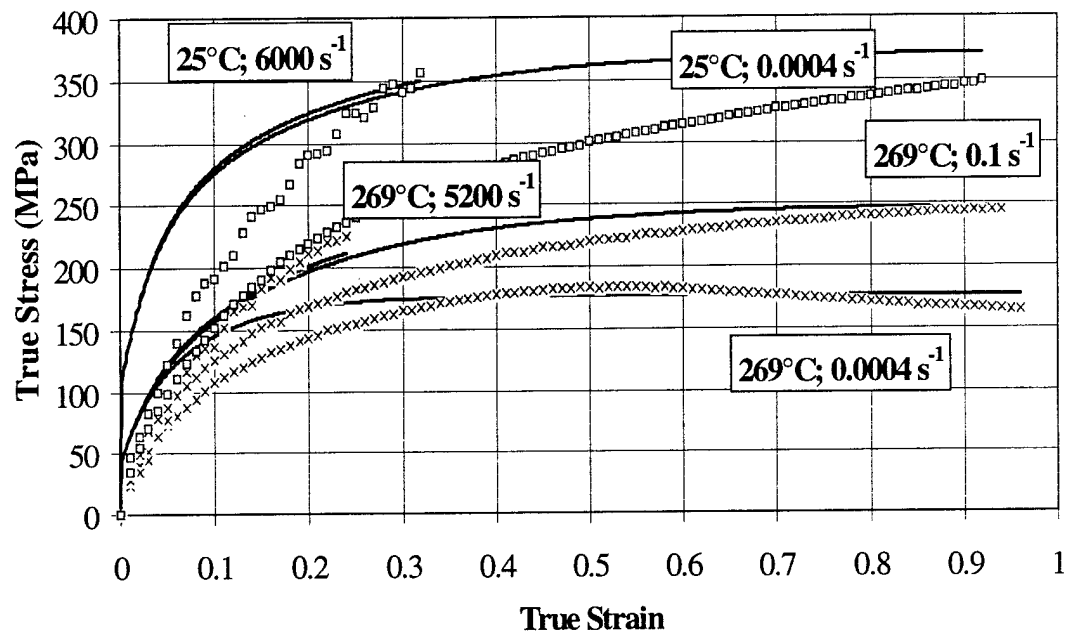


Figure V.61: Correlation to OFHC Cu compression data including the very high strain rate data 692820 s^{-1} at 298°C and 461°C (Frutschy and Clifton, 1988). The model correlations are shown using solid lines, while the experimental data are shown with open symbols. The optimization was conducted only using the data to a strain of 0.5.

V.5 Discussion

OFHC Cu exhibits many macroscopic characteristics which models must capture to accurately predict material response. These include the primary material dependencies on temperature and strain rate and, additionally, dynamic softening, resulting in an actual reduction in flow stress at 269°C, static recovery, and both temperature and strain rate history effects. The precise nature of the transition from one deformation state to another is not fully understood, but it was apparent that the changes associated with recrystallization affected the transition. As the predictive accuracy requirements for models has increased, so to has the need to include these additional features.

Flow stress is not only a function of instantaneous values of strain, strain rate and temperature, but exhibits transients, and in some cases, different asymptotic flow stress levels. A mechanical equation of state model clearly cannot capture these sequence effects. The empirical Johnson/Cook and Zerrilli-Armstrong constitutive models correlate the primary temperature and strain rate dependencies in OFHC Cu, but do not have the capability to predict sequence effects. The instantaneous response of a material depends on its current state, which in turn depends on the entire history of deformation. The MTS, BCJ-SNL, and McDowell models utilize one, two, and multiple internal variable models, respectively. The ISV evolutionary equations account for prior deformation and describe the changes in internal structure which permits transient flow stress behavior to be modeled. The McDowell and BCJ-SNL models, with internal variables, have enhanced predictive

capability relative to the MTS model for sequence effects. OFHC Cu demonstrates significant softening due to static restoration at 269°C. The MTS model does not contain any static thermal recovery terms, so does not predict any recovery while holding at elevated temperature (Figs. V.32 - V.34). The BCJ-SNL model contains static thermal recovery in both α and κ evolution equations and does predict some recovery (Figs. V.40 and V.42) but the amount is under-predicted (Fig. V.21). The isotropic static thermal recovery parameter magnitude, R_s , was too small as a result of using only constant, isothermal data for determining the parameters. The static thermal recovery terms incorporated in the BCJ-SNL model result in improved prediction of the transients occurring at 269°C. Both models best predict temperature decrease sequences, 269°C to 25°C at 0.0004 s⁻¹ (Figs. V.30 and V.41), since little or no recovery occurs at 25°C (McQueen, 1975). The McDowell model results in the lowest objective function, representing the closest correlation to the experimental data. The kinematic variable was generally not used by the optimization process to achieve the best fit. The full amount of restoration demonstrated by OFHC is not predicted by the available static thermal recovery term.

OFHC also exhibits dynamic softening at 269°C, which may be in part due to dynamic recrystallization. The greatest error associated with the correlation of the ISV models with the constant strain rate, isothermal data results from not accounting for the flow stress reduction at 269°C. The evolutionary equations for all ISV models saturate to zero, and do not become negative, which would be necessary for a flow stress reduction. Consequently, the MTS model predicts a transient behavior which demonstrates an initial

sharp increase or decrease in flow stress, staying between the two constant curves (Figs. V.27-V.31), then either an asymptotic approach to the higher constant curve (Figs. V.27, V.28, and V.30), or an immediate saturation in flow stress (Figs. V.29 and V.31). The immediate saturation is due the structure of the evolution equation for the ISV, $\hat{\sigma}$, which does not become negative.

Terms representing static and dynamic restoration processes must be included to accurately predict OFHC Cu characteristics. Capturing these features may not be sufficient. Internal stresses in a material are created by many different obstacles to dislocation motion. They have a variety of shapes and resistance, and have typically been categorized into short and long range. Peierls barriers and forest dislocations are weak obstacles which can be overcome with the assistance of thermal activation. Strong obstacles to dislocation motion are cell walls, grain boundaries, twins, etc. The effects of long range internal stresses can be distinguished from those of short range by their respective slow and fast kinetics (Lowe and Miller, 1986). A single internal state variable cannot account for these different kinetics.

The optimization procedure seems particularly effective in obtaining a parameter set which results in the best fit to experimental data. The objective function was defined as the minimization of the error norm, sum of the square of the difference between predicted and actual data. A comparison of the optimized objective function values, the error norms for each model, are shown in Table V.7. The error norms are normalized to the smallest value. The error value using parameter sets obtained using the traditional graphical technique is compared to that obtained using the optimized parameters. The optimized values all

produced much smaller error norms.

Table V.7: COMPARISON OF ERROR NORM
(normalized to smallest value).

Model	Traditional Technique	Optimized
Johnson/Cook	9200	30
Zerilli-Armstrong		30
MTS	14.4 ¹ 24.0 ²	9.0
BCJ-SNL		1.6
McD		1.0

1 (Follansbee and Kocks, 1988); 2 (Gourdin and Lassila, 1991)

CHAPTER VI

IMPROVED CONSTITUTIVE MODELS

VI.1 Modeling Approaches

Tremendous progress has been made, and is continuing, in the accuracy and precision with which material testing is now conducted. Improvements in electronics, automatic controls, digital measurements and microprocessors have resulted in a radical transformation in the capability to characterize material behavior. These testing improvements permit the precise determination of the macroscopic responses, including the transients which occur during sequences of deformation conditions. The consistency of experimental data obtained by different investigators also has improved. Additional improvements in the ability to observe actual deformation mechanisms in the microstructure has allowed the increased linkage between the macroscopic behavior and the responsible physical mechanisms. Despite the great progress that has been made in identifying actual microstructural deformation mechanisms, the understanding of viscoplasticity has not reached the point where the choice of the proper constitutive relation at any state is absolutely known. The choice of the relation remains a matter of some uncertainty and differing opinion. The particular form of the function must be formulated from the measured material behavior with an underlying understanding of the controlling deformation mechanisms.

The improvements in test procedures and microstructural examinations have allowed the development of more complex models. Additional variables are incorporated to account for the increased knowledge of physical deformation mechanisms. The limitations on capability to accurately obtain the parameters for these variables and the computing power necessary to utilize these resulting complex models are fading. In general, most existing constitutive models are too simple to represent all first order relevant mechanisms observed, for example, in this study of OFHC Cu.

Model parameters cannot be correctly identified unless a sufficient number of tests results are available which embrace a significant range of variation for each of the parameters. The utility of a predictive model is the ability to extrapolate beyond the test data available. Material constants are needed, versus the parameter determination for a particular set of data, which would then require several sets of constants suitable for a domain of variation. Parameter identification remains a difficult task. Tests are expensive and time consuming to conduct. Each model requires a variety of test matrixes with varying conditions.

This chapter explores issues related to the determination of the proper form of constitutive models and restoration functional forms. The first section details the method and results of the statistical design of experiment approach which was used to quantify the relative differences of the effects various parameters have on the minimization of the error between experimental data and modeled predictions. The next section investigates the use of artificial neural networks, which was employed for pattern recognition. The final sections

detail efforts to include restoration processes which result in flow stress softening. A methodology used for improving constitutive models is shown in Fig. VI.1. The approach incorporates the capabilities of advanced computational algorithms. This methodology may reduce the time and reduce the effort currently necessary for the creation of improved constitutive models. The process begins with the set of experimental data of interest. The particular data set requirements depends upon the range of desired predictive capabilities. Generally, the range of deformation conditions should be as broad as possible and should include as much of the deformation conditions of interest. The possibility of using a reduced set of experimental data, while retaining an accurate predictive capability, is one of the subjects of this chapter. An existing model or model hypothesis which may be applicable to the available data set is utilized in the second step. Competing model hypotheses or functional forms for particular attributes of interest can be evaluated. The capability of the chosen model to accurately capture the behavior of the material over the experimental deformation conditions can be determined. The third step depends upon the particular desired result. For the evaluation of competing models or functional forms of material representation, this step involves the optimization of the various material parameters corresponding to the experimental data. The optimization strategy maximizes the predictive capability of the chosen model. Lack of sufficient model correlations to experimental data is indicative of an inherent model shortcoming. Either the chosen model contains an incorrect functional form, representing a physical deformation mechanism, or the model needs an additional mechanism included. Model correlations within a selected threshold, indicate the

chosen model contains the proper form to accurately predict material behavior within the current deformation conditions. When the number of factors being evaluated is greater than two, a statistical design of experiments approach reduces the number of calculations necessary for the comparison and determination of the optimal set of factors. When a particular functional form is unknown, then this step involves the use of general equation forms through which the optimization strategy determines that functional form with the greatest ability of reducing the objective function value. Through application of this design process, the optimal parameter set, the experimental tests necessary, or the selection of improved functional forms for competing mechanisms (deformation mechanism maps) can be achieved.

Constitutive Model Development

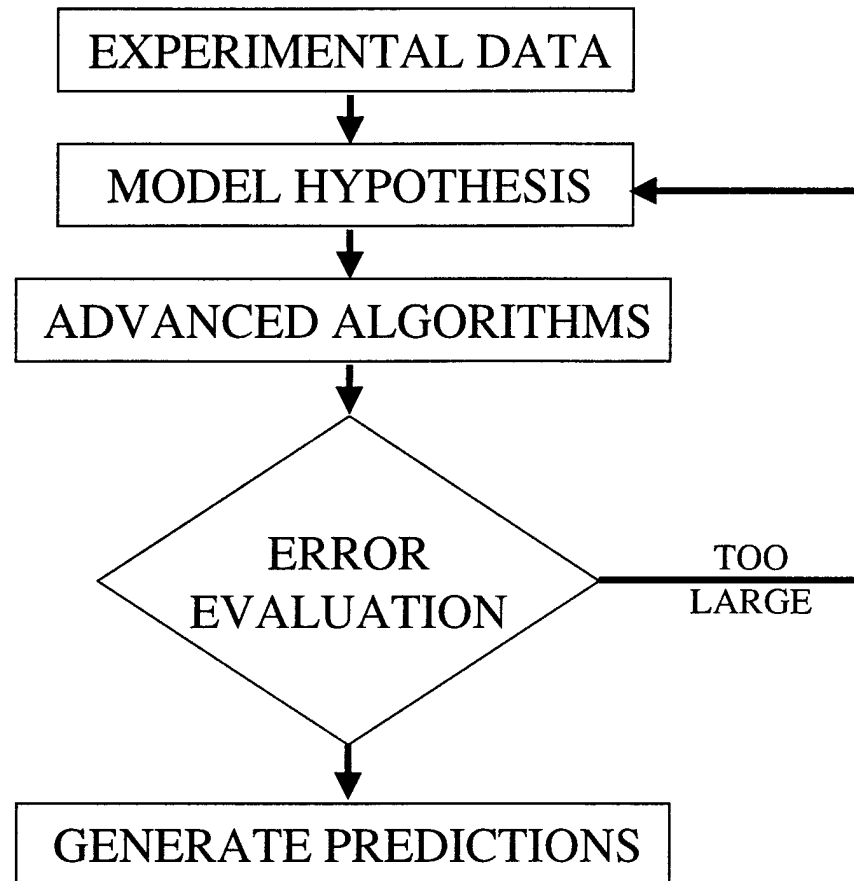


Figure VI.1: Flow chart for constitutive model development using advanced algorithms.

VI.2 Design of Experiments

The study of a large number of factors and the selection of the optimum combination of factor levels is an area where the application of statistical design of experiments (DOE) is readily suited. DOE is extensively used in manufacturing and product design. Parameter design is a method of experimentation which can be used for creating a product through the selection of the optimum conditions of controllable factors so that the product is least sensitive to uncontrollable factors. The earliest use of statistical analysis of physical experiments was applied by Sir Ronald Fisher (1935a and 1935b). Analysis of variance procedures were derived from these initial efforts for the interpretation of experimental data (Box *et al.*, 1978). The Taguchi methodology was introduced to the United States by Dr. Genichi Taguchi in 1980 (Taguchi, 1980) and who popularized the methodology for quality engineering. Parametric sensitivity studies for material constitutive model development (crystal plasticity) have been conducted by Horstemeyer (1995) using the DOE approach.

The statistical DOE strategy characterizes the effects of many parameters efficiently. This technique extracts relevant data from a relatively small number of “experiments”. The use of orthogonal arrays drastically reduces the number of combinations of “experiments” necessary to explore all the possibilities. Seven factors, each of which have two possible levels, would necessitate a total of $2^7 = 128$ different “experiments” to complete a full factorial set of calculations comparing all of the possible combinations of factors and levels. The efficient DOE approach only requires eight experiments to be conducted to obtain the relative effect, and the optimum combination, of the factors and levels. This reduction in the

number of experiments, or simulations, is possible through the use of orthogonal arrays.

Orthogonal arrays are a matrix of numbers arranged in columns and rows; each column represents a specific factor or condition that can be changed from experiment to experiment; each row represents the state of the factors in a given experiment. This matrix is called orthogonal because the levels of the various factors are balanced and can be separated from the effects of the other factors within the experiment. Table VI.1 contains an example of an L_8 orthogonal array. An $L_8 (2^7)$ orthogonal array is commonly used in design of experiments. There are seven factors and two levels per factor, which requires a total of eight experiments.

Table VI.1 ORTHOGONAL ARRAY

Experiment	A	B	C	D	E	F	G	Results
1	1	1	1	1	1	1	1	R_1
2	1	1	1	-1	-1	-1	-1	R_2
3	1	-1	-1	1	1	-1	-1	R_3
4	1	-1	-1	-1	-1	1	1	R_4
5	-1	1	-1	1	-1	1	-1	R_5
6	-1	1	-1	-1	1	-1	1	R_6
7	-1	-1	1	1	-1	-1	1	R_7
8	-1	-1	1	-1	1	1	-1	R_8

The experiments, optimization iterations in this thesis, are identified as 1 - 8, the factors as A - G and the two levels as 1 and -1. A DOE exercise does not have to use all the columns, representing different factors, in the orthogonal array; if all are used it is known as a saturated orthogonal array. The DOE approach eliminates the preconceived biases investigators may have or acquire during an investigation.

The statistical DOE procedure is an effective means of evaluating the effects of various forms and terms in constitutive models. Seven different options for the McDowell model, described in Chapter V.5, are evaluated to obtain the optimal combination and to gain insight on the relative importance of the terms.

VI.2.1 DOE Analysis Factors

The McDowell model, described in Chapter V.5, was used as an example to determine the relative importance of seven factors for obtaining the optimal correlation between experimental data and model predictions. In this section, the factors and the corresponding two levels for each factor are described.

VI.2.1.1 Temperature Dependence

Different functional forms have been proposed for the temperature dependence associated with dislocation interactions. The temperature dependence of the isotropic hardening variable has two possible forms. The first is used in equation V.37 and is given

by either an exponential or hyperbolic tangential functional form

$$\Sigma(T) = \begin{cases} [A_1 - A_2 T + A_3 \exp(-A_4 T)] \\ \text{or} \\ [A_1 - A_2 \tanh(A_3(T - A_4))] \end{cases} \quad (\text{VI.1})$$

and the second is used in equation V.38 which has the similar options as above

$$\chi^0(T) = \begin{cases} [B_1 - B_2 T + B_3 \exp(-B_4 T)] \\ \text{or} \\ [B_1 - B_2 \tanh(B_3(T - B_4))] \end{cases} \quad (\text{VI.2})$$

Figure VI.2 shows the how the above temperature factor values vary over a range of temperatures. The constants for each relationship (Equations VI.1 and VI.2) were obtained from optimization to isothermal, constant true strain rate experiments. The temperature factor for χ_1 remains constant for all temperatures. The solid symbols reflect the values corresponding to the exponential format while the open symbols show the hyperbolic tangent format. The temperature factor for χ_2 decreases with increasing temperature. The two levels for this factor, temperature dependence form for isotropic variables, were a hyperbolic

tangent form and an exponential form.

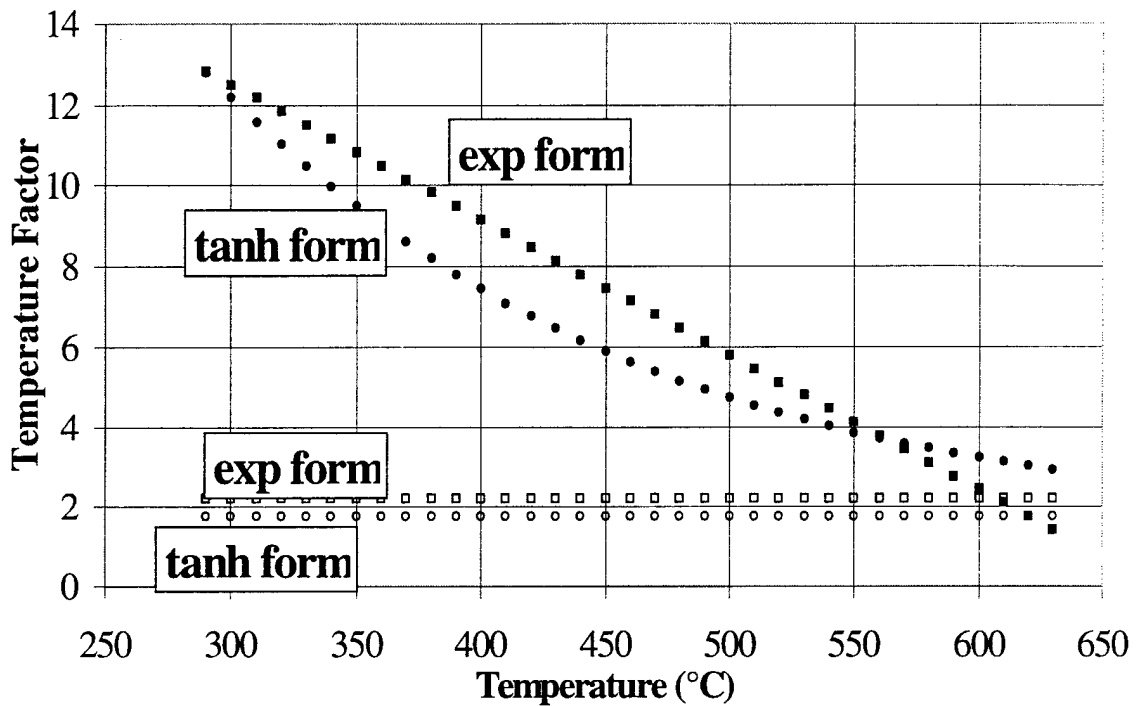


Figure VI.2: Temperature factor variance with temperature. Solid symbols reflect the dependence for χ_2 and the open symbols for χ_1 .

VI.2.1.2 Isotropic Variable Saturation

The optimization process permits the establishment of a number of constraints. This capability was used to establish the relative saturation magnitudes corresponding to the two isotropic variables. The relative magnitudes of obstacles to dislocation motion are typically categorized into short range and long range as discussed in Chapter II. The short range

obstacles are relatively easy to overcome and result in a lower saturation level, while the long range obstacles require a higher level. The two levels for the relative saturation magnitudes are established through the use of the constraint: $\chi_2 > \chi_1$ and $\chi_2 < \chi_1$.

VI.2.1.3 Kinematic Variable

The kinematic variable factor determines the utility of having a kinematic variable included, as an ISV in the McDowell model. The levels for this factor are obtained by specifying whether the parameter C is set, $C = 0$, or allowed to obtain values during the optimization process.

VI.2.1.4 Isotropic Variable Evolution Rate

The multiple ISV's formulation is often utilized by specifying the variables in terms of the obstacle barriers. The two ISV's approach, used to describe the internal structure of material, can account for the rapidly evolving, short range flow stress characteristic of initial yielding behavior and the slowly evolving long range flow stress contribution to the fully developed plastic flow regime. The short range obstacles are relatively easy to overcome and result in a faster kinetics, while the long range obstacles require a slower evolution rate. The two levels for the relative evolution rates are established through the use of the constraint: $(\chi\mu)_2 > (\chi\mu)_1$ and $(\chi\mu)_2 < (\chi\mu)_1$.

VI.2.1.5 Isotropic Variable Activation Energy

The activation energy varies for different deformation mechanisms. The activation energy for χ_i is used as a factor to obtain the necessity for inclusion in the evolution equations. The levels for this factor are obtained through specifying the value on the magnification parameter, ψ_χ is set, $\psi_\chi = 0$, or allowed to obtain values during the optimization process.

VI.2.1.6 Kinematic Variable Activation Energy

The activation energy varies for different deformation mechanisms. The activation energy for χ_i is used as a factor to obtain the necessity for inclusion in the evolution equations. The levels for this factor are obtained through specifying the value on the magnification parameter, ψ_α is set, $\psi_\alpha = 0$, or allowed to obtain values during the optimization process.

activation energy for α

VI.2.1.7 Variation in Isotropic Variable Activation Energy

Activation energy decreases with applied stress (Kocks and Mecking, 1980 and Krausz and Krausz, 1992). The kinetics of recovery increases as the internal energy, the

driving force for restoration, increases. The rate of softening, shown in Fig. IV.15, demonstrates the relationship over time. The rate of softening generally decreases with time. The variation in activation energy with increasing χ_i was established as the factor. The form for this relationship is given by

$$\dot{\chi}_i = \mu_{\chi_i} [\bar{\chi}_i - \chi_i] |\dot{\epsilon}^p| + \frac{\chi_i}{\mu_{\chi_i} \bar{\chi}_i} \frac{\partial(\mu_{\chi_i} \bar{\chi}_i)}{\partial T} \dot{T} - \mu_{\chi_i} \bar{\chi}_i (\chi_i)^{L_{\chi_i}} \psi_{\chi} \exp\left(-\frac{\Delta Q_{\chi} - V_A \chi_i}{kT}\right) \quad (VI.3)$$

where the activation energy, ΔQ_{χ} , is reduced by the term $V_A \chi_i$. The parameter V_A is the factor with levels obtained through specifying the value on the magnification parameter, V_A is set, $V_A = 0$, or allowed to obtain values during the optimization process.

VI.2.2 Macroscopic Responses

The effectiveness of the various levels were determined by the macroscopic model predictions relative to actual experimental data. Five isothermal, constant true strain rate compression experiments were used: 25°C, 0.0004 s⁻¹ and 269°C, 0.1 s⁻¹ both to a strain of 1.0, 25°C, 6000 s⁻¹ and 269°C, 5200 s⁻¹ both to a strain of 0.3, and 269°C, 0.0004 s⁻¹ to a strain of 0.5, which is prior to the dynamic recrystallization softening. The response used is the weighted sum of the error, between predicted value and data, determined for each 0.01

strain, squared. The weighting equalizes the total effect from each curve. Each DOE experiment results in a response. From the L_8 array,

$$[R] = [P] [A] \quad (VI.4)$$

where $[R]$ is the response matrix corresponding to the objective function for each optimization, $[A]$ is the output matrix and provides the relative influence of each factor, and $[P]$ is the parameter matrix.

$$[R] = \begin{bmatrix} R_1 \\ R_2 \\ R_3 \\ R_4 \\ R_5 \\ R_6 \\ R_7 \\ R_8 \end{bmatrix}, \quad [P] = \begin{bmatrix} +1 & +1 & +1 & +1 & +1 & +1 & +1 \\ +1 & +1 & +1 & -1 & -1 & -1 & -1 \\ +1 & -1 & -1 & +1 & +1 & -1 & -1 \\ +1 & -1 & -1 & -1 & -1 & +1 & +1 \\ -1 & +1 & -1 & +1 & -1 & +1 & -1 \\ -1 & +1 & -1 & -1 & +1 & -1 & +1 \\ -1 & -1 & +1 & +1 & -1 & -1 & +1 \\ -1 & -1 & +1 & -1 & +1 & +1 & -1 \end{bmatrix}, \quad \text{and} \quad [A] = \begin{bmatrix} A_1 \\ A_2 \\ A_3 \\ A_4 \\ A_5 \\ A_6 \\ A_7 \end{bmatrix} \quad (VI.5)$$

The parameter matrix $[P]$ in Equation VI.4 has an equal number of levels in each column. This provides the statistical balance in the orthogonal array. The response matrix $[R]$ contains the results for the eight optimizations. The mean of the results from the DOE analysis is given by the output matrix $[A]$. These values do not have physical significance, just statistical significance in expressing the relative influence of the associated factors on the response matrix, which is the ability to accurately predict the isothermal, constant true strain rate response of OFHC Cu. The matrix of outputs, $[A]$ is determined by transposing the parameter matrix $[P]$ and using the response matrix, $[R]$, both of which are known.

Table VI.2 PARAMETER MATRIX

Opt #	Temp	$\bar{\chi}_i$	α	μ_{χ_i}	$\left(\frac{Q}{k}\right)_\chi$	$\left(\frac{Q-V_A\chi}{k}\right)_\chi$	$\left(\frac{Q}{k}\right)_\alpha$
1	tanh	$2 < 1$	yes	$2 < 1$	yes	yes	yes
2	tanh	$2 < 1$	yes	$1 < 2$	no	no	no
3	tanh	$1 < 2$	no	$2 < 1$	yes	no	no
4	tanh	$1 < 2$	no	$1 < 2$	no		
5	exp	$2 < 1$	no	$2 < 1$	no		no
6	exp	$2 < 1$	no	$1 < 2$	yes	no	
7	exp	$1 < 2$	yes	$2 < 1$	no	no	yes
8	exp	$1 < 2$	yes	$1 < 2$	yes	yes	no

Table VI.3 RESPONSE MATRIX

Optimization #	Responses (Objective Function)
1	540000
2	150000
3	230000
4	210000
5	660000
6	355000
7	570000
8	820000

The output matrix was determined from the parameter matrix, where each factor level was converted to a plus or minus 1 value, and the response matrix. Since the values in the output matrix are relative to each other, they were normalized to the largest value to assess the relative level of influence of each factor. Figure VI.3 shows the results of this analysis, where the factor labels, numbers, correspond to the parameters listed in Table VI.4. The temperature dependence was the most influential parameter and the variation in isotropic hardening activation energy second. The remaining parameters had relatively minor influence.

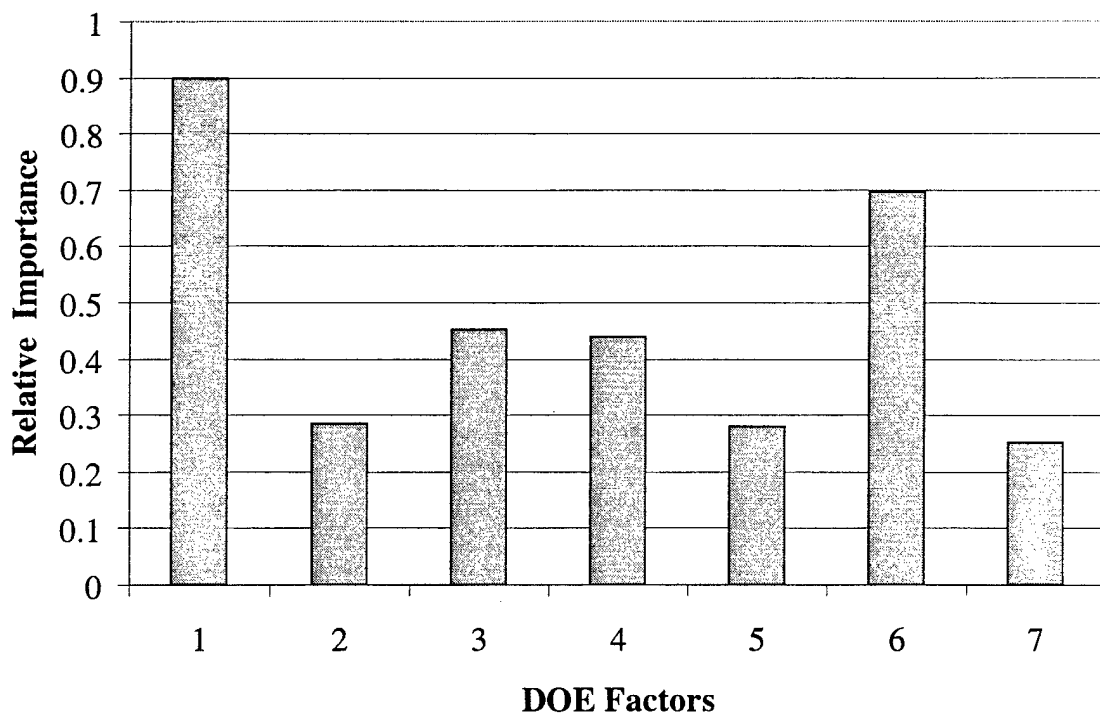


Figure VI.3 DOE results showing the relative importance that each factor has on the minimization of the objective function. The correlation of factor numbers to parameters are given in Table VI.4.

This DOE analysis also provides the information necessary to obtain the optimum combination of factors to achieve the best, minimum objective function, one where the error between the experimental data and the model predictions is the least. In accordance with this data, the optimal factor set includes temperature dependence with hyperbolic tangent function form, isotropic saturation level for 1 greater than 2, without a kinematic variable, isotropic rate term greater for 2 than 1, without the isotropic activation energy, and kinematic activation energy term. This analysis was demonstrated with an optimization iteration using these parameters, with the resulting objective function being 0.6 less than the minimum of those eight conducted for the DOE.

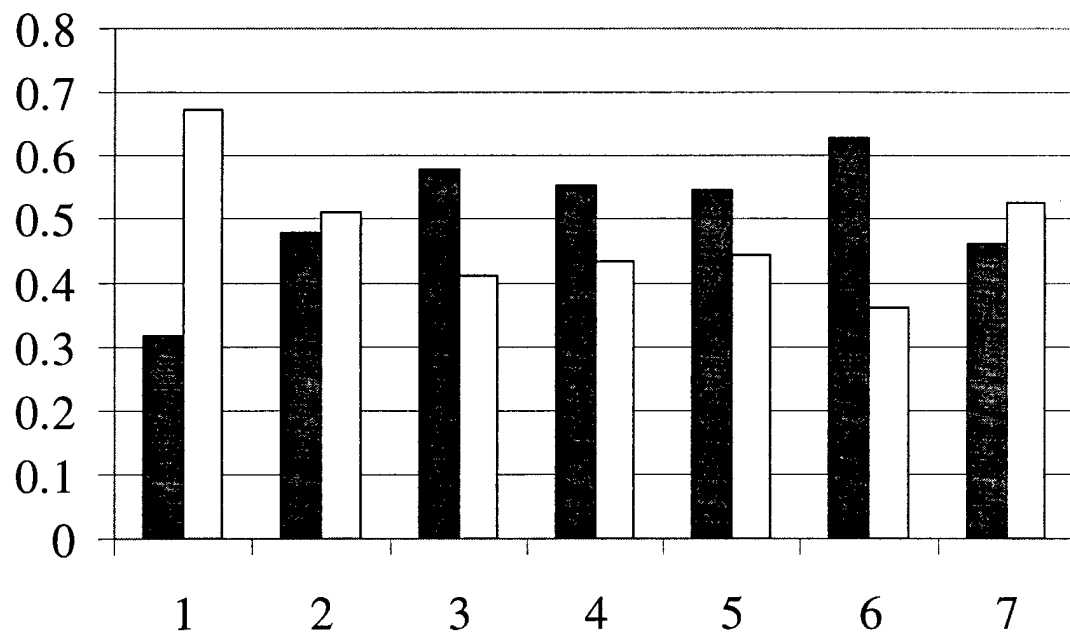


Figure VI.4: DOE results showing the relative importance each factor has on the objective function. The correlation of factor numbers to parameters are given in Table VI.4.

Table VI.4 CORRELATION OF FACTOR AND PARAMETER

Factor	1	2	3	4	5	6	7
Parameter	Temp	$\bar{\chi}_i$	α	μ_{χ_i}	$\left(\frac{Q}{k}\right)_{\chi}$	$\left(\frac{Q-V_A\chi}{k}\right)_{\chi}$	$\left(\frac{Q}{k}\right)_{\alpha}$

VI.3 Artificial Neural Networks

Material behavior is complex and difficult to accurately model. Due to the large number of dislocation processes which occur during plastic deformation, Mecking (1980) expressed that it is impossible to predict the exact evolution of dislocation structure under different deformation conditions. Another means of correlating material behavior to different conditions is through the use of artificial neural networks (ANN). Neural network models are extremely efficient in computational problems. The concept of ANN's is based on a model of the human brain. Within the cerebral cortex, lies a very dense system of interconnected neurons which form a biological neural network. Each neuron within the network performs a simple processing function based on the accumulation of signals received from hundreds of other neurons through input paths. The capabilities of the brain is due to all the neurons that work together through their interconnections. As the brain accumulates information, the connections begin to modify and adjust in terms of transmission strength and conductance. This adjustment process constitutes learning in terms of pattern recognition.

An artificial neuron also gets input from other neurons or directly from the environment. The path connecting two neurons is associated with a certain variable weight which represents the synaptic strength of the connection. The input to a neuron from another neuron is obtained by multiplying the output of the connected neuron by the synaptic strength of the connection between them. The artificial neuron then sums up all the weighted inputs. Each neuron is associated with a threshold value and a squashing function. This

function is used to compare the weighted sum of inputs and the threshold value of that neuron. If the threshold value is exceeded, the neuron goes to the higher state. The output of the i^{th} neuron is transmitted to the other neurons and this procedure is repeated until the final state is reached. Through variation of the synaptic weights, according to an adaptive algorithm, the neural network learns capabilities in the sense that desired outputs are approximated.

ANN's have been used to predict material behavior. Mukherjee *et al.* (1995) used an ANN to predict the mechanical behavior of metal matrix composites. Experimentally observed behavior material behavior was modeled directly without the necessity of developing analytical expressions. A feedforward network with sigmoidal functions and back-propagation learning was used. Hwu *et al.* (1994) used an ANN to predict the flow stress of low carbon steel at elevated temperatures, for use during on-line control. A three layer, feedforward network with back-propagation learning was used.

ANN's are also being used for functional form approximation. Somolinos (1992) uses a functional link neural network to obtain representation of functions. By choosing a complete set of linearly independent functions, any arbitrary function can be represented. Draelos and Hush (1996) employed a constructive neural network algorithm for function approximation. Function approximation involves the modeling of an unknown function from a training set of input/output pairs that represent the function. Using nonlinear activation functions, neural networks can approximate highly nonlinear surfaces. The output of a single hidden layer network forms a linear combination of adaptable basis functions. Shukla, *et al.*

(1996) also develops an ANN for function approximation. Through this process, the functional form of experimental data can be determined. Clearly, if physics of certain processes to be modeled are understood in terms of reduced models, these can be used to constrain the training of a set of basis functions.

VI.4 Modeling Improvements

VI.4.1 BCJ-SNL Modeling Improvements (split parameters)

Consistent with the categorization of obstacles into long and short range, the ISV's for the BCJ-SNL model are split into components corresponding to a short and long range obstacle value. The resulting evolution equations are given by

$$\dot{\alpha}_1 = h_1 \mu(T) \dot{\epsilon}^p - \left[r_{s1}(T) + r_{d1}(T) |\dot{\epsilon}^p| \right] \alpha_1^2 \text{sign}(\alpha_1) \quad (\text{VI.6})$$

$$\dot{\alpha}_2 = h_2 \mu(T) \dot{\epsilon}^p - \left[r_{s2}(T) + r_{d2}(T) |\dot{\epsilon}^p| \right] \alpha_2^2 \text{sign}(\alpha_2) \quad (\text{VI.7})$$

$$\dot{\kappa}_1 = H_1 \mu(T) |\dot{\epsilon}^p| - \left[R_{s1}(T) + R_{d1}(T) |\dot{\epsilon}^p| \right] \kappa_1^2 \quad (\text{VI.8})$$

$$\dot{\kappa}_2 = H_2 \mu(T) |\dot{\epsilon}^p| - \left[R_{s2}(T) + R_{d1}(T) |\dot{\epsilon}^p| \right] \kappa_2^2 \quad (\text{VI.9})$$

The optimization strategy was repeated as described in Chapter V for the BCJ-SNL model. Data correlations are shown in Fig. VI.5 with the sequence predictions in Figs. VI.6 - VI.11. The correlations are improved for the split parameter case over the single set. The objective function value for the original "single" parameter case was 1.3 times larger than the split objective function value.

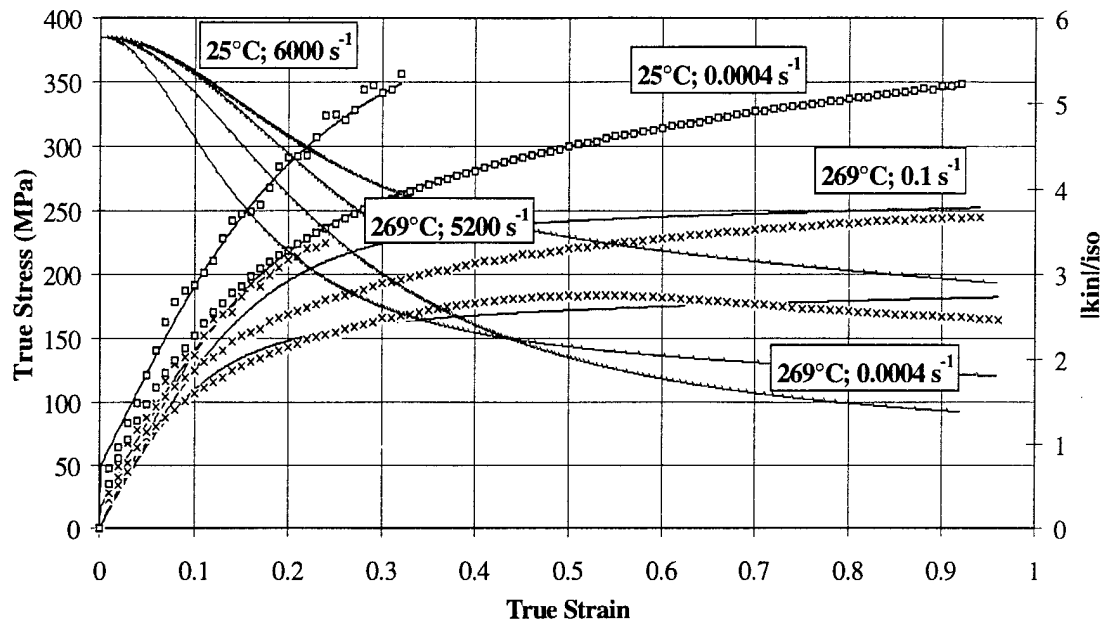


Figure VI.5: Correlation to OFHC Cu compression data using the BCJ-SNL model. The model correlations are shown using solid lines, while the experimental data are shown with open symbols. The ratio $|k|/\kappa$ are displayed using short dashed lines.

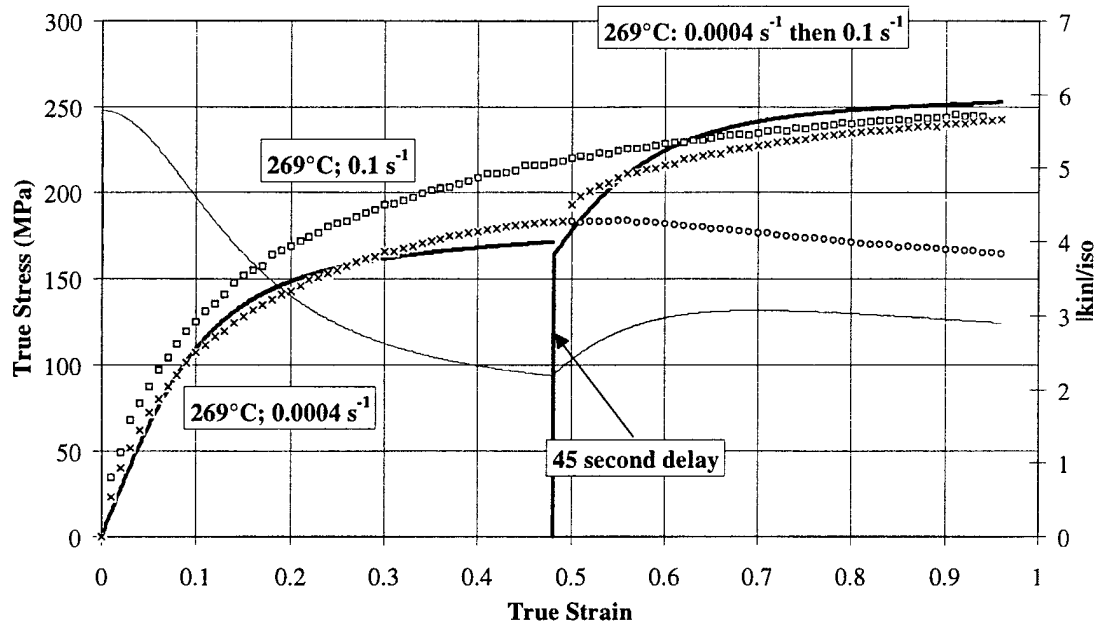


Figure VI.6: Strain rate sequence prediction for OFHC Cu using the BCJ-SNL model. Solid lines represent the model prediction, while symbols represent experimental data.

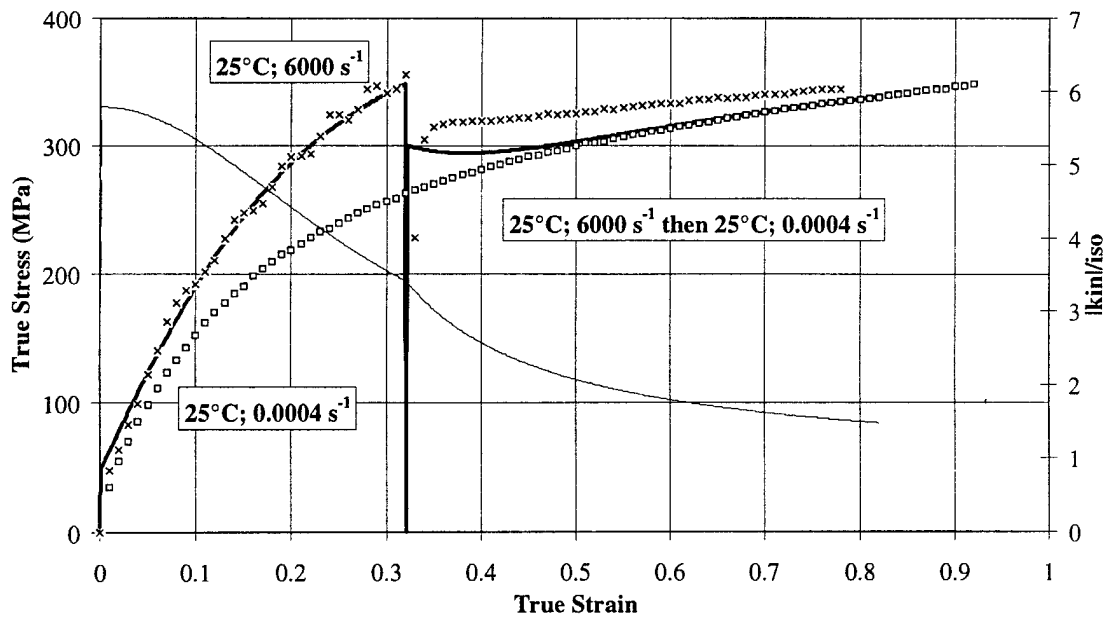


Figure VI.7: Strain rate sequence prediction for OFHC Cu using the BCJ-SNL model. Solid lines represent the model prediction, while symbols represent experimental data.

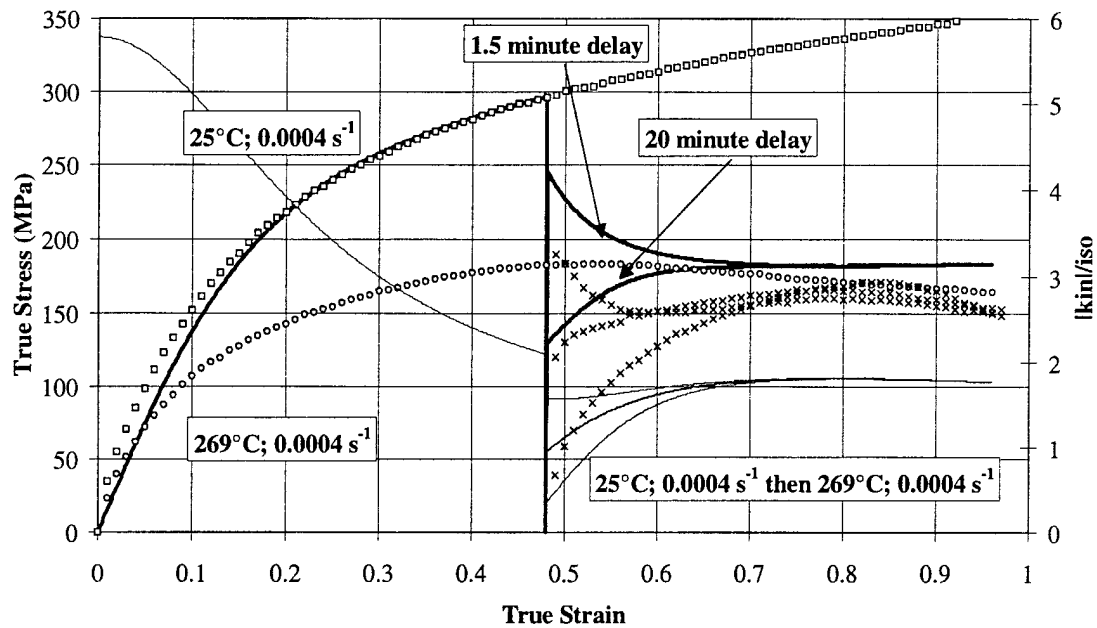


Figure VI.8: Temperature sequence prediction for OFHC Cu using the BCJ-SNL model. Solid lines represent the model prediction, while symbols represent experimental data.

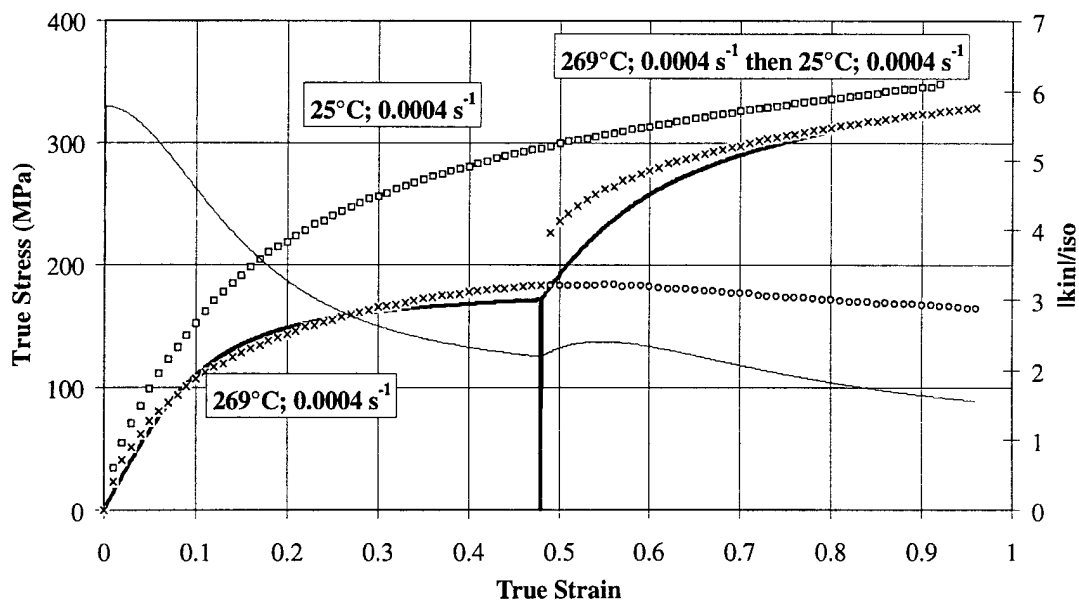


Figure VI.9: Temperature sequence prediction for OFHC Cu using the BCJ-SNL model. Solid lines represent the model prediction, while symbols represent experimental data.

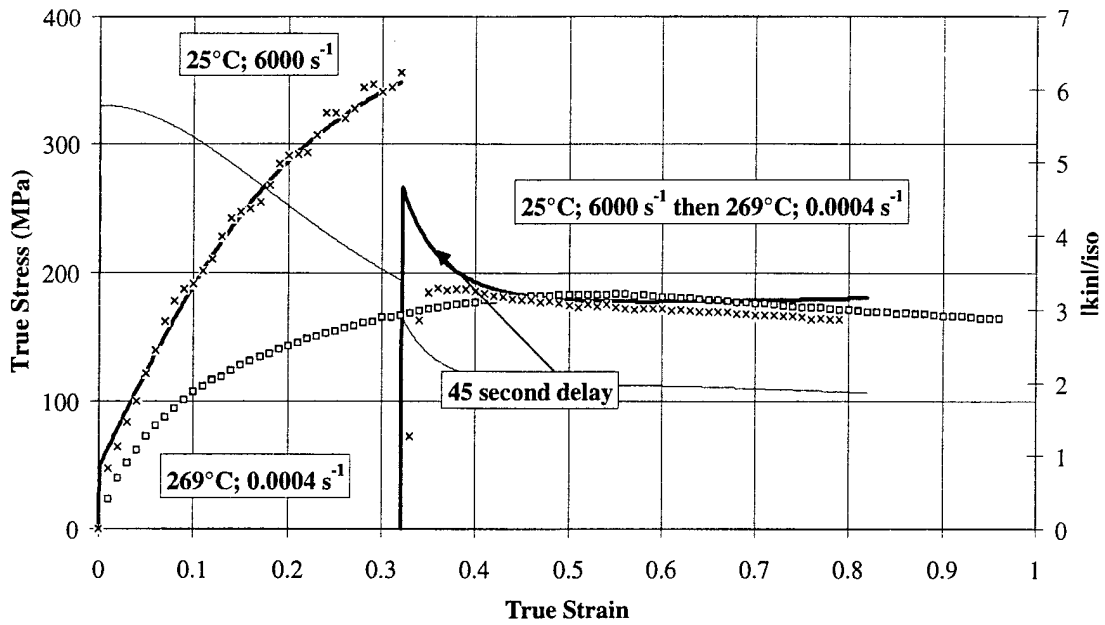


Figure VI.10: Strain rate and temperature sequence prediction for OFHC Cu using the BCJ-SNL model. Solid lines represent the model prediction, while symbols represent experimental data.

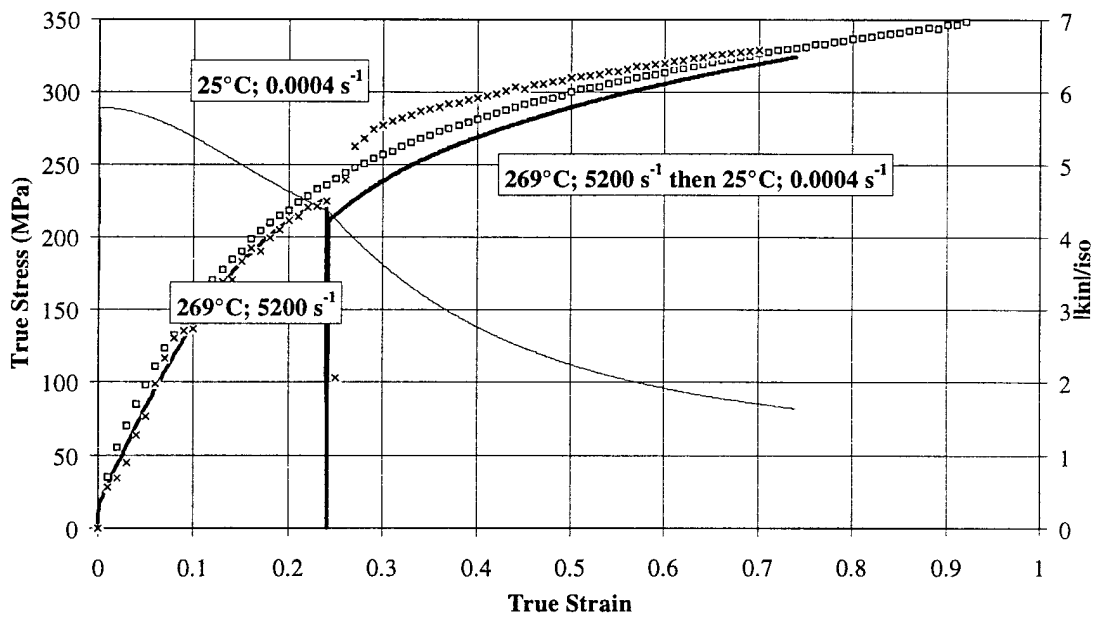


Figure VI.11: Strain rate and temperature sequence prediction for OFHC Cu using the BCJ-SNL model. Solid lines represent the model prediction, while symbols represent experimental data.

VI.4.2 Recrystallization Internal State Variable Modeling

None of the models described in Chapter V can capture the observed softening in the flow stress observed in OFHC Cu at relatively high temperature and low strain rates. This softening is attributed to recrystallization. Only the BCJ-SNL and McDowell models have the ability to include static recovery effects, which improve their predictive capabilities, but still do not fully capture either the dynamic softening nor the complete static restoration. A material softening term was necessary to account for the recrystallization processes. An additional term was included in both the BCJ-SNL and McDowell models representing the softened state of the material corresponding to the steady state following recrystallization, both static and dynamic.

During deformation of moderate or low stacking fault energy materials, like OFHC Cu, recovery mechanisms are inhibited from cross-slipping onto different glide planes by dislocations. The SFE of metals controls the relative rates of dislocation climb to form sub-boundaries. The lower the SFE, the less dislocations can climb which results in weak recovery and an increase in the local dislocation density which concentrates at cell walls. The concentration of dislocations causes the formation of polygonized dislocation cell structures. New grains nucleate at or near existing grain boundaries at dislocation pile-up sites, such as slip band and sub-boundary intersection points with grain boundaries. At these locations, dislocation gradients are high enough to force the lattice to minimize its free energy by reorienting itself and forming a new crystal. Dynamic recrystallization leads to grain refinement and the local elimination of large numbers of dislocations. The elimination

of large quantities of dislocations results in local softening and a reduction in material flow stress. The amount of softening which occurs is related to the decrease in the average dislocation density and to the size of the recrystallized grain. Eventually, a new steady state flow stress results which represents a balance between the rates of strain hardening and dynamic recovery with the sub-grains continually breaking up and reforming at an equilibrium spacing. This recrystallized steady material state is characterized by a reduction in the magnitude of hardening internal state variables which would have been achieved in the absence of recrystallization.

A critical accumulated plastic strain at which dynamic recrystallization starts, $\bar{\epsilon}_c^p$, is observed in experimental data. The onset of dynamic recrystallization is based on a material instability criterion which is dependent on a critical mean dislocation spacing (Busso, 1998). The equivalent plastic strain at which recrystallization begins is given by

$$\bar{\epsilon}_c^p = \frac{2}{\sqrt{3}} \frac{C_c}{\mu} \langle f_c S^* - S_0 \rangle \quad (\text{VI.10})$$

where S^* and S_0 characterize the isotropic deformation resistance of the material caused by dislocation density and grain and sub-grain effects. S_0 is the initial deformation resistance at zero strain, and S^* is the steady state deformation resistance. The constant, f_c , identifies the fractional amount of the steady deformation resistance, S^* , necessary for the start of recrystallization, μ is the shear modulus, and C_c is a constant. The critical strain for the

initiation of recrystallization, which identifies the state of sufficient internal stored energy, occurs shortly before the observance of a peak stress (Busso, 1998, Gottstein, *et al.*, 1991, and Blaz, *et al.*, 1983). The steady state flow stress depends on the steady state average grain size, L^* , and the initial average grain size, L_0 , as well as the temperature and strain rate.

$$S^* = X \left[\frac{\dot{\epsilon}^p}{\dot{\epsilon}_0} \exp\left(\frac{Q_R}{kT}\right) \left(\frac{L^*}{L_0}\right)^\omega \right]^{n_2} \quad (\text{VI.11})$$

where Q_R is the activation energy associated with recrystallization, ω , n_2 , and X are constants, and the recrystallized grain size, L^* , depends on strain rate and temperature

$$L^* = \left(\frac{1}{\xi X A^{n_2}} \right)^{\frac{1}{p}} \left[\ln \left(A^{n_1} + \sqrt{A^{2n_1} + 1} \right) \right]^{-\frac{1}{p}} \quad (\text{VI.12})$$

where p , n_1 , and ξ are additional constants, and A provides the dependence on strain rate and temperature through

$$A = \frac{\dot{\epsilon}^p}{\dot{\epsilon}_0} \exp\left(\frac{Q_R}{kT}\right) \left(\frac{L^*}{L_0}\right)^\omega \quad (\text{VI.13})$$

which can be obtained numerically using a Newton-type iterative procedure, or through the constraint capability within the optimization strategy.

The accumulated critical strain for the initiation of recrystallization was determined using Equations VI.10 - VI.12. The material parameters in these equations were determined using the optimization process described in Section V.2. Isothermal, constant true strain rate data for OFHC Cu at 25°C to 541°C and 0.0004 s⁻¹ to 1.0 s⁻¹ were used with the results shown in Fig. VI.12. The critical strains are accurately predicted using the parameters obtained from the optimization (Table VI.5).

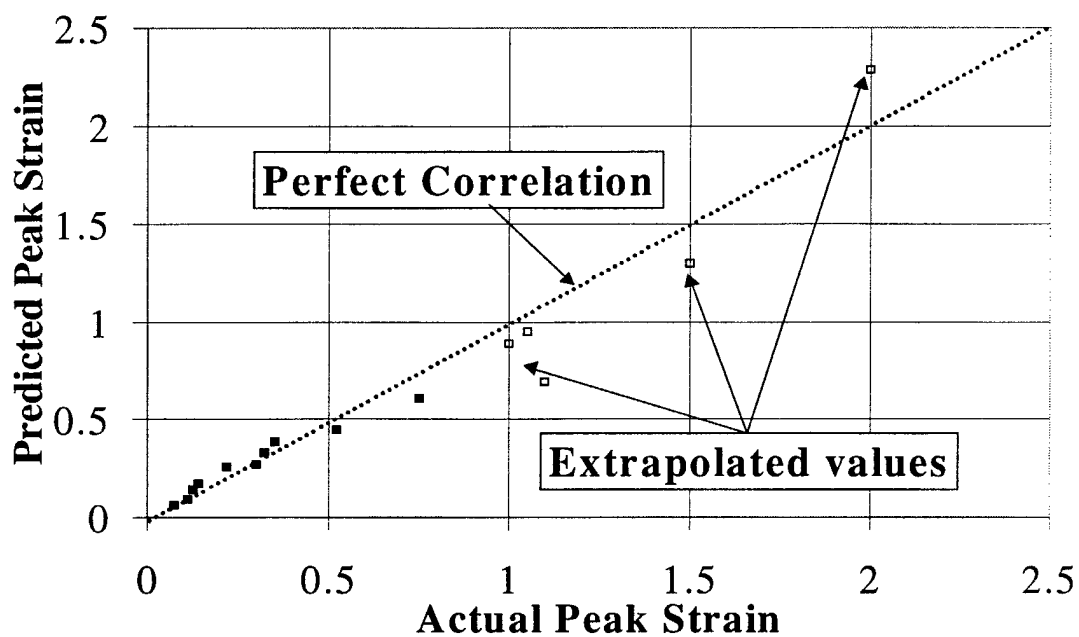


Figure VI.12: Prediction of critical strain for the initiation of recrystallization using OFHC Cu data at strain rates from 0.0004 s^{-1} to 1.0 s^{-1} and temperatures from 134°C to 541°C . Actual peak strain values are shown in closed symbols and those which were estimated from strain data limited to 1.0 are shown with open symbols.

Table VI.5: CRITICAL STRAIN PARAMETERS FOR RECRYSTALLIZATION INITIATION

Parameter	Optimized Value
C_c	5
f_c	0.003
S_0	0.000001
L_0 (μm)	100
ω	1
n_2	0.14
$\dot{\epsilon}_0$ (s^{-1})	9300
X	550000
Q/k (kJ mol^{-1})	20000
ξ	0.67
p	0.9
n_1	0.1

The critical strain identifies the critical state within the material when sufficient energy has been stored to initiate recrystallization. New grains nucleate at or near the original grain boundaries at dislocation pile-up sites, such as slip band and sub-boundary intersection points with grain boundaries, where dislocation gradients are high enough to

force the lattice to minimize its internal energy through reorientation and the formation of a new crystal. Nucleation occurs by the bulging of sections of the grain boundary, driven by the stored dislocation energy. The local driving force for the continued expansion of the grain boundary depends on the difference in dislocation densities in front of, original region, and behind the boundary, recrystallized region. The driving force is continually decreased with deformation. The recrystallized grain experiences dislocation accumulation, which increases the internal strain energy in the new region while dynamic recovery continues to annihilate some dislocations in the original grain, both processes act to reduce energy differences between the boundary and slow recrystallization.

After recrystallization is initiated, flow softening, characterized by a reduction of the true stress-true strain curve, is observed. At relatively high temperatures and low strain rates, oscillations in flow stress are usually observed which gradually reduce and achieve a steady state value. At relatively low temperatures and higher strain rates, the flow stress passes through a single peak before decreasing to a steady state value. A single peak in the flow stress has been associated with grain refinement, while oscillatory flow has been associated with grain coarsening. A microstructural deformation map was established (Jonas and Sakai, 1984) which relates the temperature corrected strain rate and the initial grain size to the characterization of dynamic recrystallization, single peak or oscillatory, and the final grain size (Fig. VI.13). Z , the Zener-Holloman parameter, provides a temperature corrected strain rate which relates temperature and strain rate into a single term.

$$Z = \dot{\epsilon} \exp\left(\frac{Q}{kT}\right) \quad (\text{VI.14})$$

Using Fig. VI.13, the change in grain size and the deformation conditions, defined with the Zener parameter, predicts the recrystallization mode. For an initial grain size, d_{01} , and low Z , Z_1 , multiple peak recrystallization occurs with an increase in the grain size. With the same initial grain size, d_{01} , but high Z , Z_2 , single peak recrystallization occurs with grain refinement, a decrease in the grain size.

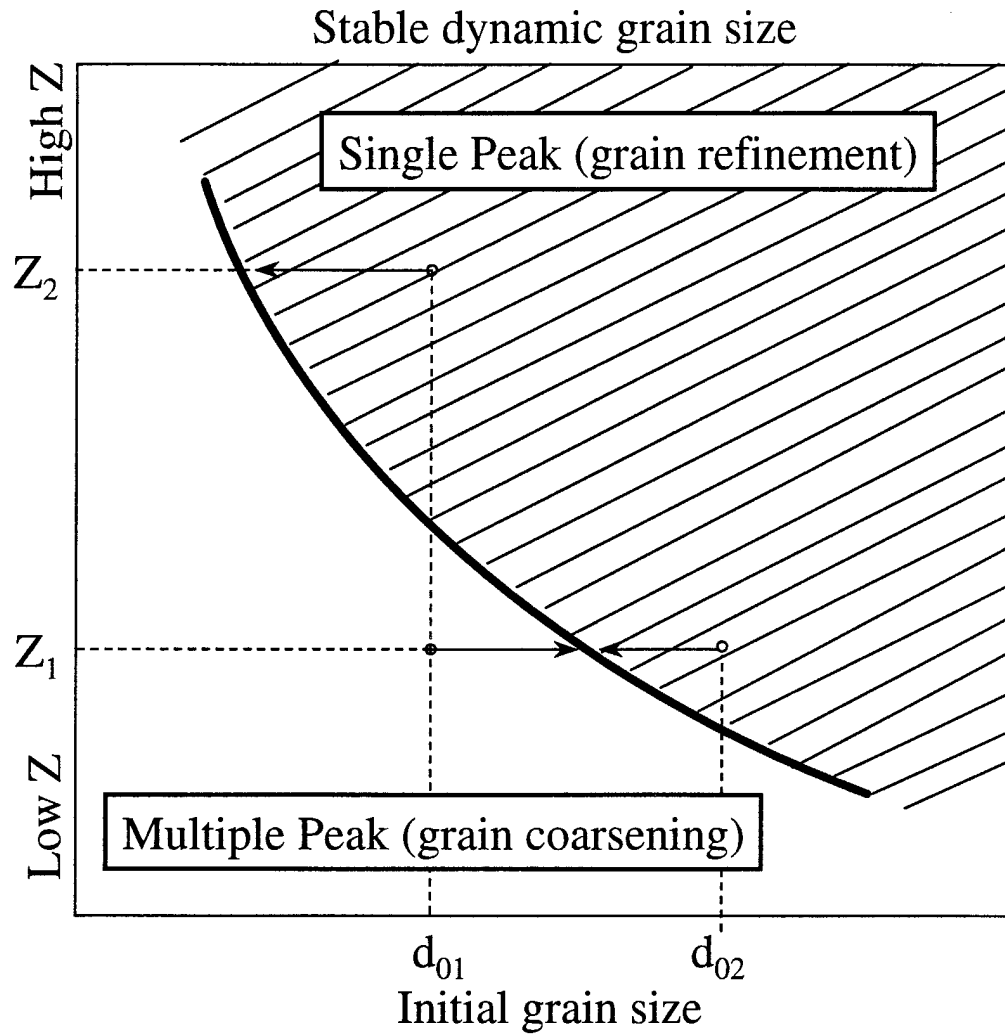


Figure VI.13: Microstructural deformation mechanism map for establishing the character of recrystallization (Jonas and Sakai, 1984).

The microstructure changes during restoration processes. Recovery is accounted for using the ISV evolution equation. The dynamic recovery term depends on the rate of deformation while static recovery depends on time. Recrystallization can be similarly

accounted for. Recrystallization also causes the microstructure to change. An auxiliary internal state variable can represent the softened state of the material resulting from the rearrangement of the microstructure, changes in the grain size, and reduction in dislocation density. The recrystallization auxiliary ISV, Ψ , represents these changes which occur during recrystallization. The change in state is driven by the recrystallization process which eliminates large quantities of dislocations and creates new, dislocation free grains. The rate of the softening reduces as dislocations accumulate in these recrystallized grains, eventually resulting in steady state. This variable evolves both statically with time and dynamically as the microstructure changes through dynamic recrystallization.

The form for the evolution of the recrystallization auxiliary ISV, Ψ , is given by

$$\dot{\Psi}_i = \hat{R}_{DX} |\dot{\epsilon}^p| + \hat{R}_{SX} - \hat{H}_X |\dot{\epsilon}^p| (\Psi_i)^2 \quad (VI.15)$$

where \hat{R}_{DX} represents the change in structure resulting from dynamic recrystallization and

\hat{R}_{SX} from static recrystallization. The continued strain hardening associated with dislocation density increases in the recrystallized grains is represented by the \hat{H}_X term. This general form for the recrystallization auxiliary ISV is then used to modify the ISV hardening variables to reflect the internal structure changes which resulted from recrystallization. This modification is implemented in both the BCJ-SNL and McDowell models.

VI.4.2.1 BCJ-SNL Model with Recrystallization Parameter

The recrystallization parameter was added to the BCJ-SNL model. The isotropic variable was selected for the additional recrystallization auxiliary ISV due to the uniform nature of the recrystallized grains. There is not a directional influence. The auxiliary ISV is added to the isotropic variable, which causes an increase in the rate of restoration. The modified isotropic hardening variable evolution equation becomes

$$\dot{\kappa} = H\mu \left| \dot{\epsilon}^p \right| - \left[R_s + R_d \left| \dot{\epsilon}^p \right| \right] \left(\kappa + \hat{\kappa} u(\bar{\epsilon}^p - \bar{\epsilon}_c^p) \right)^2 \quad (\text{VI.16})$$

where $\hat{\kappa}$ is the softening variable which evolves according to Equation VI.16. The heavy-side function, $u(\bar{\epsilon}^p - \bar{\epsilon}_c^p)$, is utilized to activate the auxiliary ISV when the critical strain level, $\bar{\epsilon}_c^p$, defined by Equation VI.10, is reached. The heavy-side function has values $u(x) = 1$ when $x > 0$; and $u(x) = 0$ when $x < 0$. Only dynamic recrystallization was included in the softening variable evolution

$$\dot{\hat{\kappa}} = \hat{R}_{D\kappa} \left| \dot{\epsilon}^p \right| - \left[\hat{H}\mu \left| \dot{\epsilon}^p \right| \right] (\hat{\kappa})^2 \quad (\text{VI.17})$$

The influence of this additional variable is shown in the following sequence of charts. The

first (Fig. VI.14) shows the optimized fit to experimental data without the recrystallization softening variable. The predicted curves typically lie between the initial high strain rate hardening portion of the data and the steady state saturated flow stress. No softening, reduction in the flow stress can occur. The second chart (Fig. VI.15) demonstrates the ability of the BCJ-SNL model to accurately predict the OFHC Cu data when the softening portion of every curve is eliminated. The fit to experiment data is very good, with the objective function being low. The last chart (Fig. VI.16) includes the softening parameters in the optimization process and the improved resulting predictions. The predicted curves capture the softening behavior and achieves a much improved prediction. The steady state flow stress, after recrystallization was well predicted. The oscillations in flow stress are not predicted using the single softening variable. The normalized objective function values which demonstrate the effect of the softening parameter is shown in Table VI.6. The softening parameter greatly reduces the error between the experimental data and the model predictions. The model does not capture any of the flow stress reduction resulting from recrystallization, and therefore the accuracy is not good.

Table VI.6: NORMALIZED OBJECTIVE FUNCTION VALUES FOR THE BCJ-SNL MODEL

Optimization Conditions	Normalized Objective Function
BCJ-SNL	4.5
BCJ-SNL (with softening parameter)	1

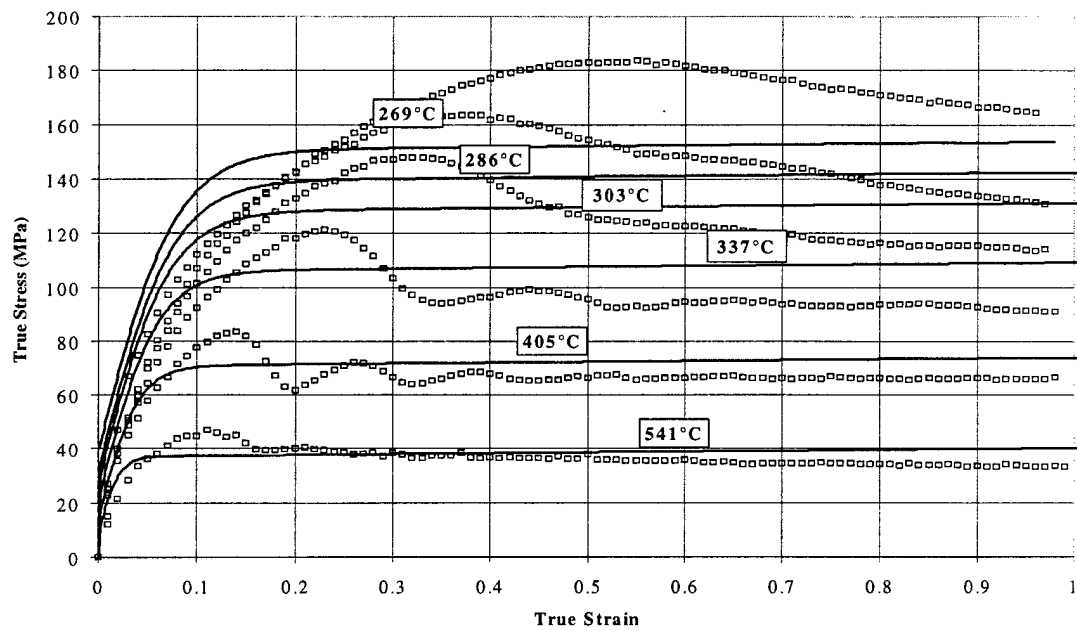


Fig. VI.14 Correlation to OFHC Cu using the BCJ-SNL model. Solid lines are model predictions which shows the optimized fit to experimental data without the recrystallization softening variable.

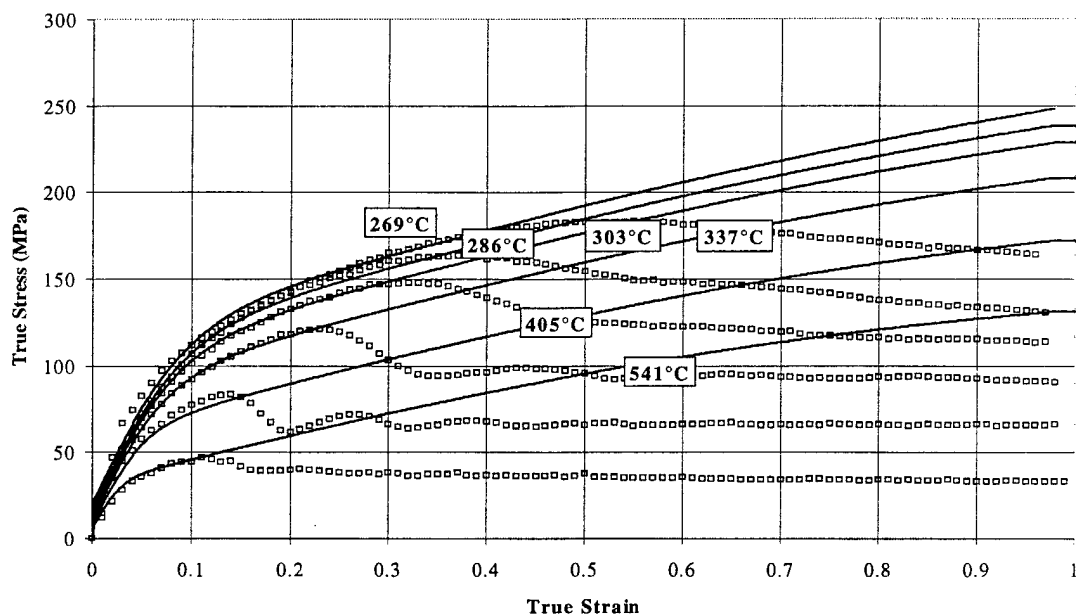


Fig. VI.15 Correlation to OFHC Cu using the BCJ-SNL model. Solid lines are model predictions which shows the optimized fit to experimental data, less the softening portion of 269°C; 0.0004 s⁻¹ without the recrystallization softening variable.

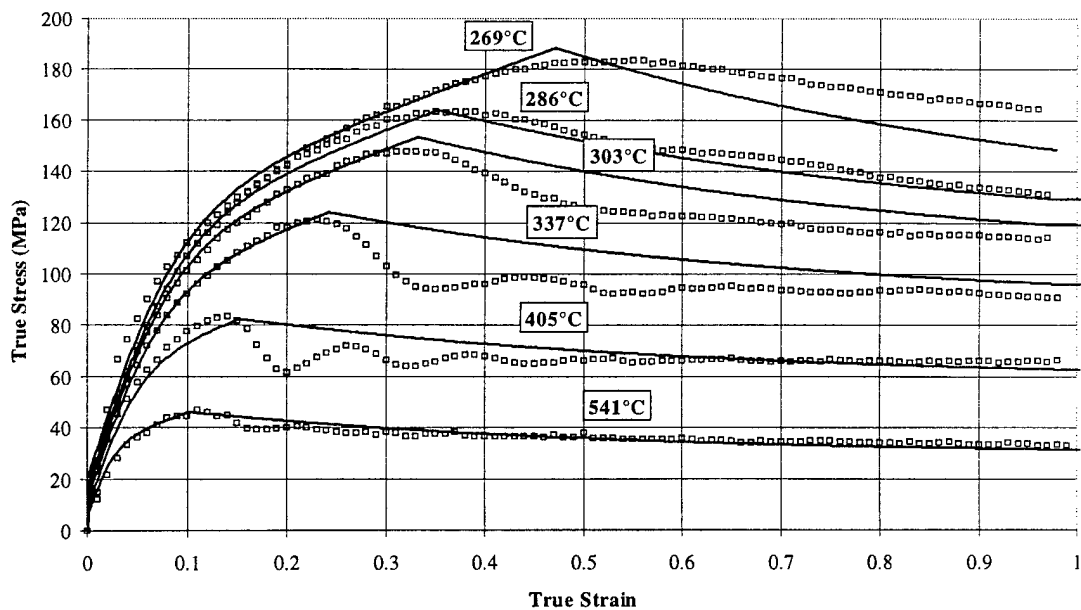


Fig. VI.16 Correlation to OFHC Cu using the BCJ-SNL model. Solid lines are model predictions which shows the optimized fit to experimental data with the recrystallization softening variable included.

VI.4.2.2 McDowell Model with Recrystallization Parameter

The recrystallization parameter was also added to the McDowell model. The isotropic variables were selected due to the uniform nature of the recrystallized grains. The modified isotropic variable evolution equations become

$$\dot{\chi}_i = \mu_{\chi_i} [\bar{\chi}_i - \chi_i] |\dot{\epsilon}^p| + \frac{\chi_i}{\mu_{\chi_i} \bar{\chi}_i} \frac{\partial(\mu_{\chi_i} \bar{\chi}_i)}{\partial T} \dot{T} - \mu_{\chi_i} \bar{\chi}_i [\chi_i - \hat{\chi}_i u(\bar{\epsilon}^p - \bar{\epsilon}^p_c)]^{L_{\chi_i}} \psi_{\chi} \exp\left(-\frac{\Delta Q_{\chi} - V_A \chi_i}{kT}\right) \quad (VI.18)$$

where $\hat{\chi}_i$ is the softening variable, and the heavy-side function, $u(\bar{\epsilon}^p - \bar{\epsilon}^p_c)$, is utilized to

activate the auxiliary ISV when the critical strain level is reached. Both dynamic and static recrystallization was included in the softening variable evolution

$$\dot{\hat{\chi}}_i = \hat{R}_{D\chi_i} |\dot{\epsilon}^p| + \hat{R}_{S\chi_i} - \left[\hat{H}_{\chi_i} \mu |\dot{\epsilon}^p| \right] (\hat{\chi}_i)^2 \quad (VI.19)$$

The influence of this additional variable is shown in the following sequence of charts. The first (Fig. VI.17) shows the McDowell model, without the recrystallization softening variable, correlations to experimental data using an optimized parameter set. The parameters were obtained, using ten isothermal, constant true strain rate experiments. The data used

were for compression at quasi-static strain rates with temperatures ranging from 25°C to 541°C. The predicted curves typically lie between the initial high strain hardening rate portion of the data and the steady state saturated flow stress. No softening is predicted, consequently, the correlations vary significantly from the experimental data.

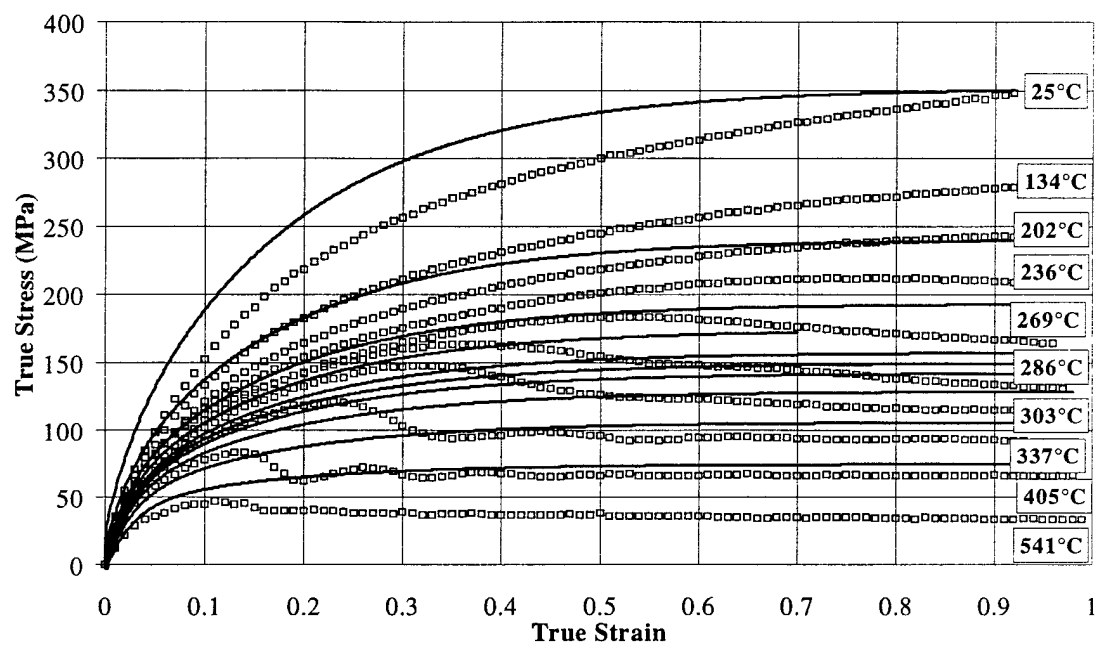


Figure VI.17: Correlation to OFHC Cu using the McDowell model, without the recrystallization softening variable. The predictions are shown using solid lines, while the experimental data are shown using open symbols.

The next figure (Fig. VI.18) shows the McDowell model, with the recrystallization softening variable, correlations to experimental data using another optimized parameter set. The parameters were also obtained, using the same ten isothermal, constant true strain rate experiments. The data used were compression at quasi-static strain rates with temperatures ranging from 25°C to 541°C. The predicted curves exhibit softening and achieve a significantly closer correlation to the experimental data.

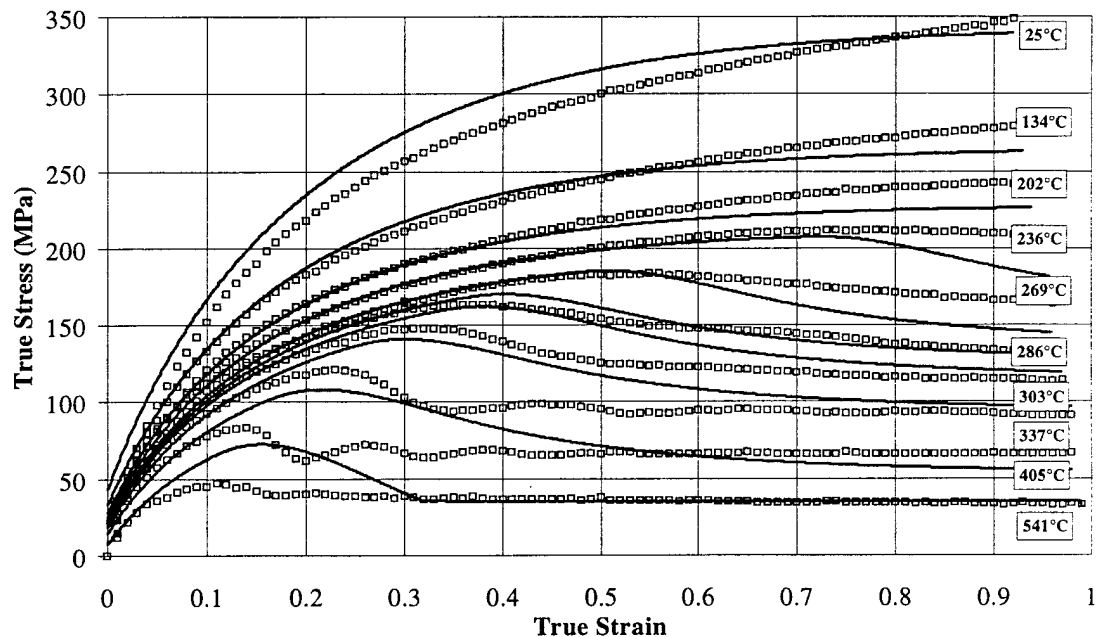


Figure VI.18 Correlation to OFHC Cu using the McDowell model, without the recrystallization softening variable. The predictions are shown using solid lines, while the experimental data are shown using open symbols.

VI.4.2.2.1 McDowell Model with Recrystallization Parameter Correlation and Sequence Predictions (limited data set)

The McDowell model was initially correlated to a limited data set to determine the capability of the recrystallization parameter functional form to capture the observed softening demonstrated during the experiments, both static and dynamic. The model was optimized using compression results from four deformation conditions, 25°C; 0.0004 s⁻¹ to 1.0 strain, 269°C, 0.0004 s⁻¹ to 1.0 strain, and two sets of 269°C, 0.0004 s⁻¹ (after compressive pre-strain to 0.5 at 25°C) at hold times of 1.5 and 20 minutes. These data represent both dynamic and static softening, and are the conditions which were not well predicted in Chapter V. The correlation is shown in Fig. VI.19. Figure VI.20 shows the correlation to the five isothermal and constant strain rate experiments. The model correlations in Fig. VI.19 are excellent. The predictions very closely correlate, for the dynamic restoration and the static restoration. The correlation to the five experiments, Fig. VI.20, does not correlate well with the higher strain rate data. The next section will consider the optimization to all five of the normal experimental data sets. Predictions are calculated using the optimized parameters for the McDowell model, with the recrystallization parameter, and correlated to the limited data set, for compression tests involving strain rate sequences (Figs. V.21 and V.22), temperature sequences (Figs. V.23 and V.24), and for combined strain rate and temperature sequences (Figs. V.25 and V.26). The solid lines represent the model prediction, while symbols represent experimental data.

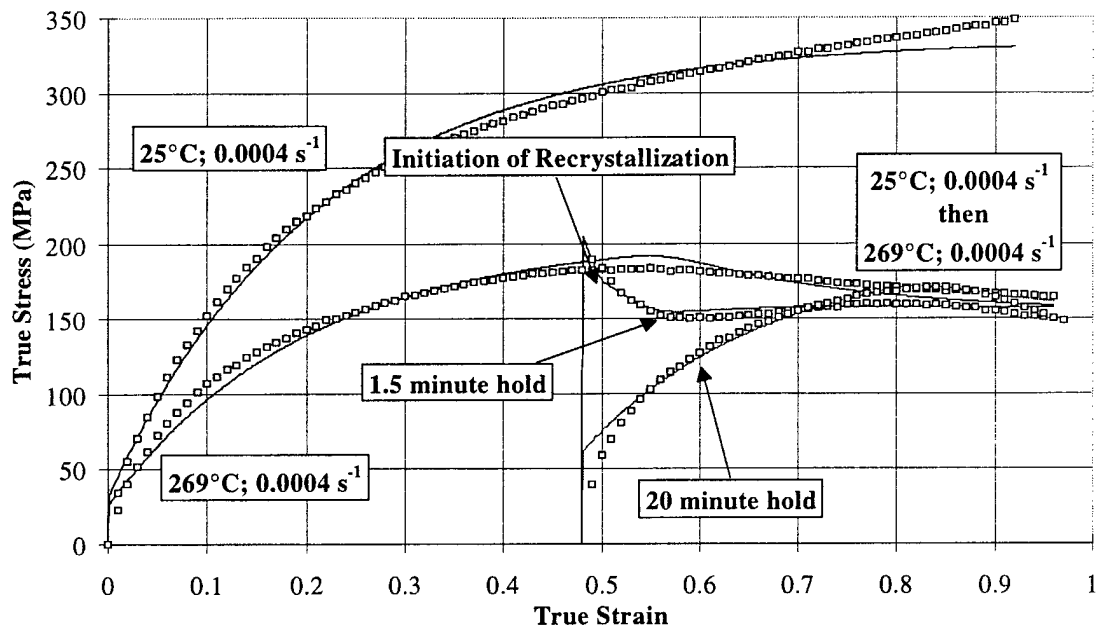


Figure VI.19: Correlation to OFHC Cu compression data using the McDowell model. The model correlations are shown using solid lines, while the experimental data are shown with open symbols.

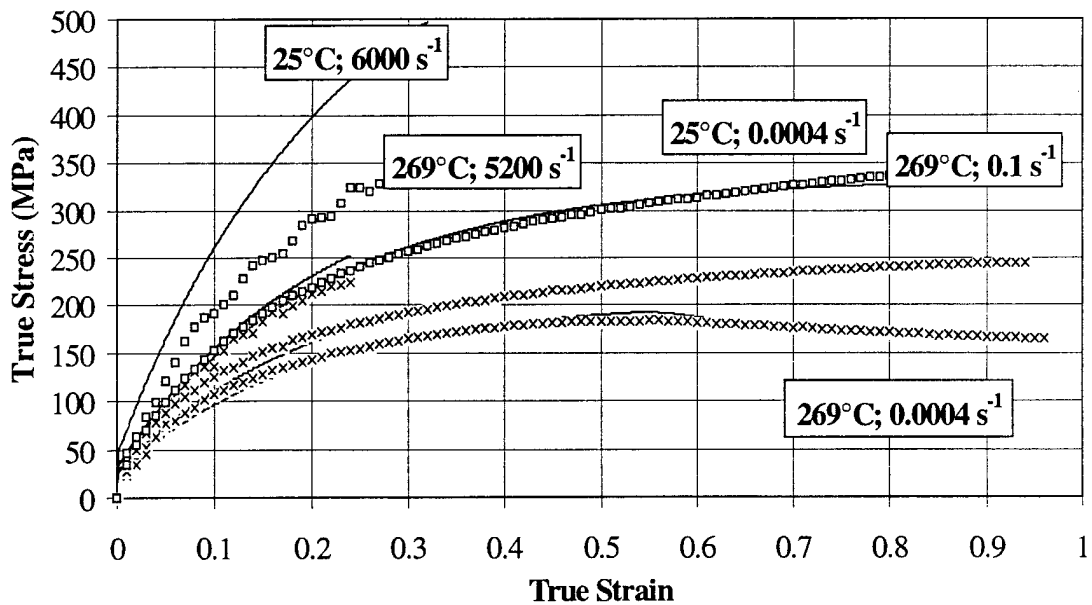


Figure VI.20: Correlation to OFHC Cu compression data using the McDowell model. The model correlations are shown using solid lines, while the experimental data are shown with open symbols.

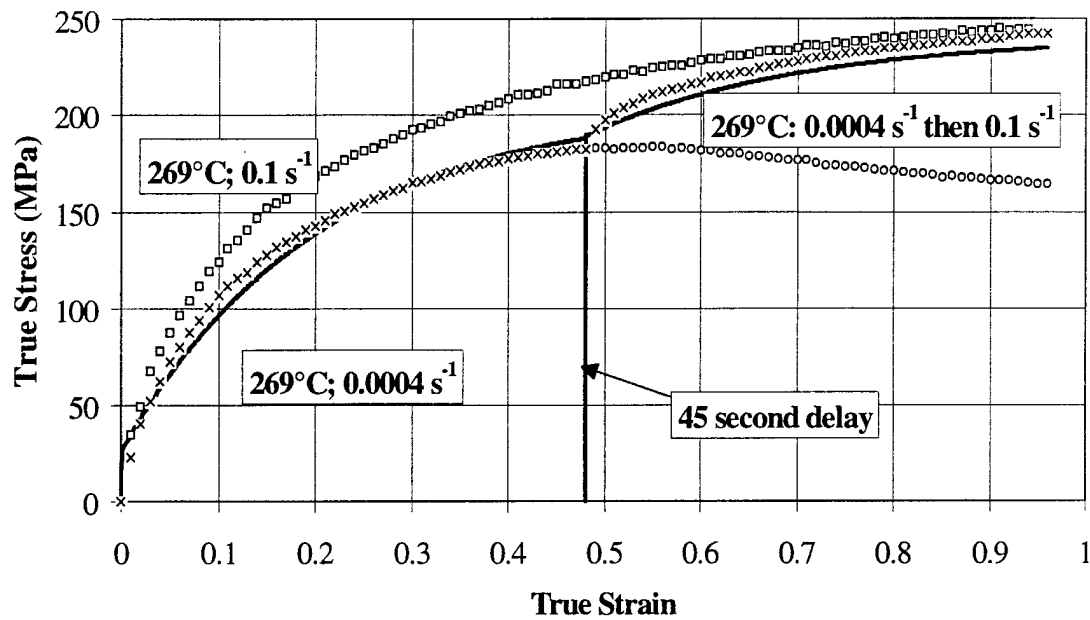


Figure VI.21: Strain rate sequence prediction for OFHC Cu using the McDowell model with recrystallization parameter. Solid lines represent the model prediction, while symbols represent experimental data.

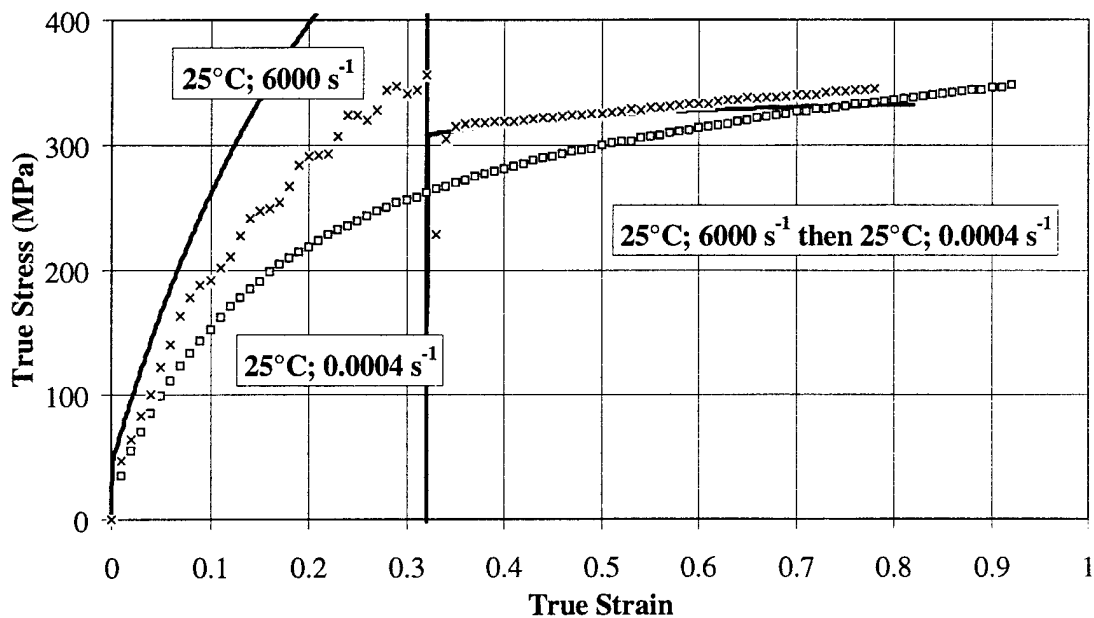


Figure VI.22: Strain rate sequence prediction for OFHC Cu using the McDowell model with recrystallization parameter. Solid lines represent the model prediction, while symbols represent experimental data.

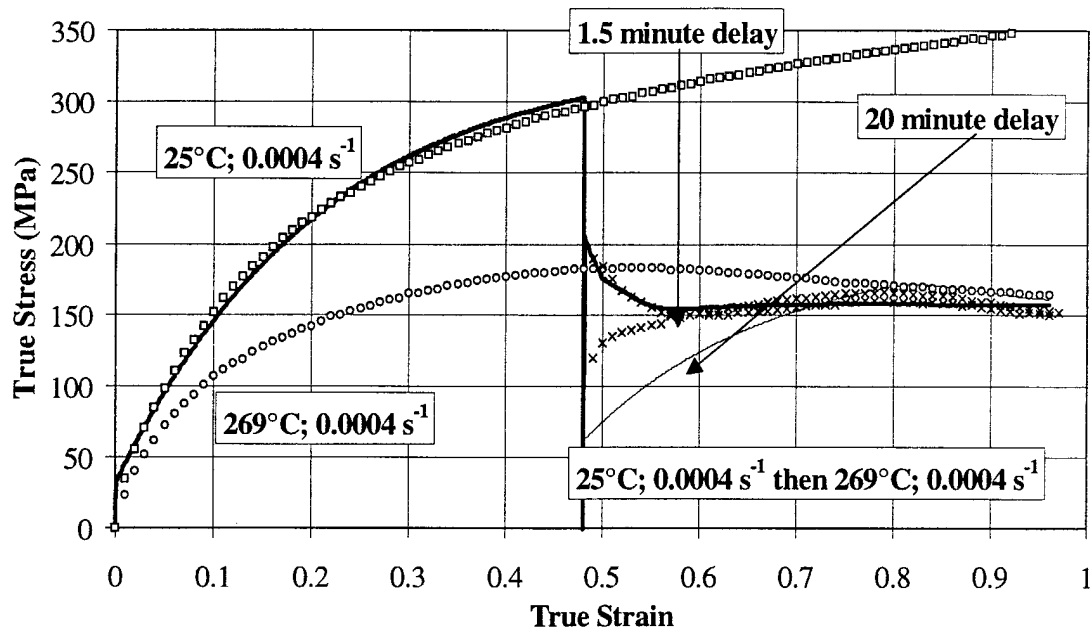


Figure VI.23: Temperature sequence prediction for OFHC Cu using the McDowell model with recrystallization parameter. Solid lines represent the model prediction, while symbols represent experimental data.

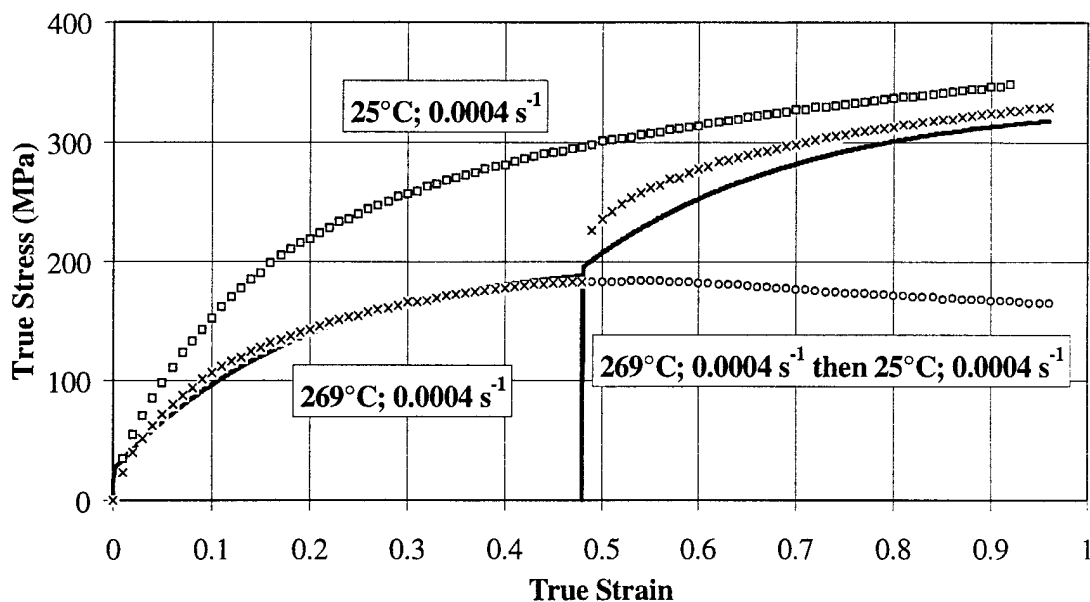


Figure VI.24: Temperature sequence prediction for OFHC Cu using the McDowell model with recrystallization parameter. Solid lines represent the model prediction, while symbols represent experimental data.

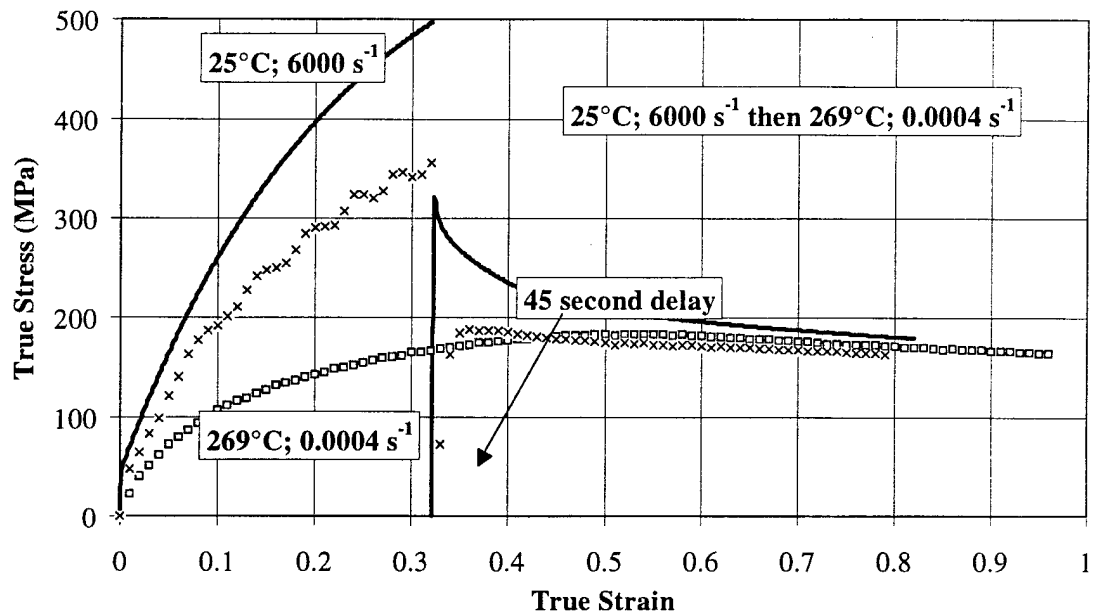


Figure VI.25: Strain rate and temperature sequence prediction for OFHC Cu using the McDowell model with recrystallization parameter. Solid lines represent the model prediction, while symbols represent experimental data.

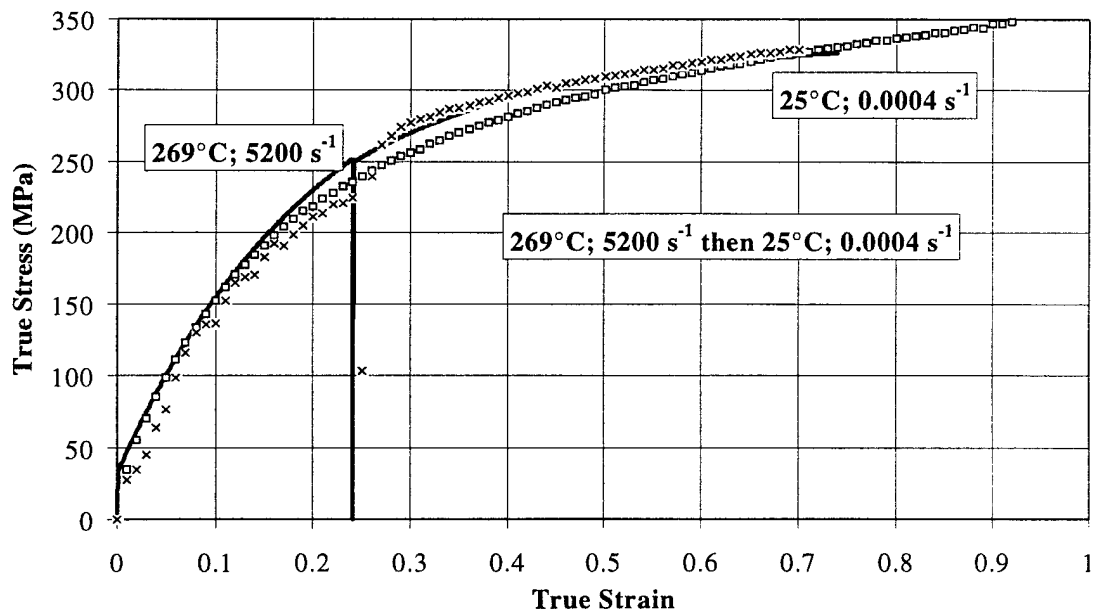


Figure VI.26: Strain rate and temperature sequence prediction for OFHC Cu using the McDowell model with recrystallization parameter. Solid lines represent the model prediction, while symbols represent experimental data.

VI.4.2.2.2 McDowell Model with Recrystallization Parameter Correlation and Sequence Predictions

The McDowell model was also correlated to a data set consisting of the five isothermal and constant strain rate data sets used in Chapter V. The model was optimized and the parameter set determined. The model correlations are shown in Fig. VI.27. Predictions are calculated using the optimized parameters for the McDowell model, with the recrystallization parameter for compression tests involving strain rate sequences (Figs. V.28 and V.29), temperature sequences (Figs. V.30 and V.31), and for combined strain rate and temperature sequences (Figs. V.32 and V.33). The solid lines represent the model prediction, while symbols represent experimental data.

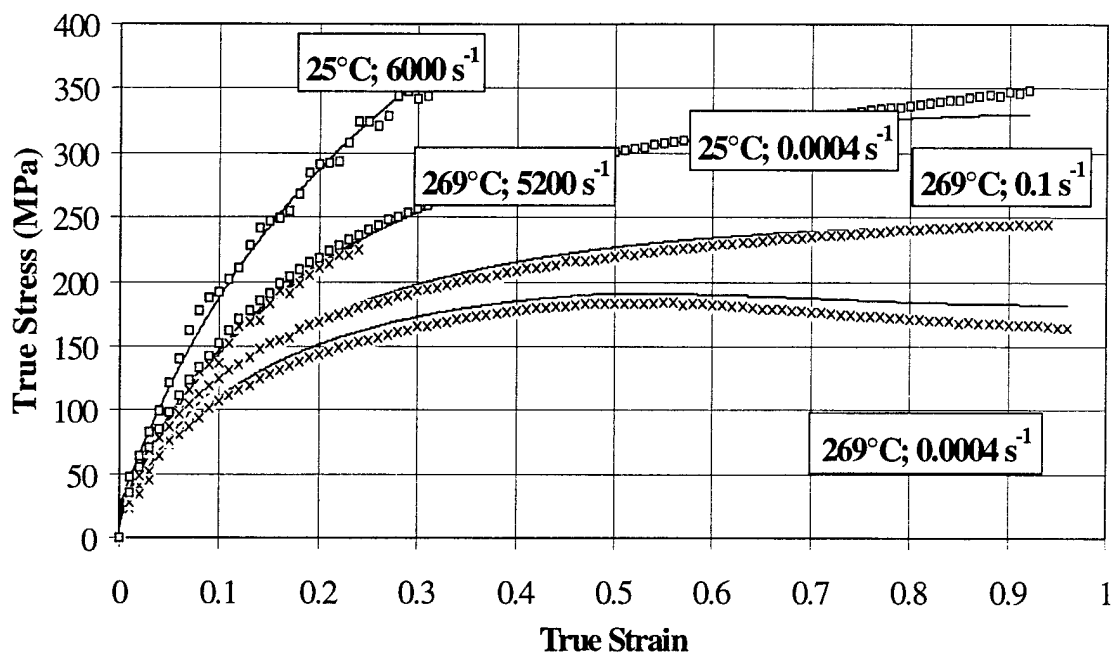


Figure VI.27: Correlation to OFHC Cu compression data using the McDowell model. The model correlations are shown using solid lines, while the experimental data are shown with open symbols.

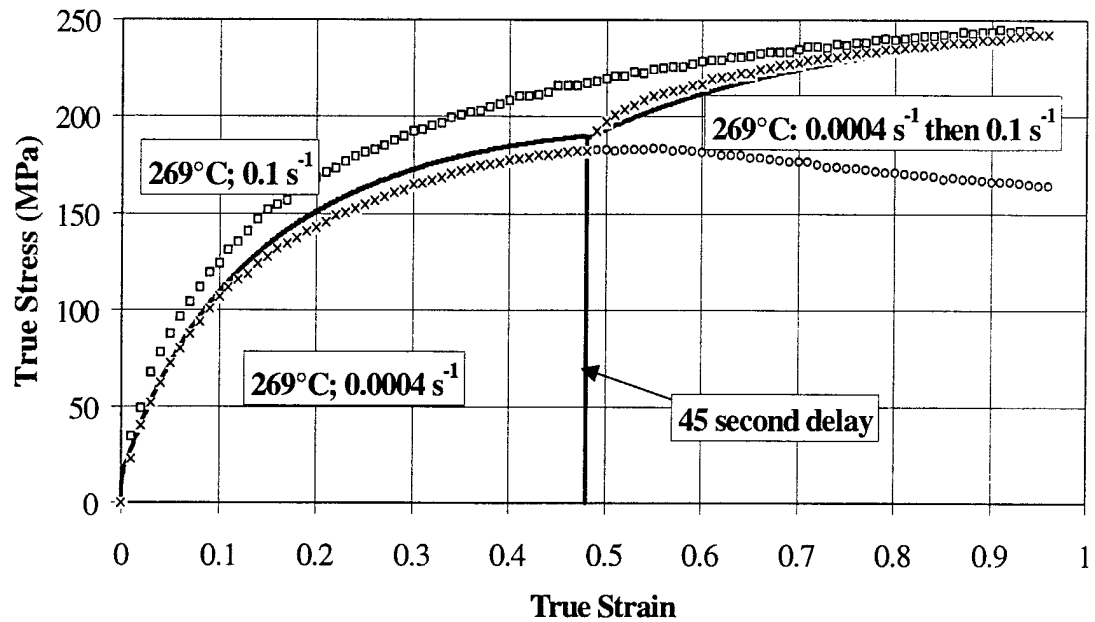


Figure VI.28: Strain rate sequence prediction for OFHC Cu using the McDowell model with recrystallization parameter. Solid lines represent the model prediction, while symbols represent experimental data.

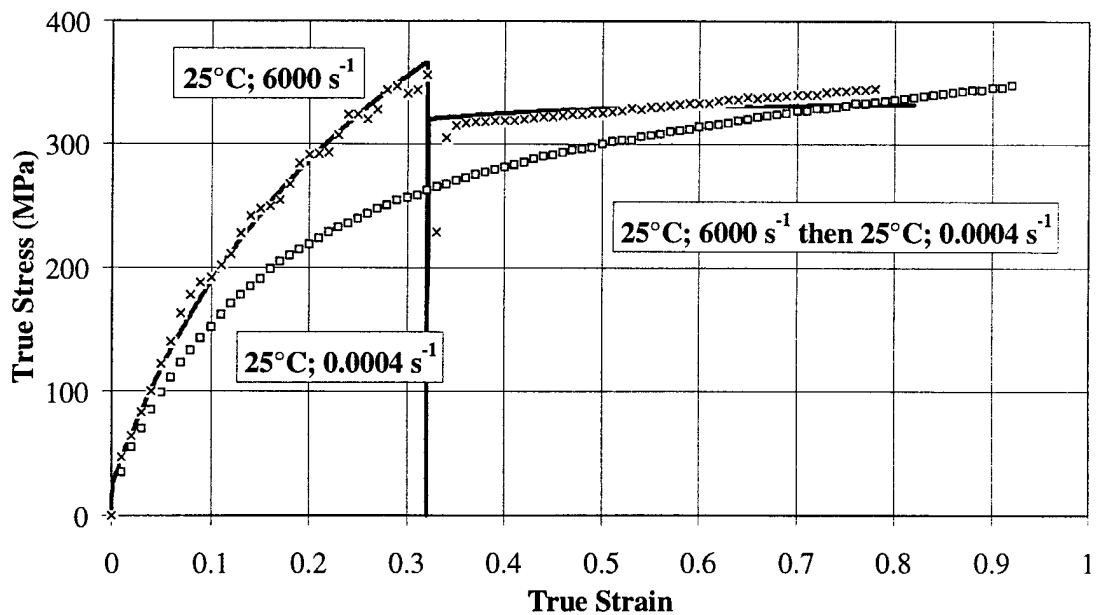


Figure VI.29: Strain rate sequence prediction for OFHC Cu using the McDowell model with recrystallization parameter. Solid lines represent the model prediction, while symbols represent experimental data.

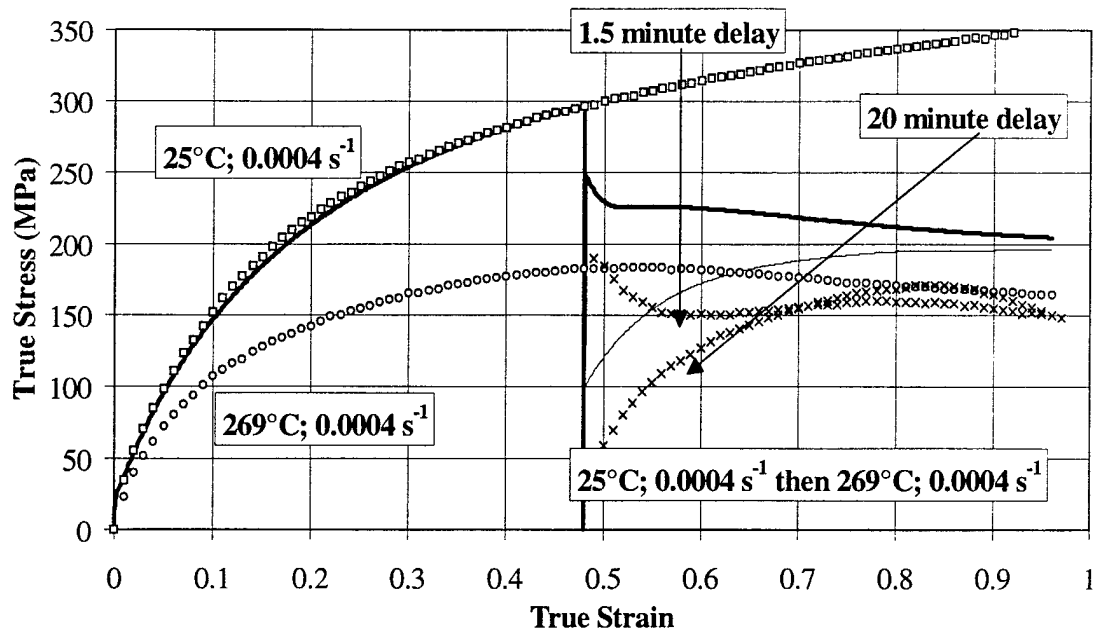


Figure VI.30: Temperature sequence prediction for OFHC Cu using the McDowell model with recrystallization parameter. Solid lines represent the model prediction, while symbols represent experimental data.

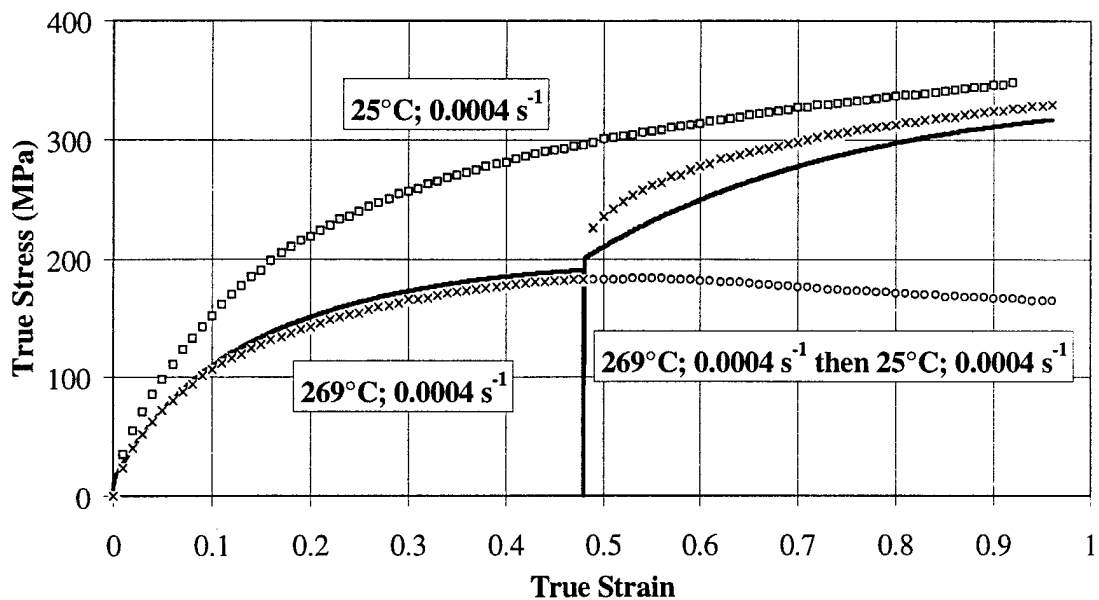


Figure VI.31: Temperature sequence prediction for OFHC Cu using the McDowell model with recrystallization parameter. Solid lines represent the model prediction, while symbols represent experimental data.

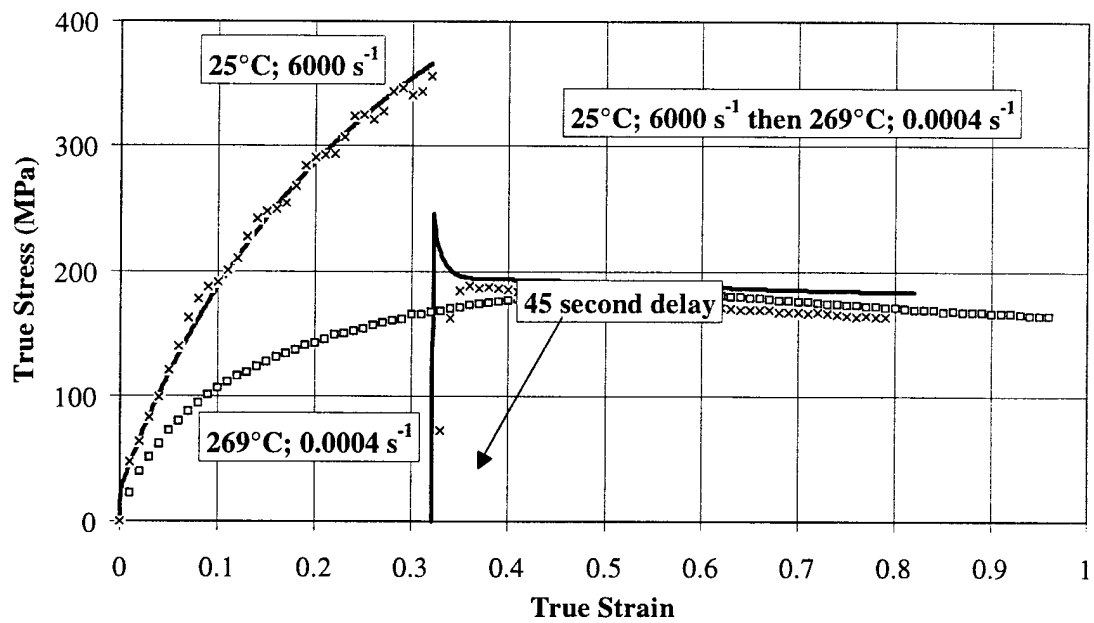


Figure VI.32: Strain rate and temperature sequence prediction for OFHC Cu using the McDowell model with recrystallization parameter. Solid lines represent the model prediction, while symbols represent experimental data.

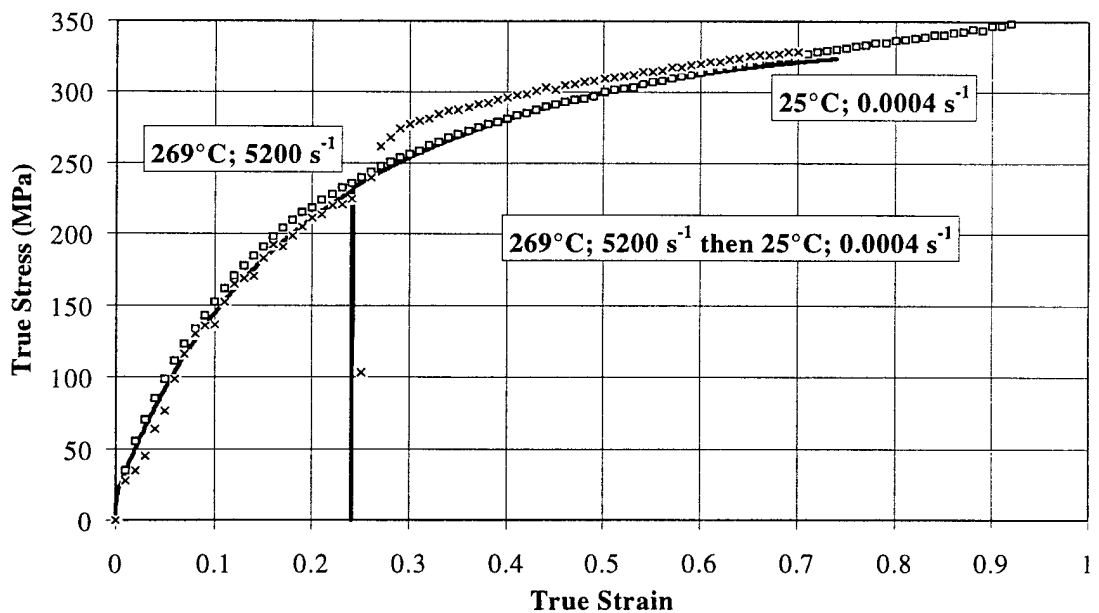


Figure VI.33: Strain rate and temperature sequence prediction for OFHC Cu using the McDowell model with recrystallization parameter. Solid lines represent the model prediction, while symbols represent experimental data.

VI.4.3 Very High Strain Rate Regime

Many applications involve large deformations at extremely high strain rates. The time scale during these is very short, prohibiting the activation of restoration mechanisms. The microstructure (e.g. dislocations) establishes a relatively homogeneous distribution, creating a strong structure due to the absence of stress screening apparent in quasi-static substructures. Chapter V detailed the inability of the current structure of the model to correlate the high strain rate regime. A general functional form, which is proportional to the effective plastic strain rate, is incorporated into the McDowell model in the isotropic hardening evolution equation. The optimization strategy was then utilized to obtain the coefficients which achieved the best correlation. This additional term, added to the isotropic hardening variable evolution equation, had the form given by

$$(A + B\dot{p} + C\dot{p}^r) \exp\left(\frac{Q_e}{kT}\right) \quad (\text{VI.20})$$

where A, B, C, r, and Q_e are parameters, k is Boltzmann's constant and \dot{p} , is the effective plastic strain rate given by

$$\dot{p} = \sqrt{\frac{2}{3} \dot{\epsilon}_{ij}^p \dot{\epsilon}_{ij}^p} \quad (\text{VI.21})$$

The resulting optimized parameters for the high strain rate term are shown in Table VI.7.

The model correlations to the very high strain rate data, as well as the lower strain rate data are shown in Fig. VI.34. The initial strain hardening rate is very rapid and then a saturated flow stress level is achieved. The softening observed in the experimental data is not predicted by the model. Additional knowledge of the dynamic restoration mechanisms involved should be investigated.

The very high strain rate creates a condition where the time available for heat dissipation is small, and much of the plastic work is converted into a temperature rise according to

$$\Delta T = \frac{\Psi}{\rho c_p} \int \sigma(\epsilon) d\epsilon \quad (\text{VI.22})$$

where ψ is the factor for amount of work converted into heat, here assumed to be 1.0. The product of the density and specific heat, ρc_p is approximately 3.43 MPa. The resultant temperature increase approaches 200°C at the very high strain rates. The model correlations including this temperature increase are shown in Fig. VI.35. The model is still able to correlate the data well. The $C\dot{p}^r$ term dominates the $B\dot{p}$ term for both the isothermal and adiabatic cases.

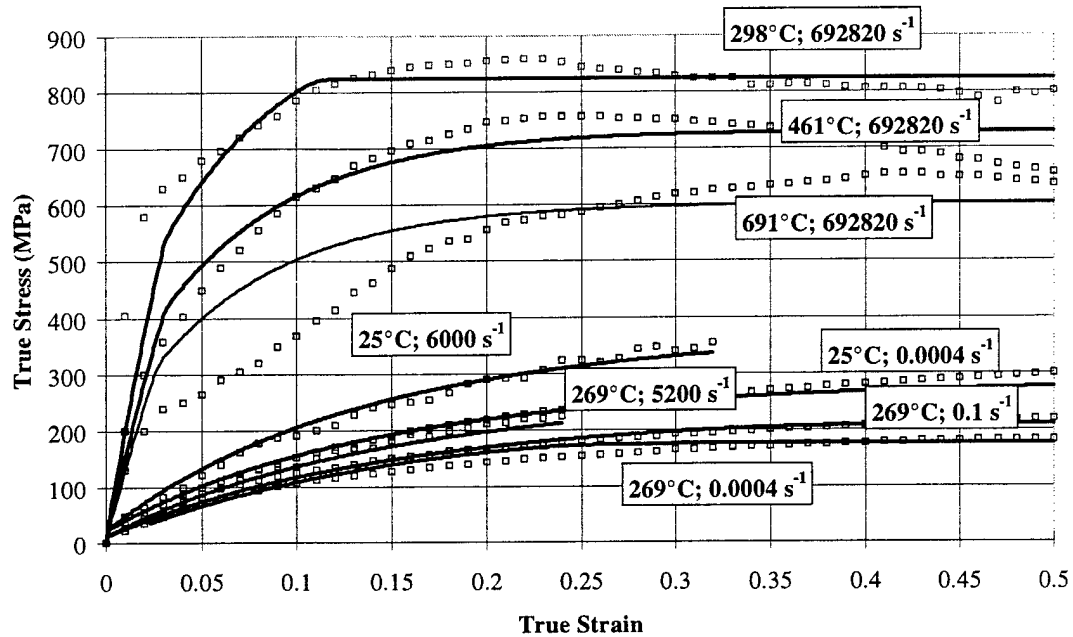


Figure VI.34: Correlation to OFHC Cu compression data using the McDowell model with the high strain rate term incorporated. The model correlations are shown using solid lines, while the experimental data are shown with open symbols.

Table VI.7 MCDOWELL MODEL HIGH STRAIN RATE TERM PARAMETERS

Parameters	Optimized Values
A	33
B	0.003
C	.09
r	0.65
Q_e	570

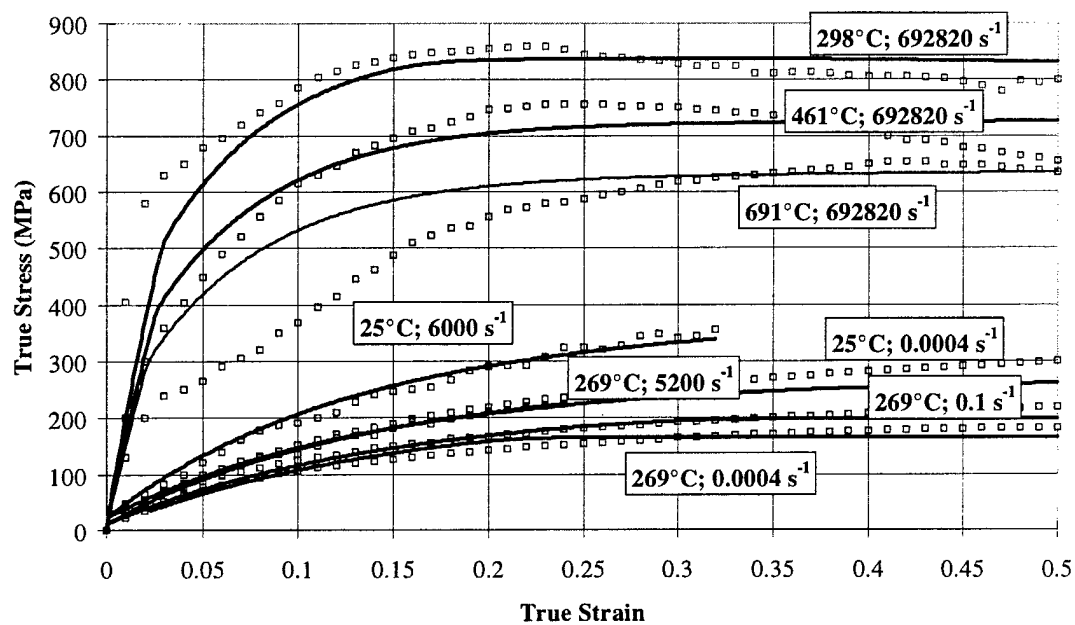


Figure VI.35: Correlation to OFHC Cu compression data using the McDowell model with the high strain rate term incorporated. A temperature increase of approximately 200°C due to adiabatic heating was included. The model correlations are shown using solid lines, while the experimental data are shown with open symbols.

Table VI.8 MCDOWELL MODEL HIGH STRAIN RATE TERM PARAMETERS
(with adiabatic heating included)

Parameters	Optimized Values
A	41
B	0.00005
C	.09
r	0.8
Q_{ϵ}	410

VI.5 Data Set Requirements for Predicting History Effects

The DOE methodology described in Section VI.2 was employed to determine the experimental data set which corresponded to the highest correlation of predicted sequences of temperature and strain rate sequences of experimental data. Additionally, the amount of experimental data and different forms for the objective function are evaluated.

VI.5.1 DOE Analysis Factors

The McDowell model, described in Chapter V.5, was used as a representative ISV model to determine the relative importance of seven factors for obtaining the optimal correlation between experimental data and model predictions. In this section, the factors and the corresponding two levels for each factor are described.

VI.5.1.1 Quantity of Experimental Data Points

Model predictions were all calculated using time step integration. The time steps were established corresponding to a strain increment of 0.001 strain. The objective function determines the difference between the predicted values and the experimental data at corresponding strain values. This factor considered two levels for the quantity of experimental data. One level utilized experimental data with a strain increment of 0.01 and the second with an interval of 0.25.

VI.5.1.2 Objective Function Form

The objective function calculates an error measurement between the model predicted value and the corresponding experimental data. Two error measurements were utilized. The first was the L2 norm. The sum of the error squared between the prediction and the experimental data at the same corresponding strain value was the first level. The second level was the maximum absolute value error between the predicted and data values.

VI.5.1.3 Experimental Deformation Conditions used for Optimization: Isothermal, Constant True Strain Rate (25°C; 6000 s⁻¹ and 0.0004 s⁻¹ and 269°C; 0.0004 s⁻¹ less than 0.5 strain, 0.1 s⁻¹ and 5200 s⁻¹)

Experimental data corresponding to the full range of temperatures (25°C to 269°C) and strain rates (0.0004 s⁻¹ to 6000 s⁻¹) used for the sequence experiment predictions were available during the optimization procedure. The two levels for this factor correspond to whether these isothermal, constant true strain rate data sets were utilized or not.

VI.5.1.4 Experimental Deformation Conditions used for Optimization: Strain Rate Sequence (269°C; 0.0004 s⁻¹ to 0.5 strain then 269°C; 0.1 s⁻¹)

Experimental data corresponding to the strain rate sequence, 269°C at 0.0004 s⁻¹ to a compressive pre-strain of 0.5 and then 269°C at 0.1 s⁻¹ to a final strain of 1.0 were available during the optimization procedure. The two levels for this factor correspond to whether this strain rate sequence data set were utilized or not.

**VI.5.1.5 Experimental Deformation Conditions used for Optimization:
Temperature Sequence (269°C; 0.0004 s⁻¹ to 0.5 strain then 25°C; 0.0004 s⁻¹)**

Experimental data corresponding to the temperature sequence, 269°C at 0.0004 s⁻¹ to a compressive pre-strain of 0.5 and then 25°C at 0.0004 s⁻¹ to a final strain of 1.0 were available during the optimization procedure. The two levels for this factor correspond to whether this temperature sequence data set were utilized or not.

**VI.5.1.6 Experimental Deformation Conditions used for Optimization:
Isothermal, Constant True Strain Rate (269°C; 0.0004 s⁻¹ 0.5 to 1.0 strain)**

Experimental data including the observed softening in flow stress, 269°C at 0.0004 s⁻¹ for strains above 0.5 were available during the optimization procedure. The two levels for this factor correspond to whether this isothermal, constant true strain rate data set, which contains the softening due to dynamic recrystallization, were utilized or not.

**VI.5.1.7 Experimental Deformation Conditions used for Optimization:
Temperature Sequence (25°C; 0.0004 s⁻¹ to 0.5 strain then 269°C; 0.0004 s⁻¹ with hold times of 1.5 and 20 minutes)**

Experimental data corresponding to the temperature sequence, 25°C at 0.0004 s⁻¹ to a compressive pre-strain of 0.5 and then 269°C at 0.0004 s⁻¹ to a final strain of 1.0 were available during the optimization procedure. Two different hold times were included, 1.5 and 20 minutes in the furnace prior to the second sequence. The two levels for this factor correspond to whether this temperature sequence data set were utilized or not.

VI.5.2 Macroscopic Responses

The effectiveness of the various levels were determined by the macroscopic McDowell model predictions relative to actual experimental data. Six different sequence experiments were used : 1) strain rate sequences of 269°C and 0.0004 s⁻¹ followed by 269°C and 0.1 s⁻¹ and 25°C and 6000 s⁻¹ followed by 25°C and 0.0004 s⁻¹; 2) temperature sequences of 25°C and 0.0004 s⁻¹ followed by 269°C and 0.0004 s⁻¹ and 269°C and 0.0004 s⁻¹ followed by 25°C and 0.0004 s⁻¹; and 3) combinations of strain rate and temperature sequences of 25°C and 6000 s⁻¹ followed by 269°C and 0.0004 s⁻¹ and 269°C and 5200 s⁻¹ followed by 25°C and 0.0004 s⁻¹. The response used was the weighted sum of the error. The weighting equalizes the total effect from each curve. Each DOE experiment results in a response.

Table VI.9 PARAMETER MATRIX

Opt #	Data Points	Error	Iso (269 < 0.5)	Rate Seq	Temp Seq (H - L)	Iso (269 > 0/5)	Temp Seq (L - H)
1	0.01	sse	yes	yes	yes	yes	yes
2	0.01	sse	yes	no	no	no	no
3	0.01	max	no	yes	yes	no	no
4	0.01	max	no	no	no	yes	yes
5	0.25	sse	no	yes	no	yes	no
6	0.25	sse	no	no	yes	no	yes
7	0.25	max	yes	yes	no	no	yes
8	0.25	max	yes	no	yes	yes	no

Table VI.10 RESPONSE MATRIX

Optimization #	Responses (Objective Function)
1	240000
2	3400000
3	1100000
4	410000
5	14000000
6	330000
7	460000
8	750000

The output matrix was determined from the parameter matrix, where each factor level was converted to a plus or minus 1 value, and the response matrix (Equation VI.4). Since the values in the output matrix are relative to each other, they are normalized to the largest value to assess the relative level of influence of each factor. Figure VI.36 shows the results of this analysis, where the factor labels, numbers, correspond to the parameters listed in Table VI.11. The temperature sequence experiments were the most influential factors and the error definition second. The temperature sequence of 25°C followed by 269°C, where the impact of static recrystallization was observed, had the greatest influence. The remaining parameters four factors had moderate influence.

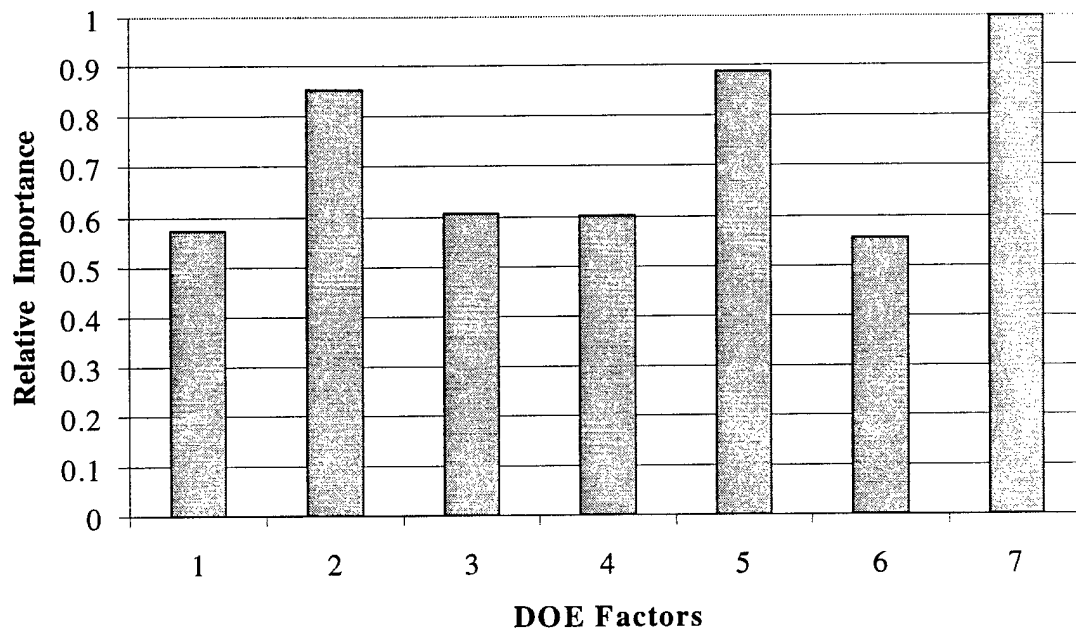


Figure VI.36 DOE results showing the relative importance that each factor has on the minimization of the objective function. The correlation of factor numbers to parameters are given in Table VI.11.

This DOE analysis also provides the information necessary to obtain the optimum combination of factors to achieve the best, minimum objective function, one where the error between the experimental data and the model predictions is the least. In accordance with this data, the optimal factor set includes more experimental data points, the use of absolute value of maximum error between experimental data and model predictions for the objective function, using experimental data including isothermal, constant true strain rate data and temperature sequence data. This analysis demonstrates the necessity for including temperature sequence experiments for the characterization of material behavior and the determination of the optimum parameter set.

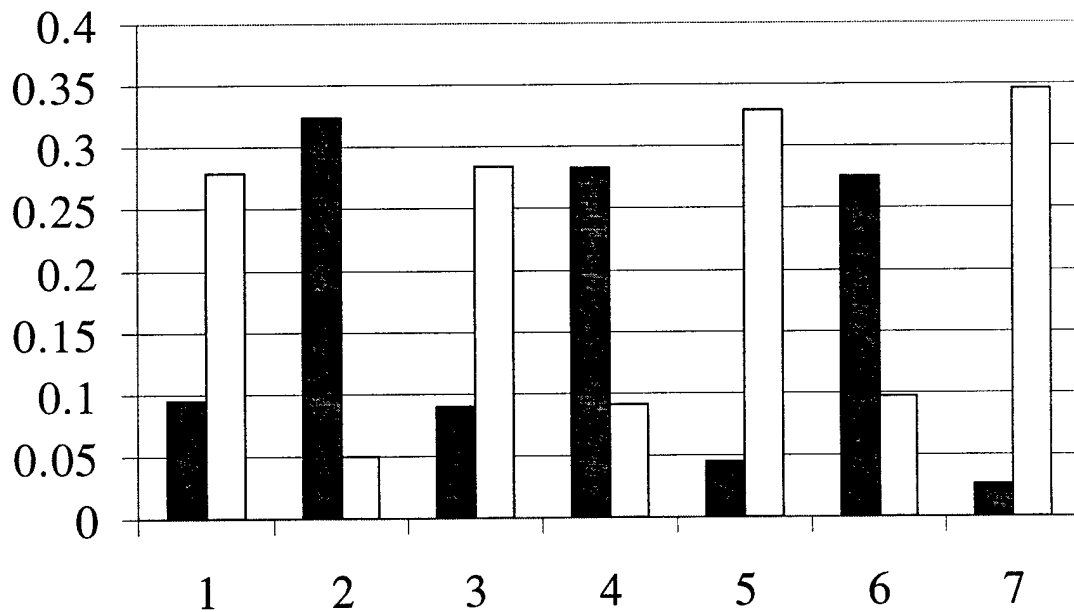


Figure VI.37: DOE results showing the relative importance each factor has on the objective function. The correlation of factor numbers to parameters are given in Table VI.11.

Table VI.11 CORRELATION OF FACTOR AND PARAMETER

Factor	1	2	3	4	5	6	7
Parameter	Data Points	Error	Iso (269 < 0.5)	Rate Seq	Temp Seq (H - L)	Iso (269 > 0.5)	Temp Seq (L - H)

VI.6 Summary

Many practical applications involve variations in loading conditions. Large changes occur during metal forming operations which have many military applications. Materials develop microstructures dependent upon these deformation conditions, which then respond differently to changing deformation conditions. Precise modeling of these microstructures, necessary for obtaining an accurate functional forms for constitutive models, result in complex relations. These complex constitutive models have often been considered too difficult. Limitations in available computing resources for the complex modeling requirements are being rapidly overcome by technology, but the difficulty in obtaining accurate parametric sets remains a significant obstacle. The procedure utilized here, a robust, non-linear optimization strategy, makes this last problem simpler.

The optimization process proved capable of determining the optimal parametric set corresponding to well correlated predictions with experimental data. When this correlation was insufficient, as when the flow stress softening was not predicted, the shortcomings of the utilized model appear. Changes or additions to the constitutive relations are then necessary to improve the correlation. The optimization process assists this procedure as well. Either alternative hypotheses can be evaluated, with the resulting objective function values used as the determination of the best alternative, or a general functional form can be utilized with the resulting parameter values determining the best form.

The softening parameter added to both the BCJ-SNL and McDowell models greatly improved their predictive capabilities of the observed flow softening. The success of this

additional term provides support for the conclusion that processes, other than static or dynamic recovery were responsible.

The following advances to constitutive modeling were established:

- A robust, non-linear optimization strategy was demonstrated and successfully utilized for the optimization of material parameters. This process was effective without regard to the quantity of parameters required by the model, five parameters or thirty. This technique was extremely efficient and greatly enhanced the ability to use constitutive models with larger numbers of physical mechanisms modeled. Moreover, it provided information on parameter sensitivity and redundancy.
- Recrystallization creates a softened state which was accurately incorporated into an ISV formulation. An auxiliary ISV, representing the changes in microstructure resulting from the growth of new, dislocation free grains, when added to both the BCJ-SNL and McDowell models, greatly improved the correlation to experimental data. The recrystallization auxiliary ISV was included in the isotropic hardening variable, due to the homogeneous nature of recrystallization.
- Very high strain hardening rates are observed at strain rates greater than 10^5 s^{-1} . The McDowell model correlation to experimental data at these very high strain rates was improved with the additional terms involving the effective plastic strain rate in the

coefficient of isotropic hardening..

- The optimization strategy, coupled with a statistical design of experiments approach was utilized for the evaluation of multiple modeling factors. This combination of approaches was effective in evaluating numerous options for model formulations, data requirements, and objective function definitions. This procedure identified the requirement to include temperature sequence experimental data when determining the optimized material parameters. A temperature sequence from 25°C at 0.0004 s⁻¹ to a pre-strain of 0.5, followed by 269°C at 0.0004 s⁻¹ was the most effective for accurately obtaining the restoration coefficients since both static and dynamic restoration mechanisms were activated. Additionally, the absolute value of the maximum difference between experimental data and model predictions was an improved objective function definition over the L_2 norm.

CHAPTER VII

SUMMARY AND CONCLUSIONS

VII.1 Overview of Experimental Results

An extensive experimental program was completed on OFHC Cu and complements the deformation path sequence experiments conducted by Graham, 1995, and investigations into the texture development by Butler *et al.*, 1998 using the same OFHC Cu material with the same initial grain size. This comprehensive experimental program included experiments to characterize the material response to a wide range of deformation conditions. The major conclusions which can be drawn from this experimental program are as follows:

- (1) OFHC Cu exhibits strain rate, temperature, and deformation path history effects. The evolution of microstructure is dependent on the initial state and the imposed deformation conditions. A transient response is observed after a change in deformation conditions which lasts on the order of the initial pre-strain, but may be permanent. The typical response during deformation sequences is for the flow stress to demonstrate an initial, instantaneous jump, towards the curve associated with the new deformation conditions. Then the flow stress transitions with a greater strain hardening rate and approaches the

new constant deformation condition curve. During deformation path sequences, from compression to torsion, the flow stress did not generally approach the torsion curve, but stayed at a greater stress level. The material response is clearly dependent on the prior deformation conditions. These strain rate, temperature, and deformation path history effects create the necessity for ISV evolution equations to accurately capture the internal structure which depends on prior deformation. The precise nature of the transition from one deformation state to another is not fully understood, but it was apparent that the changes associated with restoration processes affected the transition.

- (2) A novel specimen design was created for accomplishing path sequence experiments following a high strain rate compression experiment using the Hopkinson bar apparatus. The double shear specimen design permitted the small volume of material resulting from the high compressive strain rate experiment to be subsequently deformed in shear.
- (3) Equivalent stress results for torsion tests consistently are lower than those for compression tests at the same equivalent plastic strain. This effect, torsional softening, was observed to decrease and approach the same equivalent stress level as the deformation temperature increased. The cause of the differences

in stress levels must be temperature dependent.

- (4) Under quasi-static, 0.0004 s^{-1} , strain rates, the flow stress transitions from continued strain hardening, at 25°C , to oscillations in the flow stress with an eventual saturated flow stress level. The flow stress smoothly transitions from the fairly constant strain hardening rate, during quasi-static compression deformation, at room temperature to a saturated flow stress at 202°C and then from a single peak in the flow stress to oscillations above 337°C . These flow stresses are characteristics of the occurrence of dynamic recrystallization with single peak associated with grain refinement and multiple peak with grain coarsening. The micrograph investigation confirms the occurrence of recrystallization as the explanation of the softening in flow stress. The final grain sizes were consistent with those expected from grain refinement associated with single peak flow and grain coarsening with multiple peak flow.

VII.2 Summary of Constitutive Modeling

A comprehensive modeling effort was completed to investigate the ability of current state-of-the-art constitutive models, ranging from relatively simple empirical models, Johnson/Cook and Zerilli-Armstrong, to ISV constitutive models with various numbers of

variables. This research also incorporated a powerful optimization strategy which greatly facilitates the utility of models with many parameters. The following conclusions can be made:

- (1) OFHC Cu experiences restoration which is due to recrystallization processes during deformation under relatively high temperatures and low strain rates. This characteristic explains many of the observations made during the experimental program. None of the models described in Chapter V captured the observed softening of the flow stress at temperatures above 236°C at quasi-static strain rates. Only the BCJ-SNL and McDowell models include static recovery effects, which improve their predictive capabilities, but still do not fully capture either the dynamic softening nor the complete static restoration. A material softening term was necessary to account for the observed restoration (recrystallization) processes. An additional term was included in both the BCJ-SNL and McDowell models representing the softened state of the material corresponding to an internal structure steady state following recrystallization, both static and dynamic, which greatly improved the predictive capabilities of these models.
- (2) The very high strain data of Clifton could not be correlated without the additional hardening rate term, proportional to the strain rate. The addition

of this term improved the model correlations to experimental data. An adiabatic heating conditional was also simulated. The McDowell model with the additional hardening rate term successfully improved the correlation to the high strain rate regime.

- (3) The optimization strategy was effective in the determination of the optimal parameter set and facilitated the determination of proper functional forms. The optimization process, utilizing a combination of optimization schemes, made the determination of parameters, even when there were a great many, very efficient. The ability to establish constraints and provide a range of variation on the parameters allowed the establishment of physically realistic bounds. The path is clear for framing more physically realistic models.

VII.3 Recommendations

The deformation history effects investigation within the current research represents the continued process of a larger, more comprehensive study. This larger program includes accounting for complex paths of deformation through the development of polycrystal models incorporating the evolution of texture and slip system/grain level ISV relations. This would include the addition of ISV evolution forms of hardening minus recovery, both static and dynamic. The current modeling effort was principally oriented on uniaxial deformation

involving sequences of strain rate and temperature. The inclusion of deformation path is essential for improved modeling capabilities.

The optimization strategy was extremely effective in the determination of parameters and of the functional forms which accurately reflect the physical processes. Based on the premise that the correct functional form will result in the highest correlation, lowest objective function value, then the strategy provides a mechanism for the evaluation of different functional forms for deformation mechanisms. This technique allows the evaluation of competing hypotheses and different descriptions for similar mechanisms and should be incorporated in the polycrystal modeling.

Modeling the evolution of microstructure through the ISV evolution equations requires an understanding of the physical mechanisms involved. Investigations into the actual changes within substructures facilitates the physical based modeling. These studies should include state-of-the-art probes and observation of microstructure.

REFERENCES

- Albertini, C., Montagnani, M., and Eleiche, A.M., 1984, "The Influence of Strain-Rate History on Stress Strain Diagram of AISI 316 at High Temperature," in: Transactions of the 8th International Conference on Structural Mechanics in Reactor Technology, pp. 383-390 and Res Mechanica, Vol. 27, pp. 233-245.
- Alden, T.H., 1976, 'Microstructural Interpretation of Work Softening in Aluminum,' Metallurgica Transactions, Vol. 7, pp. 1057-1063.
- Alexopoulos, P., Keusseyan, R.L., Wire, G.L., and Li, C-Y., 1982, "Experimental Investigation of Non-elastic Deformation Emphasizing Transient Phenomena by Using a State variable Approach," in: Mechanical Testing for Deformation Model Development, ASTM STP 765, ed. R.W. Rohde and J.C. Swearingen, American Society for Testing and Materials, pp. 148-184.
- Anand, L., 1982, "Constitutive Equations for the Rate-Dependent Deformation of Metals at Elevated Temperatures," Journal of Engineering Materials and Technology, Vol. 104, pp. 12-17.
- Anand, L. and Brown, S., 1986, "Constitutive Equations for Large Deformation of Metals at High Temperatures," NTIS: PB90 121328.
- Andrade, U., 1993, "High-Strain, High-Strain-Rate Deformation of Copper", Ph.D Thesis, Brown University.
- Andrade U., Meyers, M. A., Vecchio, K. S., and Chokshi, A. H., 1994, "Dynamic Recrystallization in High-Strain-Rate Plastic Deformation of Copper," Acta Metallurgica, Vol. 42, pp. 3183-3195.
- Ashby, M.F., 1972, "A First Report on Deformation-Mechanism Maps," Acta Metallurgica, Vol. 20, pp. 887-897.
- ASTM Standard E209-65, "Standard Practice for Compression Tests of Metallic Materials at Elevated Temperatures with Conventional or Rapid Heating Rates and Strain Rates," ASTM, Philadelphia, PA., 383.

ASTM STP 808, "Compression Testing of Homogenous Materials and Composites," (eds) Chait, R. and Papirno, R., ASTM, Philadelphia, PA.

Bammann, D.J., 1984, "An Internal Variable Model of Viscoplasticity," *International Journal of Engineering Science*, Vol. 22, No. 8-1, pp. 1041-1053.

Bammann, D.J., and Johnson, G.C., 1987, "On the Kinematics of Finite-Deformation Plasticity," *Acta Mechanica*, Vol. 70, pp. 1-13.

Bammann, D.J., and Aifantis, E.C., 1987, "A Model for Finite-Deformation Plasticity," *Acta Mechanica*, Vol. 69, pp. 97-117.

Bammann, D.J. and Krieg, R.D., 1987, "Summary and Critique," in: Unified Constitutive Equations for Creep and Plasticity, ed. Miller, A.K., Elsevier Applied Science, New York, pp. 303-337.

Bammann, D.J., 1990, "Modeling Temperature and Strain Rate Dependent Large Deformations of Metals," *Applied Mechanics Review*, Vol. 43, No. 5, pp. S312-S319.

Bammann, D.J. and Dawson, P.R., 1993, "Modeling the Initial State of a Material and Its Effect on Further Deformation," Material Parameter Estimation for Modern Constitutive Equations, eds. Bertram, L.A., Brown, S.B., Freed, A.D., Vol. 43.

Bammann, D.J., Chiesa, M.L., Horstemeyer, M.F. and Weingarten, L.I., 1993, "Failure in Ductile Materials Using Finite Element Methods," in: Structural Crashworthiness and Failure, pp. 1-54.

Barlow, C.Y., Bay, B., and Hansen, N., 1985, "A Comparative Investigation of Surface Relief Structures and Dislocation Microstructures in Cold-Rolled Aluminium," *Philos. Mag.*, Vol. 51, pp. 253-275.

Barraclough, D.R. and Sellars, C.M., 1974, "The Effect of Varying Deformation Conditions During Hot Torsion Testing," in: Mechanical Properties at High Rates of Strain, Conference Series Number 21, pp. 111-123, The Institute of Physics, London.

Basinski, Z.S., 1974, "Forest Hardening in Face Centered Cubic Metals," *Scripta Metallurgica*, Vol. 8, pp. 1301-1307.

Bassim, M.N. and Liu, C.D., 1993, "Dislocation Cell Structures in Copper in Torsion and Tension," *Materials Science and Engineering*, Vol. 164, pp. 170-174.

Bay, B. and Hansen, N., 1988, in Proc. 8th Int. Conf. On the Strebgth of Metals and Alloys, eds. Kettunen, P.O., Lepisto, T.P. and Lehonon, M.E., Pergamon, Oxford.

Bay, B., Hansen, N., and Kulmann-Wilsdorf, D., 1989, "Deformation Structures in Lightly Rolled Pure Aluminium," Materials Science and Engineering, Vol. 113, pp. 385-397.

Bell, J.F. and Khan, A.S., 1980, "Finite Plastic Strain in Annealed Copper During Non-Proportional Loading," International Journal of Solids and Structures, Vol. 16, pp. 683-693..

Bertram, L.A., Lu, W.Y., and Brandon, S.L., 1993, "Constitutive Parameter Estimation for SS304L with a Hardening-Recovery Internal Variable Representation," in: Material Parameter Estimation for Modern Constitutive Equations, Vol. 43, pp. 21-33.

Blaz, L., Sakai, T., and Jonas, J.J., 1983, "Effect of Initial Grain Size on Dynamic Recrystallization of Copper," Metal Science, Vol. 17, pp. 609-616.

Bodner, S.R., 1968, "Constitutive Equations for Dynamic Material Behavior," in: Mechanical Behavior of Materials Under Dynamic Loads, Symposium San Antonio, TX, ed.. Lindholm, U.S., Springer-Verlag, New York, pp. 176-190.

Bodner, S.R. and Partom, Y., 1974, "A Representation of Elastic-Viscoplastic Strain Hardening Behavior for Generalized Straining Histories," in: Mechanical Properties at High Rates of Strain, Conference Series Number 21, pp. 102-110, The Institute of Physics, London.

Bodner, S. and Partom, Y., 1975, "Constitutive Equations for Elastic-Viscoplastic Strain Hardening Materials," ASME J. Appl. Mech., pp. 385-389.

Bodner, S. and Merzer, A., 1978, "Viscoplastic Constitutive Equations for Copper With Strain Rate History and Temperature Effects," Journal of Engineering Materials and Technology, Vol. 100, pp. 388-394.

Braasch, H., Dudeck, H., Ahrens, H., 1995, "A New Approach to Improve Material Models," Journal of Engineering Materials and Technology, Vol. 117, pp. 14-19.

Braasch, H. And Estrin, Y., 1993, "Parameter Identification for a Two-Internal-State Constitutive Model Using the Evolution Strategy," Material Parameter Estimation for Modern Constitutive Equations, Vol. 43, pp. 47-56.

Bragov, A.M., Lomunov, A.K., and Medvedev, A.A., 1991, "A Modified Kolsky Method for the Investigation of the Strain-Rate History Dependence of Mechanical Properties of Materials," Journal de Physique, Vol. IV, pp. 471-475.

Brown, S.B., Kim, K.H. and Anand, L., 1989, "An Internal Variable Constitutive Model for Hot Working of Metals," *International Journal of Plasticity*, Vol. 5, pp. 95-130.

Busso, E.P., 1998, "A Continuum Theory for Dynamic Recrystallization with Microstructure-Related Length Scales," In Press: *International Journal of Plasticity*.

Butler, G.C., McDowell, D.L., and Stock, S.R., 1998, "Application of the Taylor Polycrystal Plasticity Model to Complex Deformation Experiments," In Press: *Journal of Engineering Materials and Technology*.

Cailletaud, G. and Pilvin, P., 1993, "Identification and Inverse Problems: A Modular Approach," in: Material Parameter Estimation for Modern Constitutive Equations, Vol. 168, pp. 33-45.

Campbell, J.D. and Duby, J., 1956, "The Yield Behavior of Mild Steel in Dynamic Compression," *Proceedings of the Royal Society of London*, Vol. A236, pp. 24-40.

Campbell, J.D. and Dowling, A.R., 1970, "The Behavior of Materials Subjected to Dynamic Incremental Shear Loading," *Journal of the Mechanics and Physics of Solids*, Vol. 18, pp. 43-63.

Campbell, J.D., 1973, "Dynamic Plasticity: Macroscopic and Microscopic Aspects," *Materials Science and Engineering*, Vol. 12, pp. 3-21.

Campbell, J.D. and Briggs, T.L., 1975, "Strain-Rate History Effects in Polycrystalline Molybdenum and Niobium," *Journal of the Less-Common Metals*, Vol. 40, pp. 235-250.

Campbell, J.D., Eleiche, A.M., and Tsao, M.C.C., 1975, "Strength of Metals and Alloys at High Strains and Strain Rates," in: Fundamental Aspects of Structural Alloy Design, eds. Jaffee, R.I. and Wilcox, B.A., pp. 545-563.

Carreker, R.P. and Hibbard, W.R., 1957, "Tensile Deformation of Aluminum as a Function of Temperature, Strain rate, and Grain Size," *Journal of Metals*, pp. 1157-1163.

Chaboche, J.L. and Rousselier, G., 1983, "On the Plastic and Viscoplastic Constitutive Equations - Part I: Rules Developed with Internal Variable Concept," *Journal of Pressure Vessel Technology*, Vol. 105, pp. 153-158.

Chan, K.S., Bodner, S.R., Walker, K.P. and Lindholm, U.S., 1984, "A Survey of Unified Constitutive Theories," *Second Symposium on Nonlinear Constitutive Relations for High Temperature Applications*, Cleveland, OH.

- Chen, S.R. and Kocks, U.F., 1992, "On the Strain-Rate Dependence of Dynamic Recrystallization in Copper Polycrystals," *Scripta Metallurgica et Materialia*, Vol. 27, pp. 1587-1592.
- Chiem, C.Y. and Duffy, J., 1980, "Strain Rate History Effects in LiF Single Crystals During Dynamic Loading in Shear," *Materials Science and Engineering*, Vol. 48, pp. 207-222.
- Chiem, C.Y. and Duffy, J., 1983, "Strain Rate History Effects and Observations of Dislocation Substructure in Aluminum Single Crystals Following Dynamic Deformation," *Materials Science and Engineering*, Vol. 57, pp. 233-247.
- Christodoulou, N., Jonas, J.J., Canova, G.R., 1982, "Determination of First and Second Order Work-hardening and Rate-Sensitivity Coefficients for Oxygen-Free, High Conductivity (OFHC) Copper and 99.99 Percent Aluminum," *Mechanical Testing for Deformation Model Development*, pp. 51-66.
- Clifton, R.J., 1983, "Dynamic Plasticity," *Journal of Applied Mechanics*, Vol. 50, pp. 941-952.
- Clifton, R.J., 1990, "High Strain Rate Behavior of Metals," *Applied Mechanics Review*, Vol. 43, pp. S9-S22.
- Costin, L.S. and Duffy, J., 1979, "The Effect of Loading Rate and Temperature on the Initiation of Fracture in a Mild, Rate-Sensitive Steel," *Journal of Engineering Materials and Technology*, Vol. 101, pp. 258-264.
- Dave, V.R. and Brown, S.B., 1994, "Critical Experiments Used to Determine Flow Relations for Rate-Dependent Metal Deformation," *International Journal of Plasticity*, Vol. 10, pp. 237-262.
- Davies, E.D.H. and Hunter, S.C., 1963, "The Dynamic Compression Testing of Solids by the Methods of the Split Hopkinson Pressure Bar," *Journal of Mechanics and Physics of Solids*, Vol. 11, pp. 155-179.
- Deprez, P., Bricout, J.P. and Oudin, J., 1993, "Tensile Test on *in situ* solidified notched specimens: Effects of Temperature History and Strain Rate on the Hot Ductility of Nb and Nb-V Microalloyed Steels," *Materials Science and Engineering*, Vol. A168, pp. 17-22.
- Derby, B. and Ashbey, M. F., 1987, "On Dynamic Recrystallisation," *Scripta Metallurgica*, Vol. 21, pp. 879-884.

Derby, B., 1991, "the Dependence of Grain Size on Stress During Dynamic Recrystallization," *Acta Metallurgica*, Vol. 39, pp. 955-962.

Doner, M., Chang, H., and Conrad, H., 1974, "Plastic Flow and Dislocation Structure at Small Strains in OFHC Copper Deformed in Tension, Torsion and Combined Tension-Torsion," *Journal Mechanics and Physics of Solids*, Vol.22, pp. 555-573.

Dormeval, R. and Stelly, M., 1979, "Influence of Grain Size and Strain Rate on the Mechanical Behavior of High-Purity Polycrystalline Copper," in: Mechanical Properties at High Rates of Strain, Conference Series Number 47, pp. 154-165, The Institute of Physics, London.

Dormeval, R. and Ansart, J.P., 1985, "Heterogeneity of Deformation Under Dynamic Loading: Influence of a Local Pre-strain in Copper," in: Macro-and Micro-Mechanics of High Velocity Deformation and Fracture, ed. Kawata, K. and Shiori, J., Springer-Verlag, New York, pp. 213-222.

Dorn, D.E., Goldberg, A. and Tietz, B., 1949, "The Effect of Thermal-Mechanical History on the Strain Hardening of Metals," *Transactions of the American Institute of Mining and Metallurgical Engineering*, Vol. 180, pp. 205-225.

Draeos, T. And Hush, D., 1996, "A Constructive Neural Network Algorithm for Function Approximation," *IEEE Vol. 5*, pp. 50-55.

Duffy, J., Campbell, J.D., and Hawley, R.H., 1971, "On the Use of a Torsional Split Hopkinson Bar to Study Rate Effects in 1100-0 Aluminum," *Journal of Applied Mechanics*, Vol. 38, pp. 83-91.

Duffy, J., 1974, "Some Experimental Results in Dynamic Plasticity," in: Mechanical Properties at High Rates of Strain, Conference Series Number 21, pp. 72-80, The Institute of Physics, London.

Duffy, J., 1979, "The J.D. Campbell Memorial Lecture: Testing Techniques and Material Behavior at High rates of Strain," in: Mechanical Properties at High Rates of Strain, Conference Series Number 47, pp. 1-15, The Institute of Physics, London.

Duffy, J., 1982, "Strain Rate History Effects and Dislocation Substructure at High Strain Rates," *Proc. 29th Sagamore Army Materials Conference, Material Behavior Under High Stress and Ultrahigh Loading Rates*, July 19-23, Lake Placid, New York, Plenum Press, pp. 21-38 and in: Material Behavior Under High Stress and Ultrahigh Loading Rates, eds.. Mescall, J. and Weiss, V., pp. 21-37, Plenum Press, New York.

Dunne, F.P.E., Nanneh, M.M. and Zhou, M., 1997, "Anisothermal Large Deformation Constitutive Equations and Their Application to Modelling Titanium Alloys in Forging," *Philosophical Magazine A*, Vol. 75, No. 3, pp. 587-610.

Edington, J.W., 1967, "Effect of Strain Rate on the Dislocation Substructure in Deformed Niobium Single Crystals," in: Mechanical Behavior of Materials Under Dynamic Loads, Symposium, San Antonio, TX, Ed. Lindholm, U.S., Spring-Verlag, New York, pp.191-240.

Eleiche, A.M. and Campbell, J.D., 1974, "The Influence of Strain-Rate History on the Shear Strength of Copper and Titanium at Large Strains," University of Oxford Report.

Eleiche, A.M. and Campbell, J.D., 1976, "The Influence of Strain-Rate History and Temperature on the Shear Strength of Copper, Titanium, and Mild Steel," DTIC: AD-A031 315.

Eleiche, A.M. and Campbell, J.D., 1976, "Strain-Rate Effects During Reverse Torsional Shear," *Experimental Mechanics*, Vol. 16. Pp. 281-290.

Eleiche, A.M., Albertini, C., and Montagnani, M., 1985, "The Influence of Strain-Rate History on the Ambient Tensile Strength of AISI Type 316 Stainless Steel," *Nuclear Engineering and Design*, Vol. 88, pp. 131-141.

Ellwood, S., Griffiths, L.J., and Parry, D.J., 1984, "Strain Rate and Temperature Effects at High Strain Rates in AISI 321 Stainless Steel," in: Mechanical Properties at High Rates of Strain, Conference Series Number 70, pp. 55-62, The Institute of Physics, London.

Ellyin, F., Xia, Z. and Sasaki, K., 1993, "Effect of rate and Rate History on Plastic Deformation: Experiments and Constitutive Modelling," *International Journal of Plasticity*, Vol. 9, pp. 951-959.

Estrin, Y. And Mecking, H., 1986, "An Extension of the Bodner-Partom Model of Plastic Deformation," *International Journal of Plasticity*, Vol. 2, pp. 73-85.

Estrin, Y. and Mecking H., 1990, "A Unified Phenomenological Description of Work Hardening and Creep Based on One-Parameter Models," *Acta Metallurgica*, Vol. 32, p. 57-70.

Follansbee, P.S., Kocks, U.F., and Regazzoni, G., 1984, "The Transition to Drag-Controlled Deformation in Copper at High Strain Rates," in: Mechanical Properties at High rates of Strain, 1984, ed. Harding, J. Conference Series 70, pp. 71-80.

Follansbee, P.S., 1985, "High-Strain-Rate Deformation of FCC Metals and Alloys," in: Metallurgical Applications of Shock-Wave and High-Strain-Rate Phenomena, ed. Murr, L.E. et al, Marcel Dekker, New York, pp. 451-477.

Follansbee, P.S. and Gray, G.T., 1985, "Threshold Stress Measurements in Shock-Deformed Copper," in: Shock Waves in Condensed Matter, ed. Gupta, Y.M., Plenum Press, New York, pp. 371-376.

Follansbee, P.S., Kocks, U.F., and Regazzoni, G., 1985, "The Mechanical Threshold of Dynamically Deformed Copper and Nitronic 40," *Journal de Physique*, Vol. C5, pp. 25-34.

Follansbee, P.S. and Kocks, U.F., 1988, "A Constitutive Description of the Deformation of Copper Based on the Use of the Mechanical Threshold Stress as an Internal State Variable," *Acta Metallurgica*, Vol. 36, No. 1, pp. 81-93.

Follansbee, P.S., 1988, "The Rate Dependence of Structure Evolution in Copper and its Influence on the Stress-Strain Behavior at Very High Strain Rates," *Proc. Int. Conf. On Impact Loading and Dynamic Behavior of Materials*, eds. Chiem, C.Y., Kunze, H.D. and Meyers, L.W., Fraunhofer Institute, Bremen, Verlag, pp. 315-322.

Follansbee, P.S., 1989, "Analysis of the Strain-Rate Sensitivity at High Strain Rates in f.c.c. and b.c.c. Metals," in: Institute of Physics Conference Series, No. 102, ed. Harding, J., pp. 213-220

Follansbee, P.S., 1989, "Comparison Between the Rate and Temperature Dependent Plasticity Models of Bammann and of Kocks and Mecking," LA-11588_MS Los Alamos National Laboratory.

Follansbee, P.S. and Gray, G.T., 1989, "An Analysis of the Low Temperature, Low and High Strain-Rate Deformation of Ti-6Al-4V," *Metallurgical Transactions A*, Vol. 20, pp. 863-874.

Follansbee, P.S., Huang, J.C., and Gray, G.T., 1990, "Low-Temperature and High-Strain-Rate Deformation of Nickel and Nickel-Carbon Alloys and Analysis of Constitutive Behavior According to an Internal State Variable Model," *Acta Metallurgica*, Vol. 38, pp. 1241-1254.

Follansbee, P.S. and Gray, G.T., 1991, "The Response of Single Crystal and Polycrystal Nickel to Quasi-static and Shock Deformation," *International Journal of Plasticity*, Vol. 7, pp. 651-660.

Follansbee, P.S. and Gray, G.T., 1991, "Dynamic Deformation of Shock Pre-strained Copper," *Materials Science and Engineering*, Vol. A138, pp. 23-31.

Fossum, A.F., 1998, "Rate Data and Material Model Parameter Estimation," *Journal of Engineering Materials and Technology*, Vol. 120, pp. 7-12.

Franciosi, P., Stout, M.G., O'Rourke, J., Erskine, B. and Kocks, U.F., 1987, "Channel Die Tests on Al and Cu Polycrystals: Study of the Pre-strain History Effects on Further Large Strain Texture," *Acta Metallurgica*, Vol. 35, pp. 2115-2128.

Frantz, R.A. and Duffy, J., 1972, "The Dynamic Stress-Strain Behavior in Torsion of 1100-0 Aluminum Subjected to a Sharp Increase in Strain Rate," *Journal of Applied Mechanics*, Vol. 39, pp. 939-945.

Frantz, R.A., Follansbee, P.S., and Wright, W.T., 1984, "Experimental Techniques with the Split Hopkinson Pressure Bar," in: High Energy Rate Fabrication, eds. Berman, I. and Schoroder, J.W., pp. 229-236.

Freed, A.D. and Walker, K.P., 1993, "Viscoplastic Model Development with an Eye Towards Characterization," *Material Parameter Estimation for Modern Constitutive Equations*, Vol. 43, pp. 71-88.

Frutsky, K.J. and Clifton R.J., 1998, "High-Temperature Pressure-Shear Plate Impact Experiments on OFHC Copper," *Brown University*.

Gilat, A. and Pao, Y.H., 1988, "High-Rate Decremental-Strain-Rate Test," *Experimental Mechanics*, pp. 322-325.

Glenn, T. and Bradley, W., 1973, "The Origin of Strain-Rate Sensitivity in OFHC Copper," *Metallurgical Transactions*, Vol. 4, pp. 2343-2348.

Goldberg, A. and Hoge, K.G., 1974, "Effect of Strain Rate on Tension and Compression Stress-Strain Behavior in a TRIP Alloy," *Materials Science and Engineering*, Vol. 13, pp. 211-222.

Gottstein, G. and Kocks, U.F., 1983, "Dynamic Recrystallization and Dynamic Recovery in $\langle 111 \rangle$ Single Crystals of Nickel and Copper," *Acta Metallurgica*, Vol. 31, pp. 175-188.

Gottstein, G. and Argon, A.S., 1984, "Dislocation Theory of Strain Hardening and Steady State Deformation in Creep and Constant Strain Rate Tests," *International Conference of Creep and Fracture of Engineering Materials and Structures*, eds. Wilshire, B. et. al., pp. 15-26.

Gottstein, G., Chang, L., and Yung H. F., 1991, "Dynamic Recrystallization and Microstructural Evolution in Ni_3Al ," *Materials Science and Technology*, Vol. 7, pp. 158-166

Gourdin, W.H. and Lassila, D.H., 1991, "Flow Stress of OFE Copper at Strain Rates from 10^{-3} to 10^4 s $^{-1}$: Grain-Size Effects and Comparison to the Mechanical Threshold Stress Model," *Acta Metallurgica*, Vol. 39, No. 10, pp. 2337-2348.

Gourdin, W.H. and Lassila, D.H., 1991, "Deformation Behavior of Pre-Shocked Copper as a Function of Strain Rate and Temperature," in: Shock Compression of Condensed Matter, eds. Schmidt, S.C., Dick, R.D., Forbes, J.W., and Tasker, D.G., pp. 411-414.

Gourdin, W.H., 1992, "Characterization of Copper Shaped-Charge Linear Materials at Tensile Strain Rates of 10^4 s $^{-1}$," in: Shock-Wave and High-Strain-Rate Phenomena in Materials, eds. Meyers, M.A., Murr, L.E., and Staudhammer, K.P., pp.597-609.

Gourdin, W.H. and Lassila, D.H., 1992, "The Mechanical Behavior of Pre-Shocked Copper at Strain Rates of 10^{-3} to 10^4 and Temperatures of 25 to 400°C," *Materials Science and Engineering*, Vol. A151, pp. 11-18.

Grace, F.I., 1992, "Shaped Charge Jetting of Metals at Very High Strain Rates," in: Shock-Wave and High-Strain-Rate Phenomena in Materials, pp. 493-501.

Gray, G.T., Follansbee, P.S., and Frantz, C.E., 1989, "Effect of Residual Strain on the Substructure Development and Mechanical Response of Shock-Loaded Copper," *Materials Science and Engineering*, Vol. A111, pp. 9-16.

Gray, G.T., Chan, S.R., Wright, W. And Lopez, M.F., 1994, "Constitutive Equations for Annealed Metals Under Compression at High Strain Rates and High Temperatures," LA-12669-MS.

Green, S.J., Maiden, C.J., Babcock, S.G., and Schierloh, F.L., 1970, "The High Strain-Rate Behavior of Face-Centered Cubic Metals," in: Inelastic Behavior of Solids, eds. Kanninen, M.F., Adler, W.F., Rosenfield, A.R., and Jaffee, R.I., pp. 521-542.

Guiu, F., 1969, "On the Stress Transients Observed During Strain Rate Change Experiments," *Scripta Metallurgica*, Vol. 3, pp. 489-494.

Gulec, A.S. and Baldwin, D.H., 1973, "Some Effects of Pre-straining Nickel at Various Rates on its Subsequent Tensile Properties," *Metallurgical Transactions*, Vol. 4, pp. 1315-1321.

Hamersky, M., 1996, "Conditions for the Initiation of Strain Bursts in the Portevin-Le Chatelier Effect," *Scripta Materialia*, Vol. 35, pp. 535-538.

Hansen, N., 1992, "Deformation Microstructures," Scripta Materialia, Vol. 27, pp. 1447-1452.

Hansen, N. and Kuhlmann-Wilsdorf, D., 1986, "Low Energy Dislocation Structures Due to Unidirectional Deformation at Low Temperatures," Mater. Sci. Eng., Vol. 81, No. 1-2, pp. 141-161.

Harding, J., 1987, "The Effect of High Strain Rate on Material Properties," in: Materials at High Strain Rates, ed. Blazynski, T.Z., pp. 133-186, Elsevier Applied Science, New York.

Harding, J., 1989, "The Development of Constitutive Relations for Material Behavior at High Rates of Strain," in: Institute of Physics Conference Series No. 102, pp. 189-203.

Hart, E.W., 1976, "Constitutive Relations for the Nonelastic Deformation of Metals," Journal of Engineering Materials and Technology, Vol. 15, pp. 193-202.

Hart, E.W. and Garmestani, H., 1993, "Mechanical Testing Using Direct Control of the Inelastic Strain rate," Experimental Mechanics, pp. 1-6.

Hartley, K.A. and Duffy, J., 1984, "Strain Rate and Temperature History Effects During Deformation of f.c.c. and b.c.c. Metals," in: Mechanical Properties at High Rates of Strain, Conference Series Number 70, pp. 189-203, The Institute of Physics, London.

Hockett, J.E., 1959, Proceedings ASTM 59, p. 1309.

Horstemeyer, M.F., 1993, "Structural Analysis of a Submarine Using Statistical Design of Experiments," Advances in Numerical Simulation Techniques for Penetration and Perforation of Solids, eds. Chen, E.P. and Luk, V.K., Vol. 171, pp. 189-200.

Horstemeyer, M.F., 1995, "Physically-Motivated Modeling of Deformation-Induced Anisotropy," Ph.D Thesis, Georgia Institute of Technology.

Hughes, D.A. and Nix, W.D., 1986, "On the Limitations of Dynamic Recovery as Revealed by Temperature Change Tests at Large Strains," Scripta Metallurgica, Vol. 20, pp. 1455-1458.

Hwu, Y-J., Pang, G.K.H. and Lenard, J.G., 1994, "An Application of Artificial Neural Networks to the Prediction of Flow Stress of Steels at Elevated Temperatures," Transactions of NAMRI/SME, Vol. XXII, pp. 35-40.

Ikegami, K. and Niitsu, Y., 1987, "Plastic Behavior of 304 Stainless Steel for Complex Loading at High Temperature," in: Structural Mechanics in Reactor Technology, Vol. L, ed. Wittmann, F.H., pp. 345-356, A.A. Balkema, Boston.

Immarigeon, J.-P.A. and Jonas, J.J., 1971, "Flow Stress and Substructural Change During the Transient Deformation of Armco Iron and Silicon Steel," *Acta Metallurgica*, Vol. 19, pp. 1053-1061.

James, G.H., Imbrie, P.K., Hill, P.S., Allen, D.H. and Haisler, W.E., 1987, "An Experimental Comparison of Several Current Viscoplastic Constitutive Models at Elevated Temperature," *Journal of Engineering Materials and Technology*, Vol. 109., pp. 130-139.

Jeniski, R.A., Thanaboonsombut B., and Sanders T.H., 1996, "The Effect of Iron and Manganese on the Recrystallization Behavior of Hot-Rolled and Solution-Heat-Treated Aluminum Alloy 6013," *Metallurgical and Materials Transactions*, Vol. 27, pp. 19-27

Johnson, G.R. and Cook, W.H., 1983, "A Constitutive Model and Data for Metals Subjected to Large Strains, High Strain Rates and High Temperatures," in: Proceedings of Seventh International Symposium on Ballistics, The Hague, pp. 541-547.

Jonas, J.J. and Sakai, T., 1984, "A New Approach to Dynamic Recrystallization," ed. Krauss, G., ASM, Metals Park, OH.

Jones, W.B., Rohde, R.W., and Swearengen, J.C., 1982, "Deformation Modeling and the Strain Transient Dip Test," in: Mechanical Testing for Deformation Model Development, ASTM STP 765, eds. R.W. Rohde and J.C. Swearengen, American Society for Testing and Materials, pp. 102-118.

Karnes, C.H. and Ripperger, E.A., 1966, "Strain Rate Effects in Cold Worked High-Purity Aluminum," *Journal of the Mechanics and Physics of Solids*, Vol. 14, pp. 75-88.

Kassner, M.E. and Breithaupt, R.D., 1983, "The Yield Stress of Type 21-6-9 Stainless Steel over a Wide Range of Strain Rate (10^{-5} to 10^4 s $^{-1}$) and Temperature," DE83-017159.

Kawahara, W.A., 1990, "Effects of Specimen design in Large-Strain Compression," *Experimental Techniques*, Society for Experimental Techniques, March/April 1990, pp. 58-60.

Kessler, W. And Kessler, R.W., 1995, "Kohonen Network as a Classifier and Predictor for the Qualification of Metal-Oxide-Surfaces," in: Neural Network Engineering in Dynamic Control Systems, ed. Hunt, K.J. et al, Springer-Verlag, London, pp.201-219.

Klahn, D., Mukherjee, A.K., and Dorn, J.E., 1970, "Strain-Rate Effects," in: International Conference on the Strength of Metals and Alloys, Pacific Grove, CA. Pp. 951-982.

Klepaczko, J., 1968, "Strain Rate History Effects for Polycrystalline Aluminum and Theory of Intersections," *Journal of the Mechanics and Physics of Solids*, Vol. 16, pp. 255-266.

Klepaczko, J.R. and Duffy, J., 1974, "Strain Rate and Temperature Memory Effects for Some Polycrystalline f.c.c. Metals," in: Mechanical Properties at High Rates of Strain, Conference Series Number 21, pp. 91-101, The Institute of Physics, London.

Klepaczko, J.R., 1974, "History Effects in Polycrystalline FCC Metals Subject to Rapid Changes in Strain rate and Temperature," DTIC: AD A-004-460.

Klepaczko, J.R., 1975, "Thermally Activated Flow and Strain Rate History Effects for Some Polycrystalline f.c.c. Metals," *Materials Science and Engineering A*, Vol 18, pp. 121-135.

Klepaczko, J., Frantz, R.A. and Duffy, J., 1977, "History Effects in Polycrystalline FCC Metals Subjected to Rapid Changes in Strain Rate and Temperature," *Rozprawy Inzynierskie*, Vol. 25, pp. 3-22.

Klepaczko, J.R. and Duffy, J., 1982, "Strain Rate History Effects in b.c.c. Metals," in: Mechanical Testing for Deformation Model Development, ASTM STP 765, eds. R.W. Rohde and J.C. Swearingen, American Society for Testing and Materials, pp. 251-268.

Klepaczko, J.R. and Chiem, C.Y., 1986, "On Rate Sensitivity of f.c.c. Metals, Instantaneous Rate Sensitivity and Rate Sensitivity of Strain Hardening," *Journal of the Mechanics and Physics of Solids*, Vol. 34, pp. 29-54.

Klepaczko, J.R., 1986, "A Practical Stress-Strain-Strain Rate-Temperature Constitutive Relation of the Power Form," *Journal of Mechanical Working Technology*, Vol. 15, pp. 143-165.

Klepaczko, J.R., 1986, "Constitutive Modelling of Strain Rate and Temperature Effects in FCC Metals," in: Intense Dynamic Loading and Its Effects, eds. Zhemin, Z. and Jing, D., pp. 670-678.

Klepaczko, J.R., 1987, "A Practical Stress-Strain-Strain Rate-Temperature Constitutive Relation of the Power Form," *Journal of Mechanical Working Technology*, Vol. 15, pp. 143-165.

Klepaczko, J.R., 1987, "Modelling of Structural Evolution at Medium and High Strain Rates, f.c.c. and b.c.c. Metals," The Eighth Riso International Symposium on Metallurgy and Materials Science.

Klepaczko, J.R., 1989, "Discussion of the Microstructural Effects and Their Modelling at High Rates of Strain," in: Institute of Physics Conference Series, No. 102, pp. 283-298.

Klepaczko, J.R., 1990, "On Modeling of Structural Evolution in Metals at Different Strain Rates and Temperatures," in: Inelastic Solids and Structures, eds. Kleiber, M and Konig, J., pp. 179-196.

Klepaczko, J.R., 1990, "Short and Long Transients in Dynamic Plasticity of Metals, Modeling and Experimental Facts," in: Dynamic Plasticity of Metals, pp. 147-159.

Klepaczko, J.R., 1993, "rate Sensitivity of Copper at Large Strains and High Strain Rates," in: Large Plastic Deformations: Fundamental Aspects and Applications to Metal Forming, eds. Teodosiu, C., Raphenel, J.L., and Sidoroff, F., pp. 309-314.

Klepaczko, J.R., Sasaki, T., and Kurokawa, T., 1993, "On Rate Sensitivity of Polycrystalline Aluminum at High Strain rates," Transactions of Japan Society of Aerospace Science, Vol. 36, pp. 170-187.

Kocks, U. F., 1965, "A Statistical Theory of Flow Stress and Work-hardening," pp. 541-566.

Kocks, U.F., 1976, "Laws for Work-Hardening and Low-Temperature Creep," Journal of Engineering Materials and Technology, pp. 76-85.

Kocks, U.F. and Mecking, H., 1980, "Dislocation Kinetics at Not-So-Constant Structure," in: Dislocation Modelling of Physical Systems, eds. Ashby, M.F. et al, Pergamon, New York, pp. 173-192.

Kocks, U.F., 1982, "Strain Hardening and Strain-Rate Hardening," in: Mechanical Testing for Deformation Model Development, ASTM STP 765, eds. R.W. Rohde and J.C. Swearingen, American Society for Testing and Materials, pp.121-138.

Kocks, U.F., 1987, "Constitutive Behavior Based on Crystal Plasticity," in: Unified Constitutive Equations for Creep and Plasticity, ed. A.K. Miller, Elsevier Applied Science, Chapter 1.

Kolsky, H., 1949, "An Investigation of the Mechanical Properties of Materials at Very High Rates of Loading," Proceedings of the Royal Society of London, Vol. B62, pp. 676-700.

Kolsky, H., 1970, "Recent Experimental Studies of the Mechanical Response of Inelastic Solids to Rapidly Changing Stresses," in *Inelastic Behavior of Solids*, eds. Kanninen, M.F. et. Al., McGraw-Hill, New York, pp. 19-43.

Kreml, E., 1975, "On the Interaction of Rate and History Dependence in Structural Metals," *Acta Mechanica*, Vol. 22, pp. 53-90.

Kwon, O. and DeArdo, A.J., 1990, "On the Recovery and Recrystallization which Attend Static Softening in Hot-Deformed Copper and Aluminum," *Acta Metallurgica*, Vol. 38, pp. 41-54.

Lamba, H.S. and Sidebottom, O.M., 1978, "Cyclic Plasticity for Non-proportional Paths: Part 1 - Cyclic Hardening, Erasure of Memory, and Subsequent Strain Hardening Experiments," *Journal of Engineering Materials and Technology*, Vol. 100, pp. 96-103.

Lamba, H.S. and Sidebottom, O.M., 1978, "Cyclic Plasticity for Non-proportional Paths: Part 2 - Comparison with Predictions of Three Incremental Plasticity Models," *Journal of Engineering Materials and Technology*, Vol. 100, pp. 104-111.

Lassila, D.H. and LeBlanc, M., "High-Strain-Rate Deformation Behavior of Shocked Copper," in: Shock-Wave and High-Strain-Rate Phenomena in Materials, eds. Meyers, M.A., Murr, L.E., and Staudhammer, K.P., pp.587-595.

Lassila, D.H., LeBlanc, M.M. and Magness, F.H., 1994, "The Effect of Grain Size on Deformation and Failure of Copper Under Dynamic Loading," *Journal de Physique IV*, Vol. C8, pp. 195-199.

Lathrop, J.F., 1996, "BFIT - A Program to Analyze and Fit the BCJ Model Parameters to Experimental Data", SAND97-8218.

Lee, D. and Zaverl, F., 1978, "A Generalized Strain Rate Dependent Constitutive Equation for Anisotropic Metals," *Acta Metallurgica*, Vol. 26, pp. 1771-1780.

Lee, D. and Zaverl, F., 1979, "A Description of History Dependent Plastic Flow Behavior of Anisotropic Metals," *Journal of Engineering Materials and Technology*, Vol. 101, pp. 59-67.

Lemaitre, J. and Chaboche, J.L., 1985, Mechanics of Solid Materials, Dunod Publ., Paris.

Leroy, M., Raad, M.K., Nkule, L., and Cheron, R., 1984, "Influence of Instantaneous Dynamic Decremental/Incremental Strain Rate Tests on the Mechanical Behavior of Metals - Application to High-Purity Polycrystalline Aluminum," in Mechanical Properties at High Rates of Strain, Conference Series Number 70, pp. 31-38, The Institute of Physics, London.

Lindholm, U.S., 1964, "Some Experiments with the Split Hopkinson Pressure Bar," *Journal of the Mechanics and Physics of Solids*, Vol. 12, pp. 317-335.

Lindholm, U.S. and Yeakley, L.M., 1965, "Dynamic Deformation of Single and Polycrystalline Aluminum," *Journal of the Mechanics and Physics of Solids*, Vol. 13, pp. 41-53.

Lindholm, U.S., 1968, "Some Experiments in Dynamic Plasticity Under Combined Stress," in: Mechanical Behavior of Materials Under Dynamic Loads, Symposium San Antonio, TX, ed. Lindholm, U.S Springer-verlag, New York, pp. 77-95.

Lindholm, U.S., 1974, "Review of Dynamic Testing Techniques and Material Behaviour," in: Institute of Physics Conference Series, No 21, ed. Harding, J., pp.3-21.

Lindholm, U.S., 1977, "Deformation Maps in the Region of High Dislocation Velocity," in: High Velocity Deformation of Solids, Symposium, Tokyo, eds. Kawata, K. And Shioiri, J. Springer-Verlag, New York, pp. 26-35.

Lindholm, U.S., Nagy, A., Johnson, G.R. and Hoegfeldt, J.M., 1980, "Large Strain, High Strain Rate Testing of Copper," *Journal of Engineering Materials and Technology*, pp. 376-381.

Lindholm, U.S., 1990, "Experimental Basis for Temperature-Dependent Viscoplastic Constitutive Equations," *Applied Mechanics Reviews*, Vol. 43, No. 5, Part 2, eds. Krempl E., and McDowell, D. L., pp. S338-S344.

Lindholm, U.S., Chan, K.S. and Thacker, B.H., 1993, "On Determining Material Constants for Unified Thermo-Visco-Plastic Constitutive Equations," *Material Parameter Estimation for Modern Constitutive Equations*, Vol. 43, pp. 183-193.

Lindley, T.C., 1965, "The Effect of a Pre-Strain on the Low Temperature Mechanical Properties of a Low carbon Steel," *Acta Metallurgica*, Vol. 13, pp. 681-689.

Lipkin, J, Campbell, J.D., and Swearengen, J.C., 1978, "The Effects of Strain-Rate Variations on the Flow Stress of OFHC Copper," *Journal of the Mechanics and Physics of Solids*, Vol. 26, pp. 251-268.

Lowe, T.C. and Miller, A.K., 1984, "Improved Constitutive Equations for Modeling Strain Softening-Part I: Conceptual Development," *Journal of Engineering Materials and Technology*, Vol. 106, pp. 103-342.

Lowe, T.C. and Miller, A.K., 1984, "Improved Constitutive Equations for Modeling Strain Softening-Part II: Predictions for Aluminum," *Journal of Engineering Materials and Technology*, Vol. 106, pp. 343-348.

Lowe, T.C. and Miller, A.K., 1986, "Modeling Internal Stresses in the Nonelastic Deformation of Metals," *Journal of Engineering Materials and Technology*, Vol. 108, pp. 365-373.

Ludwick, P., 1909, Elemente der Technologischen Mechanik, Springer-Verlag, Berlin.

Lustig, S.K., 1995, "Microstructural Analysis of Finite Deformation in FCC Polycrystals," Ph.D Thesis, Georgia Institute of Technology.

Marsh, K.J. and Campbell, J.D., 1963, "The Effect of Strain Rate on the Post-Yield Flow of Mild Steel," *Journal of the Mechanics and Physics of Solids*, Vol. 11, pp. 49-63.

Mason, J.J., Rosakis, A.J., and Ravichandran, G., 1994, "On the Strain and Strain Rate Dependence of the Fraction of Plastic Work Converted to Heat: An Experimental Study Using High Speed Infrared Detectors and the Kolsky Bar," *Mechanics of Materials*, Vol. 17, pp. 135-145.

Mayer, G., 1992, "New Directions in Research on Dynamic Deformation of Materials," in: Shock-Wave and High-Strain-Rate Phenomena in Materials, eds. Meyers, M.A., Murr, L.E. and Staudhanner, K.P., Marcel Dekker, New York, pp. 35-48.

McDowell, D.L., and Voorhees, P.W., 1995, "Status of Constitutive Laws and Hydrocodes for Deformation and Damage of Structures Subjected to Impacts and Blasts," Institute for Defense Analyses, Defense Science Studies Group report, Alexandria VA.

McDowell, D.L., 1992, "A Nonlinear Kinematic Hardening Theory for Cyclic Thermoplasticity and Thermoviscoplasticity," *International Journal of Plasticity*, Vol. 8, pp. 695-728.

McQueen, H.J. and Hockett, J.E., 1970, "Microstructures of Aluminum Compressed at Various Rates and Temperatures," *Metallurgical Transactions*, Vol. 1, pp. 2997-3004.

McQueen, H.J. and Jonas, J.J., 1975, "Recovery and Recrystallization During High Temperature Deformation," in; Treatise on materials Science and Technology, ed. Arsenault, R.J., pp.393-493

McQueen, H.J. and Jonas, J.J., 1984, "Recent Advances in Hot Working: Fundamental Dynamic Softening Mechanisms," *Journal of Applied Metal Working*, Vol. 3, No. 3, pp. 233-241.

McQueen, H.J. and Vazquez, L., 1986, "Static Recovery of Copper During Annealing and Stress Relaxation Following Hot Deformation," *Materials Science and Engineering*, Vol. 81, pp. 355-369.

Mecking, H. And Lucke, K., 1970, "A New Aspect of the Theory of Flow Stress of Metals," *Scripta Metallurgica*, Vol. 34, pp. 427-432.

Mecking, H. 1980, "Strain Hardening and Dynamic Recovery," in: Dislocation Modelling of Physical Systems, eds. Ashby, M.F. et al, Pergamon Press, New York, pp. 197-211.

Mecking, H. and Kocks, U.F., 1981, "Kinetics of Flow and Strain-Hardening," *Acta Metallurgica*, Vol. 29, pp. 1865-1875.

Mecking, H., Kocks, U.F., and Hartig, C., 1996, "Taylor factors in Materials with Many Deformation Modes," *Scripta Materialia*, Vol. 35, pp. 465-471.

Messa, K., 1991, "Fitting Multivariate Functions to Data Using Genetic Algorithms," in: WNN-AIND 91, NASA, pp. 677-686.

Meyers, M.A., Chen, Y.J., Marquis, F.D.S. and Kim, D.S., 1995, "High-Strain, High-Strain-Rate Behavior of Tantalum," *Metallurgical and Materials Transactions A*, Vol. 26A, pp. 2493-2501.

Meyers, M.A., 1994, Dynamic Behavior of Materials, Wiley, New York.

Meyers, M.A., Andrade, U.R., and Chokshi, A.H., 1995, "The Effect of Grain Size on the High-Strain, High-Strain-Rate Behavior of Copper," *Metallurgica and Materials Transactions*, Vol. 26, pp. 2881-2893.

Miller, A., 1976, "An Inelastic Constitutive Model for Monotonic, Cyclic, and Creep Deformation: Part I - Equations Development and Analytical Procedures," *Journal of Engineering Materials and Technology*, Vol. 98, pp.97-105.

Miller, A., 1976, "An Inelastic Constitutive Model for Monotonic, Cyclic, and Creep Deformation: Part II - Applications to Type 304 Stainless Steel," *Journal of Engineering Materials and Technology*, Vol. 98, pp.106-113.

Miller, M.P., 1993, "Improved Constitutive Laws for Finite Strain Inelastic Deformation," Ph.D. Thesis, Georgia Institute of Technology.

Mukherjee, A., Schmauder, S. and Ruhle, M., 1995, "Artificial Neural Networks for the Prediction of Mechanical Behavior of Metal matrix Composites," *Acta Metallurgica Mater.*, Vol. 43, pp. 4083-4091.

Neu, R.W., "Nonisothermal Material Parameters for the Bodner-Partom Model," in: Material Parameter Estimation for Modern Constitutive Equations, Vol. 168, pp. 211-226.

Nicholas, T. and Whitmire, J.N., 1970, "The Effects of Strain-Rate and Strain-Rate History on the Mechanical Properties of Several Metals," AFML-TR-70-218.

Nicholas, T., 1971, "Strain-Rate and Strain-Rate-History Effects in Several Metals in Torsion," *Experimental Mechanics*, pp. 370-374.

Nicholas, T., 1973, "An Analysis of the Split Hopkinson Bar Technique for Strain-Rate-Dependent Material Behavior," *Journal of Applied Mechanics*, Vol. 40, pp. 277-282.

Pao, Y.H. and Gilat, A., 1989, "Modeling 1100-0 Aluminum Over a Wide range of Temperatures and Strain Rates," *International Journal of Plasticity*, Vol. 5, pp. 183-196.

Perzyna, P., 1962, "The Constitutive Equations for Rate Sensitive Plastic Materials," Vol. XX, No. 4, pp. 321-332.

Perzyna, P., 1968, "On Thermodynamic Foundations of Viscoplasticity," in: Mechanical Behavior of Materials Under Dynamic Loads, ed. Lindholm, U.S., Springer-Verlag, New York, pp. 61-76.

Perzyna, P., 1974, "The Constitutive Equations Describing Thermomechanical Behavior of Materials at High Rates of Strain," in: Institute of Physics Conference Series, No. 21, ed. Harding, J., pp. 138-153.

Polak, J., Obrtlík, K., and Vasek, A., 1992, "Cyclic Stress - Strain Response of Polycrystalline Copper in a Wide Range of Plastic Strain Amplitudes," *Materials Science and Engineering*, Vol. 151, pp. 19-27.

Ponter, A.R.S. and Leckie, F.A., 1976, "Constitutive Relationships for the Time-Dependent deformation of Metals," *Journal of Engineering Materials and Technology*, Vol. 98, pp. 47-51.

Regazzoni, G., Kocks, U.F. and Follansbee, P.S., 1987, "Dislocation Kinetics at High Strain Rates," *Acta Metallurgica et Materialia*, Vol. 35, No. 12, pp. 2865-2875.

Rice, J.R., 1971, "Inelastic Constitutive Relations for Solids: An Internal-Variable Theory and Its Application to Metal Plasticity," *Journal of the Mechanics and Physics of Solids*, Vol. 19, pp. 433-455.

Rosen, A. and Bodner, S.R., 1967, "The Influence of Strain Rate and Strain Aging on the Flow Stress of Commercially-Pure Aluminum," *Journal of the Mechanics and Physics of Solids*, Vol. 15, pp. 47-62.

Ruggles, M.B. and Krempl, E., 1991, "Rate-Sensitivity and Short Term Relaxation Behavior of AISI Type 304 Stainless Steel at Room Temperature and at 650 °C; Influence of Prior Aging," DE89 007823 and *Journal of Pressure Vessel Technology*, Vol. 113, pp. 385-391.

Ryan, N. D. and McQueen H. J., 1986, "Dynamic Recovery and Strain Hardening in the Hot Deformation of Type 317 Stainless Steel," *Materials Science and Engineering*, Vol. 81, pp. 259-272.

Saimoto, S., Diak, B.J., and Carlone, M., 1993, "The Evaluation of Strain Path and Strain Rate History on Strain Rate Sensitivity," in: Light Materials for Transportation Systems, ed.. Kim, N.J., pp. 937-942.

Sakai, T. and Jonas, J.J., 1984, "Dynamic Recrystallization: Mechanical and Microstructural Considerations," *Acta Metallurgica*, Vol. 32, pp. 189-209.

Sakino, K. and Shioiri, J., 1991, "Dynamic Flow Stress Response of Aluminum to Sudden Reduction in Strain Rate at Very High Strain Rates," *Journal de Physique IV*, Vol. C3, pp. 35-42.

Sakino, K. and Shioiri, J., 1996, "Effect of Steep reduction in Strain Rate on the Dynamic Flow Stress of Copper at Very High Strain Rates," *JSME International Journal*, Vol. 39, pp. 135-141.

Samanta, S.K., 1971, "Dynamic Deformation of Aluminium and Copper at Elevated Temperatures," *Journal of Mechanics and Physics of Solids*, Vol. 19, pp. 117-135.

Sample, V.M., Jaworski, A.P., and Field D.P., 1993, "A Comparison of Parameter Evaluation Procedures for a Two-Internal State Variable Constitutive Model," in: Material Parameter Estimation for Modern Constitutive Equations, eds. Bertram, L. A., Brown, S. B., Freed, A. D., ASME, New York, Vol. 43, pp. 227-242..

Schooling, J.M., Brown, M. and Reed, P.A.S., 1997, "Neurofuzzy Modelling of Fatigue Threshold Behavior in Ni-Base Superalloys," in Engineering Against Fatigue.

Schooling, J.M. and Reed, P.A.S., 1996, "The Application of Neural Computing Methods to the Modelling of Fracture in N-Base Superalloys," in: Superalloys 1996, eds. Kissinger, R.D. et al, The Minerals, Metals, & Materials Society, pp. 409-416.

Senseny, P.E., 1977, "The Effect of Strain Rate and Strain Rate History on the Flow Stress of Four Close-Packed Metals Deformed in Torsion Over a Range of Temperatures," Ph.D. Thesis, Brown University.

Senseny, P.E., Duffy, J. and Hawley, R.H., 1978, "Experiments on Strain Rate History and Temperature Effects During the Plastic Deformation of Close-packed Metals," Journal of Applied Mechanics, Vol. 45, pp. 60-66.

Senseny, P.E. and Fossum, A.F., 1993, "Parameter Evaluation for a Viscoplastic Constitutive Model," Material Parameter Estimation for Modern Constitutive Equations, Vol. 43, pp. 243-257.

Shen, W.Q., 1994, "A Temperature-Dependent Constitutive Equation for Strain-Rate Sensitive Material," Mechanical Structures and Machines, Vol. 22, pp. 457-472.

Sherwood, J.A. and Doore, R.J., 1993, "A Robust Methodology for Estimation material Parameters for the Ramaswamy - Stouffer Constitutive Model," in: Material Parameter Estimation for Modern Constitutive Equations, Vol. 168, pp. 259-273.

Shihui, H. and Clifton, R.J., 1985, "Dynamic Plastic Response of OFHC Copper at High Shear Strain Rates," in: Macro-and Micro-Mechanics of High Velocity deformation and Fracture, Symposium Tokyo, Japan, eds. Kawata, K. and Shiori, J., Springer-Verlag, New York, pp. 63-74.

Shindo, A. and Mimura, K., 1988, "The Experimental Investigation into the Strain Rate and History Dependency of Metals," in: 32nd Japan Congress on Material Research, pp. 45-51.

Shiori, J., Satoh, K. and Nishimura, K., 1977, "Experimental Studies on the Behavior of Dislocations in Copper at High Rates of Strain," High Velocity Deformation of Solids, Symposium Tokyo Japan, eds. Kawata, K. and Shioiri, J., Springer-Verlag, New York, pp. 50-66.

Shiori, J., Sakino, K. and Satoh, K., 1985, "A Constitutive Equation of f.c.c. Metals at High Strain Rates Based upon the Ultrasonic Study of Dislocation Motion," in Macro- and Micro-Mechanics of High Velocity Deformation and Fracture, Symposium Tokyo Japan, eds. Kawata, K. and Shioiri, J., Springer-Verlag, New York.

Shioiri, J., Sakino, K., and Santoh, T., 1994, "Two Strain Rate Change Tests for Derivation of Constitutive Relationships of Metals at Very High rates of Strain," Journal de Physique IV, Vol. C8, pp. 489-494.

Shoemaker, P.A., Carlin, M.J., Shimabukuro, R.L. and Priebe, C.E., 1991, "Least-Squares Learning and Approximation of Posterior Probabilities on Classification Problems by Neural Network Models," in: WNN-AIND 91, NASA, pp. 187-196.

Smith, R.C., 1961, "Studies of Effect of Dynamic Preloads on Mechanical Properties of Steel," Experimental Mechanics, pp. 153-159.

Somolinos, A.S., 1992, "Using Functional Link Neural Nets for General Linear Least Squares Model Fitting," in WNN 92, NASA, pp.113-117.

Stelly, M. and Dornmeval, R., 1974, "Some Results on the Dynamic Deformation of Copper," in: High Velocity Deformation of Solids, Symposium, Tokyo, Japan, eds. Kawata, K. and Shioiri, J., Springer-Verlag, New York.

Stout, M.G., Martin, P.L., Helling, D.E., and Canova, G.R., 1985, "Multi-axial Yield Behavior of 1100 Aluminum Following Various Magnitudes of Pre-strain," International Journal of Plasticity, Vol. 1, pp. 163-174.

Sylwestrowicz, W.D., 1958, "The Temperature Dependence of the Yield Stress of Copper and Aluminum," Transactions of the Metallurgical Society of AIME, pp. 617-624.

Takeshita, T., Kocks, U.F., and Wenk, H.-R., 1989, "Strain Path Dependence of Texture Development in Aluminum," Acta Metallurgica, Vol. 37, pp. 2595-2611.

Tanimura, S. and Duffy, J., 1984, "Strain Rate Effects and Temperature History Effects for Three Different Tempers of 4340 VAR Steel," DTIC: AD-A146 372 and International Journal of Plasticity, Vol. 2, pp. 21-35.

- Tanimura, S. and Ishikawa, K., 1991, "A Constitutive Equation Describing Strain Hardening, Strain Rate Sensitivity, Temperature Dependence and Strain Rate History Effect," in: Anisotropy and Localization of Plastic Deformation, eds. Boehler, J.-P. and Khan, A.S., pp. 417-420.
- Tasplin, D.M.R., Pandey, M.C. and Tang, N.Y., 1983, "Ashby Maps," in: Micromechanisms of Plasticity and Fracture, eds. Lewis, M.H. and Taplin, D.M.R. Waterloo, Ontario, Canada, pp. 225-260.
- Tegart, W.J.McG., 1993, "Dynamic Recrystallization - An Historical Perspective," Materials Science Forum, Vols. 113-115, pp. 1-18.
- Theocaris, P.S. and Panagiotopoulos, P.D., 1995, "Plasticity Including the Bauschinger Effect, Studied by a Neural Network Approach," Acta Mechanica, Vol. 113, pp. 63-75.
- Tong, W., 1991, "Pressure-Shear Impact Investigation of Strain-Rate History Effects in OFHC Copper," Ph.D. Thesis, Brown University.
- Tong, W. and Clifton, R.J., 1992, "Pressure-Shear Impact Investigation of Strain Rate History Effects in OFHC Copper," Journal of the Mechanics and Physics of Solids, Vol. 40, pp. 1251-1294.
- Ungar, T., Toth, L.S., Illy, J., and Kovacs, I., 1986, 'Dislocation Structure and Work Hardening in Polycrystalline OFHC Copper Rods Deformed by Torsion and Tension,' Acta Metallurgica, Vol. 34, pp. 1257-1267.
- Valanis, K.C., 1974, "Effect of Prior Deformation on Cyclic Response of Metals," Journal of Applied Mechanics, pp. 441-447.
- Valanis, K.C. and Wu, H.C., 1976, "Strain Rate and History Effects on the Deformation of Metals," DTIC: AD-A035 635.
- Venkadesan, S., Rodriguez, P., Padmanabhan, K.A., Sivaprasad, P.V., and Phaniraj, C., 1992, "Flow Transients During Strain Rate Jump Tests in a Titanium-Modified Austenitic Stainless Steel," Materials Science and Engineering, Vol. A154, pp. 69-74.
- Wang, M.L.R. and Han, M.-B., 1993, "A Kolsky Bar: Tension, Tension-Tension," Experimental Mechanics, pp. 7-14.
- Wilson, M.L., Duffy, J. and Hawley, R.H., 1979, "Strain rate and Strain Rate History Effects in Two Mild Steels," DTIC: AD-A067 204.

Wrobel, M., Dymek, S., and Blicharski, M., 1996, "The Effect of Strain Path on Microstructure and Texture Development in Copper Single Crystals with (110)[001] and (110)[110] Initial Orientations," *Scripta Materialia*, Vol. 35, pp. 417-422.

Wu, H.C. and Yip, M.C., 1980, "Strain rate and Strain Rate History Effects on the Dynamic Behavior of Metallic Materials," *International Journal of Solids and Structures*, Vol. 16, pp. 515-536.

Yip, M.-C., 1979, "The Effects of Strain Rate and Strain History on the Dynamic Behavior of Metallic Materials," Ph.D. Thesis, The University of Iowa.

Young, S.H. and Kwon, Y.W., 1996, "An Optimization Technique Using the Finite Element Method and Orthogonal Arrays," *Recent Advances in Solids/Structures*, Vol. 72, pp. 75-80.

Zandrahimi, M., Platias, S., Price, D., Barrett, D., Bate, P.S., Roberts, W.T., and Wilson, D.V., 1989, "Effects of Changes in Strain Path on Work Hardening in Cubic Metals," *Metallurgical Transactions A*, Vol. 20, pp. 2471-2482.

Zener, C. and Hollomon, J.H., 1943, "Effect of Strain rate Upon Plastic Flow of Steel," *Journal of Physics*, Vol. 15, pp. 22-32.

VITA

Albert Buck Tanner was born in Riverside, California, on September 15, 1955. He graduated from Perris Valley High School, Perris California in 1973. Buck enlisted in the Army in 1973 and graduated from United States Military Academy, West Point, New York in 1979 with a Bachelor of Science Degree. He later earned his masters degree in Mechanical Engineering from Massachusetts Institute of Technology in 1986. He has served in the Army for twenty-five years and was sponsored by the Army for his doctoral research.

Buck was married to the former Lisa G. Lucero in Denver, Colorado, on December 19, 1981, and has five children. Buck is currently a Lieutenant Colonel in the U.S. Army and will be stationed at the United States Army Research Laboratory at Aberdeen Proving Grounds, Maryland with assignment as the Senior Materials Scientist in the Weapons and Materials Research Directorate.